Using the Singularity Frequencies of Guided Waves to Obtain a Pipe's Properties and Detect and Size Notches

by

Darryl Keith Stoyko, B.Sc.(M.E.), M.Sc.(M.E.), EIT

A thesis submitted to
The Faculty of Graduate Studies of
The University of Manitoba
in partial fulfilment of the requirements for the degree of
Doctor of Philosophy

Department of Mechanical and Manufacturing Engineering
University of Manitoba
Winnipeg, Manitoba, Canada

Abstract

A survey of relevant literature on the topic of wave propagation and scattering in pipes is given first. This review is followed by a theoretical framework which is pertinent to wave propagation in homogeneous, isotropic, pipes. Emphasis is placed on approximate solutions stemming from a computer based, Semi-Analytical Finite Element (SAFE) formulation. A modal analysis of the dynamic response of homogeneous, isotropic pipes, when subjected to a transient ultrasonic excitation, demonstrates that dominant features, i.e., singularities in an unblemished pipe's displacement Frequency Response Function (FRF) coincide with its cutoff frequencies. This behaviour is confirmed experimentally. A novel technique is developed to deduce such a pipe's wall thickness and elastic properties from three cutoff frequencies. The resulting procedure is simulated numerically and verified experimentally. Agreement between the new ultrasonic procedure and traditional destructive tests is within experimental uncertainty. Then a hybrid-SAFE technique is used to simulate waves scattered by various open rectangular notches. The simulations show, for the first time, that singularities distinct from the unblemished pipe's cutoff frequencies arise in a displacement FRF when an axisymmetric notch is introduced. They also suggest that the new singularities depend on the properties of the parent pipe *and* the finite element region but effects are local to a notch. It is demonstrated further that the difference between the frequency at which a singularity introduced by a notch occurs and the nearest corresponding unblemished pipe's cutoff frequency is a function of the notch's dimensions. By plotting contours of constant frequency differences, it is shown that it is *usually* possible to characterize the notch's dimensions by using two modes. However, the frequency difference for a third mode may be also needed occasionally. The more general case of nonaxisymmetric notches is shown to be a straightforward extension of the axisymmetric case.

ACKNOWLEDGEMENTS

I wish to express my gratitude to my principal advisor Dr. N. Popplewell and co-advisor Dr. A. H. Shah, for their guidance, encouragement, and support. I wish to thank my examining committee, Drs. S. Balakrishnan and D. McNeill, for their continued advice throughout the degree. I would like to thank also Dr. J. Rose for acting as the external thesis examiner. The thoughtful and useful comments he provided during the review process helped to noticeably improve the final dissertation. The tangible assistance from my parents, Mr. Vance Stoyko and Mrs. Gail Stoyko, is acknowledged gratefully. Assistance, in various forms, from Messrs. K. Adeogun, R. Forzley, L. He, P. Lacoursiere, A. Komus, I. Penner, D. Rossong, and K. Tarte is recognized. The advice and encouragement that Dr. S. Datta provided was invaluable. The advice and contributions of Dr. H. Bai are acknowledged also. I wish to thank Dr. M. Singh for the assistance, advice, and encouragement that she provided. Moreover, the generosity of Mr. R. Thom and Stress Engineering Services Canada in permitting me the time to attend the 39th Annual Review of Progress in Quantitative Nondestructive Evaluation and revise this dissertation is acknowledged gratefully. The support of my family and friends, who are too numerous to mention by name, was essential. I found the previous work of Drs. H. Bai, A. Mahmoud, N. Rattanawangcharoen, and W. Zhuang most useful. I wish to thank further Drs. Popplewell and Shah for providing financial support from their Natural Science and Engineering Research Council (NSERC) of Canada grants. Financial aid from the Society of Automotive Engineers (SAE) International, the University of Manitoba, the Province of Manitoba, Ms. A. Toporeck and family, and the University of Manitoba Students' Union (UMSU) is recognized. Moreover, I would like to thank the Department of Mechanical and Manufacturing Engineering of the University of Manitoba for providing financial support and experience that came in the form of many teaching assistantships. The generous donation of goods in kind from the Wawanesa Mutual Insurance Company is acknowledged.

Darryl K. Stoyko
July 2012

Table of Contents

List of Tables

List of Figures

CODE LISTINGS

List of Nomenclature

Roman Letters

$\mathbf{0}$	Null matrix
$\mathbf{A}$	Vector containing the scattered wave amplitudes, nondimensional
$\mathbf{A}$	Coefficient matrix resulting from linearising the quadratic eigenvalue problem, units vary according to its sub-matrices
A	A modal amplitude, in (m)
A	Amplitude of Gaussian modulated sine wave, $\text{lb}_\text{f}/\text{in}^3$ (N m^{-3})
A	Amplitude of free vibrations of an undamped single degree of freedom oscillator, in (m)
A	Constant of integration, in^2 (m^2)
$A_{n_{\text{scat}}m_{\text{scat}}}$	Indicates the scattered amplitude of the m^{th} mode for the n^{th} circumferential wavenumber, nondimensional
a	A constant controlling the decay rate in the inputted, Gaussian modulated sine wave, s^{-2}
$\mathbf{B}$	Strain transformation matrix of a three-dimensional finite element volume, in^{-1} (m^{-1})
$\mathbf{B}$	Coefficient matrix resulting from linearising the quadratic eigenvalue problem, units vary according to its sub-matrices
$\mathbf{B}$	A vector potential, in^2/s^2 (m^2 s^{-2})
$\mathbf{B}_n$	Strain transformation matrix for the n^{th} circumferential wavenumber of an axisymmetric finite element volume, in^{-1} (m^{-1})
$\mathbf{B}_i$	Strain transformation matrices from the SAFE formulation, in^{-1} (m^{-1}) for $i = 1, 2$, and dimensionless for $i = 3$
B	Constant of integration, in^2 (m^2)
B_{nm}	"Scaling" factor resulting as a result of applying the bi-orthogonality relations from the linearised eigenvalue problem, lb_f in^2 (N m^2)
B^+	Denotes the $z = 0$ plane which is common to a finite element volume and the R^+ wave function expansion region
B^-	Denotes the plane of symmetry, $z = -l/2$, of an axisymmetric finite element volume
$\mathbf{C}$	A 3×6 matrix containing Hankel functions from the Helmholtz decomposition of the displacement field, in^{-1} (m^{-1})
c	Circumferential extent of a defect, degrees (rad)
c_1	Dilatational wave speed, in/s (m s^{-1})
c_2	Shear wave speed, in/s (m s^{-1})
$\mathbf{D}$	Symmetric matrix composed of the isotropic elastic moduli, psi (Pa)
$\mathbf{D}$	A 6×6 matrix containing Hankel functions from the Helmholtz decomposition of the strain field, in^{-2} (m^{-2})
D_o	Pipe's outer diameter, in (m)
d	Uniform depth of a notch in a pipe's radial direction in (m)
$\mathbf{E}$	A 6×6 matrix containing Hankel functions from the Helmholtz decomposition of the stress field, $\text{slug}/\text{in}^3/\text{s}^2$ (kg m^{-3} s^{-2})
E	Young's modulus, psi (Pa)

$\mathcal{E}$	Time averaged work done per period, in $-$ $\text{lb}_\text{f}/\text{s}$ (W)
$\mathcal{E}$	An arbitrary matrix element
$\hat{\mathbf{e}}$	Unit vector whose direction is indicated by a subscript
$\overline{\delta\mathcal{E}}_{\text{virt}}$	Virtual work, in $-$ lb_f (J)
$\mathbf{F}$	Force vector used to simplify the system of linear equations from the axisymmetric hybrid-SAFE formulation, lb_f (N)
$\mathbf{F}$	Consistent force vector from applying finite element methodology, lb_f (N)
$\mathbf{F}$	Consistent force vector from applying SAFE methodology, $\text{lb}_\text{f}/\text{in}$ (N m^{-1})
$\mathbf{F}_0$	Vector describing the radial distribution of an externally applied, point force, lb_f (N)
$\mathbf{F}_i$	Force vectors for $i = 1, 2$ used to simplify the system of linear equations resulting from the axisymmetric hybrid-SAFE formulation, lb_f (N)
$\mathbf{F}_{si}$	$\mathbf{F}_{s2}$ ($\mathbf{F}_{s1}$) is a matrix that "maps" a vector of scattered wave amplitudes into the first N_1 (last N_2) consistent nodal forces on the $B+$ boundary of the axisymmetric finite element region, lb_f (N)
F	Indicates a flexural mode
F	An arbitrary function, in (m)
$\mathbf{f}$	A consistent nodal force vector, lb_f (N)
$\mathbf{f}$	Body force, in/s^2 (m s^{-2})
f	Frequency, Hz
f	A component of a nodal force, lb_f (N)
f	A scalar potential, in^2/s^2 ($\text{m}^2\ \text{s}^{-2}$)
$\mathbf{G}$	Matrix containing the mode shapes of a scattered wave field, in (m)
G	Shear modulus, psi (Pa)
g	A scalar function, in^2 (m^2)
$\mathbf{H}$	Equivolume vector potential, $\mathbf{H} = (H_r, H_\theta, H_z)$, in^2 (m^2)
H	Frequency response function for the displacement of an externally excited, undamped single degree of freedom oscillator, $\text{in}/\text{lb}_\text{f}$ (m N^{-1})
H	Pipe's wall thickness, in (m)
$\mathbf{I}$	Identity matrix
I	Total number of data points assumed for the "free vibration" portion of a time history
$\mathcal{I}, \mathcal{I}'$	Arbitrary integrands
$\mathbf{J}$	Jacobian matrix
J	The number of modes assumed to contribute to a pipe's radial displacement
j	Complex unit, $\text{j} = \sqrt{-1}$
$\mathbf{K}_i$	Stiffness matrix resulting from applying the SAFE methodology, $\text{lb}_\text{f}/\text{in}^2$ (N m^{-2}) for $i = 1, 2,$ and 4, $\text{lb}_\text{f}/\text{in}$ (N m^{-1}) for $i = 3$ and 5, and lb_f (N) for $i = 6$
$\mathbf{K}_\text{I}$	Assembled stiffness matrix of finite element region, $\text{lb}_\text{f}/\text{in}$ (N/m)
$\mathbf{K}_i$	Matrices, $i = 1, 2, 3$, resulting from factoring the axisymmetric finite element's global stiffness matrix, $\text{lb}_\text{f}/\text{in}$ (N/m)
k	Axial wavenumber, in^{-1} (m^{-1})
k	Stiffness of an undamped, single degree of freedom oscillator, $\text{lb}_\text{f}/\text{in}$ (N/m)
L	Indicates a longitudinal mode
l	Length of a notch in a pipe's axial direction, in (m)

$\mathbf{M}$	Mass matrix resulting from applying SAFE methodology, slug/in (kg m^{-1})
$\mathbf{M}_{\mathrm{I}}$	Assembled mass matrix of finite element region, slug (kg)
M	A "place-holder" to indicate a mode type of one of T, L, of F
m	Positive integer indicating the m^{th} axial mode
m	Mass of an undamped, single degree of freedom oscillator, slug (kg)
$\mathbf{N}$	The assembled shape functions over an entire finite element volume
N	Number of "worker" nodes, dimensionless
N	Number of quadratic, one dimensional finite elements that discretize the pipe's thickness
$\boldsymbol{\mathcal{N}}$	A matrix containing the assembled shape functions, $\mathbf{N}$, over an entire finite element region
$\mathbf{n}$	Interpolation functions in a typical finite element
n	Circumferential wavenumber
n_{b}	Interpolation function associated with "back" (inner) nodal surface
n_{f}	Interpolation function associated with "front" (outer) nodal surface
n_{m}	Interpolation function associated with middle nodal surface
$\mathbf{P}$	Assembled vector of nodal forces, lb$_{\mathrm{f}}$ (N)
$\mathbf{P}$	A radial point force, lb$_{\mathrm{f}}$ (N)
$\mathbf{P}$	A 6×6 matrix containing Hankel functions from the Helmholtz decomposition of the stress field, slug/in^3/s^2 (kg m^{-3} s^{-2})
$\mathbf{P}_n$	Known vector of the linearised eigenvalue problem, units vary according to its sub-vectors
$\mathcal{P}$	Instantaneous power, in – lb$_{\mathrm{f}}$/s (W)
$\mathbf{p}$	External body force, lb$_{\mathrm{f}}$/in^3 (N m^{-3})
$p(t)$	Function describing the temporal variation of the input force, nondimensional
$p(t)$	Excitation force applied to an undamped, single degree of freedom oscillator, lb$_{\mathrm{f}}$ (N)
$\overline{p}(\omega)$	Fourier transform of the function, $p(t)$, describing the temporal variation of the input force, Hz^{-1} (s)
$\overline{p}(\omega)$	Fourier transform of the excitation force applied to an undamped, single degree of freedom oscillator, lb$_{\mathrm{f}}$/Hz (N Hz^{-1})
$\mathbf{Q}_n$	Solution vector of the linearised eigenvalue problem, units vary according to its sub-vectors
Q	Ratio of cutoff frequencies, dimensionless
$\mathbf{q}$	Assembled vector of nodal displacements, in (m)
q	A scalar function, in^2 (m^2)
q_0	Intensity of a narrow pulse in the circumferential direction, lb$_{\mathrm{f}}$/in^2 (N m^{-2})
$\mathbf{R}$	A force vector used to simplify the system of linear equations resulting from the axisymmetric hybrid-SAFE formulation, lb$_{\mathrm{f}}$ (N)
$\mathbf{R}_{\mathrm{B}}$	A force vector used to simplify the system of linear equations resulting from the axisymmetric hybrid-SAFE formulation, lb$_{\mathrm{f}}$ (N)
R	Pipe's mean radius, in (m)
R	Normalized reflection coefficient, dimensionless
R^2	Coefficient of determination
R^+	Denotes the reflected wave field where a wave function expansion is utilized

$\mathbf{r}$	Position vector, $\mathbf{r} = (r, \theta, z)$
$\mathbf{r}_c$	Vector containing a finite element's radial nodal coordinates, in (m)
r	Indicates the radial coordinate, in (m)
r_0	Radial coordinate at which a point force is applied, in (m)
r_{km}	Radial coordinate of the k^{th} layer's middle surface, in (m)
r_i	Radial coordinate of the pipe's inner wall, in (m)
r_o	Radial coordinate of the pipe's outer wall, in (m)
$\mathbf{S}$	Dynamic stiffness matrix, lb_f/in (N/m)
S	Speed up ratio achieved using parallel computing, dimensionless
s	Time scaling factor appearing in the inputted, Gaussian modulated sine wave
T	Kinetic energy, in-lb_f (J)
T	Normalized transmission coefficient, dimensionless
T	Indicates a torsional mode
t	Time, s
$\mathbf{U}$	Array of nodal displacements, in (m)
$\boldsymbol{\mathcal{U}}$	Array of radial displacements, in (m)
$\mathbf{u}$	Displacement vector, $\mathbf{u} = (u, v, w)$, inch (m)
u	Radial displacement, in (m)
$\boldsymbol{\mathcal{V}}$	Array of circumferential displacements, in (m)
V	Potential energy, in-lb_f (J)
V_e	Potential energy due to external forces, in $-$ lb_f (J)
v	Circumferential displacement, in (m)
v	Velocity of an undamped, single degree of freedom oscillator, in/s (m s^{-1})
$\boldsymbol{\mathcal{W}}$	Array of axial displacements, in (m)
w	Axial displacement, in (m)
x	Displacement of an undamped single degree of freedom oscillator, in (m)
$\mathbf{z}_c$	Vector containing a finite element's axial nodal coordinates, in (m)
z	Axial coordinate, in (m)
z_{FE}	One half the length of the finite element volume enclosing a nonaxisymmetric notch

Greek Letters

α^2	Parameter appearing in Bessel's differential equation, $\alpha^2 = \omega^2/c_1^2 - k^2$, in^{-2} (m^{-2})
β^2	Parameter appearing in Bessel's differential equation, $\beta^2 = \omega^2/c_2^2 - k^2$, in^{-2} (m^{-2})
$\mathbf{\Gamma}$	Matrix inverse of the Jacobian matrix
Γ	An error function which is to be minimized
γ	Engineering shear strain in which a given subscript indicates the direction, in-/in (m/m)
Δ	Indicates a change or difference in the quantity that follows
Δf	Indicates the difference from an unblemished pipe's cutoff frequency and a singularity frequency caused by a notch, Hz (rad s^{-1})
δ	Dirac delta function
δ_{mp}	Kronecker delta, $\delta_{mp} = 1$ if $m = p$, otherwise $\delta_{mp} = 0$

$\overline{\delta}$	Indicates the first variation
$\boldsymbol{\varepsilon}$	Strain tensor, in/in (m/m)
ε	Normal strain in which a given subscript indicates the direction, in/in (m/m)
ζ	Dimensionless radial coordinate in the local, isoparametric finite element's coordinate system
η	An error function which is to be minimized
η	Dimensionless axial (axisymmetric elements) or circumferential (three-dimensional elements) coordinate in the local, isoparametric element's coordinate system
$\boldsymbol{\theta}_c$	Vector containing a finite element's circumferential nodal coordinates, degrees (rad)
θ_0	Circumferential extent over which a narrow pulse approximates the Dirac delta function, degrees (rad)
θ	Indicates the circumferential coordinate, degrees (rad)
λ	First Lamé constant, psi (Pa)
μ	Second Lamé constant, psi (Pa)
ν	Poisson's ratio, dimensionless
ξ	A viscous like, damping coefficient, dimensionless
ξ	Dimensionless axial coordinate in the local, isoparametric element's coordinate system for three-dimensional elements
ρ	Mass density, slug/in^3 (kg m^{-3})
$\boldsymbol{\sigma}$	Stress tensor, psi (Pa)
σ	Normal stress in which a given subscript indicates the direction, psi (Pa)
τ	Shear stress in which a given subscript indicates the direction, psi (Pa)
τ	Time at which the "free vibration" portion of a time history is assumed to begin, s
τ	Time shifting factor appearing in the inputted, Gaussian modulated sine wave, s
$\boldsymbol{\phi}$	An eigenvector of the linearised eigenvalue problem, units vary according to its sub-vectors
Φ	Dilatational scalar potential function, in^2 (m^2)
ϕ	A modal phase angle, degrees (rad)
ϕ	Phase angle of an undamped, single degree of freedom oscillator, degrees (rad)
ω	Circular frequency, rad/s
ω_n	Undamped natural frequency of a single degree of freedom oscillator, rad s^{-1}
ω_0	Frequency appearing in the inputted, Gaussian modulated sine wave, rad s^{-1}

Roman Subscripts

0	Denotes a quantity associated with the externally applied, point force
a	Indicates the antisymmetrical loading
arr	Denotes an arrival time
B	Boundary node of a finite element region
b	A quantity associated with a "back" (inner) nodal surface
c	Indicates a vector contains finite element nodal coordinates
d	Indicates the distance from a notch's boundary

e	Indicates a quantity belonging to a single finite element
ex	A statistically expected value
F	Indicates a flexural mode
f	A quantity associated with a "front" (outer) nodal surface
I	Indicates an interior node of a finite element region
i	A quantity associated with the pipe's inner wall
in	Indicates a variable in the incident wave field
k	A quantity associated with the idealized finite element's k^{th} sublayer through the wall thickness of a pipe
L	Indicates a longitudinal mode
L	Indicates the axial coordinate at which the point force is applied
l	Denotes the lower half of a vector
M	A "place-holder," to indicate a mode type of one of T, L, of F
m	A quantity associated with a middle nodal surface
m	Positive integer indicating the m^{th} axial mode
max	Indicates a maximum value
min	Indicates a minimum value
n	Indicates the n^{th} circumferential harmonic
o	A quantity associated with the pipe's outer wall
parallel	Indicates a quantity calculated using parallel computing
ppk	Indicates a peak-to-peak value
R	Indicates the axial coordinate at which the displacement is monitored in the reflected field
r	Indicates the radial (r) direction
ref	Indicates the reference value used for nondimensionalization
s	Indicates the symmetrical loading
scat	Indicates a variable in the scattered wave field
serial	Indicates a quantity derived from serial computing
T	Indicates a torsional mode
T	Indicates the axial coordinate at which the displacement is monitored in the transmitted field
tot	Indicates a total quantity
u	Denotes the upper half of a vector
z	Indicates the axial (z) direction
$-$	Indicates a finite element node on boundary B^-
$+$	Indicates a finite element node on boundary B^+

Roman Superscripts

c	Indicates a cutoff frequency
f	Indicates the forced solutions for an undamped, single degree of freedom oscillator
h	Indicates the free vibration solutions for an undamped, single degree of freedom oscillator
in	Indicates a variable in the incident wave field
L	Denotes a left eigenvector

R	Denotes a right eigenvector
scat	Indicates a variable in the scattered wave field
T	Denotes the matrix transpose

Greek Subscripts

θ	Indicates the circumferential direction

Notation, Typeface, and Symbols

$\mathbf{X}_{,x}$	A comma followed by one or more spatial variables indicates that differentiation of the variable before the comma is to be performed with respect to any spatial variables following the comma
$\mathbf{x}$	Bold upright text indicates, in the appropriate context, a vector or matrix
∇	Del operator, $\nabla = \frac{\partial}{\partial r}\hat{\mathbf{e}}_r + \frac{1}{r}\frac{\partial}{\partial \theta}\hat{\mathbf{e}}_\theta + \frac{\partial}{\partial z}\hat{\mathbf{e}}_z$
∇^2	Laplacian operator for scalar fields, $\nabla^2 = \frac{\partial^2}{\partial r^2} + \frac{1}{r}\frac{\partial}{\partial r} + \frac{1}{r^2}\frac{\partial^2}{\partial \theta^2} + \frac{\partial^2}{\partial z^2}$
✡	Laplacian operator for vector fields, $\text{✡}\mathbf{x} = \left(\nabla^2 x_r - \frac{x_r}{r^2} - \frac{2}{r^2}\frac{\partial x_\theta}{\partial \theta}\right)\hat{\mathbf{e}}_r + \left(\nabla^2 x_\theta - \frac{x_\theta}{r^2} - \frac{2}{r^2}\frac{\partial x_r}{\partial \theta}\right)\hat{\mathbf{e}}_\theta + \nabla^2 x_z \hat{\mathbf{e}}_z$, where $\mathbf{x} = x_r\hat{\mathbf{e}}_r + x_\theta\hat{\mathbf{e}}_\theta + x_z\hat{\mathbf{e}}_z$
$\times$	Indicates the cross (vector) product or curl operation
$\cdot$	Indicates the dot (inner, scalar) product or divergence operator
$\mathfrak{I}$	Denotes the imaginary part of a complex variable
$\mathfrak{R}$	Denotes the real part of a complex variable
$\overline{\mathbf{X}}$	An over bar indicates that the Fourier transform has been applied
$\dot{x}$	Overdot(s) indicate(s) differentiation, once for each dot, with respect to time
$\hat{x}$	Overhat indicates a measured quantity
$\tilde{x}$	An over tilde indicates complex conjugation
x^*	A superscript asterisk indicates a nondimensional quantity
$\check{\mathbf{S}}$	Indicates the condensation of the interior finite element nodes for the dynamic stiffness matrix
$\mathbf{S}^{\ddagger}$	Indicates condensation of the nodes in the interior finite element region and boundary B^- for the dynamic stiffness matrix
✠	Indicates a vector or matrix where the appropriate zero displacements and reaction forces on B^- have been condensed and neglected, respectively

Abbreviations and Acronyms

AE	Acoustic Emission
API	American Petroleum Institute
BEM	Boundary Element Method
CPU	Central Processing Unit
CSA	Canadian Standards Association
DC	Direct Current
DFT	Discrete Fourier Transform
DN	Diameter Nominal
DWC	Digital Wave Corporation
EUB	(Alberta) Energy and Utilities Board
FFT	Fast Fourier Transform
FRF	Frequency Response Function
GPU	Graphics Processing Unit
IBM®	International Business Machines
MDOF	Multi Degree-Of-Freedom
NDT	Non-Destructive Testing
NPS	Nominal Pipe Size
NSERC	Natural Science and Engineering Research Council of Canada
PC	Personal Computer
PVDF	Polyvinylidene Fluoride
RAM	Random Access Memory
SAE	Society of Automotive Engineers
SAFE	Semi-Analytical Finite Element
SDOF	Single Degree-Of-Freedom
TCP/IP	Transmission Control Protocol/Internet Protocol
UI	Ultrasonic Inspection
UMSU	University of Manitoba Students' Union

Chapter 1

Introduction, Overview of Dissertation, and Literature Survey

1.1 Introduction

The Alberta Energy and Utilities Board (EUB) reports [1] that a total of 234,411 miles (377 248 km) of energy related pipeline was under its jurisdiction at the end of 2005. This total represents an increase of about 40% over the previous 8 year period [1, 2]. On the other hand, the EUB also indicates there were a total of 12 848 (12 137) pipeline "incidents"[1] between 1990 and 2005 (1980 and 1997). About 94% of the reported incidents led to a pipeline leak or rupture [1]. Moreover, corrosion was cited [1, 2] as the primary form of failure, representing between 63% and 70% of pipeline failures. Hidden, internal corrosion was responsible for around four times more failures than external corrosion [1, 2]. Although these statistics are the most currently available, they apply only to Alberta, Canada. Notwithstanding, it is clear that extensive networks of pipelines are in widespread use and they are prone to occasional failure. Given that the monetary and, less often, human costs of a pipeline failure can be extraordinarily high [3], a method of inspecting pipelines is required to detect and size defects. Furthermore, the method must be nondestructive and ideally non-invasive because the infrastructure is already in service.

DeGarmo, Black, and Kohser [4] provide a convenient summary of "classical"[2] nondestructive inspection and testing techniques, along with their relative merits. The seven "core" techniques are:

1. visual inspection,

[1] Note that incidents occurring within facilities such as satellites, batteries, or plants *are not* considered part of the pipeline system and, therefore, are not included in these statistics.

[2] Specialized inspection techniques other than ultrasonic based are beyond the scope of this thesis.

2. liquid penetrant inspection,

3. magnetic particle inspection,

4. Ultrasonic Inspection (UI),

5. radiography,

6. eddy current testing, and

7. Acoustic Emission (AE) monitoring.

A brief overview of each of these classical nondestructive inspection techniques is given next. It is based on the information presented in [4] and summarises the physical principle, advantages, disadvantages, and limitations of each of the above techniques.

A visual inspection involves examining, by eye, the surface of a specimen under illumination. Optical aids or assists may be used. The technique is simple, easy to use, portable, and inexpensive. Its application is limited, however, by the skill and knowledge of the person performing the inspection. Moreover, only an external surface of the specimen may be inspected. Records of the inspection can be made by using, for example, photographs, videotapes, or written reports.

An inspection which incorporates a liquid penetrant may be considered an enhancement of a visual inspection. It combines a visual inspection with the use of a liquid penetrant which is drawn into surface breaking flaws by a capillary action. The liquid penetrant is "revealed" subsequently by employing a developer which makes a flaw more discernible. However, the penetrant may be "washed out" of large defects which would increase the probability of "false negatives." Surface coatings may be a hindrance and specimens should not have a porous surface.

Magnetic particle inspection takes advantage of a magnetic field which is induced only in *ferromagnetic* materials. When magnetized, defects in a ferromagnetic material distort the induced magnetic field. Magnetic particles tend to be attracted strongly to surface

regions where the magnetic flux is concentrated, hopefully around any defects. This technique is relatively simple to implement, fast and easy to interpret. Moreover, portable field units are available. Subsurface flaws, having depths up to about 0.25 inch (6.4 mm), as well as "small tight" cracks may be revealed but a specimen must be relatively clean. Furthermore, the *orientation* of a flaw relative to the magnetic field affects the procedure's sensitivity so that multiple inspections may be required that utilize differently orientated magnetic fields. The process is power intensive as it requires large electrical currents to magnetize specimens. Its severest limitation is that it can be applied only to ferromagnetic materials; nonferrous materials and austenitic stainless steels cannot be inspected successfully. Specimen geometries are limited, in practice, only by the ability to induce a reasonably uniform magnetic filed. On the other hand, records of magnetic particle inspections can be preserved by applying transparent lacquer to the specimen or transferring the observation to transparent tape which can be removed later.

An Ultrasonic Inspection (UI) uses the propagation of sound waves, having 20 kHz or higher frequencies, through a specimen. Sound which is transmitted or reflected can be monitored to detect a crack or flaw with "high sensitivity." UI testing can be performed quickly and the results may be displayed or recorded "immediately." Penetration of the sound waves is relatively great with 60 feet (18 m) quoted as a possible upper limit in steel [4]. Flaws can be detected, located, and "sized" even if they are hidden whilst a material's thickness and properties can also be measured. UI can be applied to most engineering materials although interpretations for nonhomogeneous or anisotropic materials may be challenging. No radiation or other safety hazards are thought to be associated with UI [4]. On the other hand, it is more difficult to apply UI to "complex" geometries, large volumes and small, thin, or rough specimens. Couplants are required usually to minimize the differences in the acoustic impedances of the ultrasonic transducer, air, and specimen. An overriding concern is that properly "trained, experienced, and motivated" inspectors are required for its implementation.

Radiography uses the differing absorption by different materials of some form of radiation. This approach is particularly sensitive to density changes so that internal features are revealed readily. However, radiography is the "most costly" nondestructive testing method and precautions are required to avoid human exposure to radiation. Defects must be sufficiently large and cracks must be orientated favourably for their detection as cracks parallel to the radiation beam may be invisible. Locating and sizing internal defects may require at least two inspections at different illumination angles and, furthermore, two-sided access is required. Indeed, appropriate exposures for complex shapes may be difficult to determine.

Eddy current testing uses the interaction of magnetic fields, one generated by inducing surface (eddy) currents in a specimen and the other from the inducing coil itself. The eddy currents are sensitive to material properties and irregularly shaped geometries which are on or near a conductive ferrous or nonferrous metal's surface. It is also sensitive to variations in an alloy or heat treatment, a plating or coating thickness, and wall thickness. Contact with the specimen is not required and an inspection can be automated at low cost and with no clean-up requirements. As for UI, an eddy current's sensitivity to several variables may complicate the interpretation of an inspection.

Acoustic Emission (AE) monitoring takes advantage of high frequency sound which is emitted when a specimen is stressed, deformed, or changed structurally by, for example, the creation of a defect. All points of a specimen are advantageously monitored simultaneously and the source of an emission can be determined by using triangulation. An inspection can be done in harsh environments and it is not generally limited by a specimen's material. However, AE is a "passive" technique as it can only detect a flaw when it "grows." Flaws which may be present but not "active" cannot be detected. Moreover, AE does not indicate the size and shape of a flaw [4]. Furthermore, background noise can make selecting an appropriate trigger level to initiate an "event count" difficult.

Visual, liquid penetrant, and magnetic particle inspections are unsuitable for pipeline testing because they can detect only surface flaws. A magnetic particle approach is undesir-

able because it is limited to ferromagnetic materials. (It should be noted that aluminium and austenitic stainless steel are sometimes, although not commonly, used as a pipeline material.) Radiography provides a good diagnostic tool but it is not ideal for pipeline inspection because of its high cost and the risk of radiation exposure. Eddy current testing, on the other hand, lacks the penetration required for reliable detection of hidden corrosion in pipelines. Finally, acoustic emission is unsuitable because it incapable of detecting defects that are present but not active. Therefore UI appears to be one of the most suitable choices. Two principal difficulties with UI for pipeline inspection are the limited volume that can be inspected in a single measurement and the difficulty of interpreting measurements. The former disadvantage is ameliorated by employing guided waves while the latter factor is the subject of this dissertation.

Two kinds of body (bulk) waves, which are dispersionless, can exist in (semi-) infinite, homogeneous, and isotropic solids. They are shear and longitudinal waves [5, 6]. When boundaries are introduced, for example in plates, cylinders (pipes), or shells, so-called guided waves arise from the multiple interactions of body waves with the bounding surfaces [5, 6]. Body waves have been used for many years in a variety of UI applications, such as pulse-echo, through-transmission, resonance, etc., to perform tasks like flaw detection, thickness measurement, and characterization of a material's properties [6]. However, guided wave based UI is superior for the following reasons.

1. Their multi-modal and dispersive behaviour can quickly provide information over a range of frequencies [7].

2. The propagation speed of guided waves is very sensitive to material and geometrical properties [7].

3. Guided waves are capable of rapidly interrogating entire structures, including inaccessible regions [8], because they can propagate over long distances, say tens of feet or metres [8, 9].

4. Compared to body waves, guided waves have a lower rate of attenuation with increasing propagation distance [9].

The remainder of this dissertation is devoted to guided wave propagation and scattering in pipes that is relevant to UI. An introductory literature survey of these particular aspects is given next.

1.2 Literature Survey

The very advantages of guided waves which make them attractive for a pipeline inspection complicate the interpretation of data. Complications arise because, in principle, an infinite number of generally dispersive, guided wave modes can exist simultaneously in a pipe. Two excellent sources of information on guided waves in pipes can be found in [5] and [10]. Exhaustive listings of the primary literature are provided in both these texts. The second source, however, is especially useful in providing listings of the references most pertinent to the use of guided waves for pipe inspections. Two texts which address better the needs of the practitioner are [6] and [11]. Topics relevant to the guided wave inspection of pipes can be classified broadly into the following three areas:

1. the development of the dispersion relations in pipes using exact or approximate methods,

2. modelling, which is usually numerical, the scattering of waves by inhomogeneities in pipes, and

3. experimental investigations.

Of course, the three areas may overlap. Important developments are surveyed in each area next.

The first dispersion relations published for axisymmetric, harmonic waves in homogeneous, isotropic rods of infinite length appears to be the often cited, Pochhammer-Chree relation [12, 13]. (Lord Rayleigh [14] and Lamb [15] provided similar contributions for plates.) Significant developments for rods seemed to have stalled [5] until Davies [16] investigated, theoretically and experimentally, the Pochhammer-Chree relation and developed the "first few" branches [5] from this relationship for propagating modes. This important contribution was supplemented when complex wavenumbers were employed to describe the non-propagating and evanescent, axisymmetric modes [17]. Given the complexity of solving "exactly" the equations of motion for rods, particularly for a forced motion [5], a number of approximations evolved. They were surveyed by Green [18]. The most important references are [19] and [20] where axisymmetric wave modes were considered. Following Gazis's [21] approach for "hollow circular cylinders," the dispersion relation for rods was described later by Meeker and Meitzler [22] in terms of torsional, longitudinal, and (non-axisymmetric) flexural modes. Three-dimensional solutions for pipes that were based on linear elasticity theory appear to have been considered first by Gazis [21, 23].

All the references cited so far pertain to homogeneous, isotropic rods and pipes composed of a single material. Additional complexity is introduced when rods and pipes consist of several materials or an anisotropic material. To the best of the author's knowledge, there has been no analytical solution published for guided waves in cylindrical shells consisting of materials having the most general form of constitutive relations. Solutions are available, however, for special cases. Waves in infinitely long, orthotropic rods and pipes have been investigated in, for example, [24–29]. Solutions for solid rods having an internal homogeneous, isotropic core which is bonded perfectly to an outer coaxial, hollow cylinder composed of a different homogeneous, isotropic material have been developed for longitudinal [30] and torsional [31] modes. Solutions for the flexural modes of comparable bi-material rods have been investigated in, for example, [32–34]. In addition, exact solutions for longitudinal waves in infinitely long, composite hollow cylinders comprised of three different

transversely isotropic layers have been published by Keck and Armenàkas [35]. Although this technique can be extended to a cylinder created by laminating together many isotropic layers, it is cumbersome to apply [36]. A more convenient and efficient propagator matrix approach, based on three-dimensional elasticity, was developed [37] to give the dispersion characteristics of such cylinders.

Approximate solutions to the equations of motion for more general rods and pipes are appropriate when "exact" solutions are unavailable. Several approximate methods have been used. Membrane shell theory, in which only the normal and shear forces acting in the mid-surface are considered, has been applied in, for example, [38, 39] where additional membrane related references may be found. These methods are unsuitable, however, for wave scattering because they are insufficiently accurate [36]. The Rayleigh-Ritz, finite element procedure for representing the motions through a pipe's wall, combined with a separation of variables strategy for the other coordinates (i.e., a Semi-Analytical Finite Element [SAFE] approach), seems to have been reported first for cylinders in [40]. This method, which appears to be relatively easy to apply, has been also adopted for wave propagation in laminated composite cylinders. Further enhancements include the modelling of anisotropic, electrical, thermal, and viscoelastic effects. Contributions are described in, for example, [41–49].

Emphasis in the previous citations has been the determination of dispersion relations which are inherently frequency based. However actual guided wave, UI measurements are conducted necessarily in time. Early efforts to predict transient, temporal responses based on the exact equations of elasticity were limited to rods, They can be found in, for instance, [16, 50–52]. Corresponding approximate methods are located in [53–55]. Later simulations of time responses for pipes that use the SAFE methodology are given in, for example, [47, 49, 56, 57]. Of particular relevance to this thesis is the observation that singularities in an unblemished pipe's displacement response coincide with its cutoff frequencies. To the best of the author's knowledge, this aspect was reported first in [57] and confirmed later in [49].

Numerical approaches have been used most often to model guided wave scattering in rods and pipes because of the naturally inherent complexities. Investigations using approximate models of wave reflections from the free ends of such structures have been reported in, for instance, [58–61]. On the other hand, a wave propagation method employing finite elements has been utilized in [62] to investigate the effects of dispersion and end conditions on axisymmetric pulses propagating in laminated, semi-infinite cylinders possessing radial inhomogeneity. A wave expansion method, in which wave functions were calculated by using both the propagator matrix and SAFE techniques, has been employed in [63] to determine the amplitudes and energy fluxes of waves reflected from a free end of a laminated circular pipe. An extension of this approach combined a finite element model of a volume enclosing only an inhomogeneity in an otherwise blemish free pipe to create a "hybrid" method suitable for wave scattering. This approach has been applied successfully to axisymmetric and nonaxisymmetric wave scatterers in, for example, [64–68]. A mathematical crack, having an arbitrary circumferential length and radial depth in a pipe, was modelled in [69] by using a wave function expansion along the pipe's axial direction and decomposing the problem into the equivalent sum of a symmetric and an anti-symmetric component. Consequently, the otherwise three-dimensional problem was reduced to essentially two separate, quasi-one-dimensional problems to alleviate the computational burden. Approaches based on membrane models, [70, 71] for example, or solely finite element models, [70, 72–74] amongst other references, have been used to model wave scattering in pipes. The Boundary Element Method (BEM) is an attractive alternative technique because only a discretization of a structure's boundary is required [36]. Hence the dimensionality of a problem is reduced by one. The BEM has been employed in, for example [36, 75, 76], to study wave scattering by inhomogeneities in pipes.

The experimental discovery of the end mode was reported first in [77] where the reflections of axisymmetric waves from a free end of an elastic rod were investigated. Longitudinal and flexural modes induced in a rod by a "step" load were studied in [78]. Similar work

was done in [79] for axisymmetric and nonaxisymmetric modes in pipes. Early attempts in [80] and [81], for instance, of using guided waves for pipe inspection focussed on the torsional and longitudinal wave modes and considered spurious reflections as an indication of damage. More recent work, for example [8, 9, 70, 72, 74, 82–84], has focussed also on reflections of axisymmetric pipe modes from defects. The use of flexural waves for inspecting pipes has been somewhat infrequent [85–88] because "the acoustic field is much more complicated than the case of axisymmetric modes" [85].

In order to excite specific modes, or "focus" them at a desired location, special ring or "comb" transducers as well as equipment like angle beams, wedges, or time-delay, periodic linear arrays/phased arrays were employed [8, 9, 80, 81, 89, 90]. For example, electrodynamic coils with the spacing of the windings of the coils selected to excite preferentially the T(0,1) and L(0,2) modes were used in [80] to detect notches in an austenitic pipe. Similarly, the L(0,1), and to a lesser extent, the L(0,2) modes were excited by using piezoelectric ultrasonic probes in [81] to investigate the potential for employing these two modes to inspect "U-bends" and detect notches. Ditri et al. [91] described in theoretical terms the generation of waves, minimizing the contributions of nonaxisymmetric modes, through the use of a multi-element, normal incidence transducer. The use of "wedge type" transducers to excite axisymmetric modes and "comb" transducers to excite (nonaxisymmetric) modes that have wavelengths equal to the spacing between the centres of the fingers of the comb (divided by some integer) was described in [92]. Alleyne et al. [9] developed a dry-coupled, piezoelectric transducer system that utilized sixteen piezoelectric elements to approximate an axisymmetric loading. The system described in [9] was used to preferentially excite the L(0,2) mode [70] and later the T(0,1) mode [93] to detect notches in pipes. Higher order longitudinal modes, i.e., the L(0,3) and L(0,4) modes, were excited successfully using flexible Polyvinylidene Fluoride (PVDF) comb transducers in [82]. The use of variable angle beam shoes to excite the F(3,3), F(4,3), F(5,3), and F(6,3) nonaxisymmetric modes was described in [85]. These modes were used to remotely detect multiple notches cut in a pipe.

Many more examples of selecting particular modes for specific inspection purposes can be found in the literature. However, use is made in all cases of a pipe's dispersion curves and mode shapes to choose an appropriate frequency bandwidth and spatial variation in order to excite the desired mode(s).

Related to the excitation of specific modes for inspection purposes is the study of wave scatting from defects, e.g., cracks and notches. Several examples have been mentioned already. Aspects of the wave scattering problem have been studied numerically in, for example, [64–74]. Wave scattering from notches has been investigated experimentally in, for example, [8, 70, 71, 80–82, 85, 93, 94]. Common to all these examples is the concept of reflections from a notch. Either reflection coefficients are computed or reflections from a notch are simulated or measured. Numerous newer references, e.g., [95], continue to build upon the concepts developed in these seminal papers. A philosophy which complements the advances outlined in this literature survey is explored here.

The determination of an unblemished pipe's material properties *or* dimensions using guided wave speeds or dispersion curves has been reported in, for example, [96–99]. However, there appears to be only one reference [100] employing guided wave cutoff frequencies of an unblemished pipe to *simultaneously* find its wall thickness and material properties. On the other hand, although noticeably more effort has been expended in detecting damage in pipes (and plates) by using reflections as well as changes in wave speeds and also dispersion curves of guided waves, their cutoff frequencies have been used merely to detect thinning in plates [101–103]. Thinning was examined by exciting a guided wave mode near its cutoff frequency and monitoring the disappearance of the modal response when part of the plate's thickness was below the critical value for the mode to propagate. However, the seemingly straightforward extension to pipes does not seem to have been given. Moreover the identification of spatially decaying modes, which are introduced in a pipe by a notch and are analogous to end modes [77], has not been reported. The singularities corresponding to these modes are utilized here to characterise the dimensions of axisymmetric notches

in pipes. The extension to nonaxisymmetric notches is suggested. (As an aside, a comprehensive review of the use of guided waves in plates for their characterisation is given in [104]. Wave speeds, dispersion curves and reflections are featured prominently. However, there is no mention of employing an unblemished plate's cutoff frequencies for material characterisation or additional singularities arising from a defect's introduction.)

1.3 Overview of Dissertation

An introduction and overview of this dissertation is given in this chapter in addition to a survey of relevant literature. A theoretical framework, based invariably on small-strain linear elasticity, is presented in Chapter 2. It forms the basis of the inverse procedure described in Chapter 3. The procedure is used to simultaneously recover a pipe's wall thickness and elastic properties from the cutoff frequencies of ultrasonic guided waves. The scattering of guided waves by axisymmetric and more general three-dimensional notches is described in Chapter 4. An easy to measure metric is identified in Chapter 4 that allows the local detection and "sizing" of a single axisymmetric notch in a pipe. A straightforward extension to a single nonaxisymmetric notch is also suggested. The dissertation ends in Chapter 5 with conclusions and recommendations for further work. Conjectures describing the anticipated outcomes of possible future investigations are also given. A series of appendices supports the main text without disrupting its flow.

1.4 Contributions and Novelty

The mathematical bases of previously available modelling techniques are adapted and modified substantially to more readily relate numerical data and experimental results. Specifically, extensive use is made of Zhuang et al.'s [43] SAFE procedure that provides a computationally efficient method to obtain, for both axisymmetric and nonaxisymmetric modes,

approximate wavefunctions for an unblemished pipe. The related hybrid(-SAFE) technique [64–68], which makes use of the approximate wavefunctions from SAFE, provides a complementary tool and it is used to model wave scattering from various, single open rectangular notches. The computational tools were developed previously as an "end in themselves." Consequently solutions have been typically computed by using, at a given time, a new numerical method and compared to another set of numerical data or, perhaps, limited experimental measurements. Here, on the other hand, "best practices" are *combined creatively* to *simulate and interpret better* the basic behaviour of unblemished and notched pipes. Results are verified experimentally by comparisons with new and personally performed measurements for unblemished pipes and the use of previously existing, but more limited experimental data for a singly notched pipe. It is demonstrated that the computational models provide sufficiently accurate analogues to commercially available pipes and, hence, can serve as the basis of inverse solvers to characterize them. However, the inverse procedures developed are unsuitable if a rapid deviation from homogeneity, geometrical uniformity or both occurs in spatial regions where the pipe's dynamic behaviour is expressed in terms of wavefunctions, i.e., outside a finite element region. Such variations are unlikely to be encountered in commercially available pipes which comply with, for example, ASTM International 106M, American Petroleum Institute (API) SPEC 5L, or Canadian Standards Association (CSA) Z245.1. The principal contributions lie, therefore, with the *application* of the computational techniques to *fundamental* aspects arising in the Non-Destructive Testing (NDT) of pipes and represent an important step in reconciling theory and practice.

Philosophies are advanced that exploit simple experimental procedures. Furthermore, straightforward heuristics are identified that make the interpretation of measured multimodal data tractable. Moreover, the use of specialized transducers, which have numerous elements to reduce the number of excited modes, is avoided. In addition, the standard requirement for dynamically well behaved transducers and their repeatable attachments to a pipe is ameliorated because amplitude and phase independent metrics are used. However,

the results presented here are "proof of concept" in nature and they illustrate principally the overall philosophy. Further efforts are required, of course, to develop more fully the methodologies for the practical field inspection of pipes. On the other hand, suggestions are made to extend the present advances to general inverse problems related to the characterization of more arbitrary defects.

Frequencies at which singularities from an unblemished or blemished pipe arise are exploited for the first time. Distinctions are made in this dissertation between a "cutoff frequency" and a "singularity frequency." The former expression indicates a singularity which occurs in an unblemished pipe's Frequency Response Function (FRF) and, of course, coincides with one of its cutoff frequencies. The latter, on the other hand, is used to describe a singularity which is distinct from a cutoff frequency and is introduced by a notch. The term "singularity" is employed also in a generic sense with the intended meaning suggested by the context. The ultrasonic behaviour near singularities of an unblemished pipe's well known cutoff frequencies are akin to unbounded resonant responses at undamped natural frequencies of low frequency vibrations. Therefore singularities in a wave mode's displacement FRF are shown in Chapter 2 to coincide, not unexpectedly, with an unblemished pipe's cutoff frequencies. A related procedure has been applied which incorporates, for the first time, the contributions of singularities to time histories determined from an inverse Fourier transform of modal data in order to ensure causality.

A new technique is developed in Chapter 3 to simultaneously measure an unblemished, homogeneous, isotropic pipe's wall thickness and elastic constants by using three cutoff frequencies obtained from a single ultrasonic measurement. These cutoff frequencies are extracted from a time history by applying a standard nonlinear, least-squares curve fitting procedure in a novel way. The curve fitting is required to overcome the frequency limitations associated with Discrete Fourier Transform (DFT) and other frequency extraction techniques.

Singularities, similar but not coincidental with cutoff frequencies, are shown to occur,

for the first time, when an axisymmetric, outer surface breaking notch having sharp, rectangular boundaries is introduced into an otherwise unblemished pipe. Such notches are considered first because they are computationally more tractable. Moreover, computer and experimental results are available for these notches to partially validate the present computations. It is suggested that the singularities introduced by such a notch depend on the properties of the parent pipe *and* the notch but the effects are local to the notch. It is demonstrated further that the difference between the frequency at which a singularity is introduced by a notch and the nearest unblemished pipe's cutoff frequency is a function of the notch's dimensions. By plotting contours of constant frequency differences, it is shown that it is *usually* possible to characterize an axisymmetric notch's dimensions by using merely two modes. However, depending on the set of modes for which information is available, the frequency difference for a third mode may be needed occasionally for a *unique* determination. A three-dimensional, nonaxisymmetric notch having a geometry similar to that of the axisymmetric case is shown to be a straightforward, but significantly more computationally demanding, extension. The use of the singularities introduced by a notch is suggested to be a potentially useful screening tool for its local detection and characterization. It would complement, therefore, the commonplace use of a single nondispersive guided wave mode for the remote defection of flaws.

Generally applicable advances in computing are also reported here. Standard "symbolic math" engines are applied to derive approximate forms of the equations of motion suitable for a numerical simulation. Novelty is introduced by manipulating the output from these tools so that computer code is produced that actually implements the numerical simulations. This procedure has two advantages: (i) development time is reduced significantly, and (ii) the process is more reliable as fewer programming errors are likely made. Consideration is also given throughout to generate computer code which is readily parallelizable and distributable.

The overall philosophy advanced here has a number of practical advantages. It is easier

to elicit measurable responses, with modest power inputs, when exciting any pipe around the frequencies of its singularities because of the higher sensitivities there. The excitation of several modes, which is counter to current experimental practice, is required invariably for a unique characterisation. Fortunately this requirement is implementable straightforwardly and in a time effective manner by using a single, small transducer (which effectively acts at a point) to produce a pulse having a suitable frequency bandwidth. This type of excitation may simultaneously and beneficially excite all possible modes. However, the pipe's natural filter-like behaviour will make some modes easier to excite. Only modes excited most readily by a purely radial point excitation applied to the pipe's outer surface and having a frequency bandwidth between 35 kHz and 107 kHz are examined here. The spatial variation of the applied excitation is selected on the basis that it is simple to implement. The bandwidth, on the other hand, is chosen so that comparisons to previously published data can be made. This illustrative selection excites predominately the F(8,1) through F(13,1) modes, as seen later. The inverse procedures' general applicabilities, however, remain mostly unaffected by the modes selected. Indeed, as later examples suggest, *almost any* set which contains a sufficient number of accurate, non-zero[3] singularity frequencies will give the same inverse solution. This statement applies to the procedures which characterise an unblemished pipe or "size" an axisymmetric notch. Hence, the modes may be selected generally on the basis of ease of experimental implementation. For example, Figure 2.9 shows that the F(3,2) and F(11,2) modes have no radial displacement component at their respective cutoff frequencies. Consequently, neither mode would be detectable at its cutoff frequency by a transducer which measures a solely radial displacement. Hence, these modes would be unsuitable for the inverse procedure described in Chapter 3 if such a transducer is used. Finally, all the suggested characterisation techniques require, in principle, solely a single measurement to provide useful information about a pipe's condition if the desired location of inspection is known approximately.

[3]The T(0,1), L(0,1), and F(1,1) modes are excluded because they always have a zero singularity frequency for a homogeneous, isotropic pipe and, hence, they are unsuitable.

1.5 Justification of the Computational Approach

The SAFE and hybrid-SAFE techniques have been adopted for a number of pedagogical and practical reasons. The reasons are summarised briefly next.

1. SAFE is computationally very efficient because approximate solutions to three-dimensional problems are obtained from one or two-dimensional finite elements by using analytical expansions for two or one of the waveguide's spatial dimensions, respectively.

2. While somewhat pedagogical, SAFE provides *wavefunctions* which include wavenumbers and mode shapes rather than *vibration* modes. The wavenumbers are required to plot phase spectra and dispersion curves.

3. An individual wave mode's contribution to an evoked response can be extracted very straightforwardly, in either time or frequency, from a SAFE approximation. On the other hand, a determination of these contributions from a solely finite element model typically requires significant signal processing of time histories found at many spatial points. The additional signal processing is disadvantageous for two reasons: (i) it adds additional steps to an analysis, and (ii) more importantly, undesirable artefacts may be introduced to a post-processed signal.

4. Spectral data can be obtained from the SAFE and hybrid-SAFE procedures with an almost arbitrarily fine frequency resolution. Conversely, spectral data from a DFT of a short time history can have only a limited frequency resolution. This advantage is essential to the reliable identification of singularities.

5. There are no spurious reflections from the infinitely remote ends of a SAFE model. Consequently the computational expense and "tuning" required for perfectly matching or absorbing boundaries (commonly used in purely finite element approaches) is avoided.

6. Modal conversions at wave scatterers can be computed directly with no additional signal processing operations required.

7. Both the SAFE and hybrid-SAFE procedures produce mathematical forms that are embarrassingly parallelizable. (Computer run times may be reduced by about an order of magnitude by using even modest parallel computing facilities.)

8. Fast forward solvers based on SAFE and hybrid-SAFE lend themselves naturally to an "inverse" procedure which repeatedly solves the corresponding forward problem. Purely finite element models, particularly those based on commercial software packages, are not so amenable to this approach.

Chapter 2

Wavefunctions of a Pipe and the Forward Problem

2.1 Introduction

The solutions of the differential equations which model the wave motion in a pipe are considered in this chapter. They give metrics, which are developed further in Chapters 3 and 4, to serve as the basis by which actual pipes can be characterised and defects can be detected. The pipe is idealized invariably as an infinitely long, hollow, right circular cylinder so that a cylindrical coordinate system is assumed throughout. (An infinite pipe is commonly reconciled with a practical pipe having a finite length by time gating out the latter's end reflections.) One-half of the idealized pipe with the cylindrical coordinate system superimposed is shown in Figure 2.1. The pipe is taken to be uniform, homogeneous, and isotropic with negligible material damping. Moreover, displacements are assumed to be so small that linearity applies. Exact solutions based on three-dimensional elasticity are given first. These solutions are presented because of their historical significance. Moreover, they serve as a "cross-check" on the accuracy of the more convenient and computationally tractable, although approximate solutions from the Semi-Analytical Finite Element (SAFE)

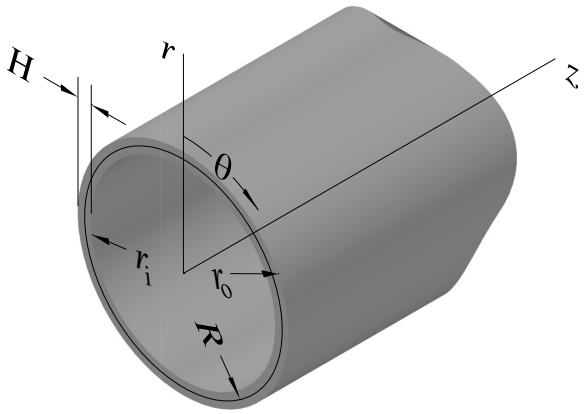

Figure 2.1. An idealized pipe and superimposed cylindrical coordinate system.

formulation to be presented in Section 2.3. A comparison between the two approaches is limited here, however, to the metric of interest, the cutoff frequencies. The chapter is concluded with an illustrative simulation which highlights salient features of an unblemished pipe's behaviour. These features are key to implementing the inverse procedure described in Chapter 3.

2.2 Exact Wavefunctions

The solution presented in this section is based upon that described first in [21]. It has been modified slightly to appear more consistent with the solutions from SAFE presented in Section 2.3. Navier's differential equations of wave motion for homogeneous and isotropic media, written in terms of displacement, are given by [5]

$$(\lambda + \mu)\nabla\nabla \cdot \mathbf{u}(\mathbf{r}, t) + \mu \text{✡}\mathbf{u}(\mathbf{r}, t) + \rho\mathbf{f}(\mathbf{r}, t) = \rho\ddot{\mathbf{u}}(\mathbf{r}, t). \tag{2.2.1}$$

Here λ and μ are Lamé's constants and ∇ is the "del" operator. The displacement vector is denoted by $\mathbf{u}$, where the bold upright typeface indicates a vector or matrix, the context of which is implied. The $\mathbf{u}$ has radial, circumferential, and axial components u, v, and w, respectively. On the other hand, the Laplacian operator for vector fields is indicated by the symbol ✡, ρ is the (mass) density and $\mathbf{f}$ is an externally applied, body force vector. Both $\mathbf{u}$ and $\mathbf{f}$ are functions of time, t, and the position vector $\mathbf{r} = (r, \theta, z)$ where r, θ, and z are the radial, circumferential and axial coordinates, respectively. See the previous Figure 2.1. An overdot indicates differentiation with respect to time, once for each dot. A centre dot symbol, $\cdot$, on the other hand, is used to indicate the divergence operator. The displacement vector is resolved, using the Helmholtz decomposition, into a dilatational scalar potential,

Φ, and an equivoluminal vector potential, $\mathbf{H}$, as in [5, 21, 105]. Then

$$\mathbf{u} = \nabla\Phi(\mathbf{r}, t) + \nabla \times \mathbf{H}(\mathbf{r}, t) \tag{2.2.2a}$$

with

$$\nabla \cdot \mathbf{H} = F(\mathbf{r}, t). \tag{2.2.2b}$$

The $\times$ in equation (2.2.2a) denotes the curl operation, while F in equation (2.2.2b) is a function of $\mathbf{r}$ and t. Function F can be chosen arbitrarily due to gauge invariance [5, 21, 105]. By substituting equation (2.2.2a) into equation (2.2.1), it can be shown [5], after tedious vector calculus manipulations, that

$$\nabla\left[(\lambda + 2\mu)\nabla^2\Phi + \rho f - \rho\ddot{\Phi}\right] + \nabla \times \left[\mu\text{✡}\mathbf{H} + \rho\mathbf{B} - \rho\ddot{\mathbf{H}}\right] = \mathbf{0}, \tag{2.2.3}$$

where the body force has been resolved into the scalar and vector potentials, $f(\mathbf{r}, t)$ and $\mathbf{B}(\mathbf{r}, t)$ respectively. Furthermore, ∇^2 is the Laplacian operator for scalar fields. Equation (2.2.3) is satisfied if both its bracketed terms vanish simultaneously, i.e.,

$$(\lambda + 2\mu)\nabla^2\Phi + \rho f - \rho\ddot{\Phi} = 0 \tag{2.2.4a}$$

and

$$\mu\text{✡}\mathbf{H} + \rho\mathbf{B} - \rho\ddot{\mathbf{H}} = \mathbf{0}. \tag{2.2.4b}$$

The former and latter equations have a scalar and vector form, respectively. A separation of variables strategy is applied next to equation (2.2.4).

Separable trial functions are assumed and harmonic solutions are sought for Φ as well as the r, θ, and z components of $\mathbf{H}$, H_r, H_θ, and H_z respectively. The resulting forms are

$$\Phi = q(r)\mathrm{e}^{\mathrm{j}n\theta}\mathrm{e}^{\mathrm{j}kz}\mathrm{e}^{-\mathrm{j}\omega t}, \tag{2.2.5a}$$

$$H_r = g_r(r)\mathrm{e}^{\mathrm{j}n\theta}\mathrm{e}^{\mathrm{j}kz}\mathrm{e}^{-\mathrm{j}\omega t}, \tag{2.2.5b}$$

$$H_\theta = g_\theta(r)\mathrm{e}^{\mathrm{j}n\theta}\mathrm{e}^{\mathrm{j}kz}\mathrm{e}^{-\mathrm{j}\omega t}, \tag{2.2.5c}$$

and

$$H_z = g_z(r)\mathrm{e}^{\mathrm{j}n\theta}\mathrm{e}^{\mathrm{j}kz}\mathrm{e}^{-\mathrm{j}\omega t}. \tag{2.2.5d}$$

The q, g_r, g_θ, and g_z in equation (2.2.5) are scalar functions of r that have to be determined still. Moreover, $\mathrm{j} = \sqrt{-1}$ is the complex unit, ω is the circular frequency, whereas n and k are the circumferential and axial wavenumbers, respectively. Note that n is permitted to take only integer values due to the requirement that the displacement field be single-valued. Substituting equation (2.2.5) into equation (2.2.4) gives, after manipulations and neglecting body forces,

$$\frac{\partial^2 q}{\partial r^2} + \frac{1}{r}\frac{\partial q}{\partial r} - \left(\frac{n^2}{r^2} - \alpha^2\right)q = 0, \tag{2.2.6a}$$

$$\frac{\partial^2 g_r}{\partial r^2} + \frac{1}{r}\frac{\partial g_r}{\partial r} - \left(\frac{(n^2+1)}{r^2} - \beta^2\right)g_r - \frac{\mathrm{j}2n}{r^2}g_\theta = 0, \tag{2.2.6b}$$

$$\frac{\partial^2 g_\theta}{\partial r^2} + \frac{1}{r}\frac{\partial g_\theta}{\partial r} - \left(\frac{(n^2+1)}{r^2} - \beta^2\right)g_\theta + \frac{\mathrm{j}2n}{r^2}g_r = 0, \tag{2.2.6c}$$

and

$$\frac{\partial^2 g_z}{\partial r^2} + \frac{1}{r}\frac{\partial g_z}{\partial r} - \left(\frac{n^2}{r^2} - \beta^2\right)g_z = 0, \tag{2.2.6d}$$

where $\alpha^2 = \omega^2/c_1^2 - k^2$ and $\beta^2 = \omega^2/c_2^2 - k^2$. The c_1 and c_2 correspond to the dilational and shear wave speeds, respectively. They can be expressed as

$$c_1 = \sqrt{(\lambda + 2\mu)/\rho}, \tag{2.2.7a}$$

and

$$c_2 = \sqrt{\mu/\rho}. \tag{2.2.7b}$$

Equations (2.2.6a) and (2.2.6d) are Bessel's differential equation in q and g_z, respectively. On the other hand, g_r and g_θ appear to be coupled in equations (2.2.6b) and (2.2.6c). They

can be decoupled by making use of the gauge invariance of F which, consequently, can be chosen arbitrarily. Making the substitution $g_\theta = -\mathrm{j}g_r$ in equations (2.2.6b) and (2.2.6c) reduces them to

$$\frac{\partial^2 g_r}{\partial r^2} + \frac{1}{r}\frac{\partial g_r}{\partial r} - \left(\frac{(n+1)^2}{r^2} - \beta^2\right) g_r = 0. \tag{2.2.8}$$

Equation (2.2.8) also has the form of Bessel's differential equation in g_r.

The solutions to equations (2.2.6a), (2.2.8), and (2.2.6d) can be written in terms of Hankel functions such that

$$q(r) = A_1 H_n^{(1)}(\alpha r) + B_1 H_n^{(2)}(\alpha r), \tag{2.2.9a}$$

$$g_r(r) = A_2 H_{n+1}^{(1)}(\beta r) + B_2 H_{n+1}^{(2)}(\beta r), \tag{2.2.9b}$$

and

$$g_z(r) = A_3 H_n^{(1)}(\beta r) + B_3 H_n^{(2)}(\beta r). \tag{2.2.9c}$$

The A_i and B_i, $i = 1, 2, 3$, are constants which need to be determined and $H_n^{(1)}$ ($H_n^{(2)}$) is a Hankel function of order n of the first (second) kind.

The dispersion relation is obtained by applying traction free boundary conditions to the inner and outer surfaces of the unblemished pipe, which correspond to $r = r_\mathrm{i}$ and $r = r_\mathrm{o}$, respectively. Equation (2.2.9), along with the relation $g_\theta = -\mathrm{j}g_r$, are substituted into equation (2.2.5). The result is substituted, in turn, into equation (2.2.2). These manipulations give the displacement field in terms of the six constants introduced in equation (2.2.9). Then displacements are substituted into the (small) strain-displacement relations to give the corresponding stress field. The detailed results are presented in Appendix A.

For traction free conditions to exist on a pipe's inner and outer surfaces, the σ_{rr}, $\tau_{r\theta}$, and τ_{rz} components of the stress tensor (defined in Appendix A) must vanish simultaneously on these surfaces. Consequently

$$\mathbf{P}\begin{bmatrix} A_1 & A_2 & A_3 & B_1 & B_2 & B_3 \end{bmatrix}^\mathrm{T} = \begin{bmatrix} 0 & 0 & 0 & 0 & 0 & 0 \end{bmatrix}^\mathrm{T}, \tag{2.2.10}$$

where **P** is matrix whose elements are given in Section A.5 of Appendix A. Superscript T indicates the matrix transpose. The determinant of matrix **P** must vanish for a nontrivial solution of equation (2.2.10) to exist, i.e.,

$$\det(\mathbf{P}) = 0, \tag{2.2.11}$$

which leads to the dispersion relation of the pipe.

Equation (2.2.11) provides a transcendental equation in the wavenumber k if the (circular) frequency ω is specified, or ω if k is specified, for a pipe having given dimensions and material properties. Although the frequency is always taken to be real here, k is generally complex. Real (imaginary) k correspond to propagating (non-propagating) waves, which may (not) propagate freely, i.e., without external excitation, in a pipe. A complex k is associated with so called evanescent waves. In principle, propagating modes can travel indefinitely in a pipe having no material damping. Non-propagating and evanescent waves, on the other hand, decay exponentially from the axial origin of their source. Evidently, if k is a wavenumber satisfying equation (2.2.11) then so are both $-k$ and $-\tilde{k}$, where an over tilde represents complex conjugation [7, 75]. The mode shape components through the wall of the pipe, which are unique apart from a multiplicative constant, can be found by using equation (2.2.10) after the roots of equation (2.2.11) have been determined. Then the response of a pipe to a prescribed excitation can be described by a linear combination of the doubly infinite (n and k) set of wave modes. It is worth remarking that the results are applicable solely to pipes which are hollow and consist of a single isotropic material. Special considerations are required for solid rods [21]. The so called propagator matrix technique [37] generalizes the previously described technique to pipes having an arbitrary number of perfectly bonded annular layers, if each layer is isotropic.

A closer examination of the matrix **P** detailed in Appendix A suggests that it is "most complicated [5]." Moreover, although the roots can be found by "some search method,"

the approach is "computationally formidable since the roots are sparsely scattered [7]." On the other hand, no analytical solution has been published, to the best of the author's knowledge, for pipes made from a material possessing general anisotropy. To overcome these difficulties, solutions based on the more convenient and computationally tractable, although approximate, Semi-Analytical Finite Element formulation are introduced next.

2.3 Wavefunctions Derived From Semi-Analytical Finite Element (SAFE)

2.3.1 Overview

The mathematical basis of the numerical procedures developed by Zhuang [43] to calculate the three dimensional, steady state Green's functions of an infinitely long cylinder is presented next. A SAFE formulation is used, in conjunction with a separation of variables, due to the complexities described previously. The axial and circumferential variations, as well as all time dependencies of a wave field, are treated analytically. The radial dependence, on the other hand, is modelled by using one-dimensional, quadratic finite elements. The governing differential equations are discretized such that a quadratic, algebraic eigenvalue problem is produced. A Fourier series representation of the circumferential dependence of the wave field allows the latter to be written as a summation. For a given circumferential wavenumber, the solution of the resulting, three parameter, quadratic eigenvalue problem provides the dispersion relation for the pipe. The response of the pipe to an external harmonic force can be described, for a given circumferential wavenumber, by a modal summation over the axial modes. A similar summation over the circumferential wavenumbers gives the steady state Green's functions. Then the (output) time response to a transient (input) point force is determined by treating each Green's function as a Frequency Response Function (FRF) and convolving it with the transient point force. An inverse Fourier transform

applied to the convolved FRF gives the time response at a spatial point of interest.

2.3.2 Discretizing and approximating the equations of motion

The unblemished pipe under consideration is assumed to have the properties described in Section 2.1. The principal difficulty in calculating numerical values from the exact solution presented earlier arises from the Hankel functions. These functions describe the radial (r) variation of the displacement field. To ameliorate this difficulty, the radial variation through the thickness is modelled approximately by using quadratic, one dimensional finite elements. The cylinder is divided into N layers through the thickness as shown in Figure 2.2 where N is illustrated as six. Each cylindrical layer corresponds to a finite element. The thickness of, say, the k^{th} layer is H_k and it extends radially from r_k to r_{k+1}, as shown in the figure.

The SAFE technique is used, in conjunction with the continuity requirements of the displacement field, to represent the governing differential equations in an approximate but more numerically tractable form. Applying the finite element methodology to the discret-

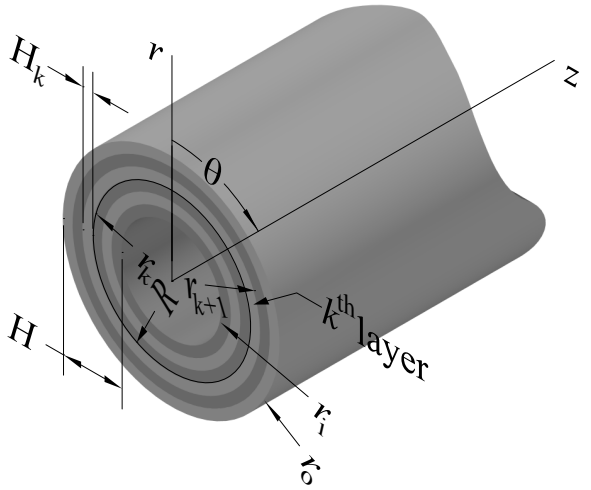

Figure 2.2. Illustrating a pipe's discretisation.

ized pipe allows the displacement field to be approximated by

$$\mathbf{u}(r,\theta,z,t) = \boldsymbol{\mathcal{N}}(r)\mathbf{U}(\theta,z,t) \tag{2.3.1}$$

where $\boldsymbol{\mathcal{N}}(r)$ interpolates the nodal displacements over the entire cylinder and $\mathbf{U}(\theta,z,t)$ is the corresponding array of nodal displacements. Approximate equations of motion are obtained by using Hamilton's principle. This procedure is described more completely in Appendix B in order not to disrupt the main text. The result may be expressed in the form

$$\mathbf{K}_1\mathbf{U} + \mathbf{K}_2\mathbf{U}_{,\theta} + \mathbf{K}_3\mathbf{U}_{,z} - \mathbf{K}_4\mathbf{U}_{,\theta\theta} - \mathbf{K}_5\mathbf{U}_{,\theta z} - \mathbf{K}_6\mathbf{U}_{,zz} + \mathbf{M}\ddot{\mathbf{U}} = \mathbf{F}, \tag{2.3.2}$$

where the $\mathbf{K}_i$, for $i = 1,2,3,\ldots,6$, are separated stiffness matrices, $\mathbf{M}$ is the mass matrix, and $\mathbf{F}$ is a consistent force vector. A comma in equation (2.3.2) indicates differentiation with respect to any spatial variable that follows. The detailed forms of the $\mathbf{K}_i$, $\mathbf{M}$, and $\mathbf{F}$ are also given in Appendix B.

2.3.3 Approximate wavefunctions

In seeking harmonic wave solutions, the consistent force vector and the resulting displacement interpolation function are assumed to be: (i) time harmonic and (ii) periodic in the circumferential coordinate. Consequently they can be expressed in a Fourier series form as

$$\mathbf{F}(\theta,z,t) = \mathrm{e}^{-\mathrm{j}\omega t}\mathbf{F}(\theta,z) = \mathrm{e}^{-\mathrm{j}\omega t}\sum_{n=-\infty}^{n=\infty}\mathrm{e}^{\mathrm{j}n\theta}\mathbf{F}_n(z), \tag{2.3.3a}$$

and

$$\mathbf{U}(\theta,z,t) = \mathrm{e}^{-\mathrm{j}\omega t}\mathbf{U}(\theta,z) = \mathrm{e}^{-\mathrm{j}\omega t}\sum_{n=-\infty}^{n=\infty}\mathrm{e}^{\mathrm{j}n\theta}\mathbf{U}_n(z), \tag{2.3.3b}$$

respectively. (Note the similarities between equations (2.3.3b) and (A.2.1) of Appendix A.) Combining equations (2.3.2) and (2.3.3) yields a system of ordinary differential equations for the Fourier coefficients, $\mathbf{U}_n$, in terms of z. The n^{th} term takes the form

$$\left(\mathbf{K}_1 + \mathrm{j}n\mathbf{K}_2 + n^2\mathbf{K}_4 - \omega^2\mathbf{M}\right)\mathbf{U}_n + \left(\mathbf{K}_3 - \mathrm{j}n\mathbf{K}_5\right)\mathbf{U}_{n,z} - \mathbf{K}_6\mathbf{U}_{n,zz} = \mathbf{F}_n. \tag{2.3.4}$$

Applying the Fourier integral transform to equation (2.3.4) transforms the governing equations from the spatial (z) domain to the (axial) wavenumber (k_n) domain. The resulting equations can be expressed as

$$\left(\mathbf{K}_1 + \mathrm{j}n\mathbf{K}_2 + n^2\mathbf{K}_4 - \omega^2\mathbf{M}\right)\overline{\mathbf{U}}_n + \mathrm{j}k_n\left(\mathbf{K}_3 - \mathrm{j}n\mathbf{K}_5\right)\overline{\mathbf{U}}_n + k_n^2\mathbf{K}_6\overline{\mathbf{U}}_n = \overline{\mathbf{F}}_n, \tag{2.3.5}$$

where an over bar indicates a Fourier transformed variable.

Equation (2.3.5) is quadratic in k_n but it can be written in first order form as

$$\left[\mathbf{A}(n,\omega) - k_n\mathbf{B}\right]\overline{\mathbf{Q}}_n = \overline{\mathbf{P}}_n, \tag{2.3.6}$$

where

$$\mathbf{A}(n,\omega) = \begin{bmatrix} \mathbf{0} & \mathbf{I} \\ \left(\mathbf{K}_1 + \mathrm{j}n\mathbf{K}_2 + n^2\mathbf{K}_4 - \omega^2\mathbf{M}\right) & \mathrm{j}\left(\mathbf{K}_3 - \mathrm{j}n\mathbf{K}_5\right) \end{bmatrix}, \tag{2.3.7a}$$

$$\mathbf{B} = \begin{bmatrix} \mathbf{I} & \mathbf{0} \\ \mathbf{0} & -\mathbf{K}_6 \end{bmatrix}, \tag{2.3.7b}$$

$$\overline{\mathbf{Q}}_n = \begin{Bmatrix} \overline{\mathbf{U}}_n \\ k_n\overline{\mathbf{U}}_n \end{Bmatrix}, \tag{2.3.7c}$$

$$\overline{\mathbf{P}}_n = \begin{Bmatrix} \mathbf{0} \\ \overline{\mathbf{F}}_n \end{Bmatrix}, \tag{2.3.7d}$$

and $\mathbf{0}$ ($\mathbf{I}$) is the null (identity) matrix. Note that equations (2.3.5) and (2.3.6) take the form

of three parameter, algebraic eigensystems in n, ω, and k_n when $\overline{\mathbf{F}}_n$ is the null matrix. The $\overline{\mathbf{U}}_n$ and $\overline{\mathbf{Q}}_n$ can be written as a modal summation of the resulting normal vectors. While any one of n, ω, or k_n can be used as the eigenvalue parameter, specific values are assigned here to n which must be an integer.

Consider now the more complicated but common form of the two eigenvalue problems. A nontrivial solution of the homogeneous form of equation (2.3.6) requires that the determinant of the coefficient matrix $\overline{\mathbf{Q}}_n$ vanish for a given ω and n. The resulting polynomial equation in k_n, whose solution yields $12N+6$ roots, is used as the (approximate) dispersion relation for the pipe. Each root, k_{nm} where m is a positive integer indicating the m^{th} axial mode, is an eigenvalue which represents an axial wavenumber for the assigned frequency and circumferential wavenumber, n. As before, a real axial wavenumber corresponds to a propagating wave travelling along an infinitely long pipe. An imaginary (complex) axial wavenumber, on the other hand, represents a spatially decaying, non-propagating (evanescent) mode in a semi-infinitely long pipe that decays exponentially as the axial (z) coordinate increases from the mode's source of excitation. One-half of the $12N + 6$ axial wavenumbers correspond to wave modes which are admissible solutions for non-negative axial coordinates; the remaining half are admissible solutions for non-positive axial coordinates. (It is assumed that the first [last] $6N + 3$ wavenumbers are admissible for non-negative [non-positive] axial coordinates.) Associated with each eigenvalue k_{nm}, is a right and left eigenvector, $\boldsymbol{\phi}^{\text{R}}_{nm}$, and $\boldsymbol{\phi}^{\text{L}}_{nm}$, respectively. The approximate wavenumbers play the same role as those found by using equation (2.2.11). On the other hand, the $\boldsymbol{\phi}^{\text{R}}_{nm}$ replace equation (2.2.10) when describing the radial variation of the displacement field. Approximate (displacement) Green's functions are constructed next by using the approximate wavefunctions.

2.3.4 Green's displacement function

The displacement field induced by a harmonic, point-like excitation is synthesized by linearly superimposing a pipe's normal modes. From the definition of the eigenvalue problem,

the eigenvectors satisfy the relations

$$[\mathbf{A}(n,\omega) - k_{nm}\mathbf{B}]\,\boldsymbol{\phi}^{\mathrm{R}}_{nm} = \mathbf{0}, \tag{2.3.8a}$$

$$\left[\mathbf{A}^{\mathrm{T}}(n,\omega) - k_{nm}\mathbf{B}^{\mathrm{T}}\right]\boldsymbol{\phi}^{\mathrm{L}}_{nm} = \mathbf{0}, \tag{2.3.8b}$$

$$\left(\boldsymbol{\phi}^{\mathrm{L}}_{nm}\right)^{\mathrm{T}}\mathbf{B}\boldsymbol{\phi}^{\mathrm{R}}_{np} = B_{nm}\delta_{mp}, \tag{2.3.8c}$$

and

$$\left(\boldsymbol{\phi}^{\mathrm{L}}_{nm}\right)^{\mathrm{T}}\mathbf{A}(n,\omega)\boldsymbol{\phi}^{\mathrm{R}}_{np} = k_{nm}B_{nm}\delta_{mp}, \tag{2.3.8d}$$

where δ_{mp} is the Kronecker delta. The right and left eigenvectors are partitioned into the following upper and lower halves:

$$\boldsymbol{\phi}^{\mathrm{R}}_{nm} = \begin{bmatrix}\boldsymbol{\phi}^{\mathrm{R}}_{nm\mathrm{u}} & \boldsymbol{\phi}^{\mathrm{R}}_{nm\mathrm{l}}\end{bmatrix}^{\mathrm{T}}, \tag{2.3.9a}$$

and

$$\boldsymbol{\phi}^{\mathrm{L}}_{nm} = \begin{bmatrix}\boldsymbol{\phi}^{\mathrm{L}}_{nm\mathrm{u}} & \boldsymbol{\phi}^{\mathrm{L}}_{nm\mathrm{l}}\end{bmatrix}^{\mathrm{T}}. \tag{2.3.9b}$$

Subscripts u and l denote the upper and lower halves, respectively[1]. Vector $\overline{\mathbf{Q}}_n$ can be represented, for a nonvanishing $\overline{\mathbf{P}}_n$, in the transformed domain of the linear eigenvalue problem by summing the $12N + 6$ right eigenvectors as

$$\overline{\mathbf{Q}}_n = \sum_{m=1}^{12N+6} Q_{nm}\boldsymbol{\phi}^{\mathrm{R}}_{nm} = \sum_{m=1}^{12N+6} \frac{\left(\boldsymbol{\phi}^{\mathrm{L}}_{mn}\right)^{\mathrm{T}}\overline{\mathbf{P}}_n}{(k_{nm} - k_n)B_{nm}}\boldsymbol{\phi}^{\mathrm{R}}_{nm}. \tag{2.3.10}$$

Use has been made here of equations (2.3.6) and (2.3.8). Then the solution vector $\overline{\mathbf{U}}_n$, which occupies the upper half of $\overline{\mathbf{Q}}_n$, can be written as

$$\overline{\mathbf{U}}_n = \sum_{m=1}^{12N+6} \frac{\left(\boldsymbol{\phi}^{\mathrm{L}}_{mn\mathrm{l}}\right)^{\mathrm{T}}\overline{\mathbf{F}}_n}{(k_{nm} - k_n)B_{nm}}\boldsymbol{\phi}^{\mathrm{R}}_{nm\mathrm{u}}, \tag{2.3.11}$$

[1]Unless noted otherwise, the right eigenvectors are normalized by using a scheme that makes the *magnitude* of the vector norm of their *upper halves* (the mode shapes) unity; the directions returned by the eigenvalue solver are unaltered.

by using equations (2.3.6), (2.3.8), and (2.3.10). Finally, the inverse Fourier transform applied to equation (2.3.11) gives the (displacement) response of the cylinder to the n^{th} circumferential harmonic in the spatial domain, $\overline{\mathbf{U}}_n(z)$, as

$$\mathbf{U}_n(z) = \frac{1}{2\pi} \sum_{m=1}^{12N+6} \int_{-\infty}^{\infty} \frac{\left(\boldsymbol{\phi}^{\mathrm{L}}_{mnl}\right)^{\mathrm{T}} \overline{\mathrm{F}}_n}{(k_{nm} - k_n) B_{nm}} \boldsymbol{\phi}^{\mathrm{R}}_{nmu} \mathrm{e}^{\mathrm{j}k_n z} \mathrm{d}k_n. \tag{2.3.12}$$

A point force applied at $r = r_0$, $\theta = 0$, $z = 0$ can be represented in the spatial domain as

$$\mathbf{F}(\theta, z) = \delta(\theta)\delta(z)\mathbf{F}_0, \tag{2.3.13}$$

where δ is the Dirac delta function and $\mathbf{F}_0$ describes the radial distribution of the force vector. Subscript 0 denotes a quantity associated with the point force. The Dirac delta function is approximated circumferentially, as shown in Figure 2.3. It can be observed that a "narrow" pulse of uniform intensity $q_0 = (2r_0\theta_0)^{-1}$, which extends over a circumferential distance $2r_0\theta_0$, is employed to avoid the non-convergence of the Dirac delta function[2]. Then

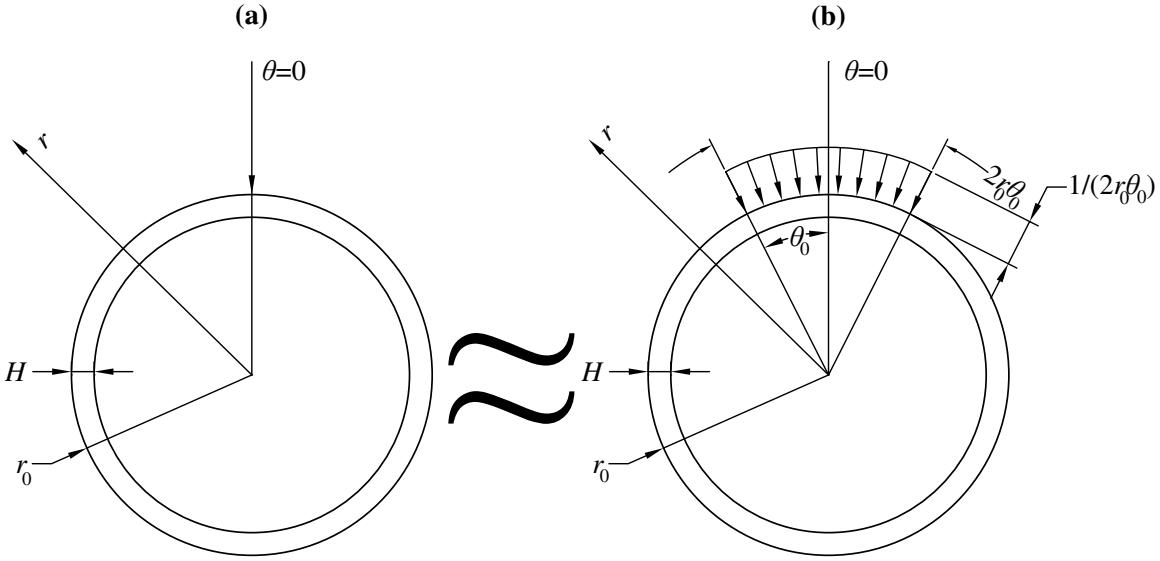

Figure 2.3. Illustrating the approximation of (a) a point force with (b) a uniform pulse.

[2]All terms in a Fourier series expansion of the Dirac delta function have an amplitude of $1/(2\pi)$ which does not decrease with increasing harmonic number.

a force which is applied at the point $r = r_0$, $\theta = 0$, $z = 0$ can be approximated spatially as

$$\mathbf{F}(\theta, z) = \begin{cases} \dfrac{1}{2r_0\theta_0}\delta(z)\mathbf{F}_0 & \text{if } -\theta_0 \leq \theta \leq \theta_0, \\ 0 & \text{otherwise.} \end{cases} \tag{2.3.14}$$

Applying the Fourier transform to the Fourier series expansion of equation (2.3.14) transforms the n^{th} term of the force's approximation from the spatial to the wavenumber domain. Substituting the result into equation (2.3.12) leads to the n^{th} circumferential harmonic of the Green's function in the spatial domain to be

$$\mathbf{U}_n(z) = \frac{\text{sinc}(n\theta_0)}{4\pi^2 r_0} \sum_{m=1}^{12N+6} \int_{-\infty}^{\infty} \frac{\left(\boldsymbol{\phi}^{\text{L}}_{mn\text{l}}\right)^{\text{T}} \overline{\mathbf{F}}_0}{(k_{nm} - k_n)B_{nm}} \boldsymbol{\phi}^{\text{R}}_{nm\text{u}} \text{e}^{\text{j}k_n z} \text{d}k_n. \tag{2.3.15}$$

Cauchy's residue theorem is applied to equation (2.3.15) to give the n^{th} circumferential mode of the Green's function as

$$\mathbf{U}_n(z) = \begin{cases} \dfrac{-\text{jsinc}(n\theta_0)}{2\pi r_0} \displaystyle\sum_{m=1}^{6N+3} \frac{\left(\boldsymbol{\phi}^{\text{L}}_{mn\text{l}}\right)^{\text{T}} \overline{\mathbf{F}}_0}{B_{nm}} \boldsymbol{\phi}^{\text{R}}_{nm\text{u}} \text{e}^{\text{j}k_{nm} z}, & z \geq 0, \\ \dfrac{\text{jsinc}(n\theta_0)}{2\pi r_0} \displaystyle\sum_{m=6N+4}^{12N+6} \frac{\left(\boldsymbol{\phi}^{\text{L}}_{mn\text{l}}\right)^{\text{T}} \overline{\mathbf{F}}_0}{B_{nm}} \boldsymbol{\phi}^{\text{R}}_{nm\text{u}} \text{e}^{\text{j}k_{nm} z}, & z \leq 0. \end{cases} \tag{2.3.16}$$

The contour of integration, which is applied in conjunction with Cauchy's residue theorem, is selected by using the radiation condition. This condition requires that (i) waves radiate outward from the applied force, and (ii) the displacement field remains finite. Substituting equation (2.3.16) into equation (2.3.3b) and using the result, in turn, in equation (2.3.1) gives the Green's displacement function for a harmonic force. The approximate strain and stress fields can be derived straightforwardly from this function by using equations (A.3.2) and (A.4.2) of Appendix A.

The displacement response to a multi-frequency, input force can be found by merely superimposing the responses caused by each individual frequency component because linear

elasticity is assumed. Hence the displacement at the radial coordinates of the finite element nodal surfaces can be written as

$$\mathbf{U}(\theta, z, t) = \frac{-\mathrm{j}}{4\pi^2 r_0} \int_{-\infty}^{\infty} \overline{p}(\omega) \mathrm{e}^{-\mathrm{j}\omega t} \sum_{n=-\infty}^{n=\infty} \mathrm{sinc}(n\theta_0) \left[\sum_{m=1}^{6N+3} \frac{\left(\boldsymbol{\phi}^{\mathrm{L}}_{mn\mathrm{l}}\right)^{\mathrm{T}} \overline{\mathbf{F}}_0}{B_{nm}} \boldsymbol{\phi}^{\mathrm{R}}_{nm\mathrm{u}} \mathrm{e}^{\mathrm{j}k_{nm}z} \right] \mathrm{e}^{\mathrm{j}n\theta} \mathrm{d}\omega, \tag{2.3.17a}$$

for $z \geq 0$, and

$$\mathbf{U}(\theta, z, t) = \frac{\mathrm{j}}{4\pi^2 r_0} \int_{-\infty}^{\infty} \overline{p}(\omega) \mathrm{e}^{-\mathrm{j}\omega t} \sum_{n=-\infty}^{n=\infty} \mathrm{sinc}(n\theta_0) \left[\sum_{m=6N+4}^{12N+6} \frac{\left(\boldsymbol{\phi}^{\mathrm{L}}_{mn\mathrm{l}}\right)^{\mathrm{T}} \overline{\mathbf{F}}_0}{B_{nm}} \boldsymbol{\phi}^{\mathrm{R}}_{nm\mathrm{u}} \mathrm{e}^{\mathrm{j}k_{nm}z} \right] \mathrm{e}^{\mathrm{j}n\theta} \mathrm{d}\omega, \tag{2.3.17b}$$

for $z \leq 0$. The $\overline{p}(\omega)$ in equation (2.3.17) is the Fourier transform of the input force which scales the amplitude and phase shifts the Green's function for each of its frequency components. The approximate displacement field throughout the entire pipe, **u**, can be found by invoking equation (2.3.1).

2.4 Overview of Computer Implementation

Computer programs to calculate the approximate wavefunctions are implemented using MATLAB® (by the MATHWORKS®) scripts and functions. Element matrices are computed first in closed (symbolic) form [106] by utilizing the (pre R2008b[3]) Symbolic Math Toolbox™ and Extended Symbolic Math Toolbox Software™ to implement equation (B.4.7) for a single element. The process is simplified by choosing the "middle" node to coincide with the geometric centre of the finite element. Then the determinant of the Jacobian matrix of the transform between r and ζ is a constant. See Section B.5 of Appendix B for details. The outputs from the symbolic engines are used as the basis of creating MATLAB® functions

[3] MATHWORKS® changed the symbolic engine in MATLAB® R2008b from a Maplesoft® Maple™ based engine to a MuPAD® (by SciFace Software GmbH & Co. KG) based engine. It was found that the new engine performed too slowly to be useful for this procedure. Hence, Maple™ 13.02, developed by Maplesoft®, and the complementary Maple Toolbox for MATLAB® was used subsequently.

to compute the element matrices. A careful choice of the names given to variables in the symbolic computations and a judicious use of the "find and replace" command in a "regular expression" capable text editor minimizes manual typing errors. Indeed minimal "hand written" code is required to complete the functions. Furthermore, functions to compute the element matrices are simplified greatly and, consequently, the software runs faster when components of the element matrices are evaluated from closed form expressions rather than by numerical integration. A conventional "direct" assembly method [107] is used to create global stiffness and mass matrices from the individual element matrices. This result is integrated into functions that also take, as input, the material and dimensional information of the unblemished pipe to produce the approximate wavefunctions. Documentation of the above process is located, along with representative annotated code listings, in Appendix C. The overall process represents a successful first step towards developing computer code that, itself, writes computer code for the finite element analysis.

2.5 Illustrative Example

2.5.1 Preamble

Computer code has been written to (a) form the previously described eigensystem, (b) solve the resulting eigenvalue problem, and (c) perform the summations and integrations inherent to equation (2.3.17), as described previously. As an illustration, a typical 3 inch Nominal Pipe Size (NPS) [80 mm Diameter Nominal (DN)], Schedule 40, carbon steel pipe, whose assumed properties[4] are summarized in Table 2.1, is considered. This pipe is used consistently for all the remaining numerical simulations. It is subjected invariably to the commonly used, Gaussian modulated sine wave excitation detailed in Appendix D. Moreover, time is

[4]Note that only two elastic properties and dimensional properties are independent. The Lamé constants, as well as the outer diameter and wall thickness, are specified directly. The remaining properties are found from these assigned values by applying standard linear elasticity equations and simple geometrical relations.

Table 2.1. Properties assigned to the unblemished pipe.

Property	Assigned Value
Density, ρ, slug/ft^3 (kg m^{-3})	15.39 (7932)
Outer diameter, D_o, in (mm)	3.496 (88.8)
Wall thickness, H, in (mm)	0.220 (5.59)
Mean radius, R, in (mm)	1.638 (41.60)
Thickness to mean radius ratio, (H/R)	0.134
Young's modulus, E, ksi (GPa)	31,460 (216.9)
Lamé constant (Shear modulus), μ (G), ksi (GPa)	12,230 (84.3)
Lamé constant, λ, ksi (GPa)	16,410 (113.2)
Ratio of Lamé constants, (λ/μ)	1.34
Poisson's ratio, ν	0.286

always measured relative to the initial instant that this excitation is applied. The excitation is orientated radially, unless specified otherwise, i.e., normal to the pipe's external surface, at $\theta = 0$ in the plane $z = 0$. Moreover, the (body force) amplitude is taken invariably as $A = \mu/H$ which corresponds to a nondimensionalized unit amplitude. This particular pipe is selected because it is commercially important. At the end of 1997, for example, there was approximately 40,300 miles (64 900 km) of such pipe in industrial use as energy related pipeline in Alberta, Canada [2]. Consequently it has been studied extensively in, for example, [70, 71]. The pipe's displacement is represented by the radial component on its outer surface at $\theta = 0$ and $z^* = z/H = 5.1$, and $\theta = 0$ and $z^* = 25.5$, where a superscript asterisk indicates a nondimensionalized variable. These locations correspond to simple axial offsets from the force's application point. Ten finite elements are used to uniformly discretise the pipe's wall thickness, H. The individual H_k are presumed to be identical for simplicity. Circumferential angle, $2\theta_0$, over which the spatial pulse approximates the Dirac delta function, is taken to be 0.002 radians (0.1°). Circumferential wavenumbers n, from 0 to ±16, and all the corresponding axial modes are incorporated into the computations.

2.5.2 Results and discussion

Figure 2.4 (a) presents the magnitudes of the spectral densities of the nondimensional, radi-

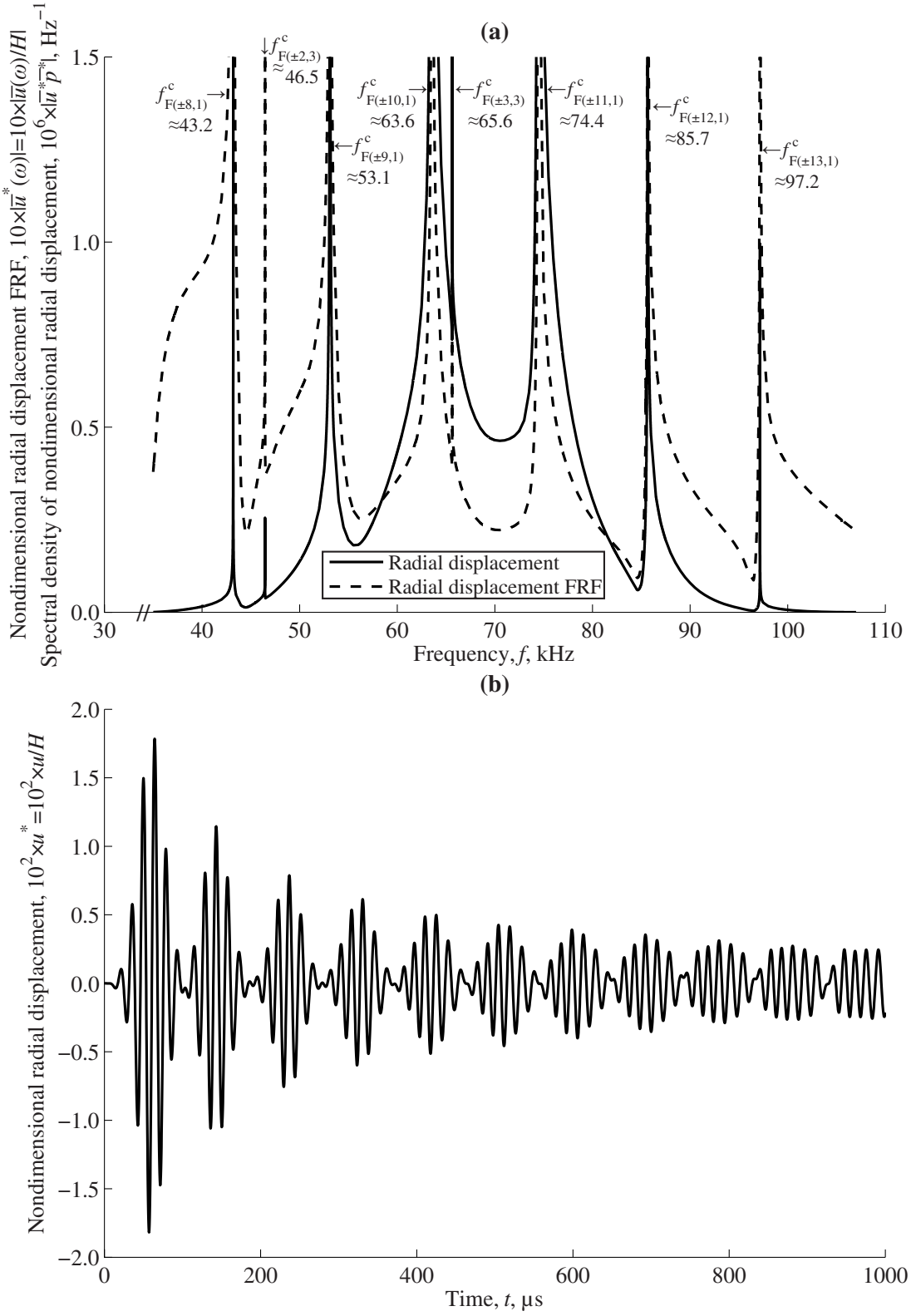

Figure 2.4. Giving (a) the spectral density of the radial displacement on the pipe's outer surface at $\theta = 0$, $z^* = z/H = 5.1$ before and after convolution with the excitation and (b) the latter's time history.

al displacement's FRF, before and after its convolution with the excitation at a purely axial offset of $5.1H$. The frequency range considered is 35 kHz to 107 kHz. It can be observed from an examination of Table 2.2, where the pipe's cutoff frequencies below 150 kHz are tabulated, and Figure 2.4 (a) that the "peaks" of a pipe's radial FRF occur at modal cutoff frequencies. The corresponding wavenumbers are zero at these particular frequencies. This behaviour can be observed also in Figures 2.5 (a) and 2.6 (a) where analogous information is shown for two representative individual modes. (Also shown in these two figures are the (axial) wavenumber and the phase and group wave speeds.) Although the character [108] or frequency locations [101] of the peaks in a FRF are seen later in Chapter 4 to be modified in the presence of a defective wall thinning, they are invariant here. Cutoff frequencies of the noticeably excited modes given in Figure 2.4 (a) are labelled as $f^{\mathrm{c}}_{\mathrm{F}(n,m)}$ where superscript c

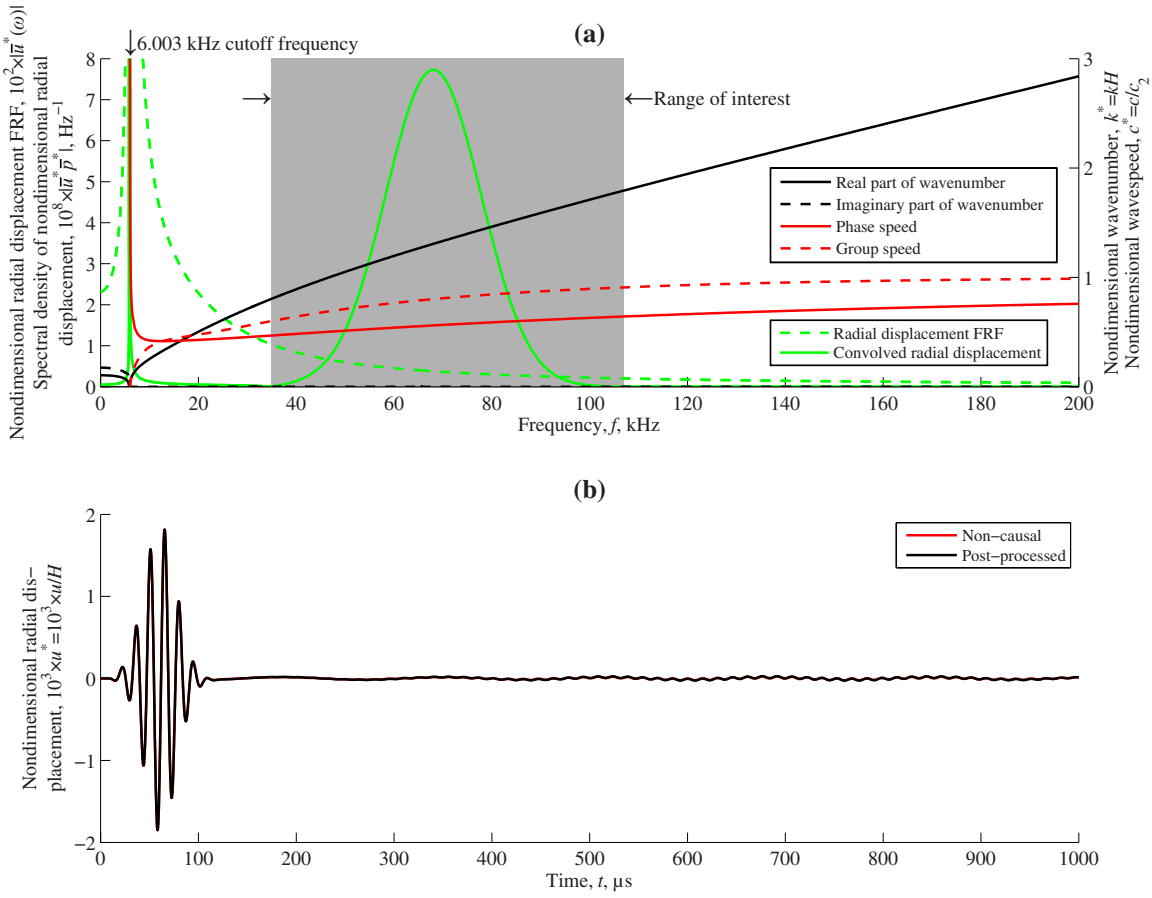

Figure 2.5. Behaviour of the F(3,1) mode on the pipe's outer surface at $\theta = 0$, $z^* = z/H = 5.1$.

Table 2.2. Cutoff frequencies below 150 kHz obtained from "exact" theory and SAFE.

Mode(s)	"Exact" cutoff frequency, kHz	Cutoff frequency from SAFE, kHz
T(0, 1)	0.000	0.000
L(0, 1)	0.000	0.034
F(±1, 1)	0.000	0.055
F(±2, 1)	2.153	2.154
F(±3, 1)	6.002	6.003
F(±4, 1)	11.281	11.282
F(±1, 2)	12.480	12.480
F(±5, 1)	17.806	17.806
L(0, 2)	20.921	20.921
F(±2, 2)	24.960	24.960
F(±6, 1)	25.405	25.406
F(±1, 3)	29.454	29.454
F(±7, 1)	33.918	33.918
F(±3, 2)	37.439	37.439
F(±8, 1)	43.196	43.197
F(±2, 3)	46.463	46.463
F(±4, 2)	49.917	49.917
F(±9, 1)	53.112	53.112
F(±5, 2)	62.393	62.393
F(±10, 1)	63.553	63.554
F(±3, 3)	65.628	65.628
F(±11, 1)	74.427	74.426
F(±6, 2)	74.867	74.867
F(±4, 3)	85.467	85.467
F(±12, 1)	85.651	85.651
F(±7, 2)	87.338	87.338
F(±13, 1)	97.164	97.163
F(±8, 2)	99.807	99.807
F(±5, 3)	105.548	105.548
F(±14, 1)	108.906	108.907
F(±9, 2)	112.272	112.273
F(±15, 1)	120.840	120.839
F(±10, 2)	124.734	124.734
F(±6, 3)	125.696	125.696
F(±16, 1)	132.919	132.921
F(±11, 2)	137.192	137.192
F(±7, 3)	145.819	145.819
F(±12, 2)	149.645	149.646

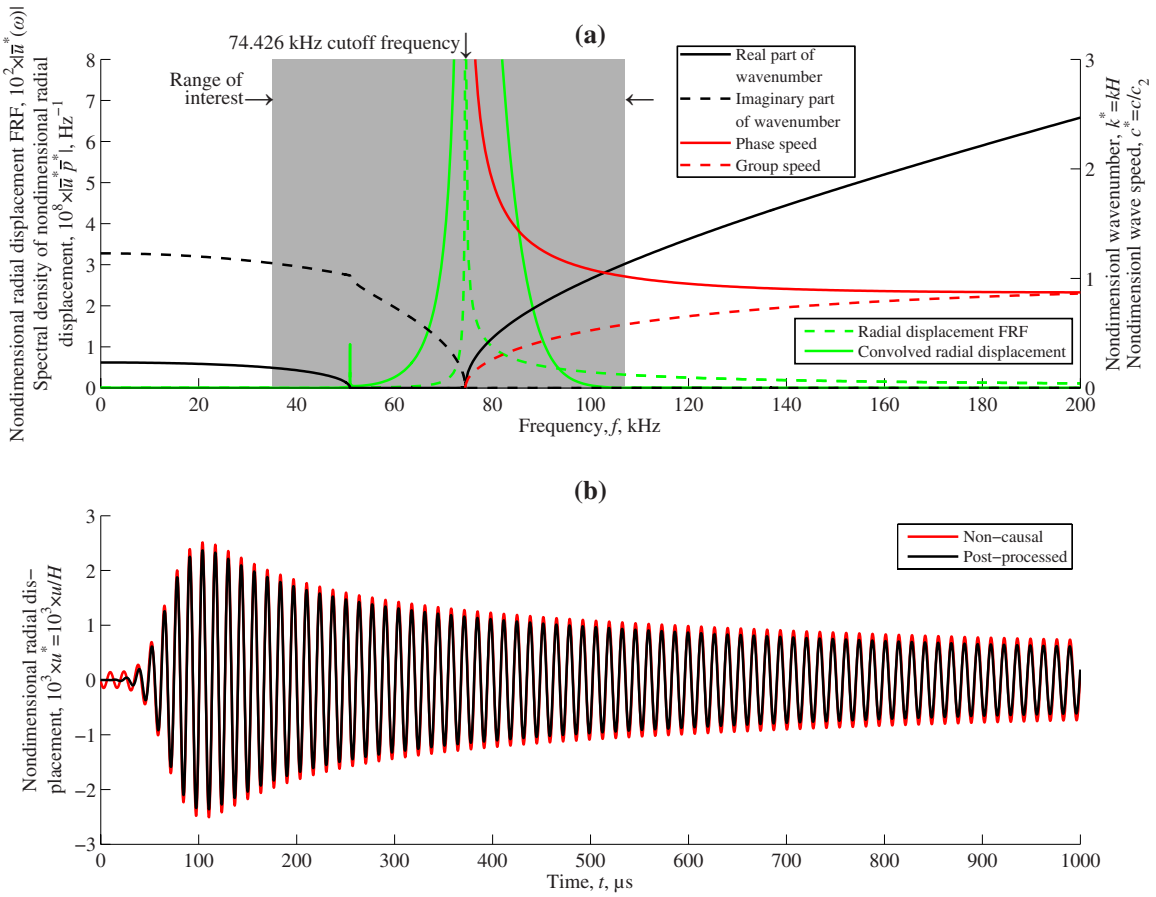

Figure 2.6. Behaviour of the F(11,1) mode on the pipe's outer surface at $\theta = 0$, $z^* = z/H = 5.1$.

indicates a cutoff frequency. Their numerical values are rounded in Figure 2.4 (a) for visual clarity. Subscript F in the label of f^{c} represents a flexural mode[5] with the circumferential wavenumber (n) and order (m) given in parentheses. A sharp increase in the magnitude of a FRF at a cutoff frequency arises because the corresponding B_{nm} in equation (2.3.17) tends to zero as the cutoff frequency is approached, i.e., a singularity happens in the nm mode's FRF. This feature occurs because there is a repeated eigenvalue[6] at each cutoff frequency. Hence a defective[7] eigensystem exists. Consequently the corresponding left and right eigenvectors are orthogonal to the $\boldsymbol{B}$ matrix defined in equation (2.3.7b). As a result B_{nm} also

[5]Modes are labelled by using the standard convention employed in [81].

[6]A repeated eigenvalue is guaranteed to exist at a cutoff frequency because zero is its own negative complex conjugate and both k_{nm} and $-\tilde{k}_{nm}$ are eigenvalues.

[7]A defective eigensystem is one in which an eigenvalue is repeated, say integer r times, but fewer than r unique (right) eigenvectors exist for the repeated eigenvalue [109].

becomes zero [109]. A physical, but somewhat philosophical explanation for singularities having large displacement amplitudes that coincide with cutoff frequencies can be found in the wavelength at a cutoff frequency. A wave mode's wavenumber is zero at its cutoff frequency, which corresponds to a wavelength that is infinitely long. No boundary conditions which restrict a pipe's motion have been applied to the pipe's ends at (plus and minus) infinity. Such a pipe has no inherent resistance to a wave mode's motions at a cutoff frequency so that large displacement amplitudes are observed. Note that, despite the assumed absence of material damping, the "resonant"-like displacement amplitudes given in Figure 2.4 (a), while large, are surprisingly not infinite. This apparently abnormal behaviour is attributable to numerical truncations and a small (1 Hz in a neighbourhood within 500 Hz of a cutoff frequency) but necessarily finite frequency increment not permitting a precise coincidence with a cutoff frequency. On the other hand, the cutoff frequencies obtained from SAFE are, with the exception of the L(0,1) and F(1,1) modes, within an acceptable 2 Hz or less of those based on "exact" three dimensional elasticity found by applying equation (2.2.11). This observation is corroborated by comparing the second and third columns of Table 2.2.

Figure 2.4 (b) shows the time history produced by superimposing the computed histories obtained, on a mode by mode basis[8], from the inverse Fourier transformation of the convolved FRF of each mode considered. (Figure 2.4 is demonstrated in Chapter 3 to reasonably represent measurements made on a physical specimen. The representation is improved even further when measured material properties and the dynamic behaviour of the measurement instrumentation are incorporated, as shown in Chapter 3.) The inverse Fourier transform is approximated by applying a standard trapezoidal integration scheme involving a variable frequency step to the transform's basic definition, with the approximation truncated outside the 35 kHz to 107 kHz range of interest. Moreover, advantageous use is made of the property that the displacement response to a real excitation is also real. This important property implies that the response at a negative frequency is the complex con-

[8]Note that the integration in equation (2.3.17) is performed before the summations.

jugate of the corresponding positive frequency. Hence, the response needs to be computed only at positive frequencies[9].

Care needs to be taken when performing the inverse Fourier transform because its direct application does not explicitly include initial conditions unlike, say, an inverse Laplace transform. Therefore, initial conditions are incorporated by enforcing causality on the sum of the homogeneous and particular solutions. The inverse Fourier transforms of the convolved FRFs are particular solutions to the equations of motion. However, they may have non-zero displacements or velocities at the instant, $t = 0$, that the excitation is applied first. "Extraneous" values are eliminated by superimposing on the particular solution, homogeneous solutions that are constrained to satisfy causality. The homogeneous solutions are sinusoids having frequencies identical to the cutoff frequencies of the unblemished pipe. Their amplitudes and phases are found from the extraneous displacement and velocity values at $t = 0$ by constraining the superimposed values to be zero. Further details are provided in Appendix E. Experience has shown that the homogeneous solution hardly contributes to the response of a mode whose cutoff frequency is outside the excitation's principal bandwidth. See Figure 2.5. Otherwise the converse is true, as indicated in Figure 2.6. The former behaviour is expected intuitively because the spectral density of a mode whose cutoff frequency lies outside the excitation's bandwidth resembles that of the excitation which is essentially causal. However a resonance is excited strongly in the opposite situation. This behaviour is supported by the distribution of energy[10] in the spectral densities of the convolved radial displacements. In the first case the energy is distributed more broadly over a range of frequencies than in the second case where the energy is localized in a narrow band of frequencies around the cutoff frequency. Although the peak radial displacements are comparable in Figures 2.5 and 2.6 (b), the radial displacement's time history shown in Figure 2.6 (b) clearly "rings" while that illustrated in Figure 2.5 (b) does not. Consequently,

[9]While two-sided (Fourier) transforms are used in the derivations, all figures, unless noted otherwise, present single-sided transforms that increase the amplitude of the nonzero frequency components by a factor of two.

[10]The term "energy" is used here in the signal processing sense [110, 111].

after a brief initial period, those modes having cutoff frequencies in the excitation's principal bandwidth dominate the convolved FRF and, hence, a displacement's time history. Figures 2.5 and 2.6 give representative radial displacement responses to exemplify the two contrasting situations at the same location of the illustrative pipe. They confirm the basic nature described earlier of the noticeably larger response component around a cutoff frequency.

Figure 2.7 shows the magnitude of the reassigned pseudo Margenau-Hill time-frequency distribution for the radial displacement history given in Figure 2.4 (b). The Margenau-Hill time-frequency distribution is an integral transform which is conceptually similar to a short period DFT or wavelet transform. It allows a nonstationary signal's frequency evolution to be visualized over time. This particular transform is selected because it appears to simultaneously reduce "smearing" on the time and frequency axes [112]. The transform is described more fully in [113]. Figures 2.7 (a) and (b) use linear and logarithmic scales for the amplitude of the transform, respectively. The amplitude scale in Figure 2.7 (a) has been "clipped[11]" at 0.01 to show more clearly the relatively small amplitudes that occur during the pipe's ringing. On the other hand, the entire range of amplitudes is presented in Figure 2.7 (b). The logarithmic scale aids the visualization of small response amplitudes but it also reduces the clarity of the image because the effects of noise are also emphasised. Both figures show that the F(±9,1), F(±10,1), F(±11,1), and F(±12,1) modes dominate the pipe's response after about 150 μs. Figure 2.7 (b), on the other hand, enhances somewhat the contributions of the additionally labelled, weakly excited F(±8,1) and F(±13,1) modes to make them more visible. The initial broadband behaviour followed by the ringing of each mode is indicated in Figure 2.7 by the broad peaks in the frequency direction narrowing after about 150 μs. Therefore, the reassigned pseudo Margenau-Hill time-frequency distribution is a useful tool for visualizing the temporal evolution of a signal. Cutoff frequencies, however, give more readily obtained, identifiable features that can be related more easily to a

[11]The value of 0.01 was assigned also to higher values.

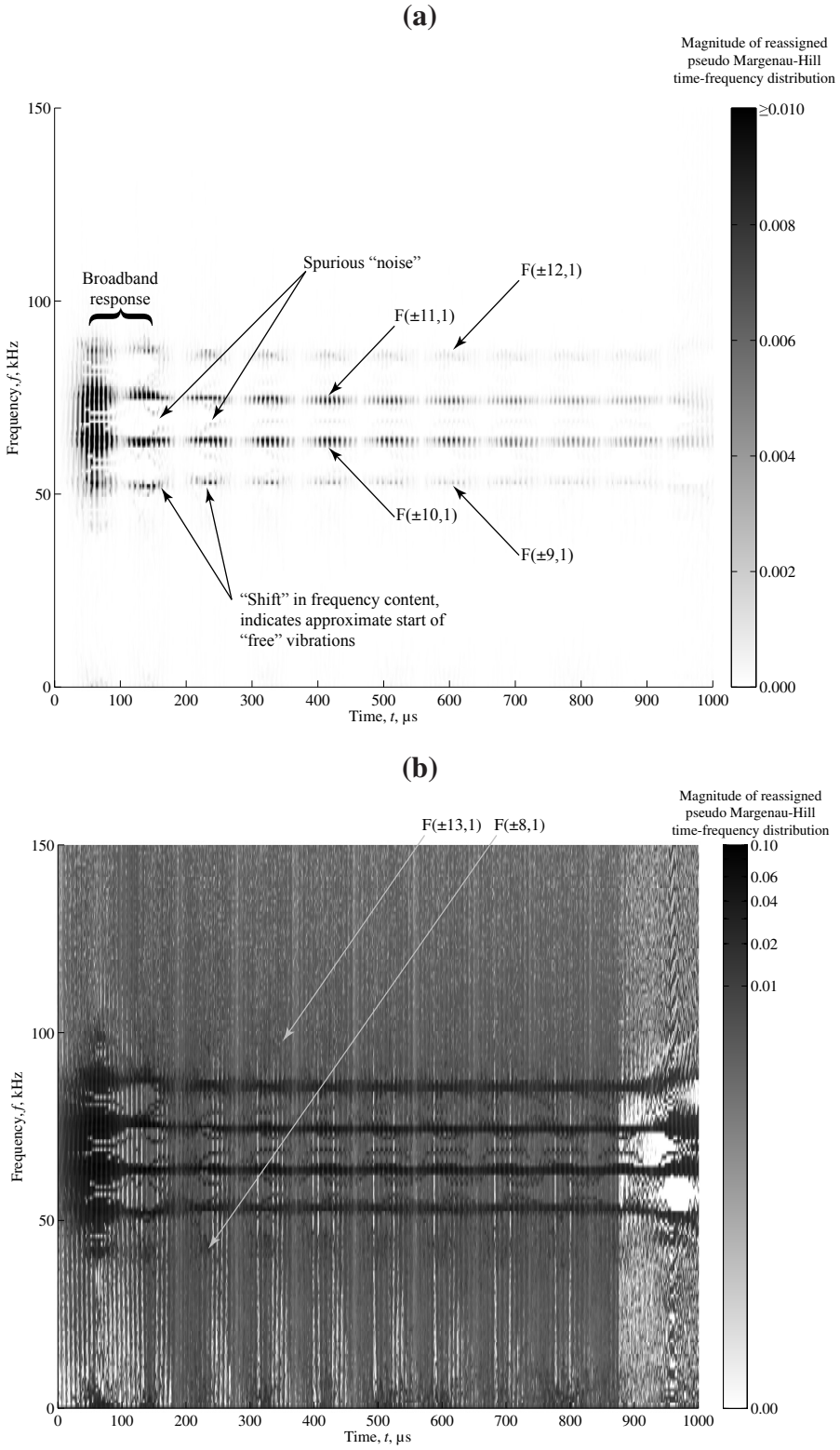

Figure 2.7. Magnitude of the reassigned pseudo Margenau-Hill time-frequency distribution for the response history given in Figure 2.4 (b) using (a) linear and (b) logarithmic scales.

mathematical model. Consequently, they are used in the next chapter to recover a homogeneous, isotropic pipe's two independent elastic constants and wall thickness from its known density and outer diameter by utilizing only a single ultrasonic measurement.

To better interpret Figure 2.4, Figure 2.8 (a) gives the (nondimensional) maximax radial displacement on the pipe's outer surface at $\theta = 0$, $z^* = z/H = 5.1$ for modes which propagate over some or all of the frequency range of interest. They are sorted by descending amplitudes with corresponding arrival times shown in Figure 2.8 (b). As an aside, the largest maximax radial displacement of the remaining non-propagating and evanescent modes is approximately 7.3×10^{-6}. The latter value corresponds to an axisymmetic mode. It is about three orders of magnitude smaller than those of the F($\pm$10, 1) modal contributions. On the other hand, the largest maximax radial displacement for a mode having a circumferential wavenumber of 16 is even smaller, being less than 3.6×10^{-7}. These clear differences suggests that the error introduced by neglecting circumferential harmonics whose wavenumber, n, is outside $\pm$16 is negligible *at distances sufficiently removed* from the force's application point. Figures 2.8 (c) and (d) present identical information to Figures 2.8 (a) and (b) but with the modal responses sorted by increasing arrival times.

Figure 2.8 simplistically quantifies the relative modal contributions and the effect of dispersion. Figures 2.8 (c) and (d), for example, demonstrate that the arrival times of the modes which propagate over the entire excitation's bandwidth are smaller than those corresponding to a transition from an evanescent or non-propagating behaviour to a propagating one. Moreover, sub-figures (a) and (c) show that the T(0,1) mode is not excited by a radial force, as expected. Somewhat more surprising is the relatively small radial contributions of the F(n, 2), $1 \leq n \leq 13$, modes. This phenomenon can be explained partly by referring to Figure 2.9. There the *magnitudes* of the normalized mode shapes through the pipe's wall, evaluated at their respective cutoff frequencies, are plotted for the representative F(3, m) and F(11, m), $m = 1, 2, 3$, modes. It can be seen that the F(n, 1) and F(n, 3) modes have no axial displacement components. Conversely the F(n, 2) modes have no radial or circum-

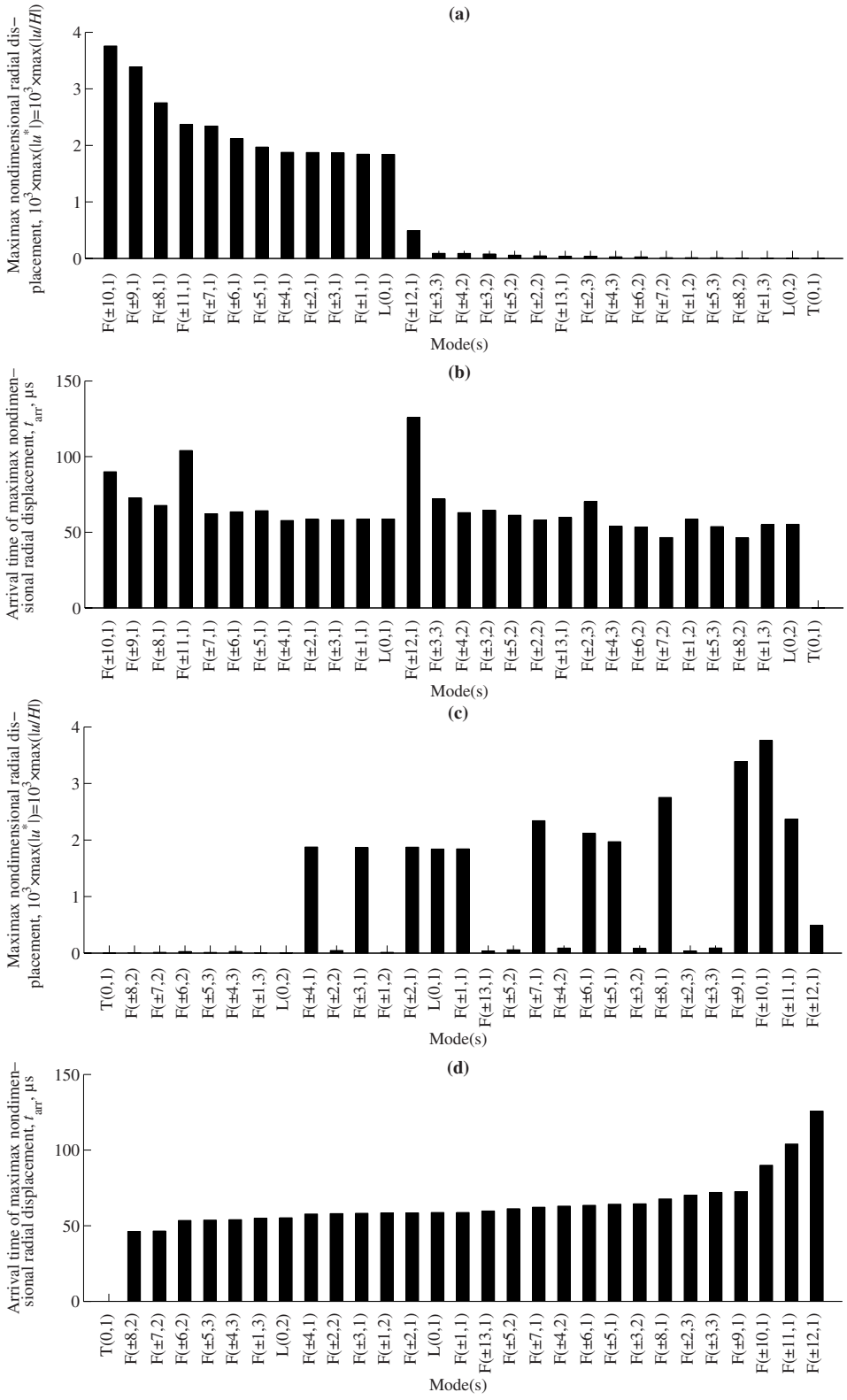

Figure 2.8. Sorting the maximax radial displacement on the pipe's outer surface at $\theta = 0$, $z^* = z/H = 5.1$ by (a), (c) amplitudes and (b), (d) arrival times for individual propagating modes.

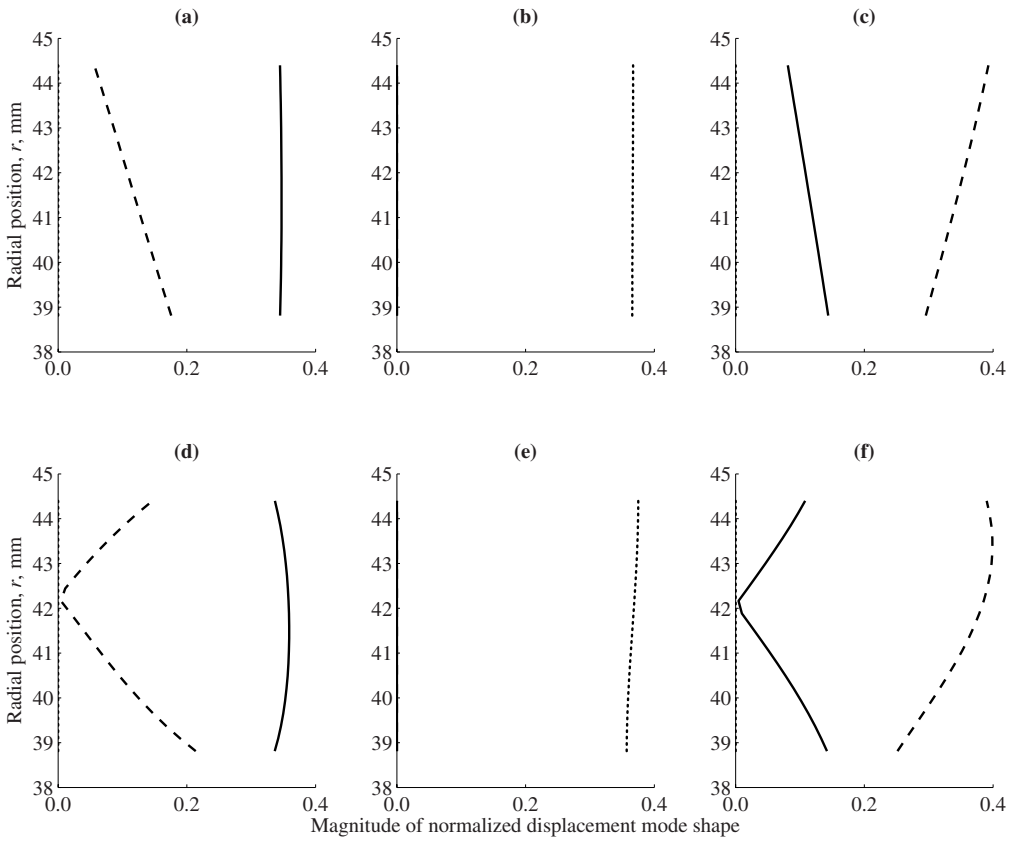

Figure 2.9. Magnitude through the pipe's wall of the (a) F(3,1), (b) F(3,2), (c) F(3,3), (d) F(11,1), (e) F(11,2), and (f) F(11,3) normalized displacement mode shapes evaluated at their respective cutoff frequencies. The solid (—) curve gives the radial component; the dashed (- -) and dotted ($\cdots$) curves correspond to the circumferential and axial components, respectively.

ferential displacement components at their respective cutoff frequencies. (Moreover, very small components occur in these directions at frequencies near the cutoff frequencies.) The disappearances at cutoff frequencies are to be expected [21]. As a practical aside, however, the ease of exciting a pipe's guided waves around the cutoff frequencies, combined with the associated vanishing displacement components, may be used to excite particular guided wave modes. For instance, a narrow band excitation applied along the pipe's axis with a centre frequency around 63.4 kHz would strongly excite the F$(5, 2)$ mode with the F$(10, 1)$ and F$(3, 3)$ modes largely suppressed. Figures 2.8 (a) and (c) support the observation arising from examining Figure 2.4 (a) that the relative modal contributions of the F$(n, 3)$ modes are significantly less than those of the F$(n, 1)$ modes. Consider, say, the en-

ergy[12] contained in the frequency bands around the F(2, 3) and F(8, 1) cutoff frequencies shown in Figure 2.4 (a). The peak around the F(2, 3) cutoff frequency is much narrower and, hence, contains less energy than that around the F(8, 1) cutoff frequency. This behaviour is beneficial because it suggests that modal summations associated with the axial wavenumbers converge quickly so that relatively few modes (and consequently finite elements) can be employed to reliably approximate displacements at distances a few wall thicknesses from the force's application point. More modes are needed, of course, for a comparable convergence of the stress or strain fields.

The results shown in Figure 2.8 correlate qualitatively with the reassigned pseudo Margenau-Hill time-frequency distribution given in Figure 2.7. Large amplitudes which are present for the entire duration of the signal are seen in the time-frequency distribution at frequencies around[13] 53 kHz, 64 kHz, 74 kHz, and 86 kHz. These frequencies are in good agreement with the cutoff frequencies listed in Table 2.2 for the F(±9,1), F(±10,1), F(±11,1), and F(±12,1) modes, i.e., the modes whose cutoff frequencies are relatively central in the excitation's bandwidth. Such modes have relatively large contributions in Figures 2.8 (a) and (c). On the other hand, a more broadband response is seen in Figure 2.7 up to about 75 μs . This time frame and the corresponding broadband response agree with the amplitudes and arrival times shown in Figures 2.8 (b) and (d) for the L(0,1) and F(±n,1), $n \leq 7$, modes.

Figures 2.10 and 2.11 provide analogues to Figures 2.4 and 2.8, respectively, but for a nondimensional axial offset of 25.5 rather than 5.1. A comparison of Figures 2.4 and 2.10 (a) indicates that, due to dispersion, a peak around a cutoff frequency widens as the axial separation from the excited point to a receiving location increases. The same effect can be also seen by comparing Figures 2.4 and 2.10 (b). This behaviour is discussed further in the next chapter in the context of the accuracy of measurements needed to determine an

[12]The term energy is used again in the signal processing sense.

[13]The frequency resolution of the reassigned pseudo Margenau-Hill time-frequency distribution shown in Figure 2.7 is limited to 1 kHz.

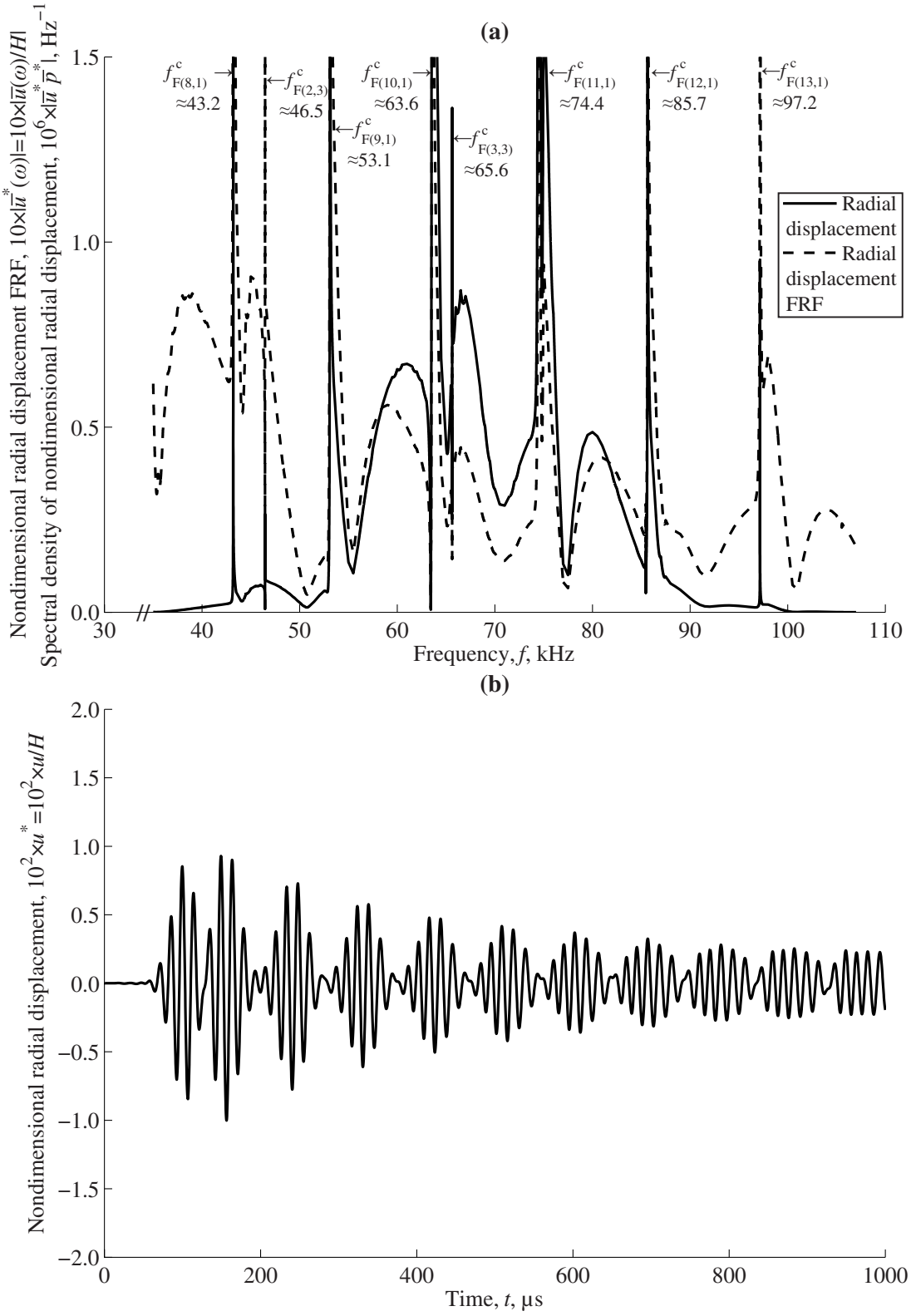

Figure 2.10. Giving (a) the spectral density of the radial displacement on the pipe's outer surface at $\theta = 0$, $z^* = z/H = 25.5$ before and after convolution with the excitation and (b) the latter's time history.

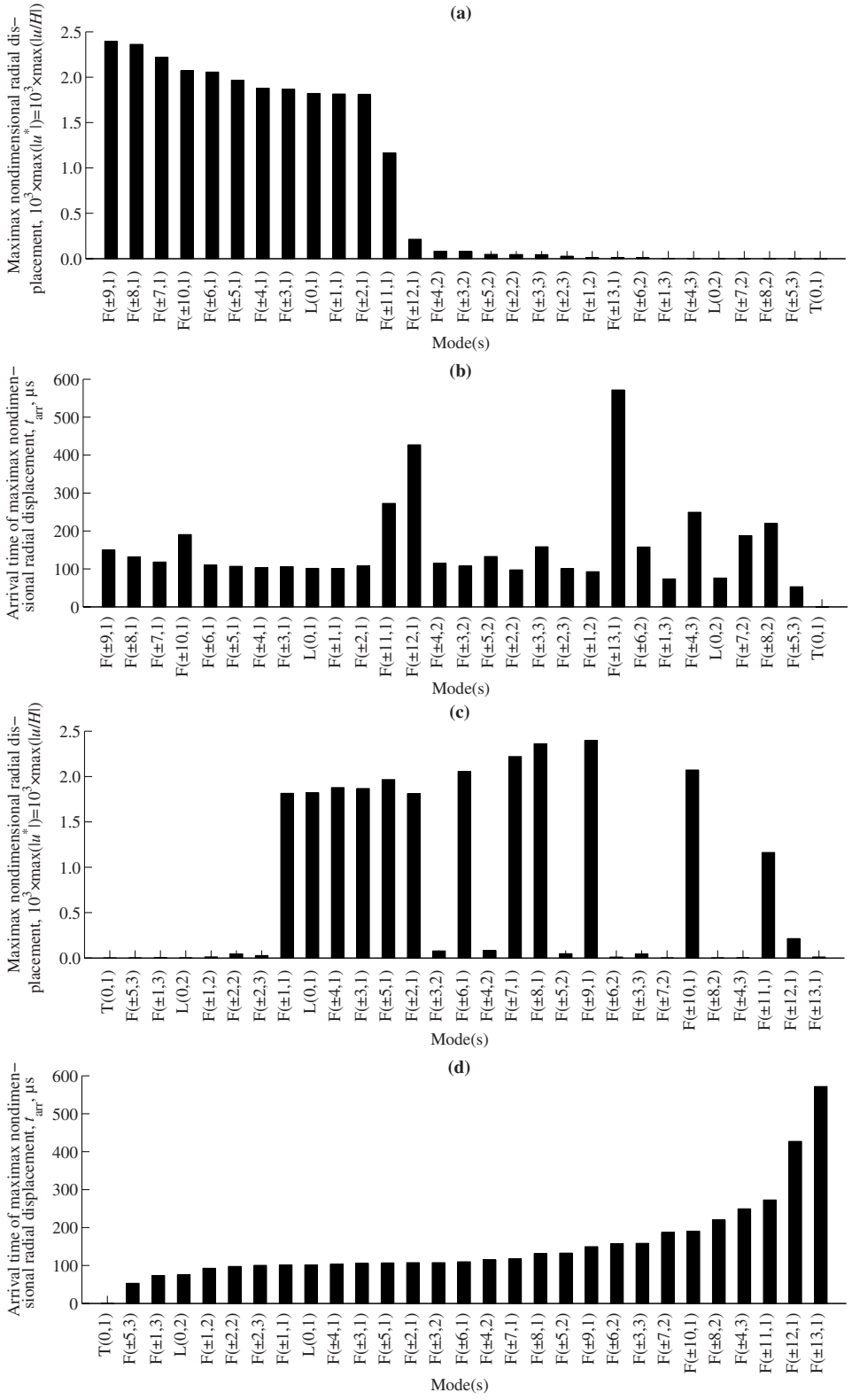

Figure 2.11. Sorting the maximax radial displacement on the pipe's outer surface at $\theta = 0$, $z^* = z/H = 25.5$ by (a), (c) amplitudes and (b), (d) arrival times for individual propagating modes.

unblemished pipe's material and dimensional properties.

Chapter 3

Unblemished Pipe's Characterization–An Inverse Problem

3.1 Introduction

Material and dimensional information constitute fundamental knowledge for assessing the current behaviour or "health" of a structure. From a practical perspective, in situ measurements should be used that are quick, reliable and non-destructive. An ultrasonic-based approach is one plausible candidate. Indeed ultrasonic body (bulk) waves are employed commonly to accurately measure fine dimensions at locations where material properties are known independently [6]. Single or "focussed guided waves," on the other hand, can propagate at least several metres so they have been used to remotely interrogate inaccessible locations [70, 71, 82, 90]. The behaviour of a single, essentially non-dispersive mode is interpreted relatively easily [70, 71] but it is quite difficult to implement. Even if excited, a single mode is likely converted to additional modes at geometrical discontinuities [70, 71]. Such modes are generally dispersive so that the form of a propagating wave packet changes as it travels along a structure. The objective here is to develop a non-destructive procedure involving several guided waves that can be automated to give material and dimensional data simultaneously. It may be extended, in the future, as a means of non-destructively screening corrosion. Although the procedure could be applied, in principle, to any plate-like structure, it is illustrated here by using a homogeneous, isotropic steel pipe. (The pipe is assumed to be reasonably modelled as uniformly right circular, homogeneous, linearly elastic, and isotropic in order to be consistent with Chapter 2.) Such pipes are employed ubiquitously in industry [2].

Defining a pipe's linear but otherwise unknown character from its measured response to a specified excitation is an example of an inverse procedure. Even a computational in-

version procedure, in which errors and uncertainties are generally less than those arising from experimental measurements, may not produce a unique solution [114]. Moreover, an inversion is often based upon a more computationally efficient forward solver [114]. (A forward solver determines the response when both the excitation and pipe's character are known.) This indirect approach is adopted here because an uncertainty analysis can be performed fairly straightforwardly. The forward solver is based upon the well known SAFE formulation described in Chapter 2. The novelty, therefore, lies in its successful practical application to solving an inverse problem. On the other hand, the linear modal decomposition produced inherently by SAFE is crucial to understanding why simple features of a pipe's temporal and corresponding frequency behaviour can be exploited in the inverse problem. However, the solution of the resulting nonlinear equations is sensitive to "noise."

An overriding concern is that a pipe's properties should be measured straightforwardly with basic equipment. Therefore, a short duration excitation is applied radially at an easily accessible external surface of the pipe. No effort is made to avoid dispersive wave modes in contrast to current common practice. The modes are received at a single, axially offset transducer which is linked to a signal processing capability. Both the transmitting and receiving transducers' dimensions are assumed to be much smaller than the excited modes' predominant wavelengths. Therefore, they are idealized as acting at points. Moreover, mass loading effects are neglected.

A Discrete Fourier Transform (DFT) is employed with a temporal curve fitting scheme to analyse the receiving transducer's time varying signal. The aim of this contorted procedure is to refine the frequency values of the predominant modal contributions before the arrival of extraneous reflections from the ends of a finite length pipe. These frequencies are generally not related harmonically. They correspond to the pipe's cutoff frequencies which are common to most pipe locations [21]. Therefore, the choice of measurement location is relatively unimportant if nodal points of modes are avoided. However, measured cutoff frequencies still have to be reconciled with their forward (SAFE) computed counterparts.

This task is accomplished by taking the "true" set of pipe properties as the one for which three measured and three corresponding computed cutoff frequencies are closest. Likely uncertainties are estimated from a sensitivity assessment around the selected set of properties. The procedure is simulated first by using the illustrative example presented previously in Chapter 2. Then the method is applied to two physical examples of metal pipes. Agreement is shown to be good with independently but destructively assessed data.

3.2 Inversion Scheme and Extraction of Cutoff Frequencies

3.2.1 Preamble

The cutoff frequencies have been demonstrated in Section 2.5 to be easily identified features that can be related to the mathematical model. They depend, through the stiffness and mass matrices produced by SAFE, on the pipe's elastic properties, density, and geometrical dimensions. It is assumed that the pipe's outer diameter and density are readily available so that the elastic properties and wall thickness remain to be determined[1]. Two independent elastic constants are sufficient to characterize a homogeneous isotropic material. Therefore, three independent parameters (two elastic constants and the wall thickness) are needed to describe an unblemished pipe.

Buckingham's π theorem [116] and physical constraints are used to reduce the search space, through nondimensionalisations, in order to make calculations more tractable. It will be seen that the application of the theorem allows the search space to be reduced from three to two dimensions. Moreover, *both* upper and lower bounds for the resulting two independent nondimensional parameters, (λ/μ) and (H/R), can be established. These seem-

[1]There are other plausible variations of this problem, e.g., when Poisson's ratio and the outer diameter are known but the wall thickness is to be determined [115].

ingly subtle differences permit a standard constrained optimization solver to be employed efficiently and straightforwardly.

To facilitate the application of Buckingham's π theorem, the nondimensional cutoff frequency ratio

$$\omega^{\mathrm{c}*}_{\mathrm{F}(n,m)} = \frac{\omega^{\mathrm{c}}_{\mathrm{F}(n,m)}}{\omega_{\mathrm{ref}}} \tag{3.2.1}$$

is introduced for a given circumferential wavenumber, n, and axial order, m. Here ω_{ref} is c_2/H and $\omega^{\mathrm{c}}_{\mathrm{F}(n,m)}$ is the cutoff frequency of the $\mathrm{F}(n,m)$ flexural mode.

The $\omega^{\mathrm{c}*}_{\mathrm{F}(n,m)}$ can be expressed more simply in terms of the nondimensional parameters (H/R) and (λ/μ) where $R = (r_{\mathrm{o}} + r_{\mathrm{i}})/2$ is the pipe's mean radius, whereas the desired elastic properties and wall thickness also require ω_{ref} as well as the unblemished pipe's presumed density and outer diameter. An inequality $0 < (H/R) < 2$ arises physically because these lower and upper bounds relate to a pipe having no wall thickness and a solid pipe, respectively. On the other hand, (λ/μ) is bounded reasonably as $0 \leq (\lambda/\mu) \lesssim 10$ by using the standard elasticity relation $0 \leq \nu \leq 0.5$ where ν is Poisson's ratio. Note that, if the Buckingham π theorem had not been applied, the equivalent dimensional problem would require two independent elastic properties (say E and G) as well as the wall thickness to be found. The elastic properties cannot be bounded but they must be non-negative. On the other hand, H is constrained by the requirement that it be less than or equal to $D_{\mathrm{o}}/2$. There is no obvious way to take further advantage of the interrelationships required to find the elastic properties and wall thickness when using a dimensional space. The disadvantage of working in a hybrid space, however, is that additional transformations are required to relate the dimensional and nondimensional variables.

If the SAFE model is perfect and the cutoff frequencies are known exactly, then

$$\omega_{\mathrm{ref}}\omega^{\mathrm{c}*}_{\mathrm{F}(n_i,m_i)} - \hat{\omega}^{\mathrm{c}}_{\mathrm{F}(n_i,m_i)} = 0 \text{ for } i = 1,2,3, \tag{3.2.2}$$

where $\omega^{\mathrm{c}*}_{\mathrm{F}(n_i,m_i)}$ are predicted by SAFE and correspond to three measurable (dimensional)

cutoff frequencies $\hat{\omega}^{c}_{F(n_i,m_i)}$. Equation (3.2.2) *implicitly* gives three relations in three unknowns, ω_{ref}, (H/R), and (λ/μ). Therefore a solution provides a largely nondimensional characterization of the pipe. The system described by equation (3.2.2) is inherently nonlinear because the eigenvalues are nonlinear functions of (H/R) and (λ/μ). Indeed, the change in a typical flexural mode's nondimensional cutoff frequency is approximately sigmoidal in (H/R) and about exponential or logarithmic in (λ/μ), depending on the value of (H/R). This behaviour is illustrated in Figure 3.1 where the typical, nondimensional cutoff frequency of the F(11,1) mode is plotted as a function of both (H/R) and (λ/μ). An estimate of (λ/μ) is more susceptible to errors because a nondimensional cutoff frequency is a much stronger function of (H/R) than of (λ/μ) in this figure.

3.2.2 Practical extraction of cutoff frequencies

Empirical experience suggests that a solution which simultaneously and exactly satisfies each constraint of equation (3.2.2) may exist only if each of three measured cutoff frequen-

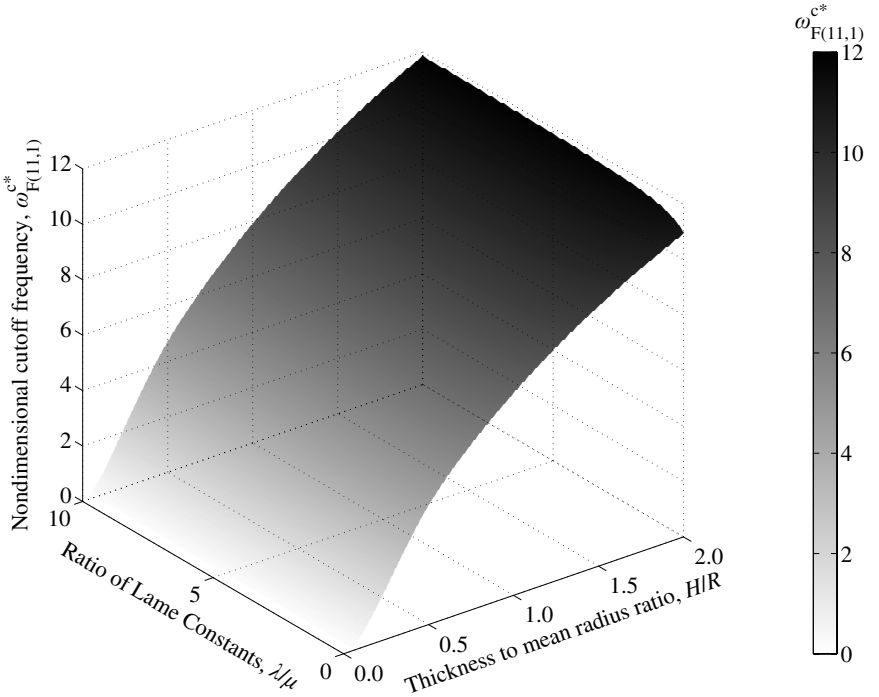

Figure 3.1. Nondimensional cutoff frequency of the F(11,1) mode.

cies are known with a precision of about 10 Hz. Unfortunately it is difficult to achieve this level of accuracy in practice. Basic experimental data are measured time histories which must be processed to extract the cutoff frequencies. In addition, a real pipe does not have the assumed infinite length. If a finite time window is introduced to truncate a response history, and thereby exclude reflections from a pipe's ends, harmonic distortion is produced in a numerically approximated Fourier transform. On the other hand a DFT, which is calculated from the truncated time history, has a finite frequency resolution. For example, a time window with about a 900 μs duration is needed to exclude end reflections from a measurement at the middle of a 3 m long, steel pipe. Then the finest frequency resolution possible with a DFT is about $(900\ \mu s)^{-1}$ or 1.1 kHz. This value is two orders of magnitude greater than the 10 Hz or so resolution required. Furthermore, the DFT implicitly presumes that the truncated history is periodic which, in turn, erroneously implies that the cutoff frequencies are related harmonically. Other DFT[2] based techniques which may potentially give a finer frequency resolution, like a "zoom" Fast Fourier Transform (FFT), require longer time records which are not feasible even for the longest (50 ft [13 m]) commonly available pipe. To overcome the frequency resolution problem, curve fitting is applied straightforwardly to a time history. Then a conventional least-square solver is employed to minimize the function

$$\eta = \sum_{i=1}^{I} \left[u_i - \sum_{j=1}^{J} \mathrm{e}^{-\xi_j (t_i - \tau_j)} A_j \cos(\omega_j^c t_i - \phi_j) \right]^2 , \tag{3.2.3}$$

where I is the total number of data points, at a given pipe location, in the "free vibration" portion of the time history[3]. Furthermore, J is the assumed number of modes contributing to this point's radial displacement, u_i, at the typical i^{th} instant, t_i. For the j^{th} mode, ξ_j rep-

[2] A cepstrum analysis can be considered a DFT based technique because it essentially post-processes a DFT.

[3] The time history of an individual modal contribution to the overall radial response (see, for instance, Figures 2.5 and 2.6 located in Chapter 2) suggests that the history can be divided into three distinct portions. An initial "forced vibration" period is followed by "free vibrations." Then a third segment can be identified which includes the first and subsequent reflections from the ends of a finite length pipe. Although a precise demarcation is not required, the "free vibrations" should exclude the other two portions as well as the transducers' ring down after the excitation's termination to advantageously avoid contamination.

resents a viscous like decay[4], τ_j is the time at which the free vibrations begin[5], whereas A_j, ω_j^c, and ϕ_j are the modal amplitude, cutoff frequency, and phase, respectively. The minimization of equation (3.2.3) is equivalent to computing a terminated, overall "best" fitting Fourier series in which the frequency components are related non-harmonically [117]. Initial approximations for the A_j, ω_j^c, and ϕ_j are provided conveniently by the DFT of a time history up to almost the first, clearly observed end reflection. Based upon experience, the ξ_j and τ_j are taken initially as zero and 200 μs, respectively.

Figure 3.2 (a) presents computer data which simulates the radial displacement on the outer surface of the illustrative pipe at $\theta = 0$ and $z^* = z/H = 5.1$. (Also see Figure 2.4 (b) given in Chapter 2.) A rectangular time window is adopted that has a duration of 600 μs

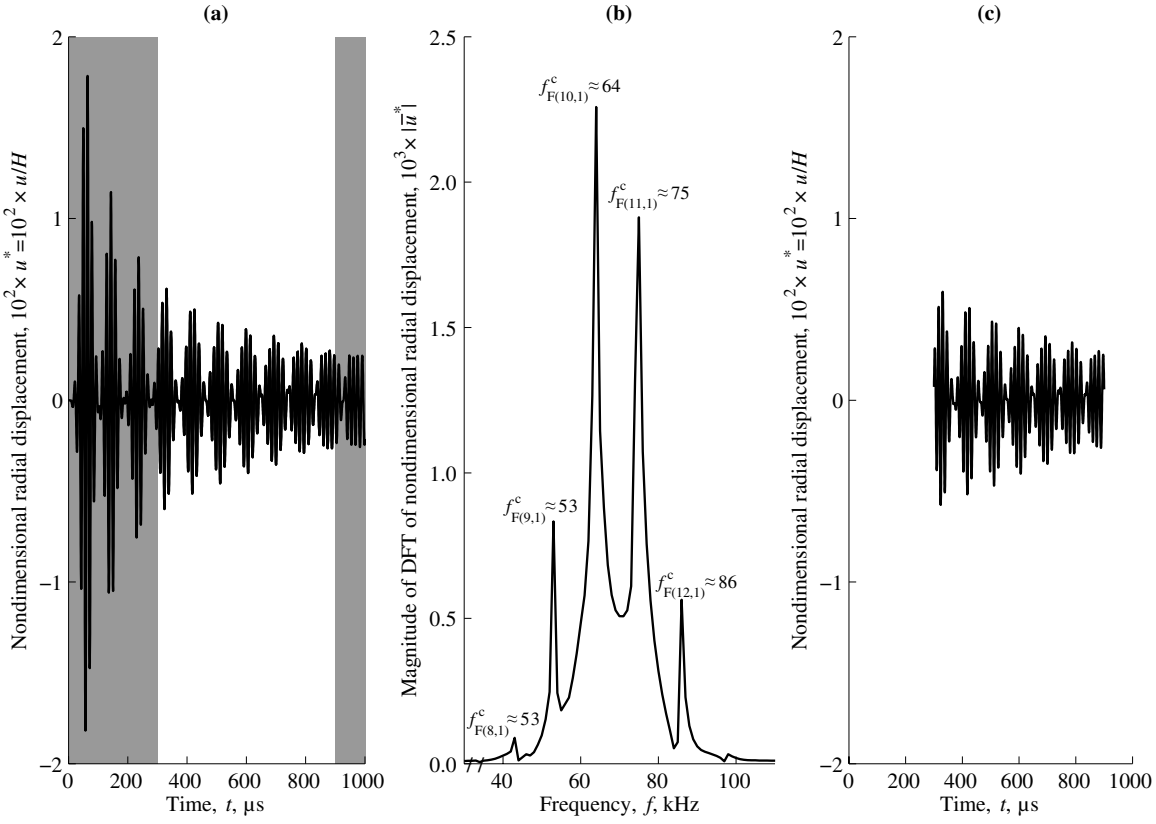

Figure 3.2. Showing (a) synthesized time history on the pipe's outer surface at $\theta = 0$ and $z^* = z/H = 5.1$ with (b) the magnitude of the corresponding DFT, and (c) the reconstructed temporal curve fit of the free vibrations.

[4]This term is included for a potential extension to damped viscoelastic materials. It is virtually zero here.

[5]Experiments with both synthesized and measured signals suggest that this term is essentially mode independent.

and is positioned between the two shaded regions of Figure 3.2 (a). Figure 3.2 (b) gives the corresponding frequency information from a DFT of the windowed history. Five obvious peaks and their cutoff frequencies are identified easily but approximately from this figure. They are related to their corresponding modes. These peaks and their relative amplitudes correlate relatively well, but imperfectly, with the modes having the largest maximax radial displacements shown in Figure 2.8. The discrepancy is due to the different techniques used in the two figures to quantify the relative contribution of a mode's radial displacement history. The peaks shown in Figure 3.2 (b) correlate nearly perfectly, however, with the frequency content for the amplitude of the reassigned pseudo Margenau-Hill time-frequency distribution shown in Figure 2.7. No simultaneous time information is available, of course, from Figure 3.2 (b) to compare with Figures 2.7 and 2.8. On the other hand, Figure 3.2 (c) shows the consequence of minimizing equation (3.2.3) and using the result to reconstruct the free vibration history. The trace shown in Figure 3.2 (c) is visually indistinguishable from the one given in Figure 3.2 (a). Table 3.1 compares the cutoff frequencies from "exact" theory (which simulates the desired ideal but practically unachievable result), the computed FRF, the DFT, and the temporal curve fitting procedure. The last procedure is seen to invariably give significantly closer estimates to the FRF than the DFT. Further improvements may be possible by including all the cutoff frequencies which are less pronounced in the DFT than those shown in Figure 3.2 (b). Moreover, taking a shorter time window which emphasises the later portion of the response history may be also advantageous because it

Table 3.1. Cutoff frequencies obtained from "exact" theory, the FRF, DFT, and temporal curve fit.

Mode	Cutoff Frequencies, kHz				Difference Between	
	"Exact"	FRF	DFT	Curve Fit	DFT and FRF, Hz	Curve Fit and FRF, Hz
F(8,1)	43.197	43.197	43.332	43.184	135	−13
F(9,1)	53.113	53.113	53.331	53.041	218	−72
F(10,1)	63.554	63.554	63.307	63.568	−247	14
F(11,1)	74.427	74.427	74.969	74.421	542	−6
F(12,1)	85.652	85.652	84.965	85.667	−687	15

would reduce the effects of initial startup transients. A more appropriate time window can be selected, however, by simply using the reassigned pseudo Margenau-Hill time-frequency distribution shown in Figure 2.7 of Chapter 2 as a guide. It can be found from this figure by noting the duration over which the bands in the frequency direction are narrowest and contributions of the noise are smallest. Consequently a more reasonable start of the window is seen to be closer to 400 μs than the approximately 300 μs used. Unfortunately this insight came retroactively. It should be noted too that a solution which satisfies equation (3.2.2) could not be found if a solver employs the F(10,1), F(11,1), and F(12,1) cutoff frequencies elicited from the temporal curve fit. This is a result of the differences between the true and curve fitted cutoff frequencies being larger than 10 Hz. Essentially exact counterparts from the FRF are required. Consequently an alternative "nearest neighbour," inversion scheme, which is based on minimizing the square of an error, is proposed next.

3.2.3 Description of inversion scheme

3.2.3.1 "Initial" inversion by finding the "nearest neighbour"

One approach to "solving" equation (3.2.2) is to find the nearest point in the (ideal) solution space to a "contaminated" result. It is located by minimizing the objective function

$$\Gamma = \sum_{i=1}^{3} \left(\omega_{\text{ref}} \omega^{\text{c*}}_{\text{F}(n_i,m_i)}(\lambda/\mu, H/R) - \hat{\omega}^{\text{c}}_{\text{F}(n_i,m_i)} \right)^2 \tag{3.2.4}$$

for which the sum of the squares of the differences between the previously extracted $\hat{\omega}^{\text{c}}_{\text{F}(n_i,m_i)}$ components and the corresponding $\omega_{\text{ref}}\omega^{\text{c*}}_{\text{F}(n_i,m_i)}$ are computed. The minimization is performed by using the robust direct search method described in [118]. Once ω_{ref}, (λ/μ) and (H/R) are known, the solution can be transformed into a physically meaningful space

by using

$$H = \frac{(H/R)D_{\mathrm{o}}}{2 + (H/R)}, \tag{3.2.5a}$$

$$\mu = G = \rho(H\omega_{\mathrm{ref}})^2, \tag{3.2.5b}$$

and

$$\lambda = \mu(\lambda/\mu). \tag{3.2.5c}$$

These expressions, along with standard geometrical and elasticity relations, are used to calculate the individual initial values given in Table 3.2. They can be seen to agree reasonably well with the corresponding values that are preassigned in the computer simulation.

Table 3.2. Comparing preassigned data with the initial nominal and revised values from the nearest neighbour inversion.

Property	Preassigned value	Initial value	Revised range
Density, ρ, slug/ft^3 (kg m^{-3})	15.39 (7932)	—	—
Outer diameter, D_{o}, in (mm)	3.496 (88.8)	—	—
Wall thickness, H, in (mm)	0.220 (5.59)	0.220 (5.59)	0.217±0.008 (5.5±0.2)
Mean radius, R, in (mm)	1.638 (41.60)	1.638 (41.60)	1.640±0.003 (41.65±0.08)
Thickness to mean radius ratio, (H/R)	0.134	0.134	0.132±0.004
Young's modulus, E, ksi (GPa)	31, 460 (216.9)	31, 430 (216.7)	32, 000±2, 200 (220±15)
Lamé constant, μ, (Shear modulus, G), ksi (GPa)	12, 230 (84.3)	12, 240 (84.4)	12, 200±700 (84±5)
Lamé constant, λ, ksi (GPa)	16, 410 (113.2)	16, 060 (110.7)	20, 600±8, 600 (142±59)
Ratio of Lamé constants, (λ/μ)	1.34	1.31	1.7±0.7
Poisson's ratio, ν	0.286	0.284	0.31±0.05

3.2.3.2 Uncertainty estimation

Estimates of uncertainties are developed more straightforwardly if they are based upon frequency ratios rather than the cutoff frequencies themselves. This is a consequence of being able to decouple the effects of (H/R) and (λ/μ) from those of ω_{ref}. Therefore, given the cutoff frequencies $\hat{\omega}^{\text{c}}_{\text{F}(n_1,m_1)}$, $\hat{\omega}^{\text{c}}_{\text{F}(n_2,m_2)}$, and $\hat{\omega}^{\text{c}}_{\text{F}(n_3,m_3)}$ of any three modes, the three independent[6] ratios

$$Q_1 = \frac{\hat{\omega}^{\text{c}}_{\text{F}(n_1,m_1)}}{\hat{\omega}^{\text{c}}_{\text{F}(n_2,m_2)}} = \frac{\omega_{\text{ref}}\omega^{\text{c}*}_{\text{F}(n_1,m_1)}}{\omega_{\text{ref}}\omega^{\text{c}*}_{\text{F}(n_2,m_2)}} = \frac{\omega^{\text{c}*}_{\text{F}(n_1,m_1)}}{\omega^{\text{c}*}_{\text{F}(n_2,m_2)}}, \tag{3.2.6a}$$

$$Q_2 = \frac{\hat{\omega}^{\text{c}}_{\text{F}(n_3,m_3)}}{\hat{\omega}^{\text{c}}_{\text{F}(n_2,m_2)}} = \frac{\omega_{\text{ref}}\omega^{\text{c}*}_{\text{F}(n_3,m_3)}}{\omega_{\text{ref}}\omega^{\text{c}*}_{\text{F}(n_2,m_2)}} = \frac{\omega^{\text{c}*}_{\text{F}(n_3,m_3)}}{\omega^{\text{c}*}_{\text{F}(n_2,m_2)}}, \tag{3.2.6b}$$

and

$$Q_3 = \frac{\hat{\omega}^{\text{c}}_{\text{F}(n_1,m_1)}}{\hat{\omega}^{\text{c}}_{\text{F}(n_3,m_3)}} = \frac{\omega_{\text{ref}}\omega^{\text{c}*}_{\text{F}(n_1,m_1)}}{\omega_{\text{ref}}\omega^{\text{c}*}_{\text{F}(n_3,m_3)}} = \frac{\omega^{\text{c}*}_{\text{F}(n_1,m_1)}}{\omega^{\text{c}*}_{\text{F}(n_3,m_3)}} \tag{3.2.6c}$$

are introduced. The rightmost sides of equation (3.2.6) indicate that the Q_i, $i = 1, 2, 3$, are independent of ω_{ref}. Consequently values of (λ/μ) may be found, for a specified (H/R), such that

$$Q_1 - \frac{\omega^{\text{c}*}_{\text{F}(n_1,m_1)}}{\omega^{\text{c}*}_{\text{F}(n_2,m_2)}} = 0, \tag{3.2.7a}$$

$$Q_2 - \frac{\omega^{\text{c}*}_{\text{F}(n_3,m_3)}}{\omega^{\text{c}*}_{\text{F}(n_2,m_2)}} = 0, \tag{3.2.7b}$$

and

$$Q_3 - \frac{\omega^{\text{c}*}_{\text{F}(n_1,m_1)}}{\omega^{\text{c}*}_{\text{F}(n_3,m_3)}} = 0 \tag{3.2.7c}$$

are satisfied individually. Reasonable approximations to the Q_i, $i = 1, 2, 3$, are given by the ratios of the values of $\omega_{\text{ref}}\omega^{\text{c}*}_{\text{F}(n_i,m_i)}$ obtained from minimizing equation (3.2.4).

Uncertainties are assessed by perturbing each $\hat{\omega}^{\text{c}}_{\text{F}(n_i,m_i)}$ in equation (3.2.6) over a range of $\pm 160\pi$ rad/s. This perturbation's magnitude corresponds to the rounded extreme of the

[6] Other combinations of the cutoff frequencies can be used to form similar ratios. However, they are simply "rearrangements" of the three selected ratios.

moduli of the cutoff frequency differences presented in the rightmost column of Table 3.1. The maximum and minimum values of (λ/μ), $(\lambda/\mu)_{\max}$ and $(\lambda/\mu)_{\min}$ respectively, which satisfy equation (3.2.7) are recorded for the perturbed Q_i when (H/R) is taken from the minimization procedure. A uniform probability density function [119] is *assumed* between $(\lambda/\mu)_{\min}$ and $(\lambda/\mu)_{\max}$. Then the expected value of (λ/μ), $(\lambda/\mu)_{\text{ex}}$, is merely the average value $(1/2)[(\lambda/\mu)_{\min} + (\lambda/\mu)_{\max}]$ [119]. The uncertainty is taken as plus or minus one standard deviation, $\pm(1/\sqrt{12})[(\lambda/\mu)_{\max} - (\lambda/\mu)_{\min}]$. A similar procedure is performed to estimate the expected (H/R), $(H/R)_{\text{ex}}$, and its uncertainty when the extreme (H/R) ratios, $(H/R)_{\min}$ and $(H/R)_{\max}$ are evaluated using $(\lambda/\mu)_{\text{ex}}$. Then the uncertainty in ω_{ref} is indicated by the absolute difference between ω_{ref}, determined by minimizing equation (3.2.4), and the average ω_{ref} found by solving equation (3.2.6) for each of the $\hat{\omega}^{\text{c}}_{\text{F}(n,m)}$, with (H/R) and (λ/μ) equalling $(H/R)_{\text{ex}}$ and $(\lambda/\mu)_{\text{ex}}$, respectively. These revised quantities are reported in Table 3.2. They can be seen to agree, within the estimated uncertainties, with the values preassigned in the simulation. The uncertainties in (H/R), (λ/μ), and ω_{ref} are propagated conventionally [120] to extend them to the individual E, H, etc., values. Note that D_{o} and ρ are assumed to be exact in the simulation. The process to estimate the uncertainty in (H/R) and (λ/μ) is illustrated graphically in Figure 3.3.

3.3 Experimental corroboration

3.3.1 Preamble

The procedure described previously is applied next to a physical specimen. The specimen is an arbitrarily selected, commercial 3 inch NPS (80 mm DN), Schedule 40, seamless, carbon steel pipe, about 114 inches (2.90 m) long. This pipe resembles closely, but not exactly, the one used in the computer simulation. The cutoff frequencies of the same three ultrasonic guided wave modes used in the simulation are measured. Conventional but destructive

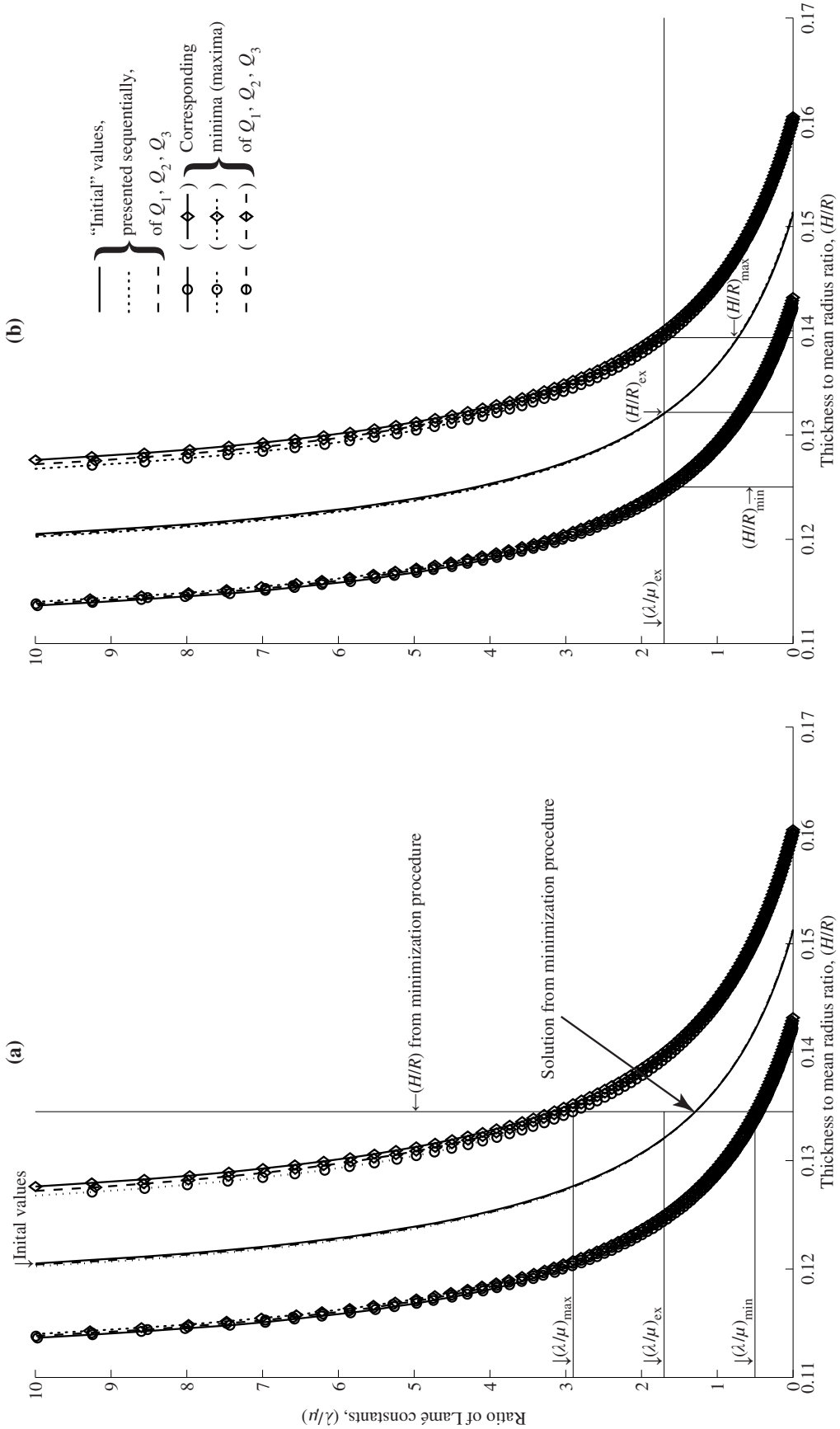

Figure 3.3. Illustrating the procedure to estimate the uncertainty in (a) (λ/μ) and (b) (H/R).

tension-compression and torsion-torsion tests are also performed on a short sample of the pipe to corroborate data.

3.3.2 Experimental apparatus

Figure 3.4 shows a schematic of the experimental apparatus. A digital representation of the pulse is programmed into an Agilent Technologies [121] 33120A, 15 MHz, function/arbitrary waveform generator. It is scaled to produce an output signal from the 33120A that is essentially 20 V_{ppk} with no Direct Current (DC) component. This voltage signal is applied to the transmitting transducer, a Digital Wave Corporation [122] (DWC) B225, broadband (30 kHz to 300 kHz) ultrasonic transducer. The transducer is "coupled" to a pipe by using a thin, fairly uniform, layer of beeswax. The transmitting transducer is assumed to produce a force which is proportional to the applied voltage signal[7]. The ensuing radial wave motion at the pipe's outer surface is measured by using a nominally identical transducer coupled similarly to the pipe. The output of the receiving transducer is conditioned by employing a DWC PA2040G/A, broadband (5 kHz to 4 MHz) preamplifier. The conditioned displacement history is captured with an Agilent Technologies DSO6014A, 100 MHz digit-

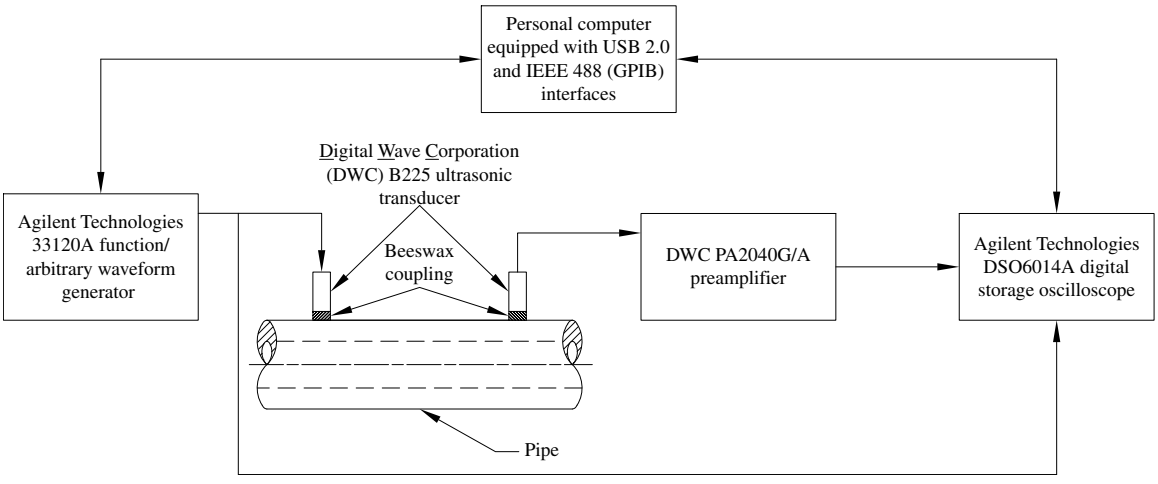

Figure 3.4. Schematic of the equipment.

[7]Note that the force was "coloured" by the transducer's and couplant's convolved FRF. See the later comment regarding the convolved FRF of the instrumentation chain.

al storage oscilloscope, which is also used to "monitor" the output of the 33120A. Both the 33120A and DSO6014A are "supervised" by a Personal Computer (PC) using bidirectional communication. All interconnections in the analogue measurement chain use shielded, coaxial cables.

3.3.3 Ultrasonic testing

Figure 3.5 (a) shows the radial displacement history measured on the steel pipe's outer surface at $\theta \approx 0$ and $z^* = z/H \approx 5$. The "free vibration" portion is shown between the two shaded regions so that the asterisked end reflection and its effect on a DFT are avoided. Initial approximations of the cutoff frequencies, their amplitudes, and phases are elicited from the DFT of the history before the right shaded region. The magnitude of this DFT is shown

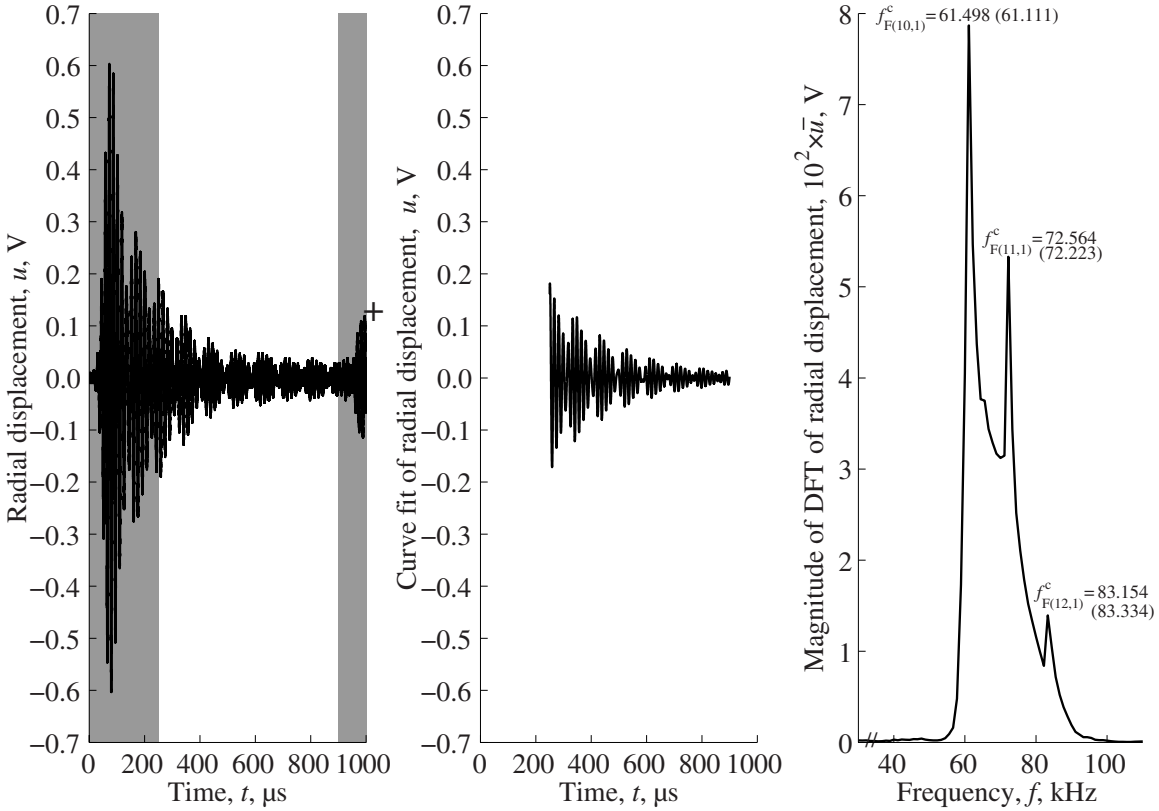

Figure 3.5. Showing (a) the radial displacement measured on the outer surface of a steel pipe at $\theta \approx 0$ and $z^* = z/H \approx 5$, (b) temporal curve fit of "free vibration" portion, and (c) DFT of time history before first end reflection's arrival in (a). $^+$End reflection.

in Figure 3.5 (c). These approximations are utilized initially in the temporal curve fitting procedure. The refined values of the cutoff frequencies are also reported in Figure 3.5 (c), with the initial approximations given in parentheses. The reconstituted time history from the refined values is presented in Figure 3.5 (b). It agrees well, over the corresponding duration, with the original history of Figure 3.5 (a). A comparison of Figure 3.5 (c) with Figure 3.2 (b) as well as Figure 2.4 (a) of Chapter 2 suggests that several modes [e.g., the F(8,1) and F(9,1) modes] are "missing" in Figure 3.5 (c). The explanation is that the missing modes are attenuated strongly by the FRF of the analogue instrumentation chain, as discussed later.

The previous inversion and uncertainty estimation procedures are applied using the cutoff frequencies obtained from the temporal curve fit of the experimental history. The results are summarized in Table 3.3. The pipe's outer diameter and density are determined separately and their measurement uncertainties are propagated in the derived quantities.

Table 3.3. Comparing conventionally and ultrasonically measured values for an actual steel pipe.

Property	Conventional approach	Initial ultrasonic value	Revised ultrasonic range
Density, ρ, slug/ft^3 (kg m^{-3})	14.9±0.4 (7700±200)	—	—
Outer diameter, D_o, in (mm)	3.496±0.004 (88.80±0.09)	—	—
Wall thickness, H, in (mm)	0.220±0.004 (5.6±0.1)	0.22 (5.6)	0.217±0.007 (5.51±0.17)
Mean radius, R, in (mm)	1.638±0.004 (41.6±0.1)	1.638 (41.6)	1.640±0.005 (41.65±0.13)
Thickness to mean radius ratio, (H/R)	0.134±0.003	0.134	0.132±0.004
Young's modulus, E, ksi (GPa)	29,300±900 (202±6)	29,200 (201)	29,600±2,300 (204±16)
Lamé constant, μ, (Shear modulus, G), ksi (GPa)	11,500±300 (79±2)	11,900 (82)	11,700±900 (81±6)
Lamé constant, λ, ksi (GPa)	14,400±7,800 (99±54)	9,900 (68)	12,900±5,900 (89±41)
Ratio of Lamé constants, (λ/μ)	1.3±0.7	0.8(4)	1.1±0.5
Poisson's ratio, ν	0.28±0.07	0.23	0.27±0.06

3.3.4 Conventional testing

Separate experiments were performed to verify the accuracy of the ultrasonic measurements. The outer diameter, D_o, and wall thickness, H, for example, were gauged at each end of the pipe, 18 and 36 times respectively, by using an outside micrometer and calliper. Dimensional data are reported in the first column of Table 3.3 as the average value plus or minus one standard deviation. The pipe's mean radius, R, and thickness to mean radius ratio, (H/R), were based upon these measurements and conventionally calculated uncertainties [120]. Its length and weight were obtained by using a tape measure and weighing scale, respectively. Then the pipe's density, ρ, was calculated straightforwardly by using standard geometrical relations. Experimental uncertainties were propagated as before. (Note that the D_o and ρ values given in Table 3.3 were used, with their corresponding uncertainties, in the ultrasonic inversion procedure.)

A standard destructive test was undertaken to determine the pipe's elastic properties. A 7 inch (18 cm) or so sample length was cut from one end of the pipe. End plates and gripping shafts were welded to this sample, as shown in Figure 3.6 (a), which was heat treated afterwards to relieve residual stresses. Two nominally identical, Vishay [123] EA-06-062RB-120 option LE, three-element strain gauge rosettes were bonded, using Vishay [123] M-Bond 610, at diametrically opposed locations in the specimen's midplane. Surface preparation and bonding followed the manufacturer's instructions [123]. The alignment of the gauges was better than $\pm 2^\circ$. Strain gauge conditioning was provided by a Vishay [123] Series 7000 Data Acquisition System. Then the instrumented pipe sample was mounted in an Instron [124] universal material testing machine, as shown in Figure 3.6 (b), and loaded pseudo-statically in either "pure" tension-compression or torsion-torsion. Elementary strength of materials calculations were performed to determine discrete data points on axial stress-strain, lateral-axial strain, and shear stress-strain curves arising from both sensors. A linear, least square regression [119] was calculated for each curve. The coefficient of determination, R^2, was invariably greater than 0.998. The curves are shown in

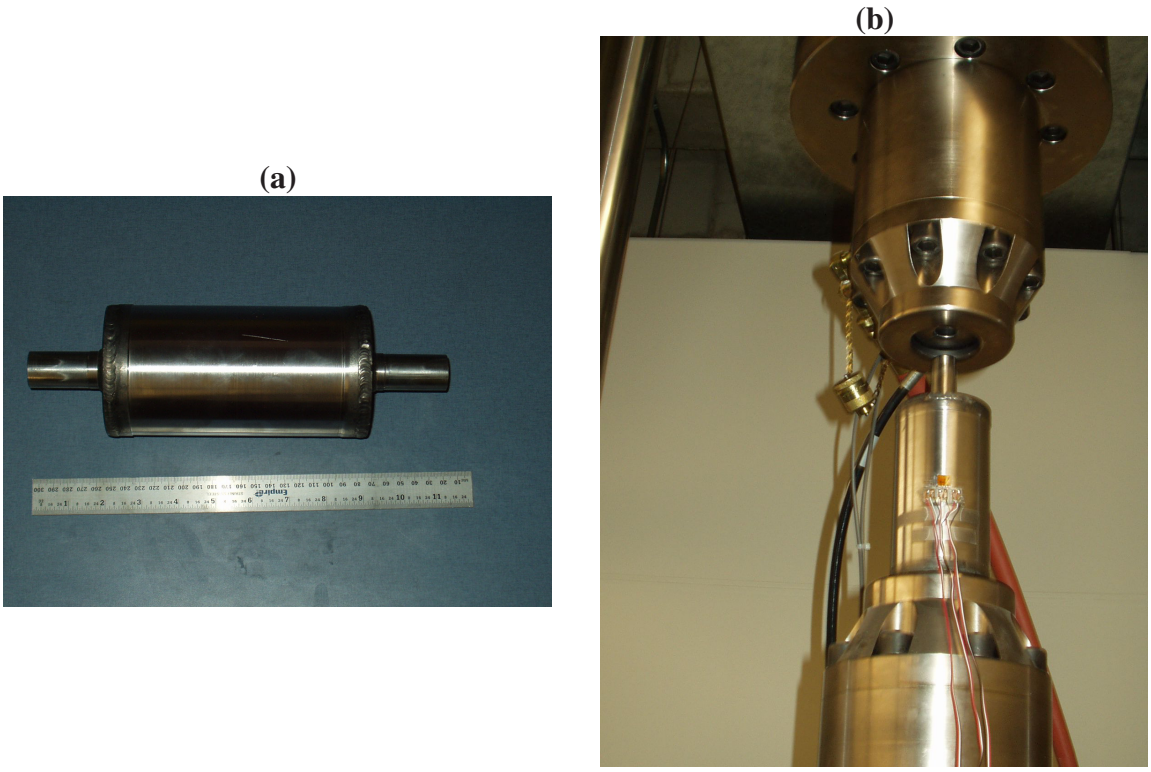

Figure 3.6. Showing (a) the tension-torsion specimen and (b) the specimen strain-gauged and mounted in the load frame.

Figure 3.7, along with the least square regression lines. The tension-compression data were used to estimate Young's modulus, E, and to provide a later cross check on the calculated Poisson's ratio, ν. The torsion test gave the shear modulus, G. These values are also reported in Table 3.3[8]. Knowing E and G, other elastic constants were calculated by using standard formulae. Uncertainties were propagated as before[9].

It can be seen from Table 3.3 that E, G, and the dimensional information found ultrasonically for the steel pipe always correlate well with corresponding values from the pseudo-static experiments. Similar uncertainties occur in this information, regardless of the approach. On the other hand, noticeably large uncertainties arise invariably in the Lamé constant, λ, and Poisson's ratio, ν. The λ, ν, and (λ/μ) agree within the estimated experimental uncertainties. It is interesting, however, that the uncertainties in the measured elastic

[8]Nominal values reported in Table 3.3 for E and G are the averages of the slopes found from the linear regression of data from the two sensors. Uncertainties are taken as one-half the corresponding differences.

[9]Note that the value of ν calculated from E and G agreed, within experimental uncertainty, with that measured from the negative ratio of the lateral to axial strains in the tension-compression experiment.

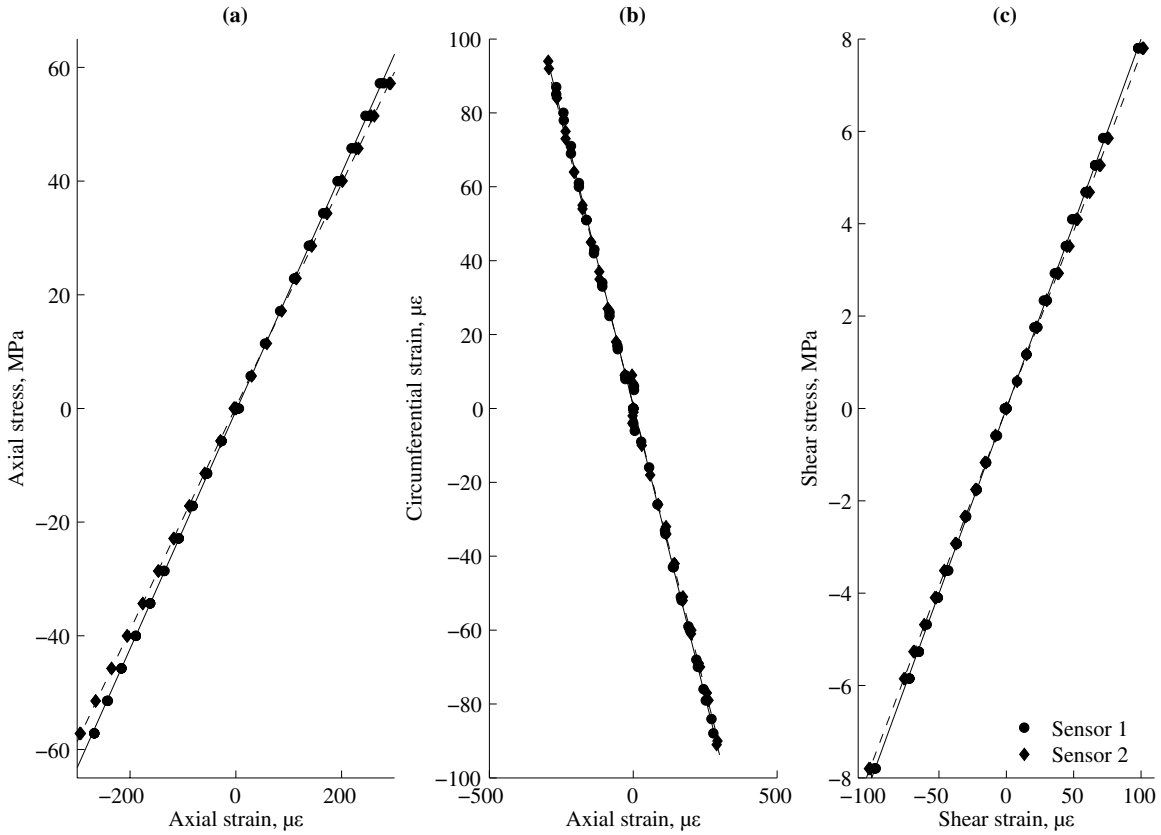

Figure 3.7. Showing the experimental (a) tension stress-strain, (b) lateral-axial strain, and (c) torsion stress-strain curves.

properties are somewhat less than in the computer simulation due to the varying sensitivity of primarily (λ/μ) around the initial solution points.

3.3.5 Frequency response of the instrumentation chain and transducer coupling

As stated previously, a comparison of Figures 3.2 (b) and 3.5 (c) suggests that the F(8,1) and F(9,1) modes, for instance, are "missing" in Figure 3.5 (c). A series of experiments were conducted [125–127] to confirm that the instrumentation chain's FRF can explain the apparent discrepancies. The experimental apparatus was arranged as shown in Figure 3.4 but with the pipe removed. The Agilent Technologies waveform generator was programmed to

produce a series of sinusoidal[10] signals having an amplitude of 20 V_{ppk} and no DC component. A signal was applied to the transmitting transducer which was coupled directly to the receiving transducer[11] by using a thin, reasonably uniform layer of beeswax. The output of the receiving transducer was conditioned by employing a DWC preamplifier configured for no voltage gain. The conditioned output from the preamplifier was captured by employing the Agilent Technologies digital storage oscilloscope. This configuration characterized not only the receiving transducer and its associated coupling and conditioning but also that of the transmitting transducer. Moreover the captured output was compared and found to be identical in frequency with the very stable and pure sinusoidal output from the waveform generator. Figure 3.8 [125] shows a representative FRF result. The magnitude in Fig-

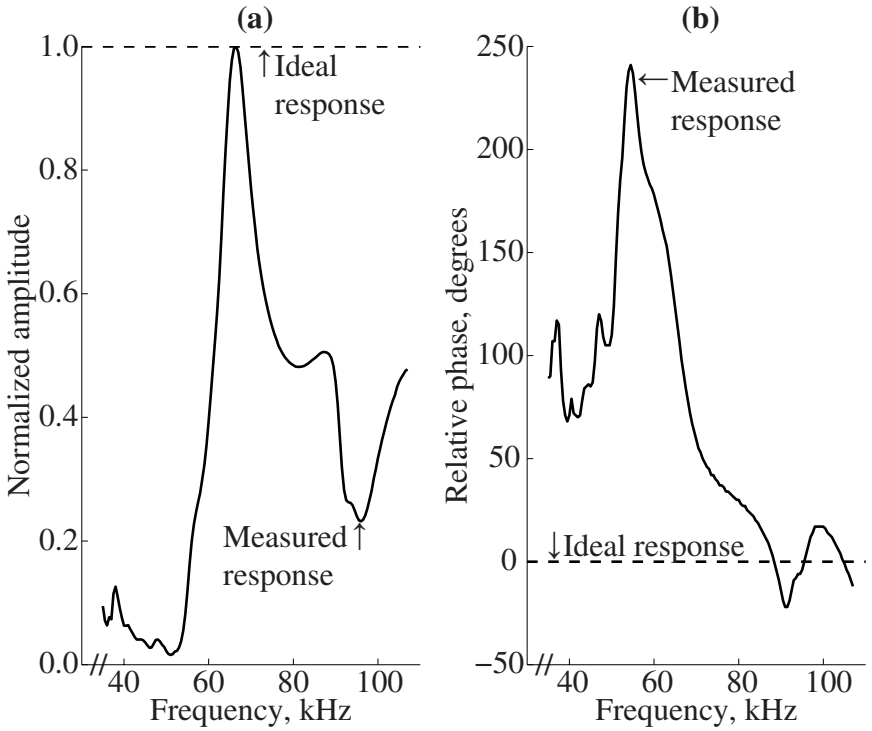

Figure 3.8. A representative measure of the (a) normalized magnitude and (b) phase angle of the instrumentation chain's FRF.

[10]One test of the linearity of a system is its response to a constant amplitude sinusoidal input having various individual frequencies. A linear system must have a sinusoidal output having the same frequency as the sinusoidal input. No marked deviation from this requirement was observed for the instrumentation chain under consideration.

[11]Reciprocity was checked by observing no difference in a given signal after interchanging the transmitting and receiving transducers.

ure 3.8 (a) has been normalized by the maximax voltage output. It is seen that the analogue instrumentation chain strongly attenuates frequency components below about 55 kHz.

Figure 3.9 compares radial displacements which are simulated and measured at $\theta = 0$ and $z^* = z/H = 5.1$. They are normalized by their corresponding maximax values so that direct comparisons are easier. The present simulation [125], unlike before, incorporates the FRF (shown in Figure 3.8) in the $\overline{p}(\omega)$ term of equation (2.3.17). An arithmetic average of the E and G reported in Table 3.3 for the conventional and ultrasonic measurements is used in the simulation. On the other hand, purely conventionally measured nominal dimensions are employed. The simulated and measured data given in Figure 3.9 show that the agreement between the simulation and measurement is improved greatly, in comparison to

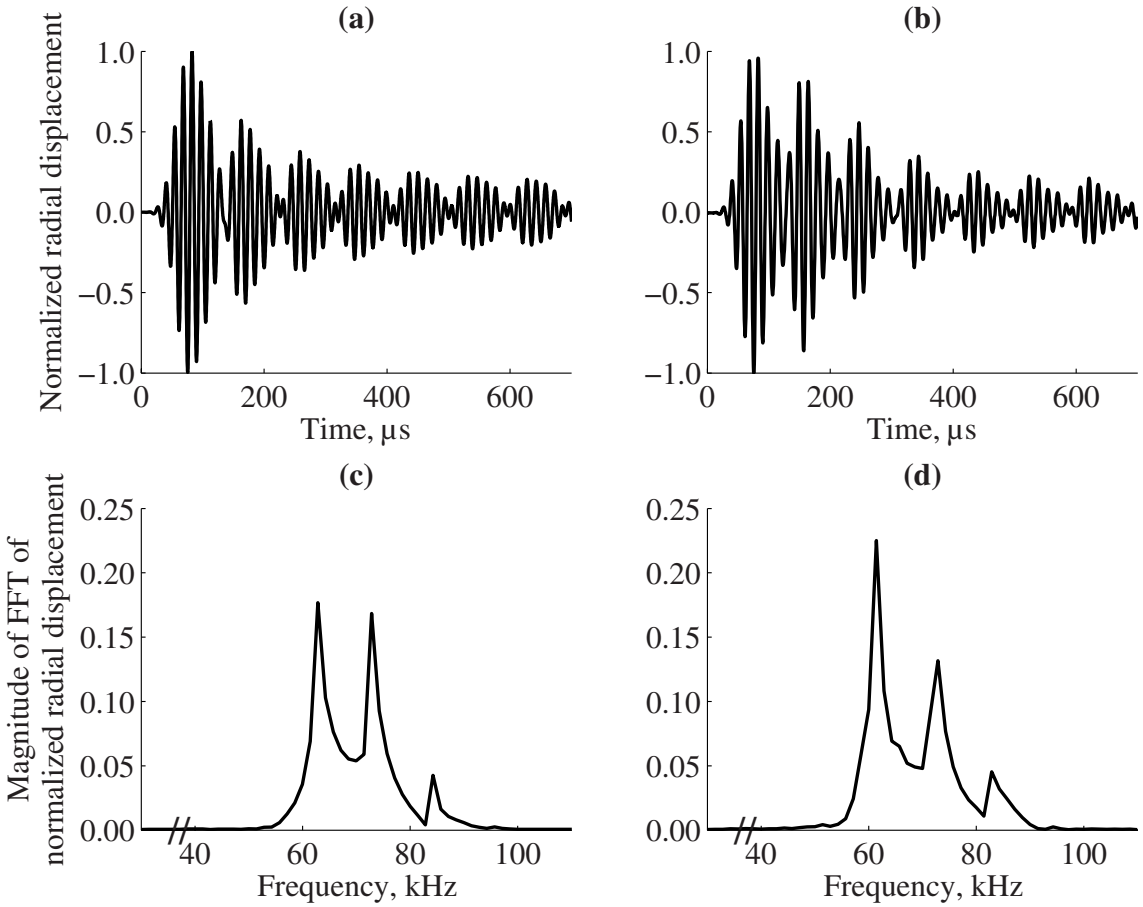

Figure 3.9. Comparing (a) and (c) simulated and (b) and (d) measured normalized radial displacements at $\theta = 0$ and $z^* = z/H = 5.1$ with allowances made for the instrumentation's frequency response.

Figures 3.2 and 3.5, by incorporating the instrumentation chain's FRF. It *may* be possible to improve the agreement even further with a more faithful characterization of the instrumentation's FRF by better controlling the coupling between the transducer and pipe in the manner described next.

Although the agreement between the more realistic simulation and the measurement is quite good, the latter must be repeatable to be practically useful. (It is unnecessary, on the other hand, for the instrumentation to have an ideal frequency response because an imperfect but consistent behaviour can be removed with post-processing [125, 127].) Therefore a series of experiments was performed to determine a measurement's repeatability [126, 127]. It was shown [126] that the ambient air temperature and the transducer coupling are the two most influential factors. The first factor may be significant as a result of seasonal changes in the field but it is relatively unimportant under controlled laboratory conditions. Therefore, only the second factor was considered in somewhat more detail.

Several coupling techniques were assessed. They included dry coupling (with a controlled force used to push back-to-back transducers together), a viscoelastic coupling, and beeswax. Of the options examined, a beeswax coupling had the greatest sensitivity and best repeatability [126]. However, the formation of a beeswax slug was found to be crucial [126]. A uniform sheet of beeswax was produced carefully at a controlled temperature. Then individual cylindrical slugs were punched from the sheet so that each slug had a diameter of 0.25 inch (6.35 mm) and a height of 0.028 ± 0.003 inch (0.53 ± 0.08 mm). A single slug was used to couple the two back-to-transducers before measuring the FRF. Normalization of a FRF followed the same procedure as that described for Figure 3.8. The results from eight different slugs are presented in Figure 3.10 [126, 127]. They are seen to be respectably repeatable.

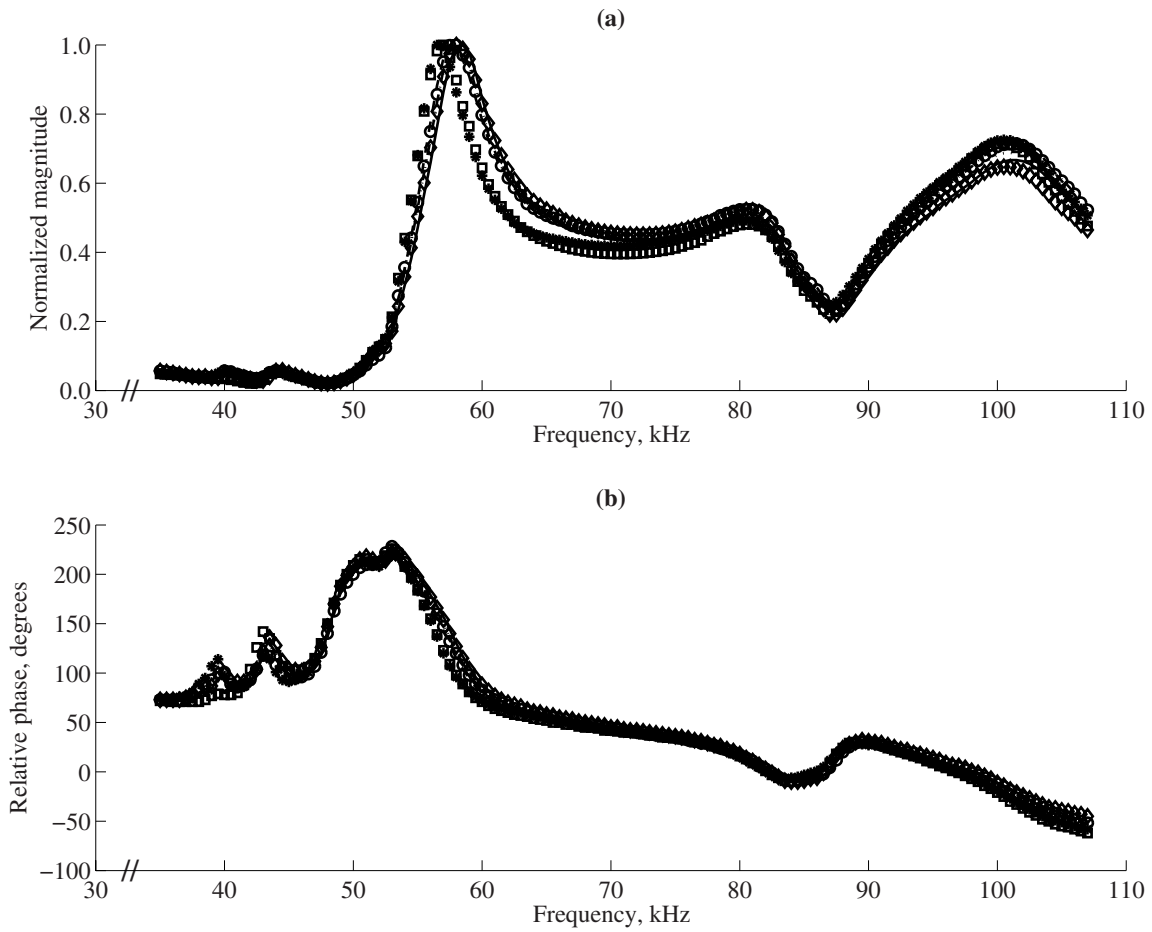

Figure 3.10. Showing the experimental (a) normalized magnitude and (b) phase angle of the instrument chain's FRF when using a controlled beeswax coupling.

3.3.6 Aluminium pipe

The procedure employed for the steel pipe was essentially repeated for an aluminium pipe. Figure 3.11 (a) shows the radial displacement history measured ultrasonically on the aluminium pipe's outer surface at $\theta \approx 0$ and $z^* = z/H \approx 5.1$. However arithmetic averaging, on a sample by sample basis, was done over 1024 separate trials to reduce the incoherent electrical noise. The selected "free vibrations" are shown, as previously, between the two shaded regions given in Figure 3.11 (a). Initial approximations of the cutoff frequencies, their amplitudes, and phases were elicited from the DFT as before. The magnitude of this DFT is shown in Figure 3.11 (c). The initial frequency approximations were utilized in the temporal curve fit of the free vibrations to refine their values. Both the initial approx-

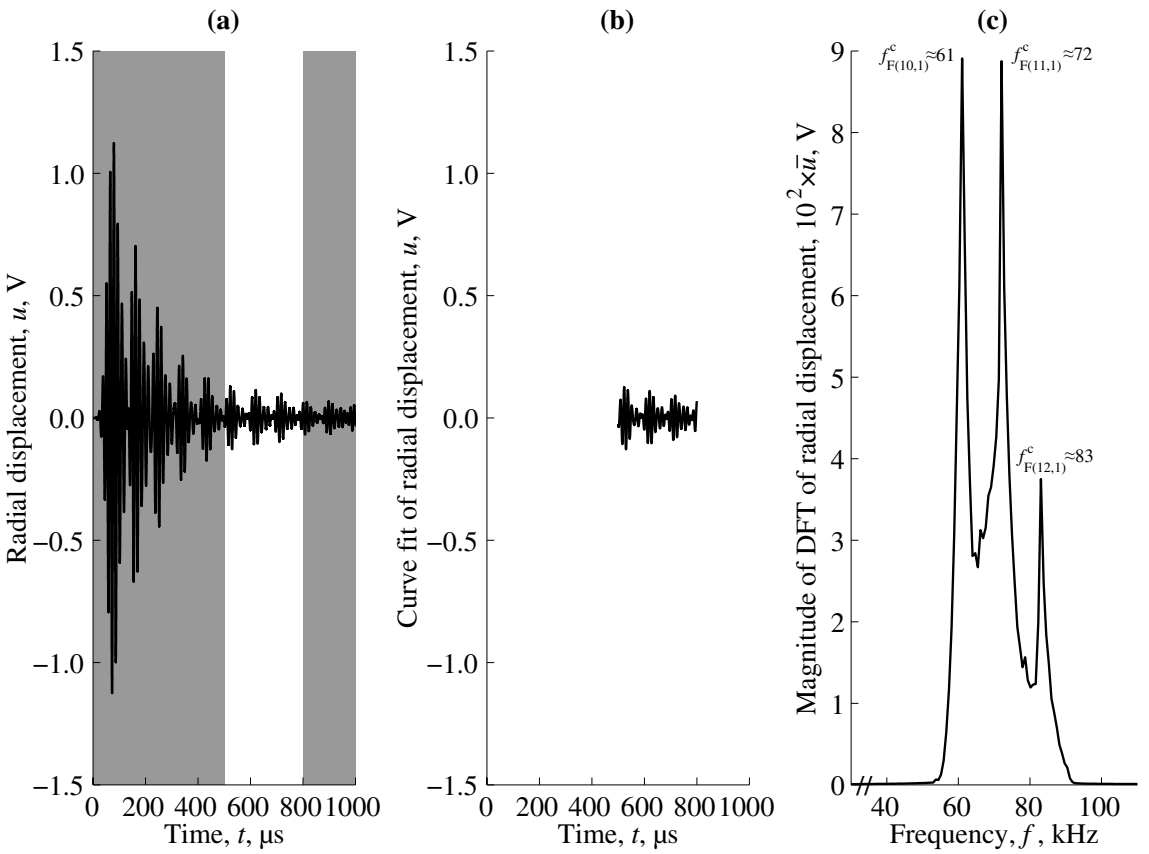

Figure 3.11. Showing (a) the radial displacement measured on the outer surface of an aluminium pipe at $\theta \approx 0$ and $z^* = z/H \approx 5.1$, (b) temporal curve fit of "free vibration" portion, and (c) DFT of time history before the first end reflection's arrival in (a).

imations and the refined cutoff frequencies are presented in Table 3.4. The reconstituted time history derived from the refined frequencies, phases, and amplitudes is shown in Figure 3.11 (b). It agrees well with the corresponding original history of Figure 3.11 (a).

The nearest neighbour inversion procedure was applied and the results are summarized in Table 3.5. The pipe's outer diameter, D_o, wall thickness, H, and density, ρ, were determined independently as before. However the elastic properties are compared now

Table 3.4. Initial and refined cutoff frequencies for the aluminium pipe.

Mode	Initial Approximation, kHz	Refined Value, kHz
F(10,1)	61.029	61.502
F(11,1)	72.059	71.771
F(12,1)	83.088	83.063

Table 3.5. Comparing (a) [(b)] conventionally [typically] and ultrasonically measured values for an aluminium pipe.

(a)

Property	Conventional approach	Initial ultrasonic value	Revised ultrasonic range
Density, ρ, slug/ft^3 (kg m^{-3})	5.0±0.4 (2600±200)	—	—
Outer diameter, D_o, in (mm)	3.50±0.01 (88.8±0.3)	—	—
Wall thickness, H, in (mm)	0.22±0.01 (5.5±0.3)	0.22 (5.6)	0.22±0.01 (5.5±0.3)
Mean radius, R, in (mm)	1.642±0.008 (41.7±0.2)	1.634 (41.5)	1.64±0.01 (41.6±0.3)
Thickness to mean radius ratio, (H/R)	0.131±0.009	0.134	0.132±0.008

(b)

Property	Typical value	Initial ultrasonic value	Revised ultrasonic range
Young's modulus, E, ksi (GPa)	10,000–10,400 (69–72)	9,900 (68)	10,000±1,500 (69±10)
Lamé constant, μ, (Shear modulus, G), ksi (GPa)	3,800–3,900 (26–27)	4,000 (28)	4,000±600 (28±4)
Lamé constant, λ, ksi (GPa)	4,800–12,600 (33–87)	3,000 (21)	3,900±3,200 (27±22)
Ratio of Lamé constants, (λ/μ)	1.2–3.3	0.76	1.0±0.8
Poisson's ratio, ν	0.28–0.38	0.22	0.2(5)±0.1

against typical values obtained from readily available, published sources. The ultrasonic measurements generally agreed, within experimental uncertainty, with the corresponding, conventionally determined or typical values.

3.4 Conclusions and closing remarks

A computer based, inverse procedure was described that simultaneously determined a homogeneous, isotropic pipe's elastic properties and wall thickness. The procedure, which is very straightforward to implement, is summarised next.

1. Choose a forcing pulse with a frequency bandwidth that contains several cutoff frequencies of the pipe of interest.

2. Carefully attach two transducers to the pipe's outer surface. Guidelines for selecting their separation are given below.

3. Pulse the transmitting transducer by using the forcing pulse selected in step 1.

4. Record a digital representation of the signal measured by the receiving transducer.

5. Estimate the cutoff frequencies from the signal recorded in step 4. The following sub-steps are required.

   (a) Compute the DFT of the signal collected in step 4.

   (b) Determine the frequencies at which the dominant peaks of the DFT's magnitude occur. Note the corresponding amplitudes and phase angles.

   (c) Apply the curve fitting technique described in Section 3.2.2 to the time history recorded in step 4 to recover refined estimates of the cutoff frequencies. An appropriate time window can be determined by computing the reassigned pseudo Margenau-Hill time-frequency distribution of the time history recorded in step 4. (Convenient initial approximations to the modal amplitudes, phase angles, and cutoff frequencies were determined in step 5b.)

6. The pipe's elastic constants and wall thickness, along with estimates of their uncertainties, can be determined by using the minimization and uncertainty estimation procedures detailed in Section 3.2.3. (The cutoff frequencies to be used in these procedures were determined in step 5c.)

The above procedural steps used the cutoff frequencies of three ultrasonic guided wave modes that were employed with a SAFE forward solver and the pipe's known density and

outer diameter. Dimensional and elastic properties were shown to agree, within estimated uncertainties, with those preassigned in a forward computer simulation. Then the practical viability was demonstrated experimentally by using two commercial pipe specimens. The dimensional and elastic properties agreed again, within estimated uncertainties, with corresponding values obtained conventionally. However, large uncertainties were encountered invariably for the Lamé constant, λ, and Poisson's ratio, ν. The F(10,1), F(11,1), and F(12,1) modes were used in this chapter to illustrate the procedure. Extensive computer simulations suggested, however, that *any* three convenient modes can be utilized in the procedure providing the caveats given in Section 1.4 are observed. A statistical analysis [128] of a data set containing approximately 125 measured time histories indicated that the cutoff frequencies extracted using the curve fitting procedure given in Section 3.2.2 agree best with predictions when they are recovered at virtually pure axial offsets around $2.55 \lesssim z/H \lesssim 10.2$. The present technique can be automated and adapted, with straightforward modifications, as a corrosion screening tool providing variations in the circularity of a pipe's cross section and its axial variations are not severe.

The previously described procedure leads inherently to a pipe that conforms to the assumptions made in the SAFE model. Of these assumptions, the ones which may most limit the procedure's application are those related to the pipe's assumed geometry. Out-of-roundness or a wall's thickness variations in a cross section may be handled straightforwardly by using a two-dimensional finite element model of the cross section rather than the one-dimensional model and Fourier series expansion used presently. A wall thickness which varies along the pipe's axis is a more difficult problem. The hybrid-SAFE technique described in Chapter 4 can be employed straightforwardly to model arbitrary wall variations if it is sufficient to consider only the variations between the input and monitoring locations. The effect of including a mating finite element region depends on the severity of the wall variations. No significant change in the cutoff frequencies is expected if the wall variations are small and smooth relative to the nominal wall thickness. However, if this is not the case,

significant wave scattering can be introduced so that the procedure described in Chapter 4 is more appropriate. On the other hand, if the wall thickness variations remote from the two transducer locations are significant then it is probable that a fully three-dimensional finite element approach using time integration is more appropriate. Such considerations are beyond the present scope.

Chapter 4

Wave Scattering–Another Forward Problem

4.1 Introduction

Detecting and sizing flaws is a first step towards assessing the "health" of a structure. From a practical perspective, in situ measurements which are quick, reliable and non-destructive are desirable. An ultrasonic-based approach is one plausible candidate. A particular attraction of single or "focussed guided waves" is that they can propagate at least several metres so they have been used to interrogate otherwise inaccessible locations [9, 70, 71, 82, 90]. In comparison to the simultaneous presence of many modes, the behaviour of a single, essentially non-dispersive mode seems capable of being interpreted more easily and, consequently, forms a more common experimental platform [70, 71]. However, a single mode's excitation is quite difficult and expensive to implement relative to the simultaneous generation of several modes by a "point"-like force. Even if excited, a single mode is likely converted to additional modes at geometrical discontinuities [69, 71]. Such modes are generally dispersive so that the form of a propagating wave packet changes as it travels along a structure. Moreover, not all modes are scattered equally by a given discontinuity [69]. The objective here is to computationally assess the feasibility of using a single Frequency Response Function (FRF) of several guided wave modes, rather than a detailed response around the circumference of the pipe at a single frequency [87], to detect and characterize notch-like defects in a homogeneous, isotropic steel pipe. This type of defect is chosen because computed and experimental results are available for the reflection coefficients of the essentially nondispersive L(0,2) mode [70]. Therefore, a useful check is provided.

An axisymmetric notch (i.e., wave scatterer) is explored first because it gives a reference for more realistic, nonaxisymmetric geometries and it permits the modelling of a variety of practical geometries (e.g., welds and flanges [65]). Moreover, a straightforward extension

of the hybrid SAFE technique [65] is possible in which finite element and wave propagation regions, around the notch and elsewhere respectively, are coupled. The extension is used to model the scattering of higher order, nonaxisymmetric guided waves with less computational burden than that expended when employing solely three-dimensional finite elements [66–68, 73]. Also, important insight is provided by the modal analysis inherent to the hybrid SAFE technique. This frequency oriented information is not obtained so readily if a time marching, finite element procedure is used.

The technique which utilized cutoff frequencies in Chapters 2 and 3 to find an unblemished pipe's dimensional and elastic properties is extended to locally detect and characterize an axisymmetric notch in the pipe. The approach proposed complements the current use of employing one non-dispersive, guided wave mode to detect a remote defect. Illustrative examples show, for apparently the first time, that singularities at frequencies in a FRF caused by a notch are *distinct*[1] from the unblemished pipe's cutoff frequencies. Moreover, the frequency differences between these singularities and an unblemished pipe's cutoff frequencies are shown to depend on a notch's dimensions. The procedure suggested for nonaxisymmetic notches is a straightforward generalization of the axisymmetric case. However, at least two frequency differences are needed even for an axisymmetric notch. Although attempts have been made previously [101–103] to use cutoff frequencies to "detect and classify" corrosion, these procedures involved a single mode's cutoff frequency which is applicable only to a spatially uniform thinning and not notches. On the other hand, predictions have been shown to improve for the analogous low frequency vibrations of a defective beam when an increasing number of up to four (natural) frequencies are employed as in, for example, [129–131].

[1]Previous studies, for example [65, 68], have noted strong wave scattering "at" cutoff frequencies. The frequency resolution was so coarse, however, that the scattering appeared artificially to coincide with a cutoff frequency of the unblemished pipe.

4.2 Axisymmetric Scatterers

4.2.1 Preamble

The idealizations of a pipe and an axisymmetric wave scatterer are described first. Then a comprehensive outline is given of the (axisymmetric) finite element model and its interface to a connecting region in which a wavefunction expansion is employed. Imposing continuity conditions on this interface allows the effect of wave scattering to be determined in the otherwise infinite waveguide. Results are presented for several simulations of wave scattering by an outer surface breaking notch[2]. Comparisons are made between the new and previous simulations as well as available experimental data. Finally, interpretations and conclusions are drawn.

4.2.2 Description of pipe, notch, and finite element region

4.2.2.1 Description of pipe and notch

The infinitely long pipe illustrated in Figure 4.1 is considered. It is assumed to be modelled reasonably as uniformly right circular, homogeneous, linearly elastic, and isotropic. Then the wavefunctions described in Chapter 2 can be used again to describe the displacement fields in the "parent" pipe which excludes the defective region. In particular, the pipe has Lamé constants λ and μ, density ρ, a constant mean radius R, outside diameter D_o, and wall thickness H, in addition to traction free, inner and outer surfaces. The radial variation in the parent pipe is modelled by utilizing N finite elements through the pipe's wall. Positions and displacements are described in terms of a right hand cylindrical coordinate system (r, θ, z), with solely the r and z axes illustrated in Figure 4.1. An axisymmetric

[2] All illustrative examples use outer surface breaking notches because they are easiest to simulate experimentally. Consequently such notches have been studied more extensively. The modelling technique can be applied, in principle, to any arbitrary axisymmetric scatterer by generating a finite element mesh appropriate to the scatterer's geometry.

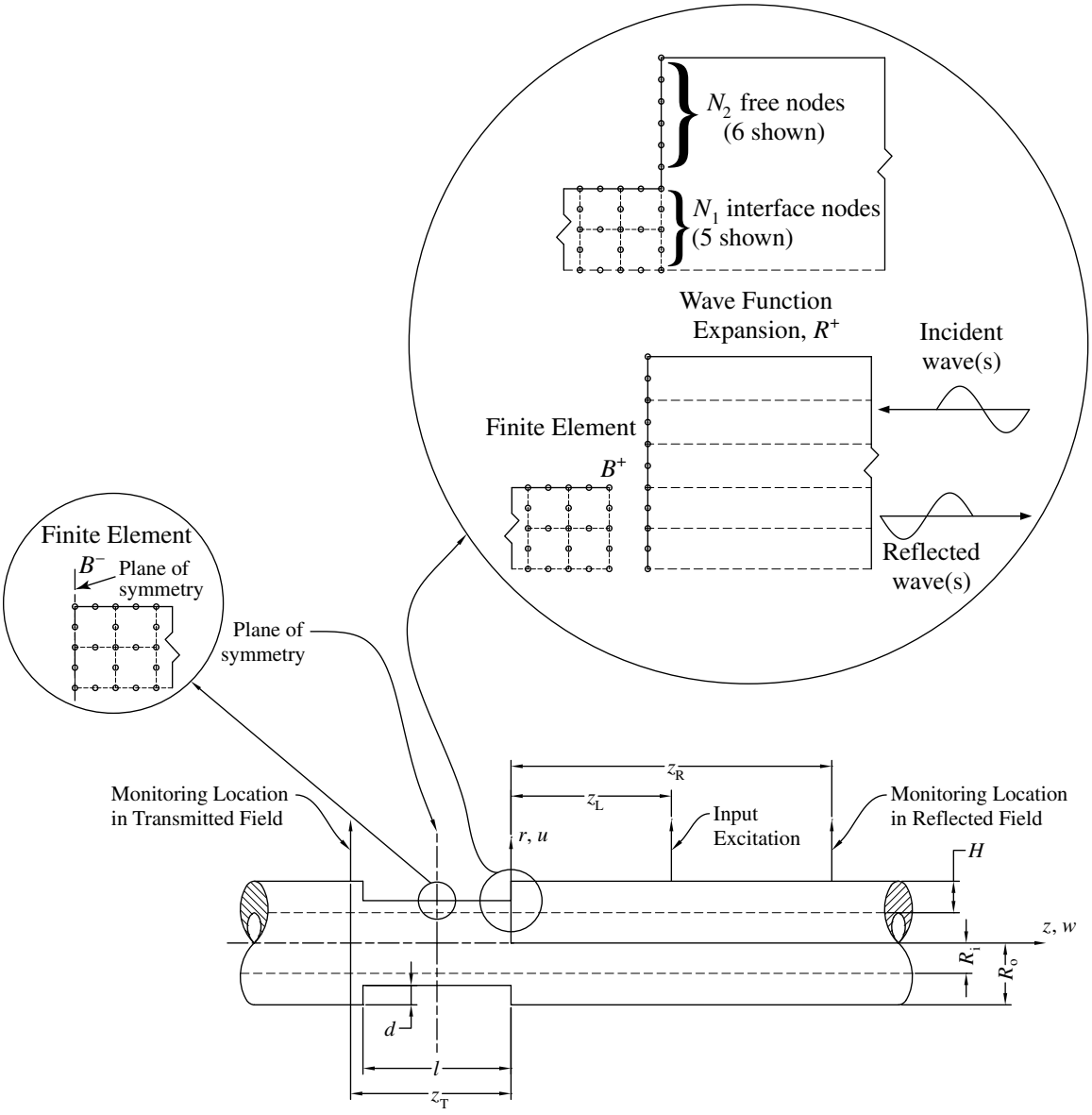

Figure 4.1. Model of part of the parent pipe and the axisymmetric notch.

wave scatterer is assumed to exist between $-l \leq z \leq 0$. This scatterer, which can have any axisymmetric geometry, is shown in the figure as a rectangular shaped, open notch having depth, d, and axial length, l. The motions caused by a transient force are modelled by using a(n approximate) wavefunction expansion in the region denoted by R^+ in addition to an axisymmetric finite element model in the region bounded by B^+ and B^-. The latter two boundaries, which coincide with the planes $z = 0$ and $z = -l/2$, define the axial extents of half the axially symmetric notch. The notch is introduced into an otherwise

unblemished pipe by simply removing finite elements, as illustrated in Figure 4.1. It is well understood [68–70, 132] that singularities in the stress field that occur at the notch's corners are not described accurately by this method[3]. However, the far field behaviour is modelled with sufficient accuracy to be meaningful [68–70, 132]. The defective pipe is symmetrical[4] about the plane $z = -l/2$ so that, as implied previously, only half the pipe and scatterer need be considered but with appropriate boundary conditions prescribed on B^-. Motions are obtained for $z \leq -l$ from those found in R^+ by using appropriate symmetry and antisymmetry arguments.

4.2.2.2 Finite element region

Eight node, quadratic, quadrilateral finite elements [107] are used to describe the motions in the finite element region bounded by the planes $z = 0$ and $z = -l/2$. The application of Hamilton's principle to the finite element region, which is described more completely in Appendix F, gives

$$\mathbf{Sq} = \mathbf{P} \tag{4.2.1}$$

where

$$\mathbf{S} = \mathbf{K}_\mathrm{I} - \omega^2 \mathbf{M}_\mathrm{I}. \tag{4.2.2}$$

$\mathbf{S}$ is a dynamic stiffness matrix whereas $\mathbf{q}$ and $\mathbf{P}$ are assembled vectors of nodal displacements and forces, respectively, for the finite element region. The $\mathbf{K}_\mathrm{I}$ and $\mathbf{M}_\mathrm{I}$ in equation (4.2.2), on the other hand, are the assembled stiffness and mass matrices, respectively, of the finite element region and ω is the angular frequency of the externally applied excita-

[3]Crack-tip elements, having their "side nodes at quarter points of their respective sides," could have been used to improve the near field accuracy [107]. However, these elements were not used for the sake of simplicity.

[4]This restriction can be removed by enclosing the *entire* scatterer in a finite element region and enforcing continuity conditions at *both* $z = 0$ and $z = -l$. The modifications can be implemented straightforwardly but more computational effort would be required.

tion. Equation (4.2.1) can be partitioned as

$$\begin{bmatrix} \mathbf{S}_{\mathrm{II}} & \mathbf{S}_{\mathrm{IB}} \\ \mathbf{S}_{\mathrm{BI}} & \mathbf{S}_{\mathrm{BB}} \end{bmatrix} \begin{Bmatrix} \mathbf{q}_{\mathrm{I}} \\ \mathbf{q}_{\mathrm{B}} \end{Bmatrix} = \begin{Bmatrix} \mathbf{P}_{\mathrm{I}} \\ \mathbf{P}_{\mathrm{B}} \end{Bmatrix} \tag{4.2.3}$$

where subscript I (B) refers to a node of the finite element region that is inside (on the boundaries [B^+ or B^-]) of the finite element region. By assuming that no external force is located in the finite element region (i.e., all the forces are applied to B^+ or B^- of the finite element region), then $\mathbf{P}_{\mathrm{I}} = \mathbf{0}$. It follows that:

$$\mathbf{S}_{\mathrm{II}}\mathbf{q}_{\mathrm{I}} + \mathbf{S}_{\mathrm{IB}}\mathbf{q}_{\mathrm{B}} = \mathbf{0} \tag{4.2.4a}$$

and

$$\mathbf{S}_{\mathrm{BI}}\mathbf{q}_{\mathrm{I}} + \mathbf{S}_{\mathrm{BB}}\mathbf{q}_{\mathrm{B}} = \mathbf{P}_{\mathrm{B}}, \tag{4.2.4b}$$

where, from equation (4.2.4a),

$$\mathbf{q}_{\mathrm{I}} = -\mathbf{S}_{\mathrm{II}}^{-1}\mathbf{S}_{\mathrm{IB}}\mathbf{q}_{\mathrm{B}}. \tag{4.2.5}$$

From equations (4.2.4b) and (4.2.5)

$$\mathbf{S}_{\mathrm{BI}}\left(-\mathbf{S}_{\mathrm{II}}^{-1}\mathbf{S}_{\mathrm{IB}}\mathbf{q}_{\mathrm{B}}\right) + \mathbf{S}_{\mathrm{BB}}\mathbf{q}_{\mathrm{B}} = \left(-\mathbf{S}_{\mathrm{BI}}\mathbf{S}_{\mathrm{II}}^{-1}\mathbf{S}_{\mathrm{IB}} + \mathbf{S}_{\mathrm{BB}}\right)\mathbf{q}_{\mathrm{B}} = \mathbf{P}_{\mathrm{B}}. \tag{4.2.6}$$

Let

$$\check{\mathbf{S}} = \left(-\mathbf{S}_{\mathrm{BI}}\mathbf{S}_{\mathrm{II}}^{-1}\mathbf{S}_{\mathrm{IB}} + \mathbf{S}_{\mathrm{BB}}\right), \tag{4.2.7}$$

so that, from equations (4.2.6) and (4.2.7),

$$\check{\mathbf{S}}\mathbf{q}_{\mathrm{B}} = \mathbf{P}_{\mathrm{B}}. \tag{4.2.8}$$

Equation (4.2.8) contains only force and displacement components on the boundaries B^+ and B^-. Matrices can be partitioned, as before, to give

$$\begin{bmatrix} \breve{\mathbf{S}}_{--} & \breve{\mathbf{S}}_{-+} \\ \breve{\mathbf{S}}_{+-} & \breve{\mathbf{S}}_{++} \end{bmatrix} \begin{Bmatrix} \mathbf{q}_- \\ \mathbf{q}_+ \end{Bmatrix} = \begin{Bmatrix} \mathbf{P}_- \\ \mathbf{P}_+ \end{Bmatrix}, \tag{4.2.9}$$

where subscript $-$ $(+)$ refers to a node of the finite element region that is on boundary B^- (B^+).

4.2.3 Boundary conditions on B^-

To take advantage of the (assumed) symmetry of a defective pipe about the plane $z = -l/2$, a force in R^+ is represented by the superposition of symmetrical and antisymmetrical forces. The principle is illustrated in Figure 4.2 for a radial point force, $\mathbf{P}$. For (anti) symmetrical loading, the displacement in the (r and θ) z direction(s), as well as the stresses (σ_{zz}) σ_{rz} and $\sigma_{\theta z}$ vanish on B^-. The disappearance of a stress gives a corresponding null (consistent) nodal force. (Nodal forces f_r, f_θ, f_z correspond to the σ_{rz}, $\sigma_{\theta z}$, σ_{zz} stress components, respectively.) The assembled displacement and force vectors, $\mathbf{q}_-$ and $\mathbf{P}_-$ respectively, are partitioned and simplified as

$$\mathbf{q}_{\mathrm{s}-} = \begin{bmatrix} \mathbf{u}_{\mathrm{s}r-} & \mathbf{u}_{\mathrm{s}\theta-} & \mathbf{0} \end{bmatrix}^{\mathrm{T}} \text{ and } \mathbf{P}_{\mathrm{s}-} = \begin{bmatrix} \mathbf{0} & \mathbf{0} & \mathbf{f}_{\mathrm{s}z-} \end{bmatrix}^{\mathrm{T}} \tag{4.2.10a}$$

$$\mathbf{q}_{\mathrm{a}-} = \begin{bmatrix} \mathbf{0} & \mathbf{0} & \mathbf{u}_{\mathrm{a}z-} \end{bmatrix}^{\mathrm{T}} \text{ and } \mathbf{P}_{\mathrm{a}-} = \begin{bmatrix} \mathbf{f}_{\mathrm{a}r-} & \mathbf{f}_{\mathrm{a}\theta-} & \mathbf{0} \end{bmatrix}^{\mathrm{T}}, \tag{4.2.10b}$$

where subscript (a) s denotes the (anti) symmetrical loading. Note that, where a displacement is known on B^-, the corresponding (reaction) force is unknown. Condensing out the zero displacements on B^- and ignoring the unknown reaction forces (as they are not of interest presently), allows the deletion of the (first) last $(2N_1)$ N_1 rows and columns of $\breve{\mathbf{S}}_{--}$, (first) last $(2N_1)$ N_1 rows of $\breve{\mathbf{S}}_{-+}$, and the (first) last $(2N_1)$ N_1 columns of $\breve{\mathbf{S}}_{+-}$ as well as the

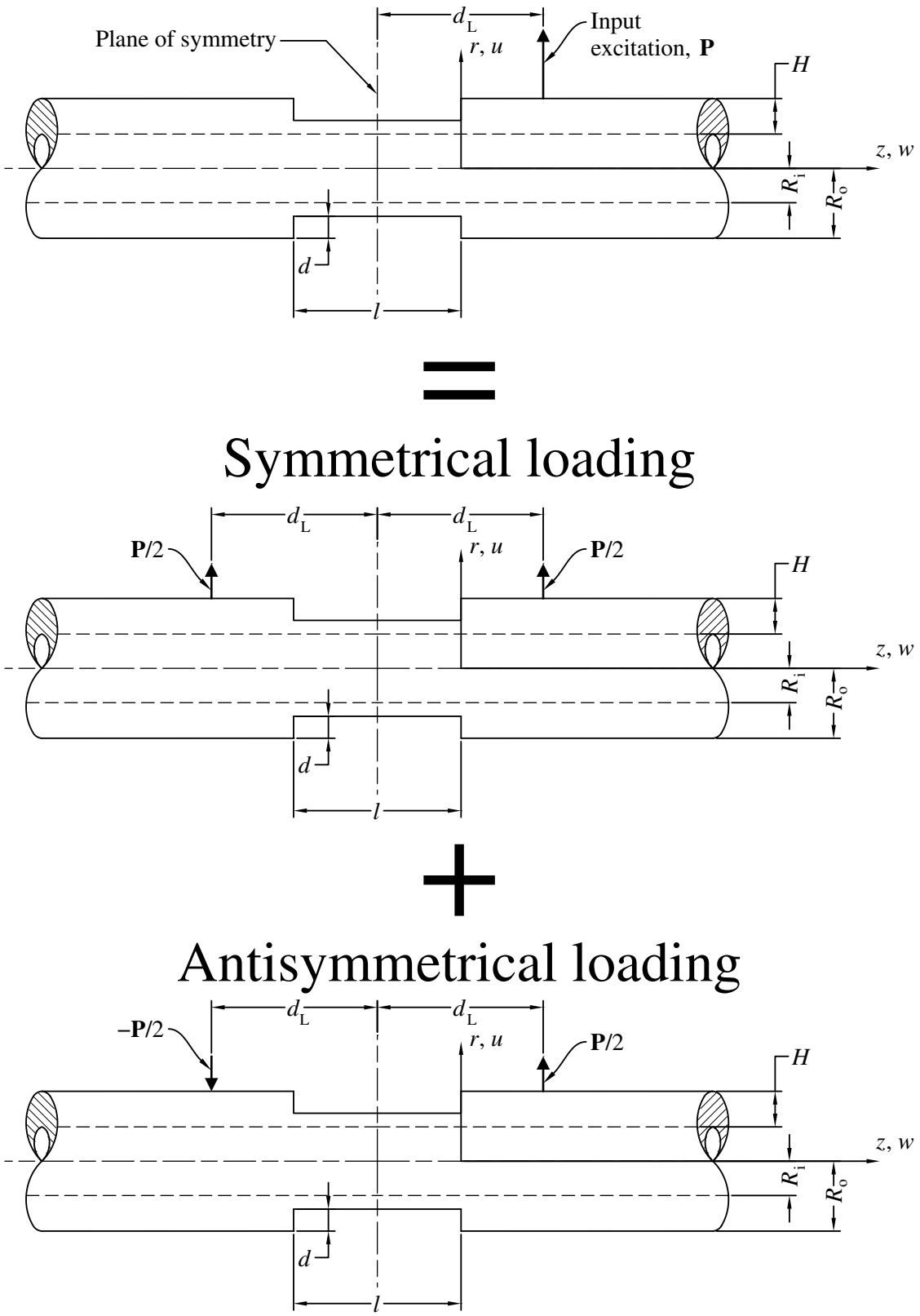

Figure 4.2. Illustrating the decomposition of a radial point force, **P**, into a superposition of two symmetrical and antisymmetrical forces, $\mathbf{P}/2$, about the plane $z = -l/2$.

corresponding rows of $\mathbf{q}_-$ and $\mathbf{P}_-$, in the (anti) symmetrical case. The N_1 is the number of nodes which are common to the finite element and wavefunction expansion regions. See Figure 4.1. Such modifications allow equation (4.2.9) to be simplified to

$$\begin{bmatrix} \mathbf{S}^{\maltese}_{--} & \mathbf{S}^{\maltese}_{-+} \\ \mathbf{S}^{\maltese}_{+-} & \mathbf{S}_{++} \end{bmatrix} \begin{Bmatrix} \mathbf{q}^{\maltese}_- \\ \mathbf{q}_+ \end{Bmatrix} = \begin{Bmatrix} \mathbf{0} \\ \mathbf{P}_+ \end{Bmatrix} \tag{4.2.11}$$

for both the symmetrical and antisymmetrical cases. Superscript ✠ indicates the condensation of the appropriate zero displacements and the neglect of the reaction forces on B^-. Equation (4.2.11) leads to

$$\mathbf{S}^{\maltese}_{--}\mathbf{q}^{\maltese}_- + \mathbf{S}^{\maltese}_{-+}\mathbf{q}_+ = \mathbf{0} \tag{4.2.12a}$$

and

$$\mathbf{S}^{\maltese}_{+-}\mathbf{q}^{\maltese}_- + \mathbf{S}_{++}\mathbf{q}_+ = \mathbf{P}_+, \tag{4.2.12b}$$

whereas, from equation (4.2.12a),

$$\mathbf{q}^{\maltese}_- = -\mathbf{S}^{\maltese\ -1}_{--}\mathbf{S}^{\maltese}_{-+}\mathbf{q}_+, \tag{4.2.13}$$

so that, from equations (4.2.12b) and (4.2.13),

$$\mathbf{S}^{\maltese}_{+-}\left(-\mathbf{S}^{\maltese\ -1}_{--}\mathbf{S}^{\maltese}_{-+}\mathbf{q}_+\right) + \mathbf{S}_{++}\mathbf{q}_+ = \left(-\mathbf{S}^{\maltese}_{+-}\mathbf{S}^{\maltese\ -1}_{--}\mathbf{S}^{\maltese}_{-+} + \mathbf{S}_{++}\right)\mathbf{q}_+ = \mathbf{P}_+. \tag{4.2.14}$$

Let

$$\mathbf{S}^{\ddagger} = \left(-\mathbf{S}^{\maltese}_{+-}\mathbf{S}^{\maltese\ -1}_{--}\mathbf{S}^{\maltese}_{-+} + \mathbf{S}_{++}\right) \tag{4.2.15}$$

so that equation (4.2.14) takes again the more convenient notational form

$$\mathbf{S}^{\ddagger}\mathbf{q}_+ = \mathbf{P}_+. \tag{4.2.16}$$

Equation (4.2.16) contains only a known dynamic stiffness matrix and, as yet, unknown displacements and forces on the boundary B^+. It is "interfaced" with the next section with the parent pipe (which acts as a waveguide) by applying continuity conditions between the finite element and wavefunction expansion regions to eliminate the unknown variables.

4.2.4 Interface between wavefunction and finite element regions

4.2.4.1 Representation of the displacement field in R^+ by a modal expansion

Consider, for convenience, a *single* harmonic wave mode with circular frequency, ω, having circumferential wavenumber n_{in}, order m_{in}, and *unit* amplitude that is incident on the plane $z = 0$. This wave is scattered generally at the interface between the parent pipe and the finite element region whose cross sectional boundaries coincide with those of a notch. Consequently, reflected and transmitted wave fields are created by the interface. The transmitted field is obtained straightforwardly from knowledge of the reflected field by taking advantage of the symmetry about the plane $z = -l/2$. Therefore only the reflected field needs to be considered in detail. The displacements in the reflected wave field (at the radial coordinates of the finite element nodal points and $\theta = 0$) that lie in region R^+ can be written, for a given circumferential wave number n_{scat}, in the form

$$\mathbf{q}_+^{\text{scat}} = \sum_{m_{\text{scat}}=1}^{6N+3} A_{n_{\text{scat}}m_{\text{scat}}} \boldsymbol{\phi}^{\text{R}}_{n_{\text{scat}}m_{\text{scat}}\text{u}} \text{e}^{\text{j}k_{n_{\text{scat}}m_{\text{scat}}}z} = \mathbf{GA}. \tag{4.2.17}$$

Here $A_{n_{\text{scat}}m_{\text{scat}}}$, $\boldsymbol{\phi}^{\text{R}}_{n_{\text{scat}}m_{\text{scat}}\text{u}}$, and $k_{n_{\text{scat}}m_{\text{scat}}}$ are the amplitude, mode shape, and axial wave number, respectively, of the m^{th} scattered mode. Only modes having non-negative (non-positive) imaginary wave number components are admissible in the reflected (incident) field as a consequence of the radiation condition described on page 32. Moreover, no modal coupling exists between different n because the parent waveguide and finite element region are both axisymmetric so that n_{scat} necessarily equals n_{in}. Furthermore, the exponential term used

in equation (4.2.17) is unity because the displacements are evaluated at $z = 0$ due to the choice of the coordinate system's origin. Consequently, $\mathbf{G}$ in equation (4.2.17) is simply a matrix containing the mode shapes of the scattered wave field. On the other hand, $\mathbf{A}$ is a vector which "collects" the scattered waves' amplitudes.

4.2.4.2 Force free nodes

The last N_2 nodes illustrated in Figure 4.1 belong solely to the parent waveguide and, hence, they are traction (force) free. It follows that:

$$\mathbf{f}^{\text{in}} + \mathbf{f}^{\text{scat}} = \mathbf{0}, \tag{4.2.18}$$

where $\mathbf{f}^{\text{in}}$ and $\mathbf{f}^{\text{scat}}$ are the assembled (consistent) forces acting at these nodes. They correspond to the incident and scattered wave fields, respectively. Nodal forces arising from the incident wave field can be calculated from the Green's function. This derivation is discussed more conveniently in Appendix F. On the other hand, $\mathbf{f}^{\text{scat}}$ may be expressed, as detailed in Appendix F, in the form

$$\mathbf{f}^{\text{scat}} = \mathbf{F}_{\text{s1}}\mathbf{A}, \tag{4.2.19}$$

where $\mathbf{F}_{\text{s1}}$ is a matrix that "maps" vector $\mathbf{A}$ (of scattered wave amplitudes) into the last N_2 nodal forces.

4.2.4.3 Continuity conditions on boundary B^+

Consider now the common boundary, B^+, between the parent waveguide and finite element regions. Continuities of the nodal forces and displacements on boundary B^+ require that

$$\mathbf{q}_+ = \mathbf{q}_+^{\text{in}} + \mathbf{q}_+^{\text{scat}} \tag{4.2.20a}$$

and

$$\mathbf{P}_+ = \mathbf{f}_+^{\text{in}} + \mathbf{f}_+^{\text{scat}}. \tag{4.2.20b}$$

Both $\mathbf{f}_+^{\text{in}}$ and $\mathbf{q}_+^{\text{in}}$ can be calculated from the known Green's function. Moreover, $\mathbf{f}_+^{\text{scat}}$ takes the same general form as $\mathbf{f}^{\text{scat}}$.

The use of equations (4.2.16) and (4.2.20) leads to

$$\mathbf{S}^{\ddagger}\mathbf{q}_+ = \mathbf{P}_+ = \mathbf{S}^{\ddagger}\left(\mathbf{q}_+^{\text{in}} + \mathbf{q}_+^{\text{scat}}\right) = \mathbf{f}_+^{\text{in}} + \mathbf{f}_+^{\text{scat}}, \tag{4.2.21}$$

which, after rearrangement, gives

$$\mathbf{S}^{\ddagger}\mathbf{q}_+^{\text{scat}} - \mathbf{f}_+^{\text{scat}} = \mathbf{f}_+^{\text{in}} - \mathbf{S}^{\ddagger}\mathbf{q}_+^{\text{in}}. \tag{4.2.22}$$

Substituting equation (4.2.17) into equation (4.2.22) produces

$$\mathbf{S}^{\ddagger}\mathbf{G}\mathbf{A} - \mathbf{F}_{s2}\mathbf{A} = \left(\mathbf{S}^{\ddagger}\mathbf{G} - \mathbf{F}_{s2}\right)\mathbf{A} = \mathbf{f}_+^{\text{in}} - \mathbf{S}^{\ddagger}\mathbf{q}_+^{\text{in}} \tag{4.2.23}$$

where $\mathbf{F}_{s2}$ is a matrix, similar to $\mathbf{F}_{s1}$, that "maps" $\mathbf{A}$ into the first N_1 scattered nodal forces.

4.2.5 Resulting system of linear equations

Suppose next that

$$\left(\mathbf{S}^{\ddagger}\mathbf{G} - \mathbf{F}_{s2}\right) = \mathbf{F}_2 \tag{4.2.24a}$$

and

$$\mathbf{f}_+^{\text{in}} - \mathbf{S}^{\ddagger}\mathbf{q}_+^{\text{in}} = \mathbf{R}_{\text{B}}. \tag{4.2.24b}$$

It can be shown, by substituting the definitions given in the last two equations into equation (4.2.23), that

$$\mathbf{F}_2\mathbf{A} = \mathbf{R}_\mathrm{B}. \tag{4.2.25}$$

Combining equations (4.2.18), (4.2.19), and (4.2.25) yields

$$\begin{bmatrix}\mathbf{F}_1\\ \mathbf{F}_2\end{bmatrix}\mathbf{A} = \begin{Bmatrix}\mathbf{f}^\mathrm{in}\\ \mathbf{R}_\mathrm{B}\end{Bmatrix} = \mathbf{F}\mathbf{A} = \mathbf{R} \tag{4.2.26}$$

where $\mathbf{F}_1 = -\mathbf{F}_{s1}$, $\mathbf{F} = \begin{bmatrix}\mathbf{F}_1 & \mathbf{F}_2\end{bmatrix}^\mathrm{T}$, and $\mathbf{R} = \begin{bmatrix}\mathbf{f}^\mathrm{in} & \mathbf{R}_\mathrm{B}\end{bmatrix}^\mathrm{T}$. The amplitudes of the scattered waves can be recovered as

$$\mathbf{A} = \mathbf{F}^{-1}\mathbf{R}. \tag{4.2.27}$$

Note that matrix $\mathbf{F}$ in equation (4.2.27) is square and invertible because *all* $6N + 3$ axial modes are retained for each circumferential harmonic wavenumber. If the effects of one or more of the axial wave modes are neglected, a minimization procedure such as the one used in [65] would be required to "solve" a linear system similar to equation (4.2.27). This last process will be employed later for three-dimensional (i.e., nonaxisymmetric) notches.

Equation (4.2.27) must be evaluated for both the symmetrical and antisymmetrical components of the excitation in order to recover their combined effect. The reflected and transmitted wave amplitudes for the nm^th scattered wave mode, $R_{\mathrm{M_{in}}(n_\mathrm{in},m_\mathrm{in}),\mathrm{M_{scat}}(n_\mathrm{scat},m_\mathrm{scat})}$ and $T_{\mathrm{M_{in}}(n_\mathrm{in},m_\mathrm{in}),\mathrm{M_{scat}}(n_\mathrm{scat},m_\mathrm{scat})}$ respectively, which are both complex, are given by

$$R_{\mathrm{M_{in}}(n_\mathrm{in},m_\mathrm{in}),\mathrm{M_{scat}}(n_\mathrm{scat},m_\mathrm{scat})} = \left(A^\mathrm{s}_{n_\mathrm{scat}m_\mathrm{scat}} + A^\mathrm{a}_{n_\mathrm{scat}m_\mathrm{scat}}\right)/2 \tag{4.2.28a}$$

and

$$T_{\mathrm{M_{in}}(n_\mathrm{in},m_\mathrm{in}),\mathrm{M_{scat}}(n_\mathrm{scat},m_\mathrm{scat})} = \left(A^\mathrm{s}_{n_\mathrm{scat}m_\mathrm{scat}} - A^\mathrm{a}_{n_\mathrm{scat}m_\mathrm{scat}}\right)/2. \tag{4.2.28b}$$

$A_{n_\mathrm{scat}m_\mathrm{scat}}$ is the nm^th scattered wave amplitude and superscript (a) s denotes the solution corresponding to the (anti) symmetrical boundary conditions. The $R_{\mathrm{M_{in}}(n_\mathrm{in},m_\mathrm{in}),\mathrm{M_{scat}}(n_\mathrm{scat},m_\mathrm{scat})}$ and

$T_{\mathrm{M_{in}}(n_{\mathrm{in}},m_{\mathrm{in}}),\mathrm{M_{scat}}(n_{\mathrm{scat}},m_{\mathrm{scat}})}$ symbolize the standard normalized reflection and transmission coefficient [70], respectively, because they are calculated for each individual incident mode by presuming it has a unit amplitude[5] at the coordinate system's origin. Moreover, these coefficients represent the amplitudes of the scattered waves at the planes $z = 0$ and $z = -l$, respectively. All the reflection and transmission coefficients are identified by utilizing subscripts that give *both* incident and scattered modes caused by cross coupling. This situation may exist between different scattered wave modes. Corresponding labels take the forms $R_{\mathrm{M_{in}}(n_{\mathrm{in}},m_{\mathrm{in}}),\mathrm{M_{scat}}(n_{\mathrm{scat}},m_{\mathrm{scat}})}$ and $T_{\mathrm{M_{in}}(n_{\mathrm{in}},m_{\mathrm{in}}),\mathrm{M_{scat}}(n_{\mathrm{scat}},m_{\mathrm{scat}})}$ for the reflection and transmission coefficients. Subscript M is a "place-holder" for one of T, L, or F which indicate a torsional, longitudinal, or flexural mode, respectively. On the other hand, n and m represent the circumferential wavenumber and axial order, respectively. Indicators "in" and "scat" are used to denote the incident and scattered wave modes. The reflection coefficient $R_{\mathrm{L(0,2),F(1,1)}}$, for example, represents the reflected contribution of the F(1,1) mode caused when the L(0,2) mode is incident on the wave scatterer[6]. The rationale for choosing the subscripts in this fashion is that they are consistent with the modal identification scheme used in [81].

4.2.6 Scattered displacement fields

The reflection and transmission coefficients defined in equation (4.2.28) are convenient mathematical concepts which have important properties that provide convenient checks of a computer program's accuracy. (Appendix H uses several of these properties to validate the numerical accuracy of the programs used here.) However, their practical usefulness is limited. Limitations are due mainly to the doubly infinite set of the unblemished regions of the notched pipe's wave modes which may exist, in principle, simultaneously. Even if a single mode is excited, it may be converted partially into other modes at the geomet-

[5]The magnitudes of $R_{\mathrm{M_{in}}(n_{\mathrm{in}},m_{\mathrm{in}}),\mathrm{M_{scat}}(n_{\mathrm{scat}},m_{\mathrm{scat}})}$ and $T_{\mathrm{M_{in}}(n_{\mathrm{in}},m_{\mathrm{in}}),\mathrm{M_{scat}}(n_{\mathrm{scat}},m_{\mathrm{scat}})}$ depend on the scaling of the mode shapes for modes excited by modal conversions, i.e, $m_{\mathrm{scat}} \neq m_{\mathrm{in}}$ for axisymmetric scatterers. All the mode shapes are scaled to have a vector norm magnitude of unity. See footnote 1 located on page 30.

[6]This particular modal conversion cannot occur with an axisymmetric scatterer but it is used to illustrate the general case.

ric discontinuity of the notch. All such modes act together so that the measurement of a *particular* mode's reflection and transmission coefficients becomes challenging because individual modal contributions need to be separated. An illustration of this difficulty is given later when considering a three-dimensional notch. The direct determination of the reflection and transmission coefficients also presumes that a scattered pulse can be isolated in time from the direct[7] wave(s). Although a point-like excitation is attractive, as it is easier to implement, it appears to make this modal resolution more difficult because the number of participating modes is generally increased. However, a simple metric is identified later whose appearance is similar to the cutoff frequencies utilized in Chapter 3 to find a pipe's properties. This metric can be used to characterize a notch when the notched pipe is "interrogated" by simultaneously using several modes having cutoff frequencies in the excitation's bandwidth. The approach taken here for the simultaneous excitation and measurement of this metric (by employing multiple modes) is similar to that used in Chapter 3. Further details will be provided later.

Two advantages of this metric, besides convenience, are that the scattered waves need not be separated from the direct waves and, furthermore, wave amplitudes are not required. Consequently the need for a transducer's consistent coupling to a pipe is ameliorated. However, a compromise must be made. The metric depends upon singularities which are introduced by the notch. Each singularity occurs at a frequency somewhat *below* that of the unblemished pipe's nearest cutoff frequency. Its effects are localized to a region around the notch which makes the metric more suitable for "spot" checks or monitoring locations close to a likely defect (e.g., a weld, say). Therefore it complements the use of propagating modes which have been employed individually for the remote inspection of long lengths of pipe [9, 70, 71, 82, 90].

Scattered wave fields are required to illustrate the usefulness of the newly identified singularities. Consequently, modal summations which describe the corresponding displace-

[7]Direct waves are defined here as waves which, after being excited externally, arrive at an observation point on a pipe *without* interacting with a wave scatterer like a notch.

ment fields are discussed next. Point-like or pencil break excitations are simple to implement. Moreover, they readily excite the desired pipe modes so that more emphasis is placed, in this thesis, on this type of excitation. Furthermore, scattering solutions for a single incident mode are merely a subset of the several modes generally produced by a point-like excitation. However, the former solutions can be "extracted" readily as a result of the modal analysis inherent to a hybrid SAFE model.

The derivation of equation (4.2.28) has assumed a single harmonic wave of unit amplitude. However, as shown in Chapter 2, a point-like transient excitation generates many modes which have frequency dependent amplitudes. The temporal variation of the displacements in the resulting reflected wave field can be found by using a modal summation and inverse Fourier transform. This procedure is similar to the one employed to derive equation (2.3.17). Then the reflected displacement field caused by an incident mode having circumferential wavenumber n_{in} and order m_{in} can be written as

$$\mathbf{U}_{n_{\text{in}}m_{\text{in}}}(\theta, z, t) = \frac{1}{2\pi}\int_{-\infty}^{\infty} \overline{p}(\omega)\mathrm{e}^{-\mathrm{j}\omega t} A^{\text{in}}_{n_{\text{in}}m_{\text{in}}} \left[\sum_{m_{\text{scat}}=1}^{6N+3} R_{\mathrm{M}_{\text{in}}(n_{\text{in}},m_{\text{in}}),\mathrm{M}_{\text{scat}}(n_{\text{scat}},m_{\text{scat}})} \boldsymbol{\phi}^{\mathrm{R}}_{n_{\text{scat}}m_{\text{scat}}\mathrm{u}} \mathrm{e}^{\mathrm{j}k_{n_{\text{scat}}m_{\text{scat}}}z}\right] \mathrm{e}^{\mathrm{j}n_{\text{scat}}\theta}\mathrm{d}\omega \tag{4.2.29}$$

at the radial coordinates of the finite elements' nodal surfaces. Note that a total of $6N + 3$ axial modes, per circumferential wavenumber, are available from the SAFE idealization to describe the reflected wave field. Moreover, $A^{\text{in}}_{n_{\text{in}}m_{\text{in}}}$ is the frequency dependent amplitude of the incident mode. It can be determined, by using equation (2.3.16), to be

$$A^{\text{in}}_{n_{\text{in}}m_{\text{in}}} = \frac{\mathrm{j}\mathrm{sinc}(n_{\text{in}}\theta_0)}{2\pi r_0} \frac{\left(\boldsymbol{\phi}^{\mathrm{L}}_{m_{\text{in}}n_{\text{in}}\mathrm{l}}\right)^{\mathrm{T}} \overline{\mathbf{F}}_0}{B_{n_{\text{in}}m_{\text{in}}}} \mathrm{e}^{-\mathrm{j}k_{n_{\text{in}}m_{\text{in}}}z_{\mathrm{L}}}, \tag{4.2.30}$$

where, from Figure 4.1, z_{L} is the axial coordinate at which the point force is applied. Summing displacement contributions produced by all the incident n and m waves gives the total

reflected field (at the radial coordinates of the finite elements' nodal surfaces) as

$$\mathbf{U}(\theta, z, t) = \sum_{n_{\text{in}}=-\infty}^{\infty} \sum_{m_{\text{in}}=6N+4}^{12N+6} \mathbf{U}_{n_{\text{in}}m_{\text{in}}}(\theta, z, t). \tag{4.2.31}$$

Note that the index for the summation over the axial modes uses the $6N + 3$ leftward admissible waves from the SAFE idealization to describe the incident wave field. The approximate reflected displacement field through the pipe's wall can be found straightforwardly by invoking equation (2.3.1). The transmitted field takes a similar form. It is recovered by using symmetric-antisymmetic arguments. Hence, $T_{\text{M}_{\text{in}}(n_{\text{in}},m_{\text{in}}),\text{M}_{\text{scat}}(n_{\text{scat}},m_{\text{scat}})}$ and $(-z - l)$, where l is the notch's (positive axial) length, replace $R_{\text{M}_{\text{in}}(n_{\text{in}},m_{\text{in}}),\text{M}_{\text{scat}}(n_{\text{scat}},m_{\text{scat}})}$ and z, respectively, in equation (4.2.29). The signs of the axial displacement components are also modified to accommodate leftward rather than rightward admissible wavefunctions. Equations (4.2.30) and (4.2.31) can be used subsequently for the transmitted wave field.

4.2.7 Work balance

A convenient useful check of predicted modal conversions is derived from the conservation of energy principle. Consider initially the instantaneous power, $\mathcal{P}^{\text{in}}_{n_{\text{in}}m_{\text{in}}}$, of a single harmonic wave mode, $\text{M}_{\text{in}}(n_{\text{in}}, m_{\text{in}})$, having circular frequency, ω, when it is incident on the finite element region's boundary B^+. The $\mathcal{P}^{\text{in}}_{n_{\text{in}}m_{\text{in}}}$ can be written mathematically as

$$\begin{aligned}\mathcal{P}^{\text{in}}_{n_{\text{in}}m_{\text{in}}} = \frac{1}{2}\int_{r_{\text{i}}}^{r_{\text{o}}}\int_{0}^{2\pi}\Bigg(&\tau_{rz}^{n_{\text{in}}m_{\text{in}}}\widetilde{\frac{\mathrm{d}u_{n_{\text{in}}m_{\text{in}}}}{\mathrm{d}t}} + \tau_{\theta z}^{n_{\text{in}}m_{\text{in}}}\widetilde{\frac{\mathrm{d}v_{n_{\text{in}}m_{\text{in}}}}{\mathrm{d}t}} + \sigma_{zz}^{n_{\text{in}}m_{\text{in}}}\widetilde{\frac{\mathrm{d}w_{n_{\text{in}}m_{\text{in}}}}{\mathrm{d}t}} \\ &+\widetilde{\tau_{rz}^{n_{\text{in}}m_{\text{in}}}}\frac{\mathrm{d}u_{n_{\text{in}}m_{\text{in}}}}{\mathrm{d}t} + \widetilde{\tau_{\theta z}^{n_{\text{in}}m_{\text{in}}}}\frac{\mathrm{d}v_{n_{\text{in}}m_{\text{in}}}}{\mathrm{d}t} + \widetilde{\sigma_{zz}^{n_{\text{in}}m_{\text{in}}}}\frac{\mathrm{d}w_{n_{\text{in}}m_{\text{in}}}}{\mathrm{d}t}\Bigg) r\mathrm{d}\theta\mathrm{d}r,\end{aligned} \tag{4.2.32}$$

where the (incident) stress and displacement fields are evaluated on B^+. The time averaged integral over one period, $2\pi/\omega$, gives the corresponding time averaged, work done per cycle

of the incident mode, $\mathcal{E}^{\text{in}}_{n_{\text{in}}m_{\text{in}}}$. Consequently,

$$\mathcal{E}^{\text{in}}_{n_{\text{in}}m_{\text{in}}} = \frac{1}{(2\pi/\omega)} \int_0^{2\pi/\omega} \mathcal{P}^{\text{in}}_{n_{\text{in}}m_{\text{in}}} \mathrm{d}t. \tag{4.2.33}$$

The total incident, time averaged work done per cycle, $\mathcal{E}^{\text{in}}_{\text{tot}}$, is simply the summed contributions of all the incident modes so that

$$\mathcal{E}^{\text{in}}_{\text{tot}} = \sum_{n_{\text{in}}=-\infty}^{\infty} \sum_{m_{\text{in}}=6N+4}^{12N+6} \mathcal{E}^{\text{in}}_{n_{\text{in}}m_{\text{in}}}. \tag{4.2.34}$$

The analogous total, time averaged work done per cycle on the finite element region due to the scattered waves, $\mathcal{E}^{\text{scat}}_{\text{tot}}$, can be deduced similarly. Equation (4.2.32), in which all the variables have been replaced by their reflected counterparts, is evaluated initially at B^+ for the reflected waves produced by each incident mode. Then the required time averaging and summations are performed. This procedure is repeated by using the symmetry-antisymmetry arguments for the transmitted waves and evaluating equation (4.2.32) at B^-. It is followed by the required time averaging and summation. The sum of the time averaged, work done by the reflected and transmitted waves gives the total, time averaged work done per cycle on the finite element region by the scattered waves. As the total energy for the finite element region is constant, on average, the conservation of energy gives

$$\mathcal{E}^{\text{in}}_{\text{tot}} - \mathcal{E}^{\text{scat}}_{\text{tot}} = 0. \tag{4.2.35}$$

On the other hand, a slight numerical deviation from the equality of equation (4.2.35) is to be expected because approximate wave functions are used computationally. The deviation's magnitude is a measure of the consistency of the solutions recovered for the scattered wave field. Note, however, that nonpropagating and evanescent[8] modes do no net[9], time aver-

[8]Evanescent modes must be taken in their complex conjugate pairs for this property to apply.

[9]Note that these modes do work on an instantaneous basis but the algebraic work done over one sinusoidal excitation period vanishes.

aged, work per cycle on the finite element volume [133, 134]. This last observation is a consequence of only the propagating modes radiating energy to infinity.

4.2.8 Illustrative examples

4.2.8.1 Overview

Computer code was written in MATLAB® to (i) solve equation (4.2.27) for the symmetrical and antisymmetrical boundary conditions, and (ii) superimpose the results. A similar approach was followed to the one adopted in Chapter 2. It is documented more conveniently in Appendices F and G. As before computer code writes the computer code for the finite element analysis.

The illustrative pipe is identical to the one described in Chapter 2. In particular, its material and dimensional properties are summarized in Table 2.1. Moreover, the same discretization and wavefunctions detailed in Section 2.5 are used to represent motions in the parent, unblemished parts of the waveguide. Transparency checks are run before a notch is introduced in order to validate the basic software. Results are given in Appendix H. Note that the smallest propagating wavelength occurring in the excitation's bandwidth[10] is about $3.4H$. This particular wavelength corresponds to that of the L(0,1) mode[11]. It is an important factor in deciding upon a sufficiently fine discretization of the finite element region in the pipe's axial direction. Approximately ten elements per shortest wavelength is considered reasonable [70, 71]. Additional elements can be used, of course, but more computational effort would be required.

Results are given first for a simulation of the one-half wall thickness deep, axisymmetric notch considered previously in a seminal paper [70]. Computed reflection coefficients are compared to more limited finite element predictions and sparse measurements to ensure that the present simulations are plausible. Then displacement time histories produced by

[10]The excitation and its bandwidth are described in Appendix H.

[11]Modes are labelled again by using the standard convention employed in [81].

an axisymmetric force applied in the pipe's axial direction are simulated. This simulation mimics the experimental configuration used in [70], but with somewhat different transducer locations. The new transducer locations are selected so that (i) the direct wave path is consistent with the transducer locations used earlier in Chapters 2 and 3, and (ii) to illustrate the difficulties which may occur when apportioning individual modal contributions from a time history, even when relatively few (propagating) modes are excited. Also, the reflected and transmitted fields created by a radial point force are computed for the same combination of notch and pipe. These simulations demonstrate that singularities caused by the notch correspond to frequencies which differ from the unblemished pipe's cutoff frequencies. Then a brief parametric study is performed to supplement previously known [70] effects of the excitation frequency and an axisymmetric notch's depth and axial length.

4.2.8.2 A familiar axisymmetric notch

An axisymmetric notch having the dimensional properties summarized in Table 4.1 was considered initially. However, a brief summary of the methodology used in [70] is warranted in view of later extensive comparisons. A specially designed "ring" transducer, described in [9], was utilized in [70] to simulate an axisymmetric force applied axially on the pipe's outer surface. The excitation was nearly axisymmetric[12] and it produced principally longitudinal wave modes. (A purely axisymmetric force can excite only modes having no circumferential variation. Torsional modes, conversely, arise only from a circumferential force.) A transient excitation was applied to the ring transducer and the reflection from

Table 4.1. Dimensions of the outer surface breaking, axisymmetric notch.

Property	Assigned Value
Depth of notch, d, in (mm)	0.110 (2.79)
Axial length of notch, l, in (mm)	0.125 (3.17)
Depth to wall thickness ratio, (d/H)	0.500
Axial length to wall thickness ratio, (l/H)	0.568

[12] Although this transducer reasonably suppresses nonaxisymmetric wave modes, traces presented in [9] suggest that they are not eliminated completely.

the free end of a pipe was measured. Then the procedure was repeated to measure the separate reflections from a series of individual notches. The invariant temporal form of the excitation was similar to the one described in Appendix H. It had the same general form and centre frequency but with a slightly narrower, 60 kHz to 85 kHz or so, frequency bandwidth as ten rather than seven temporal cycles were used. The only propagating longitudinal modes generated in this bandwidth were L(0,1) and L(0,2). A modest distance between the transducer's location and the pipe's end permitted individual end reflections from these two modes to be distinguished as a consequence of their distinct arrival times at the receiving cross section. The amplitude of the end reflection[13] of the L(0,2) mode was employed as a reference for the "strength" of this mode's reflection from various notches. The ratio, at a given location, of the reflection amplitude from a notch to that of the free end reflection was taken to be the reflection coefficient for the L(0,2) mode[14]. This particular mode was selected because it (i) had the largest group wavespeed, and (ii) was essentially nondispersive over the frequency bandwidth employed. Consequently the displacement responses created by the L(0,2) mode could be identified straightforwardly.

An axisymmetric finite element model, comparable to the one described here but involving linear (four node) finite elements and time marching integration rather than the hybrid SAFE scheme, was used in [70] for numerical simulations. Therefore additional data post-processing would have been required to identify and suppress extraneous modal effects. Such effects are completely available in the frequency domain when using SAFE. Moreover, a direct time marching scheme requires many more finite elements. For example when finite elements, each having axial lengths of 1.6 mm are used, as seems the case in [70], the idealization of the pipe's 1.2 m length would require 750 elements. In contrast, only one finite element is needed for a comparable mesh size with a hybrid-SAFE approach.

Eight node, axisymmetric finite elements [107] were utilized in the present simulations

[13]The L(0,2) mode is reflected perfectly at a free end.

[14]The only reflection coefficient considered in [70] was that of the L(0,2) mode when it was incident and scattered alone, i.e., $R_{\mathrm{L(0,2),L(0,2)}}$. When comparisons are made later to this reference, $R_{\mathrm{L(0,2),L(0,2)}}$ is termed "the reflection coefficient of the L(0,2) mode."

for the finite element region around the axisymmetric notch. Ultimately, ten (five) finite elements described the behaviour over the wall thickness in the wave function (finite element) region. Furthermore, four finite elements, which together correspond to half the notch's axial extent, were utilized axially. This uniform idealization was selected after empirically checking the convergence of the L(0,2) reflection coefficient for one notch. Convergence was assessed by using mesh configurations that included one, two, or four finite elements in the axial direction and twenty (ten), ten (five), six (three), or four (two) finite elements in the radial direction for the wave function (finite element) region, respectively. The resulting magnitudes[15] of the representative L(0,2) reflection coefficient, evaluated at 70 kHz for the notch described in Table 4.1, are presented in Table 4.2. The reflection coefficient changed by less than 1% so it is essentially independent of the different finite element meshes investigated. Similar results are seen in Table 4.1 for $|R_{\mathrm{L(0,1),L(0,1)}}|$ and $|R_{\mathrm{F(10,1),F(10,1)}}|$. The last two reflection coefficients were selected on the basis that they represent modes which propagate at 70 kHz and have the smallest axial and circumferential wavelengths. Four finite elements were used subsequently in the axial direction and ten (five) finite elements were employed radially in the wave function (finite element) region. This selection allowed longer axial notches to be represented without the need for additional axial finite elements. As noted previously, the smallest propagating wavelength over the excitation's bandwidth was about

Table 4.2. Magnitude of reflection coefficients for the L(0,2), L(0,1), and F(10,1) modes at 70 kHz for the axisymmetric notch described in Table 4.1.

Number of finite elements		Reflection coefficient		
Axial direction	Radial direction	$\lvert R_{\mathrm{L(0,2),L(0,2)}}\rvert$	$\lvert R_{\mathrm{L(0,1),L(0,1)}}\rvert$	$\lvert R_{\mathrm{F(10,1),F(10,1)}}\rvert$
One	Ten	0.4058	0.1474	0.0199
One	Five	0.4050	0.1455	0.0198
Two	Five	0.4054	0.1471	0.0195
Four	Five	0.4057	0.1480	0.0194
Four	Three	0.4033	0.1456	0.0200
Four	Two	0.4033	0.1425	0.0211

[15]The reflection and transmission coefficients are complex numbers. However, only the corresponding magnitudes are given usually.

$3.4H$. Consequently, the ratio of the smallest (axial) wavelength excited to a finite element's axial length was approximately 48, almost five times larger than the recommended guideline [70, 71] of ten elements per shortest wavelength. Furthermore, the spatial aspect ratio (i.e., the ratio of the finite elements' dimensions in the radial and axial directions) was approximately 1.4 which is near the desirable value of 1.0. Therefore, each finite element is quite "compact" and likely to behave reasonably [107].

The normalized reflection coefficient of the L(0,2) mode, $R_{\mathrm{L(0,2),L(0,2)}}$, was computed straightforwardly by using equation (4.2.28a) with all the wavefunctions required by equation (4.2.27) retained. Results are compared in Figure 4.3 with the previously published experimental and finite element values. The predicted trend for the L(0,2) reflection coefficient is similar to the experimental data but with an essentially constant offset around 13%. The earlier finite element result lies approximately midway between the current prediction and the measurement. Plausible suggestions for this difference include a slightly varying

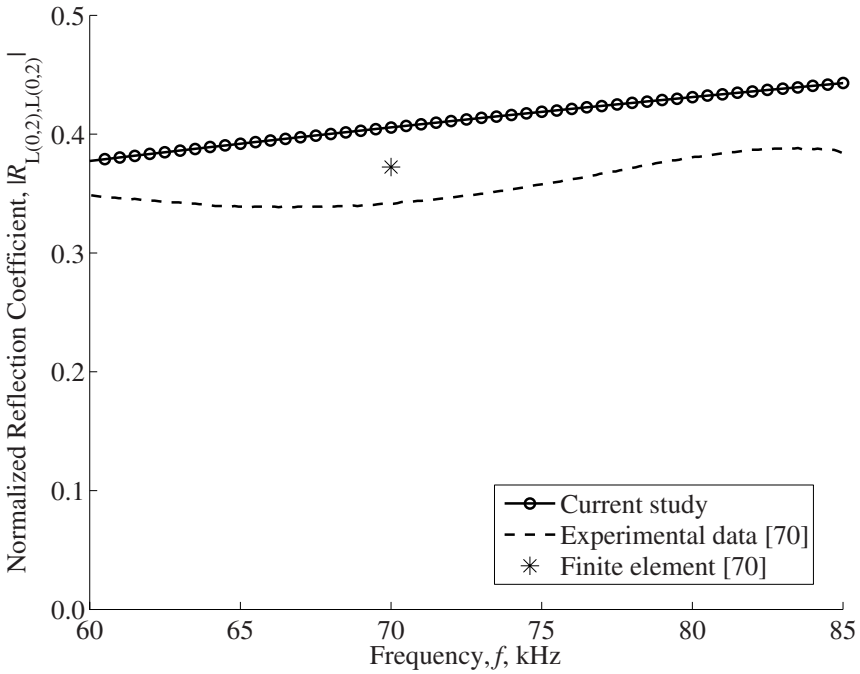

Figure 4.3. Comparing the magnitude of the computed normalized reflection coefficient of the L(0,2) mode for an axisymmetric notch with previous [70] measurements and predictions.

pipe wall thickness and a possible error in the measured, reference end reflection[16] [70]. On the other hand, the somewhat higher reflection coefficient predicted here could stem, in part, from the fewer (six) and lower order (linear) stiffer elements used in [70]. Another contributing factor could arise from an ambiguous axial extent of the notch. It was suggested to be 1.6 mm (0.062 inches) for the finite element analysis but a 3.2 mm (0.13 inches) diameter, "slot drill cutter" was used for its machining. This difference is unimportant if the notch's axial length is insignificant. To further assess the discrepancy, an axisymmetric notch was simulated that had the same depth but one-half the axial length of the notch described in Table 4.1. The calculated L(0,2) reflection coefficient was reduced from 0.41 to 0.36 which agrees very well with the value of 0.37 given in [70] for the simulation. Indeed the reflection coefficient for the L(0,2) and, later, the T(0,1) mode was found to be "sensitive to the axial extent of a part-through but not a through-wall notch" [70, 74].

To illustrate the practical difficulties associated which may be encountered when measuring the reflection coefficient, a transient axisymmetric force was applied axially to the simulated pipe's outer surface. It had the temporal form shown in Figure D.1 and was positioned at $z_{\mathrm{L}}^{*} = z_{\mathrm{L}}/H = 5.1$, where z_{L} is the transmitting transducer's axial[17] location. This force excited only longitudinal modes in which L(0,2) was dominant[18]. Moreover, no modal cutoff frequency existed in the bandwidth of this axisymmetric excitation. The resulting axial displacement was computed on the pipe's outer surface at $z_{\mathrm{R}}^{*} = 10.2$ and $z_{\mathrm{T}}^{*} = -5.1$, where z_{R} and z_{T} are the axial coordinates of the receiving transducers which are located in the reflected and transmitted fields, respectively. All pertinent positions are shown in Figure 4.1.

Figure 4.4 presents the axial displacements, in both time and frequency, for (i) the direct waves (i.e., waves which would have been observed had there been no notch), (ii) the

[16]This comment is expanded later when considering a nonaxisymmetric notch.

[17]Circumferential coordinates are immaterial in this example because the geometry and external loadings are *all* axisymmetric.

[18]The L(0,1) mode was generated also as a by-product of this stimulus. Consequently the peak axial displacement of the L(0,1) mode was a not insignificant 40% or so of that of the L(0,2) mode alone. Moreover, the L(0,1) mode was also excited by the modal conversion from L(0,2) *into* L(0,1) at the notch.

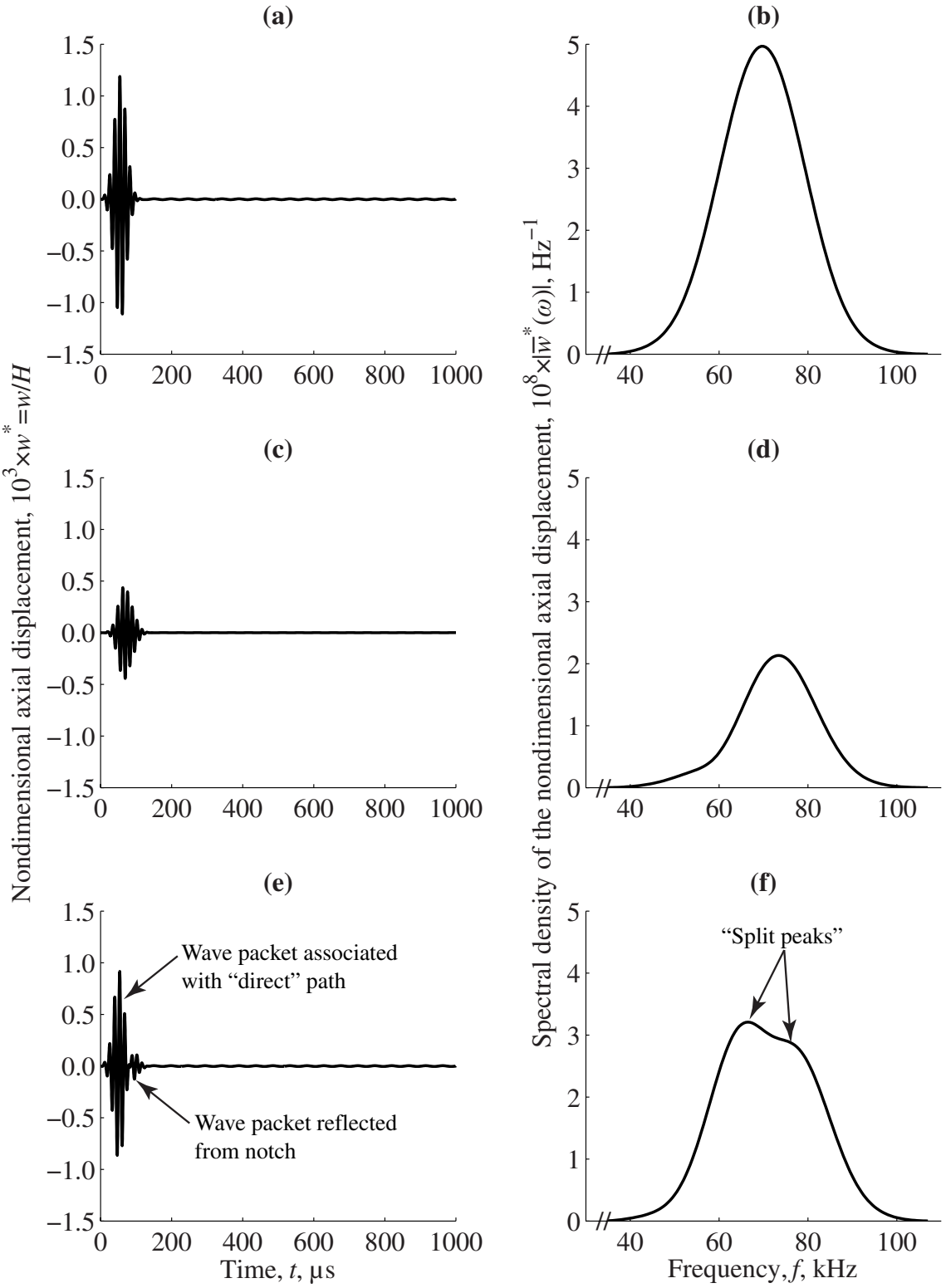

Figure 4.4. Axial displacement predicted within the reflected field for an axisymmetric notch. Sub-figures (a) and (b) [(c) and (d)] {(e) and (f)} give the direct [reflected] {superposition of direct and reflected} waves produced by an axisymmetric axial force.

reflected waves scattered "back" from the notch, and (iii) the (linear) superposition of the previous two cases. Figure 4.5 gives the corresponding information for the transmitted wave field where superposition is not required because no direct wave path exists "behind" a notch. Furthermore, Figure 4.6 graphs the spectral density produced from equation (4.2.34) for the incident waves and their scattered counterparts. The curves are indistinguishable so that, as expected for no material damping, energy is conserved.

Several interesting observations arise from Figures 4.4 and 4.5. The amplitudes of the direct waves appear to be larger in the reflected field of Figures 4.4 (a) and (b) than in the transmitted field given in Figures 4.5 (a) and (b). This seeming anomaly is a consequence of dispersion and the excitation of *both* the L(0,1) and L(0,2) modes. These modes are essentially in (out of) phase in the reflected (transmitted) field at the two reception points considered. Moreover, the individual effects of the two modes cannot be distinguished easily in either the time or frequency domains. This difficulty occurs because the difference between the wave speeds of the L(0,1) and L(0,2) modes is not great enough to separate the corresponding pulses. On the other hand, larger separation distances between the transmitting and receiving transducers would allow the modal effects to be distinguished in time. A reflection can be seen clearly in the reflected (but not the transmitted) field after introducing the notch, even though the wave packets associated with the incident and reflected waves overlap. Therefore, spatial separations required to use the technique described in [70] for measuring the reflection coefficient might not be possible. On the other hand, consider the corresponding spectral density shown in Figure 4.4 (f) which can be measured straightforwardly. This figure unmistakeably indicates the presence of the axisymmetric notch because the single peak in the spectral density of Figure 4.4 (b) becomes two local maxima, one on either side of the original peak. The change is caused by the destructive interference of the back scattered waves and the incident waves. However, it is position and defect dependent. Somewhat paradoxically, a comparison of the peaks in the spectral densities of Figure 4.5 (a) and (c) suggests that the notch's introduction has an "amplifying"

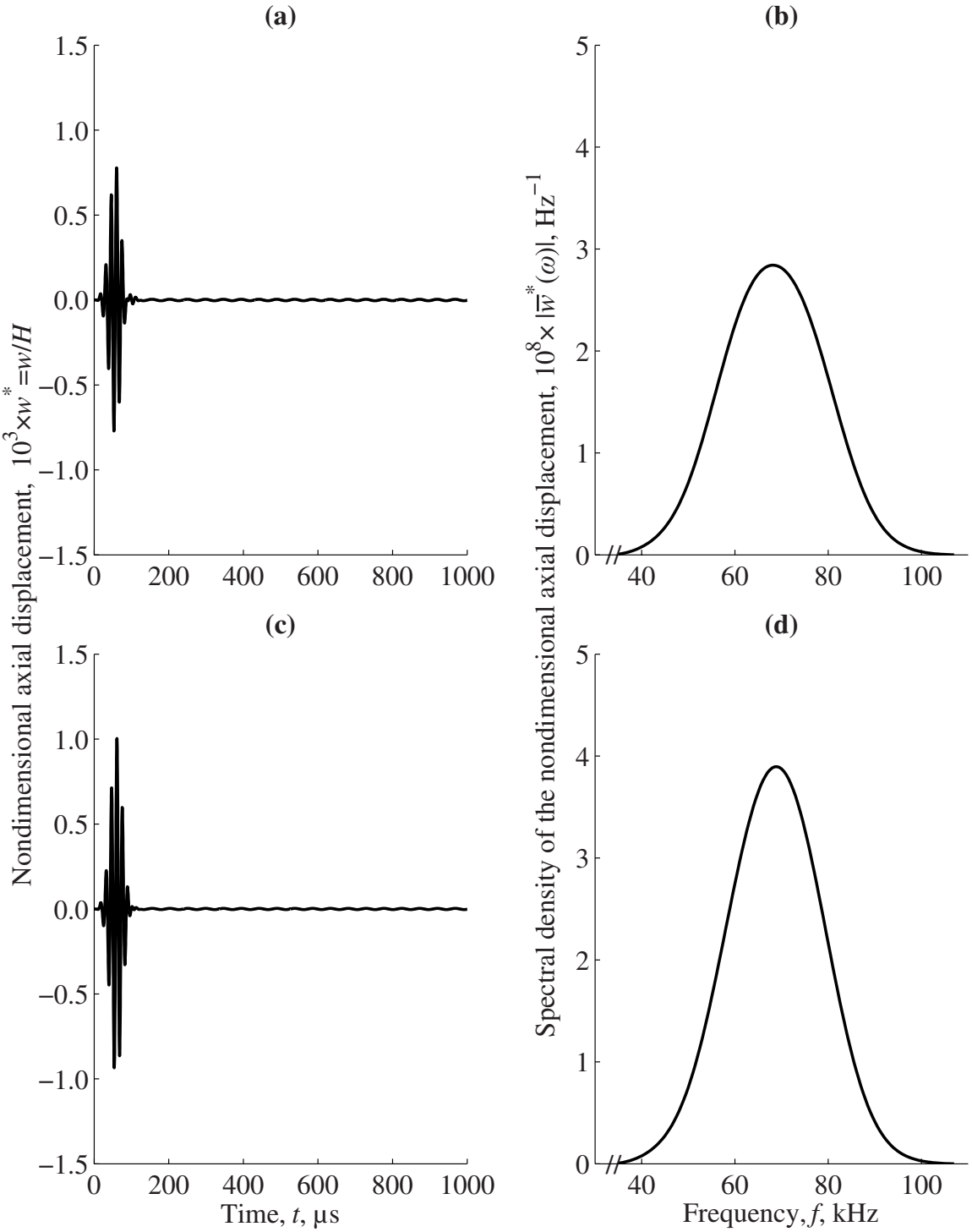

Figure 4.5. Axial displacement predicted within the transmitted field for an axisymmetric notch. Sub-figures (a) and (b) [(c) and (d)] give the direct [transmitted] waves produced by an axisymmetric axial force.

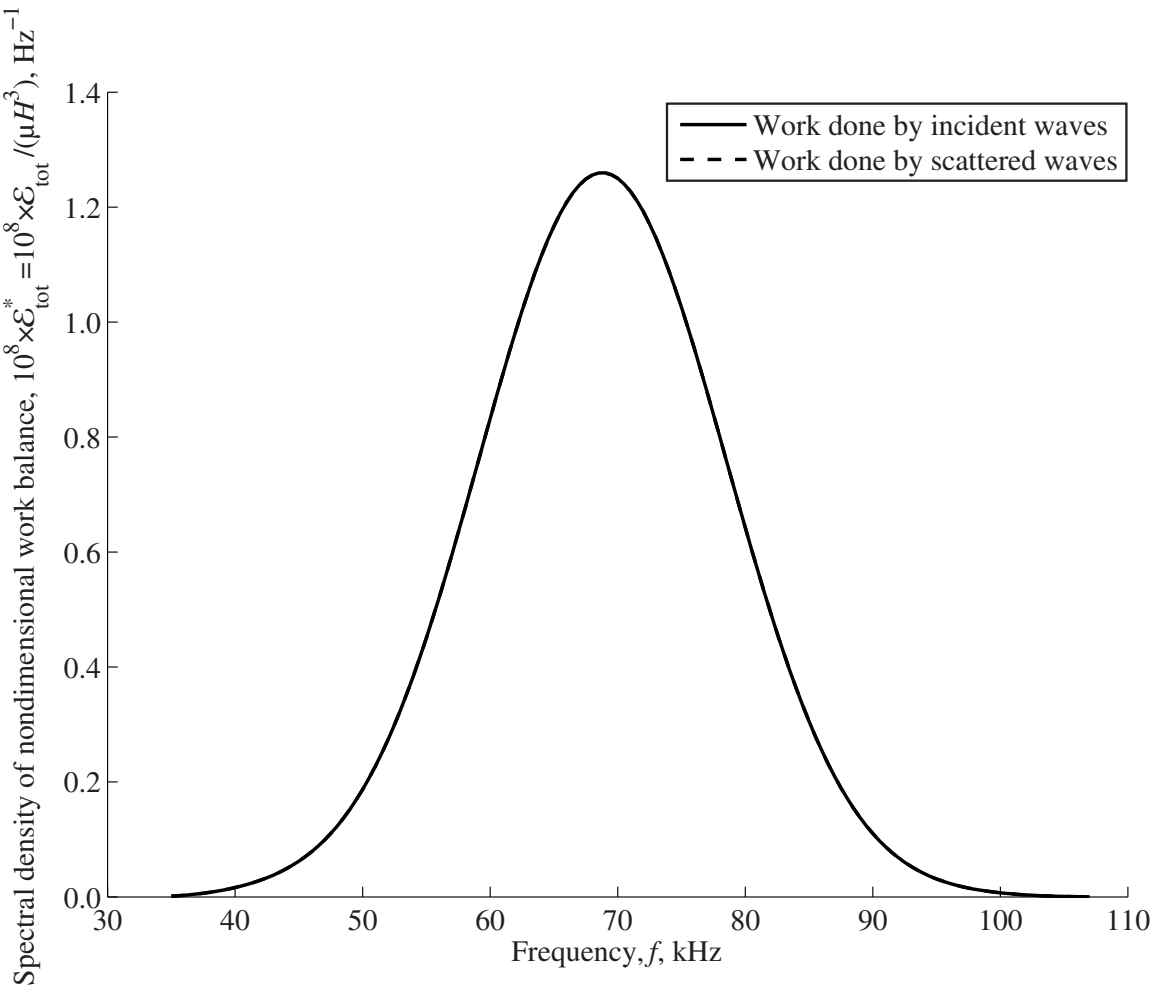

Figure 4.6. Spectral density of the work done, per period, on the finite element region by waves produced by an axisymmetric axial force and scattered by an axisymmetric notch.

effect in the transmitted field. This behaviour is explained by an amplitude reduction of the L(0,1) component[19] in the transmitted field so that it is less "destructive" to the L(0,2) component. Phase effects are obviously significant.

One phenomenon which is expected [73], but not seen, in Figures 4.4 and 4.5 are distinct wave packets representing reflections from the "front" ($z = 0$) and "back" ($z = -l$) of the notch. These wave packets are created by superimposing, both constructively and destructively, steady state waves having different frequencies and wavelengths. The excitation pulse's duration is too long and the notch's axial extent is too short in this example to

[19]The amplitude of the L(0,2) mode is also reduced in the transmitted field by the notch's introduction. The reduction of the L(0,1) mode's destructive behaviour is more important, however, in determining the overall amplitude *at this location* in the transmitted field.

see easily the separate reflections from the front and back edges of the notch.

A radial point force, whose temporal character is retained from before, is considered next for the same notch, finite element idealization, and (axial) monitoring locations. These last locations are simply offset axially from the position of the force's application. Circumferential wave numbers between $-16 \leq n \leq +16$ are used in the modal expansion, as in Section 2.5. All the available wavefunctions are kept for each circumferential wave number required in the computations of equation (4.2.27). Figures 4.7, 4.8, and 4.9 are analogous to Figures 4.4, 4.5, and 4.6. The curves in Figure 4.9 are visually indistinguishable over the excitation's entire bandwidth but, unlike Figure 4.6, they differ at singularities near but not coinciding with the F(±4,2), F(±5,2), and F(±6,2) cutoff frequencies. The work done by the incident and scattered waves no longer appear to be identical at these singularities. Discrepancies arise because corresponding wave amplitudes cannot be evaluated directly from a conventional Fourier analysis which disregards initial temporal conditions. Analogous behaviour was observed previously for the unblemished pipe when additional terms related to its cutoff frequencies needed to be introduced in order to ensure causality.

Figures 4.7 and 4.8 seem more complicated than their counterpart Figures 4.4 and 4.5. Several useful observations can be made nonetheless. A much richer palette is apparent for the point excitation because several cutoff frequencies of the (unblemished) pipe lie within its frequency bandwidth. The effects of individual modes are difficult to discern, however, because of the numerous modes that "ring." On the other hand, dominant features around the unblemished pipe's cutoff frequencies are obvious. These features occur at values slightly lower than nearby cutoff frequencies. The frequency differences are presented in Table 4.3. A typical difference is seen more clearly in Figures 4.10 (a) and (b) which reproduce Figures 4.7 (f) and 4.8 (d), respectively, but with the common frequency scale expanded about the unblemished pipe's F(±10,1) cutoff frequency of 63.554 kHz. The new singularity at 63.362 kHz does not coincide with any of the pertinent resonant frequencies given in Table 4.4 for solely the finite element region. In addition to this notch-induced

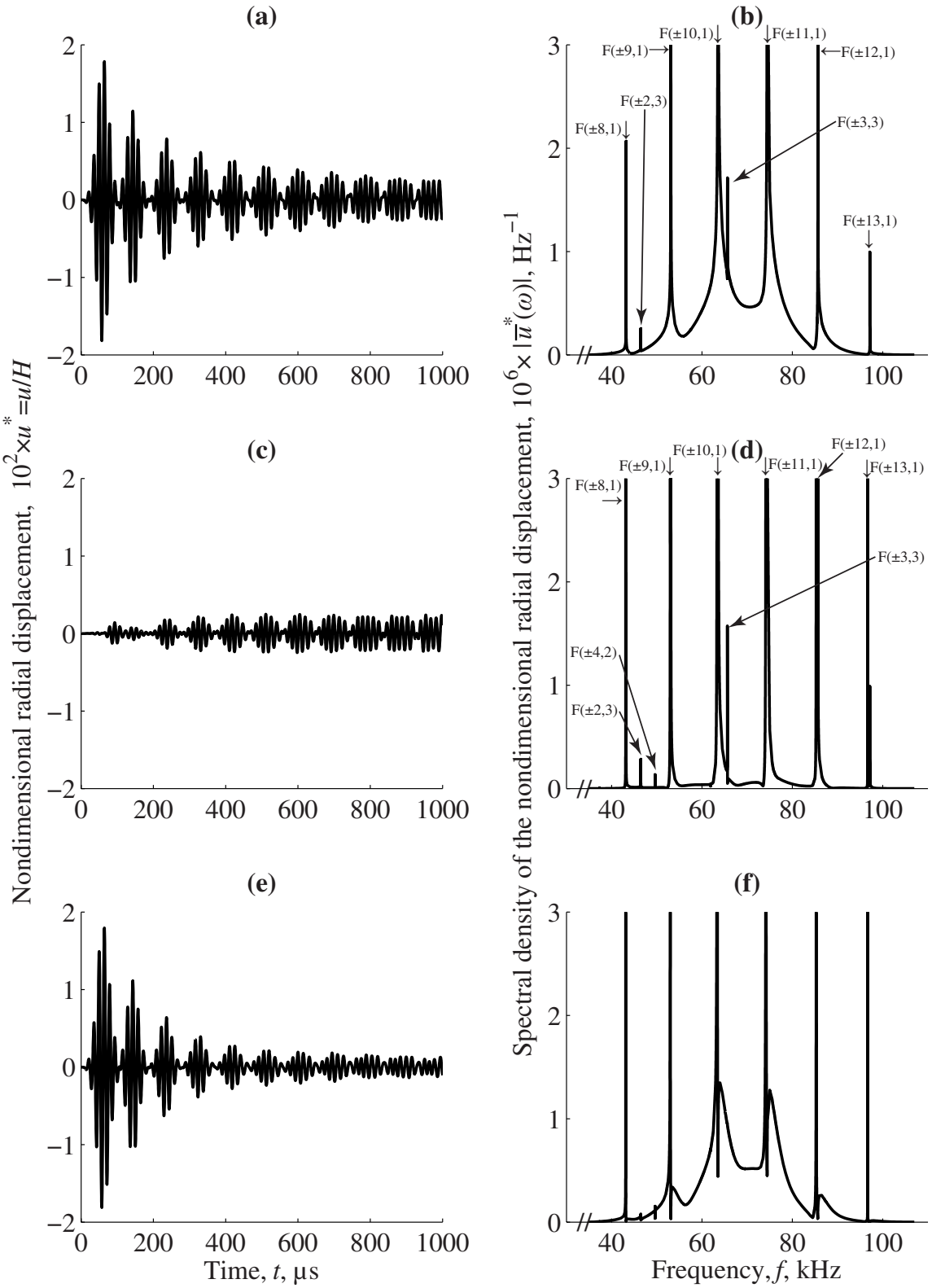

Figure 4.7. Radial displacement predicted within the reflected field for an axisymmetric notch. Sub-figures (a) and (b) [(c) and (d)] {(e) and (f)} give the direct [reflected] {superposition of direct and reflected} waves produced by a radial point force.

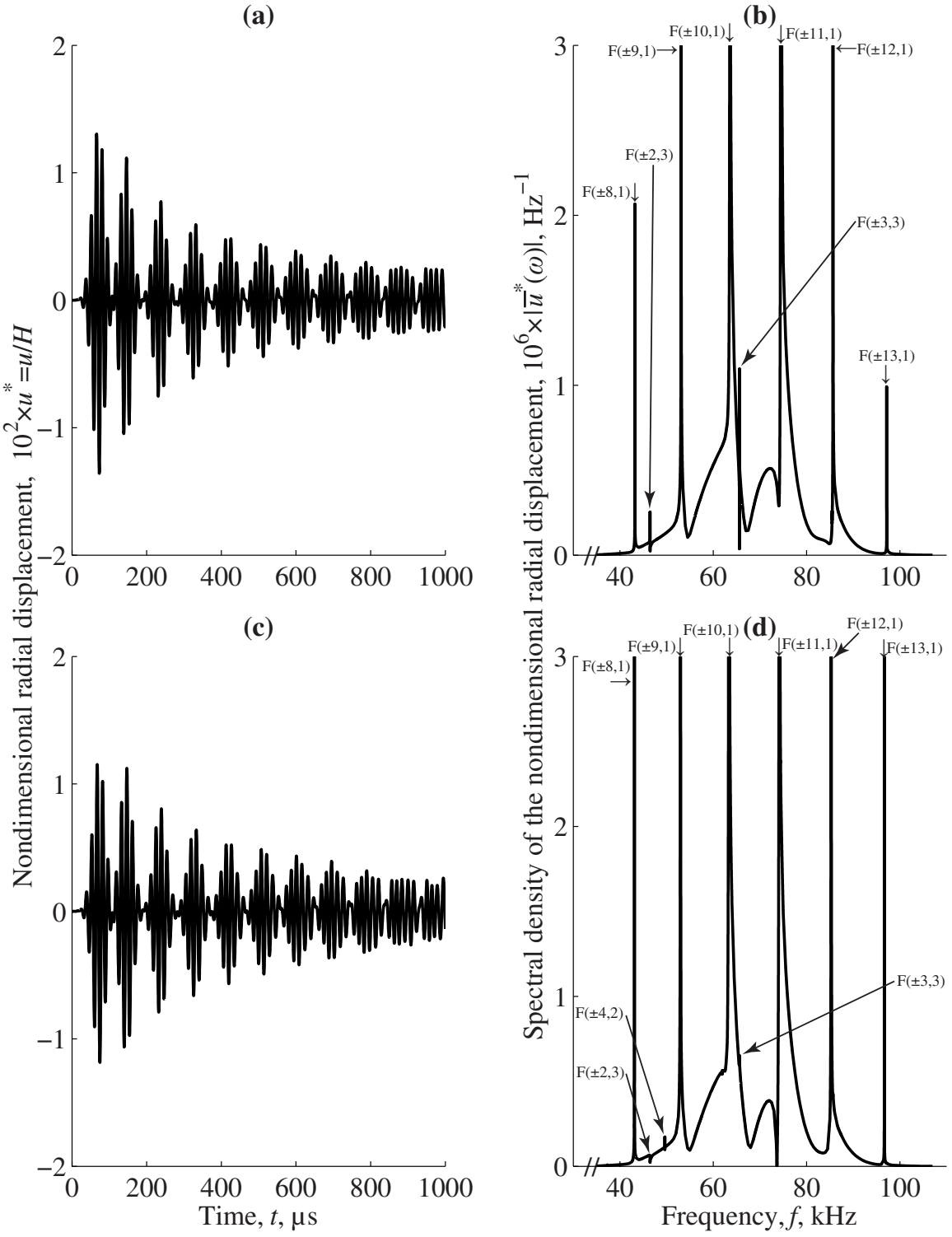

Figure 4.8. Radial displacement predicted within the transmitted field for an axisymmetric notch. Sub-figures (a) and (b) [(c) and (d)] give the direct [transmitted] waves produced by a radial point force.

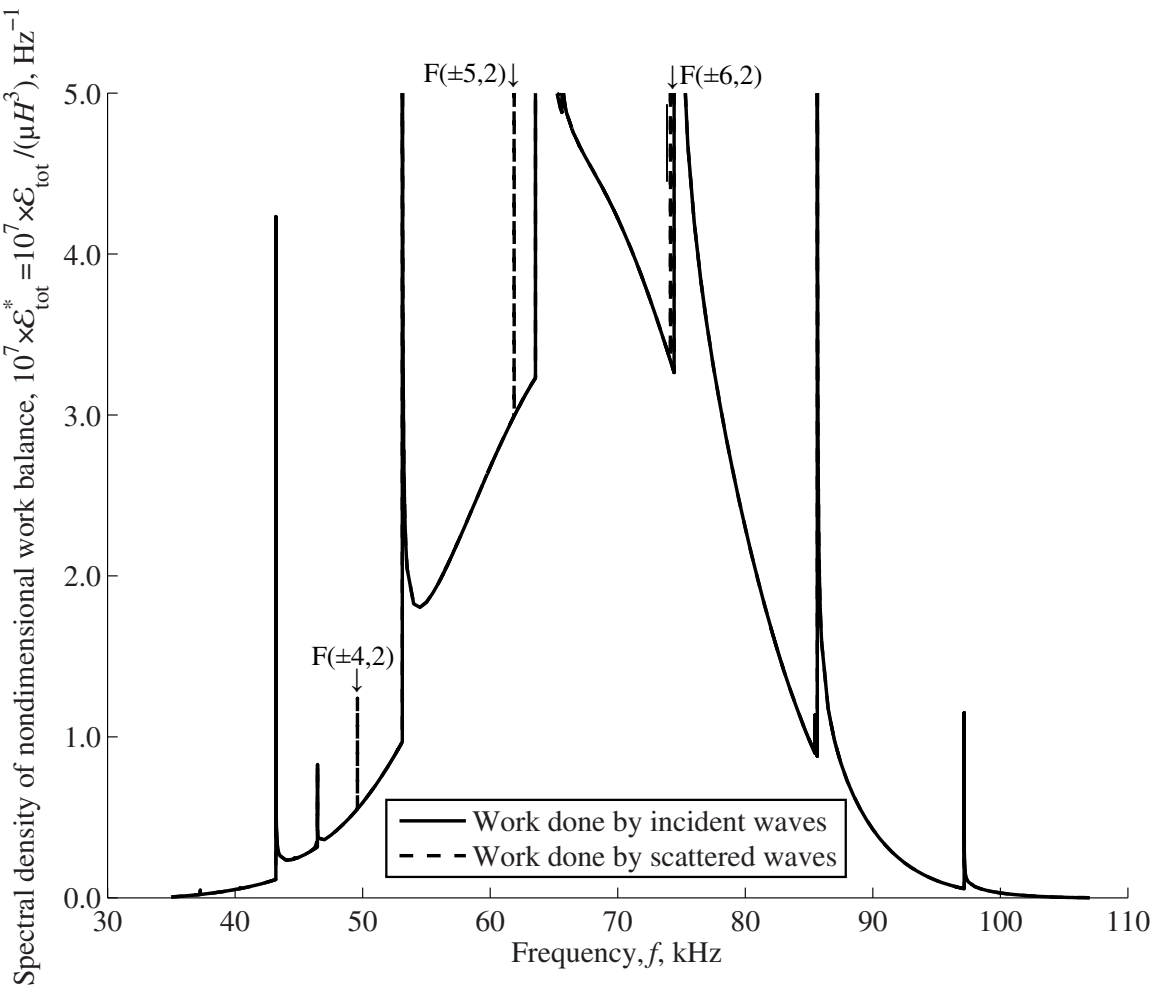

Figure 4.9. Spectral density of the work done, per period, on the finite element region by waves produced by a "point" radial force and scattered by an axisymmetric notch.

Table 4.3. Frequencies that correspond to the readily identified singularities appearing in Figures 4.7 (d) and 4.8 (d). They are distinct from the unblemished pipe's cutoff frequencies.

Circumferential wavenumber	Axial order	Frequency of singularity (kHz)	Difference between cutoff and singularity frequency (kHz)
$n = \pm 8$	$m = 1$	43.112	0.085
±2	3	46.462	0.001
±4	2	49.623	0.294
±9	1	52.983	0.129
±10	1	63.362	0.192
±11	1	74.153	0.273
±12	1	85.274	0.377
±13	1	96.660	0.503

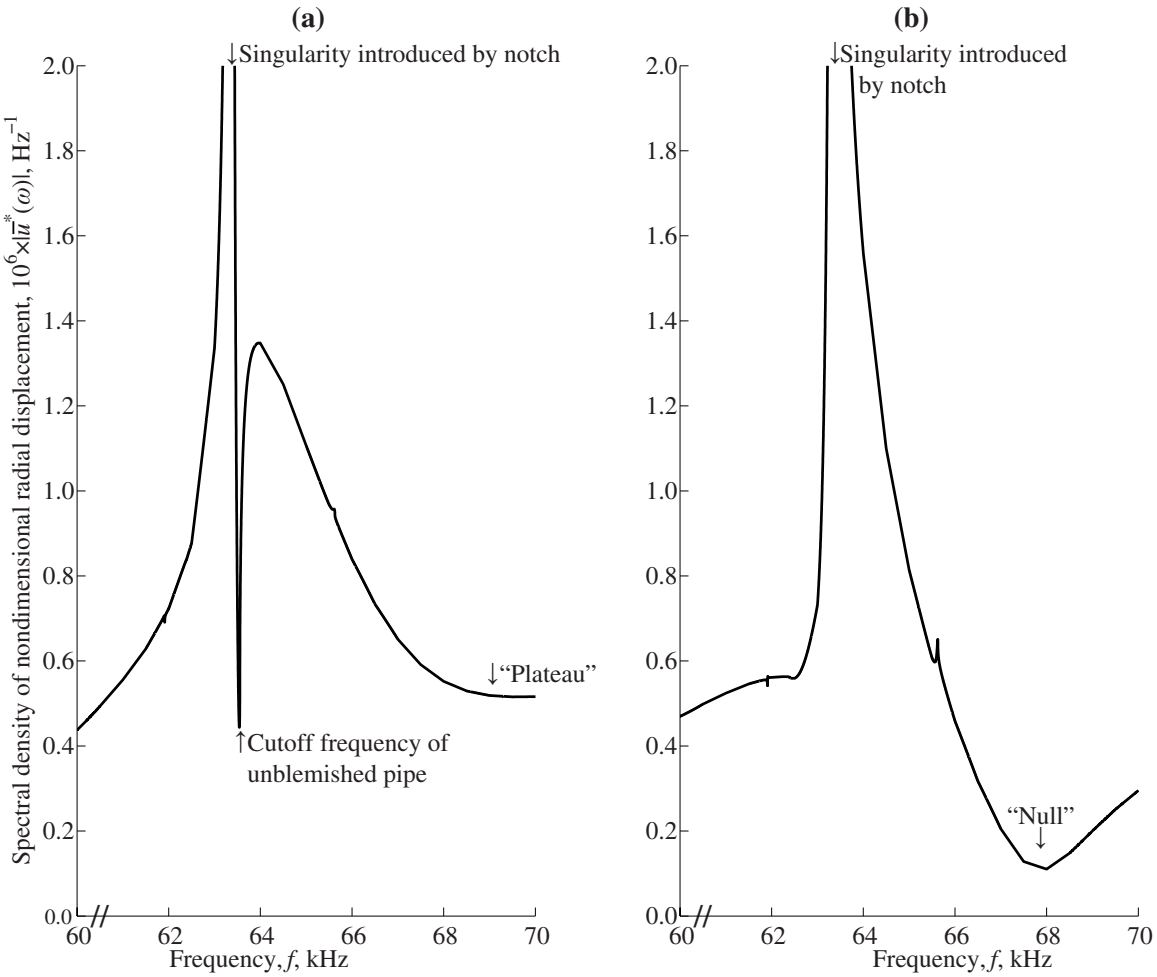

Figure 4.10. Spectral densities in the (a) reflected, and (b) transmitted field for an axisymmetric notch having $d/H = 0.500$ and $l/H = 0.568$. The frequency scales are enlarged about the unblemished pipe's F(±10,1) cutoff frequency.

singularity, which is common to the reflected and transmitted fields, a "plateau"("null") occurs in the reflected (transmitted) field above 63.554 kHz.

Figure 4.11 shows other normalized reflection and transmission coefficients predicted for the flexural F(n, 1) modes, where n equals 8 through 13, for an axisymmetric notch having $d/H = 0.500$ and $l/H = 0.568$. Each curve represents a single F(n, 1) mode which is reflected and transmitted into itself. (Modal conversions from F(n, 1) into F(n, m), $m \neq 1$, are presented in Appendix I for completeness. Such conversions are required to satisfy continuity and boundary conditions.) For easier comparisons, the frequency axis in Figure 4.11 has been normalized by the cutoff frequency of the mode in question. It is noteworthy now

Table 4.4. Resonant frequencies between 35 kHz and 110 kHz of solely the finite element region.

Circumferential wavenumber	Frequency (kHz)	Boundary conditions on B^-
$n = \pm 8$	95.593	Antisymmetric
± 9	31.177	Symmetric
± 9	34.572	Antisymmetric
± 9	107.250	Antisymmetric
± 10	38.080	Symmetric
± 10	42.202	Antisymmetric
± 11	45.587	Symmetric
± 11	50.387	Antisymmetric
± 12	53.598	Symmetric
± 12	59.077	Antisymmetric
± 13	62.072	Symmetric
± 13	68.223	Antisymmetric

that each curve can be seen to possess two singularities, rather than one. The singularity near a normalized frequency of 1.0 occurs, as before, at a frequency just below the unblemished pipe's relevant cutoff frequency. This observation can be corroborated by noting that the normalized reflection and transmission coefficients always pass through the points $(1.0, 1.0)$ and $(1.0, 0.0)$, respectively, for these modes. On the other hand, the singularity around the normalized frequency of 0.7 always corresponds to a mode transitioning from evanescent to non-propagating. The practical usefulness of this singularity, however, may be limited. Waves scattered from the axisymmetric notch at frequencies near this singularity decay exponentially from the notch's vertical boundaries at a rate of about $\exp(-z_{\mathrm{d}}^*)$. The z_{d}^* is the distance from the notch's boundary, nondimensionalized by the unblemished pipe's thickness, H. The decay rate in the axial direction is determined approximately based on the behaviour of the representative F(10,1) mode's axial wavenumber found from Figure 4.12. The latter figure shows that the imaginary part of the nondimensional axial wavenumber of this mode is almost one when the mode transitions from evanescent to non-propagating. The quite large exponent suggests that the effect is very localized and likely to be masked by the propagating modes. The singularity just below the cutoff frequency of

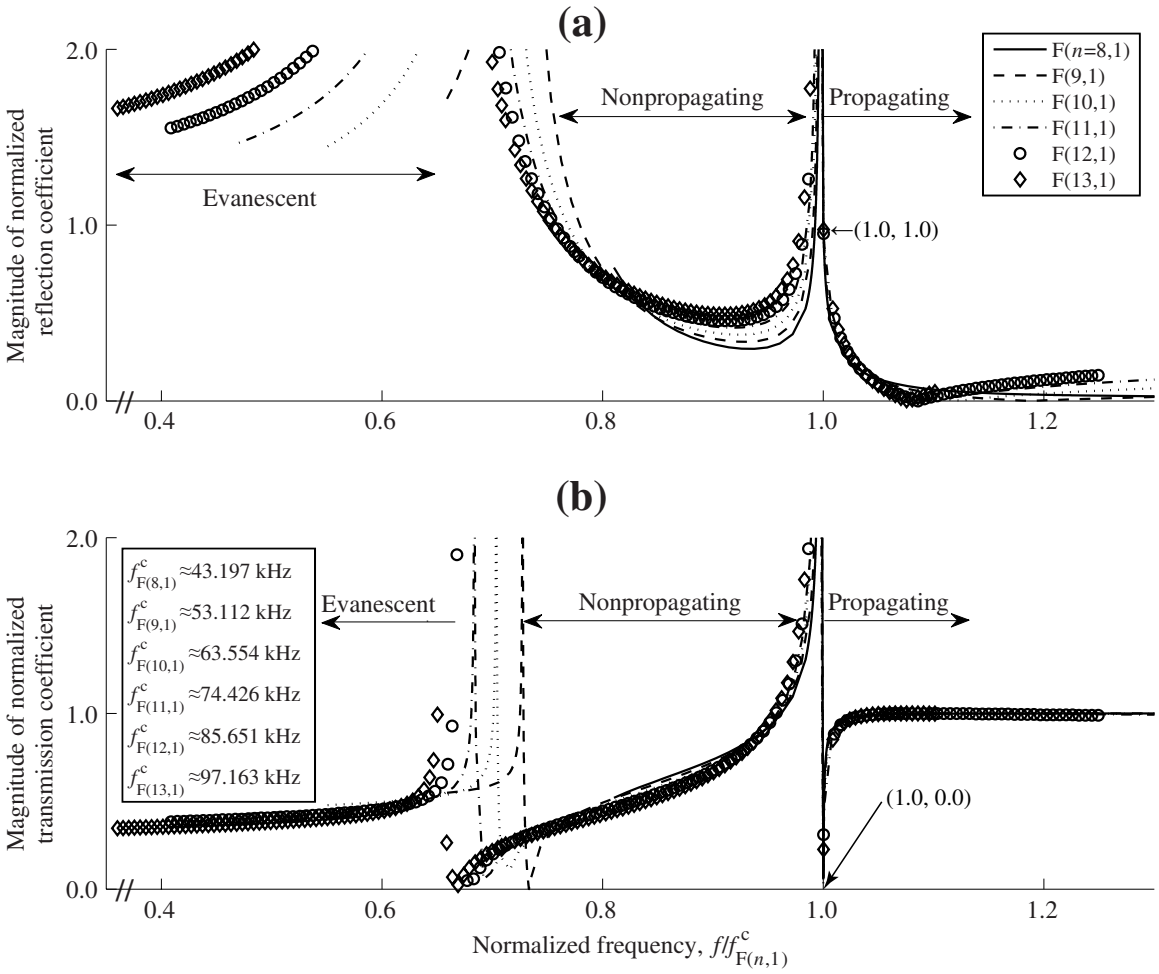

Figure 4.11. Normalized (a) reflection and (b) transmission coefficient caused by flexural F(n, 1) modes, where n is 8 through 13 inclusive, and an axisymmetric notch having $d/H = 0.500$ and $l/H = 0.568$. The $f^{c}_{F(n,1)}$ is the cutoff frequency of the unblemished pipe's F(n, 1) mode.

63.553 kHz, on the other hand, is more interesting. Its effect is not so localized because the magnitude of the imaginary part of its wavenumber is much closer to zero. Indeed, another "back of an envelope" calculation[20] based on Figure 4.10 (a) suggests that the axial decay rate is about $\exp(-0.15z^{*}_{d})$ at the notch-induced singularity. As a consequence of the smaller exponent, this last singularity may be detectable to about $10H$ or 2 inches (5 cm) from the axisymmetric notch's vertical boundaries.

Tables 4.3 and 4.4 indicate that the frequency of the possibly more important singularity

[20]This calculation plausibly assumes that the spectral density's amplitude at the higher frequency singularity is at least four times greater than that at the "plateau" or "null."

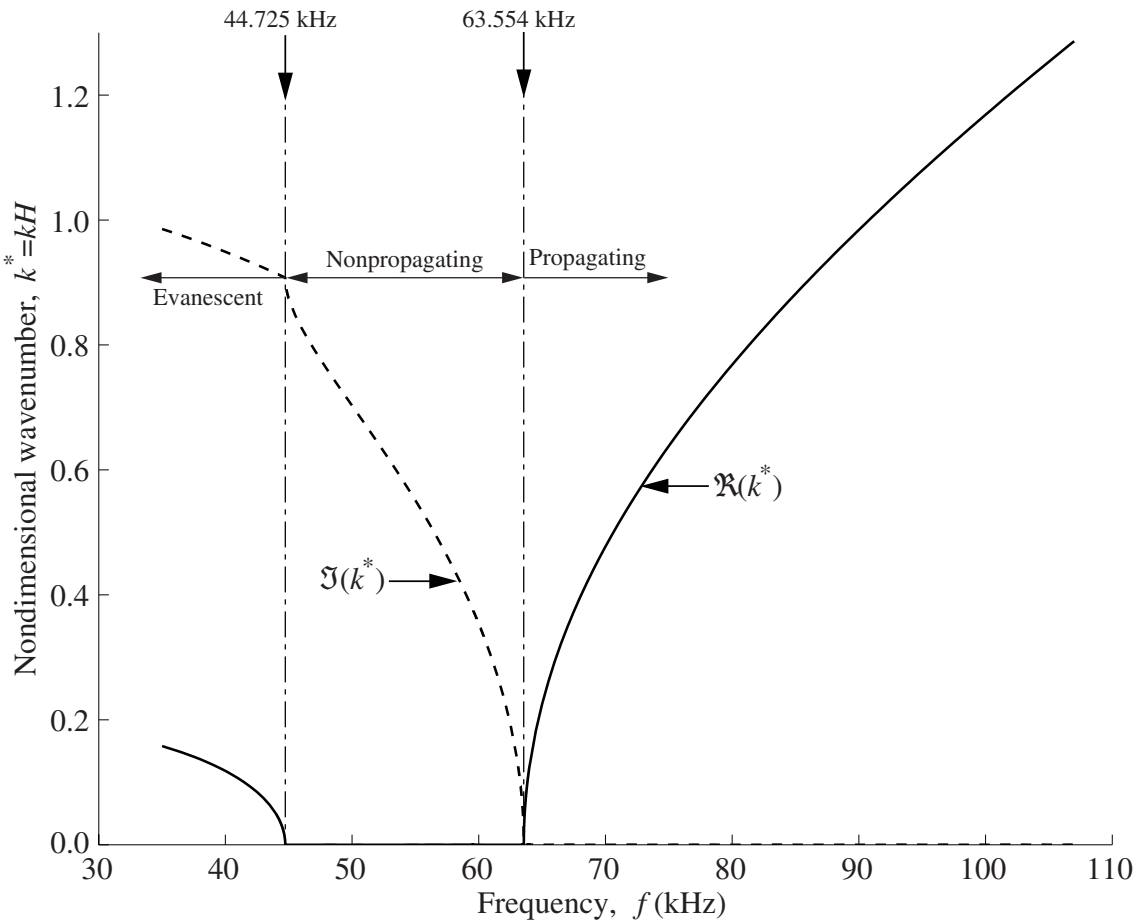

Figure 4.12. Real and imaginary parts of the unblemished pipe's F(10,1) nondimensional wavenumber, k^*, as a function of frequency.

does not correspond to a resonant frequency of the finite element region alone. It depends presumably upon the properties of *both* the finite element region and the parent waveguide. Moreover, the last column of Table 4.3 shows that the difference between the frequency of this singularity and the corresponding unblemished pipe's cutoff frequency grows continuously as the circumferential wavenumber increases. Advantage might be taken of this trend by increasing the centre frequency of the point force to excite modes having larger circumferential wavenumbers in order to make the frequency differences easier to measure.

Previous observations are summarized now. An axisymmetric notch may be detected with a single mode, whose cutoff frequency lies outside the excitation's bandwidth, by simply searching a time history for a spurious reflection providing (i) the reflection from the notch is not "masked" by the direct waves, and (ii) the reflection is sufficiently strong

that it can be separated from the measurement equipment's noise floor. The corresponding spectral density of the superimposed incident and back scattered waves indicates the notch's introduction by causing the formerly single maximum amplitude of the incident FRF to "split" into two local maxima. However, the detection in a time history of "spurious" reflections from a notch is more difficult when multiple modes are excited. On the other hand, the reflection and transmission coefficients of these modes become very large near their cutoff frequencies [65, 68]. Moreover, well defined peaks which are quite isolated in the incident FRF are mostly split into two again in the reflected wavefield. They are merely shifted (down) in frequency, however, in the transmitted field. These changes have been exemplified in Figure 4.10 by using the the representative F(10,1) mode.

4.2.8.3 Parametric study of wave scattering by axisymmetric notches

Figure 4.13 compares the present and published [70] reflection coefficient, $|R_{\mathrm{L(0,2),L(0,2)}}|$, for axisymmetric notches. A comprehensive assessment of such a notch's axial extent is provided in addition to confirming previously noted effects of different excitation frequencies as well as an axisymmetric notch's depth. Each parameter is varied individually in a given subfigure with the remaining parameters kept at constant reference values. The reference depth and axial length are presented in Table 4.1 and the reference frequency is 70 kHz. Figure 4.13 (a) shows that the reflection coefficients found by different authors is invariably within a reasonable 13%. Plausible reasons for the differences are given earlier in Section 4.2.8.2. It is seen again that $|R_{\mathrm{L(0,2),L(0,2)}}|$ is (i) a weak function of the exciation frequency over the given bandwidth, and (ii) a stronger function of the axisymmetric notch's depth for the 70 kHz excitation. Although the corresponding trend for axial length changes is more modest than that for the depth, the changes are not negligible.

Figure 4.14 gives information for the same notches considered in Figure 4.13 but for the L(0,1), T(0,1), F(3,1), and F(10,1) modes. The reflection coefficient of the T(0,1) and, to a less extent, the L(0,1) mode behave similarly to that of the L(0,2) mode. The L(0,1) and also

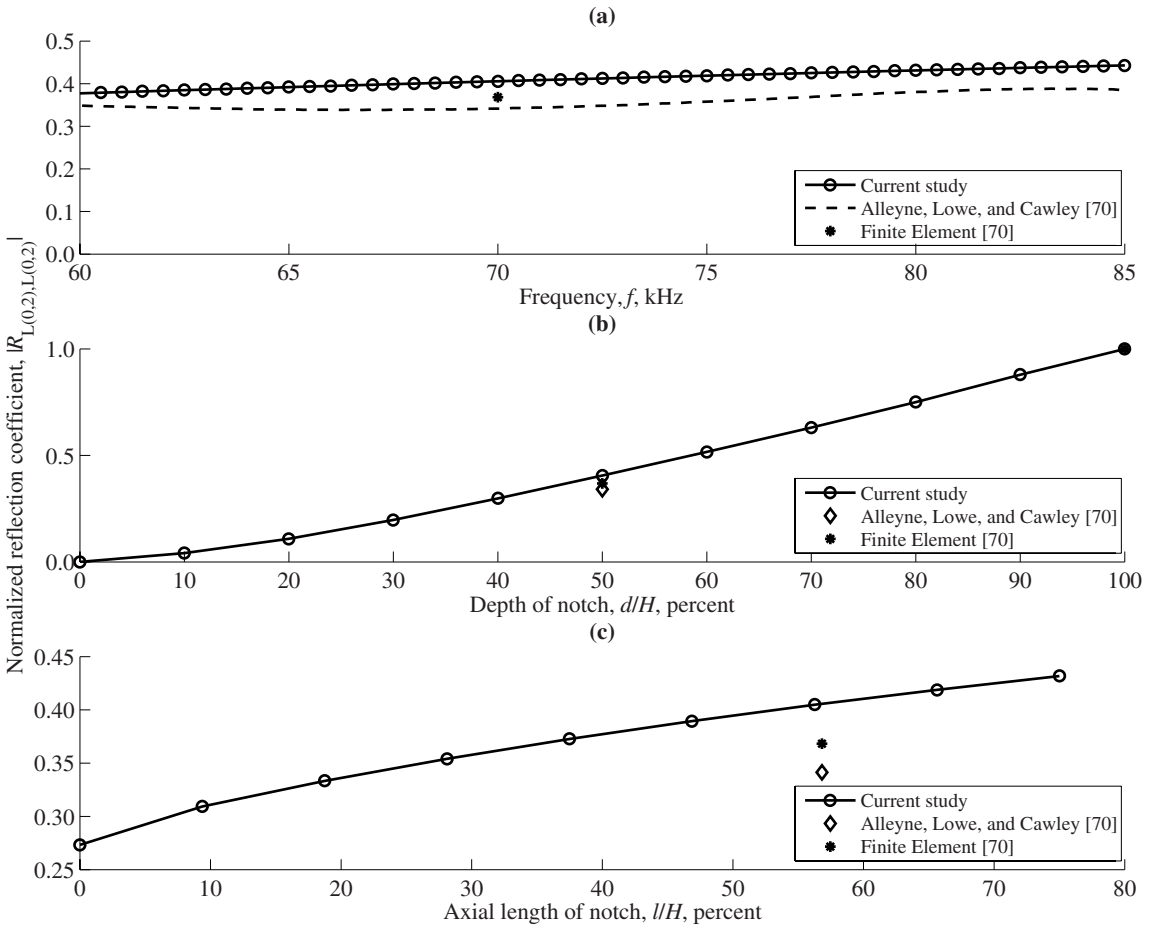

Figure 4.13. Magnitude of the reflection coefficient, $|R_{\mathrm{L(0,2),L(0,2)}}|$, for various (a) excitation frequencies and axisymmetric notches having different (b) depths, and (c) axial lengths.

the F(3,1) reflection coefficient has a high change rate (or sensitivity) in Figures 4.14 (b) and (c) when (d/H) or (l/H) increase beyond about 50%. Clearly these sensitivities are nonlinear. On the other hand, they are seen in Figure 4.14 (c) to be most sensitive to axial length changes below about 10%. Finally, the reflection coefficient of the F(10,1) mode is generally least sensitive for the modes and parametric values considered in Figure 4.14. Overall the L(0,2) and T(0,1) modes, which are both essentially nondispersive over the chosen frequency range, seem more amenable to a single mode approach for detecting and characterizing axisymmetric notches. However, even a cursory examination of Figures 4.13 (b) and (c) shows that an axisymmetric notch's dimensions *cannot be determined uniquely by using the reflection coefficient of solely one mode*. Of particular interest here,

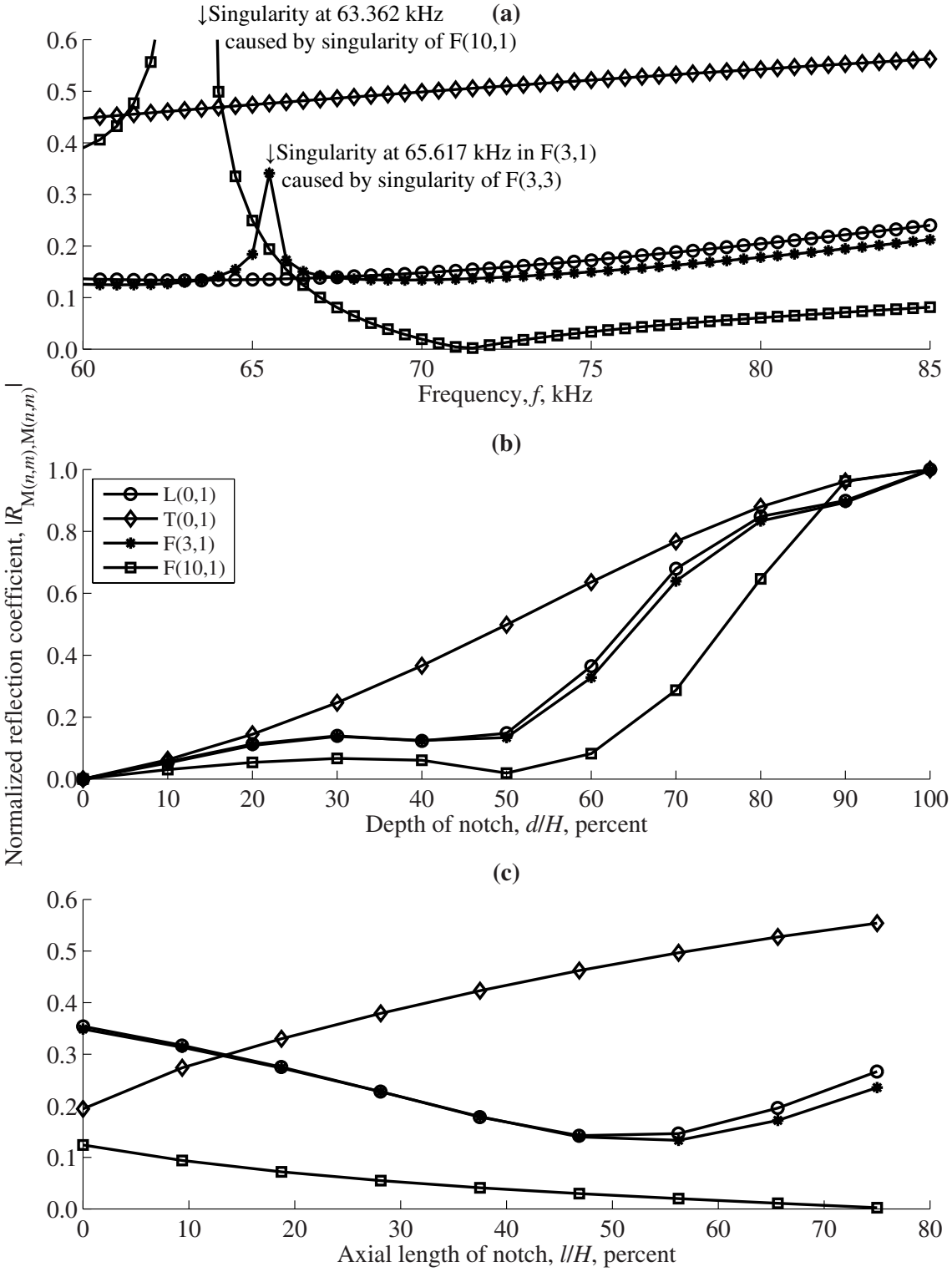

Figure 4.14. Reflection coefficients of individual L(0,1), T(0,1), F(3,1), and F(10,1) modes for different (a) excitation frequencies and axisymmetric notches having various (b) depths and (c) axial lengths. Only $|R_{\mathrm{M_{in}}(n_{\mathrm{in}},m_{\mathrm{in}}),\mathrm{M_{scat}}(n_{\mathrm{scat}},m_{\mathrm{scat}})}|$, where $\mathrm{M_{in}} = \mathrm{M_{scat}}$, $n_{\mathrm{in}} = n_{\mathrm{scat}}$, and $m_{\mathrm{in}} = m_{\mathrm{scat}}$, is plotted for each mode.

however, is the behaviour of a pipe's dominant response features near its cutoff frequencies after an axisymmetric notch is introduced. Then the F(3,1) and F(10,1) reflection coefficients presented in Figure 4.14 (a) suggest that similar, easily distinguished features still exist even after the notch's appearance. Just as importantly, the corresponding frequencies do not coincide with the unblemished pipe's cutoff frequencies. Therefore, the frequency differences may provide a more easily measured alternative to the reflection coefficient. This conjecture is assessed next by performing a preliminary parametric study that illustrates how an antisymmetric notch's dimensions may be determined uniquely by using the singularities of two or three modes, depending on the notch's dimensions.

Wave scattering by axisymmetric notches having various dimensions was modelled by using the finite element idealization described previously. Figures 4.15, 4.16, and 4.17 present the frequency difference, Δf, from the nearest cutoff frequency of the unblemished

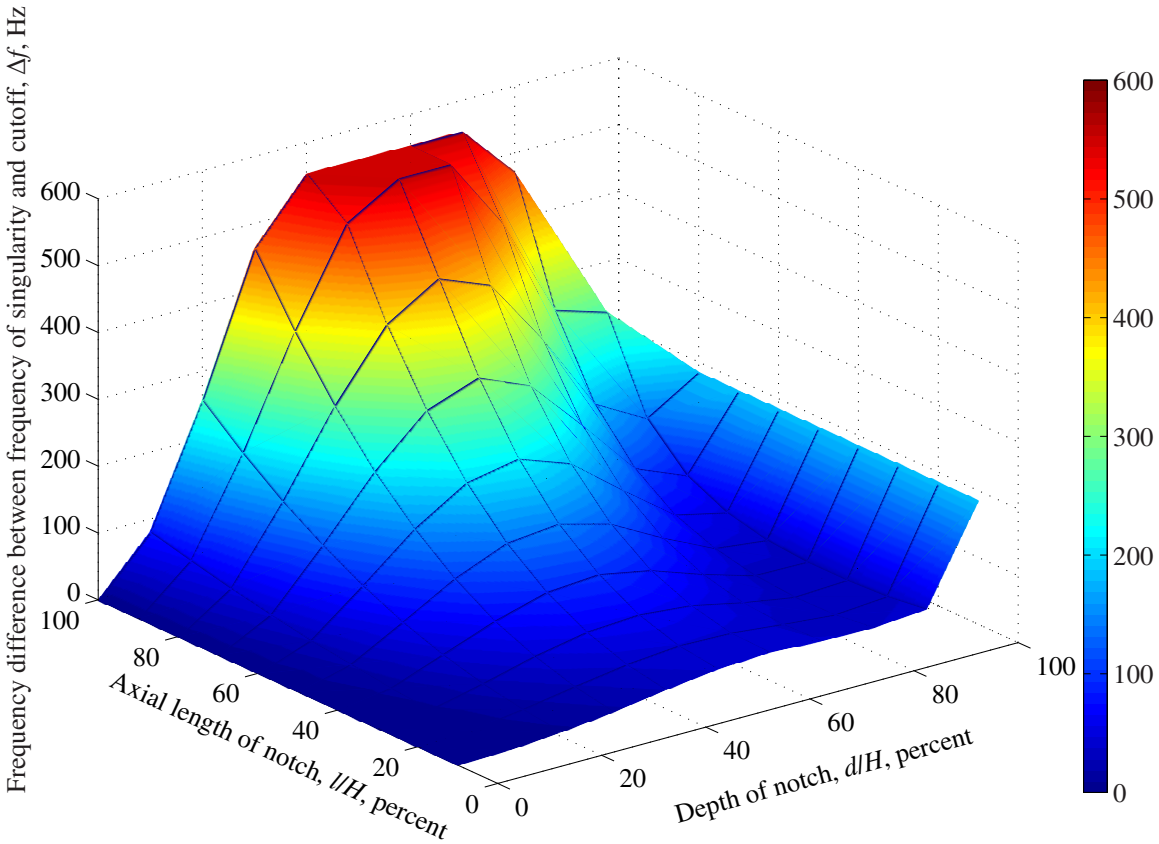

Figure 4.15. Frequency differences, Δf, from the unblemished pipe's F(10,1) cutoff frequency introduced by axisymmetric notches having various dimensions.

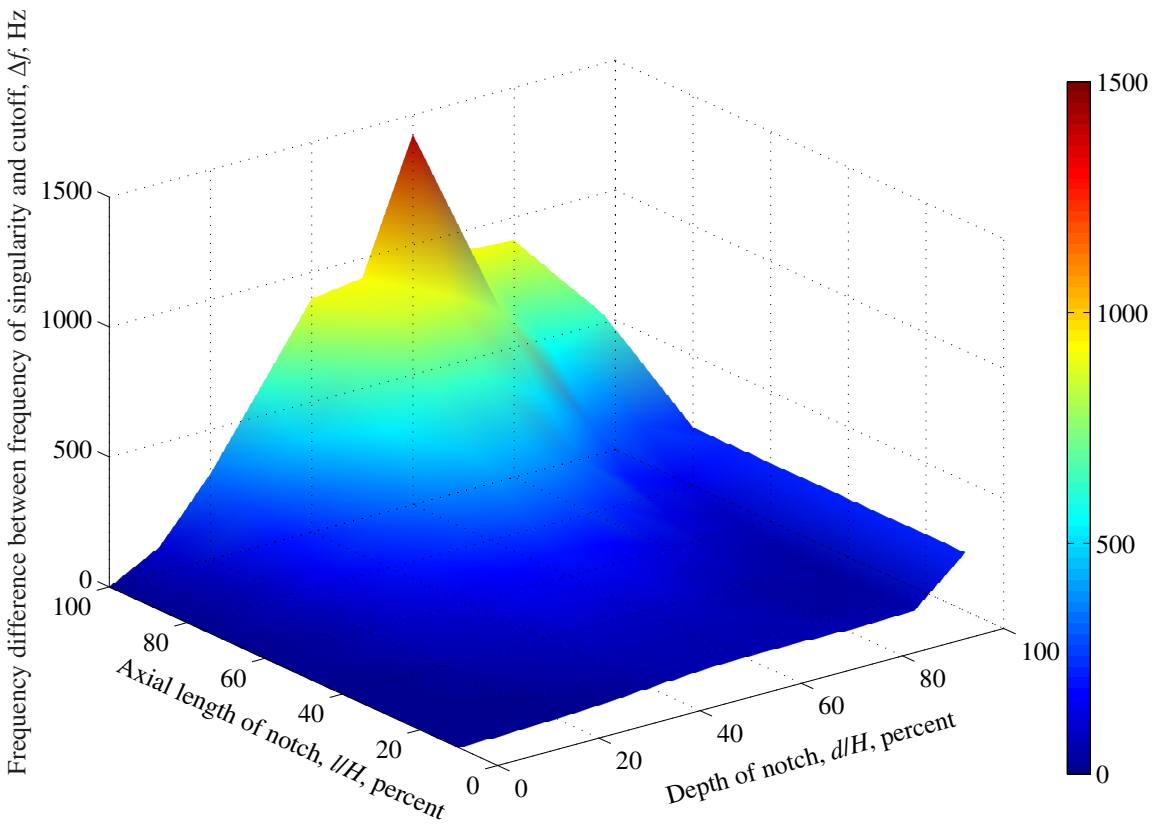

Figure 4.16. Frequency differences, Δf, from the unblemished pipe's F(11,1) cutoff frequency introduced by axisymmetric notches having various dimensions.

pipe and a singularity frequency caused by a notch. Illustrative F(10,1), F(11,1), and F(12,1) modes are shown. Frequency differences can be seen to depend upon an axisymmetric notch's depth and, to a less degree, its axial length. To determine these two dimensions, constant frequency differences for each of these modes are projected onto their common horizontal plane. The projections are superimposed in Figure 4.18. Not surprisingly it can be seen that, due to the contours' "U-shapes," the depth of a notch for a given axial length, l/H, and constant frequency difference, Δf, cannot be found absolutely from any single one of the three modes. Consequently more than one mode has to be employed—a situation which is common to a reflection based procedure [74].

The intersection of the contours of two different flexural modes is usually unique. See, for example, the 200 Hz and 300 Hz contours for the F(11,1) and F(12,1) modes, respectively. The single intersection of the contours provides two coordinates that uniquely define

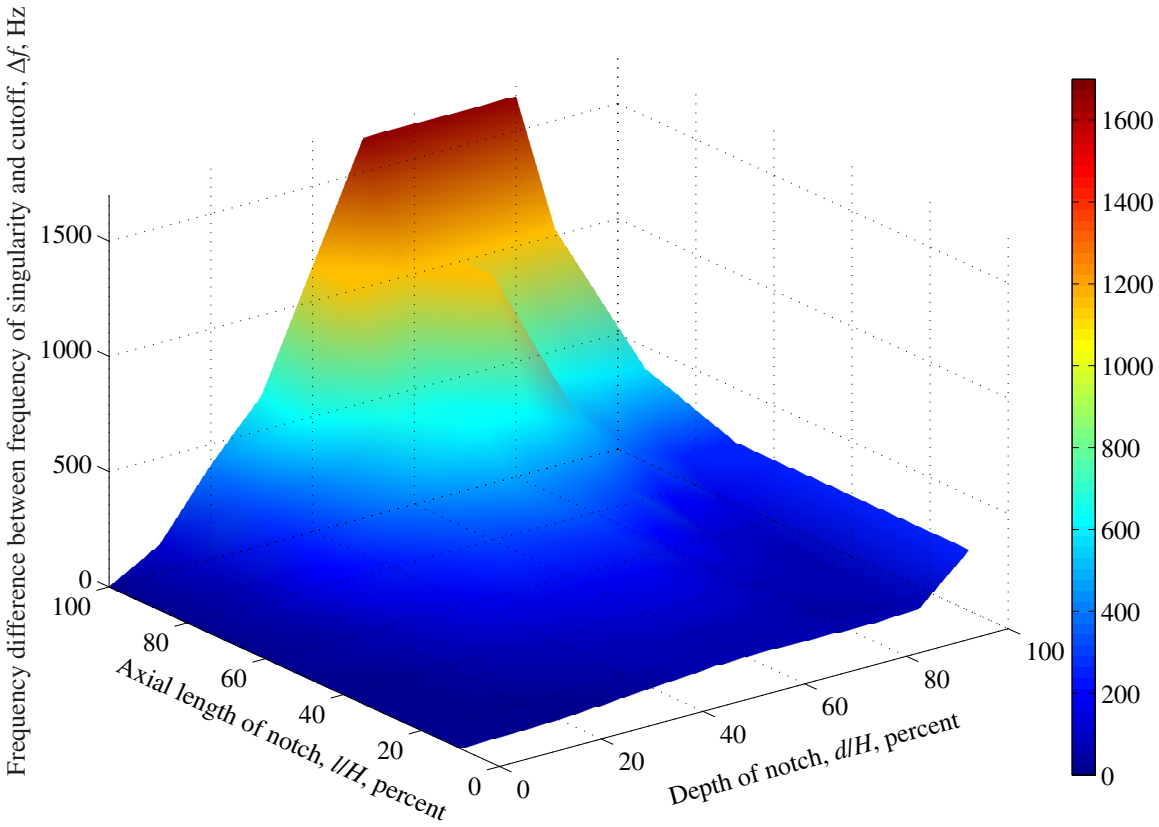

Figure 4.17. Frequency differences, Δf, from the unblemished pipe's F(12,1) cutoff frequency introduced by axisymmetric notches having various dimensions.

the two dimensions of an axisymmetric notch. (Interpolations are obviously needed if a frequency difference does not lie precisely on a contour line.) There are instances, however, when the curves for two different modes intersect more than once. One such example seen in Figure 4.18 occurs for the 400 Hz and 600 Hz contours of the F(11,1) and F(12,1) modes, respectively. In this instance the two arrowed distances from the F(10,1) mode's 200 Hz reference contour may be used to help distinguish the two intersections. Then, by interpolating linearly between the 200 Hz and 300 Hz contours of the F(10,1) mode, a frequency difference for the F(10,1) mode of around 225 Hz would suggest a notch having $(d/H) \approx 0.73$ and $(l/H) \approx 0.78$. On the other hand, a frequency difference of about 260 Hz in the F(10,1) mode would give a notch having $(d/H) \approx 0.62$ and $(l/H) \approx 0.70$. Clearly each additional intersection requires knowledge of another mode's frequency difference to uniquely determine a notch's dimensions. Note, however, that if information for the F(10,1)

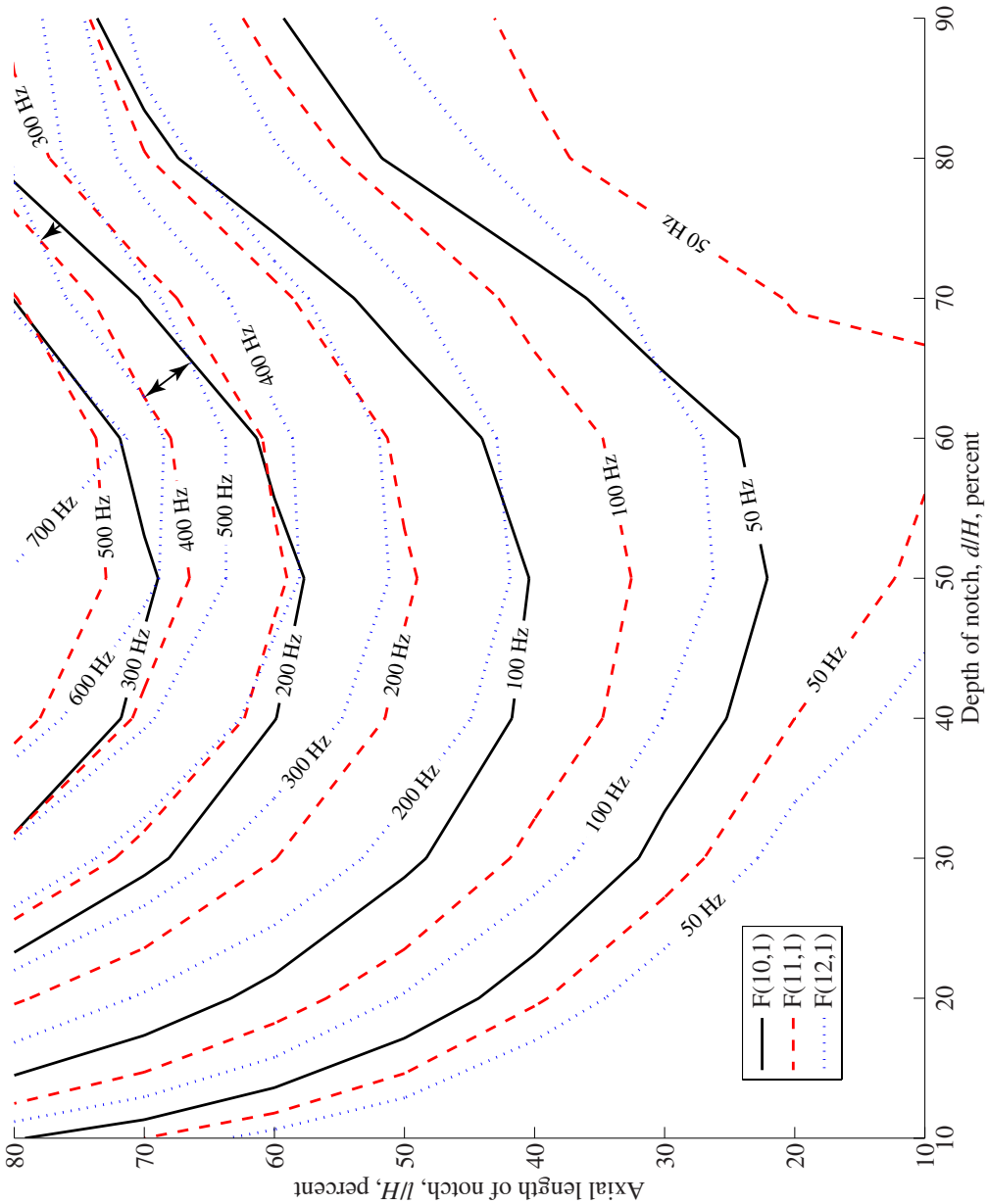

Figure 4.18. Contour maps of constant frequency differences between the singularity produced by an axisymmetric notch and the unblemished pipe's cutoff frequencies for the F(10,1), F(11,1), and F(12,1) modes. The solid [dashed] {dotted} curves correspond to contours of the F(10,1) [F(11,1)] {F(12,1)} mode.

mode and *either* the F(11,1) *or* F(12,1) mode is available, then these two notches can be sized without the need for a third mode. Apparently the selection of modes is more important if only two modes are utilized to characterise an axisymmetric notch. Fortunately the contours plotted in Figure 4.18 can be generated straightforwardly for any range of axisymmetric notch sizes once the nominal pipe and modes of interest have been identified. Furthermore an excitation such as a point force which simultaneously excites several modes becomes more advantageous as the number of required modes increases.

Figure 4.18 also suggests that, for a given frequency difference and notch depth, a flexural mode having a higher circumferential wavenumber leads to a lower ordinate position. Consequently such modes are more sensitive to notches having smaller axial extents. Furthermore, it can be observed that frequency differences for a given mode decrease for notches with progressively smaller axial extents, i.e., they become like a circumferential crack. This trend implies that the technique of measuring frequency differences is likely more effective at characterising "volumetric" voids rather than a crack. It is interesting to note that the constant frequency contours for a single mode are spaced more closely in Figure 4.18 if the axial dimension of the notch is relatively long. It follows, therefore, that sizing is likely more accurate for longer axial notches. This observation reaffirms the previous comment that the measurement of frequency differences is likely to be more challenging for crack-like defects.

The dimensions of the notch described in Table 4.1 are superimposed in Figure 4.19 on the same contour mapping of Figure 4.18. This superposition demonstrates that the selection of modes is relatively unimportant in determining an axisymmetric notch's size. Note that the Δf values for the F(10,1), F(11,1), and F(12,1) modes, obtained by linear interpolations between encompassing contours, are also given in Figure 4.19. These values also appear in Table 4.3. The two sets of (frequency) values are in excellent agreement. It may be seen from Figure 4.19 that the dimensions of the notch described in Table 4.1 can be determined uniquely given the frequency differences for *any* permutation of pairs of the

three available frequency differences. The principle illustrated in Figure 4.19 extends to other modal selections providing the caveats detailed in Section 1.4 are observed.

The size of the mark used in Figure 4.19 to indicate the dimensions of the notch described in Table 4.1 suggests how uncertainties in a notch's dimensions may be assessed from those arising in measured frequency differences. Assuming that the frequency differences are estimated by using the curve fitting technique described in Section 3.2.2, it is reasonable to assume, based on the results shown in Table 3.1, that a frequency difference might have an uncertainly of about ±25 Hz. A perturbation of ±25 Hz about the marker shown in Figure 4.19 for solely the F(10,1) frequency contours gives an uncertainty of around ±3% and ±5% for (d/H) and (l/H), respectively. Hence the procedure, not unexpectedly, produces better estimates for the depth than the length of an axisymmetric notch. These uncertainties are likely to be approximately doubled when the uncertainties for two frequency contours are considered together. It may be possible to reduce the uncertainties by considering the simultaneous, feasible solution space suggested by more than the minimum number of modes. A more precise uncertainty analysis, however, requires the actual uncertainty in each frequency difference and the gradients in the neighbourhood of the nominal solution to be considered.

4.2.8.4 Experimental procedure to determine frequency differences

Limited experiments were conducted solely by the author, Mr. K. A. Adeogun and the author, or K. A. Adeogun to confirm that singularities, distinct from those of an unblemished pipe, are introduced by a notch and that their frequencies are measurable. Reflections from a free end (i.e., an axisymmetric geometry) were investigated first as they were easiest to observe. The remainder of the notches were nonaxisymmetric. The procedure followed for the axisymmetric and nonaxisymmetric notches was identical. It is summarised next.

1. The cutoff frequencies of the pipe were determined on a section known to be "unblemished" by following the procedure given in Section 3.4.

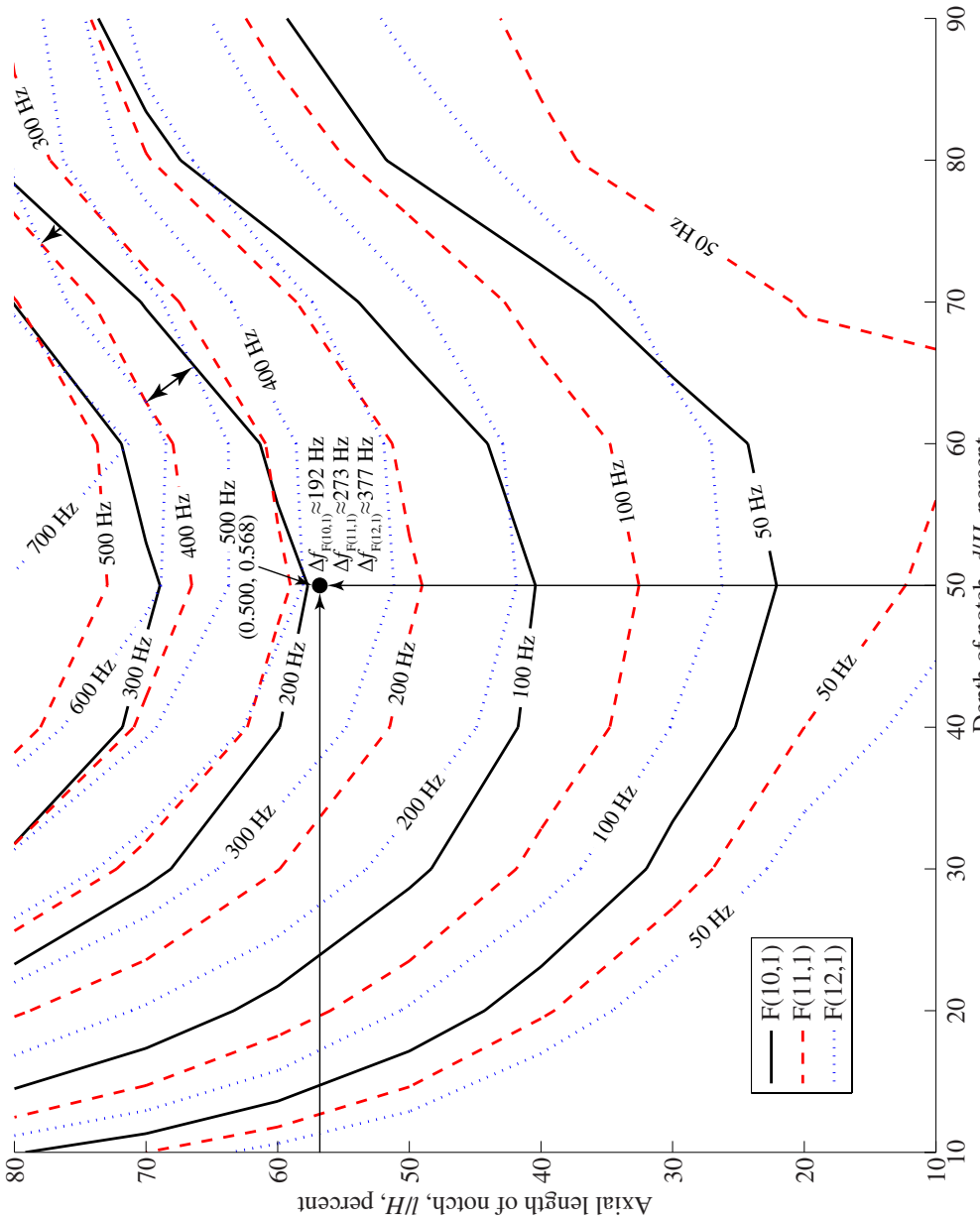

Figure 4.19. Contour maps of constant frequency differences between the singularity produced by an axisymmetric notch and the unblemished pipe's cutoff frequencies for the F(10,1), F(11,1), and F(12,1) modes with the coordinates of the notch considered in Table 4.1 identified.

2. One of the two readily accessible free ends of the pipe was used as the "notch" after which a notch was "machined" in the pipe.

3. Two transducers were attached carefully to the pipe's outer surface near the location of the notch or one of the free ends. The guidelines given in Section 3.4 for selecting transducer separations were essentially followed. Moreover, the transducer locations, relative to the notch's geometric centre, also followed these guidelines, i.e., the transducers were located between 2.55 and 10.2 wall thicknesses from the centre of the notch with essentially no circumferential offset.

4. The transmitting transducer was pulsed by using the forcing pulse described in Appendix D.

5. A digital representation of the signal measured by the receiving transducer was recorded.

6. The frequencies of the singularities were estimated from the time history recorded in the previous step. This step had the following sub-steps.

   (a) The DFT of the signal collected in step 5 was computed. Then the frequencies at which the dominant peaks of the DFT's magnitude occurred were determined, and the corresponding amplitudes and phase angles were noted.

   (b) The curve fitting technique described in Section 3.2.2 was applied to the time history recorded in step 5 to recover refined estimates of the singularities' frequencies. Convenient initial approximations to the modal amplitudes, phase angles, and singularities' frequencies were determined in step 6a.

7. The singularities' frequencies, obtained in step 6b, were compared to the unblemished pipe's cutoff frequencies found in step 1. The absolute value of the simple arithmetic difference between a singularity's frequency and the unblemished pipe's nearest cutoff frequency gave the desired frequency difference.

The procedure readily and simultaneously excited a number of modes. By following the procedural steps given above, a number of frequency differences were measured. These differences could be plotted on a contour map similar to the ones shown in Figures 4.18 and 4.19. The graphical procedure illustrated in Figure 4.19 could be applied next to estimate the notch's dimensions.

4.2.8.5 Concluding remarks for axisymmetric notches

In addition to corroborating the hybrid computational procedure, it has been confirmed that the axial length of an axisymmetric notch affects the wave reflection of the L(0,2) and T(0,1) pipe modes [70, 74] but to a less extent than the notch's depth. This conclusion has been seen to hold for flexural modes having higher order, circumferential wavenumbers. "Double" or spurious peaks in spectral densities found at receiving positions within the nearby reflected field have been demonstrated, for the first time, to be a particularly telling feature of an axisymmetric notch's presence. A preliminary parametric study has suggested that it is feasible to estimate such a notch's dimensions from frequency differences of the dominant spectral features associated with at least two modes. These differences have been seen to depend upon the properties of the combined unblemished pipe *and* finite element regions. They can be found by using a single point-like excitation and a simple receiver. Experimental investigations are required to confirm that a flexural mode having a higher circumferential wavenumber is more capable of discriminating a smaller notch at the likely expense of reducing the feasible detection distance. The computational extension to nonaxisymmetric notches is considered next.

4.3 Three-dimensional Scatterers

4.3.1 Preamble

The hyrid SAFE technique for three-dimensional scatterers is a straightforward extension [66, 67] of the procedure detailed for an axisymmetric notch. Consequently only notable differences are described and explained. The idealization of the previously considered pipe, but with a nonaxisymmetric notch, is described first. Then an overview is given of the three-dimensional finite element model and its interface to a pipe region in which a wavefunction expansion is employed again. Imposing continuity conditions on this interface allows the effect of wave scattering to be determined on the otherwise infinite waveguide. Computer results are presented for an outer surface breaking, three dimensional notch. They are compared, where possible, with published data [70]. Lastly, interpretations and conclusions are drawn.

4.3.2 Description of pipe, notch, and finite element region

4.3.2.1 Description of pipe and nonaxisymmetric notch

The infinitely long, notched pipe illustrated in Figure 4.20 is considered. The pipe is assumed, as before, to be uniformly right circular, homogeneous, linearly elastic, and isotropic. Then the wavefunctions described in Chapter 2 can be used to describe the displacement fields in the "parent" pipe on either side of the notched region. In particular, the pipe has Lamé constants λ and μ, density ρ, a constant mean radius R, outside diameter D_o, and wall thickness H, in addition to traction free, inner and outer surfaces. Positions and displacements are described in terms of the cylindrical coordinate system (r, θ, z), whose r, θ, and z axes are shown in Figure 4.20 with their origin, O . A nonaxisymmetric notch having depth d, circumferential extent c, and axial length l is bounded between the planes $z = 0$ and $z = -2z_{FE}$. Motions caused by the transient force detailed earlier are modelled by using a(n

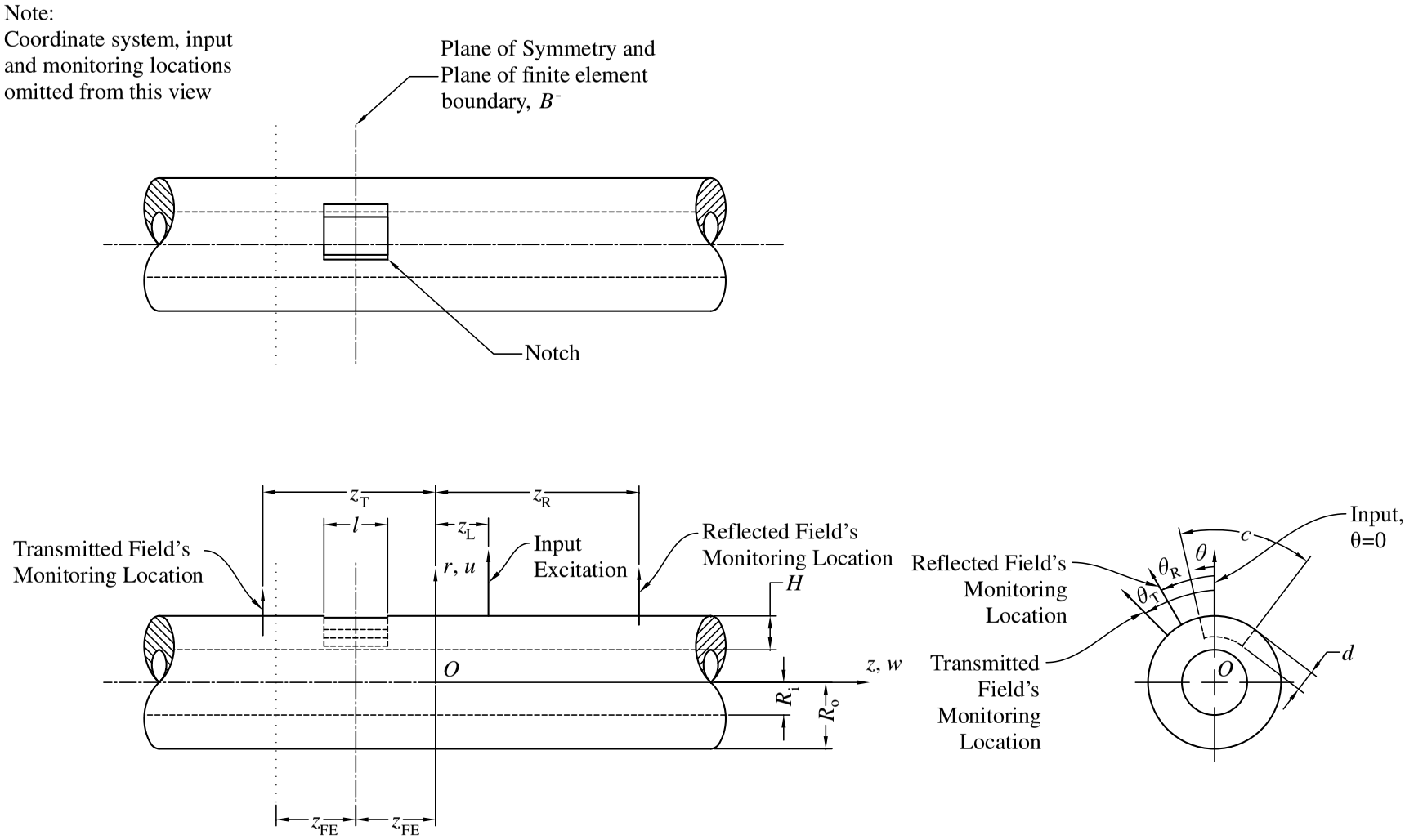

Figure 4.20. Illustrating a pipe having a nonaxisymmetric notch.

approximate) wavefunction expansion in the regions $z \geq 0$ and $z \leq -2z_{FE}$ and, now, a three-dimensional finite element model between the planes $z = 0$ and $z = -z_{FE}$. The notched pipe is assumed to be symmetrical[21] about the plane $z = -z_{FE}$ so that only half the pipe and notch is modelled with appropriate boundary conditions prescribed on $z = -z_{FE}$. Motions are obtained for $z \leq -2z_{FE}$ from those found for $z \geq 0$ by using appropriate symmetry and antisymmetry arguments again.

4.3.2.2 Finite element region

Twenty-seven node, brick finite elements based on quadratic Lagrangian interpolation functions [107] are used to describe the motions in the finite element region bounded by the planes $z = 0$ and $z = -z_{FE}$, i.e., boundaries B^+ and B^-, respectively. An arbitrary geometry can be contained in this finite element region by generating a mesh that reasonably approximates the geometry. The application of Hamilton's principle to the finite element region, which is presented more completely in Appendix J, gives equation (4.2.1) again. The procedure used to derive equation (4.2.9) from equation (4.2.1) still applies so that equation (4.2.9) also remains pertinent for the three-dimensional case.

4.3.3 Boundary conditions on $z = -z_{FE}$

To take advantage of the symmetry of the defective pipe about the plane $z = -z_{FE}$, a force applied at an arbitrary $z > 0$ is represented again by the superposition of a symmetrical and an antisymmetrical load, as illustrated in Figure 4.2. The boundary conditions on the plane $z = -z_{FE}$ do not change from the axisymmetric case so that equations (4.2.10) through (4.2.16) are still applicable.

[21] This restriction can be removed, as for the axisymmetric notch, by considering a finite element region extending from $z = 0$ to $z = -2z_{FE}$ and enforcing continuity conditions at *both* $z = 0$ and $z = -2z_{FE}$.

4.3.4 Interface between the wavefunction and finite element regions

4.3.4.1 Modal representation of the displacement field in R^+

A *single* harmonic wave mode with circular frequency, ω, circumferential wavenumber n_{in}, order m_{in}, and *unit* amplitude is considered to be incident on the plane $z = 0$. This wave is usually scattered at the interface between the parent pipe and finite element (or notched) region to create reflected and transmitted wave fields. The transmitted field may be obtained straightforwardly from a known reflected field by taking advantage of the symmetry about the plane $z = -z_{\text{FE}}$. Therefore only the reflected field needs to be detailed.

The displacements of the reflected wave field, which lie in region R^+, can be written in the form

$$\mathbf{U}_{+}^{\text{scat}} = \sum_{n_{\text{scat}}=-\infty}^{\infty} \sum_{m_{\text{scat}}=1}^{6N+3} A_{n_{\text{scat}}m_{\text{scat}}} \boldsymbol{\phi}^{\text{R}}_{n_{\text{scat}}m_{\text{scat}}\text{u}} \text{e}^{\text{j}k_{n_{\text{scat}}m_{\text{scat}}}z} \text{e}^{\text{j}n_{\text{scat}}\theta} \tag{4.3.1}$$

at the radial coordinates of the finite elements' nodal points. The nomenclature employed in equation (4.3.1) has been described previously. Only those modes having non-negative imaginary wave number components are admissible in the reflected field. However, all the circumferential wavenumbers are required now because the finite element region is no longer axisymmetric.

4.3.4.2 Continuity conditions on boundary B^+

Consider the boundary B^+ which is common to the parent waveguide and the finite element region. A schematic of this boundary is shown in Figure 4.21 by itself. At least one "complete" ring of finite elements is assumed to be coupled perfectly to the wave function region. This assumption simplifies the enforcement of continuity conditions[22] on B^+ but it does not limit the general application of the modelling. As for the axisymmetric case, continuities

[22]No finite element nodal points on B^+ are force free when this assumption is made. It follows, therefore, that mixed boundary conditions [69] need not be considered.

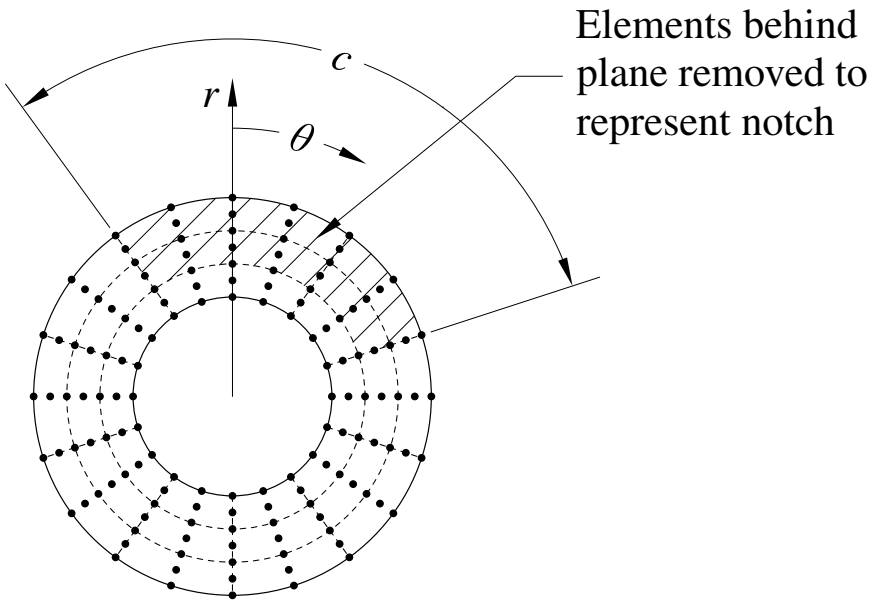

Figure 4.21. Schematic of the finite element region's B^+ boundary where no force free nodes exist.

of the nodal displacements and forces on boundary B^+ require

$$\mathbf{q}_+ = \mathbf{q}_+^{\text{in}} + \mathbf{q}_+^{\text{scat}} \tag{4.3.2a}$$

and

$$\mathbf{P}_+ = \mathbf{f}_+^{\text{in}} + \mathbf{f}_+^{\text{scat}}, \tag{4.3.2b}$$

where the incident and scattered displacements as well as the forces are evaluated at each of the nodal points on B^+ shown in Figure 4.21. Displacements created by the scattered waves can be determined by applying equation (4.3.1) at the nodal points on boundary B^+. They are written, in shorthand form, as

$$\mathbf{q}_+^{\text{scat}} = \mathbf{GA}, \tag{4.3.3}$$

where $\mathbf{G}$ is a matrix that "maps" the scattered wave amplitudes, $\mathbf{A}$, into the required nodal displacements. The $\mathbf{G}$ matrix is similar to the one encountered in the two-dimensional case but it contains (matrix) elements now that describe the circumferential variation of the wave

field. The scattered (consistent) forces are obtained straightforwardly at the nodal points on B^+ by applying standard finite element methodology [107]. They can be expressed as

$$\mathbf{f}_+^{\text{scat}} = \mathbf{F}_{\text{scat}}\mathbf{A}, \tag{4.3.4}$$

where matrix $\mathbf{F}_{\text{scat}}$ "maps" the scattered wave amplitudes, $\mathbf{A}$, into the required nodal forces. Nodal displacements and forces are determined similarly in the incident wave field from the prescribed incident wavefunctions.

4.3.5 Resulting system of linear equations

Equations (4.2.16) and (4.2.20) lead again to the result that

$$\mathbf{S}^{\ddagger}\mathbf{q}_+ = \mathbf{P}_+ = \mathbf{S}^{\ddagger}\left(\mathbf{q}_+^{\text{in}} + \mathbf{q}_+^{\text{scat}}\right) = \mathbf{f}_+^{\text{in}} + \mathbf{f}_+^{\text{scat}}. \tag{4.3.5}$$

Equation (4.3.5), however, is unlikely to produce a square order system of linear equations that can be inverted to determine the scattered wave amplitudes, $\mathbf{A}$. This difficulty arises because the number of finite element nodes on boundary B^+ is not generally identical to the number of modes assumed in the wavefunction expansion. (This difficulty was not encountered in the previous axisymmetric problem because all the available wave functions were retained so that the resulting system of linear equations was invertible.) The principle of virtual work is applied, therefore, to the finite element region in order to obtain an invertible system of equations. No real or virtual work is performed on the boundary $z = -z_{\text{FE}}$ because, at each nodal point on this boundary, all the nodal forces in each coordinate direction, or their complementary displacement components, are identically zero. Therefore, the virtual work done on the finite element region, $\bar{\delta}\mathcal{E}_{\text{virt}}$, can be written as

$$\bar{\delta}\mathcal{E}_{\text{virt}} = \frac{1}{2}(\widetilde{\bar{\delta}\mathbf{q}_+}^{\text{T}}\mathbf{P}_+ + \bar{\delta}\mathbf{q}_+^{\text{T}}\widetilde{\mathbf{P}_+}), \tag{4.3.6}$$

where $\overline{\delta}$ indicates the first variation which vanishes for equilibrium. By performing this variation, the resulting equation

$$\widetilde{\overline{\delta}\mathbf{q}_+}^{\mathrm{T}}\mathbf{P}_+ = 0 \tag{4.3.7}$$

can be shown to be sufficient for the virtual work to be stationary. The $\widetilde{\overline{\delta}\mathbf{q}_+}^{\mathrm{T}}$ can be determined, by using equation (4.3.2a), to be

$$\widetilde{\overline{\delta}\mathbf{q}_+}^{\mathrm{T}} = \widetilde{\overline{\delta}\mathbf{q}_+^{\mathrm{in}}}^{\mathrm{T}} + \widetilde{\overline{\delta}\mathbf{q}_+^{\mathrm{scat}}}^{\mathrm{T}}. \tag{4.3.8}$$

The displacements of the incident wavefield are prescribed at the finite elements' nodal points and, therefore, have no variation, i.e., $\widetilde{\overline{\delta}\mathbf{q}_+^{\mathrm{in}}}^{\mathrm{T}} = \mathbf{0}$. Consequently, equation (4.3.8) reduces to

$$\widetilde{\overline{\delta}\mathbf{q}_+}^{\mathrm{T}} = \widetilde{\overline{\delta}\mathbf{q}_+^{\mathrm{scat}}}^{\mathrm{T}}. \tag{4.3.9}$$

Substituting equation (4.3.3) into equation (4.3.9) and noting that $\mathbf{G}$ is constant gives

$$\widetilde{\overline{\delta}\mathbf{q}_+}^{\mathrm{T}} = \widetilde{\overline{\delta}\mathbf{A}}^{\mathrm{T}}\widetilde{\mathbf{G}}^{\mathrm{T}}. \tag{4.3.10}$$

Applying the principle of virtual work to equation (4.3.5) produces

$$\widetilde{\overline{\delta}\mathbf{A}}^{\mathrm{T}}\widetilde{\mathbf{G}}^{\mathrm{T}}\mathbf{S}^{\ddagger}\mathbf{q}_+ = \widetilde{\overline{\delta}\mathbf{A}}^{\mathrm{T}}\widetilde{\mathbf{G}}^{\mathrm{T}}\mathbf{P}_+ = \widetilde{\overline{\delta}\mathbf{A}}^{\mathrm{T}}\widetilde{\mathbf{G}}^{\mathrm{T}}\mathbf{S}^{\ddagger}\left(\mathbf{q}_+^{\mathrm{in}} + \mathbf{q}_+^{\mathrm{scat}}\right) = \widetilde{\overline{\delta}\mathbf{A}}^{\mathrm{T}}\widetilde{\mathbf{G}}^{\mathrm{T}}\left(\mathbf{f}_+^{\mathrm{in}} + \mathbf{f}_+^{\mathrm{scat}}\right) = 0, \tag{4.3.11}$$

when equations (4.3.7) and (4.3.10) are utilized. Equation (4.3.11) implies that

$$\widetilde{\mathbf{G}}^{\mathrm{T}}\mathbf{S}^{\ddagger}\left(\mathbf{q}_+^{\mathrm{in}} + \mathbf{q}_+^{\mathrm{scat}}\right) = \mathbf{0} \tag{4.3.12a}$$

and

$$\widetilde{\mathbf{G}}^{\mathrm{T}}\left(\mathbf{f}_+^{\mathrm{in}} + \mathbf{f}_+^{\mathrm{scat}}\right) = \mathbf{0}, \tag{4.3.12b}$$

because $\widetilde{\delta\mathbf{A}^{\mathrm{T}}}$ is arbitrary. Setting equations (4.3.12a) and (4.3.12b) equal leads, after rearrangements, to

$$\widetilde{\mathbf{G}}^{\mathrm{T}}\left(\mathbf{S}^{\ddagger}\mathbf{q}_{+}^{\mathrm{in}}-\mathbf{f}_{+}^{\mathrm{in}}\right)=\widetilde{\mathbf{G}}^{\mathrm{T}}\left(\mathbf{f}_{+}^{\mathrm{scat}}-\mathbf{S}^{\ddagger}\mathbf{q}_{+}^{\mathrm{scat}}\right). \tag{4.3.13}$$

The right side of equation (4.3.13) can be expressed in terms of the scattered wave amplitudes by using equations (4.3.3) and (4.3.4). Hence,

$$\widetilde{\mathbf{G}}^{\mathrm{T}}\left(\mathbf{S}^{\ddagger}\mathbf{q}_{+}^{\mathrm{in}}-\mathbf{f}_{+}^{\mathrm{in}}\right)=\widetilde{\mathbf{G}}^{\mathrm{T}}\left(\mathbf{F}_{\mathrm{scat}}\mathbf{A}-\mathbf{S}^{\ddagger}\mathbf{G}\mathbf{A}\right)=\widetilde{\mathbf{G}}^{\mathrm{T}}\left(\mathbf{F}_{\mathrm{scat}}-\mathbf{S}^{\ddagger}\mathbf{G}\right)\mathbf{A}. \tag{4.3.14}$$

The matrix product $\widetilde{\mathbf{G}}^{\mathrm{T}}\left(\mathbf{F}_{\mathrm{scat}}-\mathbf{S}^{\ddagger}\mathbf{G}\right)$ is square and invertible so that

$$\mathbf{A}=\left[\widetilde{\mathbf{G}}^{\mathrm{T}}\left(\mathbf{F}_{\mathrm{scat}}-\mathbf{S}^{\ddagger}\mathbf{G}\right)\right]^{-1}\widetilde{\mathbf{G}}^{\mathrm{T}}\left(\mathbf{S}^{\ddagger}\mathbf{q}_{+}^{\mathrm{in}}-\mathbf{f}_{+}^{\mathrm{in}}\right). \tag{4.3.15}$$

As for the axisymmetric case, equation (4.3.15) must be evaluated for both the symmetrical and antisymmetrical force components in order to recover their combined effect. Then the ensuing reflected and transmitted wave amplitudes may be found by using equation (4.2.28).

4.3.6 Scattered displacement fields

Modal summations required to describe the scattered displacements from a three-dimensional notch are described next. They are similar to the two-dimensional axisymmetric case but contain an additional summation to include additional conversions from one to another circumferential wavenumber. However, the modal summation and inverse Fourier transform procedures used to derive equation (2.3.17) are still pertinent. Consequently the displacements in the reflected wavefield that are caused by a typical mode having circum-

ferential wavenumber n_{in} and order m_{in}, can be written as

$$\mathbf{U}_{n_{\text{in}}m_{\text{in}}}(\theta, z, t) = \frac{1}{2\pi}\int_{-\infty}^{\infty} \overline{p}(\omega) \mathrm{e}^{-\mathrm{j}\omega t} A^{\text{in}}_{n_{\text{in}}m_{\text{in}}} \left[\sum_{n_{\text{scat}}=-\infty}^{\infty} \sum_{m_{\text{scat}}=1}^{6N+3} R_{n_{\text{scat}}m_{\text{scat}}} \boldsymbol{\phi}^{\text{R}}_{n_{\text{scat}}m_{\text{scat}}\text{u}} \mathrm{e}^{\mathrm{j}k_{n_{\text{scat}}m_{\text{scat}}}z} \right] \mathrm{e}^{\mathrm{j}n_{\text{scat}}\theta} \, \mathrm{d}\omega \tag{4.3.16}$$

at the radial coordinates of the finite elements' nodal surfaces. As before, $A^{\text{in}}_{n_{\text{in}}m_{\text{in}}}$ is the frequency dependent amplitude of an incident mode. Equations (4.2.30) and (4.2.31) can be used to recover the displacements caused by the reflected waves. Then the displacements in the transmitted wave field are found from their reflected counterparts by making the same modifications described in the axisymmetric case.

4.3.7 Illustrative examples

4.3.7.1 Overview

Computer code implementing the hybrid SAFE technique for two-dimensional problems was extended to accommodate three-dimensional wave scatterers. The unblemished pipe considered before was retained. Its material and dimensional properties are summarized in Table 2.1. Transparency tests were run to validate the extended software. These results are given in Appendix H. Note that the smallest propagating wavelength in the excitation's bandwidth, which is about $3.4H$, still corresponded to the L(0,1) mode. Consequently the discretization and wavefunctions detailed in Section 2.5 were used, after introducing a nonaxisymmetric notch, to represent motions in the parent waveguide.

Computer results are given for an outer surface breaking notch which has a depth of one-half the wall thickness, an axial length to wall thickness ratio of 0.568, and extends over one-half the pipe's circumference. The resulting reflection coefficients are compared to the measured values and finite element predictions given in [70]. These comparisons serve to add plausibility to the present numerical results. Then time histories are simulated

in the reflected and transmitted wave fields for an axisymmetric force applied in the axial (z) direction so that the experiments are mimicked. Direct comparisons are made, when possible, between the simulated histories and the measured traces given in [70]. A modal analysis, which illustrates the importance of modal conversions, is inherent to the simulations. A treatment which is analogous to that given for the axisymmetric notch is extended to a radial point force acting on the nonaxisymmetric notch. Having validated several of the present numerical results, a wider parametric study is undertaken that is similar to before.

4.3.7.2 A three-dimensional notch

A nonaxisymmetric notch having the dimensional properties summarized in Table 4.5 was considered because experimental and finite element data are again available for comparisons. Twenty seven node, brick finite elements using quadratic Lagrange interpolation polynomials in each coordinate direction [107] were employed for the finite element region around the notch. The notch was modelled again by simply removing finite elements[23]. As in the axisymmetric case, the singularities at the notch's corners are not described accurately by this method, which limits the accuracy of the stresses in the near field. The far field behaviour is, however, modelled with sufficient accuracy to be meaningful. Ultimately, ten (five) finite elements described the behaviour over the full (half) wall thickness. To minimize computer waiting time, the minimally acceptable two finite elements represented the notch's axial extent. However, 126 elements were deployed around the pipe's circumfer-

Table 4.5. Dimensional properties of the outer surface breaking, nonaxisymmetric notch.

Property	Assigned Value
Depth of notch, d, in (mm)	0.110 (2.79)
Axial length of notch, l, in (mm)	0.125 (3.17)
Circumferential extent of notch, c, degrees (rad)	180 (π)
Depth to wall thickness ratio, (d/H)	0.500
Axial length to wall thickness ratio, (l/H)	0.568

[23] Crack-tip elements, having their "side nodes at quarter points of their respective sides," *could* have been used but were not considered necessary again.

ence. The radial discretization of ten elements through the pipe's wall was selected so that the wavefunctions from the previous axisymmetric analysis could be employed.

The appropriateness of the minimal axial discretization was checked by simulating the axisymmetric notch described in Section 4.2.8.2 with the three-dimensional software. A comparison of the the two sets of reflection and transmission coefficients showed that they were essentially indistinguishable. The circumferential discretization was determined, after selecting the radial and axial discretizations, by considering the results from the transparency tests. The number of finite elements around the unblemished pipe's circumference was increased gradually until the reflection coefficient was less than 0.01 for all the modes propagating in the excitation's bandwidth. (See Appendix H and Figure H.59 in particular.) Therefore any reflection coefficient calculated with the stated circumferential mesh that has a magnitude greater than 0.01 for a propagating mode has an inconsequential error from this modelling component. Not surprisingly, the F(13,1) mode dictated the circumferential discretization as it has the the smallest ($3.6H$) circumferential wavelength of the propagating modes. On the other hand, the propagating L(0,1) mode has a somewhat smaller axial wavelength of around $3.4H$. Consequently, the ratio of the smallest axial wavelength of all the propagating modes to a finite element's axial length was approximately 12—a value which is above the recommended lower bound of ten elements per shortest wavelength [70, 71]. Similarly, the ratio of the F(13,1) mode's (circumferential) wavelength to a finite element's circumferential length was virtually 10. Moreover, the spatial aspect ratios (i.e., the ratios of the finite elements' lengths in the axial and circumferential directions to those in the radial direction) were approximately 2.4:0.4:1.0 which, experience suggests, is near the desirable value of 1.0. Hence each finite element is reasonably "compact" and likely to behave well [107].

Figures 4.22, 4.23, and 4.24 are analogous to Figures 4.4, 4.5, and 4.6, respectively. The excitation and monitoring locations were modified, however, to better mimic the experimental configuration of [70]. Therefore, the axisymmetric excitation and reflected field

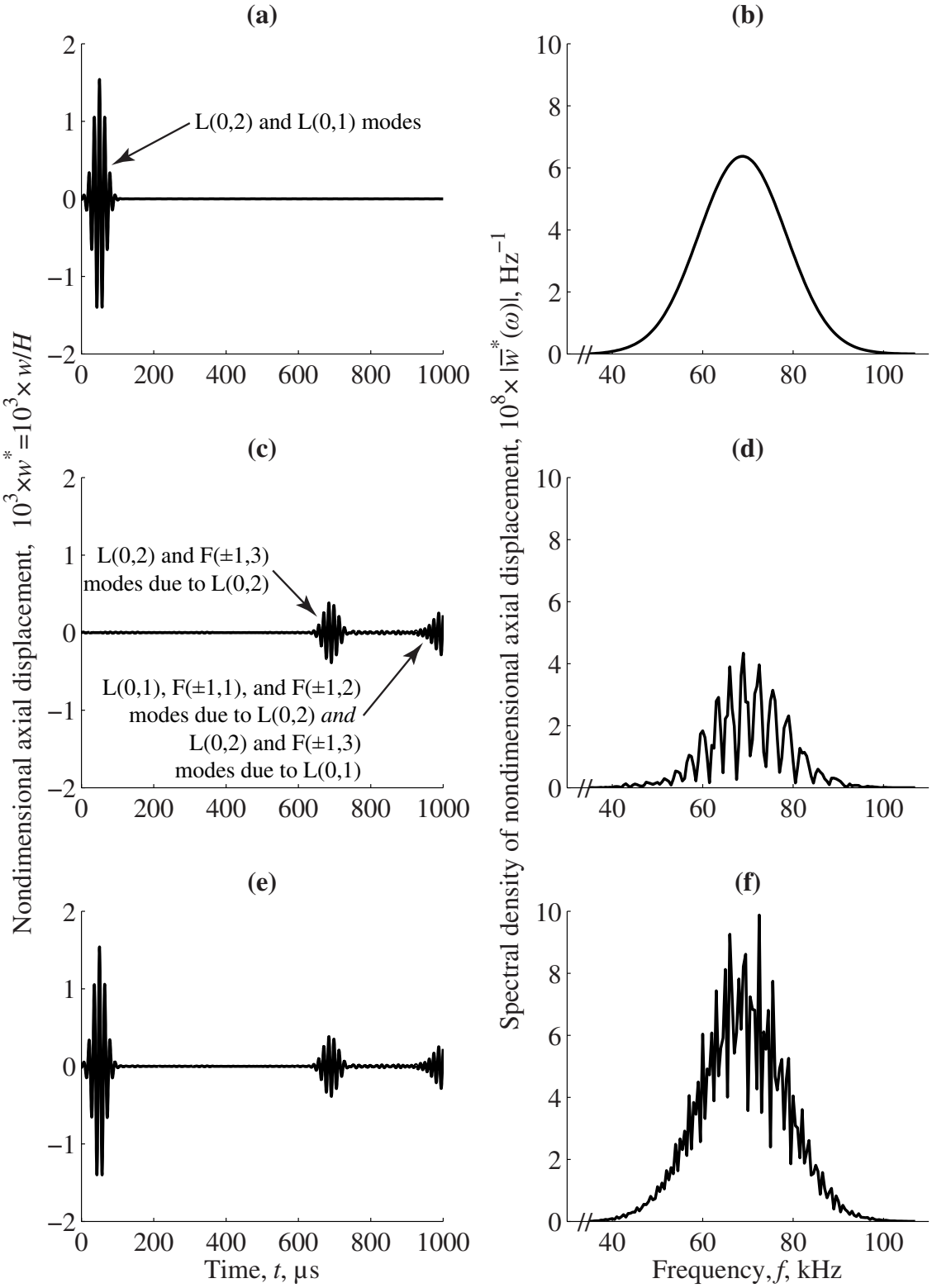

Figure 4.22. Axial displacement predicted within the reflected field for a nonaxisymmetric notch. Sub-figures (a) and (b) [(c) and (d)] {(e) and (f)} give the direct [reflected] {superposition of direct and reflected} waves resulting from an axisymmetric axial force.

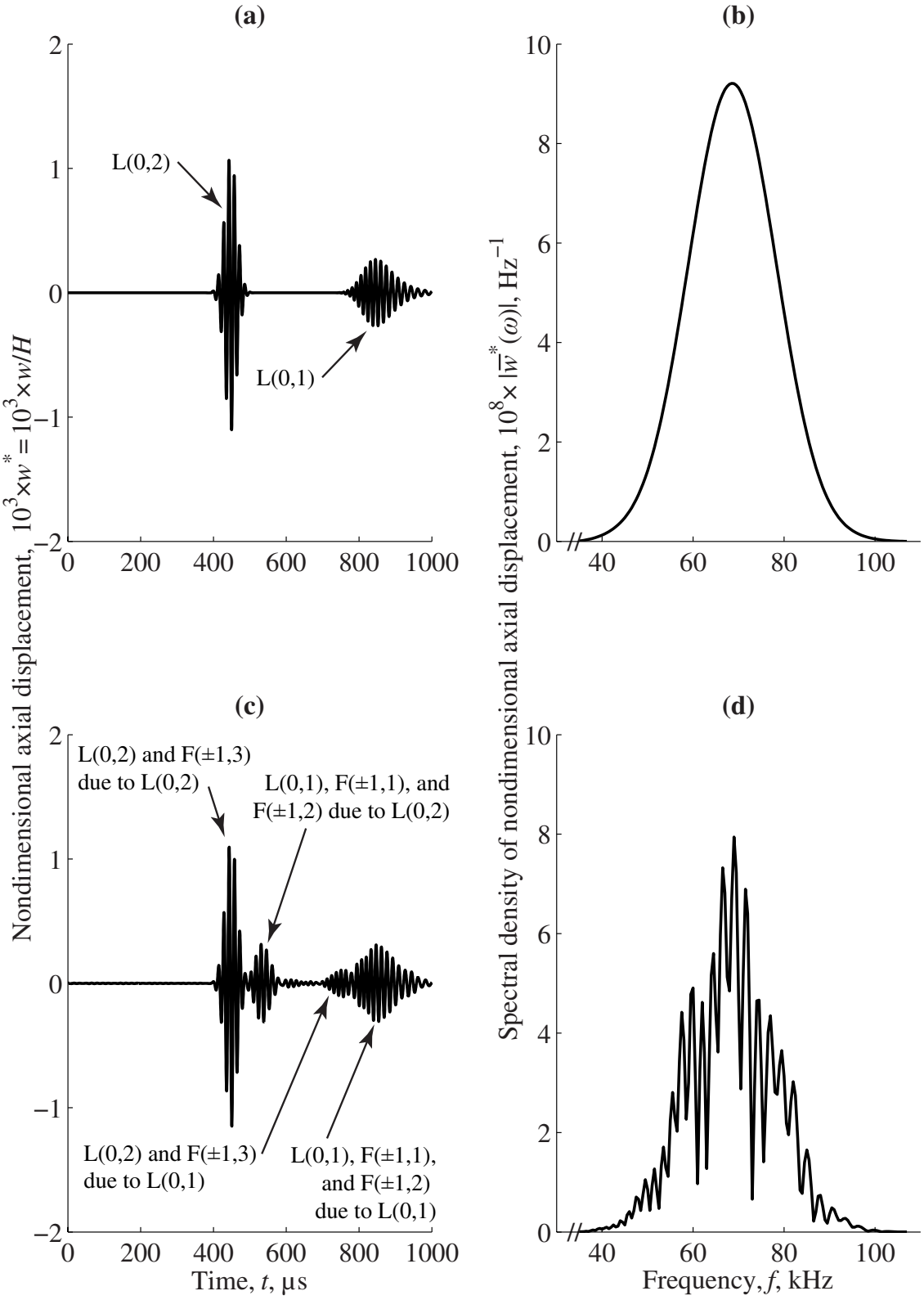

Figure 4.23. Axial displacement predicted within the transmitted field for a nonaxisymmetric notch. Sub-figures (a) and (b) [(c) and (d)] give the direct [transmitted] waves resulting from an axisymmetric axial force.

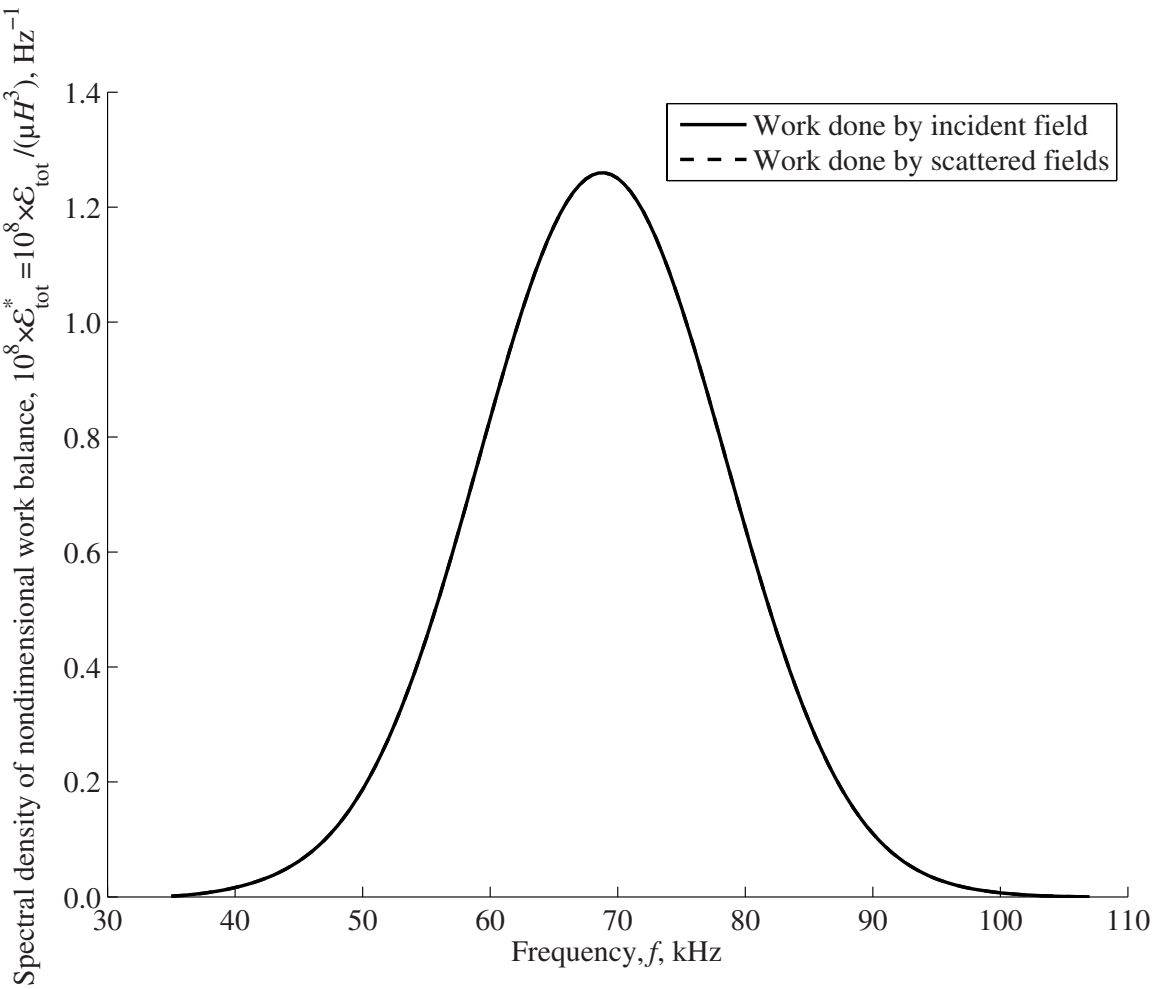

Figure 4.24. Spectral density of the work done, per period, by waves produced by an axisymmetric axial force, and scattered by a nonaxisymmetric notch.

monitoring locations were positioned on the pipe's outer surface at $z^*_{\text{L}} = z_{\text{L}}/H = z^*_{\text{R}} = z_{\text{R}}/H \approx 304$. On the other hand, the monitoring location in the transmitted wavefield was located on the pipe's outer surface at $z^*_{\text{T}} = z_{\text{T}}/H \approx -161$. As before, z_{L}, z_{R}, z_{T} are respectively the axial locations of the excitation, as well as the reflected and transmitted fields' monitoring locations. These positions are illustrated relative to the origin, O, in Figure 4.20. They are located centrally to the notch in the circumferential direction.

Figure 4.24 is identical to Figure 4.6 as the waves which carry energy to the finite element region are the same. The work done per period by the waves incident on the finite element region coincides again with that of the scattered waves. A comparison of Figures 4.22 and 4.4 shows that, as in the axisymmetric case, the contributions of the L(0,1)

and L(0,2) modes cannot be distinguished easily in the time histories of Figure 4.22 (a), (c), and (e). On the other hand, Figure 4.23 (a) indicates that the relatively large axial separation between the circumferential planes of the excitation's application and the monitoring position in the transmitted field allows the effects to be separated easily *in time*. The most noticeable modal conversions introduced by the nonaxisymmetric notch are seen in Figures 4.22 (c) and 4.23 (c). The primary involvement of the F($\pm 1, m$), $m = 1, 2, 3$ modes is investigated later. Spectral densities indicate the presence of the notch by the smooth, single peak in the spectral densities of Figures 4.22 (b) and 4.23 (b) becoming more numerous and sharper in Figures 4.22 (f) and 4.23 (d). The notch appears to act like a comb filter because a large number of modes are excited through modal conversions at the notch. Just as importantly, these conversions introduce a corresponding number of different relative phases.

A cursory comparison of the modal amplitudes annotated in Figures 4.22 and 4.23 with the appropriate reflection and transmission coefficients given in Appendix I for this notch was informative. Such a comparison showed that they were qualitatively in good agreement. Moreover the time histories appearing in these figures, which were obtained from an inverse Fourier transform of the accompanying spectral densities, appeared intuitively to be "reasonable," with the effects of dispersion clearly visible. The spectral densities in the two figures were cross-checked by computing the DFT of a recovered time history and comparing it with the corresponding spectral densities. Excellent agreement was seen in all cases.

To illustrate the importance of the modal conversions more clearly, Figures 4.25 and 4.26 present the principal modal contributions when the L(0,2) and L(0,1) modes are incident individually on the same notch. In order to be consistent with Figures 4.22 and 4.23, only modes having circumferential wavenumbers $m = 0$ or $m = \pm 1$ appear in Figures 4.25 and 4.26. Modal conversions involving a circumferential wavenumber greater than two provide negligible contributions to the reflected and transmitted wave fields for this particu-

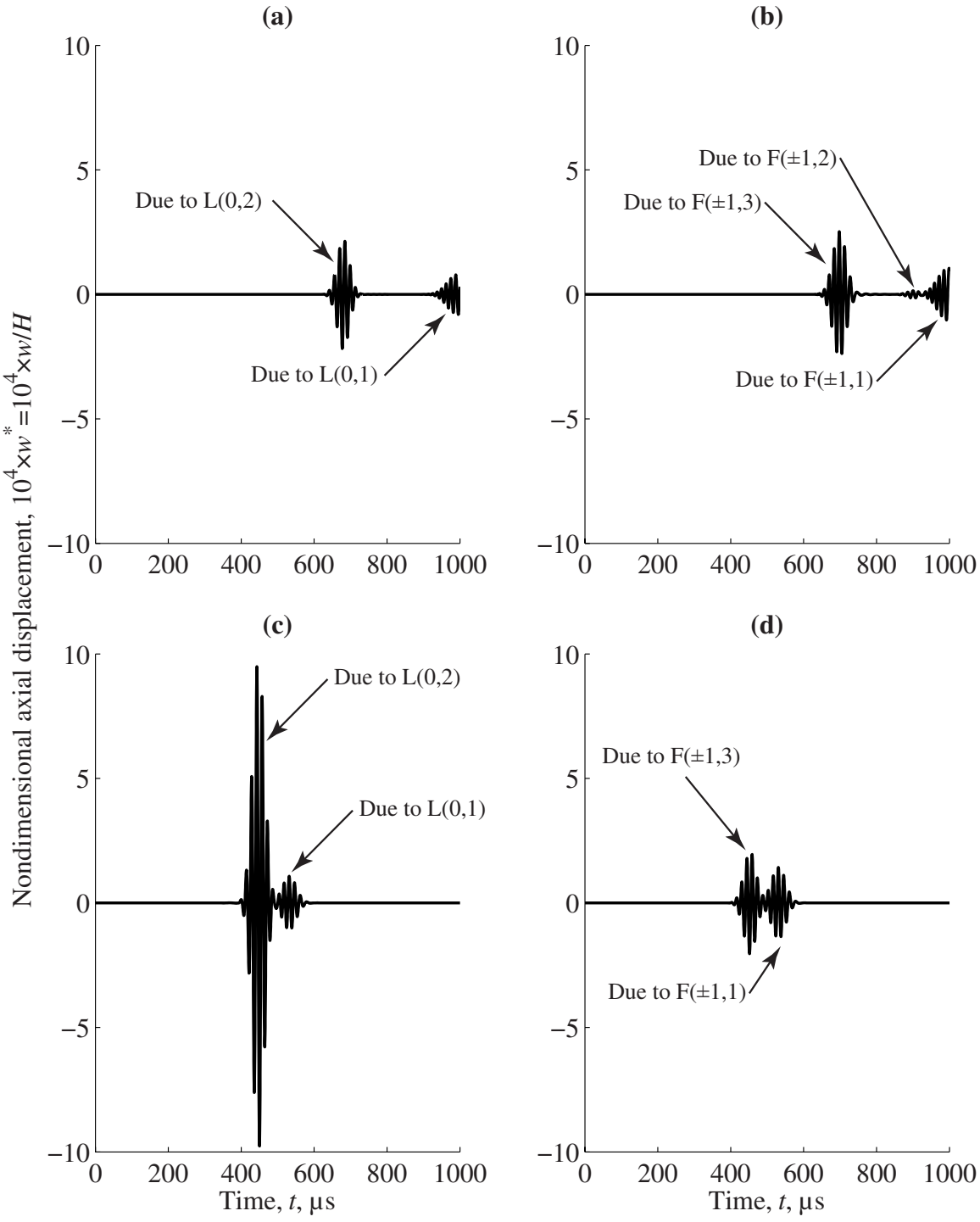

Figure 4.25. Predominant axial displacements in the (a) and (b) reflected field, and (c) and (d) transmitted field induced by the L(0,2) mode solely incident on a nonaxisymmetric notch. Subfigures (a) and (c) give the axisymmetric contributions; subfigures (b) and (d) show the contributions of the F(1,*m*) modes.

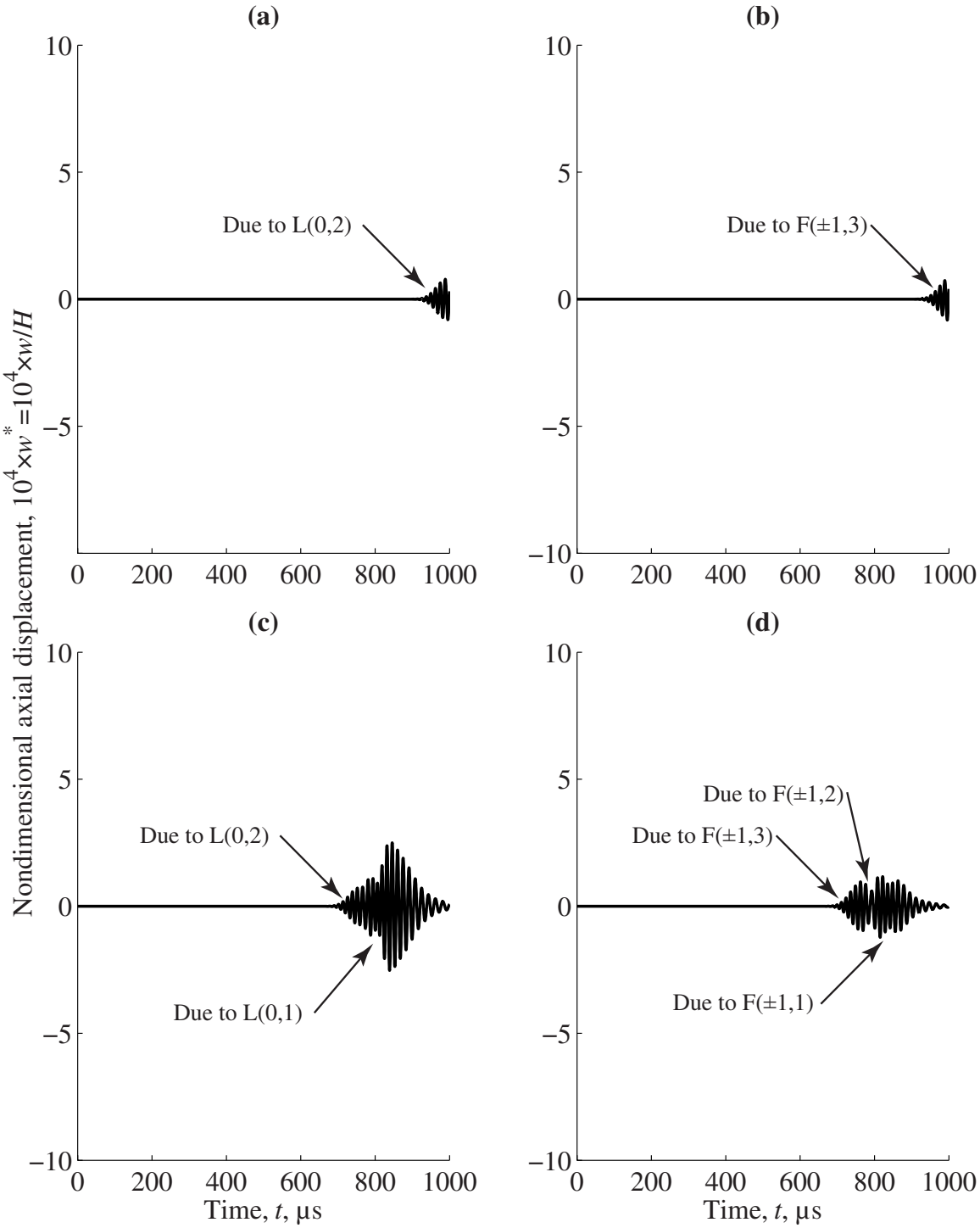

Figure 4.26. Predominant axial displacements in the (a) and (b) reflected field, and (c) and (d) transmitted field induced by the L(0,1) mode solely incident on a nonaxisymmetric notch. Subfigures (a) and (c) give the axisymmetric contributions; subfigures (b) and (d) show the contributions of the F(1,*m*) modes.

lar notch. Nevertheless, a rich pallet of modes is produced by each single incident mode. Of particular interest here is that the contributions of the L(0,2) and F(±1,3) reflections cannot be separated in time when the L(0,2) mode is incident on the notch. Therefore the measurements made in [70] *may* underestimate the reflection coefficient $|R_{\mathrm{L}(0,2),\mathrm{L}(0,2)}|$ because of the difficulty in separating these two modal contributions. *If* the separation of the F(±1,*m*) modes by the transducer used in [70] is slightly imperfect, the F(±1,3) mode will be generated and reflected from the free end of the pipe. However, the contributions of the L(0,2) and F(±1,3) modes have been seen to be virtually indistinguishable and the latter may artificially increase the amplitude of the end reflection. On the other hand, as the reflection coefficients given in Appendix I show, the F(±1,3) mode is reflected less strongly than the L(0,2) mode from the notches simulated here. These observations lead to the suspicion that the measurements made in [70] *may* underestimate $|R_{\mathrm{L}(0,2),\mathrm{L}(0,2)}|$. On the other hand, the measurement of a reflection coefficient for merely a single mode appears to be difficult, even when extraordinary care is taken.

The simulated time histories shown so far have represented displacements at a point. The transducer used in [70] is designed, however, to suppress all but the axisymmetric displacement components in either the axial or circumferential direction. Therefore all but the axisymmetric displacement components could be suppressed in Figure 4.27 (b) which reproduces the measured time history presented in [70]. On the other hand, Figure 4.27 (a) gives the *simulated* axial displacement for *solely* the reflection from the notch when all but the axisymmetric displacement components are eliminated completely. (The annotations employed in Figure 4.27 (b) are identical to those used in [70].) The two time histories are seen to be similar overall. For example, the initial arrival times of the reflections agree closely. Furthermore, the shorter excitation duration for the simulation is clearly apparent at the end of the first wave packet. Discrepancies between the relative maximum amplitudes of the first and second wave packets are, not surprisingly, evident because reflections from the free end are not simulated. Moreover, a finer comparison of the last two wave pack-

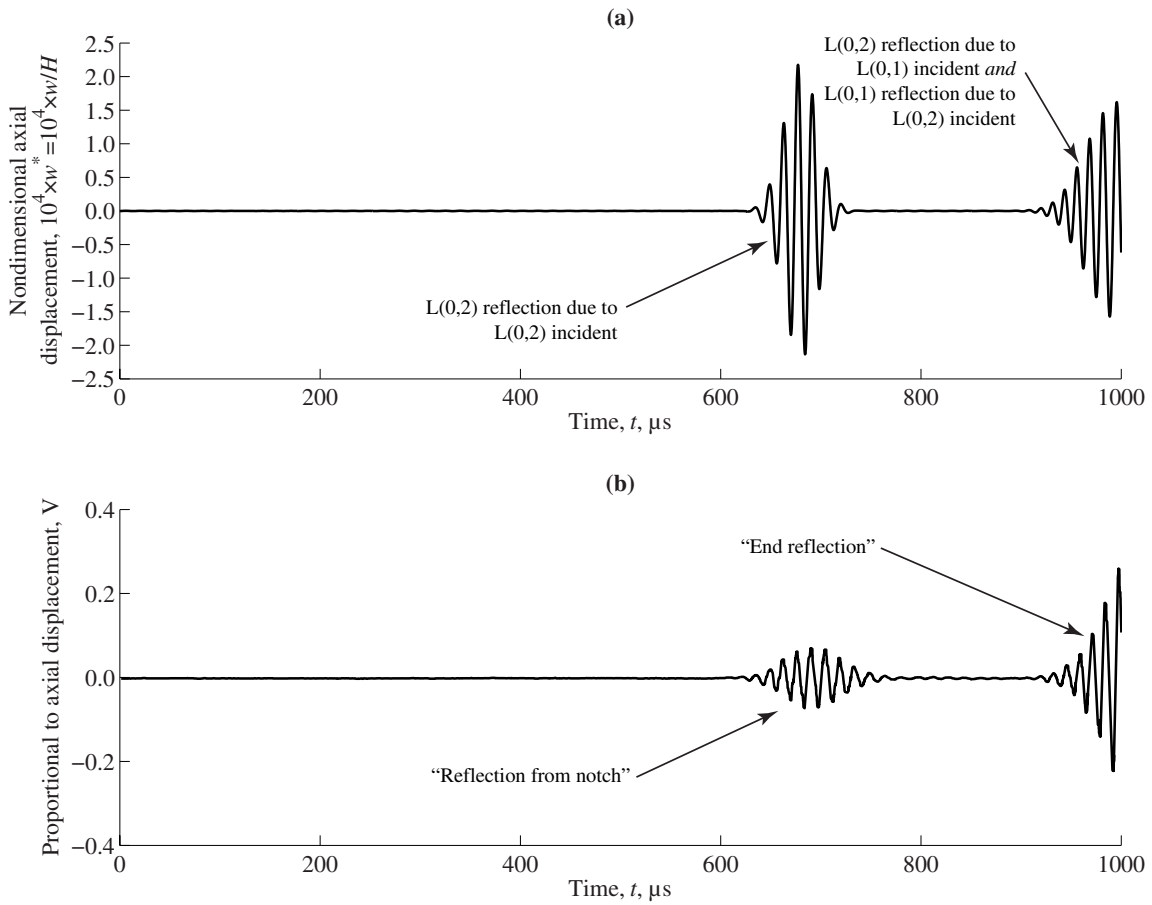

Figure 4.27. Comparing (a) the simulated axial displacement for the reflection from the nonaxisymmetric notch when all but the axisymmetric displacement components are suppressed with (b) the measured time history given in [70].

ets suggests that the measured "end reflection" labelled in Figure 4.27 (b) also contains reflected contributions from the notch. If so, the interpretations of time history is not so straightforward and the need for an alternative approach is desirable. One possibility is the procedure explored previously that is based upon global frequency differences.

Figures 4.28, 4.29, and 4.30 are analogous to Figures 4.7, 4.8, and 4.9, respectively. The excitation and monitoring locations have invariant axial coordinates but their common circumferential coordinate always coincides now with the centre of the notch. Slight differences between Figures 4.30 and 4.9 arise from a time-saving, coarser frequency step used for the former figure that limits the resolution of "spike-like" features. Nevertheless, the work done by the incident and scattered wave fields are still in good overall agreement.

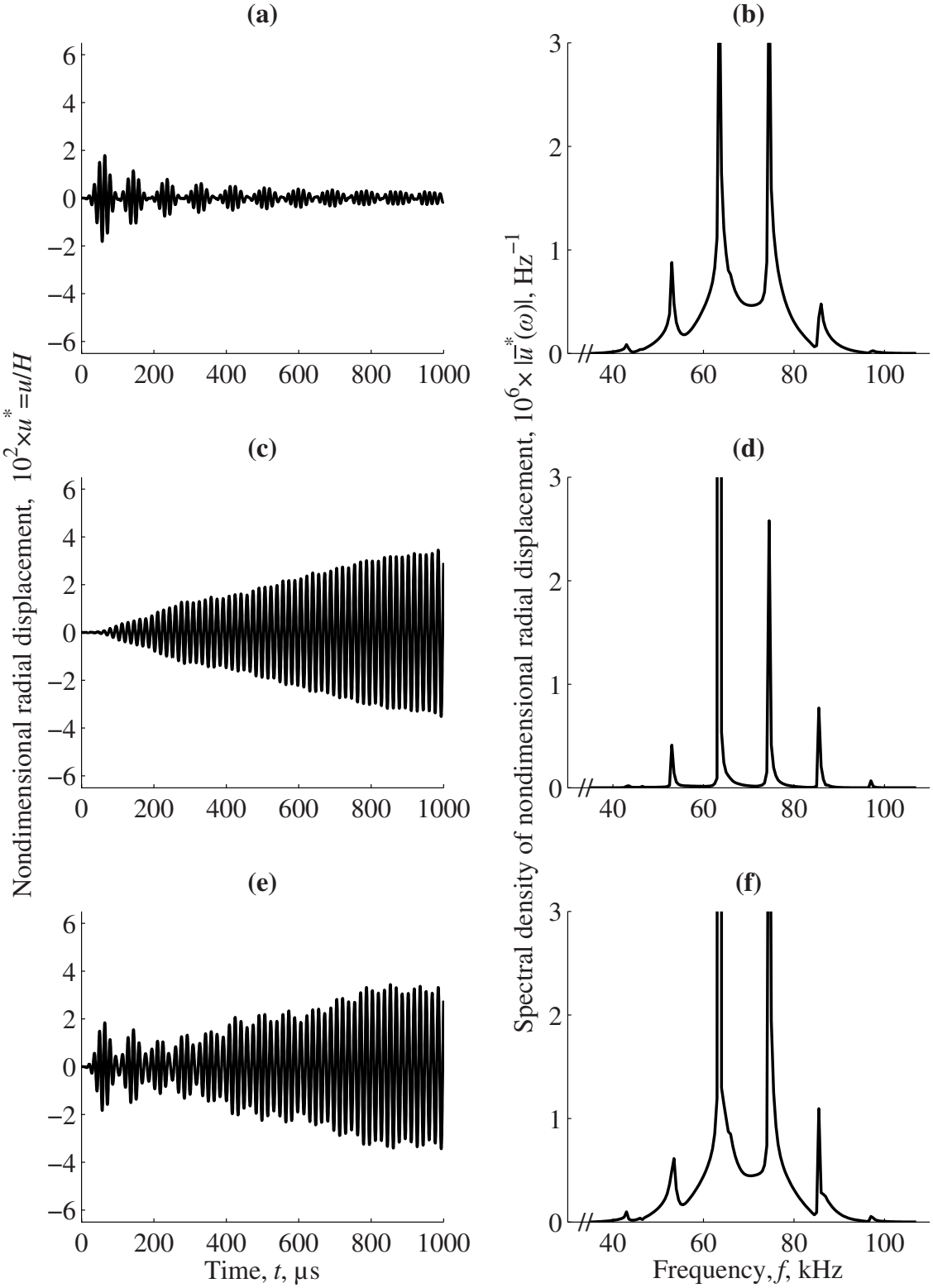

Figure 4.28. Radial displacement predicted within the reflected field when a nonaxisymmetric notch is present. Sub-figures (a) and (b) [(c) and (d)] {(e) and (f)} give the direct [reflected] {superposition of direct and reflected} waves resulting from a radial point force.

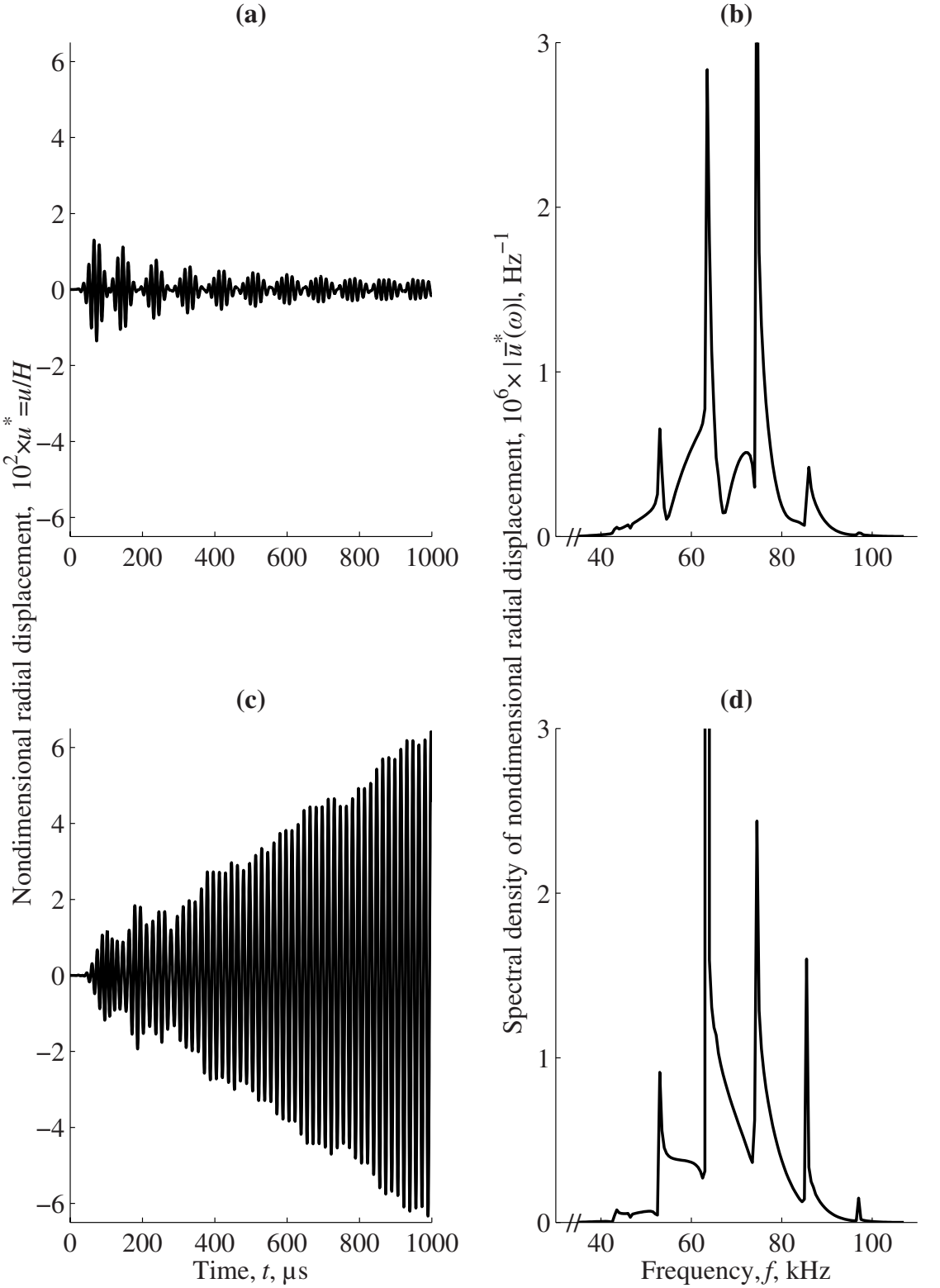

Figure 4.29. Radial displacement predicted within the transmitted field when a nonaxisymmetric notch is present. Sub-figures (a) and (b) [(c) and (d)] give the direct [transmitted] waves resulting from a radial point force.

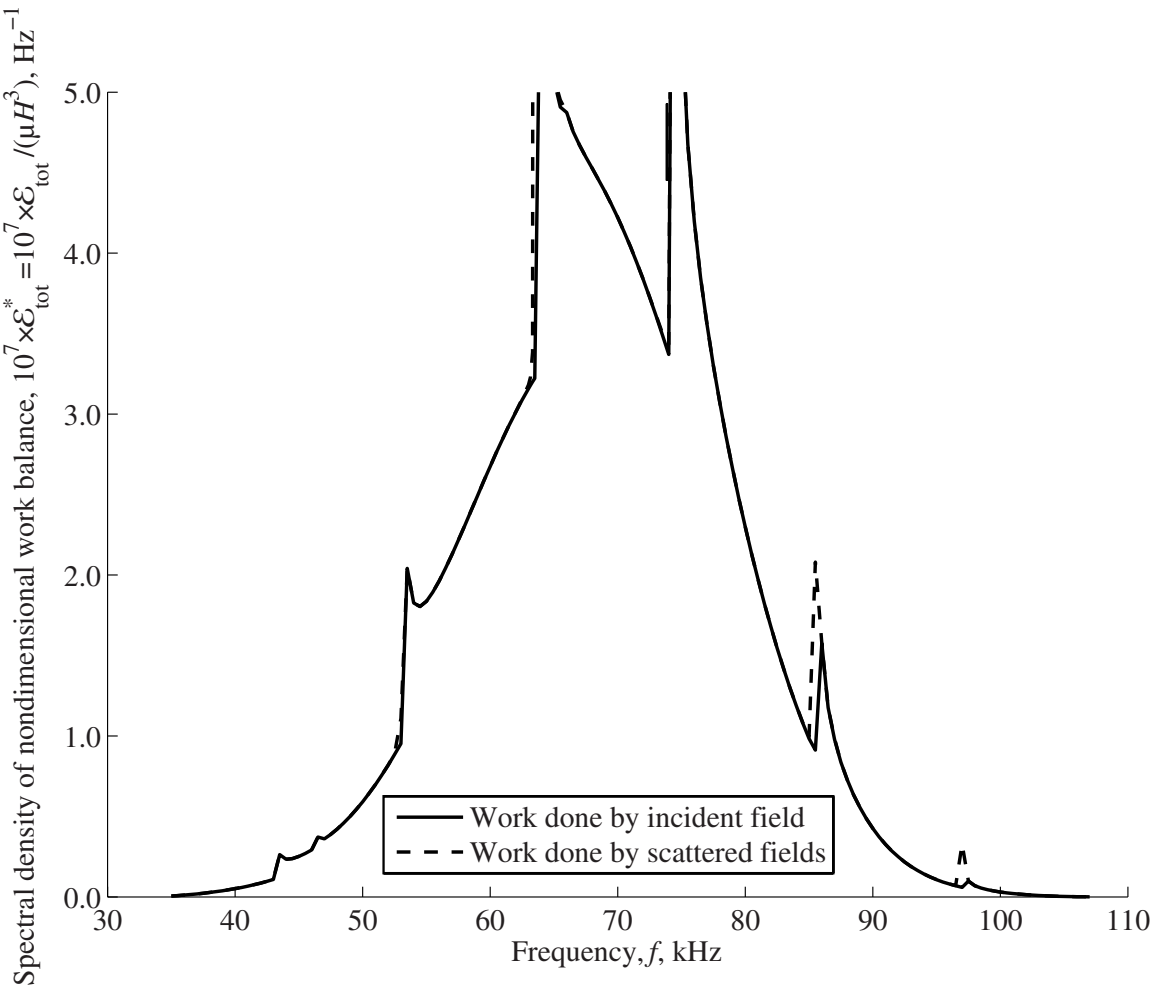

Figure 4.30. Spectral density of the work done, per period, by waves produced by a radial point force and scattered by a nonaxisymmetric notch.

Similarly the "resonant-like" behaviour seen in Figures 4.28 and 4.29 is also caused by a coarser frequency step in the computation of the corresponding spectral densities. Consequently, the energy around singularities that is introduced by the notch are narrower in frequency than around the cutoff frequencies of the unblemished pipe. As a result, the energy is overestimated which could explain the greater displacement amplitudes in Figures 4.28 and 4.29 in comparison to Figures 4.7 and 4.8. Regardless, the frequencies of the scattered waves' singularities caused by the nonaxisymmetric notch's introduction do not coincide with the unblemished pipe's cutoff frequencies. This last statement is confirmed most easily by examining Figure 4.31, where a frequency step of 50 Hz has been used in the neighbourhood of the F(13,1) mode's cutoff frequency, rather than the 500 Hz step used

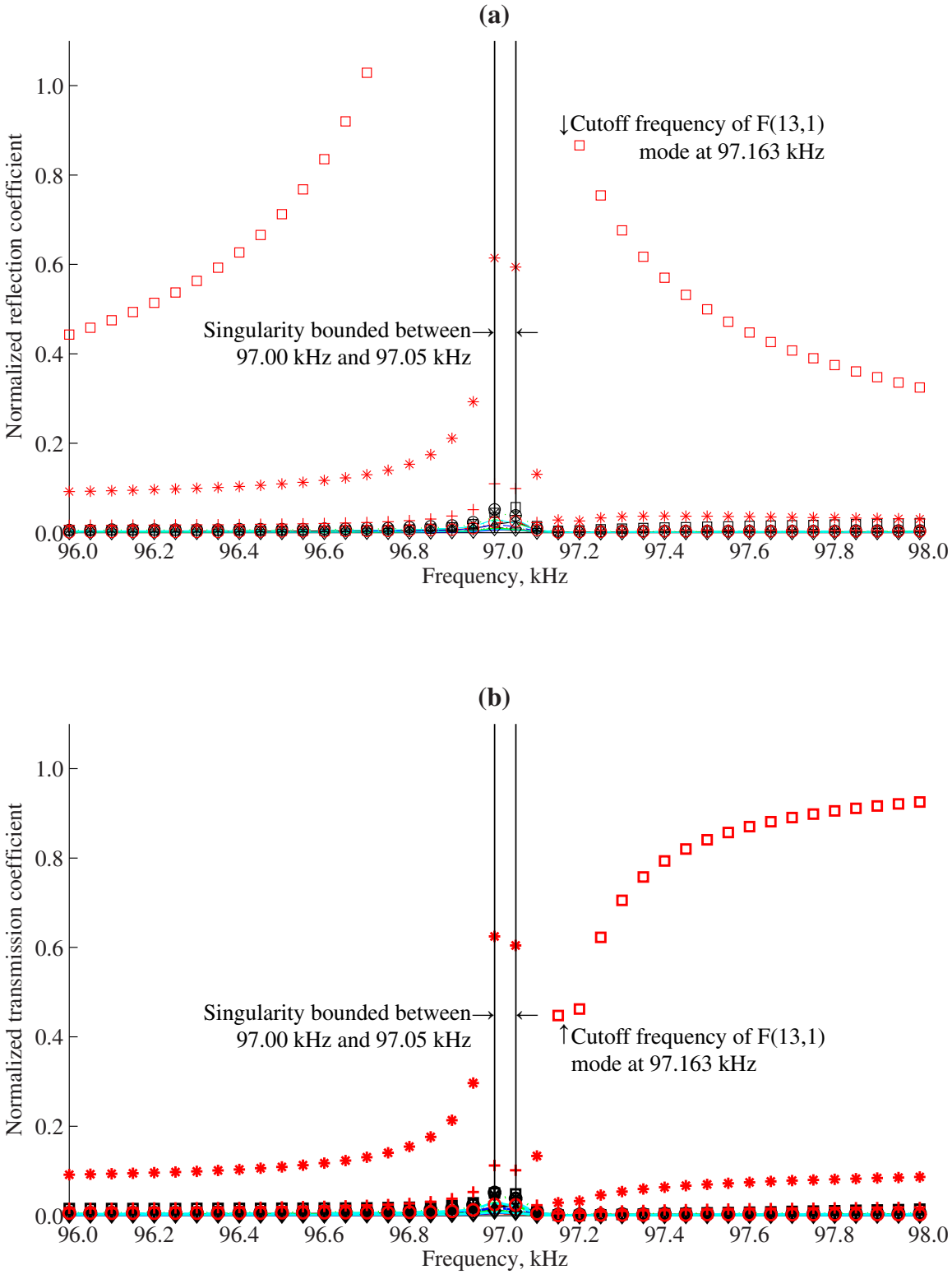

Figure 4.31. Normalized reflection and transmission coefficients for the nonaxisymmetric notch and the incident F(13,1) mode, with the frequency scale expanded around the F(13,1) mode's cutoff frequency.

elsewhere. The line and markers used in Figure 4.31 to denote the various modal reflection and transmission coefficients are consistent with Figure H.1. The singularity in the nonaxisymmetric notched pipe corresponding to the F(13,1) mode is seen to be bounded between 97.00 kHz and 97.05 kHz in this figure. On the other hand, the cutoff frequency of the F(13,1) mode is found from Table 2.2 to be 97.164 kHz. Therefore the previous assessment of an axisymmetric notch's dimensions from such differences likely extends to nonaxisymmetric notches.

4.3.7.3 Parametric study of wave scattering by three-dimensional notches

Figure 4.32 compares present and published [70] reflection coefficients, $|R_{\mathrm{L(0,2),L(0,2)}}|$, for nonaxisymmetric notches[24]. A more complete assessment of the effect of such a notch's axial extent is provided in addition to confirming previously published results. The format and reference values employed in the development of Figure 4.13 for the axisymmetric notches are retained. However, a nonaxisymmetric notch no longer extends completely around the pipe's circumference. The half (or 50%) circumferential notch considered in Figure 4.32 (a) is reduced to 11% in Figures 4.32 (b) and (d), so that direct comparisons can be made with [70]. Previous observations based upon Figure 4.13 still apply. Figure 4.33, on the other hand, gives analogous information for the nonaxisymmetric notches considered in Figure 4.32 but for the L(0,1), T(0,1), F(3,1), and F(10,1) modes. Again, observations similar to those stemming from Figure 4.14 remain valid. One important difference between Figures 4.32 (a) and Figure 4.33 (a) is noteworthy. In the former case, singularities in a reflection coefficient could be related to a modal cutoff frequency having the *same* circumferential wavenumber. In the latter case, multiple singularities are seen in a mode's reflection coefficient, that can be related to modal cutoff frequencies having *different* circumferential wavenumbers. This is due, of course, to the cross coupling between various

[24]The finite element results in [70] are extrapolated by multiplying each result from a corresponding axisymmetric notch by the percentage ratio of the part circumferential notch length to the pipe's total circumference.

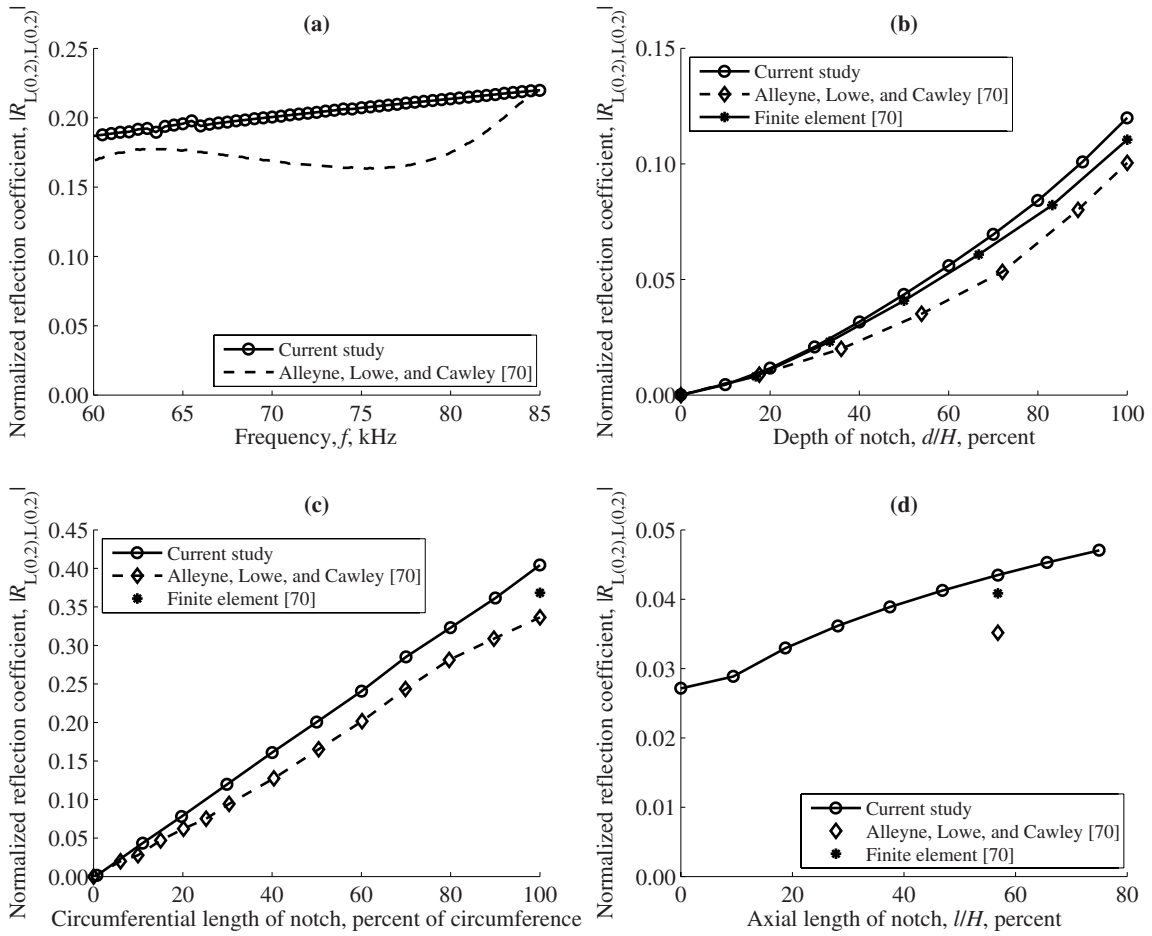

Figure 4.32. Magnitude of the normalized reflection coefficient, $|R_{L(0,2),L(0,2)}|$, for different (a) excitation frequencies, (b) depths, (c) circumferential extents, and (d) axial lengths of nonaxisymmetic notches.

circumferential wavenumbers that can occur for a nonaxisymmetric geometry. Furthermore two additional noteworthy comments can be made that arise from Figure 4.33 (c) . A linear variation of a reflection coefficient with a decreasing circumferential extent of a notch does not apply universally. This observation is substantiated by examining, for example, the curve of the F(10,1) mode given in Figure 4.33 (c). Therefore care should be taken particularly when "scaling" flexural mode data from axisymmetric notches. Moreover, no mode represented in Figure 4.33 (c) produces a particularly strong reflection at 70 kHz for (crack like) notches having a small circumferential extent. A stronger reflection may be seen, however, if the excitation is relocated to a position which is offset circumferentially from this type of defect.

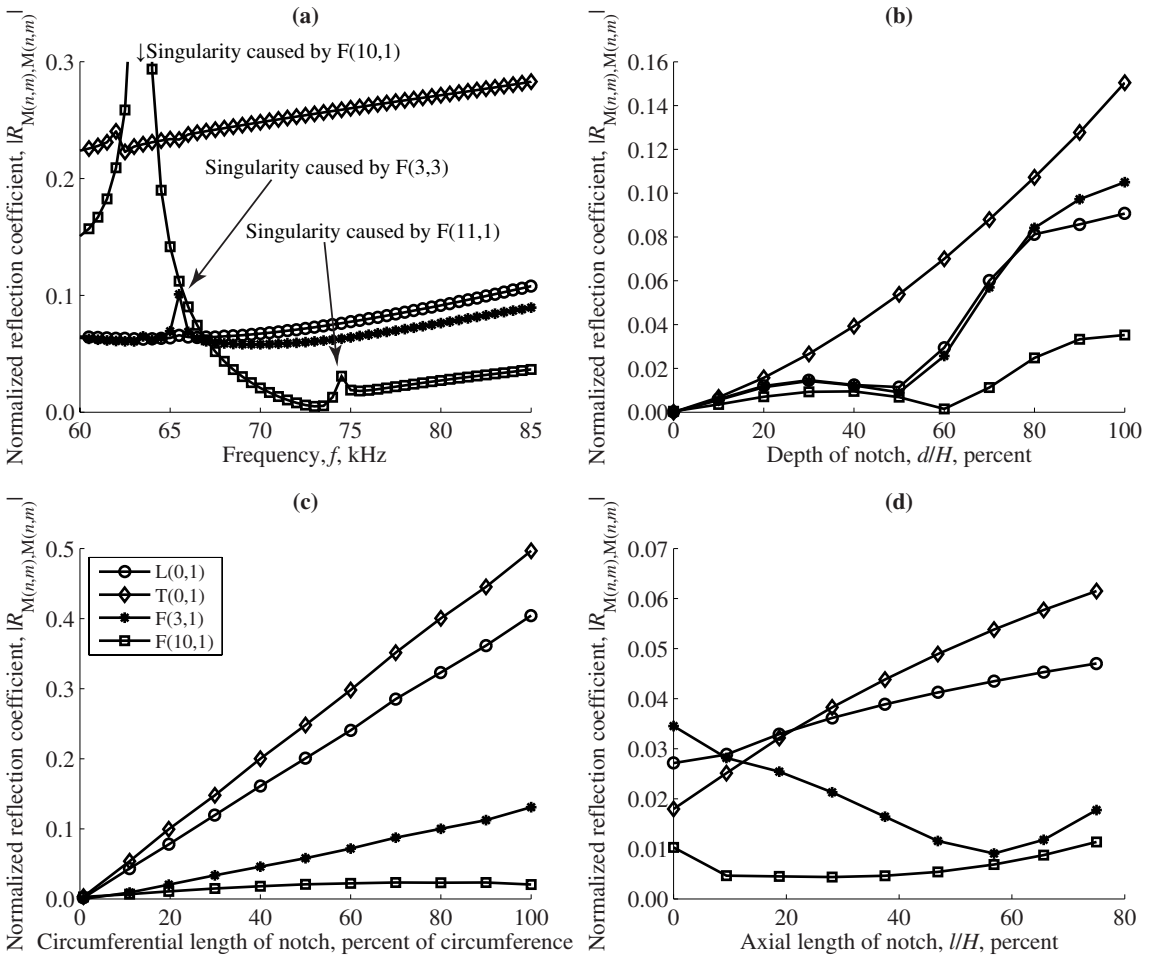

Figure 4.33. Magnitude of the normalized reflection coefficients of the L(0,1), T(0,1), F(3,1), and F(10,1) modes for different (a) excitation frequencies, (b) depths, (c) circumferential extents, and (d) axial lengths of nonaxisymmetic notches. Only $|R_{M_{in}(n_{in},m_{in}),M_{scat}(n_{scat},m_{scat})}|$, where $M_{in} = M_{scat}$, $n_{in} = n_{scat}$, and $m_{in} = m_{scat}$, is plotted for each mode.

4.3.7.4 Concluding remarks for nonaxisymmetric notches

Conclusions derived from axisymmetric notches generally extend straightforwardly to nonaxisymmetric notches. Therefore it should be possible, in principle, to use analogous frequency differences introduced by a nonaxisymmetic notch to estimate its dimensions. However, additional modes and, hence, frequency differences are most likely needed. Computational requirements could be made less onerous if advantage is taken of the need for only frequency information rather than a complete solution of the linear equations describing the wave scattering problem.

4.4 Conclusions and closing remarks

The hybrid-SAFE technique was used in this chapter to simulate wave scattering by axisymmetric and nonaxisymmetric notches. The numerical simulations showed that singularities, which are distinct from those corresponding to an unblemished pipe's cutoff frequencies, noticeably affected a notched pipe's displacement FRF. The simulations also indicated that the newly observed singularities depend on the properties of the parent pipe *and* the finite element region and could be used, therefore, to determine a notch's dimensions. However, their effects are local to a notch. Consequently, although the new singularities may provide a convenient means of estimating a notch's dimensions, they do not offer a good alternative for the "long range" detection of notch-like defects in pipelines. For short range detection of notch-like defects, on the other hand, the use of these singularities should provide generally better sensitivity than that from a single, non-dispersive mode. None of the modes surveyed produced a strong reflection at 70 kHz for crack-like notches having a small circumferential extent. An assessment of such types of defects likely requires different locations from those employed here.

Chapter 5

Conclusions and Recommendations

5.1 Conclusions

After surveying relevant literature on wave propagation and scattering in pipes in Chapter 1, theoretical frameworks pertinent to the study of wave propagation in homogeneous, isotropic pipes were reviewed in Chapter 2. Approximate, computer based solutions were based upon the Semi-Analytical Finite Element (SAFE) formulation which was shown to provide a convenient tool for studying the dynamic response of these pipes to transient, ultrasonic excitations. The principal advantage of the approach was that modal information was provided inherently and efficiently. Such information demonstrated that the dominant, easily noticed singularities in an unblemished pipe's displacement Frequency Response Function (FRF) coincided with its cutoff frequencies. This coincidence was confirmed experimentally. Practical use was made indirectly in Chapter 3 of three singularities to obtain an unblemished pipe's wall thickness and elastic properties from the corresponding cutoff frequencies. The procedure was first simulated numerically and then implemented for two physical pipe specimens. The newly developed ultrasonic procedure and more traditional destructive tests agreed within experimental uncertainty. Extensive numerical simulations suggested that, in the absence of noise, the solutions recovered by the procedure were unique. A mathematical proof was beyond the present scope.

Wave scattering by axisymmetric notches was simulated in Chapter 4. A hybrid-SAFE technique was used. This technique combined a finite element model, which enclosed a single notch whose geometry can be changed straightforwardly, with a wavefunction expansion in the remainder of the pipe. Simulations showed, for the first time, that singularities which are distinct from the unblemished pipe's cutoff frequencies were incorporated into a displacement FRF when an axisymmetric notch was introduced. The frequencies of the

new singularities depended on the properties of *both* the parent pipe and the finite element region. However, measurable effects were assessed to be local to the notch. Furthermore, it was demonstrated that the difference in frequency at which a new singularity appeared and the nearest cutoff frequency of the originally unblemished pipe depended upon an axisymmetric notch's dimensions. By plotting contours of constant frequency differences it was illustrated that it is *usually* possible to uniquely characterize an axisymmetric notch's dimensions by using such differences from two modes. However, the frequency difference of a third mode was required when the contours of two modes intersected more than once. The uniqueness was suggested only by example and not proven rigorously. If sufficient accuracy (±25 Hz) in measured singularity frequencies is accomplished, such a notch's depth and axial extent may be determined to around 5% and 10%, respectively. The more general situation of nonaxisymmetric notches was considered afterwards and it appears to be a straightforward but computationally expensive extension of the axisymmetric case. In summary, therefore, the newly discovered singularity frequencies introduced by a notch, if corroborated by further extensive laboratory and field work, could be applied in the following ways.

1. To confirm a defect's location found more remotely by using a nondispersive guided wave, and

2. locally characterise the defect's dimensions.

5.2 Recommendations

The following recommendations are made.

1. The technique developed in Chapter 3 should be extended to multilayer pipes and anisotropic materials in order to measure a coating's (e.g., chromium over a high strength low alloy steel) thickness or material properties, say.

2. The SAFE technique should be applied to elliptical cross sections to assess the effect of a pipe's out-of-roundness. As noted in Section 3.4, out-of-roundness or a wall thickness variations in a cross section may be handled straightforwardly by using a two-dimensional finite element model of the cross section rather than the one-dimensional model and Fourier series expansion used presently.

3. The frequency dependent behaviour of the present instrumentation should be measured to find its absolute sensitivity. A laser vibrometer could provide the required information.

4. Experiments should be conducted to confirm that singularities are truly introduced by a notch. Preliminary experiments, which conveniently used reflections from a pipe's free end, confirmed that the anticipated frequency shifts are observable and measurable in this case.

5. A computational technique should be developed to calculate the frequencies of the singularities introduced by notches *without* the need to find scattered wave amplitudes.

6. The minimization technique used in Chapter 3 should be automated and extended to the characterization of a notch's dimensions by using the method demonstrated in Chapter 4.

7. A plot similar to Figure 4.33 (a), but for a notch having a small circumferential extent, should be created to determine whether or not the use of the singularities provides a practical means of screening this type of defect.

8. Geometries should be investigated that are more general than straight sided notches [73]. As noted in Chapter 4, the hybrid-SAFE can be applied straightforwardly to *any* arbitrary geometry, provided that a finite element mesh suitably represents the geometry. The wave scattering caused by notches having, say, "V" or elliptical shaped

boundaries can be studied straightforwardly using hybrid-SAFE by simply replacing the existing finite element idealization with a more suitable one. Then the procedures illustrated in Chapter 4 can be applied with little or no modification. Based upon the results presented in Chapter 4, it is conjectured that notches with "V" or elliptical shaped boundaries will introduce singularities that are distinct from an unblemished pipe's cutoff frequencies. Moreover, it is speculated that the singularities introduced by such notches will occur at frequencies somewhat different from those observed here. Furthermore it is postulated that at least one frequency difference may be required per dimensional degree of freedom in an idealized notch's description in order to characterize it uniquely.

Additional recommendations to improve the computing cluster are made in Appendix L.

REFERENCES

[1] Alberta Energy and Utilities Board, "Pipeline performance in Alberta, 1990–2005," Alberta Energy and Utilities Board, Calgary, Alberta, Canada, Tech. Rep. 2007-A, Apr. 2007. [Online]. Available: http://www.ercb.ca/docs/Documents/reports/r2007-A.pdf

[2] Alberta Energy and Utilities Board, "Pipeline performance in Alberta 1980–1997," Alberta Energy and Utilities Board, Calgary, Alberta, Canada, Tech. Rep. 98-G, Dec. 1998. [Online]. Available: http://ncsp.tamu.edu/reports/AEUB/r98g.pdf

[3] T. Andersen and A. Misund, "Pipeline reliability: An investigation of pipeline failure characteristics and analysis of pipeline failure rates for submarine and cross-country pipelines," *Journal of Petroleum Technology*, vol. 35, no. 4, pp. 709–717, 1983.

[4] E. P. DeGarmo, J. T. Black, and R. A. Kohser, *Materials and Processes in Manufacturing*, 7th ed. Upper Saddle River, New Jersey, United States of America: Prentice-Hall, 1988.

[5] K. F. Graff, *Wave motion in elastic solids*. London, England: Oxford University Press, 1975.

[6] J. Krautkrämer and H. Krautkrämer, *Ultrasonic testing of materials*, 2nd ed. Berlin, Germany: Springer-Verlag, 1977.

[7] N. Rattanawangcharoen, "Propagation and scattering of elastic waves in laminated circular cylinders," Ph.D. dissertation, University of Manitoba, Winnipeg, Manitoba, Canada, 1993.

[8] J. L. Rose and M. Quarry, "Feasibility of ultrasonic guided waves for non-destructive evaluation of gas pipelines," Gas Research Institute, Chicago, Illinois, United States of America, Tech. Rep. GRI-99/0076, Apr. 1999.

[9] D. N. Alleyne and P. Cawley, "Excitation of Lamb waves in pipes using dry-coupled piezoelectric transducers," *Journal of Nondestructive Evaluation*, vol. 15, pp. 11–20, 1996.

[10] S. K. Datta and A. H. Shah, *Elastic Waves in Composite Media and Structures: With Applications to Ultrasonic Nondestructive Evaluation*. Baco Raton, Florida, United States of America: CRC Press, 2009.

[11] J. L. Rose, *Ultrasonic Waves in Solid Media*. Cambridge, United Kingdom: Cambridge University Press, 1999.

[12] L. Pochhammer, "Über die fortplanzungsgeschwindigkeiten schwingungen in einem unbegrentzten isotropen kreiscylinder," *Journal für die reine angewandte Mathematik*, vol. 81, pp. 324–336, 1876.

[13] C. Chree, "The equations of an isotropic solid in polar and cylindrical coordinates, their solutions and applications," *Transactions of the Cambridge Philosophical Society, Mathematical and Physical Sciences*, vol. 14, pp. 250–369, 1889.

[14] L. Rayleigh, "On the free vibrations of an infinite plate of homogeneous isotropic elastic matter," *Proceedings of the London Mathematical Society*, vol. 20, no. 357, pp. 225–234, Apr. 1889.

[15] H. Lamb, "On the flexure of an elastic plate," *Proceedings of the London Mathematical Society*, vol. 21, no. 375, pp. 70–90, Dec. 1889.

[16] R. M. Davies, "A critical study of the Hopkinson pressure bar," *Philosophical Transactions of the Royal Society of London. Series A (Mathematical and Physical Sciences)*, vol. 240, no. A821, pp. 375–457, Jan. 1948.

[17] M. Onoe, H. D. McNiven, and R. D. Mindlin, "Dispersion of axially symmetric waves in elastic rods," *Journal of Applied Mechanics*, vol. 29, no. 4, pp. 729–734, 1962.

[18] W. A. Green, "Dispersion relations for elastic waves in bars," in *Progress in solid mechanics*, I. Sneddon and R. Hill, Eds. Amsterdam, North Holland, Netherlands: North-Holland Publishing Company, 1960, vol. 1, ch. 5.

[19] R. Mindlin and G. Herrmann, "A one-dimensional theory of compressional waves in an elastic rod," in *Proceedings of the first U.S. National Congress of Applied Mechanics: held at Illinois Institute of Technology*, E. Sternberg, Ed. Chicago, Illinois, United States of America: American Society of Mechanical Engineers, Jun. 11–16, 1951, pp. 187–191.

[20] R. D. Mindlin and H. D. McNiven, "Axially symmetric waves in elastic rods," *Journal of Applied Mechanics*, vol. 27, no. 1, pp. 145–151, 1960.

[21] D. C. Gazis, "Three-dimensional investigation of propagation of waves in hollow circular cylinders. I. Analytical foundation," *Journal of the Acoustical Society of America*, vol. 31, no. 5, pp. 568–578, May 1959.

[22] T. R. Meeker and A. H. Meitzler, "Guided wave propagation in elongated cylinders and plates," in *Physical acoustics: principles and methods*, W. P. Mason, Ed. New York, New York, United States of America: Academic Press, 1964, vol. 1, no. A, ch. 2.

[23] D. C. Gazis, "Three-dimensional investigation of the propagation of waves in hollow circular cylinders. II. Numerical results," *Journal of the Acoustical Society of America*, vol. 31, no. 5, pp. 573–578, May 1959.

[24] I. Mirsky, "Axisymmetric vibrations of orthotropic cylinders," *Journal of the Acoustical Society of America*, vol. 36, no. 11, pp. 2106–2112, Nov. 1964.

[25] I. Mirsky, "Three-dimensional and shell-theory analysis for axisymmetric vibrations of orthotropic shells," *Journal of Acoustical Society of America*, vol. 39, no. 3, pp. 549–555, 1966.

[26] J. L. Nowinski, "Propagation of longitudinal waves in circular cylindrically orthotropic bars," *Transactions of the ASME. Series B, Journal of Engineering for Industry*, vol. 89, no. 3, pp. 408–412, Aug. 1967.

[27] F.-H. Chou and J. D. Achenbach, "Three-dimensional vibrations of orthotropic cylinders," *Journal of Engineering Mechanics*, vol. 98, pp. 813–822, 1972.

[28] A. E. Armenàkas and E. S. Reitz, "Propagation of harmonic waves in orthotropic circular cylindrical shells," *Transactions of the ASME. Series E, Journal of Applied Mechanics*, vol. 40, no. 1, pp. 168–174, Mar. 1973.

[29] S. Markus and D. J. Mead, "Axisymmetric and asymmetric wave motion in orthotropic cylinders," *Journal of Sound and Vibration*, vol. 181, no. 1, pp. 127–147, Mar. 1995.

[30] H. D. McNiven, J. L. Sackman, and A. H. Shah, "Dispersion of axially symmetric waves in composite, elastic rods," *Journal of the Acoustical Society of America*, vol. 35, no. 10, pp. 1602–1609, Oct. 1963.

[31] A. E. Armenàkas, "Torsional waves in composite rods," *Journal of the Acoustical Society of America*, vol. 38, no. 3, pp. 439–446, Sep. 1965.

[32] A. E. Armenàkas, "Propagation of harmonic waves in composite circular cylindrical shells I: Theoretical investigation," *American Institute of Aeronautics and Astronautics Journal*, vol. 5, no. 4, pp. 740–744, 1967.

[33] R. C. Reuter, Jr., "Dispersion of flexural waves in circular bimaterial cylinders—theoretical treatment," *Journal of the Acoustical Society of America*, vol. 46, no. 3, pp. 643–648, Sep. 1969.

[34] A. E. Armenàkas and H. E. Keck, "Harmonic nonaxisymmetric waves with short wavelengths propagating in composite rods," *The Journal of the Acoustical Society of America*, vol. 48, no. 5B, pp. 1160–1169, 1970.

[35] H. E. Keck and A. E. Armenàkas, "Wave propagation in transversely isotropic layered cylinders," *Journal of Engineering Mechanics*, vol. 97, pp. 541–558, 1971.

[36] H. Bai, "Elastic wave scattering in cracked cylinders," Ph.D. dissertation, University of Manitoba, Winnipeg, Manitoba, Canada, 2002.

[37] N. Rattanawangcharoen and A. H. Shah, "Guided waves in laminated isotropic circular cylinders," *Computational Mechanics*, vol. 10, no. 2, pp. 97–105, 1992.

[38] A. A. Khdeir, J. N. Reddy, and D. Frederick, "A study of bending, vibration and buckling of cross-ply circular cylindrical shells with various shell theories," *International Journal of Engineering Science*, vol. 27, no. 11, pp. 1337–1351, 1989.

[39] E. J. Barbero, J. N. Reddy, and J. L. Teply, "General two-dimensional theory of laminated cylindrical shells," *AIAA journal*, vol. 28, no. 3, pp. 544–553, 1990.

[40] R. B. Nelson, S. B. Dong, and R. D. Kalra, "Vibrations and waves in laminated orthotropic circular cylinders," *Journal of Sound and Vibration*, vol. 18, no. 3, pp. 429–444, Oct. 1971.

[41] K. H. Huang and S. B. Dong, "Propagating waves and edge vibrations in anisotropic composite cylinders," *Journal of Sound and Vibration*, vol. 96, no. 3, pp. 363–379, Oct. 1984.

[42] N. Rattanawangcharoen, A. H. Shah, and S. K. Datta, "Wave propagation in laminated composite circular cylinders," *International Journal of Solids and Structures*, vol. 29, no. 6, pp. 767–781, 1992.

[43] W. Zhuang, A. H. Shah, and S. B. Dong, "Elastodynamic Green's function for laminated anisotropic circular cylinders," *Journal of Applied Mechanics*, vol. 66, pp. 665–674, 1999.

[44] C. H. Huang and S. B. Dong, "Analysis of laminated circular cylinders of materials with the most general form of cylindrical anisotropy I. Axially symmetric deformations," *International Journal of Solids and Structures*, vol. 38, no. 34–35, pp. 6163–6182, 2001.

[45] C. H. Huang and S. B. Dong, "Analysis of laminated circular cylinders of materials with the most general form of cylindrical anisotropy. II. Flexural deformations," *International Journal of Solids and Structures*, vol. 38, no. 34–35, pp. 6183–6205, 2001.

[46] H. Bai, E. Taciroglu, S. B. Dong, and A. H. Shah, "Elastodynamic Green's functions for a laminated piezoelectric cylinder," *International Journal of Solids and Structures*, vol. 41, no. 22–23, pp. 6335–6350, 2004.

[47] A. Marzani, "Time-transient response for ultrasonic guided waves propagating in damped cylinders," *International Journal of Solids and Structures*, vol. 45, no. 25–26, pp. 6347–6368, Dec. 2008.

[48] H. Bai, R. Chitikireddy, A. H. Shah, and S. K. Datta, "Generalized thermoelastic waves in cylinders due to localized heating," *Journal of Mechanics of Materials and Structures*, vol. 6, no. 1–4, pp. 31–50, 2011.

[49] R. Chitikireddy, S. K. Datta, A. H. Shah, and H. Bai, "Transient thermoelastic waves in an anisotropic hollow cylinder due to localized heating," *International Journal of Solids and Structures*, vol. 48, no. 21, pp. 3063–3074, 2011.

[50] R. Skalak, "Longitudinal impact of semi-infinite circular elastic bar," *Journal of Applied Mechanics*, vol. 24, no. 1, pp. 59–64, 1957.

[51] R. Folk, G. Fox, C. A. Shook, and C. W. Curtis, "Elastic strain produced by sudden application of pressure to one end of a cylindrical bar I. theory," *Journal of the Acoustical Society of America*, vol. 30, no. 6, pp. 552–558, Jun. 1958.

[52] O. E. Jones and F. R. Norwood, "Axially symmetric cross-sectional strain and stress distributions in suddenly loaded cylindrical elastic bars," *Transactions of the ASME. Series E, Journal of Applied Mechanics*, vol. 34, no. 3, pp. 718–724, Sep. 1967.

[53] J. Miklowitz, "Travelling compressional waves in an elastic rod according to the more exact one-dimensional theory," in *Proceedings of the second U.S. National Congress of Applied Mechanics: held at University of Michigan*, P. M. Naghdi, Ed. Ann Arbor, Michigan, United States of America: American Society of Mechanical Engineers, Jun. 4–18, 1955, pp. 179–186.

[54] J. Miklowitz, "Propagation of compressional waves in dispersive elastic rod," *Journal of Applied Mechanics*, vol. 24, no. 2, pp. 231–244, 1957.

[55] J. Miklowitz, "On the use of approximate theories of an elastic rod in problems of longitudinal impact," in *Proceedings of the third U.S. National Congress of Applied Mechanics: held at Brown University*, R. M. Haythornthwaite, Ed. Providence, Rhode Island, United States of America: American Society of Mechanical Engineers, Jun. 11–14, 1958, pp. 231–239.

[56] D. K. Stoyko, "Interpreting wave propagation in a homogeneous, isotropic, steel cylinder," Master's thesis, University of Manitoba, Winnipeg, Manitoba, Canada, 2005. [Online]. Available: http://hdl.handle.net/1993/97

[57] D. K. Stoyko, N. Popplewell, and A. H. Shah, "Modal analysis of transient ultrasonic guided waves in a cylinder," in *Computational mechanics; proceedings of the international symposium on computational mechanics in Beijing*, Z. Yao and M. Yuan, Eds. Berlin, Heidelberg: Springer, 2007, p. 411, abstract p. 411, full manuscript (p. 1215–1225) on accompanying CD-ROM, 211_FP-136-PopplewellN.pdf.

[58] H. D. McNiven, "Extensional waves in a semi-infinite elastic rod," *Journal of the Acoustical Society of America*, vol. 33, no. 1, pp. 23–27, Jan. 1961.

[59] H. D. McNiven and A. H. Shah, "The influence of the end mode on the resonant frequencies of finite, hollow, elastic rods," *Journal of Sound and Vibration*, vol. 6, no. 1, pp. 8–19, Jul. 1967.

[60] J. Zemanek, Jr., "An experimental and theoretical investigation of elastic wave propagation in a cylinder," *Journal of the Acoustical Society of America*, vol. 51, no. 1, pp. 265–283, Jan. 1972.

[61] R. D. Gregory and I. Gladwell, "Axisymmetric waves in a semi-infinite elastic rod," *Quarterly Journal of Mechanics and Applied Mathematics*, vol. 42, pp. 327–337, May 1989.

[62] T. Kohl, S. K. Datta, and A. H. Shah, "Axially symmetric pulse propagation in semi-infinite hollow cylinders," *AIAA journal*, vol. 30, no. 6, pp. 1617–1624, 1992.

[63] N. Rattanawangcharoen, A. H. Shah, and S. K. Datta, "Reflection of waves at the free edge of a laminated circular cylinder," *Journal of Applied Mechanics, Transactions ASME*, vol. 61, no. 2, pp. 323–329, 1994.

[64] N. Rattanawangcharoen, W. Zhuang, A. H. Shah, and S. K. Datta, "Axisymmetric guided waves in jointed laminated cylinders," *Journal of Engineering Mechanics*, vol. 123, no. 10, pp. 1020–1026, 1997.

[65] W. Zhuang, A. H. Shah, and S. K. Datta, "Axisymmetric guided wave scattering by cracks in welded steel pipes," *Journal of Pressure Vessel Technology*, vol. 119, no. 4, pp. 401–406, 1997.

[66] A. Mahmoud, "Hybrid formulation of wave scattering in a cracked circular cylinder," Master's thesis, University of Manitoba, Winnipeg, Manitoba, Canada, 2002.

[67] A. Mahmoud, A. H. Shah, and N. Popplewell, "Parallel hybrid algorithm for three-dimensional elastic wave scattering in steel pipes," *Journal of Pressure Vessel Technology, Transactions of the ASME*, vol. 126, no. 4, pp. 510–517, 2004.

[68] F. Benmeddour, F. Treyssède, and L. Laguerre, "Numerical modeling of guided wave interaction with non-axisymmetric cracks in elastic cylinders," *International Journal of Solids and Structures*, vol. 48, no. 5, pp. 764–774, 2011.

[69] H. Bai, A. H. Shah, N. Popplewell, and S. K. Datta, "Scattering of guided waves by circumferential cracks in steel pipes," *Journal of Applied Mechanics*, vol. 68, no. 4, pp. 619–631, 2001.

[70] D. N. Alleyne, M. J. S. Lowe, and P. Cawley, "Reflection of guided waves from circumferential notches in pipes," *Journal of Applied Mechanics*, vol. 65, no. 3, pp. 635–641, 1998.

[71] M. J. S. Lowe, D. N. Alleyne, and P. Cawley, "Mode conversion of a guided wave by a part-circumferential notch in a pipe," *Journal of Applied Mechanics*, vol. 65, no. 3, pp. 649–656, 1998.

[72] P. Cawley, M. J. S. Lowe, F. Simonetti, C. Chevalier, and A. Roosenbrand, "The variation of the reflection coefficient of extensional guided waves in pipes from defects as a function of defect depth, axial extent, circumferential extent and frequency," *Proceedings of the Institution of Mechanical Engineers, Part C: Journal of Mechanical Engineering Science*, vol. 216, no. 11, pp. 1131–1144, 2002.

[73] W. Zhu, "An FEM simulation for guided elastic wave generation and reflection in hollow cylinders with corrosion defects," *Journal of Pressure Vessel Technology*, vol. 124, no. 1, pp. 108–117, 2002.

[74] A. Demma, P. Cawley, M. J. S. Lowe, A. G. Roosenbrand, and B. Pavlakovic, "The reflection of guided waves from notches in pipes: A guide for interpreting corrosion measurements," *NDT and E International*, vol. 37, no. 3, pp. 167–180, 2004. [Online]. Available: http://dx.doi.org/10.1016/j.ndteint.2003.09.004

[75] W. Zhuang, "Numerical modeling for elastodynamic problems in laminated composite cylinders," Ph.D. dissertation, University of Manitoba, Winnipeg, Manitoba, Canada, 1998.

[76] H. Bai and A. H. Shah, "Application of boundary element method for 3D wave scattering in cylinders," *International Journal of Computational Methods*, vol. 8, no. 1, pp. 57–76, 2011.

[77] J. Oliver, "Elastic wave dispersion in a cylindrical rod by a wide-band short-duration pulse technique," *Journal of the Acoustical Society of America*, vol. 29, no. 2, pp. 189–195, Feb. 1957.

[78] G. Fox and C. W. Curtis, "Elastic strain produced by sudden application of pressure to one end of a cylindrical bar II. experimental observations," *Journal of the Acoustical Society of America*, vol. 30, no. 6, pp. 559–563, Jun. 1958.

[79] A. H. Fitch, "Observation of elastic-pulse propagation in axially symmetric and nonaxially symmetric longitudinal modes of hollow cylinders," *Journal of the Acoustical Society of America*, vol. 35, no. 5, pp. 706–708, May 1963.

[80] W. Mohr and P. Hoeller, "On inspection of thin-walled tubes for transverse and longitudinal flaws by guided ultrasonic waves," *IEEE Transactions on Sonics and Ultrasonics*, vol. SU-23, no. 5, pp. 369–374, 1976.

[81] M. Silk and K. Bainton, "Propagation in metal tubing of ultrasonic wave modes equivalent to Lamb waves," *Ultrasonics*, vol. 17, pp. 11–19, 1979.

[82] T. Hay and J. L. Rose, "Flexible PVDF comb transducers for excitation of axisymmetric guided waves in pipe," *Sensors and Actuators A: Physical*, vol. A100, no. 1, pp. 18–23, 2002.

[83] J. Ma, F. Simonetti, and M. J. S. Lowe, "Scattering of the fundamental torsional mode by an axisymmetric layer inside a pipe," *Journal of the Acoustical Society of America*, vol. 120, no. 4, pp. 1871–1880, Oct. 2006.

[84] D. N. Alleyne, T. Vogt, and P. Cawley, "The choice of torsional or longitudinal excitation in guided wave pipe inspection," *Insight: Non-Destructive Testing and Condition Monitoring*, vol. 51, no. 7, pp. 373–377, 2009. [Online]. Available: http://dx.doi.org/10.1784/insi.2009.51.7.373

[85] H. J. Shin and J. L. Rose, "Guided wave tuning principles for defect detection in tubing," *Journal of Nondestructive Evaluation*, vol. 17, no. 1, pp. 27–36, Mar. 1998. [Online]. Available: http://dx.doi.org/10.1023/A:1022680429232

[86] H. J. Shin and J. L. Rose, "Guided waves by axisymmetric and non-axisymmetric surface loading on hollow cylinders," *Ultrasonics*, vol. 37, no. 5, pp. 355–363, Jun. 1999.

[87] J. Li and J. L. Rose, "Excitation and propagation of non-axisymmetric guided waves in a hollow cylinder," *Journal of the Acoustical Society of America*, vol. 109, no. 2, pp. 457–464, 2001.

[88] J. L. Rose, Z. Sun, P. J. Mudge, and M. J. Avioli, "Guided wave flexural mode tuning and focusing for pipe testing," *Materials Evaluation*, vol. 61, no. 2, pp. 162–167, 2003.

[89] J. L. Rose, D. Jiao, and J. Spanner, Jr., "Ultrasonic guided wave NDE for piping," *Materials Evaluation*, vol. 54, no. 11, pp. 1310–1313, 1996.

[90] J. Mu, L. Zhang, and J. L. Rose, "Defect circumferential sizing by using long range ultrasonic guided wave focusing techniques in pipe," *Nondestructive Testing And Evaluation*, vol. 22, no. 4, pp. 239–253, 2007.

[91] J. Ditri and J. Rose, "Excitation of guided elastic wave modes in hollow cylinders by applied surface tractions," *Journal of Applied Physics*, vol. 72, no. 7, pp. 2589–2597, Oct. 1992. [Online]. Available: http://dx.doi.org/10.1063/1.351558

[92] J. J. Ditri, J. L. Rose, and A. Pilarski, "Generation of guided waves in hollow cylinders by wedge and comb type transducers," in *Review of progress in quantitative nondestructive evaluation, Volume 12A*, D. O. Thompson and D. E. Chimenti, Eds. New York, New York: Plenum Press, 1993, pp. 211–218.

[93] A. Demma, P. Cawley, M. Lowe, and A. Roosenbrand, "The reflection of the fundamental torsional mode from cracks and notches in pipes," *Journal of the Acoustical Society of America*, vol. 114, no. 2, pp. 611–625, Aug. 2003. [Online]. Available: http://dx.doi.org/10.1121/1.1582439

[94] M. Ratassepp, S. Fletcher, and M. Lowe, "Scattering of the fundamental torsional mode at an axial crack in a pipe," *Journal of the Acoustical Society of America*, vol. 127, no. 2, pp. 730–740, Feb. 2010. [Online]. Available: http://dx.doi.org/10.1121/1.3277185

[95] D. Alleyne, T. Vogt, and P. Cawley, "The choice of torsional or longitudinal excitation in guided wave pipe inspection," *Insight: Non-Destructive Testing and Condition Monitoring*, vol. 51, no. 7, pp. 373–377, 2009. [Online]. Available: http://dx.doi.org/10.1784/insi.2009.51.7.373

[96] F. Simonetti and P. Cawley, "A guided wave technique for the characterization of highly attenuative viscoelastic materials," *Journal of the Acoustical Society of America*, vol. 114, no. 1, pp. 158–165, 2003.

[97] H. Nishino, N. Chubachi, H. Cho, and M. Takemoto, "A novel method of estimating the aspect ratio of pipe wall thickness to diameter utilizing the characteristics of a hollow cylindrical guided wave," in *2004 ASME/JSME Pressure Vessels and Piping Conference*, vol. 484, San Diego, CA, United states, Jul. 5–9, 2004, pp. 1–6.

[98] J.-H. Park, J.-H. Lee, and M.-R. Lee, "Evaluation of wall-thinning in pipes using laser-generated guided waves," *Key Engineering Materials*, vol. 326–328, pp. 705–708, 2006.

[99] Y. Jiangong, "Determination of material properties of functionally graded hollow cylinders using artificial neural network," in *2009 International Conference on Measuring Technology and Mechatronics Automation, ICMTMA 2009*, vol. 3, Zhangjiajie, Hunan, China, Apr. 11–12, 2009, pp. 202–205.

[100] D. K. Stoyko, N. Popplewell, and A. H. Shah, "Finding a pipe's elastic and dimensional properties using ultrasonic guided wave cut-off frequencies," *NDT and E International*, vol. 43, no. 7, pp. 568–578, 2010. [Online]. Available: http://dx.doi.org/10.1016/j.ndteint.2010.05.013

[101] J. L. Rose and J. N. Barshinger, "Using ultrasonic guided wave mode cutoff for corrosion detection and classification," *Proceedings of the IEEE Ultrasonic Symposium*, vol. 1, pp. 851–854, 1998.

[102] W. Zhu, J. L. Rose, J. N. Barshinger, and V. Agarwala, "Ultrasonic guided wave NDT for hidden corrosion detection," *Research in Nondestructive Evaluation*, vol. 10, no. 4, pp. 205–225, 1998.

[103] M. Z. Silva, R. Gouyon, and F. Lepoutre, "Hidden corrosion detection in aircraft aluminum structures using laser ultrasonics and wavelet transform signal analysis," *Ultrasonics*, vol. 41, no. 4, pp. 301–305, 2003.

[104] D. E. Chimenti, "Guided waves in plates and their use in materials characterization," *Applied Mechanics Reviews*, vol. 50, no. 5, pp. 247–284, 1997.

[105] P. M. Morse and H. Feshbach, *Methods of theoretical physics*. New York, New York, United States of America: McGraw-Hill Book Company, Incorporated, 1953.

[106] D. V. Griffiths, "Stiffness matrix of the four-node quadrilateral element in closed form," *International Journal for Numerical Methods in Engineering*, vol. 37, no. 6, pp. 1027–1038, 1994.

[107] R. Cook, *Concepts and Applications of Finite Element Analysis*, 2nd ed. New York, New York, United States of America: John Wiley and Sons, 1981.

[108] D. K. Stoyko, A. H. Shah, and N. Popplewell, "Detection of a pipe's localized wall thinning using ultrasonic guided waves," in *Proceedings of the* 10^{th} *International Conference on Recent Advances in Structural Dynamics (RASD 2010)*, M. Brennan, Ed. Southampton: Institute Sound and Vibration Research, 2010, accepted for inclusion.

[109] J. Wilkinson, *The algebraic eigenvalue problem*. Oxford, England: Oxford University Press, 1965.

[110] C. C. Goodyear, *Signals and information*. New York, New York, United States of America: Wiley-Interscience, 1971.

[111] J. C. Santamarina and D. Fratta, *Introduction to discrete signals and inverse problems in civil engineering*. Reston, Virginia, United States of America: ASCE Press, 1998.

[112] L. He, "Time-frequency analysis of ultrasound signal in non-destructive testing using reassignment method," University of Manitoba, Project report, 2011.

[113] P. Flandrin, *Time-frequency/time-scale analysis*. London, England, United Kingdom: Academic Press, Sep. 1998.

[114] G. Liu and X. Han, *Computational inverse techniques in nondestructive evaluation*. Boca Raton, Florida, United States of America: CRC Press, 2003.

[115] D. K. Stoyko, N. Popplewell, and A. H. Shah, "Ultrasonic measurement of a cylinder's wall thickness," in *Proceedings of the Dynamics Behavior of Cylindrical Structures (DBCS) Conference 2009*, F. Delfanian and A. Luo, Eds., 2009, full manuscript on conference proceedings CD-ROM.

[116] E. Buckingham, "On physically similar systems: illustrations of the use of dimensional equations," *Physical Review*, vol. 4, pp. 345–376, Oct. 1914.

[117] W. Elmore and M. Heald, *Physics of waves*. Mineola, New York, United States of America: Dover Publications, 1985.

[118] The MathWorks®, Incorporated, *Genetic algorithm and direct search toolbox™ 2 user's guide*, The MathWorks®, Incorporated, Natick, Massachusetts, 2008. [Online]. Available: http://www.mathworks.com/help/toolbox/gads/rn/br3ldvx-1.html

[119] R. E. Walpole, R. H. Myers, and S. L. Myers, *Probability and statistics for engineers and scientists*, 6th ed. Upper Saddle River, New Jersey, United States of America: Prentice Hall, 1998.

[120] J. P. Holman, *Experimental methods for engineers*, 2nd ed. New York, New York, United States of America: McGraw-Hill, 1971.

[121] Agilent Technologies, http://www.agilent.com, 2009.

[122] Digital Wave Corporation, http://www.digitalwavecorp.com/, 2009.

[123] Vishay Micro-Measurements, http://www.vishay.com/strain-gages/, 2009.

[124] Instron, http://www.instron.us/wa/home/default_en.aspx, 2009.

[125] K. A. Adeogun, "Eliminating the extraneous behaviour of an ultrasonic transducer in non-destructive testing," University of Manitoba, Project report, 2011.

[126] P. Lacoursiere, "Characterization of transducer coupling," B.Sc. Thesis, University of Manitoba, Winnipeg, Manitoba, Canada, 2011.

[127] D. Stoyko, K. Adeogun, N. Popplewell, and H. Bai, "Principal challenges in predicting guided wave behavior in NDT," in *Review of progress in quantitative nondestructive evaluation: proceedings of the 38th annual review of progress in quantitative nondestructive evaluation*, D. O. Thompson and D. E. Chimenti, Eds. Melville, New York: American Institute of Physics, 2011, p. In press.

[128] K. A. Adeogun, "Extraction and statistical analysis of cut-off frequencies of homogeneous isotropic pipe's using curve fitting techniques," University of Manitoba, MECG 7780 project report, Aug. 2010.

[129] Y.-S. Lee and M.-J. Chung, "Study on crack detection using eigenfrequency test data," *Computers and Structures*, vol. 77, no. 3, pp. 327–342, 2000. [Online]. Available: http://dx.doi.org/10.1016/S0045-7949(99)00194-7

[130] B. P. Nandwana and S. K. Maiti, "Detection of the location and size of a crack in stepped cantilever beams based on measurements of natural frequencies," *Journal of Sound and Vibration*, vol. 203, no. 3, pp. 435–446, 1997. [Online]. Available: http://dx.doi.org/10.1006/jsvi.1996.0856

[131] X. F. Chen, Z. J. He, and J. W. Xiang, "Experiments on crack identification in cantilever beams," *Proceedings of the Society for Experimental Mechanics*, vol. 52, pp. 295–300, 2005. [Online]. Available: http://dx.doi.org/10.1177/0014485105054328

[132] D. R. J. Owen and A. J. Fawkes, *Engineering fracture mechanics: Numerical methods and applications*. Swansea, U.K.: Pineridge Press, 1983.

[133] W. M. Karunasena, "Elastic waves in laminated composite plates for application in ultrasonic nondestructive testing," Ph.D. dissertation, University of Manitoba, Winnipeg, Manitoba, Canada, 1992.

[134] W. M. Karunasena, "Fundamentals of elastic wave propagation," Lecture notes for wave propagation course in the Department of Civil Engineering, University of Manitoba.

[135] R. R. Craig, *Structural dynamics: an introduction to computer methods*. New York, New York, United States of America: John Wiley & Sons, 1981.

[136] M. J. Hine, "Transient synthesis using a fourier transform envelope: an alternative to swept-sine vibration testing," *Journal of the Institute of Environmental Sciences*, vol. 39, no. 5, pp. 17–22, September–October 1996.

[137] X. D. Wang and G. L. Huang, "Identification of embedded cracks using back-propagating elastic waves," *Inverse Problems*, vol. 20, no. 5, pp. 1393–1409, Oct. 2004.

[138] T. W. Körner, *Fourier analysis*. Cambridge, England, United Kingdom: Cambridge University Press, 1995.

[139] S. S. Rao, *Mechanical vibrations*, 4th ed. Upper Saddle River, New Jersey, United States of America: Pearson Prentice Hall, 2004.

[140] D. J. Ewins, *Modal testing: theory, practice, and application*, 2nd ed. Baldock, Hertfordshire, England: Research Studies Press Limited, 2000.

[141] K. G. McConnell, *Vibration testing: theory and practice*. New York, New York, United States of America: Wiley-Interscience, 1995.

[142] D. W. Trim, *Calculus for engineers*, 2nd ed. Toronto, Ontario, Canada: Pearson Hall, 2001.

Appendix A

Results From the Derivation of Exact Wavefunctions

A.1 Introduction

The displacement, strain, and stress fields that result from the Helmholtz decomposition presented in Chapter 2 are summarized in this appendix. The fields are presented in matrix form and the nomenclature defined in Chapter 2 is used. This appendix is concluded with the requirements needed for a hollow isotropic pipe to have traction free, inner and outer surfaces. Finally, the elements of the matrix $\mathbf{P}$, whose determinant serves as the dispersion relation for such a pipe, are described.

A.2 Displacement Field

The displacement field is given by

$$\mathbf{u} = \begin{bmatrix} u & v & w \end{bmatrix}^{\mathrm{T}} = \mathbf{C}\begin{bmatrix} A_1 & A_2 & A_3 & B_1 & B_2 & B_3 \end{bmatrix}^{\mathrm{T}} \mathrm{e}^{\mathrm{j}n\theta}\mathrm{e}^{\mathrm{j}kz}\mathrm{e}^{-\mathrm{j}\omega t}, \tag{A.2.1}$$

where $\mathbf{C}$ is a 3×6 matrix having the elements:

$$C_{1,1} = -\frac{\alpha r H_{n+1}^{(1)}(\alpha r) - n H_n^{(1)}(\alpha r)}{r}, \tag{A.2.2a}$$

$$C_{1,2} = -k H_{n+1}^{(1)}(\beta r), \tag{A.2.2b}$$

$$C_{1,3} = \frac{\mathrm{j}n H_n^{(1)}(\beta r)}{r}, \tag{A.2.2c}$$

$$C_{1,4} = -\frac{\alpha r H_{n+1}^{(2)}(\alpha r) - n H_n^{(2)}(\alpha r)}{r}, \tag{A.2.2d}$$

$$C_{1,5} = -k H_{n+1}^{(2)}(\beta r), \tag{A.2.2e}$$

$$C_{1,6} = \frac{\mathrm{j}nH_n^{(2)}(\beta r)}{r}, \tag{A.2.2f}$$

$$C_{2,1} = \frac{\mathrm{j}kH_n^{(1)}(\alpha r)}{r}, \tag{A.2.2g}$$

$$C_{2,2} = \mathrm{j}kH_{n+1}^{(1)}(\beta r), \tag{A.2.2h}$$

$$C_{2,3} = \frac{\beta r H_{n+1}^{(1)}(\beta r) - nH_n^{(1)}(\beta r)}{r}, \tag{A.2.2i}$$

$$C_{2,4} = \frac{\mathrm{j}kH_n^{(2)}(\alpha r)}{r}, \tag{A.2.2j}$$

$$C_{2,5} = \mathrm{j}kH_{n+1}^{(2)}(\beta r), \tag{A.2.2k}$$

$$C_{2,6} = \frac{\beta r H_{n+1}^{(2)}(\beta r) - nH_n^{(2)}(\beta r)}{r}, \tag{A.2.2l}$$

$$C_{3,1} = \mathrm{j}kH_n^{(1)}(\alpha r), \tag{A.2.2m}$$

$$C_{3,2} = -\mathrm{j}\beta H_n^{(1)}(\beta r), \tag{A.2.2n}$$

$$C_{3,3} = 0, \tag{A.2.2o}$$

$$C_{3,4} = \mathrm{j}kH_n^{(2)}(\alpha r), \tag{A.2.2p}$$

$$C_{3,5} = -\mathrm{j}\beta H_n^{(2)}(\beta r), \tag{A.2.2q}$$

and

$$C_{3,6} = 0. \tag{A.2.2r}$$

A.3 Strain Field

The strain field is given by

$$\boldsymbol{\varepsilon} = \begin{bmatrix} \varepsilon_{rr} & \varepsilon_{\theta\theta} & \varepsilon_{zz} & \gamma_{r\theta} & \gamma_{rz} & \gamma_{\theta z} \end{bmatrix}^{\mathrm{T}}, \tag{A.3.1}$$

where $\boldsymbol{\varepsilon}$ represents the strain tensor expressed in vector form. Moreover, ε is a normal strain and γ is a(n engineering) shear strain. The double subscripts for ε and γ give the directions of the strain. The first subscript indicates the normal of the plane in which the

quantity in measured; the second subscript gives the direction. Moreover, the strain tensor is symmetrical so that the order of the subscripts may be reversed without changing the value. The elements of the strain tensor are related to the displacement field by the (small) strain-displacement relations. These are given in cylindrical coordinates by

$$\varepsilon_{rr} = \frac{\partial u}{\partial r}, \tag{A.3.2a}$$

$$\varepsilon_{\theta\theta} = \frac{1}{r}\frac{\partial v}{\partial \theta} + \frac{u}{r}, \tag{A.3.2b}$$

$$\varepsilon_{zz} = \frac{\partial w}{\partial z}, \tag{A.3.2c}$$

$$\gamma_{r\theta} = \frac{1}{r}\frac{\partial u}{\partial \theta} + \frac{\partial v}{\partial r} - \frac{v}{r}, \tag{A.3.2d}$$

$$\gamma_{rz} = \frac{\partial w}{\partial r} + \frac{\partial u}{\partial z}, \tag{A.3.2e}$$

and

$$\gamma_{\theta z} = \frac{\partial v}{\partial z} + \frac{1}{r}\frac{\partial w}{\partial \theta}. \tag{A.3.2f}$$

Substituting the displacement field into equation (A.3.1) and making use of equation (A.3.2) gives

$$\boldsymbol{\varepsilon} = \mathbf{D}\Big[\, A_1 \; A_2 \; A_3 \; B_1 \; B_2 \; B_3 \,\Big]^{\mathrm{T}} \mathrm{e}^{\mathrm{j}n\theta} \mathrm{e}^{\mathrm{j}kz} \mathrm{e}^{-\mathrm{j}\omega t}, \tag{A.3.3}$$

where $\mathbf{D}$ is a 6×6 matrix having the elements:

$$D_{1,1} = \frac{-\alpha^2 r^2 H_n^{(1)}(\alpha r) + n^2 H_n^{(1)}(\alpha r) + \alpha r H_{n+1}^{(1)} - n H_n^{(1)}(\alpha r)}{r^2}, \tag{A.3.4.i}$$

$$D_{1,2} = \frac{k\left(-\beta r H_n^{(1)}(\beta r) + n H_{n+1}^{(1)}(\beta r) + H_{n+1}^{(1)}(\beta r)\right)}{r}, \tag{A.3.4.ii}$$

$$D_{1,3} = \frac{-\mathrm{j}n\left(\beta r H_{n+1}^{(1)}(\beta r) + H_n^{(1)}(\beta r) - n H_n^{(1)}(\beta r)\right)}{r^2}, \tag{A.3.4.iii}$$

$$D_{1,4} = \frac{-\alpha^2 r^2 H_n^{(2)}(\alpha r) + n^2 H_n^{(2)}(\alpha r) + \alpha r H_{n+1}^{(2)} - n H_n^{(2)}(\alpha r)}{r^2}, \tag{A.3.4.iv}$$

$$D_{1,5} = \frac{k\left(-\beta r H_n^{(2)}(\beta r) + n H_{n+1}^{(2)}(\beta r) + H_{n+1}^{(2)}(\beta r)\right)}{r}, \tag{A.3.4.v}$$

$$D_{1,6} = \frac{-\mathrm{j}n\left(\beta r H_{n+1}^{(2)}(\beta r) + H_n^{(2)}(\beta r) - n H_n^{(2)}(\beta r)\right)}{r^2}, \tag{A.3.4.vi}$$

$$D_{2,1} = \frac{-n^2 H_n^{(1)}(\alpha r) - \alpha r H_{n+1}^{(1)}(\alpha r) + n H_n^{(1)}(\alpha r)}{r^2}, \tag{A.3.4.vii}$$

$$D_{2,2} = \frac{-k(n+1) H_{n+1}^{(1)}(\beta r)}{r}, \tag{A.3.4.viii}$$

$$D_{2,3} = \frac{\mathrm{j}n\left(\beta r H_{n+1}^{(1)}(\beta r) - n H_n^{(1)}(\beta r) + H_n^{(1)}(\beta r)\right)}{r^2}, \tag{A.3.4.ix}$$

$$D_{2,4} = \frac{-n^2 H_n^{(2)}(\alpha r) - \alpha r H_{n+1}^{(2)}(\alpha r) + n H_n^{(2)}(\alpha r)}{r^2}, \tag{A.3.4.x}$$

$$D_{2,5} = \frac{-k(n+1) H_{n+1}^{(2)}(\beta r)}{r}, \tag{A.3.4.xi}$$

$$D_{2,6} = \frac{\mathrm{j}n\left(\beta r H_{n+1}^{(2)}(\beta r) - n H_n^{(2)}(\beta r) + H_n^{(2)}(\beta r)\right)}{r^2}, \tag{A.3.4.xii}$$

$$D_{3,1} = -k^2 H_n^{(1)}(\alpha r), \tag{A.3.4.xiii}$$

$$D_{3,2} = \beta k H_n^{(1)}(\beta r), \tag{A.3.4.xiv}$$

$$D_{3,3} = 0, \tag{A.3.4.xv}$$

$$D_{3,4} = -k^2 H_n^{(2)}(\alpha r), \tag{A.3.4.xvi}$$

$$D_{3,5} = \beta k H_n^{(2)}(\beta r), \tag{A.3.4.xvii}$$

$$D_{3,6} = 0, \tag{A.3.4.xviii}$$

$$D_{4,1} = \frac{-2\mathrm{j}n\left(H_n^{(1)}(\alpha r) - n H_n^{(1)}(\alpha r) + \alpha r H_{n+1}^{(1)}(\alpha r)\right)}{r^2}, \tag{A.3.4.xix}$$

$$D_{4,2} = \frac{-\mathrm{j}k\left(2H_{n+1}^{(1)}(\beta r) - \beta r H_n^{(1)}(\beta r) + 2n H_{n+1}^{(1)}(\beta r)\right)}{r}, \tag{A.3.4.xx}$$

$$D_{4,3} = \frac{-2n^2 H_n^{(1)}(\beta r) - 2\beta r H_{n+1}^{(1)}(\beta r) + \beta^2 r^2 H_n^{(1)}(\beta r) + 2n H_n^{(1)}(\beta r)}{r^2}, \tag{A.3.4.xxi}$$

$$D_{4,4} = \frac{-2\mathrm{j}n\left(H_n^{(2)}(\alpha r) - n H_n^{(2)}(\alpha r) + \alpha r H_{n+1}^{(2)}(\alpha r)\right)}{r^2}, \tag{A.3.4.xxii}$$

$$D_{4,5} = \frac{-\mathrm{j}k\left(2H_{n+1}^{(2)}(\beta r) - \beta r H_n^{(2)}(\beta r) + 2n H_{n+1}^{(2)}(\beta r)\right)}{r}, \tag{A.3.4.xxiii}$$

$$D_{4,6} = \frac{-2n^2 H_n^{(2)}(\beta r) - 2\beta r H_{n+1}^{(2)}(\beta r) + \beta^2 r^2 H_n^{(2)}(\beta r) + 2n H_n^{(2)}(\beta r)}{r^2}, \tag{A.3.4.xxiv}$$

$$D_{5,1} = \frac{-2\mathrm{j}k\left(\alpha r H_{n+1}^{(1)}(\alpha r) - n H_n^{(1)}(\alpha r)\right)}{r}, \tag{A.3.4.xxv}$$

$$D_{5,2} = \frac{-\mathrm{j}\left(-\beta^2 r H_{n+1}^{(1)}(\beta r) + \beta n H_n^{(1)}(\beta r) + k^2 r H_{n+1}^{(1)}(\beta r)\right)}{r}, \tag{A.3.4.xxvi}$$

$$D_{5,3} = \frac{-knH_n^{(1)}(\beta r)}{r}, \tag{A.3.4.xxvii}$$

$$D_{5,4} = \frac{-2\mathrm{j}k\left(\alpha r H_{n+1}^{(2)}(\alpha r) - nH_n^{(2)}(\alpha r)\right)}{r}, \tag{A.3.4.xxviii}$$

$$D_{5,5} = \frac{-\mathrm{j}\left(-\beta^2 r H_{n+1}^{(2)}(\beta r) + \beta n H_n^{(2)}(\beta r) + k^2 r H_{n+1}^{(2)}(\beta r)\right)}{r}, \tag{A.3.4.xxix}$$

$$D_{5,6} = \frac{-knH_n^{(2)}(\beta r)}{r}, \tag{A.3.4.xxx}$$

$$D_{6,1} = \frac{-2knH_n^{(1)}(\alpha r)}{r}, \tag{A.3.4.xxxi}$$

$$D_{6,2} = \frac{-k^2 r H_{n+1}^{(1)}(\beta r) + \beta n H_n^{(1)}(\beta r)}{r}, \tag{A.3.4.xxxii}$$

$$D_{6,3} = \frac{\mathrm{j}k\left(\beta r H_{n+1}^{(1)}(\beta r) - nH_n^{(1)}(\beta r)\right)}{r}, \tag{A.3.4.xxxiii}$$

$$D_{6,4} = \frac{-2knH_n^{(2)}(\alpha r)}{r}, \tag{A.3.4.xxxiv}$$

$$D_{6,5} = \frac{-k^2 r H_{n+1}^{(2)}(\beta r) + \beta n H_n^{(2)}(\beta r)}{r}, \tag{A.3.4.xxxv}$$

and

$$D_{6,6} = \frac{\mathrm{j}k\left(\beta r H_{n+1}^{(2)}(\beta r) - nH_n^{(2)}(\beta r)\right)}{r}. \tag{A.3.4.xxxvi}$$

A.4 Stress Field

The stress field is given by

$$\boldsymbol{\sigma} = \left[\, \sigma_{rr}\ \sigma_{\theta\theta}\ \sigma_{zz}\ \tau_{r\theta}\ \tau_{rz}\ \tau_{\theta z} \,\right]^{\mathrm{T}}, \tag{A.4.1}$$

where $\boldsymbol{\sigma}$ represents the stress tensor expressed in vector form. The σ and τ in equation (A.4.1) are a normal and shearing stress, respectively. As before, the double subscripts indicate the directions of the stress. The strain tensor is also symmetrical. For isotropic materials, elements of the stress tensor are related to the strain field, when cylindrical

coordinates are employed, by

$$\sigma_{rr} = (\lambda + 2\mu)\varepsilon_{rr} + \lambda\varepsilon_{\theta\theta} + \lambda\varepsilon_{zz}, \tag{A.4.2a}$$

$$\sigma_{\theta\theta} = \lambda\varepsilon_{rr} + (\lambda + 2\mu)\varepsilon_{\theta\theta} + \lambda\varepsilon_{zz}, \tag{A.4.2b}$$

$$\sigma_{zz} = \lambda\varepsilon_{rr} + \lambda\varepsilon_{\theta\theta} + (\lambda + 2\mu)\varepsilon_{zz}, \tag{A.4.2c}$$

$$\tau_{r\theta} = \mu\gamma_{r\theta}, \tag{A.4.2d}$$

$$\tau_{rz} = \mu\gamma_{rz}, \tag{A.4.2e}$$

and

$$\tau_{\theta z} = \mu\gamma_{\theta z} \tag{A.4.2f}$$

Substituting the displacement field into equation (A.4.1) and making use of equation (A.4.2) gives

$$\boldsymbol{\sigma} = \mathbf{E}\Big[\, A_1 \;\; A_2 \;\; A_3 \;\; B_1 \;\; B_2 \;\; B_3 \,\Big]^{\mathrm{T}} \mathrm{e}^{\mathrm{j}n\theta} \mathrm{e}^{\mathrm{j}kz} \mathrm{e}^{-\mathrm{j}\omega t}, \tag{A.4.3}$$

where $\mathbf{E}$ is a 6×6 matrix having the elements:

$$E_{1,1} = -\frac{\left(\lambda\alpha^2 r^2 + 2\mu\alpha^2 r^2 + \lambda k^2 r^2 - 2\mu n^2 + 2\mu n\right) H_n^{(1)}(\alpha r)}{r^2} + 2\frac{\mu\alpha H_{n+1}^{(1)}(\alpha r)}{r}, \tag{A.4.4.i}$$

$$E_{1,2} = \frac{2\mu k(n+1) H_{n+1}^{(1)}(\beta r)}{r} - 2\mu k\beta H_n^{(1)}(\beta r), \tag{A.4.4.ii}$$

$$E_{1,3} = \frac{-2\mathrm{j}\mu n(-n+1) H_n^{(1)}(\beta r)}{r^2} - \frac{2\mathrm{j}\mu n\beta H_{n+1}^{(1)}(\beta r)}{r}, \tag{A.4.4.iii}$$

$$E_{1,4} = -\frac{\left(\lambda\alpha^2 r^2 + 2\mu\alpha^2 r^2 + \lambda k^2 r^2 - 2\mu n^2 + 2\mu n\right) H_n^{(2)}(\alpha r)}{r^2} + 2\frac{\mu\alpha H_{n+1}^{(2)}(\alpha r)}{r}, \tag{A.4.4.iv}$$

$$E_{1,5} = \frac{2\mu k(n+1) H_{n+1}^{(2)}(\beta r)}{r} - 2\mu k\beta H_n^{(2)}(\beta r), \tag{A.4.4.v}$$

$$E_{1,6} = \frac{-2\mathrm{j}\mu n(-n+1) H_n^{(2)}(\beta r)}{r^2} - \frac{2\mathrm{j}\mu n\beta H_{n+1}^{(2)}(\beta r)}{r}, \tag{A.4.4.vi}$$

$$E_{2,1} = -\frac{\left(\lambda\alpha^2 r^2 + \lambda k^2 r^2 + 2\mu n^2 - 2\mu n\right) H_n^{(1)}(\alpha r)}{r^2} - \frac{2\mu\alpha H_{n+1}^{(1)}(\alpha r)}{r}, \tag{A.4.4.vii}$$

$$E_{2,2} = \frac{-2\mu k(n+1) H_{n+1}^{(1)}(\beta r)}{r}, \tag{A.4.4.viii}$$

$$E_{2,3} = \frac{2\mathrm{j}\mu n(-n+1)H_n^{(1)}(\beta r)}{r^2} + \frac{2\mathrm{j}\mu n H_{n+1}^{(1)}(\beta r)}{r}, \tag{A.4.4.ix}$$

$$E_{2,4} = -\frac{\left(\lambda\alpha^2 r^2 + \lambda k^2 r^2 + 2\mu n^2 - 2\mu n\right) H_n^{(2)}(\alpha r)}{r^2} - \frac{2\mu\alpha H_{n+1}^{(2)}(\alpha r)}{r}, \tag{A.4.4.x}$$

$$E_{2,5} = \frac{-2\mu k(n+1)H_{n+1}^{(2)}(\beta r)}{r}, \tag{A.4.4.xi}$$

$$E_{2,6} = \frac{2\mathrm{j}\mu n(-n+1)H_n^{(2)}(\beta r)}{r^2} + \frac{2\mathrm{j}\mu n H_{n+1}^{(2)}(\beta r)}{r}, \tag{A.4.4.xii}$$

$$E_{3,1} = \left(-\lambda\alpha^2 - \lambda k^2 - 2k^2\mu\right) H_n^{(1)}(\alpha r), \tag{A.4.4.xiii}$$

$$E_{3,2} = 2\mu k\beta H_n^{(1)}(\beta r), \tag{A.4.4.xiv}$$

$$E_{3,3} = 0, \tag{A.4.4.xv}$$

$$E_{3,4} = \left(-\lambda\alpha^2 - \lambda k^2 - 2k^2\mu\right) H_n^{(2)}(\alpha r), \tag{A.4.4.xvi}$$

$$E_{3,5} = 2\mu k\beta H_n^{(2)}(\beta r), \tag{A.4.4.xvii}$$

$$E_{3,6} = 0, \tag{A.4.4.xviii}$$

$$E_{4,1} = \frac{-2\mu\mathrm{j}n\left(H_n^{(1)}(\alpha r) - nH_n^{(1)}(\alpha r) + \alpha r H_{n+1}^{(1)}(\alpha r)\right)}{r^2}, \tag{A.4.4.xix}$$

$$E_{4,2} = \frac{-\mathrm{j}\mu k\left(2H_{n+1}^{(1)}(\beta r) - \beta r H_n^{(1)}(\beta r) + 2nH_{n+1}^{(1)}(\beta r)\right)}{r}, \tag{A.4.4.xx}$$

$$E_{4,3} = \frac{-2\mu n^2 H_n^{(1)}(\beta r) - 2\mu\beta r H_{n+1}^{(1)}(\beta r) + \mu\beta^2 r^2 H_n^{(1)}(\beta r) + 2\mu n H_n^{(1)}(\beta r)}{r^2}, \tag{A.4.4.xxi}$$

$$E_{4,4} = \frac{-2\mu\mathrm{j}n\left(H_n^{(2)}(\alpha r) - nH_n^{(2)}(\alpha r) + \alpha r H_{n+1}^{(2)}(\alpha r)\right)}{r^2}, \tag{A.4.4.xxii}$$

$$E_{4,5} = \frac{-\mathrm{j}\mu k\left(2H_{n+1}^{(2)}(\beta r) - \beta r H_n^{(2)}(\beta r) + 2nH_{n+1}^{(2)}(\beta r)\right)}{r}, \tag{A.4.4.xxiii}$$

$$E_{4,6} = \frac{-2\mu n^2 H_n^{(2)}(\beta r) - 2\mu\beta r H_{n+1}^{(2)}(\beta r) + \mu\beta^2 r^2 H_n^{(2)}(\beta r) + 2\mu n H_n^{(2)}(\beta r)}{r^2}, \tag{A.4.4.xxiv}$$

$$E_{5,1} = \frac{-2\mathrm{j}\mu k\left(\alpha r H_{n+1}^{(1)}(\alpha r) - nH_n^{(1)}(\alpha r)\right)}{r}, \tag{A.4.4.xxv}$$

$$E_{5,2} = \frac{-\mathrm{j}\mu\left(-\beta^2 r H_{n+1}^{(1)}(\beta r) + \beta n H_n^{(1)}(\beta r) + k^2 r H_{n+1}^{(1)}(\beta r)\right)}{r}, \tag{A.4.4.xxvi}$$

$$E_{5,3} = \frac{-\mu k n H_n^{(1)}(\beta r)}{r}, \tag{A.4.4.xxvii}$$

$$E_{5,4} = \frac{-2\mathrm{j}\mu k\left(\alpha r H_{n+1}^{(2)}(\alpha r) - nH_n^{(2)}(\alpha r)\right)}{r}, \tag{A.4.4.xxviii}$$

$$E_{5,5} = \frac{-\mathrm{j}\mu\left(-\beta^2 r H_{n+1}^{(2)}(\beta r) + \beta n H_n^{(2)}(\beta r) + k^2 r H_{n+1}^{(2)}(\beta r)\right)}{r}, \tag{A.4.4.xxix}$$

$$E_{5,6} = \frac{-\mu k n H_n^{(2)}(\beta r)}{r}, \tag{A.4.4.xxx}$$

$$E_{6,1} = \frac{-2\mu k n H_n^{(1)}(\alpha r)}{r}, \tag{A.4.4.xxxi}$$

$$E_{6,2} = \frac{-\mu k^2 r H_{n+1}^{(1)}(\beta r) + \mu\beta n H_n^{(1)}(\beta r)}{r}, \tag{A.4.4.xxxii}$$

$$E_{6,3} = \frac{\mathrm{j}\mu k\left(\beta r H_{n+1}^{(1)}(\beta r) - n H_n^{(1)}(\beta r)\right)}{r}, \tag{A.4.4.xxxiii}$$

$$E_{6,4} = \frac{-2\mu k n H_n^{(2)}(\alpha r)}{r}, \tag{A.4.4.xxxiv}$$

$$E_{6,5} = \frac{-\mu k^2 r H_{n+1}^{(2)}(\beta r) + \mu\beta n H_n^{(2)}(\beta r)}{r}, \tag{A.4.4.xxxv}$$

and

$$E_{6,6} = \frac{\mathrm{j}\mu k\left(\beta r H_{n+1}^{(2)}(\beta r) - n H_n^{(2)}(\beta r)\right)}{r}. \tag{A.4.4.xxxvi}$$

A.5 Traction Free Inner and Outer Surfaces

The σ_{rr}, $\tau_{r\theta}$, and τ_{rz} components of the stress tensor must vanish simultaneously on the inner and outer surfaces of the pipe for these two surfaces to be traction free. These constraints require, as stated in equation (2.2.10) and repeated here, that

$$\mathbf{P}\left[A_1\ A_2\ A_3\ B_1\ B_2\ B_3\right]^{\mathrm{T}} = \left[0\ 0\ 0\ 0\ 0\ 0\right]^{\mathrm{T}}. \tag{A.5.1}$$

Components of matrix **P** are:

$$P_{1,1} = -\frac{\left(\lambda\alpha^2 r_{\mathrm{i}}^2 + 2\mu\alpha^2 r_{\mathrm{i}}^2 + \lambda k^2 r_{\mathrm{i}}^2 - 2\mu n^2 + 2\mu n\right) H_n^{(1)}(\alpha r_{\mathrm{i}})}{r_{\mathrm{i}}^2} + 2\frac{\mu\alpha H_{n+1}^{(1)}(\alpha r_{\mathrm{i}})}{r_{\mathrm{i}}}, \tag{A.5.2.i}$$

$$P_{1,2} = \frac{2\mu k(n+1) H_{n+1}^{(1)}(\beta r_{\mathrm{i}})}{r_{\mathrm{i}}} - 2\mu k\beta H_n^{(1)}(\beta r_{\mathrm{i}}), \tag{A.5.2.ii}$$

$$P_{1,3} = \frac{-2\mathrm{j}\mu n(-n+1) H_n^{(1)}(\beta r_{\mathrm{i}})}{r_{\mathrm{i}}^2} - \frac{2\mathrm{j}\mu n\beta H_{n+1}^{(1)}(\beta r_{\mathrm{i}})}{r_{\mathrm{i}}}, \tag{A.5.2.iii}$$

$$P_{1,4} = -\frac{\left(\lambda\alpha^2 r_\mathrm{i}^2 + 2\mu\alpha^2 r_\mathrm{i}^2 + \lambda k^2 r^2 - 2\mu n^2 + 2\mu n\right) H_n^{(2)}(\alpha r_\mathrm{i})}{r_\mathrm{i}^2} + 2\frac{\mu\alpha H_{n+1}^{(2)}(\alpha r_\mathrm{i})}{r_\mathrm{i}}, \quad \text{(A.5.2.iv)}$$

$$P_{1,5} = \frac{2\mu k(n+1)H_{n+1}^{(2)}(\beta r_\mathrm{i})}{r_\mathrm{i}} - 2\mu k\beta H_n^{(2)}(\beta r_\mathrm{i}), \quad \text{(A.5.2.v)}$$

$$P_{1,6} = \frac{-2\mathrm{j}\mu n(-n+1)H_n^{(2)}(\beta r_\mathrm{i})}{r_\mathrm{i}^2} - \frac{2\mathrm{j}\mu n\beta H_{n+1}^{(2)}(\beta r_\mathrm{i})}{r_\mathrm{i}}, \quad \text{(A.5.2.vi)}$$

$$P_{2,1} = -\frac{\left(\lambda\alpha^2 r_\mathrm{o}^2 + 2\mu\alpha^2 r_\mathrm{o}^2 + \lambda k^2 r_\mathrm{o}^2 - 2\mu n^2 + 2\mu n\right) H_n^{(1)}(\alpha r_\mathrm{o})}{r_\mathrm{o}^2} + 2\frac{\mu\alpha H_{n+1}^{(1)}(\alpha r_\mathrm{o})}{r_\mathrm{o}}, \quad \text{(A.5.2.vii)}$$

$$P_{2,2} = \frac{2\mu k(n+1)H_{n+1}^{(1)}(\beta r_\mathrm{o})}{r_\mathrm{o}} - 2\mu k\beta H_n^{(1)}(\beta r_\mathrm{o}), \quad \text{(A.5.2.viii)}$$

$$P_{2,3} = \frac{-2\mathrm{j}\mu n(-n+1)H_n^{(1)}(\beta r_\mathrm{o})}{r_\mathrm{o}^2} - \frac{2\mathrm{j}\mu n\beta H_{n+1}^{(1)}(\beta r_\mathrm{o})}{r_\mathrm{o}}, \quad \text{(A.5.2.ix)}$$

$$P_{2,4} = -\frac{\left(\lambda\alpha^2 r_\mathrm{o}^2 + 2\mu\alpha^2 r_\mathrm{o}^2 + \lambda k^2 r^2 - 2\mu n^2 + 2\mu n\right) H_n^{(2)}(\alpha r_\mathrm{o})}{r_\mathrm{o}^2} + 2\frac{\mu\alpha H_{n+1}^{(2)}(\alpha r_\mathrm{o})}{r_\mathrm{o}}, \quad \text{(A.5.2.x)}$$

$$P_{2,5} = \frac{2\mu k(n+1)H_{n+1}^{(2)}(\beta r_\mathrm{o})}{r_\mathrm{o}} - 2\mu k\beta H_n^{(2)}(\beta r_\mathrm{o}), \quad \text{(A.5.2.xi)}$$

$$P_{2,6} = \frac{-2\mathrm{j}\mu n(-n+1)H_n^{(2)}(\beta r_\mathrm{o})}{r_\mathrm{o}^2} - \frac{2\mathrm{j}\mu n\beta H_{n+1}^{(2)}(\beta r_\mathrm{o})}{r_\mathrm{o}}, \quad \text{(A.5.2.xii)}$$

$$P_{3,1} = \frac{-2\mu\mathrm{j}n\left(H_n^{(1)}(\alpha r_\mathrm{i}) - nH_n^{(1)}(\alpha r_\mathrm{i}) + \alpha r_\mathrm{i} H_{n+1}^{(1)}(\alpha r_\mathrm{i})\right)}{r_\mathrm{i}^2}, \quad \text{(A.5.2.xiii)}$$

$$P_{3,2} = \frac{-\mathrm{j}\mu k\left(2H_{n+1}^{(1)}(\beta r_\mathrm{i}) - \beta r_\mathrm{i} H_n^{(1)}(\beta r_\mathrm{i}) + 2nH_{n+1}^{(1)}(\beta r_\mathrm{i})\right)}{r_\mathrm{i}}, \quad \text{(A.5.2.xiv)}$$

$$P_{3,3} = \frac{-2\mu n^2 H_n^{(1)}(\beta r_\mathrm{i}) - 2\mu\beta r_\mathrm{i} H_{n+1}^{(1)}(\beta r_\mathrm{i}) + \mu\beta^2 r_\mathrm{i}^2 H_n^{(1)}(\beta r_\mathrm{i}) + 2\mu n H_n^{(1)}(\beta r_\mathrm{i})}{r_\mathrm{i}^2}, \quad \text{(A.5.2.xv)}$$

$$P_{3,4} = \frac{-2\mu\mathrm{j}n\left(H_n^{(2)}(\alpha r_\mathrm{i}) - nH_n^{(2)}(\alpha r_\mathrm{i}) + \alpha r_\mathrm{i} H_{n+1}^{(2)}(\alpha r_\mathrm{i})\right)}{r_\mathrm{i}^2}, \quad \text{(A.5.2.xvi)}$$

$$P_{3,5} = \frac{-\mathrm{j}\mu k\left(2H_{n+1}^{(2)}(\beta r_\mathrm{i}) - \beta r_\mathrm{i} H_n^{(2)}(\beta r_\mathrm{i}) + 2nH_{n+1}^{(2)}(\beta r_\mathrm{i})\right)}{r_\mathrm{i}}, \quad \text{(A.5.2.xvii)}$$

$$P_{3,6} = \frac{-2\mu n^2 H_n^{(2)}(\beta r_\mathrm{i}) - 2\mu\beta r_\mathrm{i} H_{n+1}^{(2)}(\beta r_\mathrm{i}) + \mu\beta^2 r_\mathrm{i}^2 H_n^{(2)}(\beta r_\mathrm{i}) + 2\mu n H_n^{(1)}(\beta r_\mathrm{i})}{r_\mathrm{i}^2}, \quad \text{(A.5.2.xviii)}$$

$$P_{4,1} = \frac{-2\mu\mathrm{j}n\left(H_n^{(1)}(\alpha r_\mathrm{o}) - nH_n^{(1)}(\alpha r_\mathrm{o}) + \alpha r_\mathrm{o} H_{n+1}^{(1)}(\alpha r_\mathrm{o})\right)}{r_\mathrm{o}^2}, \quad \text{(A.5.2.xix)}$$

$$P_{4,2} = \frac{-\mathrm{j}\mu k\left(2H_{n+1}^{(1)}(\beta r_\mathrm{o}) - \beta r_\mathrm{o} H_n^{(1)}(\beta r_\mathrm{o}) + 2nH_{n+1}^{(1)}(\beta r_\mathrm{o})\right)}{r_\mathrm{o}}, \quad \text{(A.5.2.xx)}$$

$$P_{4,3} = \frac{-2\mu n^2 H_n^{(1)}(\beta r_o) - 2\mu\beta r_o H_{n+1}^{(1)}(\beta r_o) + \mu\beta^2 r_o^2 H_n^{(1)}(\beta r_o) + 2\mu n H_n^{(1)}(\beta r_o)}{r_o^2}, \quad \text{(A.5.2.xxi)}$$

$$P_{4,4} = \frac{-2\mu j n \left(H_n^{(2)}(\alpha r_o) - n H_n^{(2)}(\alpha r_o) + \alpha r_o H_{n+1}^{(2)}(\alpha r_o)\right)}{r_o^2}, \quad \text{(A.5.2.xxii)}$$

$$P_{4,5} = \frac{-j\mu k \left(2H_{n+1}^{(2)}(\beta r_o) - \beta r_o H_n^{(2)}(\beta r_o) + 2n H_{n+1}^{(2)}(\beta r_o)\right)}{r_o}, \quad \text{(A.5.2.xxiii)}$$

$$P_{4,6} = \frac{-2\mu n^2 H_n^{(2)}(\beta r_o) - 2\mu\beta r_o H_{n+1}^{(2)}(\beta r_o) + \mu\beta^2 r_o^2 H_n^{(2)}(\beta r_o) + 2\mu n H_n^{(2)}(\beta r_o)}{r_o^2}, \quad \text{(A.5.2.xxiv)}$$

$$P_{5,1} = \frac{-2j\mu k \left(\alpha r_i H_{n+1}^{(1)}(\alpha r_i) - n H_n^{(1)}(\alpha r_i)\right)}{r_i}, \quad \text{(A.5.2.xxv)}$$

$$P_{5,2} = \frac{-j\mu \left(-\beta^2 r_i H_{n+1}^{(1)}(\beta r_i) + \beta n H_n^{(1)}(\beta r_i) + k^2 r_i H_{n+1}^{(1)}(\beta r_i)\right)}{r_i}, \quad \text{(A.5.2.xxvi)}$$

$$P_{5,3} = \frac{-\mu k n H_n^{(1)}(\beta r_i)}{r_i}, \quad \text{(A.5.2.xxvii)}$$

$$P_{5,4} = \frac{-2j\mu k \left(\alpha r_i H_{n+1}^{(2)}(\alpha r_i) - n H_n^{(2)}(\alpha r_i)\right)}{r_i}, \quad \text{(A.5.2.xxviii)}$$

$$P_{5,5} = \frac{-j\mu \left(-\beta^2 r_i H_{n+1}^{(2)}(\beta r_i) + \beta n H_n^{(2)}(\beta r_i) + k^2 r_i H_{n+1}^{(2)}(\beta r_i)\right)}{r_i}, \quad \text{(A.5.2.xxix)}$$

$$P_{5,6} = \frac{-\mu k n H_n^{(2)}(\beta r_i)}{r_i}, \quad \text{(A.5.2.xxx)}$$

$$P_{6,1} = \frac{-2j\mu k \left(\alpha r_o H_{n+1}^{(1)}(\alpha r_o) - n H_n^{(1)}(\alpha r_o)\right)}{r_o}, \quad \text{(A.5.2.xxxi)}$$

$$P_{6,2} = \frac{-j\mu \left(-\beta^2 r_o H_{n+1}^{(1)}(\beta r_o) + \beta n H_n^{(1)}(\beta r_o) + k^2 r_o H_{n+1}^{(1)}(\beta r_o)\right)}{r_o}, \quad \text{(A.5.2.xxxii)}$$

$$P_{6,3} = \frac{-\mu k n H_n^{(1)}(\beta r_o)}{r_o}, \quad \text{(A.5.2.xxxiii)}$$

$$P_{6,4} = \frac{-2j\mu k \left(\alpha r_o H_{n+1}^{(2)}(\alpha r_o) - n H_n^{(2)}(\alpha r_o)\right)}{r_o}, \quad \text{(A.5.2.xxxiv)}$$

$$P_{6,5} = \frac{-j\mu \left(-\beta^2 r_o H_{n+1}^{(2)}(\beta r_o) + \beta n H_n^{(2)}(\beta r_o) + k^2 r_o H_{n+1}^{(2)}(\beta r_o)\right)}{r_o}, \quad \text{(A.5.2.xxxv)}$$

and

$$P_{6,6} = \frac{-\mu k n H_n^{(2)}(\beta r_o)}{r_o}. \quad \text{(A.5.2.xxxvi)}$$

The previous components are obtained from equation (A.4.3) by evaluating σ_{rr} (first and second rows of $\mathbf{P}$), $\tau_{r\theta}$ (third and fourth rows of $\mathbf{P}$), and τ_{rz} (fifth and sixth rows of $\mathbf{P}$) at the

inner and outer surfaces of the pipe, respectively.

The axisymmetric case is special. Substituting $n = 0$ into equation (A.5.2) yields:

$$P_{1,3} = 0, \tag{A.5.3a}$$

$$P_{1,6} = 0, \tag{A.5.3b}$$

$$P_{2,3} = 0, \tag{A.5.3c}$$

$$P_{2,6} = 0, \tag{A.5.3d}$$

$$P_{3,1} = 0, \tag{A.5.3e}$$

$$P_{3,4} = 0, \tag{A.5.3f}$$

$$P_{4,1} = 0, \tag{A.5.3g}$$

$$P_{4,4} = 0, \tag{A.5.3h}$$

$$P_{5,3} = 0, \tag{A.5.3i}$$

$$P_{5,6} = 0, \tag{A.5.3j}$$

$$P_{6,3} = 0, \tag{A.5.3k}$$

and

$$P_{6,6} = 0. \tag{A.5.3l}$$

Then the determinant of matrix $\mathbf{P}$ can be written as the product of two subdeterminants. This observation can be verified by expanding the determinant down the sixth column. The result is

$$\det(\mathbf{P}) = \det\left(\begin{bmatrix} P_{3,6} & P_{4,6} \\ P_{3,3} & P_{4,3} \end{bmatrix}\right) \det\left(\begin{bmatrix} P_{1,1} & P_{1,2} & P_{1,4} & P_{1,5} \\ P_{2,1} & P_{2,2} & P_{2,4} & P_{2,5} \\ P_{5,1} & P_{5,2} & P_{5,4} & P_{5,5} \\ P_{6,1} & P_{6,2} & P_{6,4} & P_{6,5} \end{bmatrix}\right). \tag{A.5.4}$$

The second subdeterminant corresponds to longitudinal modes where radial and axial displacements appear to be coupled. On the other hand, the first subdeterminant in equation

(A.5.4) corresponds to torsional modes, which involve a displacement component only in the circumferential direction. It is interesting to note that $\beta = 0$ causes the first subdeterminant to vanish. This case corresponds to the non-dispersive, lowest torsional mode.

Appendix B

Derivation of Approximate Equations of Motion Using SAFE

B.1 Introduction

The approximate displacement field is written in this appendix in terms of interpolation functions and a nodal displacement vector. The strain-displacement matrices are introduced to describe the strain and stress fields in terms of the approximate displacement field. Then approximate equations of motion are obtained, along with initial and boundary conditions, by applying Hamilton's principle to the appropriate functional for the complex displacement fields when no material damping is present.

B.2 Approximate Displacement Field

The displacement field is approximated initially as

$$\mathbf{u}(r,\theta,z,t) = \boldsymbol{\mathcal{N}}(r)\mathbf{U}(\theta,z,t), \tag{B.2.1}$$

where

$$\boldsymbol{\mathcal{N}}(r) = \begin{bmatrix} \mathbf{N}(r) & \mathbf{0} & \mathbf{0} \\ \mathbf{0} & \mathbf{N}(r) & \mathbf{0} \\ \mathbf{0} & \mathbf{0} & \mathbf{N}(r) \end{bmatrix}, \tag{B.2.2}$$

$\mathbf{N}$ are the assembled interpolation functions over the entire cylinder, and $\mathbf{U}(\theta,z,t)$ is the corresponding array of nodal displacements. The $\mathbf{N}$ is obtained by a conventional finite assembly process over all elements. (See, for example, [107].) The $\mathbf{U}(\theta,z,t)$, can be written

as

$$\mathbf{U}(\theta, z, t) = \left[\begin{array}{ccc} \boldsymbol{\mathcal{U}}(\theta, z, t) & \boldsymbol{\mathcal{V}}(\theta, z, t) & \boldsymbol{\mathcal{W}}(\theta, z, t) \end{array} \right]^{\mathrm{T}}, \tag{B.2.3}$$

where $\boldsymbol{\mathcal{U}}$, $\boldsymbol{\mathcal{V}}$, and $\boldsymbol{\mathcal{W}}$ are arrays containing $2N + 1$ elements corresponding to the radial, circumferential, and axial nodal displacements, respectively. The interpolation functions, $\mathbf{n}$, used here in any sublayer of the pipe, are quadratic isoparametric elements having the specific forms

$$\mathbf{n}(\zeta) = \left[\begin{array}{ccc} n_{\mathrm{b}}(\zeta) & n_{\mathrm{m}}(\zeta) & n_{\mathrm{f}}(\zeta) \end{array} \right] = \left[\begin{array}{ccc} \frac{1}{2}\zeta(\zeta - 1) & (1 - \zeta^2) & \frac{1}{2}\zeta(\zeta + 1) \end{array} \right]. \tag{B.2.4}$$

The n_{b}, n_{m}, n_{f} are shape functions associated with the "back" (inner), "middle", and "front" (outer) nodal surfaces, respectively. Moreover, ζ is a dimensionless radial coordinate in the local, isoparametric finite element's coordinate system that is given by

$$\zeta = \frac{2(r - r_{k\mathrm{m}})}{H_k}, -1 \leq \zeta \leq 1. \tag{B.2.5}$$

The $r_{k\mathrm{m}}$ in the above equation is the radial coordinate of the k^{th} layer's middle surface, which is taken to be the arithmetic average of the element's inner and outer radial coordinates.

B.3 Approximate Strain and Stress Fields

The following three strain transformation matrices are introduced:

$$\mathbf{B}_1 = \begin{bmatrix} \mathbf{N}_{,r} & \mathbf{N}/r & \mathbf{0} & \mathbf{0} & \mathbf{0} & \mathbf{0} \\ \mathbf{0} & \mathbf{0} & \mathbf{0} & \mathbf{N}_{,r} - \mathbf{N}/r & \mathbf{0} & \mathbf{0} \\ \mathbf{0} & \mathbf{0} & \mathbf{0} & \mathbf{0} & \mathbf{N}_{,r} & \mathbf{0} \end{bmatrix}^{\mathrm{T}}, \tag{B.3.1a}$$

$$\mathbf{B}_2 = \begin{bmatrix} \mathbf{0} & \mathbf{0} & \mathbf{0} & \mathbf{N}/r & \mathbf{0} & \mathbf{0} \\ \mathbf{0} & \mathbf{N}/r & \mathbf{0} & \mathbf{0} & \mathbf{0} & \mathbf{0} \\ \mathbf{0} & \mathbf{0} & \mathbf{0} & \mathbf{0} & \mathbf{0} & \mathbf{N}/r \end{bmatrix}^{\mathrm{T}}, \tag{B.3.1b}$$

and

$$\mathbf{B}_3 = \begin{bmatrix} \mathbf{0} & \mathbf{0} & \mathbf{0} & \mathbf{0} & \mathbf{N} & \mathbf{0} \\ \mathbf{0} & \mathbf{0} & \mathbf{0} & \mathbf{0} & \mathbf{0} & \mathbf{N} \\ \mathbf{0} & \mathbf{0} & \mathbf{N} & \mathbf{0} & \mathbf{0} & \mathbf{0} \end{bmatrix}^{\mathrm{T}} \tag{B.3.1c}$$

to simplify the computation of the approximate strain field. Then the strain and stress tensors can be written in vector form as

$$\boldsymbol{\varepsilon} = \mathbf{B}_1\mathbf{U} + \mathbf{B}_2\mathbf{U}_{,\theta} + \mathbf{B}_3\mathbf{U}_{,z} \tag{B.3.2a}$$

and

$$\boldsymbol{\sigma} = \mathbf{D}\mathbf{B}_1\mathbf{U} + \mathbf{D}\mathbf{B}_2\mathbf{U}_{,\theta} + \mathbf{D}\mathbf{B}_3\mathbf{U}_{,z}, \tag{B.3.2b}$$

respectively, where $\mathbf{D}$ is a symmetric matrix composed of the isotropic elastic moduli given by

$$\mathbf{D} = \begin{bmatrix} \lambda+2\mu & \lambda & \lambda & 0 & 0 & 0 \\ \lambda & \lambda+2\mu & \lambda & 0 & 0 & 0 \\ \lambda & \lambda & \lambda+2\mu & 0 & 0 & 0 \\ 0 & 0 & 0 & \mu & 0 & 0 \\ 0 & 0 & 0 & 0 & \mu & 0 \\ 0 & 0 & 0 & 0 & 0 & \mu \end{bmatrix}. \tag{B.3.3}$$

B.4 Application of Hamilton's Principle

Hamilton's principle can be expressed in the form

$$\overline{\delta} \int_{t_1}^{t_2} (T - V)\mathrm{d}t = 0, \tag{B.4.1}$$

where $\overline{\delta}$ indicates the first variation and T and V are the total kinetic and potential energies, respectively. They are given by

$$T = \frac{1}{2} \int_z \int_\theta \int_r \rho \dot{\tilde{\mathbf{u}}}^{\mathrm{T}} \dot{\mathbf{u}} r \mathrm{d}r\mathrm{d}\theta\mathrm{d}z \tag{B.4.2a}$$

and

$$V = \frac{1}{2} \int_z \int_\theta \int_r \tilde{\boldsymbol{\varepsilon}}^{\mathrm{T}} \boldsymbol{\sigma} r \mathrm{d}r\mathrm{d}\theta\mathrm{d}z + V_{\mathrm{e}} = \frac{1}{2} \int_z \int_\theta \int_r \tilde{\boldsymbol{\varepsilon}}^{\mathrm{T}} \mathbf{D}\boldsymbol{\varepsilon} r \mathrm{d}r\mathrm{d}\theta\mathrm{d}z + V_{\mathrm{e}}, \tag{B.4.2b}$$

where use has been made of equation (B.3.2b) and V_e is the potential energy due to the external forces. External forces that are body-force like are assumed now for convenience. Surface tractions are assumed not to exist. This assumption is the same one made when the exact wavefunctions were derived. With this assumption, the V_{e} can be represented as

$$V_{\mathrm{e}} = -\frac{1}{2} \int_z \int_\theta \int_r \left(\tilde{\mathbf{u}}^{\mathrm{T}} \mathbf{p} + \tilde{\mathbf{p}}^{\mathrm{T}} \mathbf{u} \right) r \mathrm{d}r\mathrm{d}\theta\mathrm{d}z, \tag{B.4.3}$$

where $\mathbf{p}$ is a body force vector that is a function of the spatial coordinates and whose specific form depends on the external forces. (The only external loadings considered here are "point-like" forces applied at a finite element model's nodal points so that the form of $\mathbf{p}$ is quite simple.) Substituting equation (B.2.1) into equation (B.4.2), making use of equation (B.3.2a) and noting that $\mathbf{N}$ and $\mathbf{D}$ are both real and independent of time, gives

$$T = \frac{1}{2} \int_z \int_\theta \int_r \rho \dot{\tilde{\mathbf{U}}}^{\mathrm{T}} \boldsymbol{\mathcal{N}}^{\mathrm{T}} \boldsymbol{\mathcal{N}} \dot{\mathbf{U}} r \mathrm{d}r\mathrm{d}\theta\mathrm{d}z \tag{B.4.4a}$$

and

$$\begin{aligned} V = \frac{1}{2}\int_z\int_\theta\int_r \Big(&\tilde{\mathbf{U}}^{\mathrm{T}}\mathbf{B}_1^{\mathrm{T}}\mathbf{D}\mathbf{B}_1\mathbf{U} + \tilde{\mathbf{U}}^{\mathrm{T}}\mathbf{B}_1^{\mathrm{T}}\mathbf{D}\mathbf{B}_2\mathbf{U}_{,\theta} + \tilde{\mathbf{U}}^{\mathrm{T}}\mathbf{B}_1^{\mathrm{T}}\mathbf{D}\mathbf{B}_3\mathbf{U}_{,z} \\ &+ \tilde{\mathbf{U}}_{,\theta}^{\mathrm{T}}\mathbf{B}_2^{\mathrm{T}}\mathbf{D}\mathbf{B}_1\mathbf{U} + \tilde{\mathbf{U}}_{,\theta}^{\mathrm{T}}\mathbf{B}_2^{\mathrm{T}}\mathbf{D}\mathbf{B}_2\mathbf{U}_{,\theta} + \tilde{\mathbf{U}}_{,\theta}^{\mathrm{T}}\mathbf{B}_2^{\mathrm{T}}\mathbf{D}\mathbf{B}_3\mathbf{U}_{,z} \\ &+ \tilde{\mathbf{U}}_{,z}^{\mathrm{T}}\mathbf{B}_3^{\mathrm{T}}\mathbf{D}\mathbf{B}_1\mathbf{U} + \tilde{\mathbf{U}}_{,z}^{\mathrm{T}}\mathbf{B}_3^{\mathrm{T}}\mathbf{D}\mathbf{B}_2\mathbf{U}_{,\theta} + \tilde{\mathbf{U}}_{,z}^{\mathrm{T}}\mathbf{B}_3^{\mathrm{T}}\mathbf{D}\mathbf{B}_3\mathbf{U}_{,z}\Big)\, r\mathrm{d}r\mathrm{d}\theta\mathrm{d}z \\ &- \frac{1}{2}\int_z\int_\theta\int_r \Big(\tilde{\mathbf{U}}^{\mathrm{T}}\boldsymbol{\mathcal{N}}^{\mathrm{T}}\mathbf{p} + \tilde{\mathbf{p}}^{\mathrm{T}}\boldsymbol{\mathcal{N}}\mathbf{U}\Big)\, r\mathrm{d}r\mathrm{d}\theta\mathrm{d}z, \end{aligned} \tag{B.4.4b}$$

by making use of equation (B.4.3). Making the substitutions $\mathbf{U} = \Re(\mathbf{U}) + \mathrm{j}\Im(\mathbf{U})$ and $\mathbf{p} = \Re(\mathbf{p}) + \mathrm{j}\Im(\mathbf{p})$, where $\Re$ and $\Im$ indicate the real and imaginary part respectively, into equation (B.4.4) gives

$$T = \frac{1}{2}\int_z\int_\theta\int_r \rho\Big(\Re(\dot{\mathbf{U}})^{\mathrm{T}}\boldsymbol{\mathcal{N}}^{\mathrm{T}}\boldsymbol{\mathcal{N}}\Re(\dot{\mathbf{U}}) + \Im(\dot{\mathbf{U}})^{\mathrm{T}}\boldsymbol{\mathcal{N}}^{\mathrm{T}}\boldsymbol{\mathcal{N}}\Im(\dot{\mathbf{U}})\Big)\, r\mathrm{d}r\mathrm{d}\theta\mathrm{d}z \tag{B.4.5a}$$

and

$$\begin{aligned} V = \frac{1}{2}\int_z\int_\theta\int_r \Big(&\Re(\mathbf{U})^{\mathrm{T}}\mathbf{B}_1^{\mathrm{T}}\mathbf{D}\mathbf{B}_1\Re(\mathbf{U}) + \Re(\mathbf{U})^{\mathrm{T}}\mathbf{B}_1^{\mathrm{T}}\mathbf{D}\mathbf{B}_2\Re(\mathbf{U}_{,\theta}) \\ &+ \Re(\mathbf{U})^{\mathrm{T}}\mathbf{B}_1^{\mathrm{T}}\mathbf{D}\mathbf{B}_3\Re(\mathbf{U}_{,z}) + \Re(\mathbf{U}_{,\theta})^{\mathrm{T}}\mathbf{B}_2^{\mathrm{T}}\mathbf{D}\mathbf{B}_1\Re(\mathbf{U}) \\ &+ \Re(\mathbf{U}_{,\theta})^{\mathrm{T}}\mathbf{B}_2^{\mathrm{T}}\mathbf{D}\mathbf{B}_2\Re(\mathbf{U}_{,\theta}) + \Re(\mathbf{U}_{,\theta})^{\mathrm{T}}\mathbf{B}_2^{\mathrm{T}}\mathbf{D}\mathbf{B}_3\Re(\mathbf{U}_{,z}) \\ &+ \Re(\mathbf{U}_{,z})^{\mathrm{T}}\mathbf{B}_3^{\mathrm{T}}\mathbf{D}\mathbf{B}_1\Re(\mathbf{U}) + \Re(\mathbf{U}_{,z})^{\mathrm{T}}\mathbf{B}_3^{\mathrm{T}}\mathbf{D}\mathbf{B}_2\Re(\mathbf{U}_{,\theta}) \\ &+ \Re(\mathbf{U}_{,z})^{\mathrm{T}}\mathbf{B}_3^{\mathrm{T}}\mathbf{D}\mathbf{B}_3\Re(\mathbf{U}_{,z}) + \Im(\mathbf{U})^{\mathrm{T}}\mathbf{B}_1^{\mathrm{T}}\mathbf{D}\mathbf{B}_1\Im(\mathbf{U}) \\ &+ \Im(\mathbf{U})^{\mathrm{T}}\mathbf{B}_1^{\mathrm{T}}\mathbf{D}\mathbf{B}_2\Im(\mathbf{U}_{,\theta}) + \Im(\mathbf{U})^{\mathrm{T}}\mathbf{B}_1^{\mathrm{T}}\mathbf{D}\mathbf{B}_3\Im(\mathbf{U}_{,z}) \\ &+ \Im(\mathbf{U}_{,\theta})^{\mathrm{T}}\mathbf{B}_2^{\mathrm{T}}\mathbf{D}\mathbf{B}_1\Im(\mathbf{U}) + \Im(\mathbf{U}_{,\theta})^{\mathrm{T}}\mathbf{B}_2^{\mathrm{T}}\mathbf{D}\mathbf{B}_2\Im(\mathbf{U}_{,\theta}) \\ &+ \Im(\mathbf{U}_{,\theta})^{\mathrm{T}}\mathbf{B}_2^{\mathrm{T}}\mathbf{D}\mathbf{B}_3\Im(\mathbf{U}_{,z}) + \Im(\mathbf{U}_{,z})^{\mathrm{T}}\mathbf{B}_3^{\mathrm{T}}\mathbf{D}\mathbf{B}_1\Im(\mathbf{U}) \\ &+ \Im(\mathbf{U}_{,z})^{\mathrm{T}}\mathbf{B}_3^{\mathrm{T}}\mathbf{D}\mathbf{B}_2\Im(\mathbf{U}_{,\theta}) + \Im(\mathbf{U}_{,z})^{\mathrm{T}}\mathbf{B}_3^{\mathrm{T}}\mathbf{D}\mathbf{B}_3\Im(\mathbf{U}_{,z}) \\ &-2\Re(\mathbf{U})^{\mathrm{T}}\boldsymbol{\mathcal{N}}^{\mathrm{T}}\Re(\mathbf{p}) - 2\Im(\mathbf{U})^{\mathrm{T}}\boldsymbol{\mathcal{N}}^{\mathrm{T}}\Im(\mathbf{p})\Big)\, r\mathrm{d}r\mathrm{d}\theta\mathrm{d}z, \end{aligned} \tag{B.4.5b}$$

by making use of the fact that each matrix product gives rise to a scalar. Hence $\mathrm{j}\Im(\dot{\mathbf{U}})^{\mathrm{T}}\boldsymbol{\mathcal{N}}^{\mathrm{T}}\boldsymbol{\mathcal{N}}\Re(\dot{\mathbf{U}}) = \Re(\dot{\mathbf{U}})^{\mathrm{T}}\boldsymbol{\mathcal{N}}^{\mathrm{T}}\boldsymbol{\mathcal{N}}\mathrm{j}\Im(\dot{\mathbf{U}})$, for example.

Substituting equation (B.4.5) into equation (B.4.1) and taking the first variation gives

$$
\begin{aligned}
&\frac{1}{2}\int_{t_1}^{t_2}\Bigg(\int_z\int_\theta\int_r -2\Big\{\overline{\delta}\mathfrak{R}(\mathbf{U})^{\mathrm{T}}\Big[\rho\boldsymbol{\mathcal{N}}^{\mathrm{T}}\boldsymbol{\mathcal{N}}\mathfrak{R}(\ddot{\mathbf{U}})+\mathbf{B}_1^{\mathrm{T}}\mathbf{D}\mathbf{B}_1\mathfrak{R}(\mathbf{U})\\
&\quad+\left(\mathbf{B}_1^{\mathrm{T}}\mathbf{D}\mathbf{B}_2-\mathbf{B}_2^{\mathrm{T}}\mathbf{D}\mathbf{B}_1\right)\mathfrak{R}(\mathbf{U}_{,\theta})+\left(\mathbf{B}_1^{\mathrm{T}}\mathbf{D}\mathbf{B}_3-\mathbf{B}_3^{\mathrm{T}}\mathbf{D}\mathbf{B}_1\right)\mathfrak{R}(\mathbf{U}_{,z})\\
&\quad-\mathbf{B}_2^{\mathrm{T}}\mathbf{D}\mathbf{B}_2\mathfrak{R}(\mathbf{U}_{,\theta\theta})-\left(\mathbf{B}_2^{\mathrm{T}}\mathbf{D}\mathbf{B}_3+\mathbf{B}_3^{\mathrm{T}}\mathbf{D}\mathbf{B}_2\right)\mathfrak{R}(\mathbf{U}_{,\theta z})-\mathbf{B}_3^{\mathrm{T}}\mathbf{D}\mathbf{B}_3\mathfrak{R}(\mathbf{U}_{,zz})\\
&\quad-\boldsymbol{\mathcal{N}}^{\mathrm{T}}\mathfrak{R}(\mathbf{p})\Big]+\overline{\delta}\mathfrak{I}(\mathbf{U})^{\mathrm{T}}\Big[\rho\boldsymbol{\mathcal{N}}^{\mathrm{T}}\boldsymbol{\mathcal{N}}\mathfrak{I}(\ddot{\mathbf{U}})+\mathbf{B}_1^{\mathrm{T}}\mathbf{D}\mathbf{B}_1\mathfrak{I}(\mathbf{U})\\
&\quad+\left(\mathbf{B}_1^{\mathrm{T}}\mathbf{D}\mathbf{B}_2-\mathbf{B}_2^{\mathrm{T}}\mathbf{D}\mathbf{B}_1\right)\mathfrak{I}(\mathbf{U}_{,\theta})+\left(\mathbf{B}_1^{\mathrm{T}}\mathbf{D}\mathbf{B}_3-\mathbf{B}_3^{\mathrm{T}}\mathbf{D}\mathbf{B}_1\right)\mathfrak{I}(\mathbf{U}_{,z})-\mathbf{B}_2^{\mathrm{T}}\mathbf{D}\mathbf{B}_2\mathfrak{I}(\mathbf{U}_{,\theta\theta})\\
&\quad-\left(\mathbf{B}_2^{\mathrm{T}}\mathbf{D}\mathbf{B}_3+\mathbf{B}_3^{\mathrm{T}}\mathbf{D}\mathbf{B}_2\right)\mathfrak{I}(\mathbf{U}_{,\theta z})-\mathbf{B}_3^{\mathrm{T}}\mathbf{D}\mathbf{B}_3\mathfrak{R}(\mathbf{U}_{,zz})-\boldsymbol{\mathcal{N}}^{\mathrm{T}}\mathfrak{I}(\mathbf{p})\Big]\Big\}\,r\mathrm{d}r\mathrm{d}\theta\mathrm{d}z\Bigg)\mathrm{d}t\\
&+\frac{1}{2}\int_{t_1}^{t_2}\int_z\int_\theta\int_r 2\left\{\frac{\mathrm{d}}{\mathrm{d}t}\left[\overline{\delta}\mathfrak{R}(\mathbf{U})^{\mathrm{T}}\rho\boldsymbol{\mathcal{N}}^{\mathrm{T}}\boldsymbol{\mathcal{N}}\mathfrak{R}(\dot{\mathbf{U}})\right]\right.\\
&\quad\left.+\frac{\mathrm{d}}{\mathrm{d}t}\left[\overline{\delta}\mathfrak{I}(\mathbf{U})^{\mathrm{T}}\rho\boldsymbol{\mathcal{N}}^{\mathrm{T}}\boldsymbol{\mathcal{N}}\mathfrak{I}(\dot{\mathbf{U}})\right]\right\}r\mathrm{d}r\mathrm{d}\theta\mathrm{d}z\mathrm{d}t\\
&+\frac{1}{2}\int_{t_1}^{t_2}\int_z\int_\theta\int_r 2\Bigg\{\frac{\mathrm{d}}{\mathrm{d}\theta}\Big(\overline{\delta}\mathfrak{R}(\mathbf{U})^{\mathrm{T}}\left[\mathbf{B}_2^{\mathrm{T}}\mathbf{D}\mathbf{B}_1\mathfrak{R}(\mathbf{U})+\mathbf{B}_2^{\mathrm{T}}\mathbf{D}\mathbf{B}_2\mathfrak{R}(\mathbf{U}_{,\theta})\right.\\
&\quad\left.+\mathbf{B}_2^{\mathrm{T}}\mathbf{D}\mathbf{B}_3\mathfrak{R}(\mathbf{U}_{,z})\right]\Big)+\frac{\mathrm{d}}{\mathrm{d}z}\Big(\overline{\delta}\mathfrak{R}(\mathbf{U})^{\mathrm{T}}\left[\mathbf{B}_3^{\mathrm{T}}\mathbf{D}\mathbf{B}_1\mathfrak{R}(\mathbf{U})+\mathbf{B}_3^{\mathrm{T}}\mathbf{D}\mathbf{B}_2\mathfrak{R}(\mathbf{U}_{,\theta})\right.\\
&\quad\left.+\mathbf{B}_3^{\mathrm{T}}\mathbf{D}\mathbf{B}_3\mathfrak{R}(\mathbf{U}_{,z})\right]\Big)+\frac{\mathrm{d}}{\mathrm{d}\theta}\Big(\overline{\delta}\mathfrak{I}(\mathbf{U})^{\mathrm{T}}\left[\mathbf{B}_2^{\mathrm{T}}\mathbf{D}\mathbf{B}_1\mathfrak{I}(\mathbf{U})+\mathbf{B}_2^{\mathrm{T}}\mathbf{D}\mathbf{B}_2\mathfrak{I}(\mathbf{U}_{,\theta})\right.\\
&\quad\left.+\mathbf{B}_2^{\mathrm{T}}\mathbf{D}\mathbf{B}_3\mathfrak{I}(\mathbf{U}_{,z})\right]\Big)+\frac{\mathrm{d}}{\mathrm{d}z}\Big(\overline{\delta}\mathfrak{I}(\mathbf{U})^{\mathrm{T}}\left[\mathbf{B}_3^{\mathrm{T}}\mathbf{D}\mathbf{B}_1\mathfrak{I}(\mathbf{U})+\mathbf{B}_3^{\mathrm{T}}\mathbf{D}\mathbf{B}_2\mathfrak{I}(\mathbf{U}_{,\theta})\right.\\
&\quad\left.+\mathbf{B}_3^{\mathrm{T}}\mathbf{D}\mathbf{B}_3\mathfrak{I}(\mathbf{U}_{,z})\right]\Big)\Bigg\}\,r\mathrm{d}r\mathrm{d}\theta\mathrm{d}z\mathrm{d}t=0.
\end{aligned}
\tag{B.4.6}
$$

The first integral in equation (B.4.6) represents the approximate equations of motion. On the other hand, the second and third integrals give approximate initial conditions and boundary conditions, respectively. The mass, $\mathbf{M}$, stiffness $\mathbf{K}_i$, $i=1,2,3,\ldots,6$, and consistent force, $\mathbf{F}$, matrices are defined now as:

$$\mathbf{M}=\int_{r_{\mathrm{i}}}^{r_{\mathrm{o}}}\rho\boldsymbol{\mathcal{N}}^{\mathrm{T}}\boldsymbol{\mathcal{N}}r\mathrm{d}r, \tag{B.4.7a}$$

$$\mathbf{K}_1=\int_{r_{\mathrm{i}}}^{r_{\mathrm{o}}}\mathbf{B}_1^{\mathrm{T}}\mathbf{D}\mathbf{B}_1r\mathrm{d}r, \tag{B.4.7b}$$

$$\mathbf{K}_2=\int_{r_{\mathrm{i}}}^{r_{\mathrm{o}}}\left(\mathbf{B}_1^{\mathrm{T}}\mathbf{D}\mathbf{B}_2-\mathbf{B}_2^{\mathrm{T}}\mathbf{D}\mathbf{B}_2\right)r\mathrm{d}r, \tag{B.4.7c}$$

$$\mathbf{K}_3 = \int_{r_\mathrm{i}}^{r_\mathrm{o}} \left(\mathbf{B}_1^\mathrm{T}\mathbf{D}\mathbf{B}_3 - \mathbf{B}_3^\mathrm{T}\mathbf{D}\mathbf{B}_1\right) r\mathrm{d}r, \tag{B.4.7d}$$

$$\mathbf{K}_4 = \int_{r_\mathrm{i}}^{r_\mathrm{o}} \mathbf{B}_2^\mathrm{T}\mathbf{D}\mathbf{B}_2 r\mathrm{d}r, \tag{B.4.7e}$$

$$\mathbf{K}_5 = \int_{r_\mathrm{i}}^{r_\mathrm{o}} \left(\mathbf{B}_2^\mathrm{T}\mathbf{D}\mathbf{B}_3 + \mathbf{B}_3^\mathrm{T}\mathbf{D}\mathbf{B}_2\right) r\mathrm{d}r, \tag{B.4.7f}$$

$$\mathbf{K}_6 = \int_{r_\mathrm{i}}^{r_\mathrm{o}} \mathbf{B}_3^\mathrm{T}\mathbf{D}\mathbf{B}_3 r\mathrm{d}r, \tag{B.4.7g}$$

and

$$\mathbf{F} = \int_{r_\mathrm{i}}^{r_\mathrm{o}} \mathcal{N}^\mathrm{T}\mathbf{p} r\mathrm{d}r. \tag{B.4.7h}$$

Note that $\mathbf{M}$, $\mathbf{K}_1$, $\mathbf{K}_4$, $\mathbf{K}_5$, and $\mathbf{K}_6$ are symmetric but $\mathbf{K}_2$ and $\mathbf{K}_3$ are antisymmetric. Substituting equation (B.4.7) into the approximate equations of motion gives

$$\begin{aligned}
\frac{1}{2}\int_{t_1}^{t_2}\Bigg\{\int_z\int_\theta -2\Big(\overline{\delta}\mathfrak{R}(\mathbf{U})^\mathrm{T}\Big[&\mathbf{M}\mathfrak{R}(\ddot{\mathbf{U}}) + \mathbf{K}_1\mathfrak{R}(\mathbf{U}) + \mathbf{K}_2\mathfrak{R}(\mathbf{U}_{,\theta}) + \mathbf{K}_3\mathfrak{R}(\mathbf{U}_{,z})\\
&-\mathbf{K}_4\mathfrak{R}(\mathbf{U}_{,\theta\theta}) - \mathbf{K}_5\mathfrak{R}(\mathbf{U}_{,\theta z}) - \mathbf{K}_6\mathfrak{R}(\mathbf{U}_{,zz}) - \mathfrak{R}(\mathbf{F})\Big]\\
+\overline{\delta}\mathfrak{I}(\mathbf{U})^\mathrm{T}\Big[&\rho\mathbf{M}\mathfrak{I}(\ddot{\mathbf{U}}) + \mathbf{K}_1\mathfrak{I}(\mathbf{U}) + \mathbf{K}_2\mathfrak{I}(\mathbf{U}_{,\theta}) + \mathbf{K}_3\mathfrak{I}(\mathbf{U}_{,z}) - \mathbf{K}_4\mathfrak{I}(\mathbf{U}_{,\theta\theta})\\
&-\mathbf{K}_5\mathfrak{I}(\mathbf{U}_{,\theta z}) - \mathbf{K}_6\mathfrak{I}(\mathbf{U}_{,zz}) - \mathfrak{I}(\mathbf{F})\Big]\Big)\mathrm{d}\theta\mathrm{d}z\Bigg\}\mathrm{d}t = 0.
\end{aligned} \tag{B.4.8}$$

It follows that

$$\begin{aligned}
&\mathbf{M}\mathfrak{R}(\ddot{\mathbf{U}}) + \mathbf{K}_1\mathfrak{R}(\mathbf{U}) + \mathbf{K}_2\mathfrak{R}(\mathbf{U}_{,\theta}) + \mathbf{K}_3\mathfrak{R}(\mathbf{U}_{,z}) - \mathbf{K}_4\mathfrak{R}(\mathbf{U}_{,\theta\theta})\\
&\qquad - \mathbf{K}_5\mathfrak{R}(\mathbf{U}_{,\theta z}) - \mathbf{K}_6\mathfrak{R}(\mathbf{U}_{,zz}) - \mathfrak{R}(\mathbf{F}) = 0
\end{aligned} \tag{B.4.9a}$$

and

$$\begin{aligned}
&\mathbf{M}\mathfrak{I}(\ddot{\mathbf{U}}) + \mathbf{K}_1\mathfrak{I}(\mathbf{U}) + \mathbf{K}_2\mathfrak{I}(\mathbf{U}_{,\theta}) + \mathbf{K}_3\mathfrak{I}(\mathbf{U}_{,z}) - \mathbf{K}_4\mathfrak{I}(\mathbf{U}_{,\theta\theta})\\
&\qquad - \mathbf{K}_5\mathfrak{I}(\mathbf{U}_{,\theta z}) - \mathbf{K}_6\mathfrak{I}(\mathbf{U}_{,zz}) - \mathfrak{I}(\mathbf{F}) = 0
\end{aligned} \tag{B.4.9b}$$

for equation (B.4.8) to be generally satisfied because $\overline{\delta}\mathfrak{R}(\mathbf{U})^\mathrm{T}$ and $\overline{\delta}\mathfrak{I}(\mathbf{U})^\mathrm{T}$ are independent. Multiplying equation (B.4.9b) by j and adding the result to equation (B.4.9a) gives

$$\mathbf{M}\ddot{\mathbf{U}} + \mathbf{K}_1\mathbf{U} + \mathbf{K}_2\mathbf{U}_{,\theta} + \mathbf{K}_3\mathbf{U}_{,z} - \mathbf{K}_4\mathbf{U}_{,\theta\theta} - \mathbf{K}_5\mathbf{U}_{,\theta z} - \mathbf{K}_6\mathbf{U}_{,zz} = \mathbf{F}. \tag{B.4.10}$$

Equation (B.4.10) is identical to equation (2.3.2) given in the main text and it is the desired result.

B.5 Note on Integrating the Finite Element Matrices

In practice the matrices given in equation (B.4.7) are evaluated by "assembling" finite element matrices. The element matrices for the k^{th} element take the same form as the matrices in equation (B.4.7) but with integration limits of r_k and r_{k+1} instead of r_{i} and r_{o}. (See also subsection 2.3.2 and Figure 2.2.) A typical element of these matrices can be written in the form

$$\mathcal{E} = \int_{r_k}^{r_{k+1}} \mathcal{I}(r,\zeta) r \mathrm{d}r, \tag{B.5.1}$$

where $\mathcal{E}$ is an arbitrary matrix element and $\mathcal{I}$ is the integrand arising from the required matrix multiplications. The variable of integration in equation (B.5.1) is r but the integrand is a function of both r and ζ (which is also a function of r). The well known change of variables theorem from multivariable calculus is invoked to evaluate equation (B.5.1). The result is

$$\mathcal{E} = \int_{r_k}^{r_{k+1}} \mathcal{I}(r,\zeta) r \mathrm{d}r = \int_{-1}^{1} \mathcal{I}'(\zeta) \left(\frac{H_k\zeta + r_{k\text{m}}}{2}\right)\left(\frac{H_k}{2}\right)\mathrm{d}\zeta. \tag{B.5.2}$$

Use is made of the relation $r = (H_k\zeta + r_{k\text{m}})/2$ which is obtained from equation (B.2.5). Moreover, $\mathcal{I}'(\zeta)$ can be derived straightforwardly from $\mathcal{I}(r,\zeta)$ by using the chain rule and the previously stated relation between r and ζ. On the other hand, the $H_k/2$ factor appearing in equation (B.5.2) arises from the use of the determinant of the Jacobian matrix in the change of variables theorem. For this particular case, the Jacobian matrix, $\mathbf{J}$, is a scalar and it is given simply by

$$\mathbf{J} = \frac{\partial r}{\partial \zeta} = \frac{H_k}{2} \tag{B.5.3}$$

so its determinant, $|\mathbf{J}|$, is merely

$$|\mathbf{J}| = \frac{H_k}{2}. \tag{B.5.4}$$

The Jacobian matrix is a scalar as a result of using a one-dimensional finite element. On the other hand, the Jacobian matrix given by equation (B.5.3) is a constant when the radial coordinate of the k^{th} layer's middle surface is chosen to coincide with the arithmetic average of a finite element's inner and outer radial coordinates.

APPENDIX C

CODE LISTINGS AND SKETCHES TO IMPLEMENT SAFE

C.1 Overview

This appendix contains annotated code listings and "sketches" (where sections of code are removed for brevity) of illustrative MATLAB® scripts and functions used to implement the SAFE method. This method is described for isotropic pipes in Chapter 2 and Appendix B. The code listings and sketches introduce an approach which allows a partial automation of writing finite element programs by taking advantage of readily available commercial tools. Moreover, several MATLAB® "best practices," such as preallocating memory for arrays and "vectorizing code" rather than using a loop, are illustrated as a matter of course in the numerical implementations. Although the programs presented in this appendix have been "parallelized" to run simultaneously on a several computing cores, only "serial" or single computer[1] versions are presented here. A discussion of parallel and distributed computing is deferred to Appendix L.

C.2 Annotated Code Listings

An annotated MATLAB® code listing to evaluate (in closed form) the finite element stiffness and mass matrices is provided in Listing C.1. A high level flowchart for this program is given in Figure C.1. Listing C.2, on the other hand, gives *illustrative* code to assemble the global $\mathbf{K}_1$ stiffness matrix from the element matrices. Figure C.2 gives a high level flowchart for this listing. The script is run once for each $\mathbf{K}_i$ and $\mathbf{M}$. A "find and replace" is used to change a matrix designation. The output of the two previously described scripts is copied into programs which implement the eigenvalue problems to produce the approx-

[1]Note that MATLAB® supports implicit parallelization that speeds code execution for serial programs.

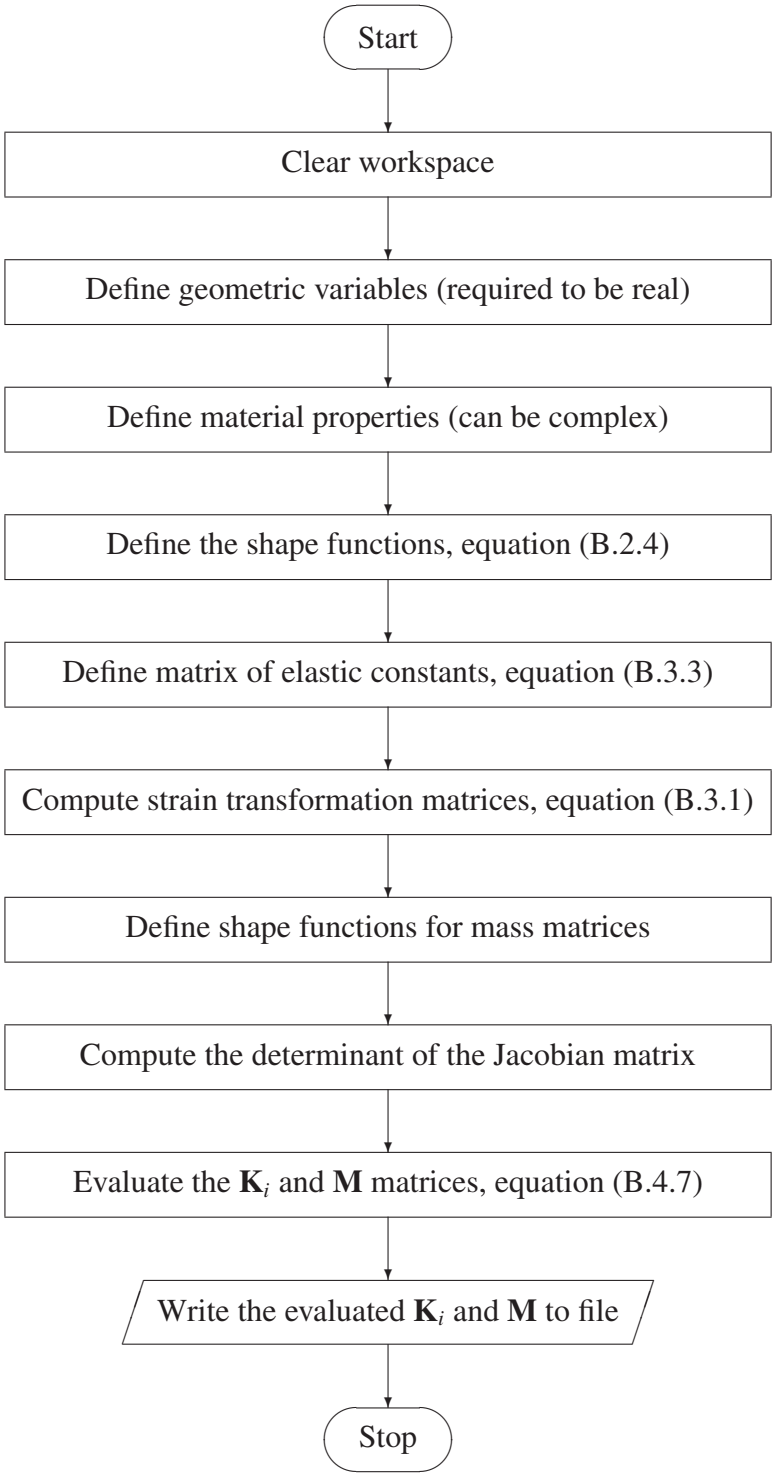

Figure C.1. A high level flowchart for Listing C.1.

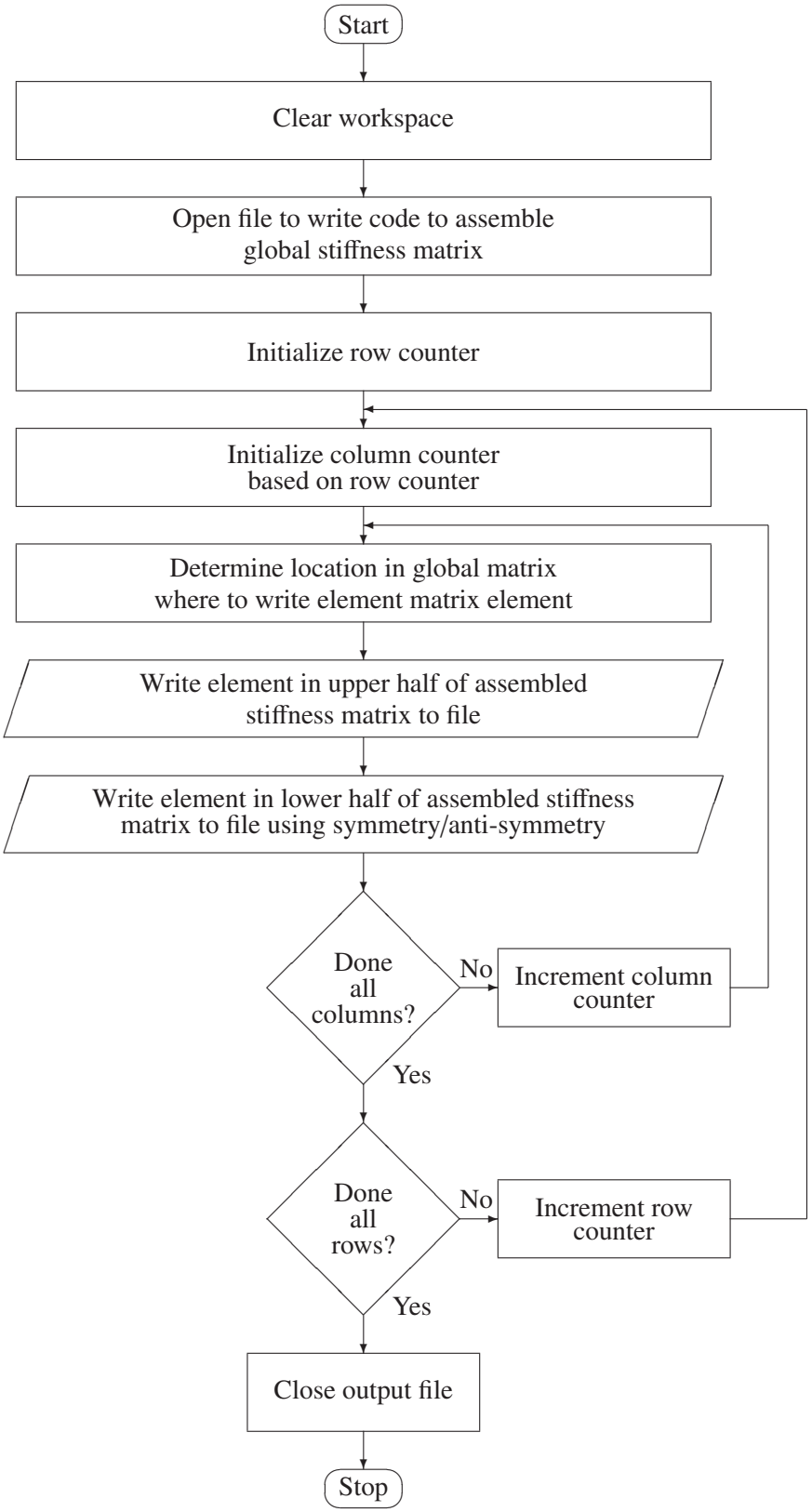

Figure C.2. A high level flowchart for Listing C.2.

imate wavefunctions. Listings C.3 and C.4 provide "sketches" of these MATLAB® programs. High level flowcharts for the listings are provided in Figures C.3 and C.4, respectively. The first of these two listings solves the eigenvalue problem given in equation (2.3.5); the second implements the eigenvalue problem of equation (2.3.6). Both eigenvalue problems have practical interest but in different scenarios. Note that the program Listings C.3 and C.4 implement not only the general three-dimensional case (where displacements in the radial, circumferential and axial directions can exist simultaneously) but also simplifications arising from the axisymmetric case. Both axisymmetric wave types labelled either torsional, which involve purely circumferential displacements, or longitudinal, in which radial and axial displacements can exist simultaneously, are implemented. The element and global stiffness and mass matrices for these special cases are derived using programs that are similar, yet simpler, than those presented in Listings C.1 and C.2. These listings are modified by deleting the relevant displacement components and accommodating the deletions in the assembly process. Discussions of the additional code required to distribute the programs to a cluster of computers are deferred until Appendix L. (Note that in later implementations of these programs the [frequency independent] global mass and stiffness matrices are written to disk to be "read in" when required, rather than recomputing them for each frequency and circumferential wavenumber of interest. These matrices are stored by using MATLAB®'s built-in, binary storage scheme which encodes numerical information much more efficiently than a "plain text" storage scheme.)

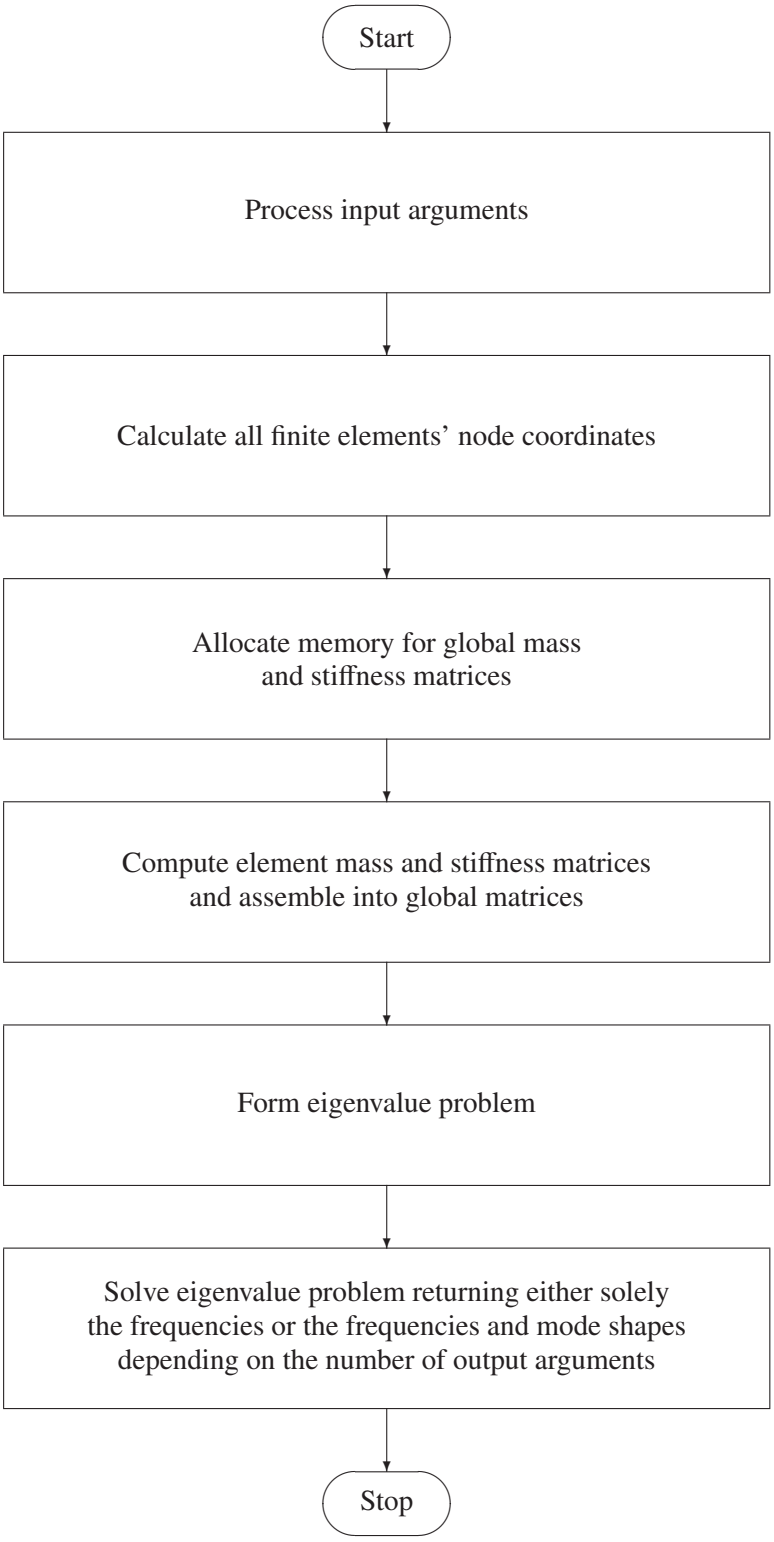

Figure C.3. A high level flowchart for Listing C.3.

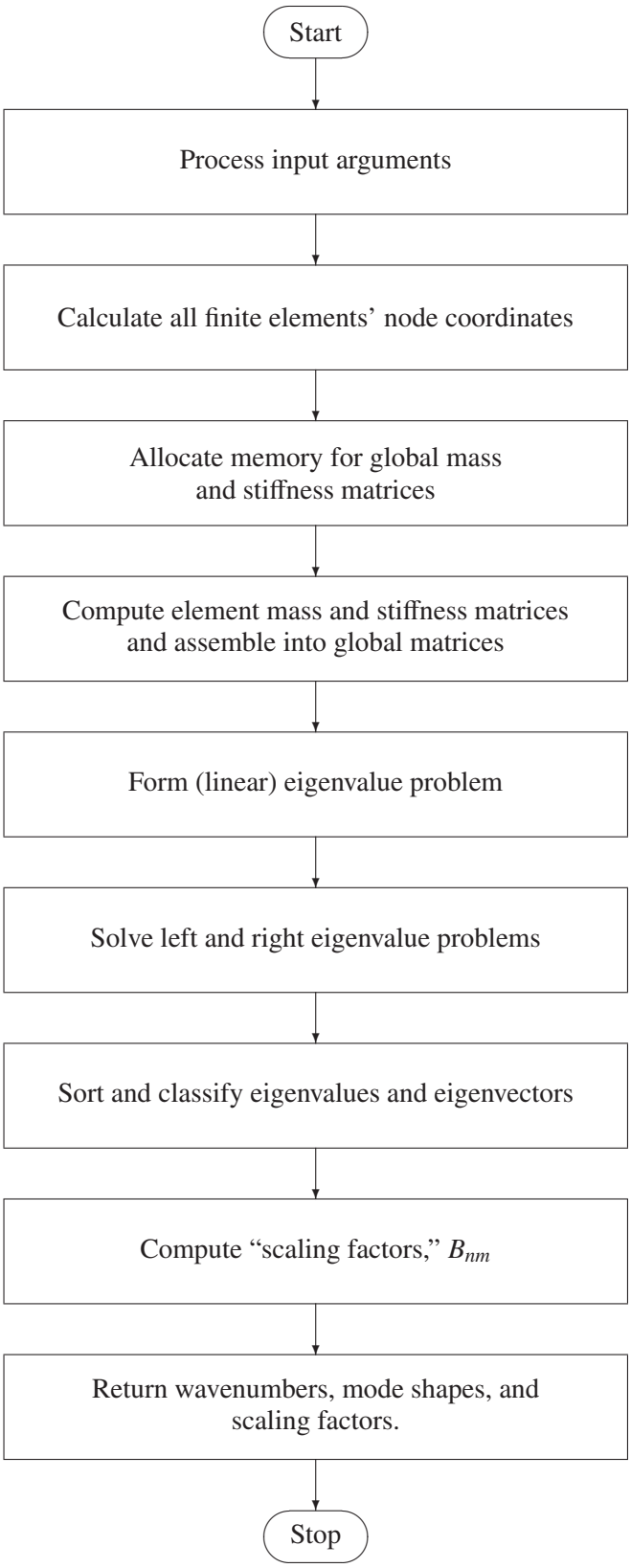

Figure C.4. A high level flowchart for Listing C.4.

Listing C.1. MATLAB® code to compute (finite) element stiffness and mass matrices.

```
clear; %Clear the workspace.
clc; %Clear the screen.

syms xi r rkm Hk rki rko real %Define the "base" symbolic variables
                                    %which are required to be real.
syms lambda mu rho %Define the symbolic variables which correspond
                         %to the material properties.

N=[1/2*xi*(xi-1) (1-xi^2) 1/2*xi*(xi+1)] %Define the shape functions,
                                        %i.e., equation (B.2.4).

%Note: xi=2*(r-rkm)/Hk, equation (B.2.5).

%Compute derivative of shape functions using "Chain rule."
%N_r=diff(N,'xi')*diff(xi,'r').
N_r=diff(N,'xi')*2/Hk

%Matrix of elastic constants for equation (B.3.3).
D=[lambda+2*mu lambda lambda 0 0 0;
   lambda lambda+2*mu lambda 0 0 0;
   lambda lambda lambda+2*mu 0 0 0;
   0      0      0          mu 0 0;
   0      0      0          0 mu 0;
   0      0      0          0  0 mu]

%Note: r=Hk*xi/2+rkm [Derived from equation (B.2.5).]

%Compute strain transformation matrices, equation (B.3.1).

B1=[N_r 0 0 0 0 0 0;
    N/(Hk*xi/2+rkm) 0 0 0 0 0 0;
    0 0 0 0 0 0 0 0 0;
    0 0 0 N_r-N/(Hk*xi/2+rkm) 0 0 0;
    0 0 0 0 0 0 N_r;
    0 0 0 0 0 0 0 0 0];

B2=[0 0 0 0 0 0 0 0 0;
    0 0 0 N/(Hk*xi/2+rkm) 0 0 0;
    0 0 0 0 0 0 0 0 0;
    N/(Hk*xi/2+rkm) 0 0 0 0 0 0;
    0 0 0 0 0 0 0 0 0;
    0 0 0 0 0 0 N/(Hk*xi/2+rkm)];

B3=[0 0 0 0 0 0 0 0 0;
    0 0 0 0 0 0 0 0 0;
    0 0 0 0 0 0 N;
    0 0 0 0 0 0 0;
    N 0 0 0 0 0 0;
    0 0 0 N 0 0 0]
```

(Continued on next page...)

Listing C.1. MATLAB® code to compute (finite) element stiffness and mass matrices. (Continued from previous page.)

```
%Set up shape functions for element mass matrix.
NM=[N 0 0 0 0 0 0;
    0 0 0 N 0 0 0;
    0 0 0 0 0 0 N];

%Notes on the Jacobian:
%X=N*[rkm-Hk/2 rkm rkm+Hk/2]',
%dXdxi=diff(X,'xi').

%Compute determinant of the Jacobian matrix.
detJ=Hk/2;

%Symbolically evaluate the element stiffness and mass matrices,
%equation (B.4.7).
K1=simple(int(B1'*D*B1*(Hk*xi/2+rkm)*detJ,'xi',-1,1))
K2=simple(int((B1'*D*B2-B2'*D*B1)*(Hk*xi/2+rkm)*detJ,'xi',-1,1))
K3=simple(int((B1'*D*B3-B3'*D*B1)*(Hk*xi/2+rkm)*detJ,'xi',-1,1))
K4=simple(int(B2'*D*B2*(Hk*xi/2+rkm)*detJ,'xi',-1,1))
K5=simple(int((B2'*D*B3+B3'*D*B2)*(Hk*xi/2+rkm)*detJ,'xi',-1,1))
K6=simple(int(B3'*D*B3*(Hk*xi/2+rkm)*detJ,'xi',-1,1))
M=simple(int(rho*NM'*NM*(Hk*xi/2+rkm)*detJ,'xi',-1,1))

%Write individual stiffness and mass matrices to ASCII plain text
%files for later use by assembly routine.  Use the ccode command
%to convert from symbolic data type to a string of characters.

fid=fopen('K1.txt', 'wt');
for i=1:1:9
    for j=i:1:9
        fprintf(fid,'%s%d%d%c%c\n','K1_',i,j,'=',ccode(K1(i,j)));
    end
end
fclose(fid);

fid=fopen('K2.txt', 'wt');
for i=1:1:9
    for j=i:1:9
        fprintf(fid,'%s%d%d%c%c\n','K2_',i,j,'=',ccode(K2(i,j)));
    end
end
fclose(fid);

fid=fopen('K3.txt', 'wt');
for i=1:1:9
    for j=i:1:9
        fprintf(fid,'%s%d%d%c%c\n','K3_',i,j,'=',ccode(K3(i,j)));
    end
end
fclose(fid);
```

(Continued on next page...)

Listing C.1. MATLAB® code to compute (finite) element stiffness and mass matrices. (Continued from previous page.)

```
100
101 fid=fopen('K4.txt', 'wt');
102 for i=1:1:9
103     for j=i:1:9
104         fprintf(fid,'%s%d%d%c%c\n','K4_',i,j,'=',ccode(K4(i,j)));
105     end
106 end
107 fclose(fid);
108
109 fid=fopen('K5.txt', 'wt');
110 for i=1:1:9
111     for j=i:1:9
112         fprintf(fid,'%s%d%d%c%c\n','K5_',i,j,'=',ccode(K5(i,j)));
113     end
114 end
115 fclose(fid);
116
117 fid=fopen('K6.txt', 'wt');
118 for i=1:1:9
119     for j=i:1:9
120         fprintf(fid,'%s%d%d%c%c\n','K6_',i,j,'=',ccode(K6(i,j)));
121     end
122 end
123 fclose(fid);
124
125 fid=fopen('M.txt', 'wt');
126 for i=1:1:9
127     for j=i:1:9
128         fprintf(fid,'%s%d%d%c%c\n','M_',i,j,'=',ccode(M(i,j)));
129     end
130 end
131 fclose(fid);
```

Listing C.2. Sample MATLAB® code to assemble global matrices from element matrices using the $\mathbf{K}_1$ stiffness matrix as an illustration.

```
clear; %Clear the workspace.
clc; %Clear the screen.

fid=fopen('assemble.txt', 'wt'); %Open file to write the assembled
%global matrix.

%There are 9 rows and 9 columns of each element stiffness and mass
%matrix giving a total of 81 elements.  Loop over all elements and
%assign them to the correct location in the global matrix.  Note
%that "i" is the element number and (2*N+1) is the total number of
%nodes.  This value is used to "offset" the circumferential and axial
%components of the element matrices to the global matrices.

%Loop over all element matrix components.
for n=1:1:9
    for m=n:1:9
        %Main diagonal.
        if m==n
            if n<4
                if m<4
                    %No row or column offset needed.
                    str=['K1(2*(i-1)+' num2str(n) ',2*(i-1)+'...
                        num2str(m) ')=K1(2*(i-1)+' num2str(n)...
                        ',2*(i-1)+' num2str(m) ')+K1_' num2str(n)...
                        num2str(m) ';%K1(' num2str(n) ','...
                        num2str(m) ')'];
                    fprintf(fid,'%s\n',str);
                elseif m<7
                    %No row and one column offset needed.
                    str=['K1(2*(i-1)+' num2str(n) ',2*(i-1)+'...
                        num2str(m-3) '+2*N+1)=K1(2*(i-1)+'...
                        num2str(n) ',2*(i-1)+' num2str(m-3)...
                        '+2*N+1)+K1_' num2str(n) num2str(m)...
                        ';%K1(' num2str(n) ',' num2str(m) ')'];
                    fprintf(fid,'%s\n',str);
                else
                    %No row and two column offsets needed.
                    str=['K1(2*(i-1)+' num2str(n) ',2*(i-1)+'...
                        num2str(m-6) '+4*N+2)=K1(2*(i-1)+'...
                        num2str(n) ',2*(i-1)+' num2str(m-6)...
                        '+4*N+2)+K1_' num2str(n) num2str(m)...
                        ';%K1(' num2str(n) ',' num2str(m) ')'];
                    fprintf(fid,'%s\n',str);
                end
            elseif n<7
                if m<4
                    %One row and no column offset needed.
                    str=['K1(2*(i-1)+' num2str(n-3)...
                        '+2*N+1,2*(i-1)+' num2str(m)...
```

(Continued on next page...)

Listing C.2. Sample MATLAB® code to assemble global matrices from element matrices using the $\mathbf{K}_1$ stiffness matrix as an illustration. (Continued from previous page.)

```
                        ')=K1(2*(i-1)+' num2str(n-3)...
                        '+2*N+1,2*(i-1)+' num2str(m) ')+K1_'...
                        num2str(n) num2str(m) ';%K1(' num2str(n)...
                        ',' num2str(m) ')'];
                    fprintf(fid,'%s\n',str);
                elseif m<7
                    %One row and column offset needed.
                    str=['K1(2*(i-1)+' num2str(n-3)...
                        '+2*N+1,2*(i-1)+' num2str(m-3)...
                        '+2*N+1)=K1(2*(i-1)+' num2str(n-3)...
                        '+2*N+1,2*(i-1)+' num2str(m-3)...
                        '+2*N+1)+K1_' num2str(n) num2str(m)...
                        ';%K1(' num2str(n) ',' num2str(m) ')'];
                    fprintf(fid,'%s\n',str);
                else
                    %One row and two column offsets needed.
                    str=['K1(2*(i-1)+' num2str(n-3)...
                        '+2*N+1,2*(i-1)+' num2str(m-6)...
                        '+4*N+2)=K1(2*(i-1)+' num2str(n-3)...
                        '+2*N+1,2*(i-1)+' num2str(m-6)...
                        '+4*N+2)+K1_' num2str(n) num2str(m)...
                        ';%K1(' num2str(n) ',' num2str(m) ')'];
                    fprintf(fid,'%s\n',str);
                end
            else
                if m<4
                    %Two row and no column offsets needed.
                    str=['K1(2*(i-1)+' num2str(n-6)...
                        '+4*N+2,2*(i-1)+' num2str(m)...
                        ')=K1(2*(i-1)+' num2str(n-6)...
                        '+4*N+2,2*(i-1)+' num2str(m) ')+K1_'...
                        num2str(n) num2str(m) ';%K1(' num2str(n)...
                        ',' num2str(m) ')'];
                    fprintf(fid,'%s\n',str);
                elseif m<7
                    %Two row and one column offsets needed.
                    str=['K1(2*(i-1)+' num2str(n-6)...
                        '+4*N+2,2*(i-1)+' num2str(m-3)...
                        '+2*N+1)=K1(2*(i-1)+' num2str(n-6)...
                        '+4*N+2,2*(i-1)+' num2str(m-3)...
                        '+2*N+1)+K1_' num2str(n) num2str(m)...
                        ';%K1(' num2str(n) ',' num2str(m) ')'];
                    fprintf(fid,'%s\n',str);
                else
                    %Two row and column offsets needed.
                    str=['K1(2*(i-1)+' num2str(n-6)...
                        '+4*N+2,2*(i-1)+' num2str(m-6)...
                        '+4*N+2)=K1(2*(i-1)+' num2str(n-6)...
                        '+4*N+2,2*(i-1)+' num2str(m-6)...
```

(Continued on next page...)

Listing C.2. Sample MATLAB® code to assemble global matrices from element matrices using the $\mathbf{K}_1$ stiffness matrix as an illustration. (Continued from previous page.)

```
                        '+4*N+2)+K1_' num2str(n) num2str(m)...
                        ';%K1(' num2str(n) ',' num2str(m) ')'];
                    fprintf(fid,'%s\n',str);
                end
            end
        else
            %Off diagonal terms.  Take advantage of symmetry (in
            %this case).  Note the usefulness of interchanging
              %indices.
            if n<4
                if m<4
                    %No row or column offset needed.
                    str=['K1(2*(i-1)+' num2str(n) ',2*(i-1)+'...
                        num2str(m) ')=K1(2*(i-1)+' num2str(n)...
                        ',2*(i-1)+' num2str(m) ')+K1_' num2str(n)...
                        num2str(m) ';%K1(' num2str(n) ','...
                        num2str(m) ')'];
                    fprintf(fid,'%s\n',str);
                    str=['K1(2*(i-1)+' num2str(m) ',2*(i-1)+'...
                        num2str(n) ')=K1(2*(i-1)+' num2str(m)...
                        ',2*(i-1)+' num2str(n) ')+K1_' num2str(n)...
                        num2str(m) ';%K1(' num2str(m) ','...
                        num2str(n) ')'];
                    fprintf(fid,'%s\n',str);
                elseif m<7
                    %No row and one column offset needed.
                    str=['K1(2*(i-1)+' num2str(n) ',2*(i-1)+'...
                        num2str(m-3) '+2*N+1)=K1(2*(i-1)+'...
                        num2str(n) ',2*(i-1)+' num2str(m-3)...
                        '+2*N+1)+K1_' num2str(n) num2str(m)...
                        ';%K1(' num2str(n) ',' num2str(m) ')'];
                    fprintf(fid,'%s\n',str);
                    str=['K1(2*(i-1)+' num2str(m-3)...
                        '+2*N+1,2*(i-1)+' num2str(n)...
                        ')=K1(2*(i-1)+' num2str(m-3)...
                        '+2*N+1,2*(i-1)+' num2str(n) ')+K1_'...
                        num2str(n) num2str(m) ';%K1(' num2str(m)...
                        ',' num2str(n) ')'];
                    fprintf(fid,'%s\n',str);
                else
                    %No row and two column offsets needed.
                    str=['K1(2*(i-1)+' num2str(n) ',2*(i-1)+'...
                        num2str(m-6) '+4*N+2)=K1(2*(i-1)+'...
                        num2str(n) ',2*(i-1)+' num2str(m-6)...
                        '+4*N+2)+K1_' num2str(n)  num2str(m)...
                        ';%K1(' num2str(n) ',' num2str(m) ')'];
                    fprintf(fid,'%s\n',str);
                    str=['K1(2*(i-1)+' num2str(m-6)...
                        '+4*N+2,2*(i-1)+' num2str(n)...
```

(Continued on next page...)

Listing C.2. Sample MATLAB® code to assemble global matrices from element matrices using the $\mathbf{K}_1$ stiffness matrix as an illustration. (Continued from previous page.)

```
148                         ')=K1(2*(i-1)+' num2str(m-6)...
149                         '+4*N+2,2*(i-1)+' num2str(n) ')+K1_'...
150                         num2str(n) num2str(m) ';%K1(' num2str(m)...
151                         ',' num2str(n) ')'];
152                     fprintf(fid,'%s\n',str);
153                 end
154             elseif n<7
155                 if m<4
156                     %One row and no column offset needed.
157                     str=['K1(2*(i-1)+' num2str(n-3)...
158                         '+2*N+1,2*(i-1)+' num2str(m)...
159                         ')=K1(2*(i-1)+' num2str(n-3)...
160                         '+2*N+1,2*(i-1)+' num2str(m) ')+K1_'...
161                         num2str(n) num2str(m) ';%K1(' num2str(n)...
162                         ',' num2str(m) ')'];
163                     fprintf(fid,'%s\n',str);
164                     str=['K1(2*(i-1)+' num2str(m) ',2*(i-1)+'...
165                         num2str(n-3) '+2*N+1)=K1(2*(i-1)+'...
166                         num2str(m) ',2*(i-1)+' num2str(n-3)...
167                         '+2*N+1)+K1_' num2str(n) num2str(m)...
168                         ';%K1(' num2str(m) ',' num2str(n) ')'];
169                     fprintf(fid,'%s\n',str);
170                 elseif m<7
171                     %One row and column offset needed.
172                     str=['K1(2*(i-1)+' num2str(n-3)...
173                         '+2*N+1,2*(i-1)+' num2str(m-3)...
174                         '+2*N+1)=K1(2*(i-1)+' num2str(n-3)...
175                         '+2*N+1,2*(i-1)+' num2str(m-3)...
176                         '+2*N+1)+K1_' num2str(n)  num2str(m)...
177                         ';%K1(' num2str(n) ',' num2str(m) ')'];
178                     fprintf(fid,'%s\n',str);
179                     str=['K1(2*(i-1)+' num2str(m-3)...
180                         '+2*N+1,2*(i-1)+' num2str(n-3)...
181                         '+2*N+1)=K1(2*(i-1)+' num2str(m-3)...
182                         '+2*N+1,2*(i-1)+' num2str(n-3)...
183                         '+2*N+1)+K1_' num2str(n) num2str(m)...
184                         ';%K1(' num2str(m) ',' num2str(n) ')'];
185                     fprintf(fid,'%s\n',str);
186                 else
187                     %Two row and column offsets needed.
188                     str=['K1(2*(i-1)+' num2str(n-3)...
189                         '+2*N+1,2*(i-1)+' num2str(m-6)...
190                         '+4*N+2)=K1(2*(i-1)+' num2str(n-3)...
191                         '+2*N+1,2*(i-1)+' num2str(m-6)...
192                         '+4*N+2)+K1_' num2str(n) num2str(m)...
193                         ';%K1(' num2str(n) ',' num2str(m) ')'];
194                     fprintf(fid,'%s\n',str);
195                     str=['K1(2*(i-1)+' num2str(m-6)...
196                         '+4*N+2,2*(i-1)+' num2str(m-6)...
```

(Continued on next page...)

Listing C.2. Sample MATLAB® code to assemble global matrices from element matrices using the $\mathbf{K}_1$ stiffness matrix as an illustration. (Continued from previous page.)

```
                        '+2*N+1)=K1(2*(i-1)+' num2str(m-6)...
                        '+4*N+2,2*(i-1)+' num2str(m-6)...
                        '+2*N+1)+K1_' num2str(n) num2str(m)...
                        ';%K1(' num2str(m) ',' num2str(n) ')'];
                    fprintf(fid,'%s\n',str);
                end
            else
                if m<4
                    %No row or column offsets needed.
                    str=['K1(2*(i-1)+' num2str(n-6)...
                        '+4*N+2,2*(i-1)+' num2str(m)...
                        ')=K1(2*(i-1)+' num2str(n-6)...
                        '+4*N+2,2*(i-1)+' num2str(m) ')+K1_'...
                        num2str(n) num2str(m) ';%K1(' num2str(n)...
                        ',' num2str(m) ')'];
                    fprintf(fid,'%s\n',str);
                    str=['K1(2*(i-1)+' num2str(m) ',2*(i-1)+'...
                        num2str(n-6) '+4*N+2)=K1(2*(i-1)+'...
                        num2str(m) ',2*(i-1)+' num2str(n-6)...
                        '+4*N+2)+K1_' num2str(n) num2str(m)...
                        ';%K1(' num2str(m) ',' num2str(n) ')'];
                    fprintf(fid,'%s\n',str);
                elseif m<7
                    %One row and column offset needed.
                    str=['K1(2*(i-1)+' num2str(n-6)...
                        '+4*N+2,2*(i-1)+' num2str(m-3)...
                        '+2*N+1)=K1(2*(i-1)+' num2str(n-6)...
                        '+4*N+2,2*(i-1)+' num2str(m-3)...
                        '+2*N+1)+K1_' num2str(n) num2str(m)...
                        ';%K1(' num2str(n) ',' num2str(m) ')'];
                    fprintf(fid,'%s\n',str);
                    str=['K1(2*(i-1)+' num2str(m-3)...
                        '+2*N+1,2*(i-1)+' num2str(n-6)...
                        '+4*N+2)=K1(2*(i-1)+' num2str(m-3)...
                        '+2*N+1,2*(i-1)+' num2str(n-6)...
                        '+4*N+2)+K1_' num2str(n) num2str(m)...
                        ';%K1(' num2str(m) ',' num2str(n) ')'];
                    fprintf(fid,'%s\n',str);
                else
                    %Two row and column offsets needed.
                    str=['K1(2*(i-1)+' num2str(n-6)...
                        '+4*N+2,2*(i-1)+' num2str(m-6)...
                        '+4*N+2)=K1(2*(i-1)+' num2str(n-6)...
                        '+4*N+2,2*(i-1)+' num2str(m-6)...
                        '+4*N+2)+K1_' num2str(n) num2str(m)...
                        ';%K1(' num2str(n) ',' num2str(m) ')'];
                    fprintf(fid,'%s\n',str);
                    str=['K1(2*(i-1)+' num2str(m-6)...
                        '+4*N+2,2*(i-1)+' num2str(n-6)...
```

(Continued on next page...)

Listing C.2. Sample MATLAB® code to assemble global matrices from element matrices using the $\mathbf{K}_1$ stiffness matrix as an illustration. (Continued from previous page.)

```
                            '+4*N+2)=K1(2*(i-1)+' num2str(m-6)...
                            '+4*N+2,2*(i-1)+' num2str(n-6)...
                            '+4*N+2)+K1_' num2str(n) num2str(m)...
                            ';%K1(' num2str(m) ',' num2str(n) ')'];
                        fprintf(fid,'%s\n',str);
                    end
                end
            end
        end
    end

    fclose(fid); %Close the output file.
```

Listing C.3. Sketch of the MATLAB® code used to compute the approximate wave functions from equation (2.3.5).

```
function [Omega,CEV]=Omegakin(lambda_mu,H_R,n,k,N,dof)
% Returns the non-dimensional frequency for a homogeneous,
% isotropic cylinder when given the wave-number.
% Omegakin(lambda_mu,H_R,n,k,N,dof) returns the non-dimensional
% frequency for a homogeneous, isotropic cylinder when given the
% non-dimensional wave-number, k.
% lambda_mu = ratio of Lame constants lambda and mu.
% H_R = ratio of wall thickness, H, to mean pipe radius, R.
% n = circumferential wave-number (defaults to 0).
% k = non-dimensional wave-number (defaults to 0).
% N = number of finite elements (defaults to 10).
% dof = number of displacement degrees of freedom at each node
% (defaults to 3).

% Code to check number and type of inputs and set default values.
% Actual code removed for brevity.

% Code to perform "sanity" checks.  %Actual code removed for brevity.

% Set H=1, mu=1, rho=1, non-dimensional values are used throughout.
H=1;
mu=1;
rho=1;

%Calculate R and lambda
R=H/H_R;
lambda=mu*lambda_mu;

%Pre-allocate memory for coordinates of finite elements' middle
%nodes.
rkm=zeros(N,1);

%Calculate element thicknesses and mean radii
Hk=H/N*ones(N,1);

% Inner radius of pipe.
Ri=(2-H_R)/2/H_R*H;

% First middle node location.
rkm(1)=Ri+Hk(1)/2;

% Remaining middle node locations
for i=2:1:N
    rkm(i)=rkm(i-1)+(Hk(i)+Hk(i-1))/2;
end

% Element and global stiffness and mass matrices for the general
%case.
if dof==3
```

(Continued on next page...)

Listing C.3. Sketch of the MATLAB® code used to compute the approximate wave functions from equation (2.3.5). (Continued from previous page.)

```
50      %Allocate memory for K1 and M (always used).
51      K1=zeros(dof*(2*N+1));
52      M=zeros(dof*(2*N+1));
53      %Allocate memory for K2 and K4 (used if n~=0).
54      if n~=0
55          K2=zeros(dof*(2*N+1));
56          K4=zeros(dof*(2*N+1));
57      end
58      %Allocate memory for K3 and K6 (used if k~=0).
59      if k~=0
60          K3=zeros(dof*(2*N+1));
61          K6=zeros(dof*(2*N+1));
62          %If n~=0 K5 is also required.
63          if n~=0
64              K5=zeros(dof*(2*N+1));
65          end
66      end
67
68      %Compute element matrices and assemble.
69      %Loop over all elements.
70      for i=1:1:N
71          %Compute non-zero elements of K1.  This code is pasted
72          %from the output of Listing C.1.
73          %Zero elements are ignored and advantage is taken of
74          %symmetry.
75
76          %Actual code removed for brevity.
77
78          %Perform assembly for K1.  This code is pasted from the
79          %modified output of Listing C.2.
80          %Zero elements are ignored and advantage is taken of
81          %symmetry.
82
83          %Actual code removed for brevity.
84
85           %Compute non-zero elements of M.  This code is pasted
86          %from the output of Listing C.1.
87          %Zero elements are ignored and advantage is taken of
88          %symmetry.
89
90          %Actual code removed for brevity.
91
92          %Perform assembly for M.  This code is pasted from the
93          %modified output of Listing C.2.
94          %Zero elements are ignored and advantage is taken of
95          %symmetry.
96
97          %Actual code removed for brevity.
```

(Continued on next page...)

Listing C.3. Sketch of the MATLAB® code used to compute the approximate wave functions from equation (2.3.5). (Continued from previous page.)

```
99          if n~=0
100             %Compute non-zero elements of K2.  This code is pasted
101             %from the output of Listing C.1.
102             %Zero elements are ignored and advantage is taken of
103             %anti-symmetry.
104
105             %Actual code removed for brevity.
106
107             %Perform assembly for K2.  This code is pasted from the
108             %modified output of Listing C.2.
109             %Zero elements are ignored and advantage is taken of
110             %anti-symmetry.
111
112             %Actual code removed for brevity.
113
114             %Compute non-zero elements of K4.  This code is pasted
115             %from the output of Listing C.1.
116             %Zero elements are ignored and advantage is taken of
117             %symmetry.
118
119             %Actual code removed for brevity.
120
121             %Perform assembly for K4.  This code is pasted from the
122             %modified output of Listing C.2.
123             %Zero elements are ignored and advantage is taken of
124             %symmetry.
125
126             %Actual code removed for brevity.
127         end
128
129         if k~=0
130             %Compute non-zero elements of K3.  This code is pasted
131             %from the output of Listing C.1.
132             %Zero elements are ignored and advantage is taken of
133             %anti-symmetry.
134
135             %Actual code removed for brevity.
136
137             %Perform assembly for K3.  This code is pasted from the
138             %modified output of Listing C.2.
139             %Zero elements are ignored and advantage is taken of
140             %anti-symmetry.
141
142             %Actual code removed for brevity.
143
144             %Compute non-zero elements of K6.  This code is pasted
145             %from the output of Listing C.1.
146             %Zero elements are ignored and advantage is taken of
147             %symmetry.
```

(Continued on next page...)

Listing C.3. Sketch of the MATLAB® code used to compute the approximate wave functions from equation (2.3.5). (Continued from previous page.)

```
148             %Actual code removed for brevity.
149
150             %Perform assembly for K6.  This code is pasted from the
151             %modified output of Listing C.2.
152             %Zero elements are ignored and advantage is taken of
153             %symmetry.
154
155             %Actual code removed for brevity.
156
157             if n~=0
158                 %Compute non-zero elements of K5.  This code is
159                 %pasted from the output of Listing C.1.
160                 %Zero elements are ignored and advantage is taken
161                 %of symmetry.
162
163                 %Actual code removed for brevity.
164
165                 %Perform assembly for K5.  This code is pasted
166                 %from the modified output of Listing C.2.
167                 %Zero elements are ignored and advantage is taken of
168                 %anti-symmetry.
169
170                 %Actual code removed for brevity.
171             end
172         end
173     end
174 %Longitudinal modes.  Already checked to ensure that n=0.
175 elseif dof==2
176     %Allocate memory for K1 and M (always used).
177     K1=zeros(dof*(2*N+1));
178     M=zeros(dof*(2*N+1));
179
180     %Allocate memory for K3 and K6 (used if k~=0).
181     if k~=0
182         K3=zeros(dof*(2*N+1));
183         K6=zeros(dof*(2*N+1));
184     end
185
186     %Compute element matrices and assemble.
187     %Loop over all elements.
188     for i=1:1:N
189         %Compute non-zero elements of K1.  This code is pasted
190         %from the output of Listing C.1.
191         %Zero elements are ignored and advantage is taken of
192         %symmetry.
193
194         %Actual code removed for brevity.
```

(Continued on next page...)

Listing C.3. Sketch of the MATLAB® code used to compute the approximate wave functions from equation (2.3.5). (Continued from previous page.)

```
195         %Perform assembly for K1.  This code is pasted from the
196         %modified output of Listing C.2.
197         %Zero elements are ignored and advantage is taken of
198         %symmetry.
199
200         %Actual code removed for brevity.
201
202         %Compute non-zero elements of M.  This code is pasted
203         %from the output of Listing C.1.
204         %Zero elements are ignored and advantage is taken of
205         %symmetry.
206
207         %Actual code removed for brevity.
208
209         %Perform assembly for M.  This code is pasted from the
210         %modified output of Listing C.2.
211         %Zero elements are ignored and advantage is taken of
212         %symmetry.
213
214         %Actual code removed for brevity.
215
216         if k~=0
217             %Compute non-zero elements of K3.  This code is pasted
218             %from the output of Listing C.1.
219             %Zero elements are ignored and advantage is taken of
220             %anti-symmetry.
221
222             %Actual code removed for brevity.
223
224             %Perform assembly for K3.  This code is pasted from the
225             %modified output of Listing C.2.
226             %Zero elements are ignored and advantage is taken of
227             %anti-symmetry.
228
229             %Actual code removed for brevity.
230
231             %Compute non-zero elements of K6.  This code is pasted
232             %from the output of Listing C.1.
233             %Zero elements are ignored and advantage is taken of
234             %symmetry.
235
236             %Actual code removed for brevity.
237
238             %Perform assembly for K6.  This code is pasted from the
239             %modified output of Listing C.2.
240             %Zero elements are ignored and advantage is taken of
241             %symmetry.
242
243             %Actual code removed for brevity.
```

(Continued on next page...)

Listing C.3. Sketch of the MATLAB® code used to compute the approximate wave functions from equation (2.3.5). (Continued from previous page.)

```
244         end
245     end
246
247 %Torsional modes.  Already checked to ensure that n=0.
248 else
249     %Allocate memory for K1 and M (always used).
250     K1=zeros(dof*(2*N+1));
251     M=zeros(dof*(2*N+1));
252
253     %Allocate memory for K6 (used if k~=0).  (K3 vanishes for
254     %this case.)
255     if k~=0
256         K6=zeros(dof*(2*N+1));
257     end
258
259     %Compute element matrices and assemble.
260     %Loop over all elements.
261     for i=1:1:N
262         %Compute non-zero elements of K1.  This code is pasted
263         %from the output of Listing C.1.
264         %Zero elements are ignored and advantage is taken of
265         %symmetry.
266
267         %Actual code removed for brevity.
268
269         %Perform assembly for K1.  This code is pasted from the
270         %modified output of Listing C.2.
271         %Zero elements are ignored and advantage is taken of
272         %symmetry.
273
274         %Actual code removed for brevity.
275
276         %Compute non-zero elements of M.  This code is pasted
277         %from the output of Listing C.1.
278         %Zero elements are ignored and advantage is taken of
279         %symmetry.
280
281         %Actual code removed for brevity.
282
283         %Perform assembly for M.  This code is pasted from the
284         %modified output of Listing C.2.
285         %Zero elements are ignored and advantage is taken of
286         %symmetry.
287
288         %Actual code removed for brevity.
289
290         if k~=0
291             %Compute non-zero elements of K6.  This code is pasted
292             %from the output of Listing C.1.
```

(Continued on next page...)

Listing C.3. Sketch of the MATLAB® code used to compute the approximate wave functions from equation (2.3.5). (Continued from previous page.)

```
293             %Zero elements are ignored and advantage is taken of
294             %symmetry.
295             %Actual code removed for brevity.
296
297             %Perform assembly for K6.  This code is pasted from the
298             %modified output of Listing C.2.
299             %Zero elements are ignored and advantage is taken of
300             %symmetry.
301
302             %Actual code removed for brevity.
303         end
304     end
305 end
306
307 %Solution phase.
308
309 %Form the coefficient matrices for the generalized eigenvalue
310 %problem described by equation (2.3.5).
311 if dof==3
312     if k~=0
313         if n~=0
314             A=K1+j*n*K2+n*n*K4+j*k*(K3-j*n*K5)+k*k*K6;
315         else
316             A=K1+j*k*K3+k*k*K6;
317         end
318     else
319         if n~=0
320             A=K1+j*n*K2+n*n*K4;
321         else
322             A=K1;
323         end
324     end
325 elseif dof==2
326     if k~=0
327         A=K1+j*k*K3+k*k*K6;
328    else
329         A=K1;
330     end
331 else
332     if k~=0
333         A=K1+k*k*K6;
334     else
335         A=K1;
336     end
337 end
338
339 if nargout==1
340 %Solve eigenvalue problem and take the square root to get the
341 %frequencies corresponding to the assigned wave-numbers.
```

(Continued on next page...)

Listing C.3. Sketch of the MATLAB® code used to compute the approximate wave functions from equation (2.3.5). (Continued from previous page.)

```
342 Omega=sort(sqrt(eig(A,M)));
343 else
344 %Solve for the mode shapes as well as the frequencies because the
345 %user supplied two output arguments.  See MATLAB documentation for
346 %use of sort command.
347     [CEV,EV]=eig(A,M);
348     [Omega,idx]=sort(sqrt(diag(EV)));
349     CEV=CEV(:,idx);
350 end
```

Listing C.4. Sketch of the MATLAB® code used to compute the approximate wave functions using equation (2.3.6).

```
function [RREV,kR,RLEV,kL,Bnm]=kOmegain(lambda_mu,H_R,n,Omega,N,dof)
% Returns the right and left eigenvalues and eigenvectors and
% "scaling factor," Bnm, between the left and right eigenvectors,
% for positive axial offsets, for a homogeneous, isotropic cylinder
% when given the frequency and circumferential wave number.
% [RREV,kR,RLEV,kL,Bnm]=Ring_Loads(lambda_mu,H_R,n,Omega,N,dof)
% takes:
% lambda_mu = ratio of Lame constants lambda and mu,
% H_R = ratio of wall thickness, H, to pipe mean radius, R,
% n = circumferential wave-number (defaults to 0),
% Omega = non-dimensional frequency (defaults to 0),
% N = number of finite elements (defaults to 10),
% dof = number of displacement degrees of freedom at each node
% (defaults to 3), and returns
% RREV[2*dof*(2N+1)xdof*(2N+1)] = right eigenvectors,
% kR[2*dof*(2N+1)x1] = right eigenvalues,
% RLEV[2*dof*(2N+1)xdof*(2N+1)] = left eigenvectors,
% kR[2*dof*(2N+1)x1] = left eigenvectors,
% Bnm[2*dof*(2N+1)x1] = "scaling factors." See
% equation (2.3.8).

% Code to check number and type of inputs and set default values.
% Actual code removed for brevity.

% Code to perform "sanity" checks.
% Actual code removed for brevity.

% Set H=1, mu=1, rho=1, non-dimensional values are used throughout.
H=1;
mu=1;
rho=1;

%Calculate R and lambda
R=H/H_R;
lambda=mu*lambda_mu;

%Pre-allocate memory for coordinates of finite elements' middle
%nodes.
rkm=zeros(N,1);

%Calculate element thicknesses and mean radii
Hk=H/N*ones(N,1);

% Inner radius of pipe.
Ri=(2-H_R)/2/H_R*H;

% First middle node location.
rkm(1)=Ri+Hk(1)/2;
```

(Continued on next page...)

Listing C.4. Sketch of the MATLAB® code used to compute the approximate wave functions using equation (2.3.6). (Continued from previous page.)

```
% Remaining middle node locations
for i=2:1:N
    rkm(i)=rkm(i-1)+(Hk(i)+Hk(i-1))/2;
end

% Element and global stiffness and mass matrices for the general
% nonaxisymmetric case.
if dof==3
    %Allocate memory for K1, K3, and K6 (always used).
    K1=zeros(dof*(2*N+1));
    K3=zeros(dof*(2*N+1));
    K6=zeros(dof*(2*N+1));

    %Allocate memory for K2, K4, and K5 (used if n~=0).
    if n~=0
        K2=zeros(dof*(2*N+1));
        K4=zeros(dof*(2*N+1));
        K5=zeros(dof*(2*N+1));
    end

    %Allocate memory for M (used if Omega~=0).
    if Omega~=0
        M=zeros(dof*(2*N+1));
    end

    %Compute element matrices and assemble.
    %Loop over all elements.
    for i=1:1:N

        %Compute non-zero elements of K1.  This code is pasted
        %from the output of Listing C.1.
        %Zero elements are ignored and advantage is taken of
        %symmetry.

        %Actual code removed for brevity.

        %Perform assembly for K1.  This code is pasted from the
        %modified output of Listing C.2.
        %Zero elements are ignored and advantage is taken of
        %symmetry.

        %Actual code removed for brevity.

        %Compute non-zero elements of K3.  This code is pasted
        %from the output of Listing C.1.
        %Zero elements are ignored and advantage is taken of
        %anti-symmetry.

        %Actual code removed for brevity.
```

(Continued on next page...)

Listing C.4. Sketch of the MATLAB® code used to compute the approximate wave functions using equation (2.3.6). (Continued from previous page.)

```
98          %Perform assembly for K3.  This code is pasted from the
99          %modified output of Listing C.2.
100         %Zero elements are ignored and advantage is taken of
101         %anti-symmetry.
102
103         %Actual code removed for brevity.
104
105         %Compute non-zero elements of K6.  This code is pasted
106         %from the output of Listing C.1.
107         %Zero elements are ignored and advantage is taken of
108         %symmetry.
109
110         %Actual code removed for brevity.
111
112         %Perform assembly for K6.  This code is pasted from the
113         %modified output of Listing C.2.
114         %Zero elements are ignored and advantage is taken of
115         %symmetry.
116
117         %Actual code removed for brevity.
118
119         if Omega~=0
120             %Compute non-zero elements of M.  This code is pasted
121             %from the output of Listing C.1.
122             %Zero elements are ignored and advantage is taken of
123             %symmetry.
124
125             %Actual code removed for brevity.
126
127             %Perform assembly for M.  This code is pasted from the
128             %modified output of Listing C.2.
129             %Zero elements are ignored and advantage is taken of
130             %symmetry.
131
132             %Actual code removed for brevity.
133         end
134
135         if n~=0
136             %Compute non-zero elements of K2.  This code is pasted
137             %from the output of Listing C.1.
138             %Zero elements are ignored and advantage is taken of
139             %anti-symmetry.
140
141             %Actual code removed for brevity.
142
143             %Perform assembly for K2.  This code is pasted from the
144             %modified output of Listing C.2.
145             %Zero elements are ignored and advantage is taken of
146             %anti-symmetry.
```

(Continued on next page...)

Listing C.4. Sketch of the MATLAB® code used to compute the approximate wave functions using equation (2.3.6). (Continued from previous page.)

```
148             %Actual code removed for brevity.
149
150             %Compute non-zero elements of K4.  This code is pasted
151             %from the output of Listing C.1.
152             %Zero elements are ignored and advantage is taken of
153             %symmetry.
154
155             %Actual code removed for brevity.
156
157             %Perform assembly for K4.  This code is pasted from the
158             %modified output of Listing C.2.
159             %Zero elements are ignored and advantage is taken of
160             %symmetry.
161
162             %Actual code removed for brevity.
163
164             %Compute non-zero elements of K5.  This code is pasted
165             %from the output of Listing C.1.
166             %Zero elements are ignored and advantage is taken of
167             %symmetry.
168
169             %Actual code removed for brevity.
170
171             %Perform assembly for K5.  This code is pasted from the
172             %modified output of Listing C.2.
173             %Zero elements are ignored and advantage is taken of
174             %symmetry.
175
176             %Actual code removed for brevity.
177         end
178     end
179     %Longitudinal modes.  Already checked to ensure that n=0.
180 elseif dof==2
181     %Allocate memory for K1, K3, and K6 (always used).
182     K1=zeros(dof*(2*N+1));
183     K3=zeros(dof*(2*N+1));
184     K6=zeros(dof*(2*N+1));
185
186     %Allocate memory for M (used if Omega~=0).
187     if Omega~=0
188         M=zeros(dof*(2*N+1));
189     end
190
191     %Compute element matrices and assemble.
192     %Loop over all elements.
193     for i=1:1:N
194         %Compute non-zero elements of K1.  This code is pasted
195         %from the output of Listing C.1.
196         %Zero elements are ignored and advantage is taken of
```

(Continued on next page...)

Listing C.4. Sketch of the MATLAB® code used to compute the approximate wave functions using equation (2.3.6). (Continued from previous page.)

```
197         %symmetry.
198
199         %Actual code removed for brevity.
200
201         %Perform assembly for K1.  This code is pasted from the
202         %modified output of Listing C.2.
203         %Zero elements are ignored and advantage is taken of
204         %symmetry.
205
206         %Actual code removed for brevity.
207
208         %Compute non-zero elements of K3.  This code is pasted
209         %from the output of Listing C.1.
210         %Zero elements are ignored and advantage is taken of
211         %anti-symmetry.
212
213         %Actual code removed for brevity.
214
215         %Perform assembly for K3.  This code is pasted from the
216         %modified output of Listing C.2.
217         %Zero elements are ignored and advantage is taken of
218         %anti-symmetry.
219
220         %Actual code removed for brevity.
221
222         %Compute non-zero elements of K6.  This code is pasted
223         %from the output of Listing C.1.
224         %Zero elements are ignored and advantage is taken of
225         %symmetry.
226
227         %Actual code removed for brevity.
228
229         %Perform assembly for K6.  This code is pasted from the
230         %modified output of Listing C.2.
231         %Zero elements are ignored and advantage is taken of
232         %symmetry.
233
234         %Actual code removed for brevity.
235
236         if Omega~=0
237             %Compute non-zero elements of M.  This code is pasted
238             %from the output of Listing C.1.
239             %Zero elements are ignored and advantage is taken of
240             %symmetry.
241
242             %Actual code removed for brevity.
243
244             %Perform assembly for M.  This code is pasted from the
245             %modified output of Listing C.2.
```

(Continued on next page...)

Listing C.4. Sketch of the MATLAB® code used to compute the approximate wave functions using equation (2.3.6). (Continued from previous page.)

```
246             %Zero elements are ignored and advantage is taken of
247             %symmetry.
248
249             %Actual code removed for brevity.
250         end
251     end
252 %Torsional modes.  Already checked to ensure that n=0.
253 else
254     %Allocate memory for K1 and K6 (always used).
255     K1=zeros(dof*(2*N+1));
256     K6=zeros(dof*(2*N+1));
257     if Omega~=0
258         M=zeros(dof*(2*N+1));
259     end
260
261     for i=1:1:N
262         %Compute non-zero elements of K1.  This code is pasted
263         %from the output of Listing C.1.
264         %Zero elements are ignored and advantage is taken of
265         %symmetry.
266
267         %Actual code removed for brevity.
268
269         %Perform assembly for K1.  This code is pasted from the
270         %modified output of Listing C.2.
271         %Zero elements are ignored and advantage is taken of
272         %symmetry.
273
274         %Actual code removed for brevity.
275
276         %Compute non-zero elements of K6.  This code is pasted
277         %from the output of Listing C.1.
278         %Zero elements are ignored and advantage is taken of
279         %symmetry.
280
281         %Actual code removed for brevity.
282
283         %Perform assembly for K6.  This code is pasted from the
284         %modified output of Listing C.2.
285         %Zero elements are ignored and advantage is taken of
286         %symmetry.
287
288         %Actual code removed for brevity.
289         if Omega~=0
290             %Compute non-zero elements of M.  This code is pasted
291             %from the output of Listing C.1.
292             %Zero elements are ignored and advantage is taken of
293             %symmetry.
```

(Continued on next page...)

Listing C.4. Sketch of the MATLAB® code used to compute the approximate wave functions using equation (2.3.6). (Continued from previous page.)

```
            %Actual code removed for brevity.

            %Perform assembly for M.  This code is pasted from the
            %modified output of Listing C.2.
            %Zero elements are ignored and advantage is taken of
            %symmetry.

            %Actual code removed for brevity.
        end
    end
end

%Solution phase.

%Form the coefficient matrices for the generalized eigenvalue
%problem described by equation (2.3.6).
%Convert quadratic eigenvalue problem to linear eigenvalue problem.
if dof==3
    if n~=0
        if Omega~=0
            A=[zeros(dof*(2*N+1)) eye(dof*(2*N+1)); ...
                K1+j*n*K2+n*n*K4-Omega*Omega*M j*(K3-j*n*K5)];
            B=[eye(dof*(2*N+1)) zeros(dof*(2*N+1)); ...
                zeros(dof*(2*N+1)) -K6];
        else
            A=[zeros(dof*(2*N+1)) eye(dof*(2*N+1)); ...
                K1+j*n*K2+n*n*K4 j*(K3-j*n*K5)];
            B=[eye(dof*(2*N+1)) zeros(dof*(2*N+1)); ...
                zeros(dof*(2*N+1)) -K6];
        end
    else
        if Omega~=0
            A=[zeros(dof*(2*N+1)) eye(dof*(2*N+1)); ...
                K1-Omega*Omega*M j*K3];
            B=[eye(dof*(2*N+1)) zeros(dof*(2*N+1)); ...
                zeros(dof*(2*N+1)) -K6];
        else
            A=[zeros(dof*(2*N+1)) eye(dof*(2*N+1)); ...
                K1 j*K3];
            B=[eye(dof*(2*N+1)) zeros(dof*(2*N+1)); ...
                zeros(dof*(2*N+1)) -K6];
        end
    end
elseif dof==2
    if Omega~=0
        A=[zeros(dof*(2*N+1)) eye(dof*(2*N+1)); ...
            K1-Omega*Omega*M j*K3];
        B=[eye(dof*(2*N+1)) zeros(dof*(2*N+1)); ...
            zeros(dof*(2*N+1)) -K6];
```

(Continued on next page...)

Listing C.4. Sketch of the MATLAB® code used to compute the approximate wave functions using equation (2.3.6). (Continued from previous page.)

```
344     else
345         A=[zeros(dof*(2*N+1)) eye(dof*(2*N+1)); K1 j*K3];
346         B=[eye(dof*(2*N+1)) zeros(dof*(2*N+1)); ...
347             zeros(dof*(2*N+1)) -K6];
348     end
349 else
350     if Omega~=0
351         A=[zeros(dof*(2*N+1)) eye(dof*(2*N+1)); ...
352             K1-Omega*Omega*M zeros(dof*(2*N+1))];
353         B=[eye(dof*(2*N+1)) zeros(dof*(2*N+1)); ...
354             zeros(dof*(2*N+1)) -K6];
355     else
356         A=[zeros(dof*(2*N+1)) eye(dof*(2*N+1)); ...
357             K1 zeros(dof*(2*N+1))];
358         B=[eye(dof*(2*N+1)) zeros(dof*(2*N+1)); ...
359             zeros(dof*(2*N+1)) -K6];
360     end
361 end
362
363 %Call eigenvalue solver.
364
365 %Right Eigenvalue Problem.
366 [REV,Rval]=eig(A,B);
367 Rval=diag(Rval);
368 %Left Eigenvalue Problem.
369 [LEV,Lval]=eig(A.',B.');
370 Lval=diag(Lval);
371
372 %Sort Eigenvalues, keep only those propagating and/or stable to
373 %the right.
374
375 %Right Eigenvalue Problem.
376
377 %Real Eigenvalues:
378
379 %Handle eigenvalues almost equal to zero, select based on stability.
380 krrR=Rval(abs(Rval)<1E-6&imag(Rval)>=0);
381 krrR=[krrR Rval((abs(imag(Rval)))<1E-4&real(Rval)>=0&...
382     abs(Rval)>=1E-6)];
383 tmp=real(krrR);
384 [tmp,Index]=sort(tmp,'descend');
385 krrR=krrR(Index);
386
387 %Imaginary Eigenvalues:
388 kirR=Rval(imag(Rval)>=1E-4&abs(real(Rval))<1E-4);
389 tmp=imag(kirR);
390 [tmp,Index]=sort(tmp,'ascend');
391 kirR=kirR(Index);
```

(Continued on next page...)

Listing C.4. Sketch of the MATLAB® code used to compute the approximate wave functions using equation (2.3.6). (Continued from previous page.)

```
%Complex Eigenvalues:
kcrR=Rval(imag(Rval)>=1E-4&abs(real(Rval))>=1E-4);
kcrR=sort(kcrR,'ascend');

if mod(length(kcrR),2)~=0
    warning(['Complex eigenvalues for the right eigenproblem do'...
        'not occur in pairs.']);
end

for i=1:1:length(kcrR)/2
    if real(kcrR(2*i-1))<0
        tmp=kcrR(2*i-1);
        kcrR(2*i-1)=kcrR(2*i);
        kcrR(2*i)=tmp;
    end

    if abs(conj(kcrR(2*i-1))+kcrR(2*i))>1E-4
        warning(['Complex eigenvalues for the right eigenproblem'...
            'do not occur in negative complex conjugate pairs.']);
    end
end

if ~isempty(krrR)&&~isempty(kirR)
    kR=[krrR;kirR];
elseif ~isempty(kirR)&&isempty(krrR)
    kR=kirR;
elseif ~isempty(krrR)&&isempty(kirR)
    kR=krrR;
elseif isempty(krrR)&&isempty(kirR)
    kR=[];
else
    error(['Unhandled number of propagating and non-propagating'...
            ' modes']);
end

kR=sort(kR,'ascend');
for i=1:1:length(kcrR)/2
    Index=sum(abs(kR)<abs(kcrR(2*i-1)));
    kR=[kR(1:Index);kcrR(2*i-1);kcrR(2*i);kR(Index+1:end)];
end

%Left Eigenvalue Problem.

%Real Eigenvalues:
%Handle eigenvalues almost equal to zero, select based on stability.
krrL=Lval(abs(Lval)<1E-6&imag(Lval)>=0);
krrL=[krrL Lval((abs(imag(Lval)))<1E-4&real(Lval)>=0&...
    abs(Lval)>=1E-6)];
tmp=real(krrL);
```

(Continued on next page...)

Listing C.4. Sketch of the MATLAB® code used to compute the approximate wave functions using equation (2.3.6). (Continued from previous page.)

```
[tmp,Index]=sort(tmp,'descend');
krrL=krrL(Index);

%Imaginary Eigenvalues:
kirL=Lval(imag(Lval)>=1E-4&abs(real(Lval))<1E-4);
tmp=imag(kirL);
[tmp,Index]=sort(tmp,'ascend');
kirL=kirL(Index);

%Complex Eigenvalues:
kcrL=Lval(imag(Lval)>=1E-4&abs(real(Lval))>=1E-4);
kcrL=sort(kcrL,'ascend');

if mod(length(kcrL),2)~=0
    warning(['Complex eigenvalues for the left eigenproblem'...
        'do not occur in pairs.']);
end

for i=1:1:length(kcrL)/2
    if real(kcrL(2*i-1))<0
        tmp=kcrL(2*i-1);
        kcrL(2*i-1)=kcrL(2*i);
        kcrL(2*i)=tmp;
    end

    if abs(conj(kcrL(2*i-1))+kcrL(2*i))>1E-4
        warning(['Complex eigenvalues for the right eigenproblem'...
            'do not occur in negative complex conjugate pairs.']);
    end
end

if ~isempty(krrL)&&~isempty(kirL)
    kL=[krrL;kirL];
elseif ~isempty(kirL)&&isempty(krrL)
    kL=kirL;
elseif ~isempty(krrL)&&isempty(kirL)
    kL=krrL;
elseif isempty(krrL)&&isempty(kirL)
    kL=[];
else
    error(['Unhandled number of propagating and non-propagating'...
            ' modes']);
end
kL=sort(kL,'ascend');

for i=1:1:length(kcrL)/2
    Index=sum(abs(kL)<abs(kcrL(2*i-1)));
    kL=[kL(1:Index);kcrL(2*i-1);kcrL(2*i);kL(Index+1:end)];
end
```

(Continued on next page...)

Listing C.4. Sketch of the MATLAB® code used to compute the approximate wave functions using equation (2.3.6). (Continued from previous page.)

```
491
492 if max(abs(kR-kL))>=1E-7
493     disp(['Eigenvalues for the left and right eigenvalue problems'...
494         'are not equal.']);
495     warning(['Maximum difference in magnitude of difference: '...
496         num2str(max(abs(kR-kL))) '.']);
497 end
498
499 %Reorder Eigenvectors by using the previously sorted Eigenvalues
500 %Right Eigenvectors and Left Eigenvectors
501 RREV=zeros(2*length(kR),length(kR));
502 RLEV=zeros(2*length(kL),length(kL));
503 for i=1:1:length(kR)
504     RREV(:,i)=REV(:,Rval==kR(i));
505     RLEV(:,i)=LEV(:,Lval==kL(i));
506 end
507
508 %Compute "scaling" factor
509 Bnm=diag(RLEV.'*B*RREV);
```

Appendix D

Input Signal

D.1 Excitation

The function p which describes the variation of the applied force and is associated with equation (2.3.17) is idealized as the commonly used Gaussian modulated sine wave that has the temporal form

$$p(t) = \begin{cases} 0, & t < 0 \\ A\mathrm{e}^{-a(st-\tau)^2} \sin(s\omega_0 t), & t \geq 0, \end{cases} \tag{D.1.1}$$

where A is an amplitude, a determines the rate of decay of the pulse, s serves to "scale" time, τ centres the pulse in time, t, and ω_0 sets the centre frequency of the sine wave. The Fourier transform of equation (D.1.1) is

$$\begin{aligned} \overline{p}(\omega) = \frac{-\mathrm{j}A\sqrt{\pi}}{4s\sqrt{a}} \Bigg[& \exp\left(\frac{(\omega + s\omega_0)(-\omega - s\omega_0 + 4\mathrm{j}\tau as)}{4as^2}\right) \\ & - \exp\left(\frac{(\omega - s\omega_0)(-\omega + s\omega_0 + 4\mathrm{j}\tau as)}{4as^2}\right) \\ & + \operatorname{erf}\left(\frac{\mathrm{j}\omega + 2as\tau + \mathrm{j}s\omega_0}{2s\sqrt{a}}\right) \exp\left(\frac{(\omega + s\omega_0)(-\omega - s\omega_0 + 4\mathrm{j}\tau as)}{4as^2}\right) \\ & - \operatorname{erf}\left(\frac{2as\tau + \mathrm{j}\omega - \mathrm{j}s\omega_0}{2s\sqrt{a}}\right) \exp\left(\frac{(\omega - s\omega_0)(-\omega + s\omega_0 + 4\mathrm{j}\tau as)}{4as^2}\right) \Bigg] \end{aligned} \tag{D.1.2}$$

where exp is the exponential function and erf is the error function which takes complex arguments. The constant a, s, τ, and ω_0 are taken invariably in this thesis to be

$$a = 2.29595 \times 10^{10}\ \mathrm{s}^{-2} \tag{D.1.3a}$$

$$s = 0.28 \tag{D.1.3b}$$

$$\tau = 1.4 \times 10^{-5}\ \mathrm{s} \tag{D.1.3c}$$

and

$$\omega_0 = (5 \times 10^5)\pi \text{ rad/s}. \tag{D.1.3d}$$

The previously described pulse is smooth (i.e., differentiable) in both time and frequency and, with the chosen constants, simultaneously has a relatively short duration, narrow frequency bandwidth. The short duration is useful for "time of flight" applications; the narrow band frequency character allows the Fourier transform to be approximated by assuming a finite bandwidth. For the given constants, the force has a 70 kHz centre frequency and over 99% of its energy is contained within a 35 to 107 kHz bandwidth. Therefore the Fourier integral transform of $p(t)$, $\overline{p}(\omega)$, may be assumed reasonably to be contained within this finite bandwidth. The resulting forms of $p(t)$ and $|\overline{p}(\omega)|$ are illustrated in Figure D.1.

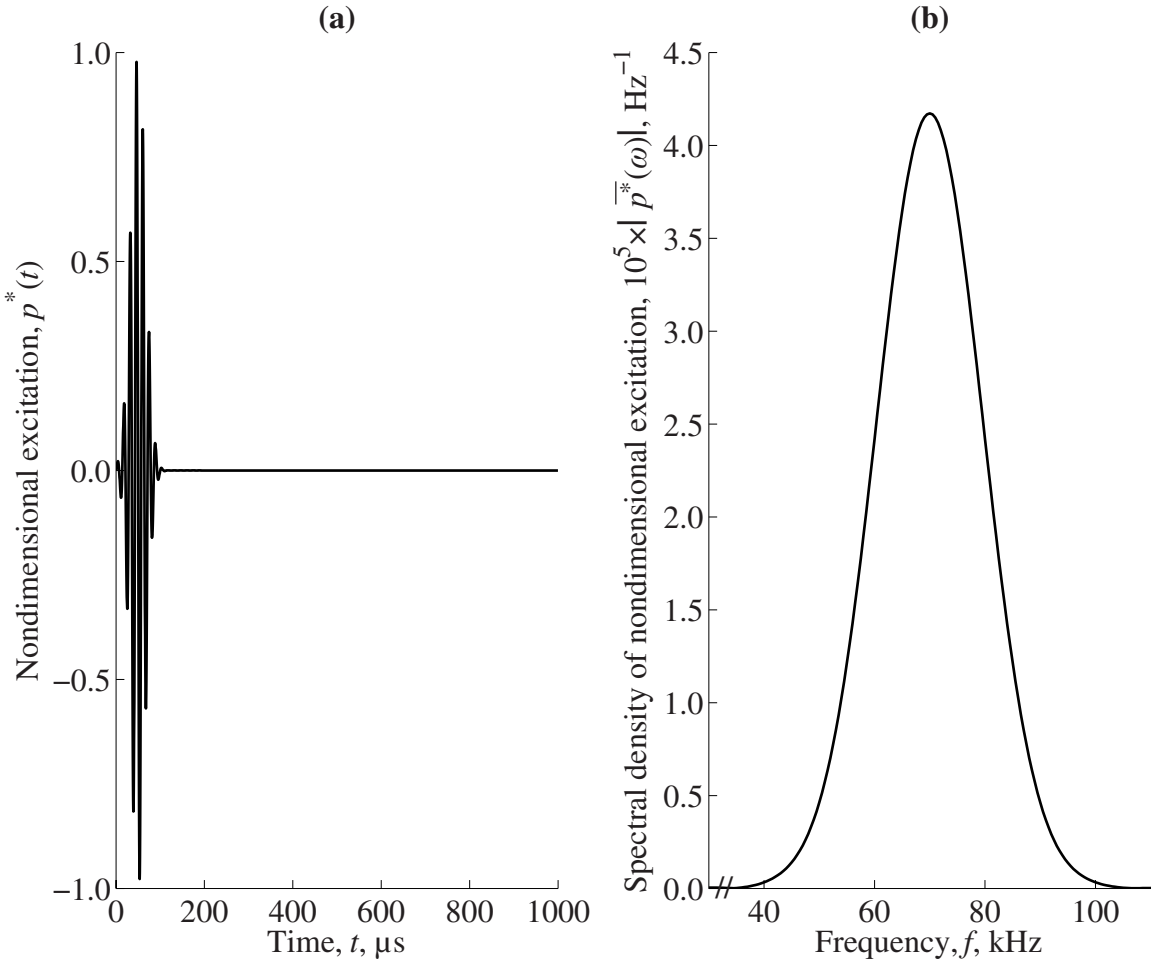

Figure D.1. Applied excitation in (a) time and (b) frequency.

APPENDIX E

ENFORCING CAUSALITY

E.1 Introduction

Although the superposition of modal responses from a steady-state excitation is generally applicable to linear systems, this procedure is used most commonly in vibration and wave propagation problems. The inverse Fourier transform of the modal summation gives the corresponding temporal behaviour. The purpose of this appendix is to demonstrate that the latter need not automatically satisfy the physical requirement of causality. Then a straightforward extension of the better known mathematical procedure for a periodic excitation is proposed as a remedy. Two illustrative examples are given that arise in calculating time responses to a known pulse which is adapted to excite i) vibrations of an ideal single oscillator or ii) numerous ultrasonic waves in a steel pipe.

Finding the response of a linear, time invariant system is usually somewhat easier for a steady sinusoidal excitation than for a transient pulse. Moreover, physical insight into the system's dynamic behaviour is often gained advantageously in the process of computing its Frequency Response Function (FRF). The FRF describes the magnitude and phase of a steady-state motion as a function of frequency [135]. The well known inverse and forward Fourier transforms permit a transient temporal response to be determined from knowledge of an excitation's Fourier transform and a system's FRF, and vice-versa. A Fourier transform is a simpler concept than the alternative Laplace transform because sinusoidal excitations are visualized and interpreted not only more easily than their complex exponential counterparts but they can be implemented physically. Furthermore, the evaluation of an inverse Fourier transform involves a more tractable integration along the real (frequency) axis rather than the contour integration in the complex domain required by an inverse Laplace transform. Unfortunately the inverse Fourier transform, unlike its Laplace

counterpart, does not contain explicit information about a system's initial conditions—a deficiency which may lead to a non-causal response.

Situations exist when a computed prediction and a physical measurement must be compared in the time domain. This comparison can be troublesome when predictions are non-causal. See, for example, [56, 136, 137][1]. While non-causal responses are merely undesirable numerical artefacts for most vibration work, there are situations (e.g., simulating shock loadings) where knowledge of the initial conditions is critical. Similarly, non-causality from a wave's propagation makes it impossible to accurately compute its time of flight, a duration which is used frequently to characterize or detect defects [6]. Therefore, a procedure is presented here in which non-causal predictions arising from an inverse Fourier transform are remedied straightforwardly. Although conceptually comparable to a mathematical approach developed for a periodic excitation [135, 138, 139], the albeit simple extension to transient excitations, as well as dependent practical applications, has not been reported to the best of the author's knowledge . The procedure is illustrated by first considering a Single Degree Of Freedom (SDOF) oscillator's vibrations when excited over both a continuous and discretized time base. Then a practical example is presented that arises when predicting the analogous time response of an industrial pipe to the same excitation shifted upwards into the ultrasonic frequency range.

E.2 Theoretical and Physical Arguments

The following outline considers the linear vibrations of an illustrative, undamped SDOF oscillator which is excited transiently. Similar arguments can be made for any form of *linear* damping (e.g., viscous, proportional and hysteretic damping [135, 140]) although the resulting FRFs are more complicated. By taking advantage of the decoupling inherent to a modal analysis, the theory can be extended straightforwardly to Multi-Degree Of Free-

[1] Note that these last two references use the more computationally efficient Fast Fourier Transform (FFT) pairs.

dom (MDOF) vibration and wave propagation problems involving excitations applied at multiple locations. Brevity precludes these developments. Although a continuous time base is assumed in the present derivations the principle applies also to discrete time systems, as illustrated later.

The *forced* displacement and velocity at any instant t, $x^{\mathrm{f}}(t)$ and $v^{\mathrm{f}}(t)$ respectively, of an *undamped* SDOF oscillator produced by an excitation $p(t)$ are [135, 139–141][2]:

$$x^{\mathrm{f}}(t) = \frac{1}{2\pi}\int_{-\infty}^{\infty}\left(\frac{\overline{p}(\omega)}{k-\omega^2 m}\right)\mathrm{e}^{-\mathrm{j}\omega t}\mathrm{d}\omega \tag{E.2.1a}$$

(E.2.1b)

and

$$v^{\mathrm{f}}(t) = \frac{1}{2\pi}\int_{-\infty}^{\infty}\left(\frac{-\mathrm{j}\omega\overline{p}(\omega)}{k-\omega^2 m}\right)\mathrm{e}^{-\mathrm{j}\omega t}\mathrm{d}\omega. \tag{E.2.1c}$$

The displacement FRF, $H(\omega)$, which depends more generally upon the existence and form of damping, corresponds to $(k-\omega^2 m)^{-1}$ in the above equations. The k and m are the oscillator's stiffness and mass, respectively, whilst ω (f) represents frequency in rad/s (Hz). $\overline{p}(\omega)$ is the Fourier transform of $p(t)$ and $\mathrm{j} = \sqrt{-1}$. The integrands of equation (E.2.1) are singular but a standard integration of improper integrals can be applied if limits exist [142]. Then the *forced* displacement and corresponding velocity, $x^{\mathrm{f}}(0)$ and $v^{\mathrm{f}}(0)$, *which are caused solely by the excitation* can be determined at $t = 0$, the instant of initially applying the excitation. These values are real and sometimes negligibly small as a later example demonstrates.

Formulae for the *free* vibration displacement and velocity , $x^{\mathrm{h}}(t)$ and $v^{\mathrm{h}}(t)$, of the undamped oscillator are well known [135, 139–141] to be:

$$x^{\mathrm{h}}(t) = A^{\mathrm{h}}\cos\left(\omega_{\mathrm{n}}t - \phi\right) \tag{E.2.2a}$$

[2]It is implied in these references that the expressions give the *total* displacement and velocity. Note that the Fourier transform pairs defined here are comparable but inconsequentially different from those given in [135, 139–141].

and

$$v^{\mathrm{h}}(t) = -\omega_n A^{\mathrm{h}} \sin(\omega_{\mathrm{n}} t - \phi) \tag{E.2.2b}$$

where $\omega_n = \sqrt{k/m}$. The amplitude, A^h, and phase, ϕ, are found by enforcing causality at $t = 0$ for the linearly superimposed forced *and* free vibration solutions. Hence;

$$x^{\mathrm{f}}(0) + x^{\mathrm{h}}(0) = 0 \tag{E.2.3a}$$

and

$$v^{\mathrm{f}}(0) + v^{\mathrm{h}}(0) = 0, \tag{E.2.3b}$$

which lead, in conjunction with equations (E.2.1) and (E.2.2), to:

$$A^{\mathrm{h}} = \frac{-x^{\mathrm{f}}(0)}{\cos(-\phi)}, \tag{E.2.4a}$$

and

$$\phi = \arctan\left(\frac{v^{\mathrm{f}}(0)}{\omega_n x^{\mathrm{f}}(0)}\right). \tag{E.2.4b}$$

Causality is enforced for a MDOF rather than a SDOF system on a mode by mode basis at each location of interest.

E.3 Illustrative Examples

Two examples are given. One relates to the time varying vibrations of an undamped SDOF oscillator caused by a transient excitation. The second, more complex example arises from the Semi-Analytical Finite Element (SAFE) formulation for ultrasonically generated waves in a continuous pipe having negligible material damping. See, for example, [46]. The pipe's cutoff frequencies (at which the wave number is identically zero) represents a juncture where the "character" of a pipe mode changes from an overall vibration to a propagating

wave [21]. Moreover, the displacement at a cutoff frequency becomes unbounded in the absence of damping so it is analogous to the behaviour at an undamped natural vibration frequency [21].

E.3.1 Excitation

A transient excitation having the invariant character in the time and frequency domains shown in Figure E.1 is applied to both the SDOF oscillator and on the outer surface of a

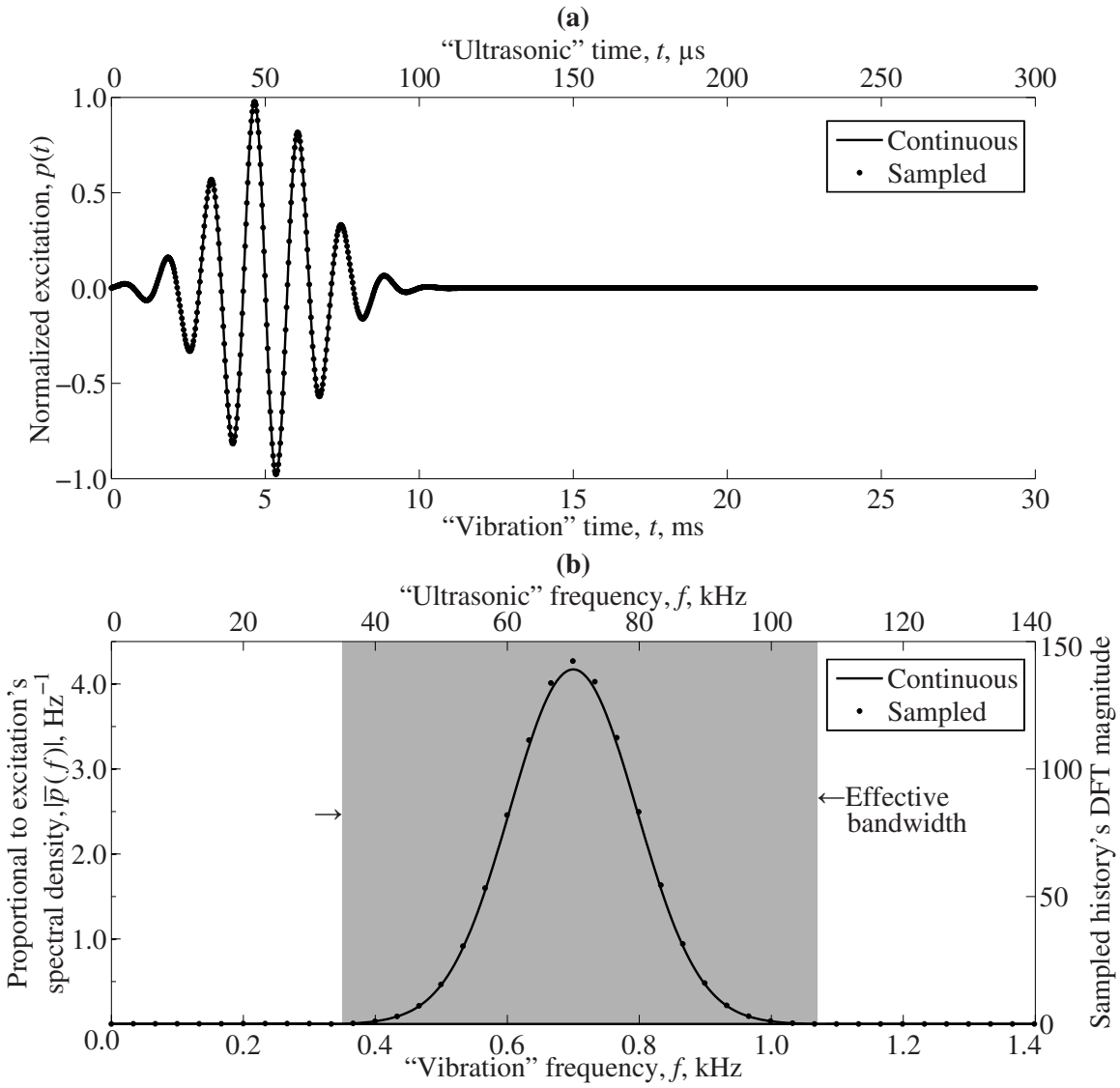

Figure E.1. Applied excitations in (a) time and (b) frequency.

hollow steel pipe. The lower (upper) time and frequency scales labelled "vibration" ("ultrasonic") are for the pulse applied to the SDOF system (pipe). The transposed time and frequency scales reflect the low and high frequencies inherent to the SODF vibrations and ultrasonic pipe waves, respectively. Vertical scales on the left are for continuous time while those on the right are for discrete representations. (See [111] for discrete time expressions similar to those used in the current development.) The excitation is effectively band-limited because over 99.9% of its energy[3] is contained between 350 Hz and 1070 Hz or between 35 kHz and 107 kHz for the vibration and ultrasonic cases, respectively.

E.3.2 SDOF example

The vibration producing excitation is applied to the undamped SDOF oscillator whose mass and stiffness values are given in Table E.1. The oscillator's resulting frequency and time behaviours are shown in Figure E.2. Plots presented in the left (right) column of this figure correspond to continuous (discrete) time calculations. Figures E.2 (a) and E.2 (b) give the FRFs in which the oscillator's 450 Hz natural frequency is seen to be superimposed on the excitation's spectrum of Figure E.1 (b). (Note that the spectral densities shown involve the convolution of a FRF with the excitation's spectral density.) Reference displacement histories are presented, on the other hand, in Figures E.2 (c) and E.2 (d). They are derived from the convolution integral [111, 135, 139] of closed form expressions and are essentially exact. Corresponding time histories found from the inverse Fourier transforms of Figures E.2 (a) and E.2 (b) are illustrated in Figures E.2 (e) and E.2 (f), respectively. However, only every

Table E.1. Properties assigned to the SDOF oscillator.

Property	Assigned Value
Mass, m, slug (kg)	6.8522×10^{-2} (1.0000)
Stiffness, k, kip/ft (MN m^{-1})	547.79 (7.9944)
Undamped natural Frequency, ω_n (f_n)	2.8274×10^3 rad s^{-1} (450.00 Hz)

[3]The term "energy" is used here in the signal processing sense [110, 111].

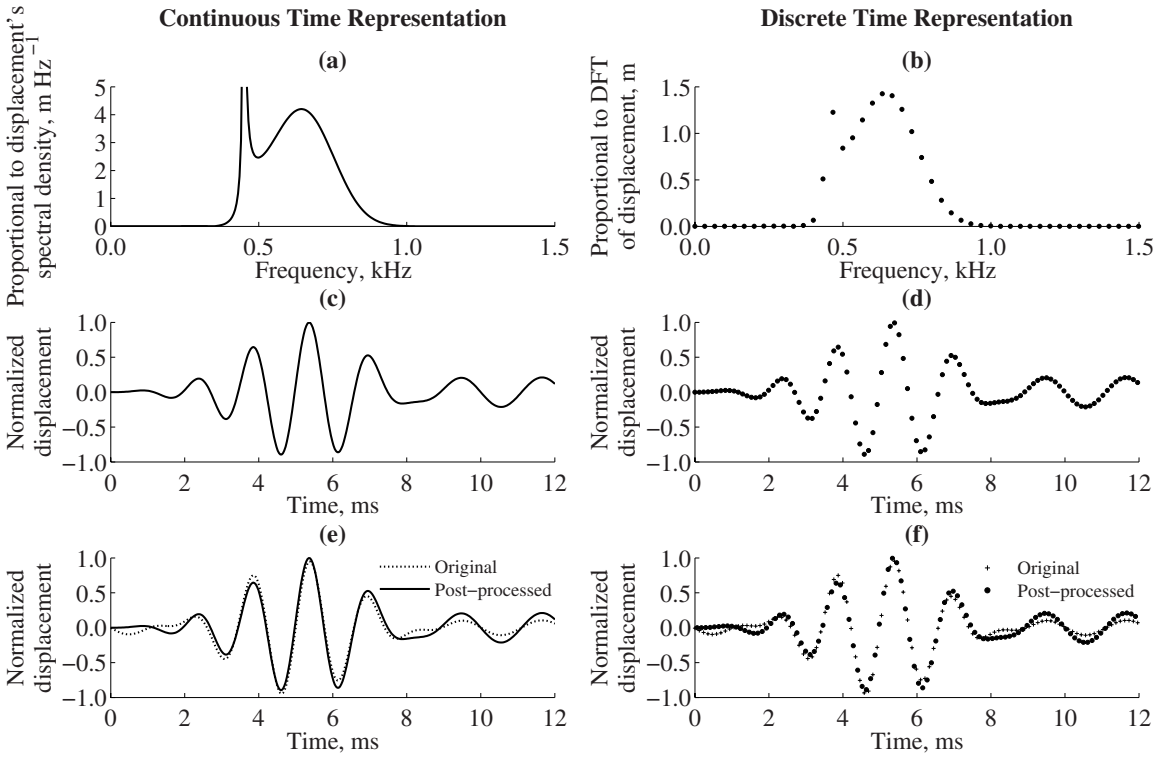

Figure E.2. Representative response of a SDOF oscillator in (a) and (b) frequency and (c) through (e) time.

fourth sample over the first 12 ms [rather than the 30 ms duration implicit to Figure E.2 (b)] of the discretized history in Figure E.2 (f) is shown to enhance visual clarity. Other time histories are made, as far as possible, compatible with Figure E.2 (f). Histories labelled "original" are unprocessed inverse transforms; "post-processed" histories incorporate the additional causality conditions, i.e., equations (E.2.3a) and (E.2.3b).

A comparison of Figures E.2 (c) and E.2 (d) establishes that the discrete counterpart coincides with the exact continuous time history. Similar agreement holds not only between the original but also the post-processed histories of Figures E.2 (e) and E.2 (f). Therefore discretization is not the source of the non-causality exhibited by the original history of Figure E.2 (f). Moreover, imposition of the causality conditions consistently corrects the deficiency regardless of whether the history is discrete or continuous. Consequently there is a need to specifically incorporate equations (E.2.3a) and (E.2.3b) for the (discrete or continuous) inverse Fourier transform to be complete and *always* precise.

E.3.3 MDOF example

The previous SDOF example is extended to a MDOF steel pipe. The hollow pipe is excited radially on its outer surface by using a pulse have the same overall character as before but shifted upwards in frequency. The pipe's dimensional and material properties are identical to those given in Table 2.1. They match those encountered commonly in the petrochemical industry. Ensuing individual radial displacement components on the pipe's outer surface at a location having a purely axial offset (which is 5.1 wall thicknesses from the pulse's point of application) are extracted initially for two instructive wave modes. The first mode has a 6.004 kHz cutoff frequency which is outside the excitation's 35 kHz and 107 kHz effective bandwidth. Conversely the 74.426 kHz cutoff frequency of the second mode lies almost centrally within this bandwidth. The frequency and time behaviours of the two modes are presented separately on the left and right, respectively, of Figures E.3 (a) through E.3 (d). On the other hand, Figures E.3 (e) through E.3 (f) show the analogous but total radial displacement when all the 2000 or so modes which are considered are superimposed. The previous meanings of "original" and "post-processed" are retained in these figures.

The contribution of a mode acting individually is indicated by a noticeable spike at its corresponding cutoff frequency in Figures E.3 (a) and E.3 (c). This behaviour is similar to that observed earlier in Figures E.2 (a) and E.2 (b) for the SODF oscillator. The corresponding time histories given in Figures E.3 (b) and E.3 (d) show that the free vibrations occurring after the pulse's termination are prolonged only when a spike is within the pulse's frequency bandwidth. This was also the situation for the oscillator and, not surprisingly, each individual mode's post-processed displacement history is always causal. On the other hand, the agreement between the original and post-processed histories given in Figure E.3 (b) suggests a less imperative need for post-processing when a cutoff frequency is outside the pulse's bandwidth. This is not the case in Figure E.3 (d) or Figure E.3 (f) where the 2000 or so modes considered introduce several cutoff frequencies in this bandwidth.

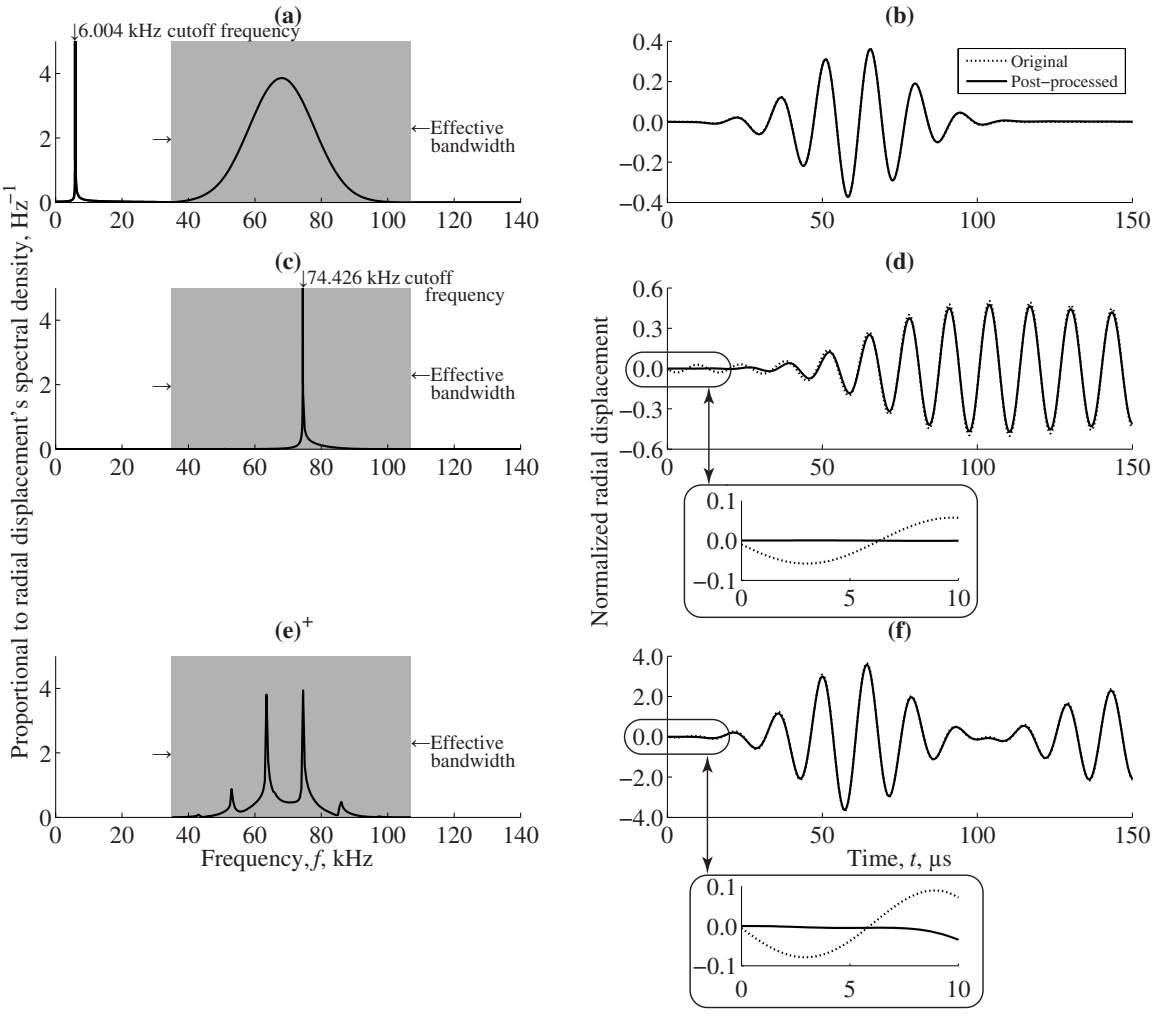

Figure E.3. Representative responses in frequency and time for (a) and (b) [(c) and (d)] a single mode whose cutoff frequency lies outside [inside] the excitation's effective bandwidth and (e) and (f) the superposition of about 2000 wave modes. $^{+}$Scales are insufficiently sensitive to clearly delineate all the cutoff frequencies, most of which lie outside the excitation's bandwidth.

E.4 Conclusions

A mathematical procedure for a periodic excitation is extended to a transient pulse which is used commonly in ultrasonic testing. The extremes of a single vibration mode of a simple oscillator and the many wave modes propagating simultaneously in a real pipe illustrate that the extended procedure can remedy non-causal predictions. The extension is shown to apply to both continuous and discrete time problems but it must be applied disadvantageously to each mode of a MDOF system.

APPENDIX F

AXISYMMETRIC FINITE ELEMENT MODELLING

F.1 Introduction

The approximate displacement field of an axisymmetric finite element volume is written in this appendix in terms of interpolation functions and a nodal displacement vector. The strain-displacement matrices are introduced to describe the strain and stress fields in terms of the approximate displacement field. Then approximate equations of undamped motion are obtained by applying Hamilton's principle to the appropriate functional for complex displacement fields.

F.2 Approximate Displacement Field

The displacement field in the axisymmetric finite element region is approximated initially as

$$\mathbf{u}(r,\theta,z,t) = \sum_{n=-\infty}^{\infty} \boldsymbol{\mathcal{N}}_n(r,\theta,z)\mathrm{e}^{-\mathrm{j}\omega t}\mathbf{U}_n, \tag{F.2.1}$$

where

$$\boldsymbol{\mathcal{N}}(r,\theta,z) = \begin{bmatrix} \mathbf{N}_n(r,\theta,z) & \mathbf{0} & \mathbf{0} \\ \mathbf{0} & \mathbf{N}_n(r,\theta,z) & \mathbf{0} \\ \mathbf{0} & \mathbf{0} & \mathbf{N}_n(r,\theta,z) \end{bmatrix}. \tag{F.2.2}$$

The $\mathbf{N}_n$ are the assembled interpolation functions over the finite element region and $\mathbf{U}_n$ is the corresponding array of nodal displacements. A time, t, harmonic excitation and displacement response, both having circular frequency ω, have been assumed implicitly in equation (F.2.1). The $\mathbf{N}_n$ and $\mathbf{U}_n$ both depend on the circumferential harmonic (wavenumber), n. The $\mathbf{N}_n$ is obtained by a conventional finite assembly process over all elements. See,

for example, [107]. The $\mathbf{U}_n$ are represented, as in Appendix B, by

$$\mathbf{U}_n = \left[\begin{array}{ccc} \mathcal{U}_n & \mathcal{V}_n & \mathcal{W}_n \end{array} \right]^{\mathrm{T}}, \tag{F.2.3}$$

where $\mathcal{U}_n$, $\mathcal{V}_n$, and $\mathcal{W}_n$ are arrays containing the radial, circumferential, and axial nodal displacements, respectively, for the n^{th} circumferential wavenumber. Isoparametric, axisymmetric finite elements are utilized. A representative finite element with its numbering is shown in Figure F.1 for an elevation perspective. In addition, global coordinates, (r, z), are shown in Figure F.1 (a) whereas the local coordinates (ζ, η) are illustrated in Figure F.1 (b). The radial coordinates of the finite element's nodal coordinates are selected so that:

$$r_1 = r_{\mathrm{i}}, \tag{F.2.4a}$$

$$r_2 = (r_{\mathrm{i}} + r_{\mathrm{o}})/2, \tag{F.2.4b}$$

$$r_3 = r_{\mathrm{o}}, \tag{F.2.4c}$$

$$r_4 = r_{\mathrm{i}}, \tag{F.2.4d}$$

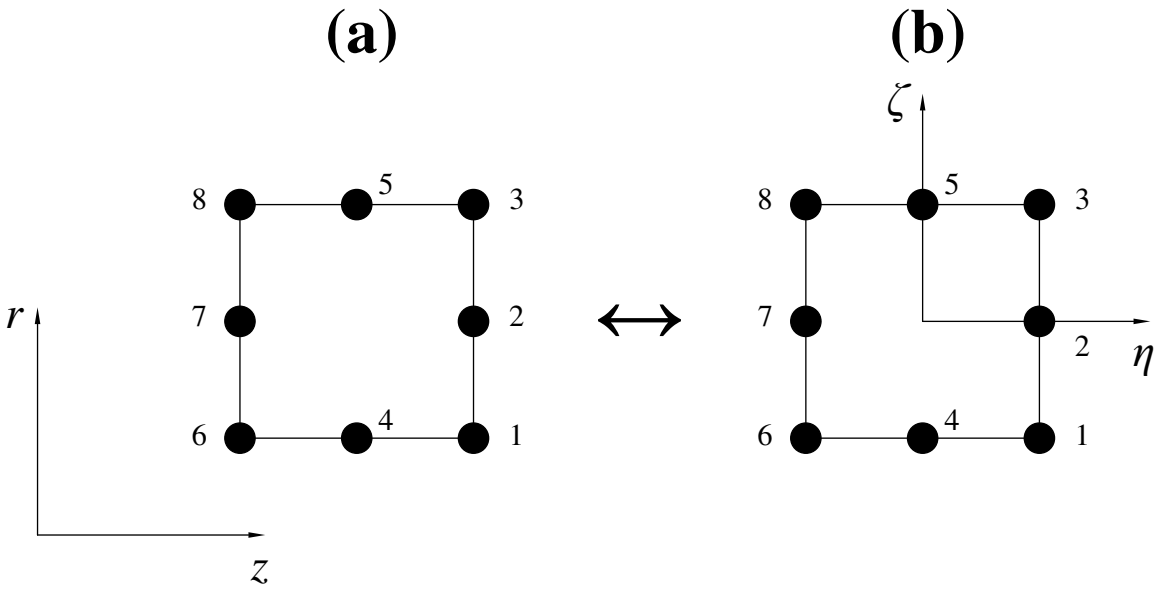

Figure F.1. Showing a representative isoparametric, axisymmetric finite element's nodal numbering in (a) global, and (b) local coordinate frames.

$$r_5 = r_o, \tag{F.2.4e}$$

$$r_6 = r_i, \tag{F.2.4f}$$

$$r_7 = (r_i + r_o)/2, \tag{F.2.4g}$$

and

$$r_8 = r_o. \tag{F.2.4h}$$

Here r_i (r_o) is the radial coordinate of the finite element's inner (outer) surface. (Note that *in this context* r_i and r_o refer to a finite element's inner and outer radii, and not to the pipe's inner and outer radii.) Similarly the axial coordinates of the finite element's nodal coordinates are selected so that:

$$z_1 = z_f, \tag{F.2.5a}$$

$$z_2 = z_f, \tag{F.2.5b}$$

$$z_3 = z_f, \tag{F.2.5c}$$

$$z_4 = (z_b + z_f)/2, \tag{F.2.5d}$$

$$z_5 = (z_b + z_f)/2, \tag{F.2.5e}$$

$$z_6 = z_b, \tag{F.2.5f}$$

$$z_7 = z_b, \tag{F.2.5g}$$

and

$$z_8 = z_b, \tag{F.2.5h}$$

where z_f (z_b) is the axial coordinate of the finite element's front (back) face and $z_f > z_b$.

With the finite element's nodal coordinates selected in the fashion described by equations (F.2.4) and (F.2.5), the individual matrix elements of the shape function vector, **n**,

(which is used in each finite element) can be expressed as

$$n_{1,1} = \left(-1/4 + 1/4\zeta^2 - 1/4\eta\zeta + 1/4\eta^2 + 1/4\eta\zeta^2 - 1/4\eta^2\zeta\right)\mathrm{e}^{\mathrm{j}n\theta}, \tag{F.2.6a}$$

$$n_{1,2} = \left(1/2 + 1/2\eta - 1/2\zeta^2 - 1/2\eta\zeta^2\right)\mathrm{e}^{\mathrm{j}n\theta}, \tag{F.2.6b}$$

$$n_{1,3} = \left(-1/4 + 1/4\zeta^2 + 1/4\eta\zeta + 1/4\eta^2 + 1/4\eta\zeta^2 + 1/4\eta^2\zeta\right)\mathrm{e}^{\mathrm{j}n\theta}, \tag{F.2.6c}$$

$$n_{1,4} = \left(1/2 - 1/2\zeta - 1/2\eta^2 + 1/2\eta^2\zeta\right)\mathrm{e}^{\mathrm{j}n\theta}, \tag{F.2.6d}$$

$$n_{1,5} = \left(1/2 + 1/2\zeta - 1/2\eta^2 - 1/2\eta^2\zeta\right)\mathrm{e}^{\mathrm{j}n\theta}, \tag{F.2.6e}$$

$$n_{1,6} = \left(-1/4 + 1/4\zeta^2 + 1/4\eta\zeta + 1/4\eta^2 - 1/4\eta\zeta^2 - 1/4\eta^2\zeta\right)\mathrm{e}^{\mathrm{j}n\theta}, \tag{F.2.6f}$$

$$n_{1,7} = \left(1/2 - 1/2\eta - 1/2\zeta^2 + 1/2\eta\zeta^2\right)\mathrm{e}^{\mathrm{j}n\theta}, \tag{F.2.6g}$$

and

$$n_{1,8} = \left(-1/4 + 1/4\zeta^2 - 1/4\eta\zeta + 1/4\eta^2 - 1/4\eta\zeta^2 + 1/4\eta^2\zeta\right)\mathrm{e}^{\mathrm{j}n\theta}. \tag{F.2.6h}$$

The ζ and η are dimensionless radial and axial coordinates, respectively, that are specified in the local, isoparametric element coordinate system. They are related to the global coordinate system by

$$\zeta = \frac{2r - (r_\mathrm{o} + r_\mathrm{i})}{(r_\mathrm{o} - r_\mathrm{i})}, -1 \leq \zeta \leq 1 \tag{F.2.7a}$$

and

$$\eta = \frac{2z - (z_\mathrm{f} + z_\mathrm{b})}{(z_\mathrm{f} - z_\mathrm{b})}, -1 \leq \eta \leq 1. \tag{F.2.7b}$$

F.3 Approximate Strain and Stress Fields

The following strain-displacement transformation matrix:

$$\mathbf{B}_n = \begin{bmatrix} \mathbf{N}_{n,r} & \mathbf{N}_n/r & \mathbf{0} & \mathrm{j}n\mathbf{N}_n/r & \mathbf{N}_{n,z} & \mathbf{0} \\ \mathbf{0} & \mathrm{j}n\mathbf{N}_n/r & \mathbf{0} & \mathbf{N}_{n,r} - \mathbf{N}_n/r & \mathbf{0} & \mathbf{N}_{n,z} \\ \mathbf{0} & \mathbf{0} & \mathbf{N}_{n,z} & \mathbf{0} & \mathbf{N}_{n,r} & \mathrm{j}n\mathbf{N}_n/r \end{bmatrix}^{\mathrm{T}} \tag{F.3.1}$$

is introduced to simplify the computation of the approximate strain field in the axisymmetric, finite element volume, for the n^{th} circumferential wavenumber. Then the corresponding strain and stress tensors which are expressed in vector form, can be written as

$$\boldsymbol{\varepsilon} = \mathbf{B}\mathbf{U}_n \tag{F.3.2a}$$

and

$$\boldsymbol{\sigma} = \mathbf{D}\mathbf{B}\mathbf{U}_n, \tag{F.3.2b}$$

respectively, for a given circumferential wavenumber, n. The $\mathbf{D}$ is a symmetric matrix which is composed from the isotropic elastic moduli given in equation (B.3.3).

F.4 Application of Hamilton's Principle

Hamilton's principle can be expressed for the axisymmetric finite element volume in the form used in equation (B.4.1). Moreover, the kinetic and total potential energies are still given by equation (B.4.2). By following a procedure similar to the one used in Section B.4 to derive equation (B.4.10) from equation (B.4.1), the approximate equations of motions of the axisymmetric finite element volume can be shown, for a single circumferential harmonic, to be

$$\left(\mathbf{K}_{\mathrm{I}}(n) - \omega^2\mathbf{M}_{\mathrm{I}}\right)\mathbf{U}_n = \mathbf{F}_n. \tag{F.4.1}$$

Equation (F.4.1) becomes identical to equation (4.2.1) when $\mathbf{U}_n$ and $\mathbf{F}_n$ are replaced by $\mathbf{q}$ and $\mathbf{P}$, respectively, in the last equation.

The $\mathbf{K}_\mathrm{I}$ and $\mathbf{M}_\mathrm{I}$ appearing in equation (F.4.1) can be computed by evaluating the integrals

$$\mathbf{K}_\mathrm{I}(n) = \int_{-l/2}^{0}\int_{-\pi}^{\pi}\int_{r_i}^{r_o} \widetilde{\mathbf{B}_n}^\mathrm{T}\mathbf{D}\mathbf{B}_n r\mathrm{d}r\mathrm{d}\theta\mathrm{d}z \tag{F.4.2a}$$

and

$$\mathbf{M}_\mathrm{I} = \int_{-l/2}^{0}\int_{-\pi}^{\pi}\int_{r_i}^{r_o} \rho\widetilde{\boldsymbol{\mathcal{N}}_n}^\mathrm{T}\boldsymbol{\mathcal{N}}_n r\mathrm{d}r\mathrm{d}\theta\mathrm{d}z, \tag{F.4.2b}$$

where the limits of integration are determined by referring to Figure 4.1. Note that $\mathbf{K}_\mathrm{I}$ is a function of n, but $\mathbf{M}_\mathrm{I}$ is independent of n. However, it is possible [107] to express $\mathbf{K}_\mathrm{I}(n)$ as

$$\mathbf{K}_\mathrm{I}(n) = \mathbf{K}_0 + n\mathbf{K}_1 + n^2\mathbf{K}_2, \tag{F.4.3}$$

where $\mathbf{K}_0$, $\mathbf{K}_1$ and $\mathbf{K}_2$ are all independent of n. On the other hand, $\mathbf{F}_n$ can be found by following the procedure given in [107] for the computation of consistent force vectors for external forces. The integral

$$\mathbf{F}_n = \int_{-\pi}^{\pi}\int_{r_i}^{r_o} \widetilde{\boldsymbol{\mathcal{N}}_n}^\mathrm{T}\begin{Bmatrix}\tau_{rz}\\ \tau_{\theta z}\\ \sigma_{zz}\end{Bmatrix} r\mathrm{d}r\mathrm{d}\theta, \tag{F.4.4}$$

gives the required consistent force vector. The $\widetilde{\boldsymbol{\mathcal{N}}_n}$ in equation (F.4.4) is evaluated on the plane $z = 0$. Moreover, τ_{rz}, $\tau_{\theta z}$, and σ_{zz} are stresses from the wavefunction expansion that act on the plane $z = 0$. This is the only plane where distributed external forces are applied to the finite element region. They may be found for a single mode of the wavefunction expansion region by applying equations (A.3.2) and (A.4.2) of Appendix A to the (approximate) displacement field given in equation (B.2.1) for that mode. Briefly, the displacement,

$\mathbf{u}_{nm}$, in the wavefunction expansion region can be expressed, for a single mode having unit amplitude, as

$$\mathbf{u}_{nm} = \mathcal{N}\boldsymbol{\phi}^{\mathrm{R}}_{nm\mathrm{u}} \mathrm{e}^{\mathrm{j}k_{nm}z} \mathrm{e}^{\mathrm{j}n\theta}. \tag{F.4.5}$$

As before, $\mathcal{N}$ are the assembled interpolation functions over the entire pipe in the wavefunction expansion region. Furthermore, $\boldsymbol{\phi}^{\mathrm{R}}_{nm\mathrm{u}}$ is the nm^{th} mode shape for which k_{nm} and n are the axial and circumferential wavenumbers, respectively. Applying equations (A.3.2) and (A.4.2) to equation (F.4.5) and making evaluations in the $z = 0$ plane gives the required stresses as

$$\begin{Bmatrix} \tau_{rz} \\ \tau_{\theta z} \\ \sigma_{zz} \end{Bmatrix} = \mathbf{D} \begin{bmatrix} \mathrm{j}k_{nm}\mathbf{N} & \mathbf{0} & \mathbf{N}_{,r} \\ \mathbf{0} & \mathrm{j}k_{nm}\mathbf{N} & \mathrm{j}n\mathbf{N}/r \\ \mathbf{0} & \mathbf{0} & \mathrm{j}k_{nm}\mathbf{N} \end{bmatrix} \boldsymbol{\phi}^{\mathrm{R}}_{nm\mathrm{u}} \mathrm{e}^{\mathrm{j}n\theta}. \tag{F.4.6}$$

Substituting equation (F.4.6) into equation (F.4.4) and evaluating the result leads to a column vector. Collecting the column vectors for all the scattered modes (essentially containing both the $\mathbf{F}_{\mathrm{s}1}$ and $\mathbf{F}_{\mathrm{s}2}$ used in Section 4.2.4) results in the shorthand notations used for $\mathbf{f}^{\mathrm{scat}}$ and $\mathbf{f}^{\mathrm{scat}}_{+}$ given in Section 4.2.4. Similarly, the $\mathbf{f}^{\mathrm{in}}$ is a single column vector as a result of applying equation (F.4.4) for a single incident mode.

F.5 Note on Integrating the Finite Element Matrices

In practice the matrices given in equation (F.4.2) are evaluated by "assembling" element matrices. The element matrices for the k^{th} element take the same form as the matrices in equation (F.4.2) but they have integration limits which span each finite element's local dimensions only. (See equations (F.2.4) and (F.2.5) as well as Figure F.1.) A typical component in these matrices can be written in the form

$$\mathcal{E} = \int_{z_{\mathrm{b}}}^{z_{\mathrm{f}}} \int_{-\pi}^{\pi} \int_{r_{\mathrm{i}}}^{r_{\mathrm{o}}} \mathcal{I}(r, \theta, z, \zeta, \eta) r \mathrm{d}r \mathrm{d}\theta \mathrm{d}z, \tag{F.5.1}$$

where, as before, $\mathcal{E}$ is an arbitrary matrix element and $\mathcal{I}$ is the integrand arising from the required matrix multiplications. The variables of integration in equation (F.5.1) are r, θ, and z but the integrand contains ζ and η which are functions of the other spatial variables. The well known change of variables theorem from multivariable calculus is invoked to evaluate equation (F.5.1). The result is

$$\begin{aligned}\mathcal{E} &= \int_{z_\mathrm{b}}^{z_\mathrm{f}} \int_{-\pi}^{\pi} \int_{r_\mathrm{i}}^{r_\mathrm{o}} \mathcal{I}(r,\theta,z,\zeta,\eta) r \mathrm{d}r\mathrm{d}\theta\mathrm{d}z \\ &= \int_{-\pi}^{\pi} \int_{-1}^{1} \int_{-1}^{1} \mathcal{I}'(\theta,\zeta,\eta) \left(\frac{[r_\mathrm{o}-r_\mathrm{i}]\zeta + [r_\mathrm{o}+r_\mathrm{i}]}{2}\right)\left(\frac{[z_\mathrm{f}-z_\mathrm{b}][r_\mathrm{o}-r_\mathrm{i}]}{4}\right) \mathrm{d}\zeta\mathrm{d}\eta\mathrm{d}\theta\end{aligned} \tag{F.5.2}$$

Equation (F.5.2) makes use of the relation $r = (r_\mathrm{o}\zeta - r_\mathrm{i}\zeta + r_\mathrm{o} + r_\mathrm{i})/2$ which is obtained from equation (F.2.7a). Moreover, $\mathcal{I}'(\zeta)$ can be derived straightforwardly from $\mathcal{I}(r,\zeta)$ by using the chain rule and the previously stated relations between r and ζ as well as z and η. On the other hand, the $(z_\mathrm{f} - z_\mathrm{b})(r_\mathrm{o} - r_\mathrm{i})/4$ factor appearing in equation (F.5.2) arises from the determinant of the Jacobian matrix in the change of variables theorem. For this particular case, the Jacobian matrix, $\mathbf{J}$, is given by

$$\mathbf{J} = \begin{bmatrix} \frac{\partial r}{\partial \zeta} & \frac{\partial z}{\partial \zeta} \\ \frac{\partial r}{\partial \eta} & \frac{\partial z}{\partial \eta} \end{bmatrix} = \begin{bmatrix} \frac{(r_\mathrm{o}-r_\mathrm{i})}{2} & 0 \\ 0 & \frac{(z_\mathrm{f}-z_\mathrm{b})}{2} \end{bmatrix} \tag{F.5.3}$$

so that the determinant, $|\mathbf{J}|$, is

$$|\mathbf{J}| = \frac{(z_\mathrm{f} - z_\mathrm{b})(r_\mathrm{o} - r_\mathrm{i})}{4}. \tag{F.5.4}$$

A similar procedure can be applied to evaluate the consistent force vector given in equation (F.4.4).

APPENDIX G

CODE LISTINGS AND SKETCHES IMPLEMENTING HYBRID SAFE FOR AXISYMMETRIC SCATTERERS

G.1 Overview

This appendix contains annotated code listings and "sketches" (in which sections of code are removed for brevity) of illustrative MATLAB® scripts and functions. The code is used to implement the hybrid SAFE method for axisymmetric scatters. This method is described in Section 4.2 of Chapter 4 and Appendix F. Code listings and sketches illustrate a work flow which allows the writing of finite element programs to be automated partially by taking advantage of readily available commercial tools. Moreover, several MATLAB® "best practices," such as preallocating memory for arrays and "vectorizing code" rather than using a loop, are illustrated as a matter of course. Although the programs presented in this appendix have been "parallelized" to run simultaneously on a several computing cores, only "serial" or single computer[1] versions are presented here. A discussion of parallel and distributed computing is deferred to Appendix L.

G.2 Annotated Code Listings

An annotated MATLAB® code listing to evaluate (in closed form) the axisymmetric finite element stiffness and mass matrices is provided in Listing C.1. A high level flowchart for this program is given in Figure G.1. Listing G.2, on the other hand, gives code to evaluate (in closed form) the consistent force vector for external forces acting on the B^+ surface of the axisymmetric finite element volume. Figure G.2 gives a high level flowchart for this listing. Finally, Listing G.3 provides a "sketch" of the MATLAB® program that implements

[1] Note that MATLAB® supports some implicit parallelization that speeds code execution for serial programs.

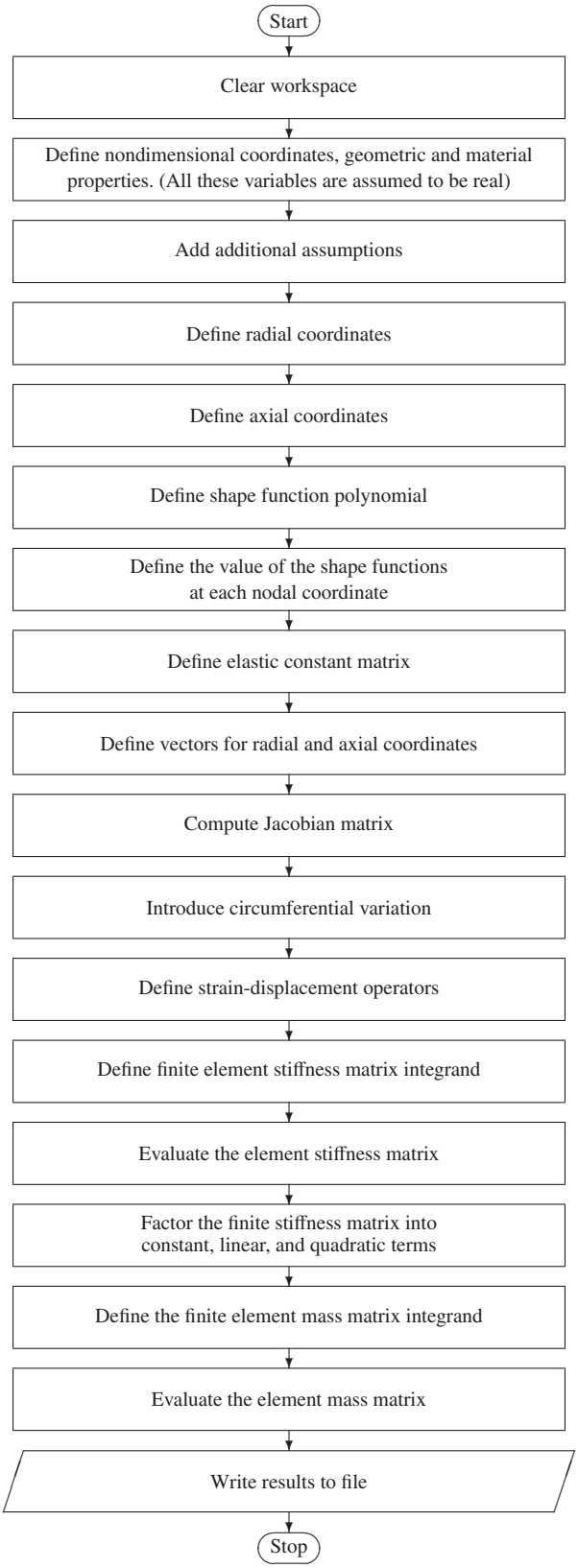

Figure G.1. A high level flowchart for Listing G.1.

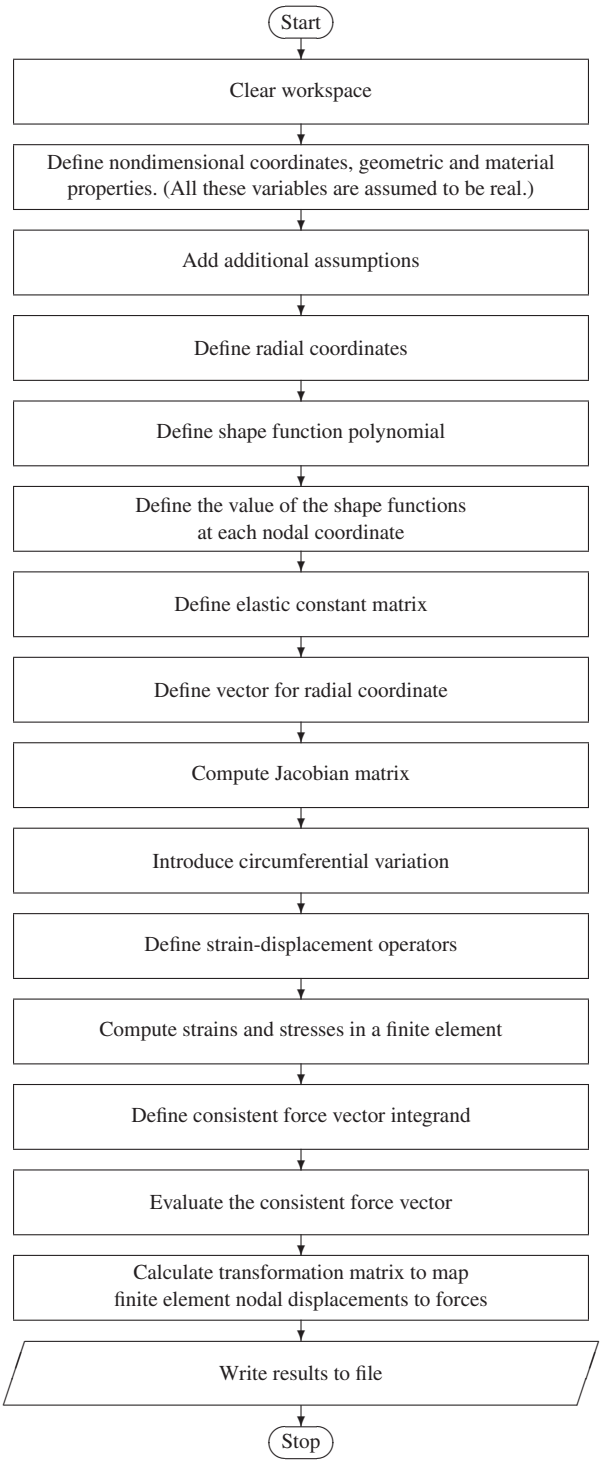

Figure G.2. A high level flowchart for Listing G.2.

the hybrid-SAFE procedure for axisymmetric notches. Note that reflections from a free end are also accommodated in this program. A high level flowchart for this listing is given in Figure G.3.

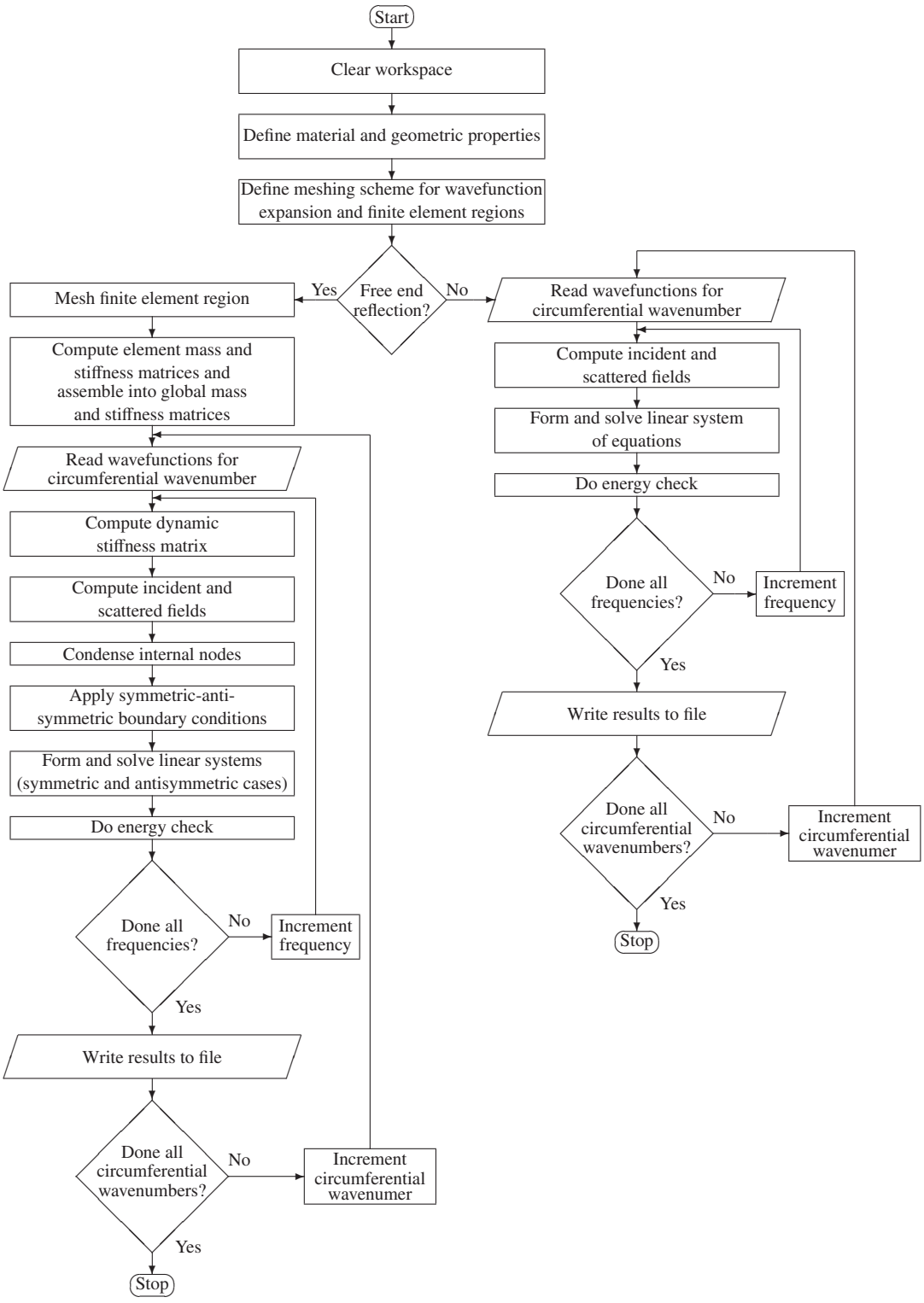

Figure G.3. A high level flowchart for Listing G.3.

Listing G.1. MATLAB® code to compute axisymmetric element stiffness and mass matrices for the axisymmetric case.

```
%Clear workspace
clear;
clc;

%Define symbolic variables using real values
syms xi eta ri ro zu zl n theta lambda mu rho real;

%Add additional assumptions
maple('assume(n,integer)');
maple('assume(ri,positive)');
maple('assume(ro,positive)');
maple('assume(lambda,positive)');
maple('assume(mu,positive)');
maple('assume(rho,positive)');
maple('additionally(ri<ro)');
maple('additionally(zl<zu)');

%Define radial coordinate locations
r1=ri;
r3=ro;
r2=(r1+r3)/2;
r4=r1;
r5=r3;
r6=r1;
r7=r2;
r8=r3;

%Define axial coordinate locations
z1=zu;
z2=zu;
z3=zu;
z4=(zu+zl)/2;
z5=z4;
z6=zl;
z7=zl;
z8=zl;

%Define shape function polynomial.  See [107].
P=[1 xi eta xi^2 xi*eta eta^2 xi^2*eta xi*eta^2];

%Define values of P at nodal coordinates.
%See [107].
A=[1 -1 1 1 -1 1 1 -1;
    1 0 1 0 0 1 0 0;
    1 1 1 1 1 1 1 1;
    1 -1 0 1 0 0 0 0;
    1 1 0 1 0 0 0 0;
    1 -1 -1 1 1 1 -1 -1;
    1 0 -1 0 0 1 0 0;
```

(Continued on next page...)

Listing G.1. MATLAB® code to compute axisymmetric element stiffness and mass matrices for the axisymmetric case. (Continued from previous page.)

```
51      1 1 -1 1 -1 1 -1 1];
52
53  %Define matrix of elastic constants
54  E=[lambda+2*mu lambda lambda 0 0 0;
55      lambda lambda+2*mu lambda 0 0 0;
56      lambda lambda lambda+2*mu 0 0 0;
57      0 0 0 mu 0 0;
58      0 0 0 0 mu 0;
59      0 0 0 0 0 mu];
60
61  %Convert A from numeric to symbolic variables
62  A=sym(A);
63
64  %Derive shape functions from P and A.
65  %See [107].
66  N=simple(P*inv(A));
67
68  %Define vectors of radial and axial
69  %nodal coordinates
70  rc=[r1; r2; r3; r4; r5; r6; r7; r8];
71  zc=[z1; z2; z3; z4; z5; z6; z7; z8];
72
73  %Define continuous radial and axial
74  %coordinate variable
75  r=simple(N*rc);
76  z=simple(N*zc);
77
78  %Compute the Jacobian matrix
79  J=simple([diff(z,eta) diff(r,eta);diff(z,xi) diff(r,xi)]);
80
81  %Compute the inverse of the Jacobian matrix
82  Gamma=simple(inv(J));
83
84  %Define the assumed circumferential variation
85  N2=simple(N*exp(j*n*theta));
86
87  %Define operators to give the radial, circumferential, and axial
88  %displacement and their derivatives which are required to compute
89  %the strain tensor
90  ou=simple([N2 zeros(1,16)]);
91  our=simple([diff(N2,eta)*Gamma(2,1)+diff(N2,xi)*Gamma(2,2) ...
92      zeros(1,16)]);
93  ouz=simple([diff(N2,eta)*Gamma(1,1)+diff(N2,xi)*Gamma(1,2) ...
94      zeros(1,16)]);
95  out=simple([diff(N2,theta) zeros(1,16)]);
96  ov=simple([zeros(1,8) N2 zeros(1,8)]);
97  ovr=simple([zeros(1,8) diff(N2,eta)*Gamma(2,1)+diff(N2,xi)*...
98      Gamma(2,2) zeros(1,8)]);
99  ovz=simple([zeros(1,8) diff(N2,eta)*Gamma(1,1)+diff(N2,xi)*...
```

(Continued on next page...)

Listing G.1. MATLAB® code to compute axisymmetric element stiffness and mass matrices for the axisymmetric case. (Continued from previous page.)

```
    Gamma(1,2) zeros(1,8)]);
ovt=simple([zeros(1,8) diff(N2,theta) zeros(1,8)]);
owr=simple([zeros(1,16) diff(N2,eta)*Gamma(2,1)+diff(N2,xi)*...
    Gamma(2,2)]);
owz=simple([zeros(1,16) diff(N2,eta)*Gamma(1,1)+diff(N2,xi)*...
    Gamma(1,2)]);
owt=simple([zeros(1,16) diff(N2,theta)]);

%Assemble a strain displacement operator
B=simple([our;ou/r+ovt/r;owz;ovz+owt/r;ouz+owr;out/r+ovr-ov/r]);


%Define the integrand for the finite element stiffness matrix
IK=B'*E*B*r*det(J);

%Define a matrix to hold the integrated finite element stiffness
%matrix
K=sym(zeros(size(IK)));

%Integrate the integrand of the finite element stiffness matrix
for a=1:1:size(IK,1)
    for b=1:1:size(IK,2)
        disp(['a=' int2str(a) ', b=' int2str(b)]);
        K(a,b)=simple(int(int(int(IK(a,b),xi,-1,1),theta,-pi,pi),...
            eta,-1,1));
    end
end

%Define matrices to factor the finite element stiffness matrix into
%terms that are constant, linear, and quadratic in n.  See [107].
K0=sym(zeros(size(K)));
K1=sym(zeros(size(K)));
K2=sym(zeros(size(K)));

%A test matrix
K3test=sym(zeros(size(K)));

%Define two working matrices
I1=sym(zeros(size(K)));
I2=sym(zeros(size(K)));

%Loop over all matrix components
for a=1:1:size(IK,1)
    for b=1:1:size(IK,2)
        disp(['a=' int2str(a) ', b=' int2str(b)]);

        %Set n=0 in K to get constant term
        if (subs(K(a,b),n,0)==0)
            K0(a,b)=sym(0);
```

(Continued on next page...)

Listing G.1. MATLAB® code to compute axisymmetric element stiffness and mass matrices for the axisymmetric case. (Continued from previous page.)

```
149         else
150             K0(a,b)=simple(subs(K(a,b),n,0));
151         end
152
153         %Compute result of removing constant term and store
154         %the result in the first working matrix
155         I1(a,b)=simple(K(a,b)-K0(a,b));
156
157         %Divide the working matrix by n and subsequently set n=0.
158         %This leaves only the terms linear in n.
159         I1(a,b)=simple(I1(a,b)/n);
160         if (subs(I1(a,b),n,0)==0)
161             K1(a,b)=sym(0);
162         else
163             K1(a,b)=simple(subs(I1(a,b),n,0));
164         end
165
166         %Compute result of removing constant term and linear terms
167         %and store the result in the second working matrix
168         I2(a,b)=simple((K(a,b)-K0(a,b)-K1(a,b)*n));
169
170         %Divide the working matrix by n^2 and subsequently set n=0.
171         %This leaves only the terms quadratic in n.
172         I2(a,b)=simple(I2(a,b)/n^2);
173         if (subs(I2(a,b),n,0)==0)
174             K2(a,b)=sym(0);
175         else
176             K2(a,b)=simple(subs(I2(a,b),n,0));
177         end
178
179         %Test that the sum of K0+n*K1+n^2*K2=K
180         K3test(a,b)=simple(K(a,b)-K0(a,b)-K1(a,b)*n-K2(a,b)*n^2);
181     end
182 end
183
184 %Define the integrand for the finite element mass matrix
185 IM=rho*[N2 zeros(1,16);zeros(1,8) N2 zeros(1,8);zeros(1,16) N2]'*...
186     [N2 zeros(1,16);zeros(1,8) N2 zeros(1,8);zeros(1,16) N2]*...
187     r*det(J);
188
189 %Define a matrix to hold the integrated finite element mass matrix
190 M=sym(zeros(size(IM)));
191
192 %Integrate the integrand of the finite element mass matrix
193 for a=1:1:size(IM,1)
194     for b=1:1:size(IM,2)
195         disp(['a=' int2str(a) ', b=' int2str(b)]);
196         M(a,b)=simple(int(int(int(IM(a,b),theta,-pi,pi),xi,-1,1),...
197             eta,-1,1));
```

(Continued on next page...)

Listing G.1. MATLAB® code to compute axisymmetric element stiffness and mass matrices for the axisymmetric case. (Continued from previous page.)

```
    end
end
%Write K0, K1, K2, and M to m files.
fid=fopen('K0.m','wt')

for a=1:1:size(K0,1)
    for b=1:1:size(K0,2)
        disp(['a=' int2str(a) ', b=' int2str(b)]);
        fprintf(fid,'K0fe(%d,%d)=%s;\n',a,b,char(simple(K0(a,b))));
    end
end

fclose(fid)

fid=fopen('K1.m','wt')

for a=1:1:size(K1,1)
    for b=1:1:size(K1,2)
        disp(['a=' int2str(a) ', b=' int2str(b)]);
        fprintf(fid,'K1fe(%d,%d)=%s;\n',a,b,char(simple(K1(a,b))));
    end
end

fclose(fid)

fid=fopen('K2.m','wt')

for a=1:1:size(K2,1)
    for b=1:1:size(K2,2)
        disp(['a=' int2str(a) ', b=' int2str(b)]);
        fprintf(fid,'K2fe(%d,%d)=%s;\n',a,b,char(simple(K2(a,b))));
    end
end

fclose(fid);
```

Listing G.2. MATLAB® code to evaluate the consistent, finite element force matrices for the axisymmetric case.

```
%Clear the workspace
clear;
clc;

%Define symbolic variables which are required to be real
syms xi ri ro n theta lambda mu rho z real;

%Define nodal displacements in a layer
syms u1 u2 u3 v1 v2 v3 w1 w2 w3 k;

%Add additional assumptions
maple('assume(n,integer)');
maple('assume(ri,positive)');
maple('assume(ro,positive)');
maple('assume(lambda,positive)');
maple('assume(mu,positive)');
maple('assume(rho,positive)');
maple('additionally(ri<ro)');

%Define radial coordinate locations
r1=ri;
r3=ro;
r2=(r1+r3)/2;

%Define shape function polynomial.  See [107].
P=[1 xi xi^2];

%Define values of P at nodal coordinates.
%See [107].
A=[1 -1 1;
   1  0 0;
   1 1 1];

%Define matrix of elastic constants
E=[lambda+2*mu lambda lambda 0 0 0;
    lambda lambda+2*mu lambda 0 0 0;
    lambda lambda lambda+2*mu 0 0 0;
    0 0 0 mu 0 0;
    0 0 0 0 mu 0;
    0 0 0 0 0 mu];

%Convert A from numeric to symbolic variables
A=sym(A);

%Derive shape functions from P and A.
%See [107].
N=simple(P*inv(A));

%Define vectors of radial coordinates
```

(Continued on next page...)

Listing G.2. MATLAB® code to evaluate the consistent, finite element force matrices for the axisymmetric case. (Continued from previous page.)

```
rc=[r1; r2; r3];

%Define continuous radial coordinate variable
r=simple(N*rc);

%Define continuous displacement variables
u=simple(N*[u1;u2;u3]);
v=simple(N*[v1;v2;v3]);
w=simple(N*[w1;w2;w3]);

%Compute the Jacobian matrix
J=simple([diff(r,xi)]);

%Incorporate the circumferential and axial variations in the
%displacement variables
u=u*exp(j*n*theta)*exp(j*k*z);
v=v*exp(j*n*theta)*exp(j*k*z);
w=w*exp(j*n*theta)*exp(j*k*z);

%Compute the strain over the layer
e=simple([diff(u,xi)/J;
   u/r+diff(v,theta)/r;
   diff(w,z);
   diff(u,z)+diff(w,xi)/J;
   diff(u,theta)/r+diff(v,xi)/J-v/r;
   diff(v,z)+diff(w,theta)/r]);

%Remove the circumferential variations from the strain.
%(It will be reintroduced later.)
e=e/exp(j*k*z);

%Compute the stress over the layer
s=simple(E*e);

%Reintroduce the circumferential variations from the stress
Nt=(N*exp(j*n*theta))';

%Compute the consistent force vectors by integrating over the
%axisymmetric element's face.  See [107].

%Radial
Fr=simple(int(int(Nt*s(4)*r*J,theta,sym('-pi'),sym('pi')),xi,...
    sym('-1'),sym('1')));
%Circumferential
Ft=simple(int(int(Nt*s(6)*r*J,theta,sym('-pi'),sym('pi')),xi,...
    sym('-1'),sym('1')));
%Axial
Fz=simple(int(int(Nt*s(3)*r*J,theta,sym('-pi'),sym('pi')),xi,...
    sym('-1'),sym('1')));
```

(Continued on next page...)

Listing G.2. MATLAB® code to evaluate the consistent, finite element force matrices for the axisymmetric case. (Continued from previous page.)

```
99  %Assemble the force vector
100 F=[Fr;Ft;Fz];
101
102 %Define a matrix to map the nodal displacements in a layer into
103 %consistent nodal forces
104 AT=sym(zeros(9,9));
105
106 %Loop over all elements of the matrix that maps the nodal
107 %displacements into consistent nodal forces, AT.  Set all
108 %displacements except one to zero to get the contribution
109 %to the nodal force vector of that one displacement
110 %component.
111 for a=1:1:9
112     for b=1:1:9
113         dv=sym(zeros(1,9));
114         dv(b)=sym(1);
115         AT(a,b)=simple(subs(F(a),{u1,u2,u3,v1,v2,v3,w1,w2,w3},dv));
116     end
117 end
118
119 %A test, Chk should be a null vector.
120 Chk=simple(F-AT*[u1;u2;u3;v1;v2;v3;w1;w2;w3])
121
122 %Write the matrix that maps the nodal
123 %displacements into consistent nodal forces, AT, to file.
124 %Minimal hand written code is required to complete
125 %a function which takes the nodal displacements in a layer
126 %and computes the (consistent) nodal force vector.
127 fid=fopen('AT.m','wt');
128
129 fprintf(fid,'%s\n',a,b,char(simple(AT)));
130
131 fclose(fid);
```

Listing G.3. MATLAB® code to implement the axisymmetric scattering problem.

```
%Clear workspace
clear;
clc;

%Control Information
%Define circumferential wavenumbers
Nm=[-16:1:16];

%Common Information, material and dimensional properties
lambdap=113.2E9; %First Lame constant
mup=84.3E9; %Second Lame constant
l_m=lambdap/mup; %Ratio of Lame constants
rhop=7932; %Density
Hp=0.220*25.4E-3; %Wall thickness
Do=3.4960*25.4E-3; %Outer diameter
Rp=(Do-Hp)/2; %Mean radius
H_R=Hp/Rp; %Wall thickness to mean radius ratio
wref=1/Hp*sqrt(mup/rhop);%Reference frequency
mu=1; %Nondimensional shear modulus
lambda=l_m*mu; %Nondimensional Lame constant
rho=1; %Nondimensional mass density


%Wave function expansion information
H=1; %Nondimensional wall thickness
N=10; %Number of elements in wave function expansion region
dof=3; %Number of nodal degrees of freedom
L=(2*N+1)*dof; %Length of mode shape vectors, number of axial modes

%Finite element region information
Rip=(2-H_R)/2/H_R*H; %Inner radius of finite element region
Rop=Rip+1; %Outer radius of finite element region
zby2=3.1750E-3/Hp*1/4; %Half length of finite element region
Nz=4; %Number of elements in the axial direction


%Mesh in radial direction
[rife,rofe,rmfe,rki,rko,rkm,FE,Er]=HMesh(H_R,N,Rip,Rop);

if Er
    error('An error was detected in HMesh.');
end

%Mesh in axial direction
[zl,zu,Er]=ZMesh(zby2,Nz,FE);
if Er
    error('An error was detected in ZMesh.');
end
```

(Continued on next page...)

Listing G.3. MATLAB® code to implement the axisymmetric scattering problem. (Continued from previous page.)

```
49 if ~FE %This is the case for a notch
50
51     %Create FE mesh...
52
53     %Number of nodes in FE region
54     Nfe=length(rife); %Number of elements in the radial direction...
55     %in the FE region
56     Mfe=length(zl); %Number of elements in the axial direction in...
57     %the FE region
58     FEN=(3*Mfe+2)*Nfe+2*Mfe+1; %Total number of nodes in the FE...
59     %region
60
61     %Assign memory for global mass and stiff matrices
62     Mg=sparse(3*FEN,3*FEN); %Mass matrix
63     K0g=sparse(3*FEN,3*FEN); %Constant stiffness matrix
64     K1g=sparse(3*FEN,3*FEN); %Stiffness matrix in n
65     K2g=sparse(3*FEN,3*FEN); %Stiffness matrix in n^2
66
67     %Loop over all elements
68     for nfe=1:1:Nfe
69         for mfe=1:1:Mfe
70             %Element matrices
71
72             %Mass matrices
73             [Me,Er]=M(rife(nfe),rofe(nfe),zl(mfe),zu(mfe),rho);
74             if Er
75                 error('An error was detected in M.');
76             end
77
78             %Constant stiffness matrices
79             [K0e,Er]=K0(rife(nfe),rofe(nfe),zl(mfe),zu(mfe),...
80                 lambda,mu);
81             if Er
82                 error('An error was detected in K0.');
83             end
84
85             %Stiffness matrix in n
86             [K1e,Er]=K1(rife(nfe),rofe(nfe),zl(mfe),zu(mfe),...
87                 lambda,mu);
88             if Er
89                 error('An error was detected in K1.');
90             end
91
92             %Stiffness matrix in n^2
93             [K2e,Er]=K2(rife(nfe),rofe(nfe),zl(mfe),zu(mfe),...
94                 lambda,mu);
95             if Er
```

(Continued on next page...)

Listing G.3. MATLAB® code to implement the axisymmetric scattering problem. (Continued from previous page.)

```
96                  error('An error was detected in K2.');
97              end
98
99              %Assembly
100             %Calculate element nodes
101             Nodenums=Nodes(Nfe,nfe,mfe);
102             Rows=[Nodenums;FEN+Nodenums;2*FEN+Nodenums];
103             Cols=Rows;%[Nodenums;FEN+Nodenums;2*FEN+Nodenums];
104
105             %Do assembly
106             for a=1:1:length(Rows)
107                 Mg(Rows(a),Cols)=Mg(Rows(a),Cols)+Me(a,:);
108                 K0g(Rows(a),Cols)=K0g(Rows(a),Cols)+K0e(a,:);
109                 K1g(Rows(a),Cols)=K1g(Rows(a),Cols)+K1e(a,:);
110                 K2g(Rows(a),Cols)=K2g(Rows(a),Cols)+K2e(a,:);
111             end
112         end
113     end
114
115     %Loop over all circumferential wavenumbers
116     for n=1:1:length(Nm)
117
118         disp(['n= ' num2str(Nm(n)) ' out of ' num2str(length(Nm))]);
119
120         %Clear data from previous circumferential wavenumber
121         if n~=1
122             clear 'fwhole' 'Rvalf' 'REVf' 'LRvalf' 'LREVf';
123         end
124
125         %Load wavefunctions from file
126         load(['L:\RASD2010\WF\F_' num2str(Nm(n)) '.mat'],...
127             'fwhole', 'Rvalf', 'REVf', 'LRvalf', 'LREVf');
128
129         %Define arrays
130         %Solutions to symmetric and antisymmetric loading problems
131         Asym=zeros(length(fwhole),size(Rvalf,2),size(Rvalf,2));
132         Aasym=zeros(length(fwhole),size(Rvalf,2),size(Rvalf,2));
133         %Work balance
134         %Incident
135         workin=zeros(length(fwhole),L);
136         %Reflected
137         workr=zeros(length(fwhole),L,L);
138         %Transmitted
139         workt=zeros(length(fwhole),L,L);
140
141         %Calculate FE global mass and stiffness matrices
142         K=K0g+Nm(n)*K1g+Nm(n)^2*K2g;
143         M=Mg;
```

(Continued on next page...)

Listing G.3. MATLAB® code to implement the axisymmetric scattering problem. (Continued from previous page.)

```
144  %Loop over all frequencies
145         for f=1:1:length(fwhole)
146
147             disp(['f= ' num2str(f) ' out of '...
148                 num2str(length(fwhole))]);
149
150             %Compute dynamic stiffness matrix
151             S=K0g+Nm(n)*K1g+Nm(n)^2*K2g-(fwhole(f)/wref)^2*Mg;
152
153             %Find (force) free nodes on B+
154
155             %Nodes on Wave Function Expansion (WFE)
156             rnwfe=sort([rki;rkm;rko(end)],'ascend');
157
158             %Nodes on Finite Element Region (FER)
159             rnfer=sort([rife;rmfe;rofe(end)],'ascend');
160
161             %Find free nodes on FER
162             FNFE=[];
163             for a=1:1:length(rnfer)
164                 if min(abs(rnfer(a)-rnwfe))>1E-6
165                     FNFE=[FNFE;a];
166                 end
167             end
168
169             %Find free nodes on WFE
170             FNWF=[];
171             for a=1:1:length(rnwfe)
172                 if min(abs(rnwfe(a)-rnfer))>1E-6
173                     FNWF=[FNWF;a];
174                 end
175             end
176
177             %Define array of incident nodal forces
178             Fin=zeros(3*(2*N+1),size(LRvalf,2));
179
180             %Calculate incident field.  Assume only one mode
181             %having unit magnitude
182
183             %Nodal displacements
184             qin=zeros(3*(2*N+1),size(LRvalf,2));
185
186             for mm=1:1:size(LRvalf,2)
187                 qin(:,mm)=(squeeze(LREVf(f,:,mm))).';
188             end
189
190             %Find incident nodal forces
191             for mm=1:1:L
192                 for a=1:1:N
```

(Continued on next page...)

Listing G.3. MATLAB® code to implement the axisymmetric scattering problem. (Continued from previous page.)

```
                        %Force in each finite element
                        [fint,Er]=fin(lambda,mu,rko(a),rki(a),Nm(n),...
                          LRvalf(f,mm),qin([2*(a-1)+1:1:2*(a-1)+3 ...
                          2*(a-1)+1+(2*N+1):1:2*(a-1)+3+(2*N+1)...
                          2*(a-1)+1+2*(2*N+1):1:2*(a-1)+3+2*(2*N+1)],...
                          mm));
                        %Assembled forces
                        Fin([2*(a-1)+1:1:2*(a-1)+3 ...
                          2*(a-1)+1+(2*N+1):1:2*(a-1)+3+(2*N+1)...
                          2*(a-1)+1+2*(2*N+1):1:2*(a-1)+3+2*(2*N+1)],...
                          mm)=Fin([2*(a-1)+1:1:2*(a-1)+3 ...
                          2*(a-1)+1+(2*N+1):1:2*(a-1)+3+(2*N+1)...
                          2*(a-1)+1+2*(2*N+1):1:2*(a-1)+3+2*(2*N+1)],...
                          mm)+fint;
                    end
                end

                %Scattered displacements
                G=squeeze(REVf(f,:,:));

                %Find scattered nodal forces
                Fscat=zeros(3*(2*N+1),3*(2*N+1));

                for b=1:1:3*(2*N+1)
                    for a=1:1:N
                        %Force in each finite element
                        [fint,Er]=fin(lambda,mu,rko(a),rki(a),Nm(n),...
                          Rvalf(f,b),G([2*(a-1)+1:1:2*(a-1)+3 ...
                          2*(a-1)+1+(2*N+1):1:2*(a-1)+3+(2*N+1)...
                          2*(a-1)+1+2*(2*N+1):1:2*(a-1)+3+2*(2*N+1)],...
                          b));
                        %Assembled forces
                        Fscat([2*(a-1)+1:1:2*(a-1)+3 ...
                          2*(a-1)+1+(2*N+1):1:2*(a-1)+3+(2*N+1)...
                          2*(a-1)+1+2*(2*N+1):1:2*(a-1)+3+2*(2*N+1)],...
                          b)=Fscat([2*(a-1)+1:1:2*(a-1)+3 ...
                          2*(a-1)+1+(2*N+1):1:2*(a-1)+3+(2*N+1)...
                          2*(a-1)+1+2*(2*N+1):1:2*(a-1)+3+2*(2*N+1)],...
                          b)+fint;
                    end
                end

                %Do condensation of internal nodes of FE region...
                %SII=[SIIrr SIItr SIIzr];
                SII=[S(2*Nfe+2:1:FEN-2*Nfe-1,[2*Nfe+2:1:FEN-2*Nfe-1 ...
                    2*Nfe+2+FEN:1:FEN-2*Nfe-1+FEN 2*Nfe+2+2*FEN:1:FEN-...
                    2*Nfe-1+2*FEN]);
                    S(2*Nfe+2+FEN:1:FEN-2*Nfe-1+FEN,...
                    [2*Nfe+2:1:FEN-2*Nfe-1 2*Nfe+2+FEN:1:FEN-2*Nfe-1 ...
```

(Continued on next page...)

Listing G.3. MATLAB® code to implement the axisymmetric scattering problem. (Continued from previous page.)

```
                +FEN 2*Nfe+2+2*FEN:1:FEN-2*Nfe-1+2*FEN]);
                S(2*Nfe+2+2*FEN:1:FEN-2*Nfe-1+2*FEN,...
                [2*Nfe+2:1:FEN-2*Nfe-1 2*Nfe+2+FEN:1:FEN-2*Nfe-1 ...
                +FEN 2*Nfe+2+2*FEN:1:FEN-2*Nfe-1+2*FEN])];
            %SIB=[SIBrr SIBtr SIIzr];
            SIB=[S(2*Nfe+2:1:FEN-2*Nfe-1,[1:1:2*Nfe+1 ...
                FEN-2*Nfe:1:FEN FEN+1:1:FEN+2*Nfe+1 ...
                FEN+FEN-2*Nfe:1:FEN+FEN 2*FEN+1:1:2*FEN+2*Nfe+1 ...
                2*FEN+FEN-2*Nfe:1:2*FEN+FEN]);
                S(2*Nfe+2+FEN:1:FEN-2*Nfe-1+FEN,[1:1:2*Nfe+1 ...
                FEN-2*Nfe:1:FEN FEN+1:1:FEN+2*Nfe+1 ...
                FEN+FEN-2*Nfe:1:FEN+FEN 2*FEN+1:1:2*FEN+2*Nfe+1 ...
                2*FEN+FEN-2*Nfe:1:2*FEN+FEN]);
                S(2*Nfe+2+2*FEN:1:FEN-2*Nfe-1+2*FEN,...
                [1:1:2*Nfe+1 FEN-2*Nfe:1:FEN FEN+1:1:FEN+2*Nfe+1 ...
                FEN+FEN-2*Nfe:1:FEN+FEN 2*FEN+1:1:2*FEN+2*Nfe+1 ...
                2*FEN+FEN-2*Nfe:1:2*FEN+FEN])];

            %SBI=[SBIrr SBItr SBIzr];
            SBI=[S([1:1:2*Nfe+1 FEN-2*Nfe:1:FEN],...
                [2*Nfe+2:1:FEN-2*Nfe-1 2*Nfe+2+FEN:1:FEN-2*Nfe-1+...
                FEN 2*Nfe+2+2*FEN:1:FEN-2*Nfe-1+2*FEN]);
                S([FEN+1:1:FEN+2*Nfe+1 FEN+FEN-2*Nfe:1:FEN+FEN],...
                [2*Nfe+2:1:FEN-2*Nfe-1 2*Nfe+2+FEN:1:FEN-2*Nfe-1+...
                FEN 2*Nfe+2+2*FEN:1:FEN-2*Nfe-1+2*FEN]);
                S([2*FEN+1:1:2*FEN+2*Nfe+1 2*FEN+FEN-2*Nfe:1:2*FEN...
                +FEN],[2*Nfe+2:1:FEN-2*Nfe-1 2*Nfe+2+FEN:1:FEN-2 ...
                *Nfe-1+FEN 2*Nfe+2+2*FEN:1:FEN-2*Nfe-1+2*FEN])];
            %SBB=[SBBrr SBBtr SBIzr];
            SBB=[S([1:1:2*Nfe+1 FEN-2*Nfe:1:FEN],[1:1:2*Nfe+1 ...
                FEN-2*Nfe:1:FEN FEN+1:1:FEN+2*Nfe+1 ...
                FEN+FEN-2*Nfe:1:FEN+FEN 2*FEN+1:1:2*FEN+2*Nfe+1 ...
                2*FEN+FEN-2*Nfe:1:2*FEN+FEN]);
                S([FEN+1:1:FEN+2*Nfe+1 FEN+FEN-2*Nfe:1:FEN+FEN],...
                [1:1:2*Nfe+1 FEN-2*Nfe:1:FEN FEN+1:1:FEN+2*Nfe+1 ...
                FEN+FEN-2*Nfe:1:FEN+FEN 2*FEN+1:1:2*FEN+2*Nfe+1 ...
                2*FEN+FEN-2*Nfe:1:2*FEN+FEN]);
                S([2*FEN+1:1:2*FEN+2*Nfe+1 2*FEN+FEN-2*Nfe:1:2 ...
                *FEN+FEN],[1:1:2*Nfe+1 FEN-2*Nfe:1:FEN...
                FEN+1:1:FEN+2*Nfe+1 FEN+FEN-2*Nfe:1:FEN+FEN...
                2*FEN+1:1:2*FEN+2*Nfe+1 ...
                2*FEN+FEN-2*Nfe:1:2*FEN+FEN])];

            %Sq=P

            %[SII SIB;SBI SBB]{qI qB}^T={PI PB}^T={0 PB}^T
            %SII*qI+SIB*qB=0 -> qI=-SII^-1*SIB*qB
            %So: (-SBI*SII^-1*SIB+SBB)=PB=Scup*qb
```

(Continued on next page...)

Listing G.3. MATLAB® code to implement the axisymmetric scattering problem. (Continued from previous page.)

```
292             Scup=-SBI*(SII\SIB)+SBB;
293
294             %Number of nodes now in FE region
295             FENcup=2*(2*Nfe+1);
296
297             %Modify Scup for free nodes on B+ of the FE region
298             if ~isempty(FNFE)
299
300                 %Non-free nodes on B+
301                 NFFE=1:1:FENcup;
302                 NFFE(FNFE)=[];
303
304                 %[Scup00 Scup0f;Scupf0 Scupff]{q0 qf}^T={0 P}^T
305                 Scup00=[Scup(FNFE,[FNFE FNFE+FENcup FNFE+2*FENcup]);
306                     Scup(FNFE+FENcup,[FNFE FNFE+FENcup...
307                     FNFE+2*FENcup]);
308                     Scup(FNFE+2*FENcup,[FNFE FNFE+FENcup...
309                     FNFE+2*FENcup])];
310
311                 Scup0f=[Scup(FNFE,[NFFE NFFE+FENcup NFFE+2*FENcup]);
312                     Scup(FNFE+FENcup,[NFFE NFFE+FENcup...
313                     NFFE+2*FENcup]);
314                     Scup(FNFE+2*FENcup,[NFFE NFFE+FENcup...
315                     NFFE+2*FENcup])];
316
317                 Scupf0=[Scup(NFFE,[FNFE FNFE+FENcup FNFE+2*FENcup]);
318                     Scup(NFFE+FENcup,[FNFE FNFE+FENcup...
319                     FNFE+2*FENcup]);
320                     Scup(NFFE+2*FENcup,[FNFE FNFE+FENcup...
321                     FNFE+2*FENcup])];
322
323                 Scupff=[Scup(NFFE,[NFFE NFFE+FENcup NFFE+2*FENcup]);
324                     Scup(NFFE+FENcup,[NFFE NFFE+FENcup...
325                     NFFE+2*FENcup]);
326                     Scup(NFFE+FENcup,[NFFE NFFE+FENcup...
327                     NFFE+2*FENcup])];
328                 Scup=-Scupf0*(Scup00\Scup0f)+Scupff;
329                 size(Scup)
330             end
331
332             %Nodes on B+
333             NBplus=1:1:2*Nfe+1-length(FNFE);
334             %Nodes on B-
335             NBminus=NBplus(end)+1:1:NBplus(end)+(2*Nfe+1);
336
337             %Numbr of remaining nodes now in FE region
338             FENcup=length(NBplus)+length(NBminus);
339
340             %Symmetric case
```

(Continued on next page...)

Listing G.3. MATLAB® code to implement the axisymmetric scattering problem. (Continued from previous page.)

```
342             %[Sscup-- Sscup-+;Sscup+- Sscup++]{q- q+}^T={P- P+}^T
343             %q-={ur- ut- 0}^T P-={0 0 fz-}^T
344
345             %Ignore fz-, condense out uz-
346             Sstars=Scup;
347             %Delete columns corresponding to uz-
348             Sstars(:,NBminus+2*FENcup)=[];
349             %Delete rows corresonding to fz- (not of interest)
350             Sstars(NBminus+2*FENcup,:)=[];
351
352             %[Sstars-- Sstars-+;Sstars+- Sstars++]*...
353             %[q-stars q+stars]^T=[0 P+]^T
354
355             %Eliminate q-stars (Note, no z component for
356             %displacement on B- and no r
357             %or theta component for force on B-).
358
359             Sstarsmm=[Sstars(NBminus, [NBminus NBminus+FENcup]);
360                 Sstars(NBminus+FENcup, [NBminus NBminus+FENcup])];
361
362             Sstarsmp=[Sstars(NBminus, [NBplus NBplus+FENcup...
363                 NBplus+2*FENcup]);
364                 Sstars(NBminus+FENcup, [NBplus NBplus+FENcup ...
365                 NBplus+2*FENcup])];
366
367             Sstarspm=[Sstars(NBplus, [NBminus NBminus+FENcup]);
368                 Sstars(NBplus+FENcup, [NBminus NBminus+FENcup]);
369                 Sstars(NBplus+2*FENcup, [NBminus NBminus+FENcup])];
370
371             Sstarspp=[Sstars(NBplus, [NBplus NBplus+FENcup...
372                 NBplus+2*FENcup]);
373                 Sstars(NBplus+FENcup, [NBplus NBplus+FENcup...
374                 NBplus+2*FENcup]);
375                 Sstars(NBplus+2*FENcup, [NBplus NBplus+FENcup...
376                 NBplus+2*FENcup])];
377
378             Sstars=-Sstarspm*(Sstarsmm\Sstarsmp)+Sstarspp;
379
380
381             %Anti-symmetric case
382             %[Sscup-- Sscup-+;Sscup+- Sscup++]{q- q+}^T={P- P+}^T
383             %q-={0 0 uz-}^T P-={fr- ft- 0}^T
384
385             %Ignore fr- fr+, condense out ur- and ut-
386             Sstara=Scup;
387             %Delete columns corresponding to ur- and ut-
388             Sstara(:,[NBminus NBminus+FENcup])=[];
389             %Delete rows corresponding to fr- and ft- (not of
390             %interest)...
```

(Continued on next page...)

Listing G.3. MATLAB® code to implement the axisymmetric scattering problem. (Continued from previous page.)

```
392             Sstara([NBminus NBminus+FENcup],:)=[];
393
394             %[Sstara-- Sstara-+;Sstara+- Sstara++]...
395             %[q-stara q+stara]^T=[0 P+]^T
396
397             %Eliminate q-stara (Note, no r or theta component for
398             %displacement on B- and no z
399             %component for force on B-).
400
401             Sstaramm=Sstara(NBminus+2*length(NBplus),...
402                 NBminus+2*length(NBplus));
403
404             Sstaramp=Sstara(NBminus+2*length(NBplus),...
405                 [NBplus NBplus+length(NBplus)...
406                 NBplus+2*length(NBplus)]);
407
408             Sstarapm=[Sstara(NBplus, NBminus+2*length(NBplus));
409                 Sstara(NBplus+length(NBplus),...
410                 NBminus+2*length(NBplus));
411                 Sstara(NBplus+2*length(NBplus),...
412                 NBminus+2*length(NBplus))];
413
414             Sstarapp=[Sstara(NBplus, [NBplus NBplus+length(NBplus)...
415                 NBplus+2*length(NBplus)]);
416                 Sstara(NBplus+length(NBplus), [NBplus NBplus+...
417                 length(NBplus) NBplus+2*length(NBplus)]);
418                 Sstara(NBplus+2*length(NBplus), [NBplus NBplus+...
419                 length(NBplus) NBplus+2*length(NBplus)])];
420
421             Sstara=-Sstarapm*(Sstaramm\Sstaramp)+Sstarapp;
422
423             %Form linear systems...
424             %Find matching nodes from FE and WFE
425             %First node
426             FN=find(abs(rnfer(1)-rnwfe)==min(abs(rnfer(1)-rnwfe)));
427             %Last node
428             LN=find(abs(rnfer(end)-rnwfe)==min(abs(rnfer(end)...
429                     -rnwfe)));
430
431             %Symmetric case...
432             Rs=Fin;
433             Kfinals=-Fscat;
434
435             %Force free nodes already done...
436             Rs([FN:1:LN FN+(2*N+1):1:LN+(2*N+1) FN+2*(2*N+1):1:LN+...
437               2*(2*N+1)],:)=Rs([FN:1:LN FN+(2*N+1):1:LN+(2*N+1)...
438               FN+2*(2*N+1):1:LN+2*(2*N+1)],:)-Sstars*qin([FN:1:LN...
439               FN+(2*N+1):1:LN+(2*N+1) ...
440               FN+2*(2*N+1):1:LN+2*(2*N+1)],:);
```

(Continued on next page...)

Listing G.3. MATLAB® code to implement the axisymmetric scattering problem. (Continued from previous page.)

```
441                 Kfinals([FN:1:LN FN+(2*N+1):1:LN+(2*N+1) ...
442                   FN+2*(2*N+1):1:LN+2*(2*N+1)],:)=Kfinals([FN:1:LN FN...
443                   +(2*N+1):1:LN+(2*N+1) FN+2*(2*N+1):1:LN+2*(2*N+1)],...
444                   :)+Sstars*G([FN:1:LN FN+(2*N+1):1:LN+(2*N+1)...
445                   FN+2*(2*N+1):1:LN+2*(2*N+1)],:);
446
447                 As=Kfinals\Rs;
448                 Asym(f,:,:)=As;
449
450                 %Anti-symmetric case...
451                 Ra=Fin;
452                 Kfinala=-Fscat;
453
454                 %Force free nodes already done...
455                 Ra([FN:1:LN FN+(2*N+1):1:LN+(2*N+1) ...
456                     FN+2*(2*N+1):1:LN+2*(2*N+1)],:)=Ra([FN:1:LN FN+...
457                     (2*N+1):1:LN+(2*N+1) FN+2*(2*N+1):1:LN+2*(2*N+1)]...
458                     ,:)-Sstara*qin([FN:1:LN FN+(2*N+1):1:LN+(2*N+1)...
459                     FN+2*(2*N+1):1:LN+2*(2*N+1)],:);
460                 Kfinala([FN:1:LN FN+(2*N+1):1:LN+(2*N+1) ...
461                   FN+2*(2*N+1):1:LN+2*(2*N+1)],:)=Kfinala([FN:1:LN FN...
462                   +(2*N+1):1:LN+(2*N+1) FN+2*(2*N+1):1:LN+2*(2*N+1)]...
463                   ,:)+Sstara*G([FN:1:LN FN+(2*N+1):1:LN+(2*N+1)...
464                   FN+2*(2*N+1):1:LN+2*(2*N+1)],:);
465
466                 Aa=Kfinala\Ra;
467                 Aasym(f,:,:)=Aa;
468
469                 %Energy Check - This code works but is slow.
470                 %An alternative method is used in practice.
471
472                 %Incident
473                 for mm=1:1:L
474                     for a=1:1:N
475                         %Work in each layer
476                         [workl,Er]=Work(lambda,mu,rko(a),rki(a),...
477                             Nm(n),LRvalf(f,mm),squeeze(LREVf(f,...
478                             [2*(a-1)+1:1:2*(a-1)+3 2*(a-1)+1+...
479                             (2*N+1):1:2*(a-1)+3+(2*N+1) 2*(a-1)+1+2*...
480                             (2*N+1):1:2*(a-1)+3+2*(2*N+1)],mm)).');
481                         %Total over all layers
482                         workin(f,mm)=workin(f,mm)+workl;
483                     end
484                 end
485
486                 %Reflected
487                 for mm=1:1:L
488                     for b=1:1:L
489                         for a=1:1:N
```

(Continued on next page...)

Listing G.3. MATLAB® code to implement the axisymmetric scattering problem. (Continued from previous page.)

```
                            %Work in each layer
                            [workl,Er]=Work(lambda,mu,rko(a),rki(a),...
                                Nm(n),Rvalf(f,b),(Asym(f,b,mm)+...
                                Aasym(f,b,mm))/2*squeeze(REVf(f,...
                                [2*(a-1)+1:1:2*(a-1)+3 2*(a-1)+1+...
                                (2*N+1):1:2*(a-1)+3+(2*N+1)...
                                2*(a-1)+1+2*(2*N+1):1:2*(a-1)...
                                +3+2*(2*N+1)],b)).');
                            %Total over all layers
                            workr(f,b,mm)=workr(f,b,mm)+workl;
                        end
                    end

                    %Transmitted
                    for b=1:1:3*(2*N+1)
                        for a=1:1:N
                            %Work in each layer
                            [workl,Er]=Work(lambda,mu,rko(a),rki(a),...
                                Nm(n),LRvalf(f,b),(Asym(f,b,mm)-...
                                Aasym(f,b,mm))/2*squeeze(LREVf(f,...
                                [2*(a-1)+1:1:2*(a-1)+3 2*(a-1)+1+...
                                (2*N+1):1:2*(a-1)+3+(2*N+1) 2*...
                                (a-1)+1+2*(2*N+1):1:2*(a-1)+3+2*...
                                (2*N+1)],b)).');
                            %Total over all layers
                            workt(f,b,mm)=workt(f,b,mm)+workl;
                        end
                    end
                end
            end

            %Write results to file
            save(['F_' num2str(Nm(n)) '.mat'], 'fwhole', 'Asym',...
                'Aasym','workin','workr','workt');
        end
    else %Free end...

        %Loop over all circumferential wavenumbers
        for n=1:1:length(Nm)

            disp(['n= ' num2str(Nm(n)) ' out of ' num2str(length(Nm))]);

            %Clear data from previous circumferential wavenumber
            if n~=1
                clear 'fwhole' 'Rvalf' 'REVf' 'LRvalf' 'LREVf';
            end

            %Load wavefunctions from file
```

(Continued on next page...)

Listing G.3. MATLAB® code to implement the axisymmetric scattering problem. (Continued from previous page.)

```
538         load(['L:\RASD2010\WF\F_' num2str(Nm(n)) '.mat'],...
539             'fwhole', 'Rvalf', 'REVf', 'LRvalf', 'LREVf');
540
541         %Define arrays for solutions
542         %Amplitude of reflection
543         AFE=zeros(length(fwhole),size(Rvalf,2),size(Rvalf,2));
544         %Work done by incident waves
545         workin=zeros(length(fwhole),L);
546         %Work done by reflected waves
547         workr=zeros(length(fwhole),L,L);
548
549         %Loop over all frequencies
550         for f=1:1:length(fwhole)
551
552             disp(['f= ' num2str(f) ' out of '...
553                 num2str(length(fwhole))]);
554
555             %Define array for incident nodal forces
556             Fin=zeros(3*(2*N+1),size(LRvalf,2));
557
558             %Calculate incident field.  Assume only one mode
559             %having unit magnitude
560             qin=zeros(3*(2*N+1),size(LRvalf,2));
561
562             for mm=1:1:size(LRvalf,2)
563                 qin(:,mm)=(squeeze(LREVf(f,:,mm))).';
564             end
565
566             %Find incident nodal forces
567             for mm=1:1:L
568                 for a=1:1:N
569                     %Force in each element
570                     [fint,Er]=fin(lambda,mu,rko(a),rki(a),Nm(n),...
571                       LRvalf(f,mm),qin([2*(a-1)+1:1:2*(a-1)+3 ...
572                       2*(a-1)+1+(2*N+1):1:2*(a-1)+3+(2*N+1)...
573                       2*(a-1)+1+2*(2*N+1):1:2*(a-1)+3+2*(2*N+1)],...
574                       mm));
575                     %Assembled nodal forces
576                     Fin([2*(a-1)+1:1:2*(a-1)+3 ...
577                       2*(a-1)+1+(2*N+1):1:2*(a-1)+3+(2*N+1) ...
578                       2*(a-1)+1+2*(2*N+1):1:2*(a-1)+3+2*(2*N+1)],...
579                       mm)=Fin([2*(a-1)+1:1:2*(a-1)+3 ...
580                       2*(a-1)+1+(2*N+1):1:2*(a-1)+3+(2*N+1)...
581                       2*(a-1)+1+2*(2*N+1):1:2*(a-1)+3+2*(2*N+1)],...
582                       mm)+fint;
583                 end
584             end
585
586             %Scattered displacements
```

(Continued on next page...)

Listing G.3. MATLAB® code to implement the axisymmetric scattering problem. (Continued from previous page.)

```
587             G=squeeze(REVf(f,:,:));
588
589             %Find scattered nodal forces
590             Fscat=zeros(3*(2*N+1),3*(2*N+1));
591
592             for b=1:1:3*(2*N+1)
593                 for a=1:1:N
594                     %Force for each element
595                     [fint,Er]=fin(lambda,mu,rko(a),rki(a),Nm(n),...
596                         Rvalf(f,b),G([2*(a-1)+1:1:2*(a-1)+3 ...
597                         2*(a-1)+1+(2*N+1):1:2*(a-1)+3+(2*N+1)...
598                         2*(a-1)+1+2*(2*N+1):1:2*(a-1)+3+2*(2*N+1)]...
599                         ,b));
600                     %Assembled nodal forces
601                     Fscat([2*(a-1)+1:1:2*(a-1)+3 ...
602                       2*(a-1)+1+(2*N+1):1:2*(a-1)+3+(2*N+1)...
603                       2*(a-1)+1+2*(2*N+1):1:2*(a-1)+3+2*(2*N+1)],...
604                       b)=Fscat([2*(a-1)+1:1:2*(a-1)+3 ...
605                       2*(a-1)+1+(2*N+1):1:2*(a-1)+3+(2*N+1) ...
606                       2*(a-1)+1+2*(2*N+1):1:2*(a-1)+3+2*(2*N+1)],...
607                       b)+fint;
608                 end
609             end
610
611             %Form linear systems...
612
613             R=Fin;
614             Kfinal=-Fscat;
615
616             A=Kfinal\R;
617             AFE(f,:,:)=A;
618
619             %Energy Check - This code works but is slow.
620             %An alternative method is used in practice.
621
622             %Incident
623             for mm=1:1:L
624                 for a=1:1:N
625                     %Work done in each layer
626                     [workl,Er]=Work(lambda,mu,rko(a),rki(a),Nm(n),...
627                         LRvalf(f,mm),squeeze(LREVf(f,...
628                         [2*(a-1)+1:1:2*(a-1)+3 2*(a-1)+1+...
629                         (2*N+1):1:2*(a-1)+3+(2*N+1) 2*(a-1)+...
630                         1+2*(2*N+1):1:2*(a-1)+3+2*(2*N+1)],mm)).');
631                     %Total work over all layers
632                     workin(f,mm)=workin(f,mm)+workl;
633                 end
634             end
```

(Continued on next page...)

Listing G.3. MATLAB® code to implement the axisymmetric scattering problem. (Continued from previous page.)

```
635                 %Reflected
636                 for mm=1:1:L
637                     for b=1:1:L
638                         for a=1:1:N
639                             %Work done in each layer
640                             [workl,Er]=Work(lambda,mu,rko(a),rki(a),...
641                                 Nm(n),Rvalf(f,b),AFE(f,b,mm)*...
642                                 squeeze(REVf(f,[2*(a-1)+1:1:2*(a-1)+3 ...
643                                 2*(a-1)+1+(2*N+1):1:2*(a-1)+3+(2*N+1)...
644                                 2*(a-1)+1+2*(2*N+1):1:2*(a-1)+3+...
645                                 2*(2*N+1)],b)).');
646                             %Total work over all layers
647                             workr(f,b,mm)=workr(f,b,mm)+workl;
648                         end
649                     end
650                 end
651             end
652
653             %Save results to file
654             save(['F_' num2str(Nm(n)) '.mat'], 'fwhole', 'AFE',...
655             'workin','workr');
656         end
657     end
```

APPENDIX H

TRANSPARENCY CHECKS

H.1 Summary

This appendix gives the magnitudes of the normalized reflection and transmission coefficients for selected modes which are incident on and scattered by the finite element region. They provide transparency checks for the axisymmetric and three-dimensional computer programs. The finite element meshes which produced the results presented here are identical to those employed in Chapter 4 *but with no elements removed* to represent the notches described in Tables 4.1 and 4.5. The modes selected for inclusion have a non-negative circumferential wavenumber and propagate over at least part of the excitation's bandwidth. This selection is compatible with Appendix I. The lines and markers employed in Figures H.2 through H.59 to denote various modal reflection and transmission coefficients are summarized in Figure H.1. (Note that Figure H.1 is identical to Figure I.1.) Each incident mode is indicated in a figure's caption.

Regardless of frequency, every normalized reflection coefficient should be zero to satisfy the transparency check. All reflection coefficient values in the following figures have a magnitude that is less than an insignificant 0.02. Similarly the normalized transmission

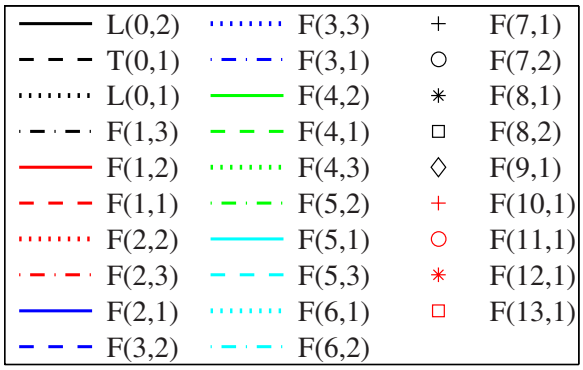

Figure H.1. Legend indicating mode line and marker styles.

coefficient should be unity for an incident propagating mode. Moreover, no modal conversations should be seen. Visual inspections indicate that this situation always holds. However, the normalized transmission coefficient should be less than one for incident, nonpropagating and evanescent modes because these modes decay as they travel from the origin of the coordinate system. The incident mode is assumed to have unit magnitude at the origin. No modal conversations to other modes should be seen. This is visually the case again. (Note that differences between the transmission coefficients computed by separately using the axisymmetric and three-dimensional computer programs for the nonpropagating and evanescent modes is due to the different axial extents used in the two finite element meshes. This change modifies the axial separation between the coordinate system's origin and the axial cross section where the transmission coefficient is evaluated.) Frequencies at which a mode transitions from evanescent to nonpropagating are seen easily in Figures H.2 through H.59. For convenient illustrative purposes, these points are labelled only in Figure H.16 where both types of transitions occur.

H.2 Transparency Check for Axisymmetric Program

Normalized reflection and transmission coefficients for selected modes incident on and scattered by the finite element region are given in Figures H.2 through H.30 as a check for the transparency of the axisymmetric program when no scatterer is present. The summary of annotations given in Section H.1 remains applicable.

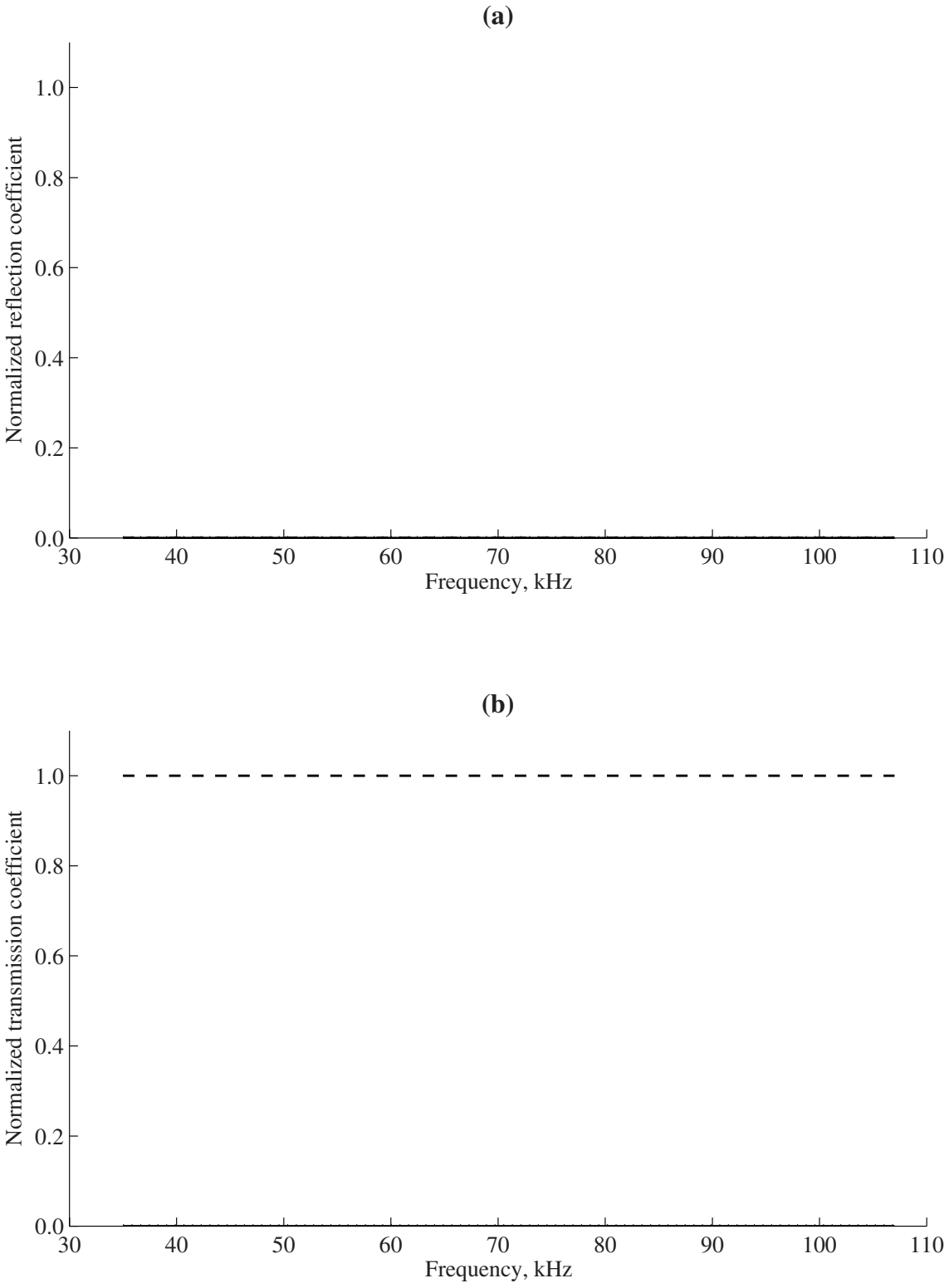

Figure H.2. Normalized reflection and transmission coefficients for the axisymmetric transparency check and the incident T(0,1) mode.

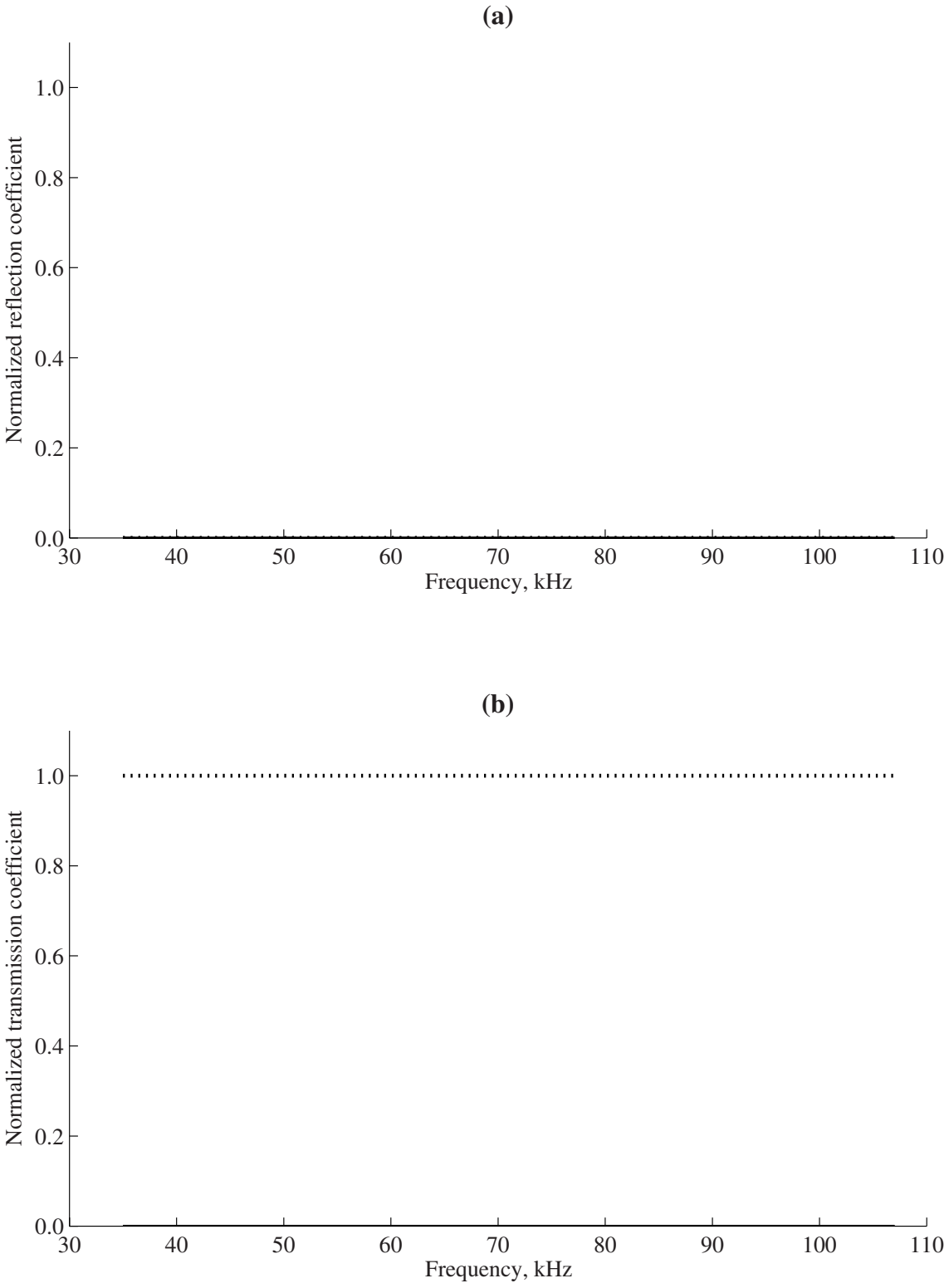

Figure H.3. Normalized reflection and transmission coefficients for the axisymmetric transparency check and the incident L(0,1) mode.

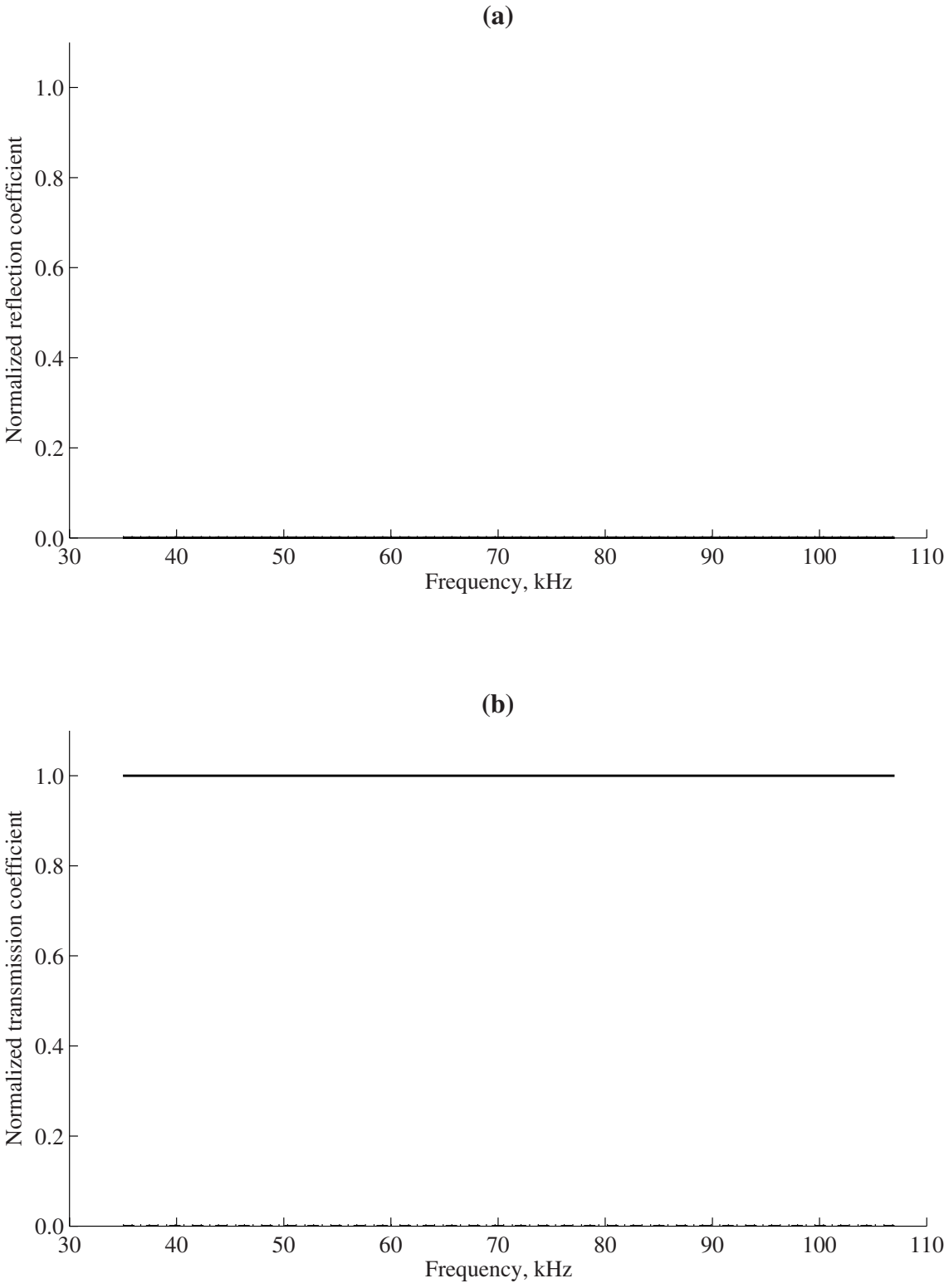

Figure H.4. Normalized reflection and transmission coefficients for the axisymmetric transparency check and the incident L(0,2) mode.

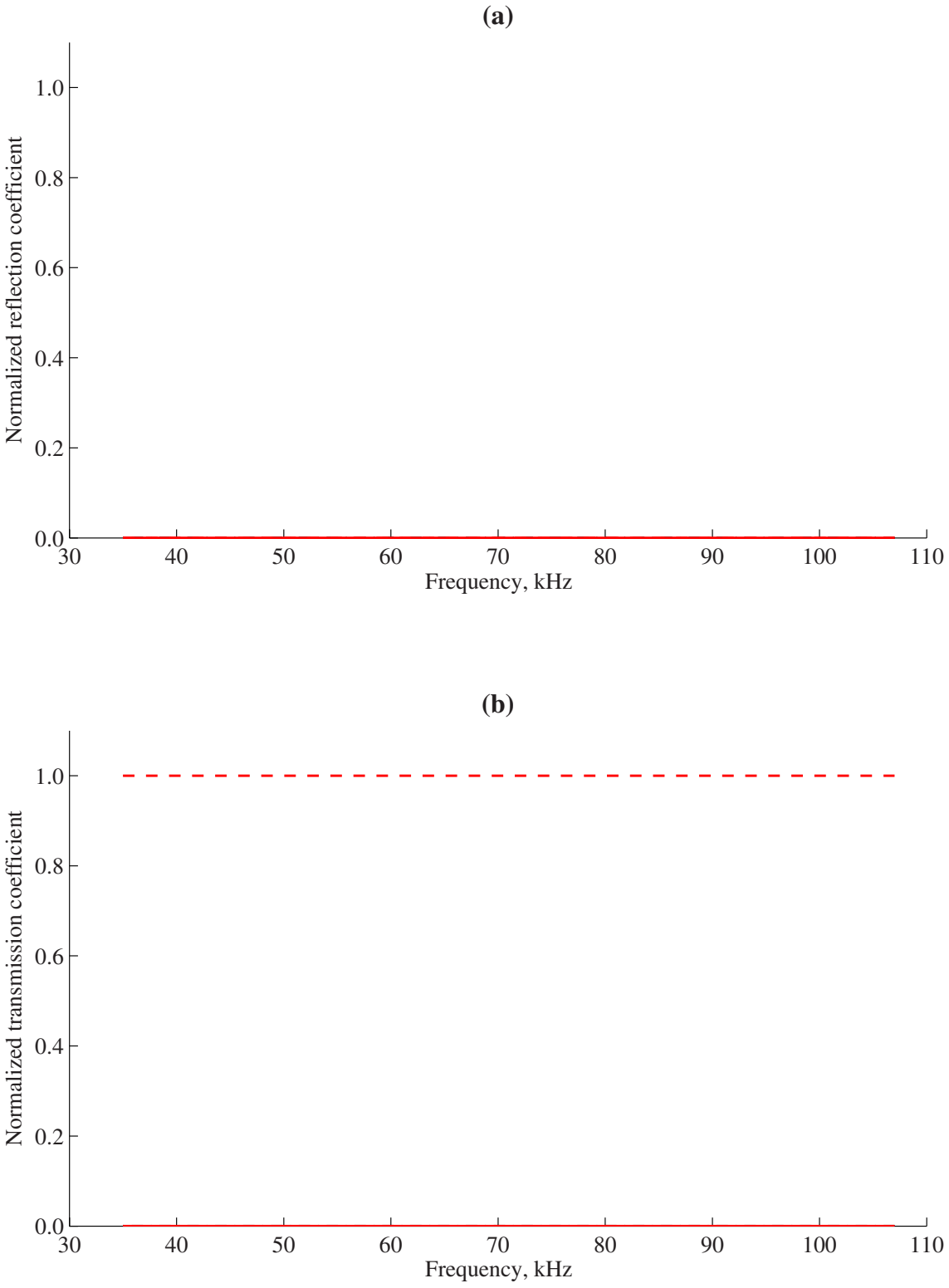

Figure H.5. Normalized reflection and transmission coefficients for the axisymmetric transparency check and the incident F(1,1) mode.

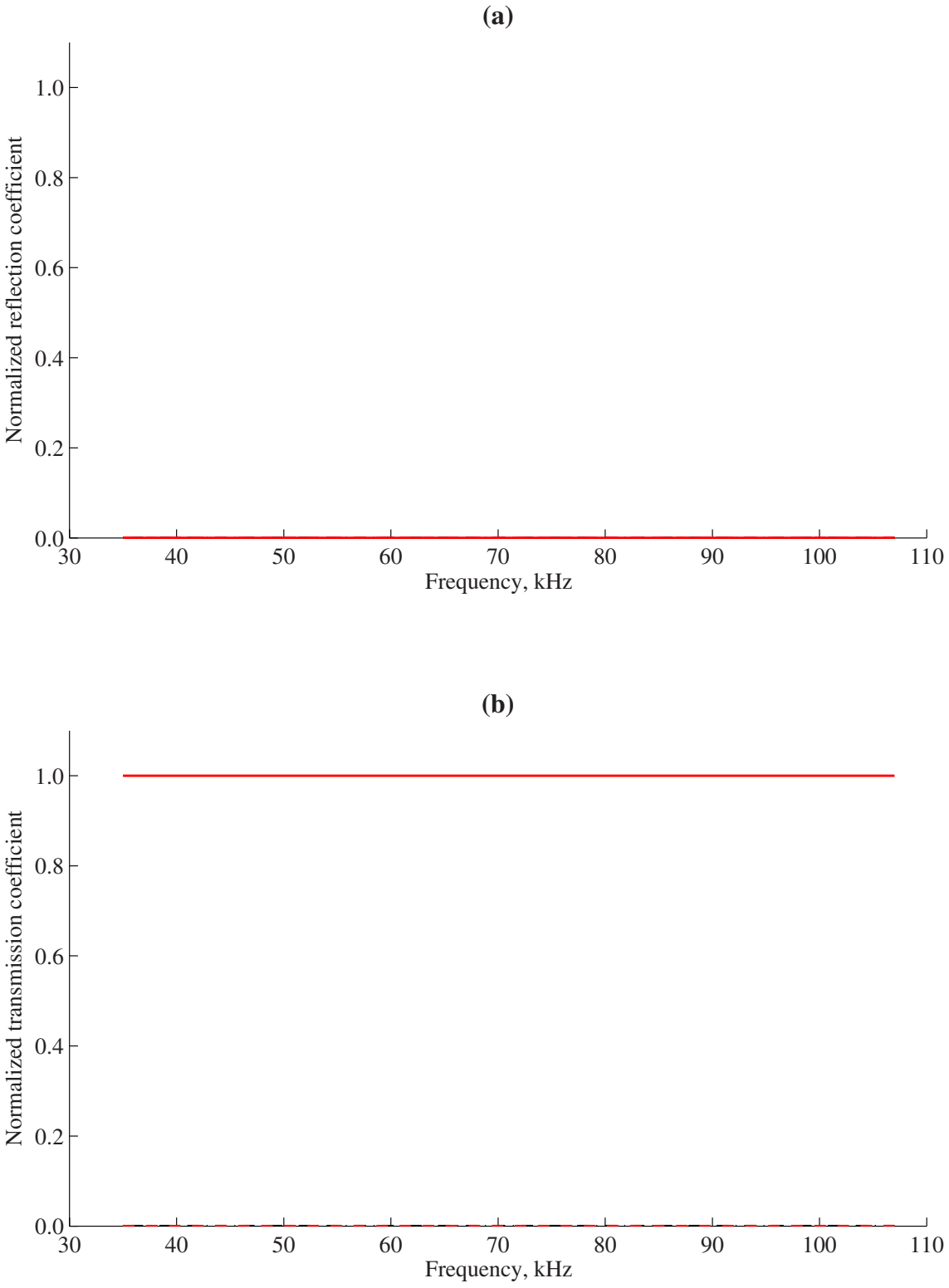

Figure H.6. Normalized reflection and transmission coefficients for the axisymmetric transparency check and the incident F(1,2) mode.

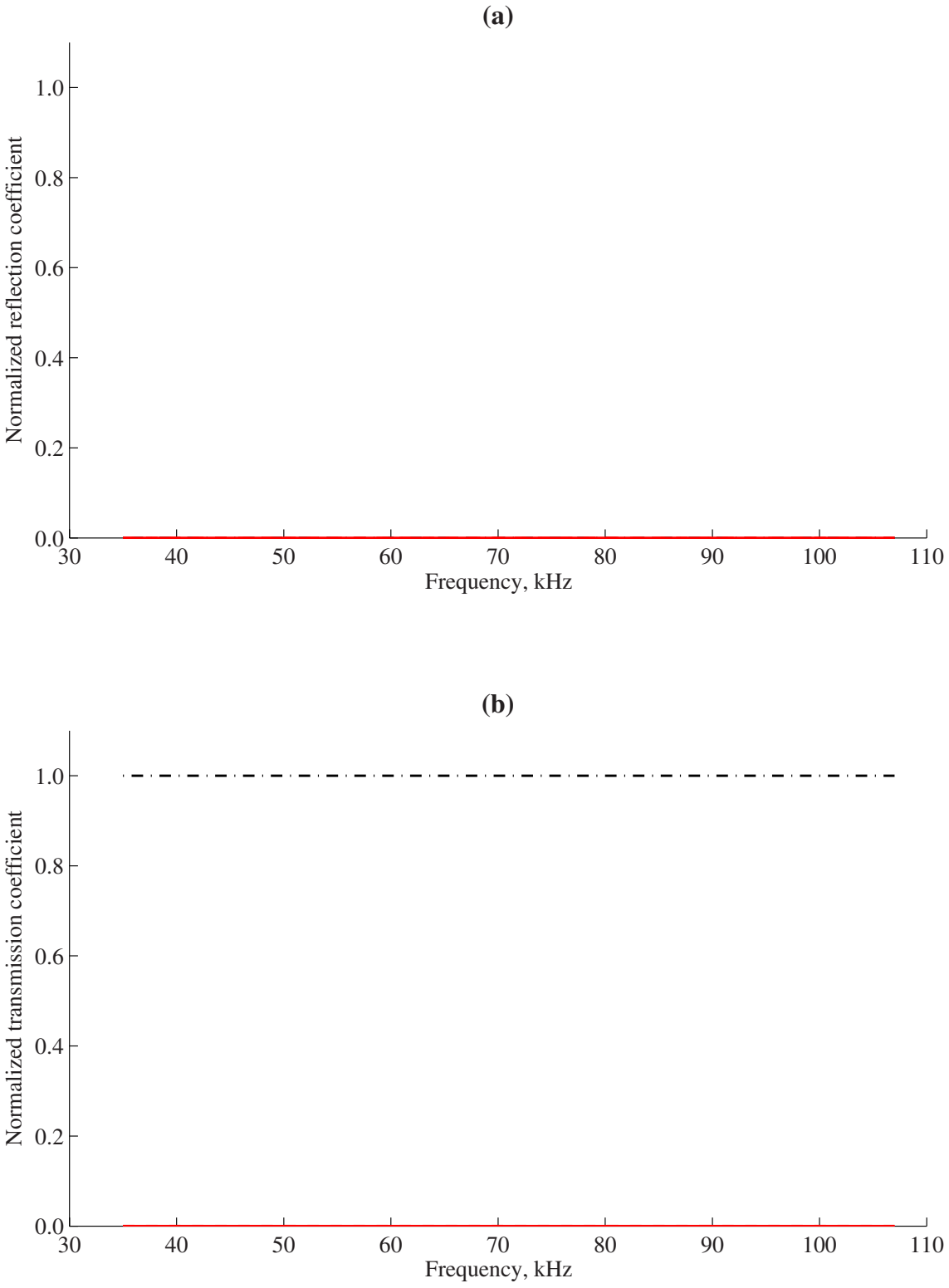

Figure H.7. Normalized reflection and transmission coefficients for the axisymmetric transparency check and the incident F(1,3) mode.

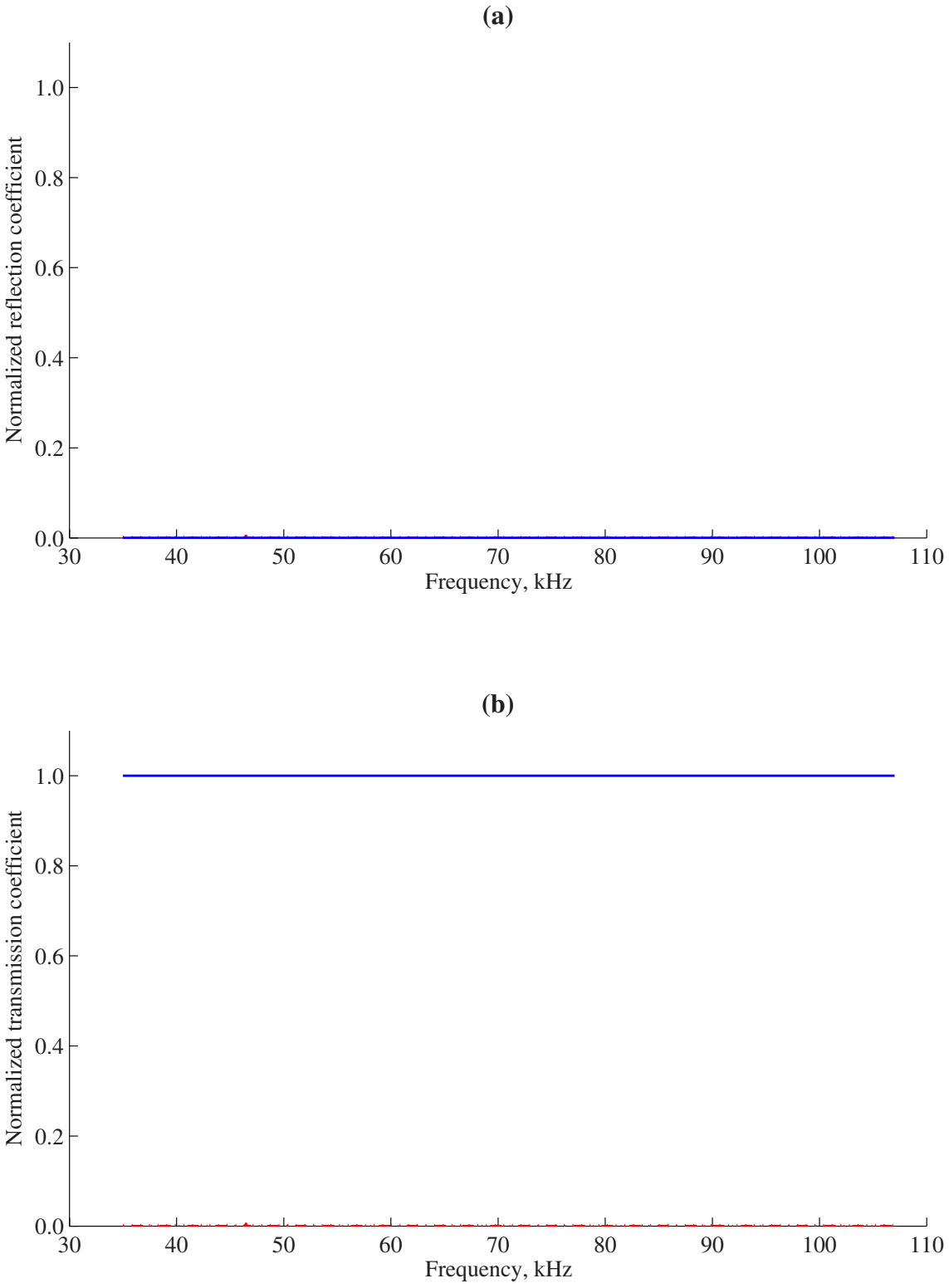

Figure H.8. Normalized reflection and transmission coefficients for the axisymmetric transparency check and the incident F(2,1) mode.

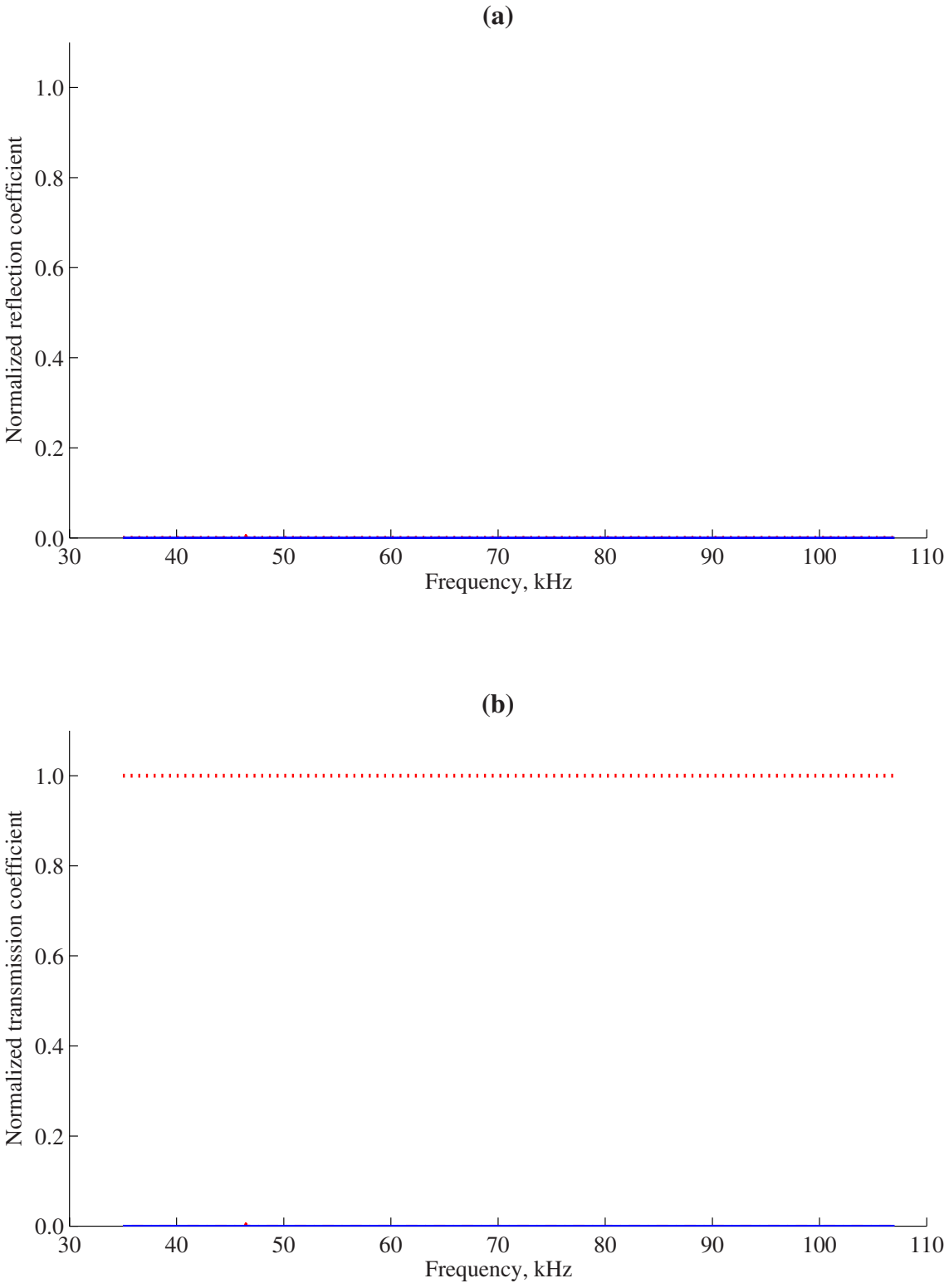

Figure H.9. Normalized reflection and transmission coefficients for the axisymmetric transparency check and the incident F(2,2) mode.

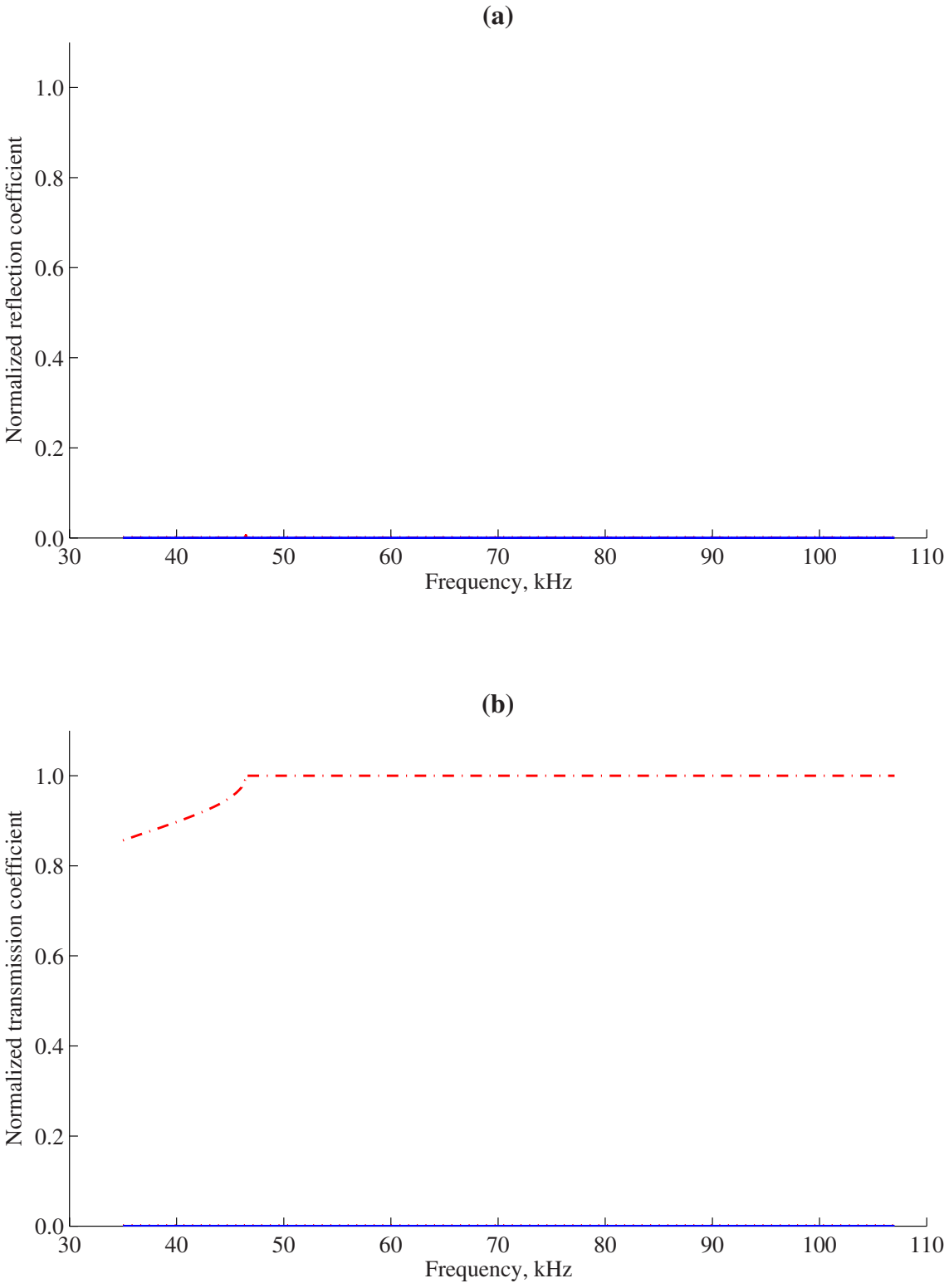

Figure H.10. Normalized reflection and transmission coefficients for the axisymmetric transparency check and the incident F(2,3) mode.

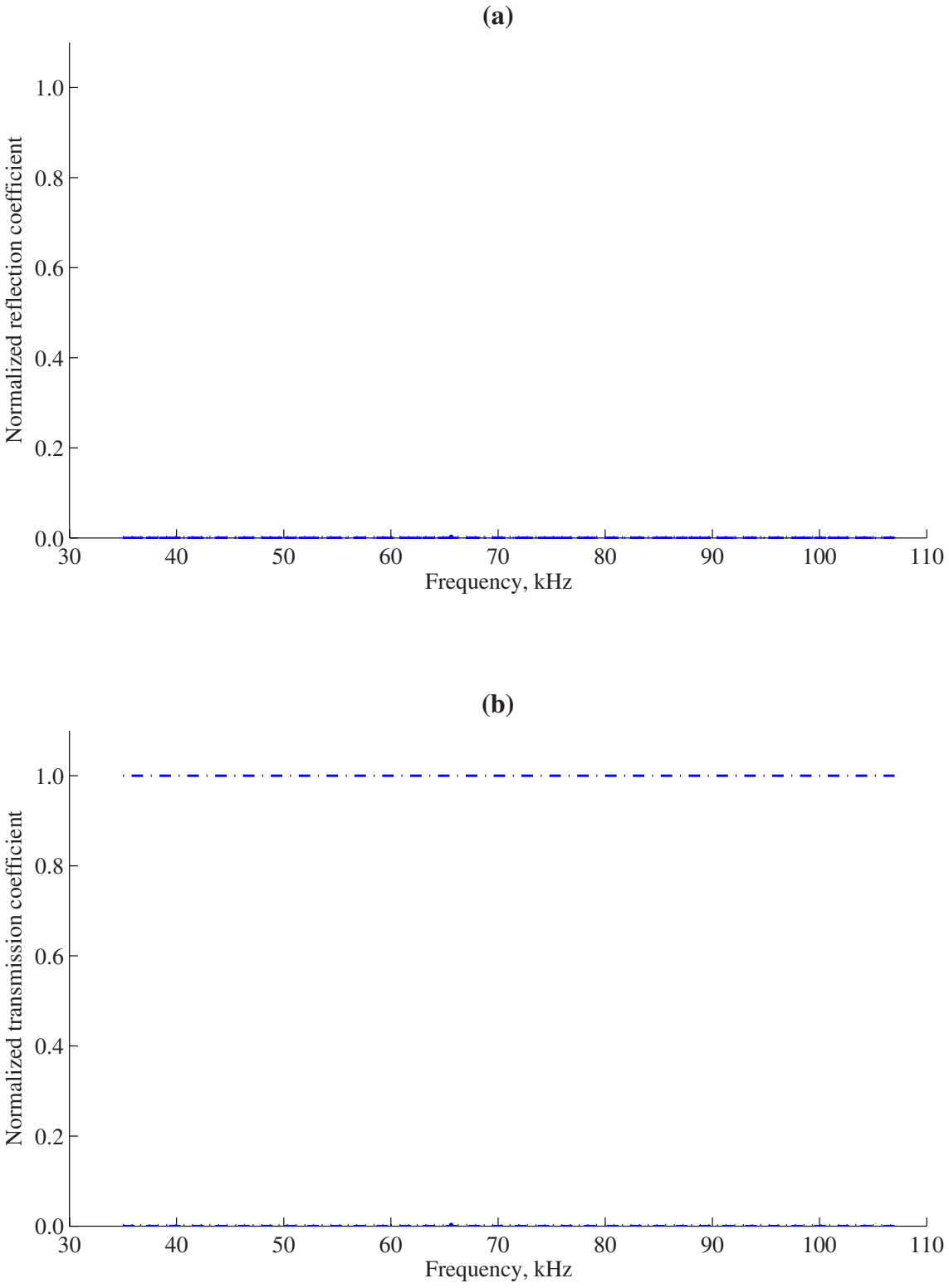

Figure H.11. Normalized reflection and transmission coefficients for the axisymmetric transparency check and the incident F(3,1) mode.

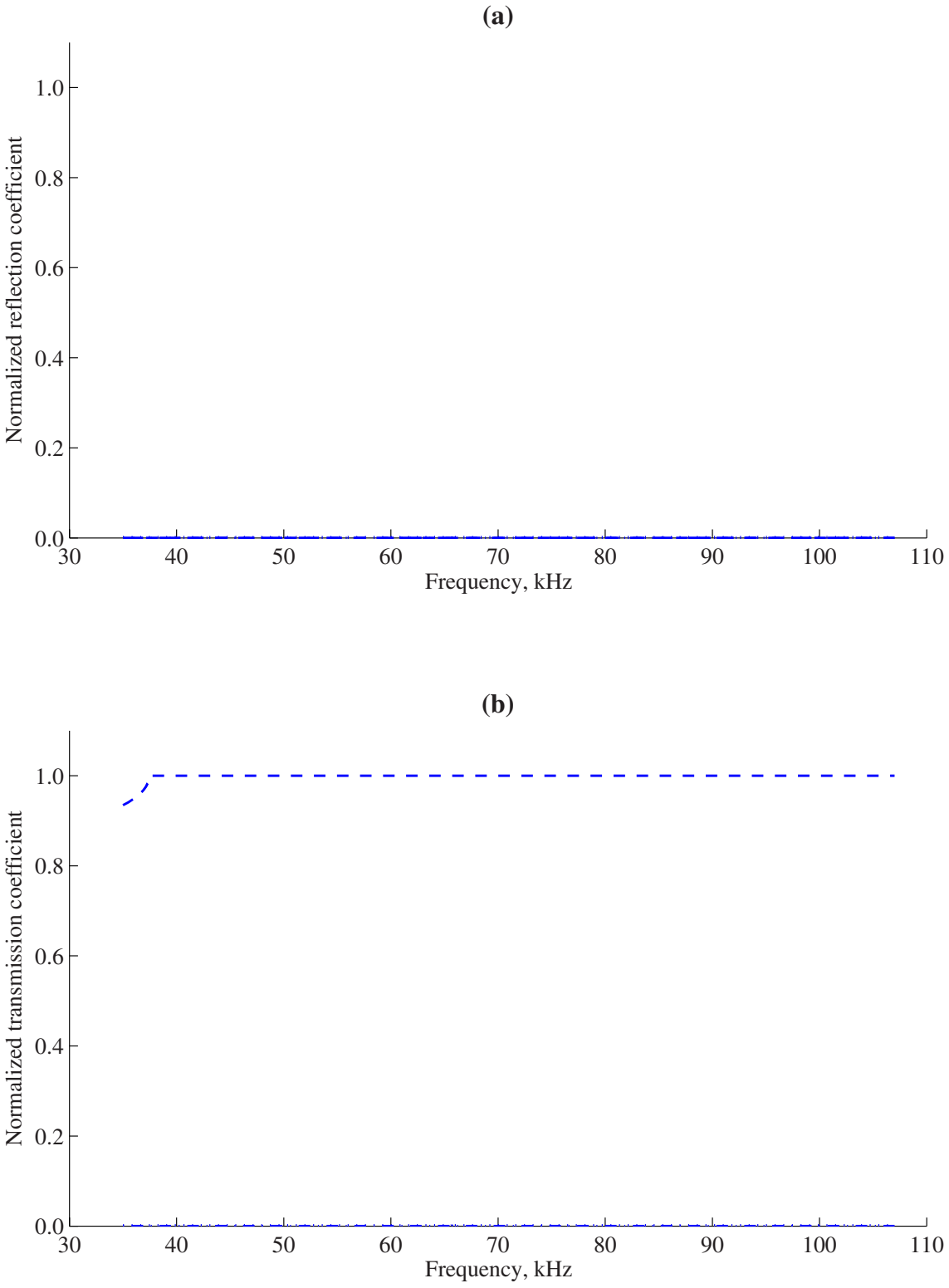

Figure H.12. Normalized reflection and transmission coefficients for the axisymmetric transparency check and the incident F(3,2) mode.

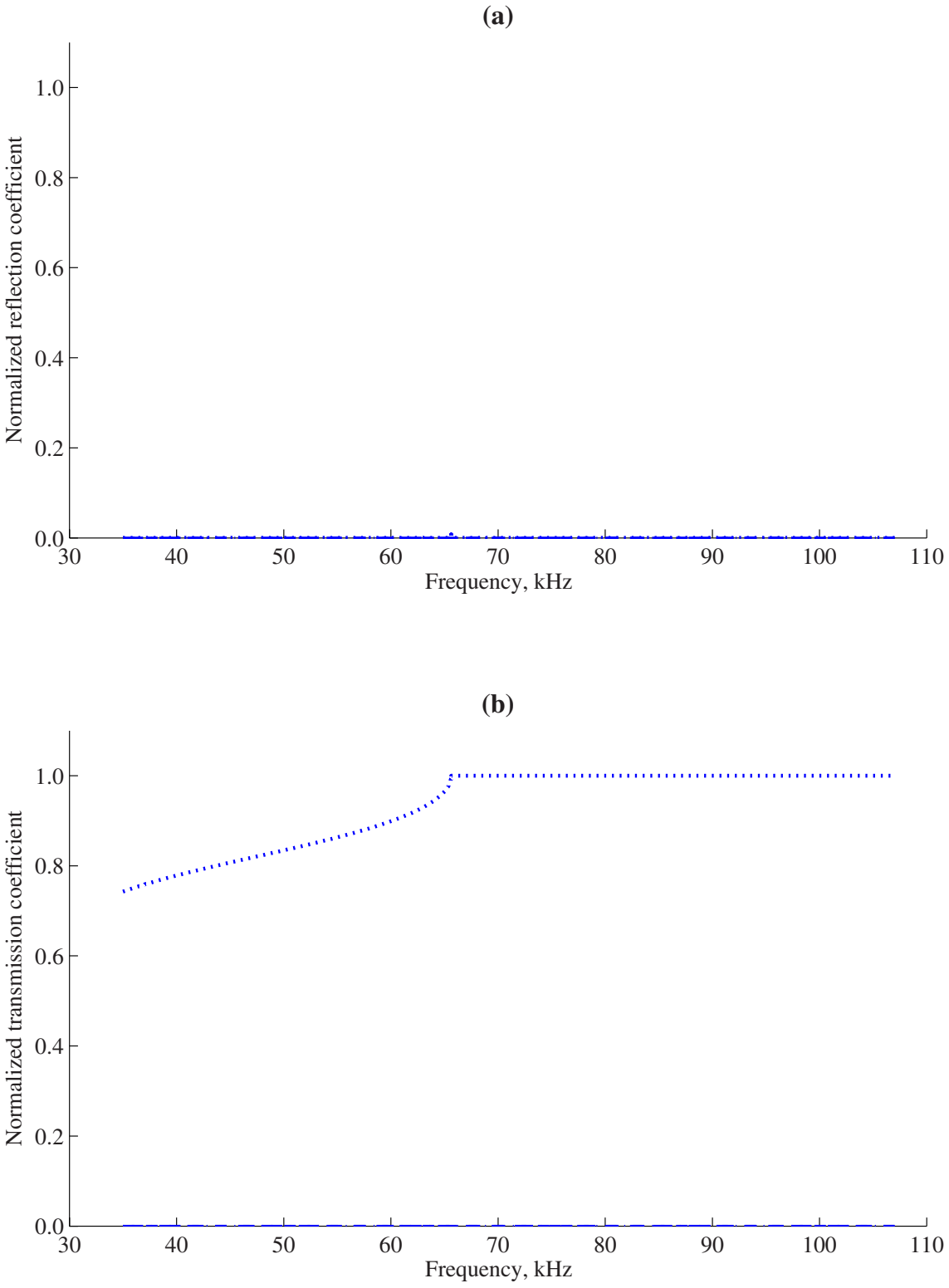

Figure H.13. Normalized reflection and transmission coefficients for the axisymmetric transparency check and the incident F(3,3) mode.

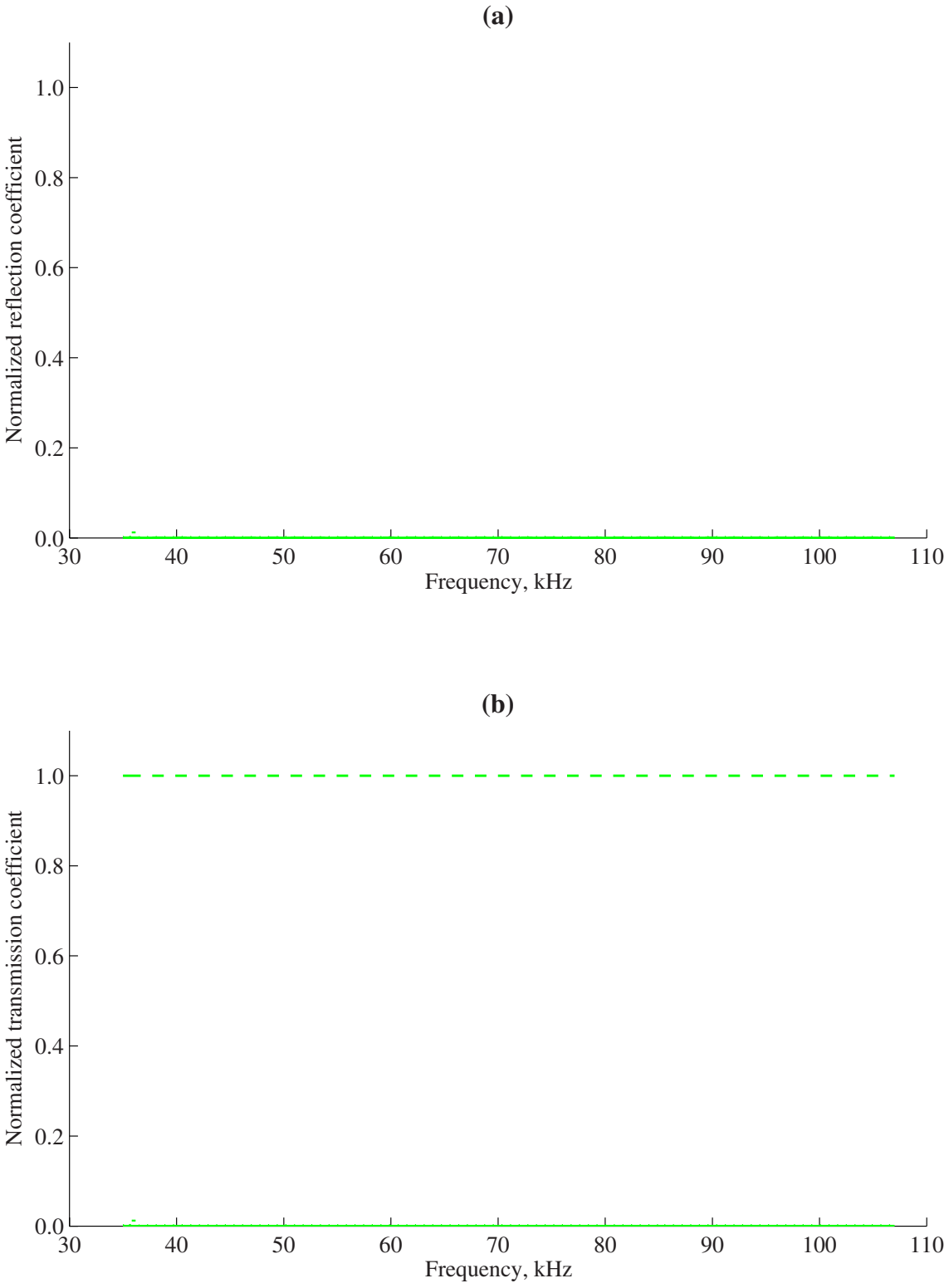

Figure H.14. Normalized reflection and transmission coefficients for the axisymmetric transparency check and the incident F(4,1) mode.

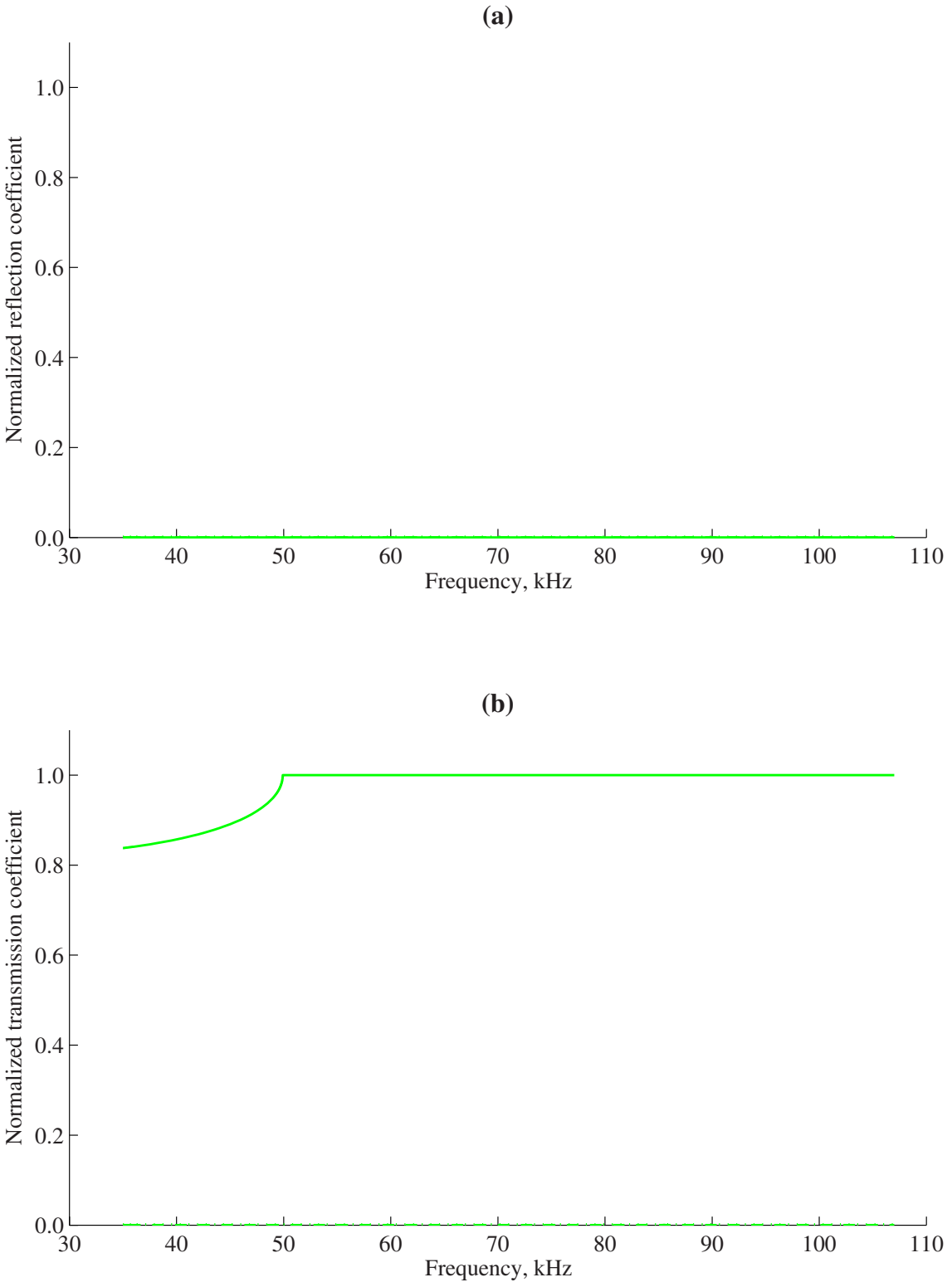

Figure H.15. Normalized reflection and transmission coefficients for the axisymmetric transparency check and the incident F(4,2) mode.

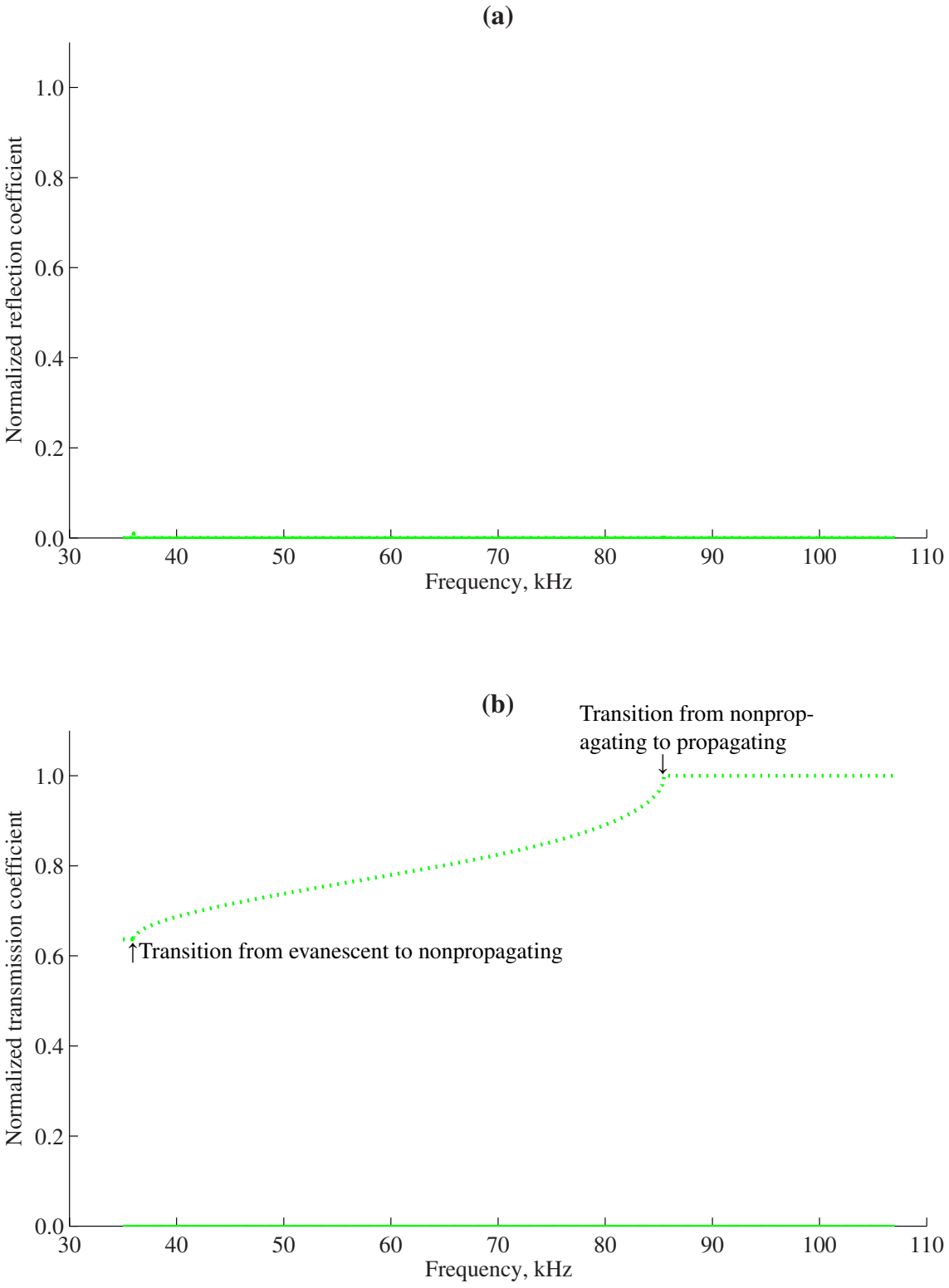

Figure H.16. Normalized reflection and transmission coefficients for the axisymmetric transparency check and the incident F(4,3) mode.

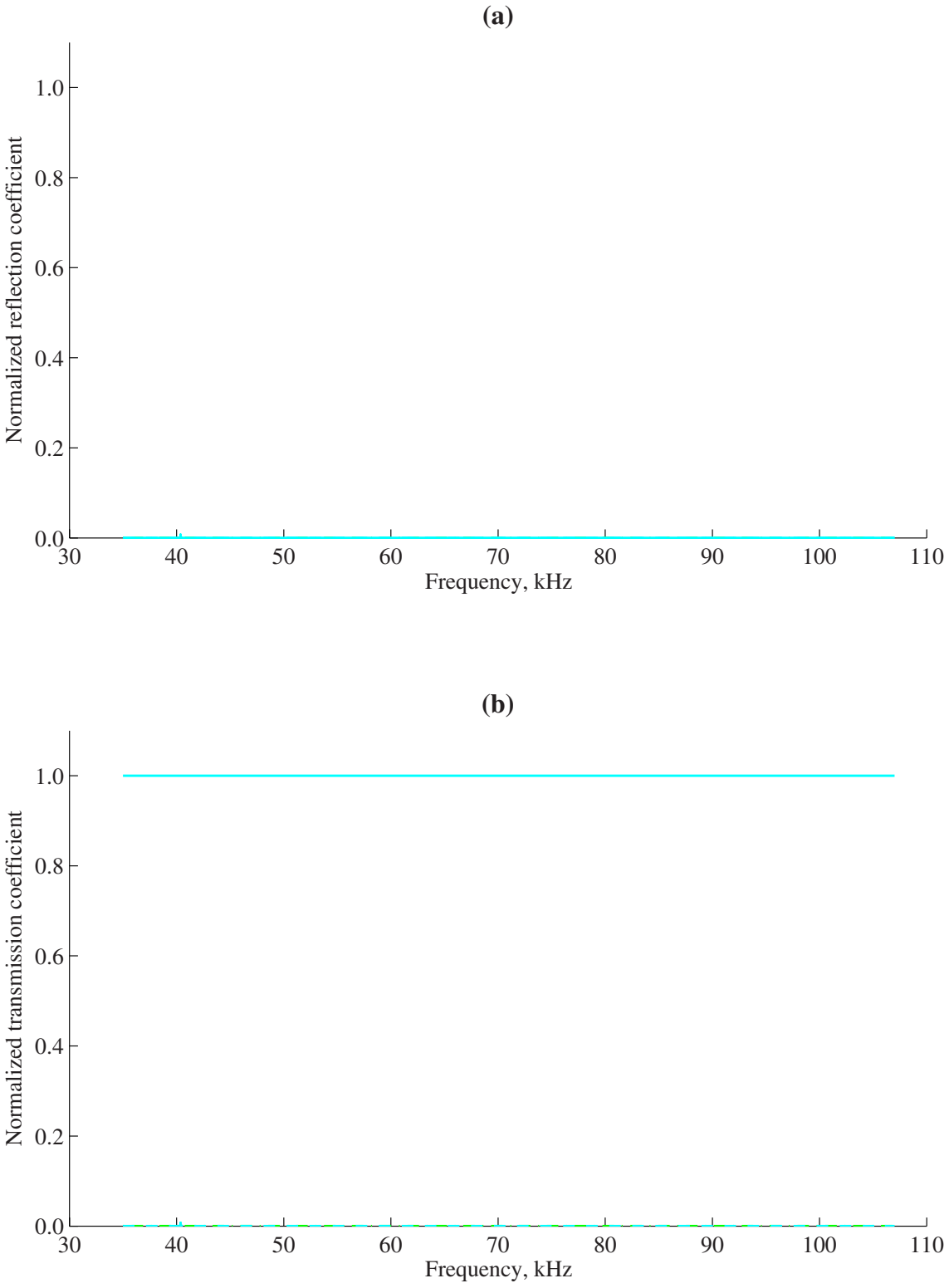

Figure H.17. Normalized reflection and transmission coefficients for the axisymmetric transparency check and the incident F(5,1) mode.

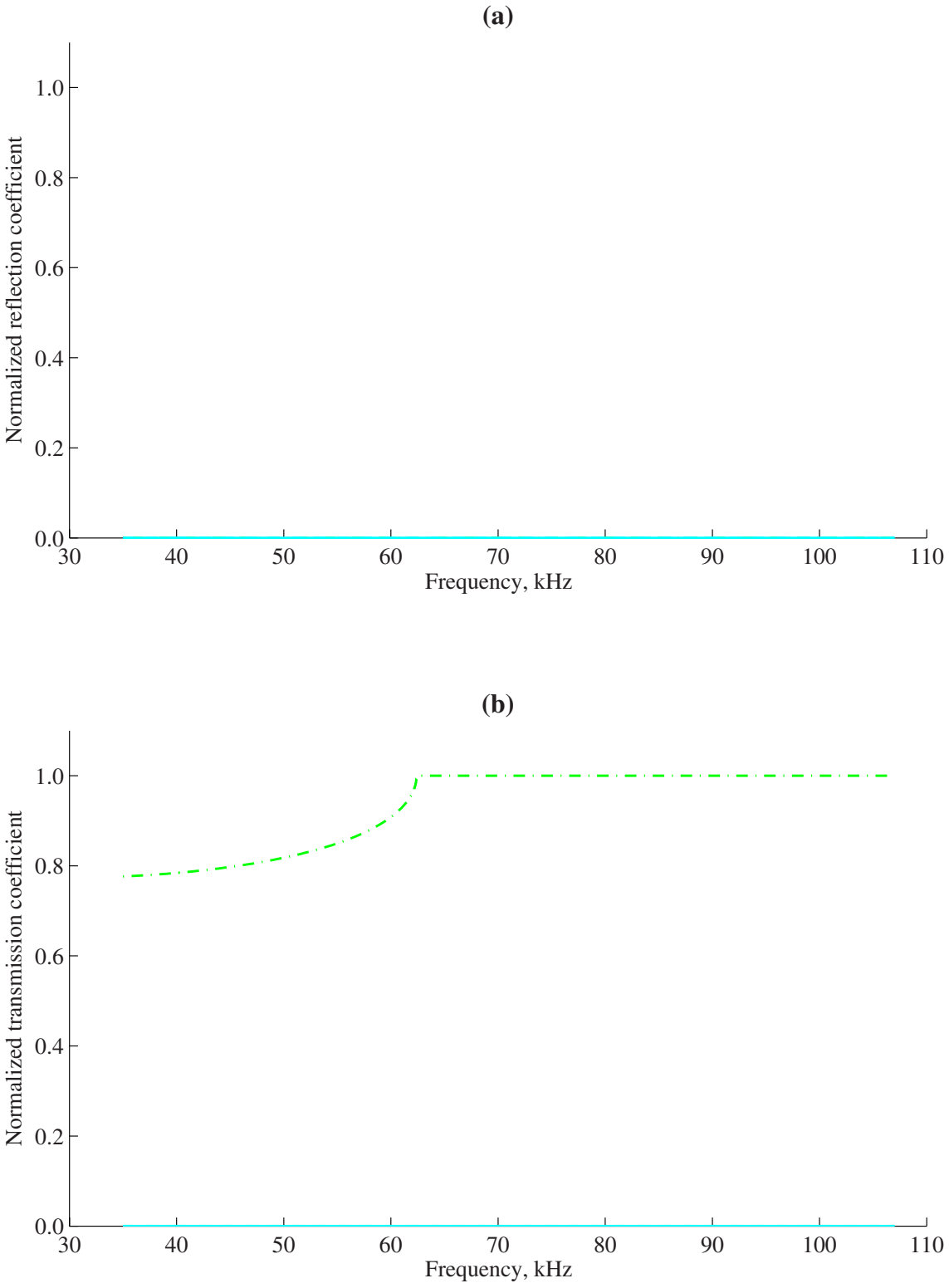

Figure H.18. Normalized reflection and transmission coefficients for the axisymmetric transparency check and the incident F(5,2) mode.

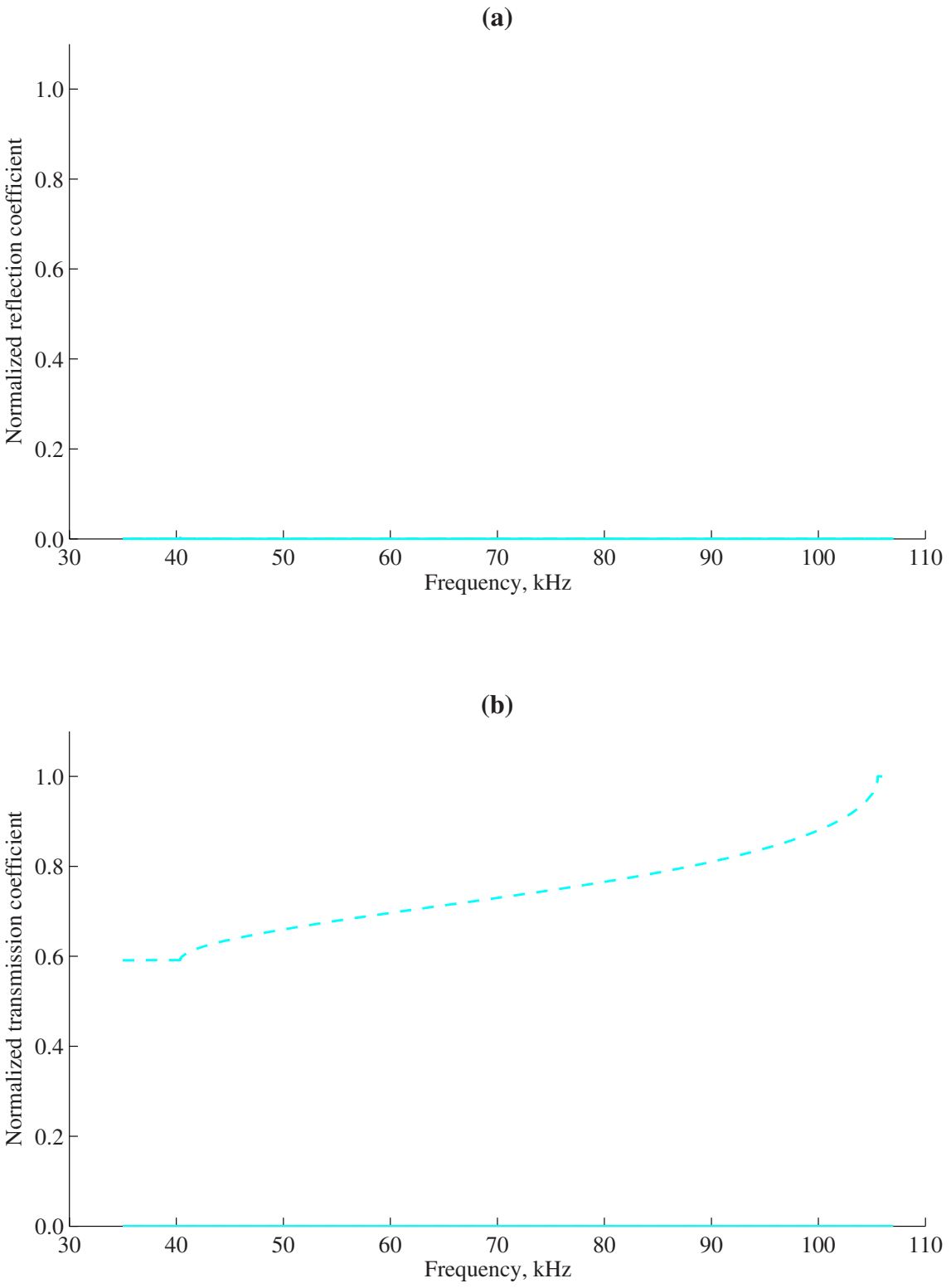

Figure H.19. Normalized reflection and transmission coefficients for the axisymmetric transparency check and the incident F(5,3) mode.

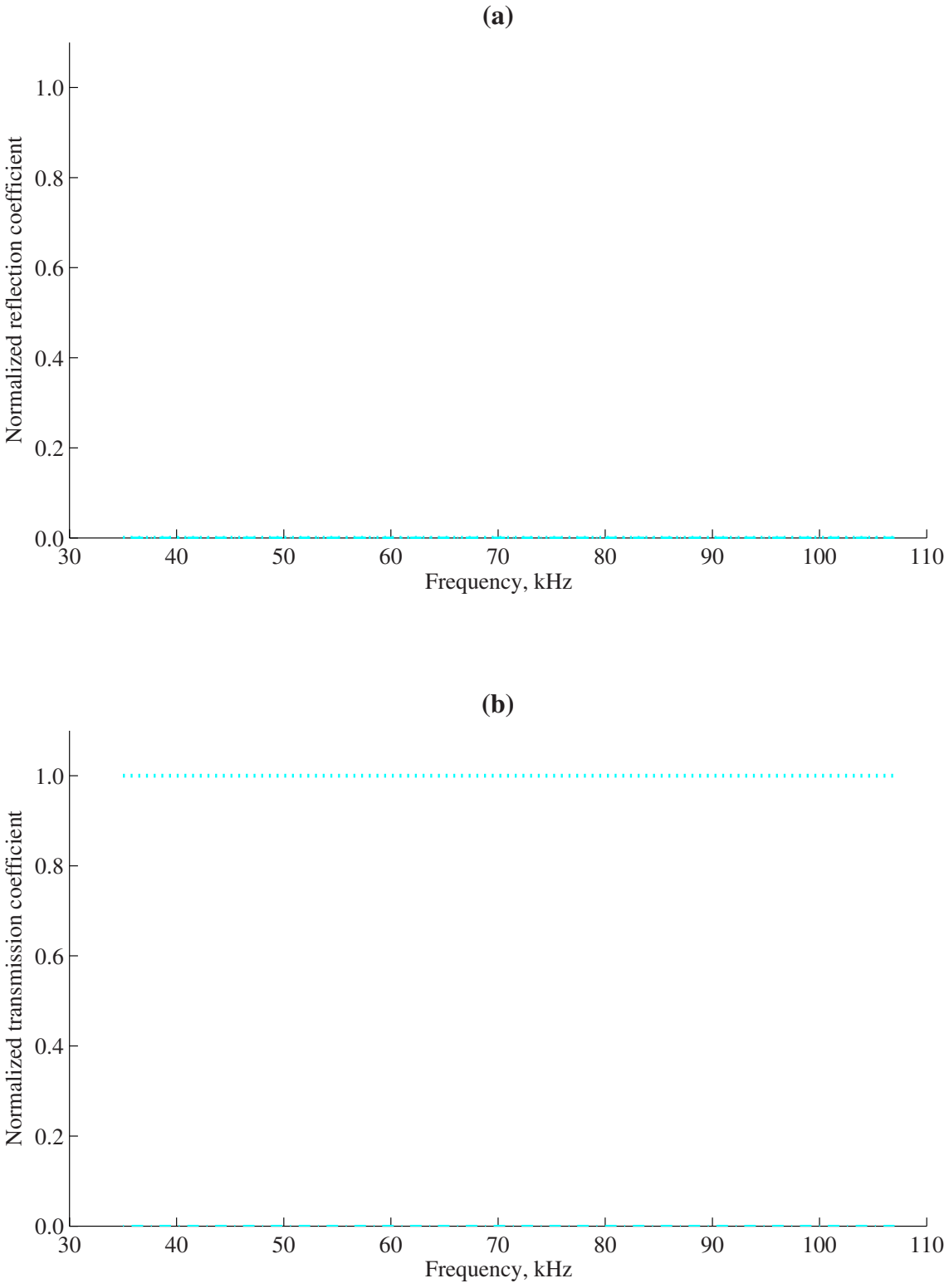

Figure H.20. Normalized reflection and transmission coefficients for the axisymmetric transparency check and the incident F(6,1) mode.

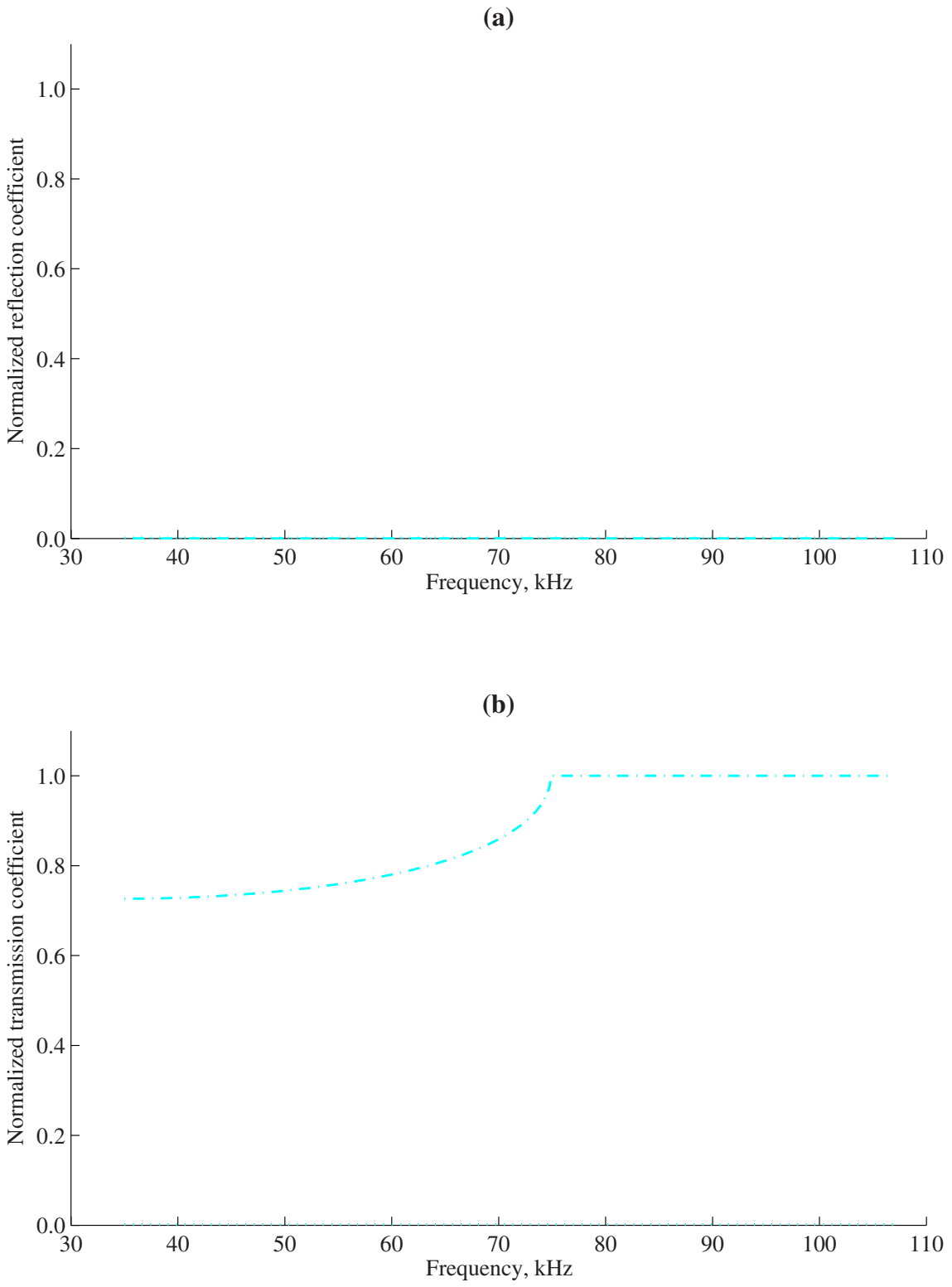

Figure H.21. Normalized reflection and transmission coefficients for the axisymmetric transparency check and the incident F(6,2) mode.

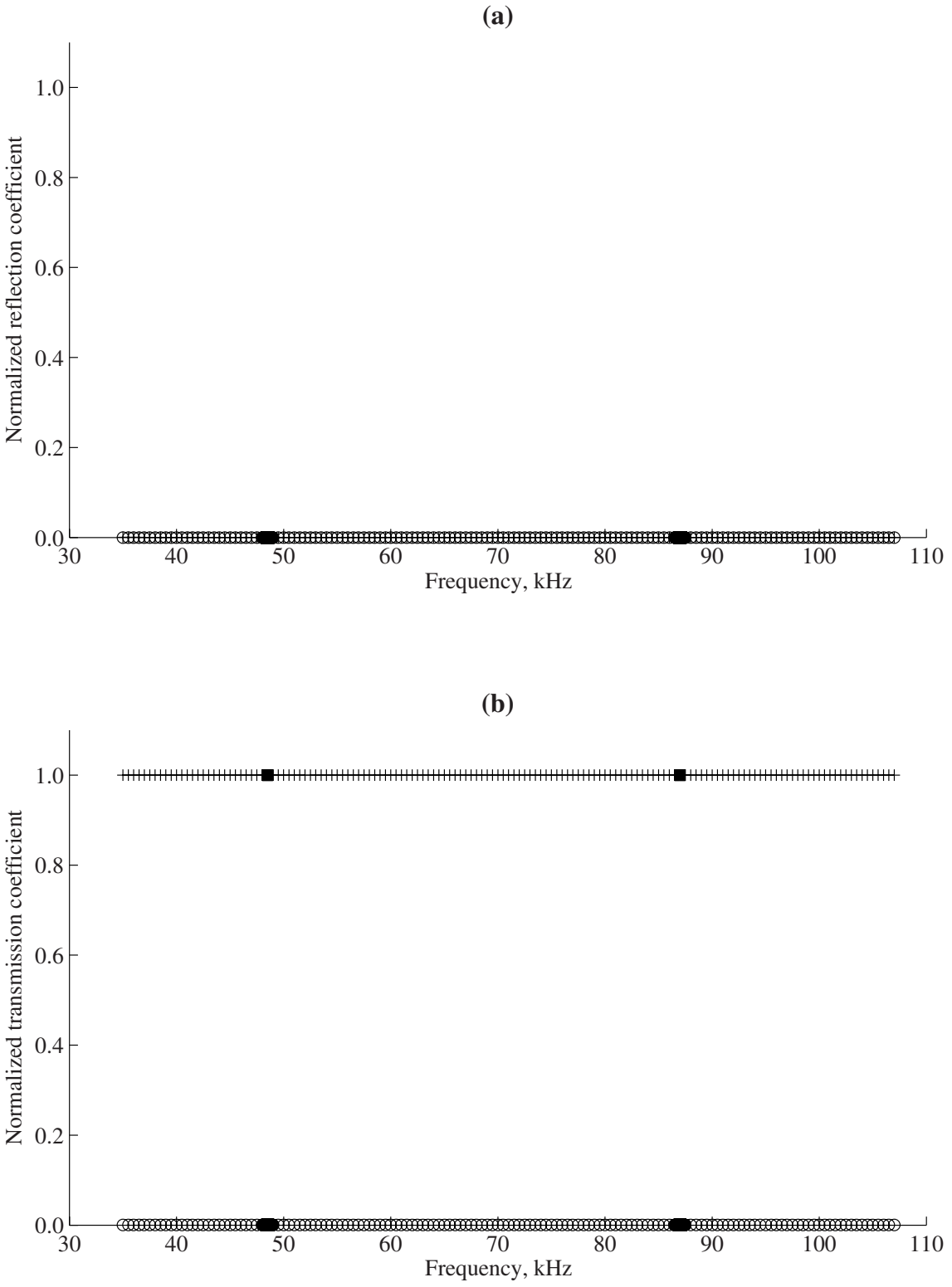

Figure H.22. Normalized reflection and transmission coefficients for the axisymmetric transparency check and the incident F(7,1) mode.

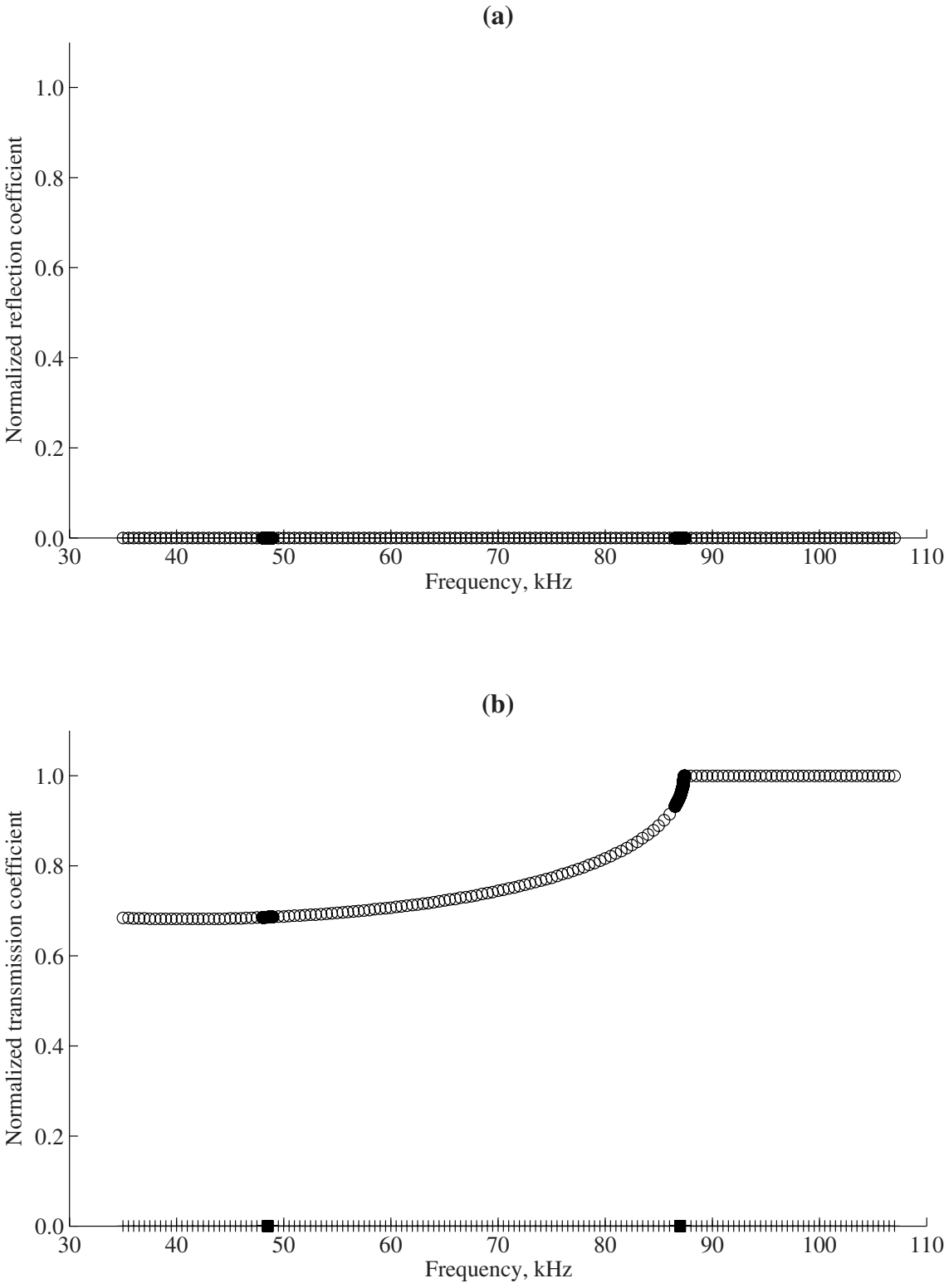

Figure H.23. Normalized reflection and transmission coefficients for the axisymmetric transparency check and the incident F(7,2) mode.

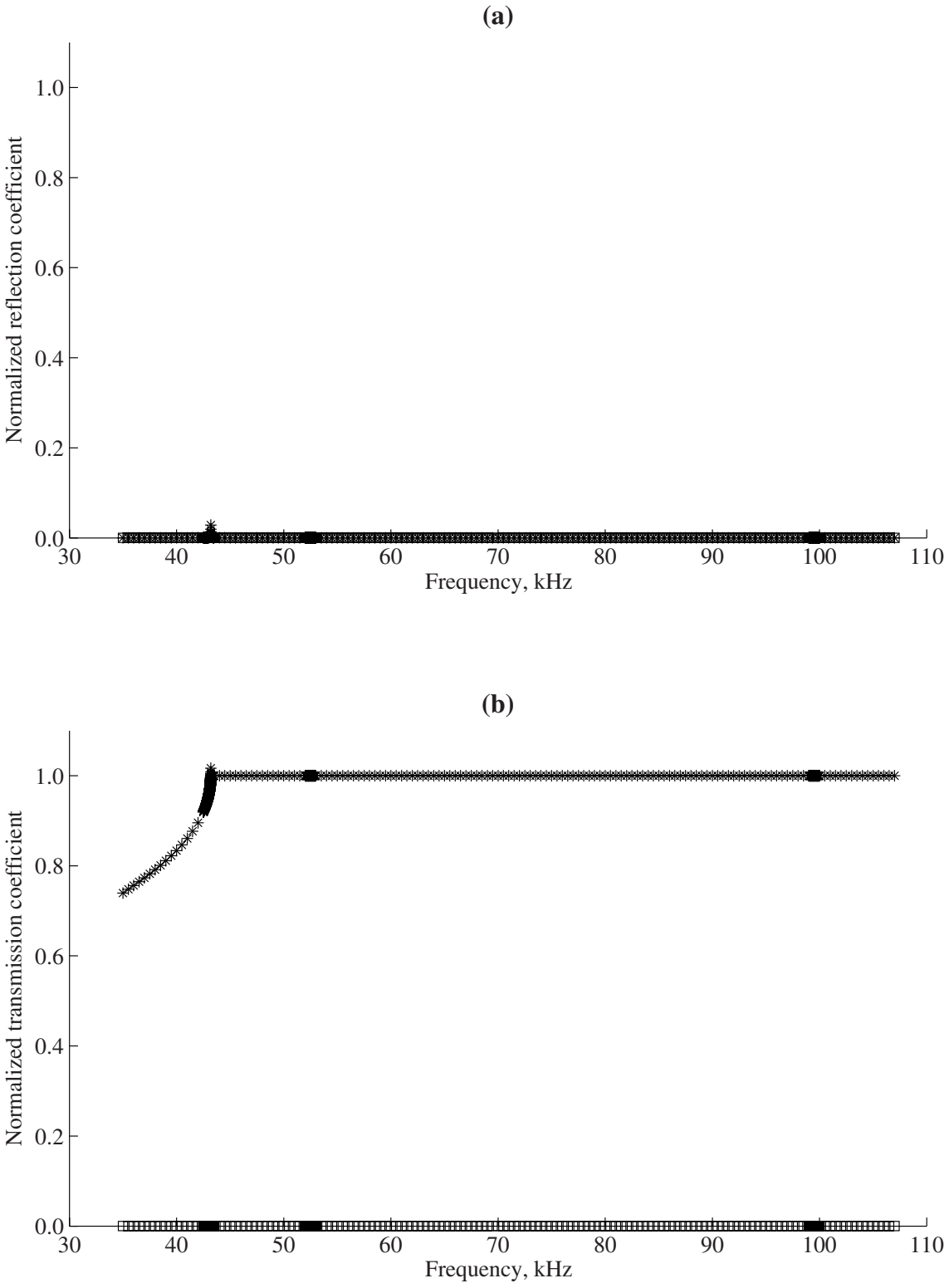

Figure H.24. Normalized reflection and transmission coefficients for the axisymmetric transparency check and the incident F(8,1) mode.

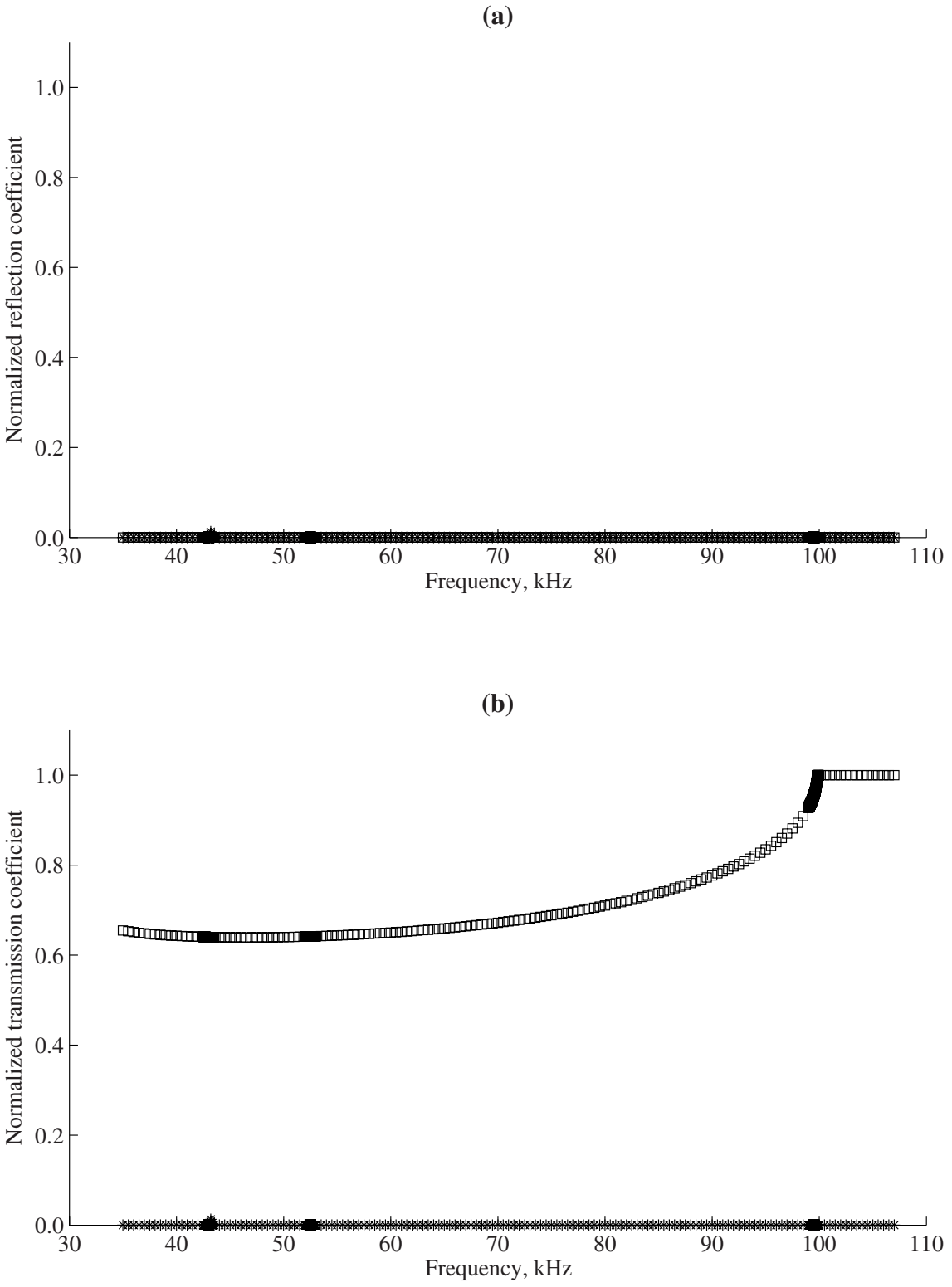

Figure H.25. Normalized reflection and transmission coefficients for the axisymmetric transparency check and the incident F(8,2) mode.

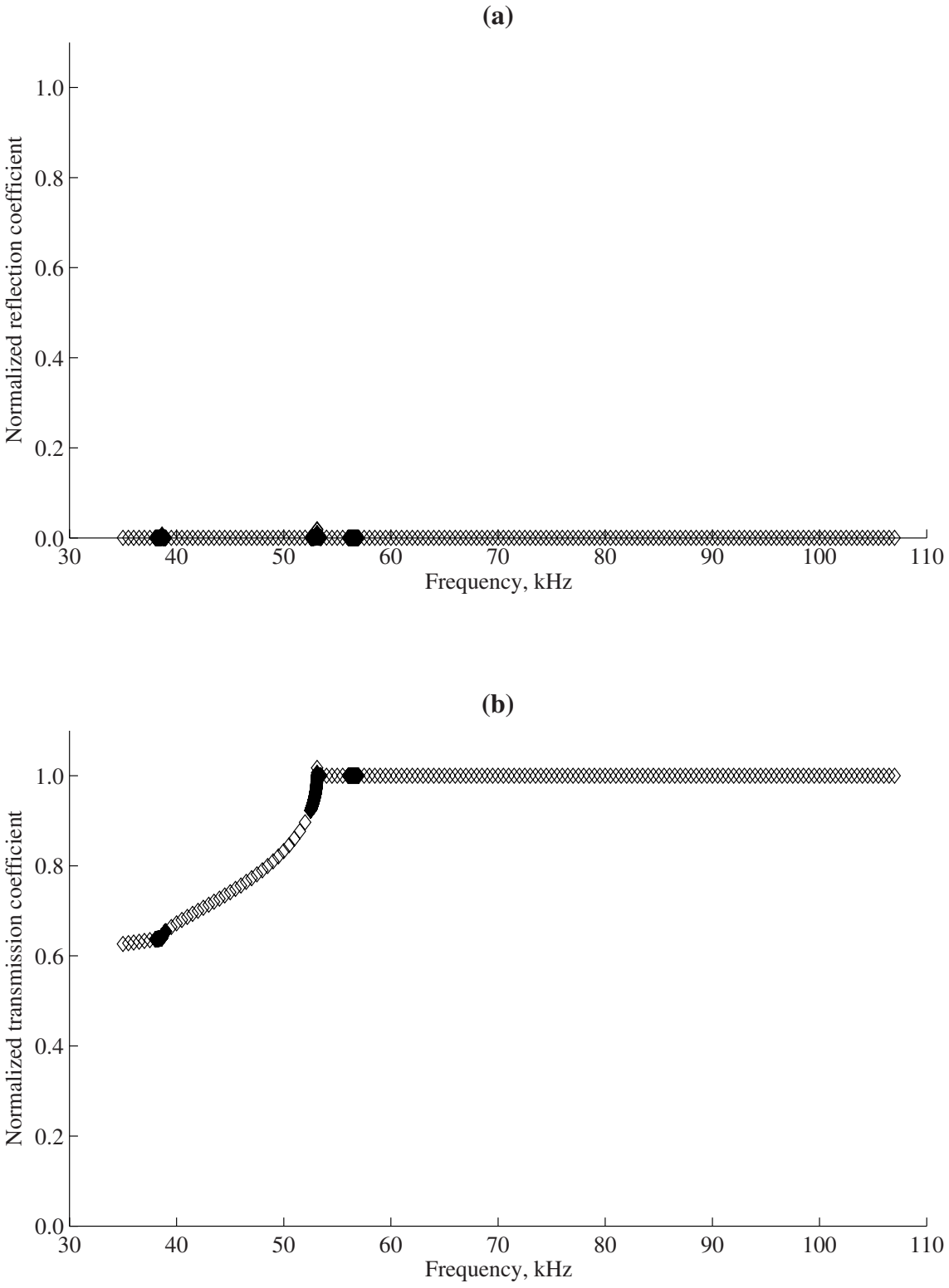

Figure H.26. Normalized reflection and transmission coefficients for the axisymmetric transparency check and the incident F(9,1) mode.

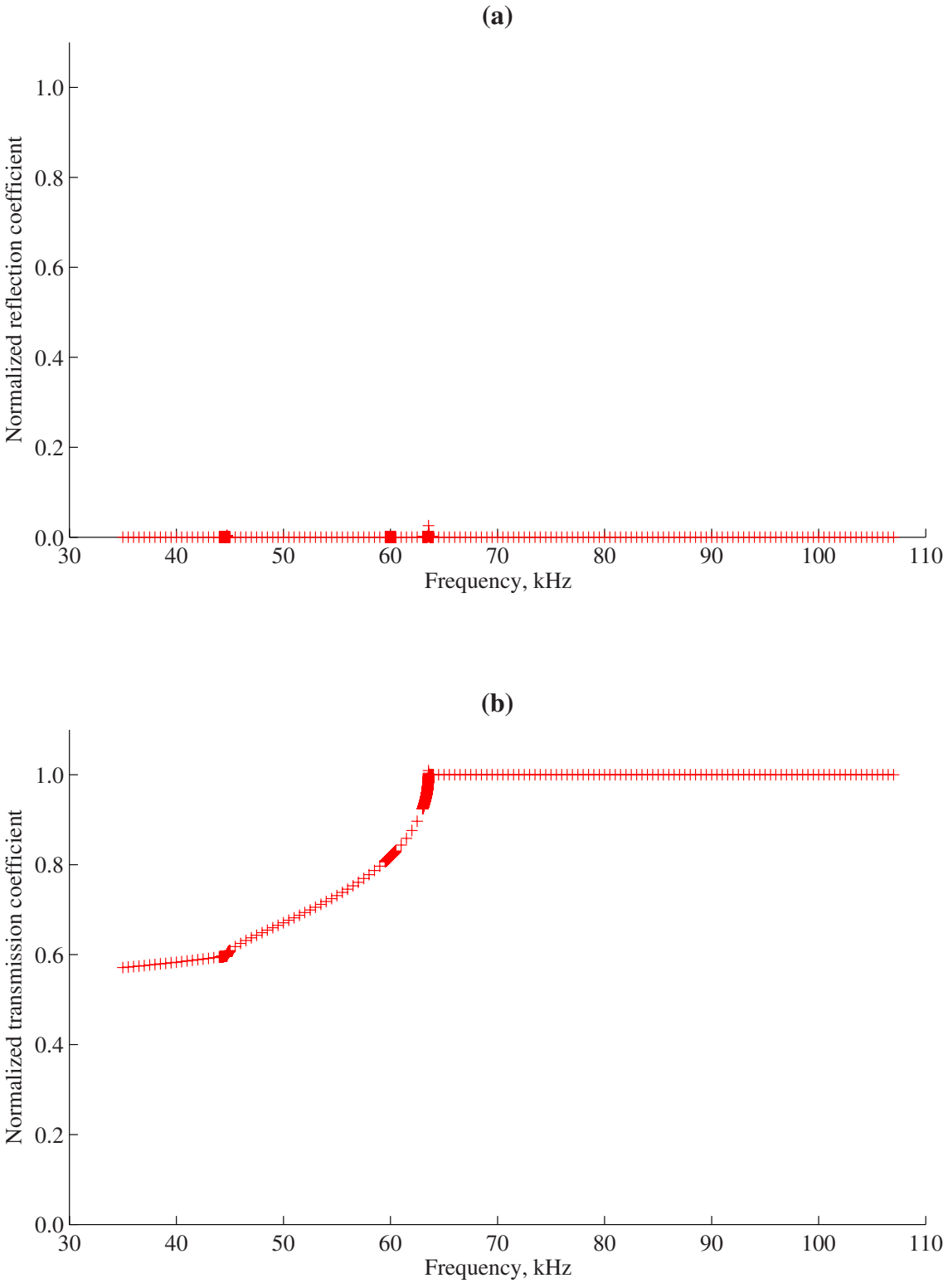

Figure H.27. Normalized reflection and transmission coefficients for the axisymmetric transparency check and the incident F(10,1) mode.

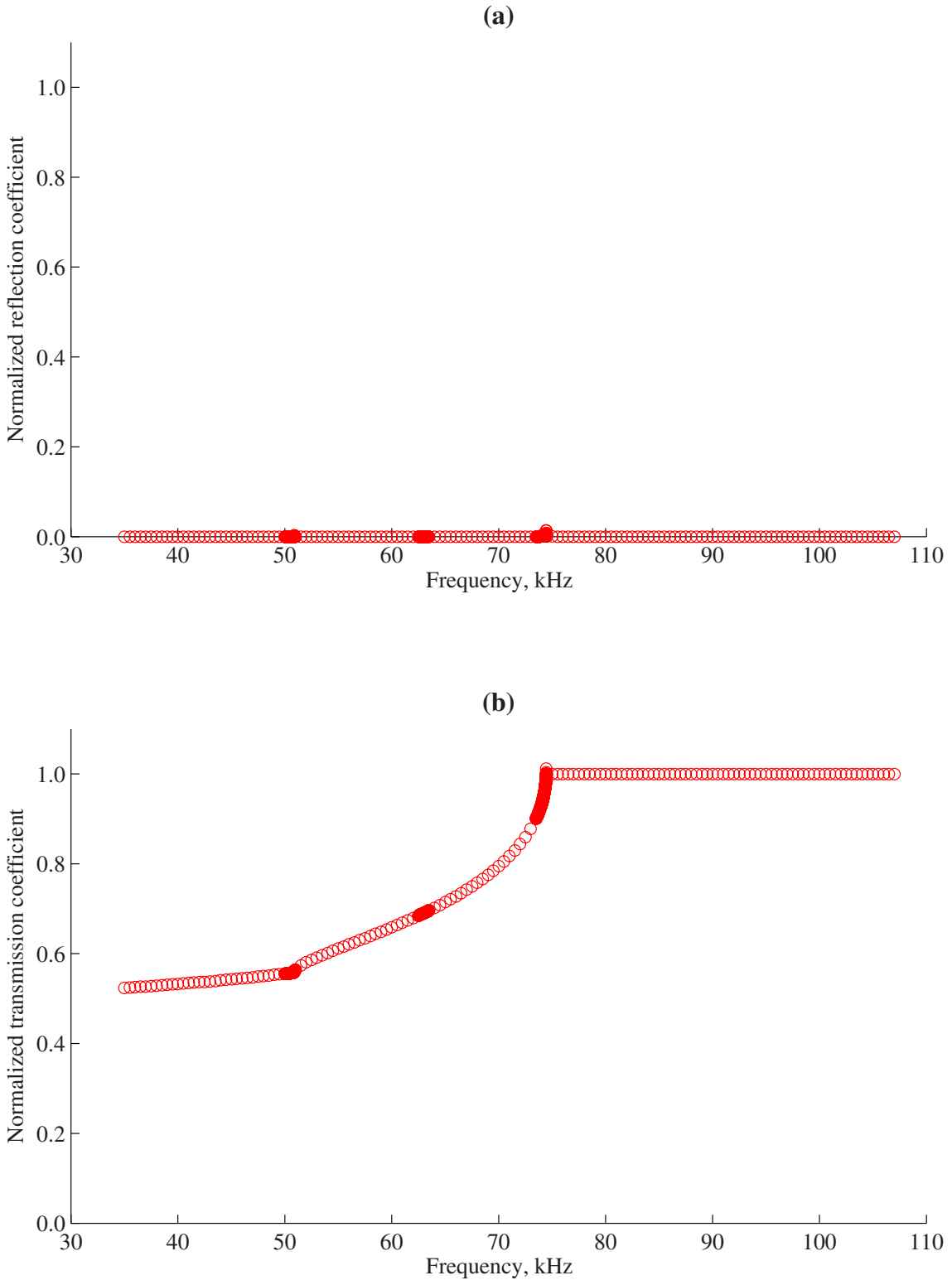

Figure H.28. Normalized reflection and transmission coefficients for the axisymmetric transparency check and the incident F(11,1) mode.

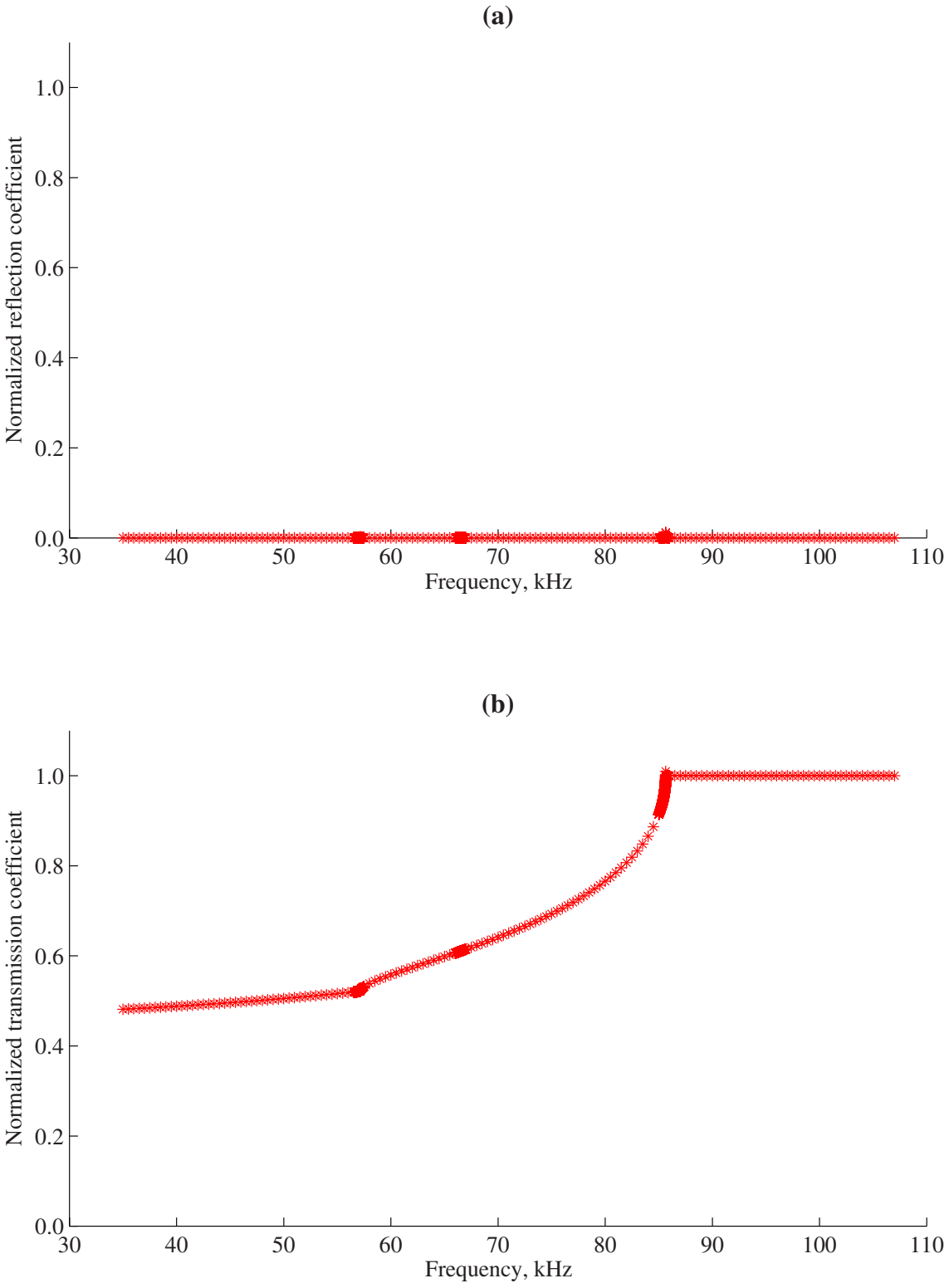

Figure H.29. Normalized reflection and transmission coefficients for the axisymmetric transparency check and the incident F(12,1) mode.

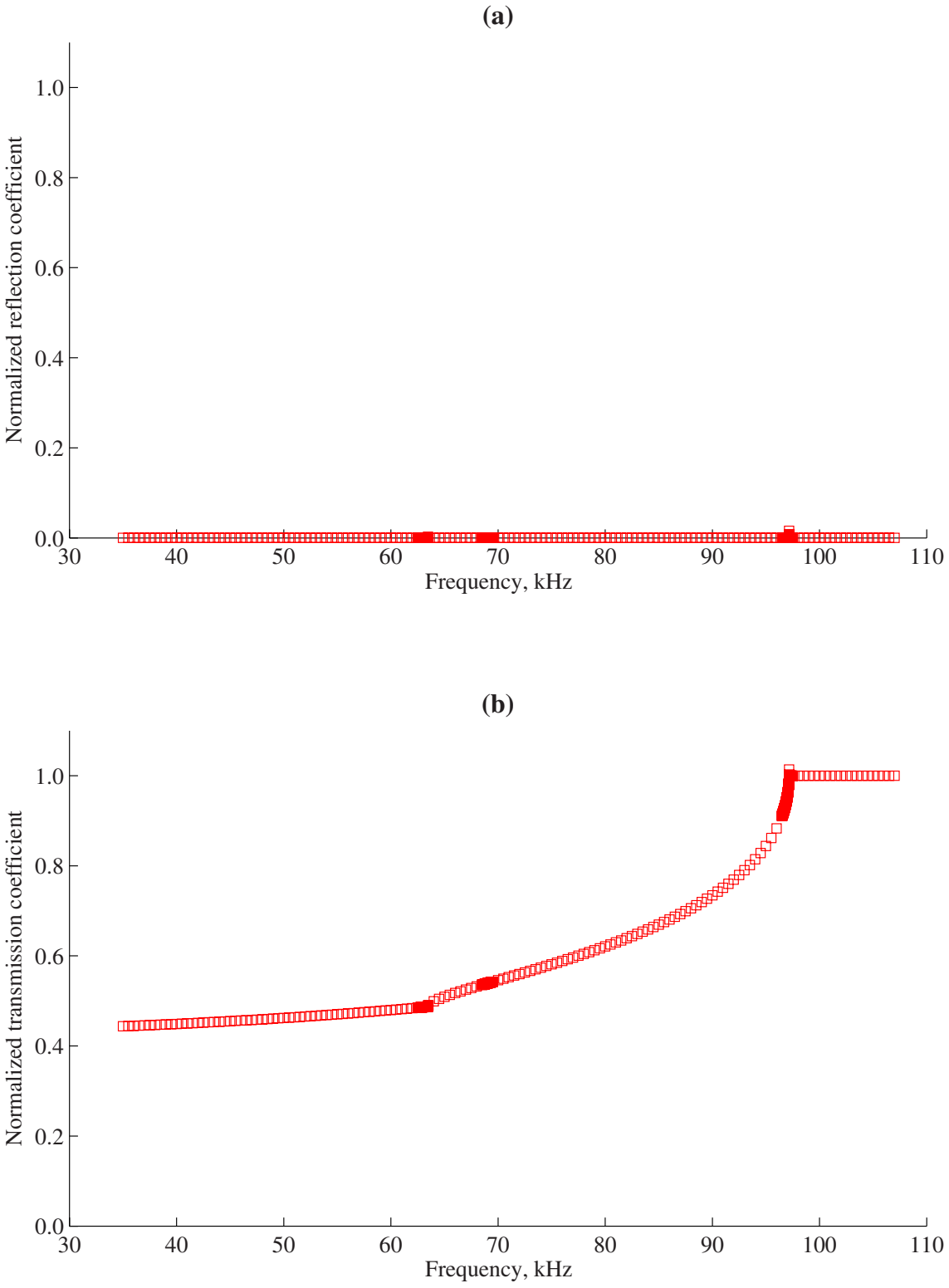

Figure H.30. Normalized reflection and transmission coefficients for the axisymmetric transparency check and the incident F(13,1) mode.

H.3 Transparency Check for Three-dimensional Program

Normalized reflection and transmission coefficients for selected modes incident on and scattered by the finite element region are given in Figures H.31 through H.59 as a check for the transparency of the nonaxisymmetric program when no scatterer is present. The summary of annotations given in Section H.1 remains applicable.

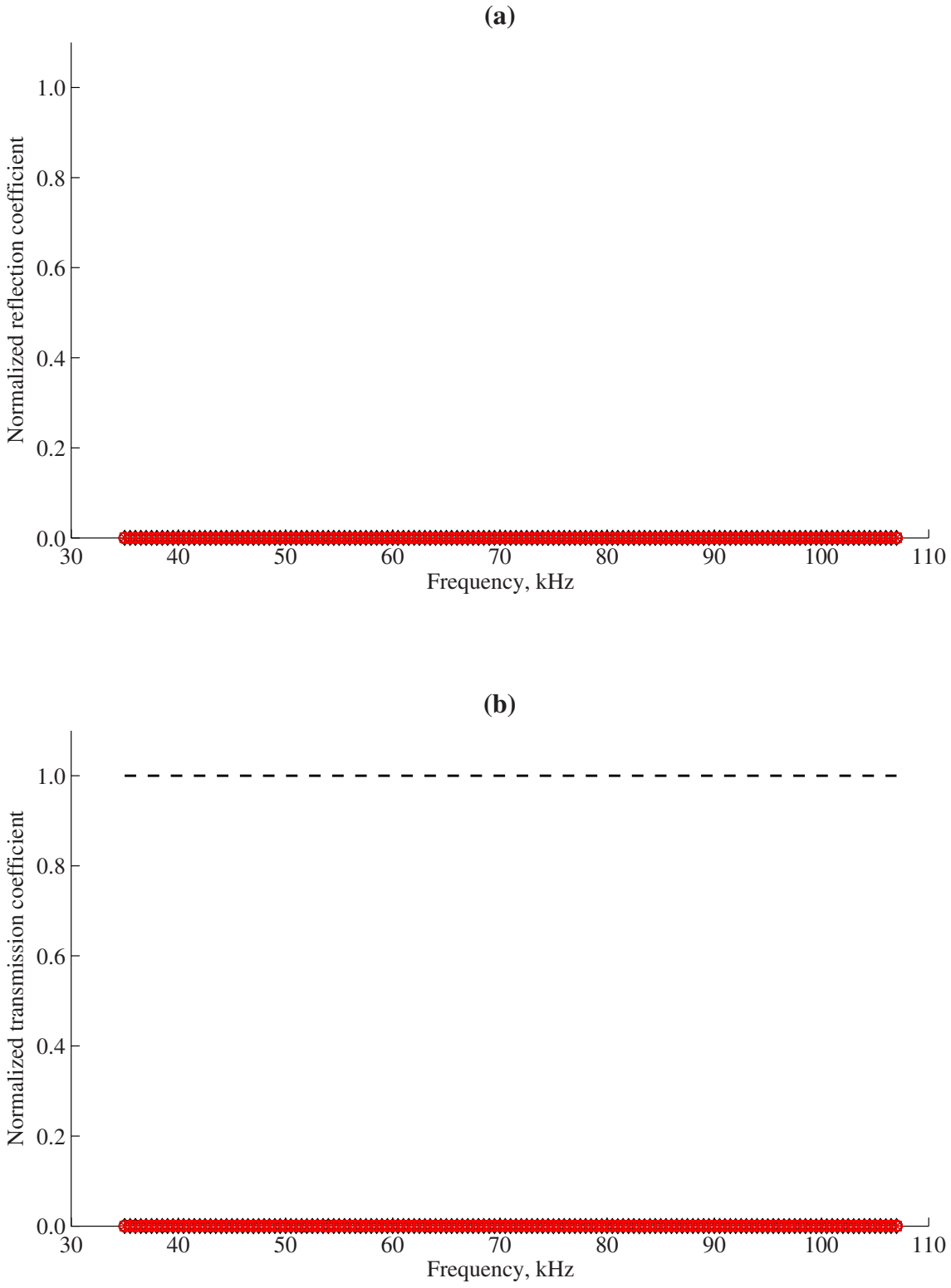

Figure H.31. Normalized reflection and transmission coefficients for the three-dimensional transparency check and the incident T(0,1) mode.

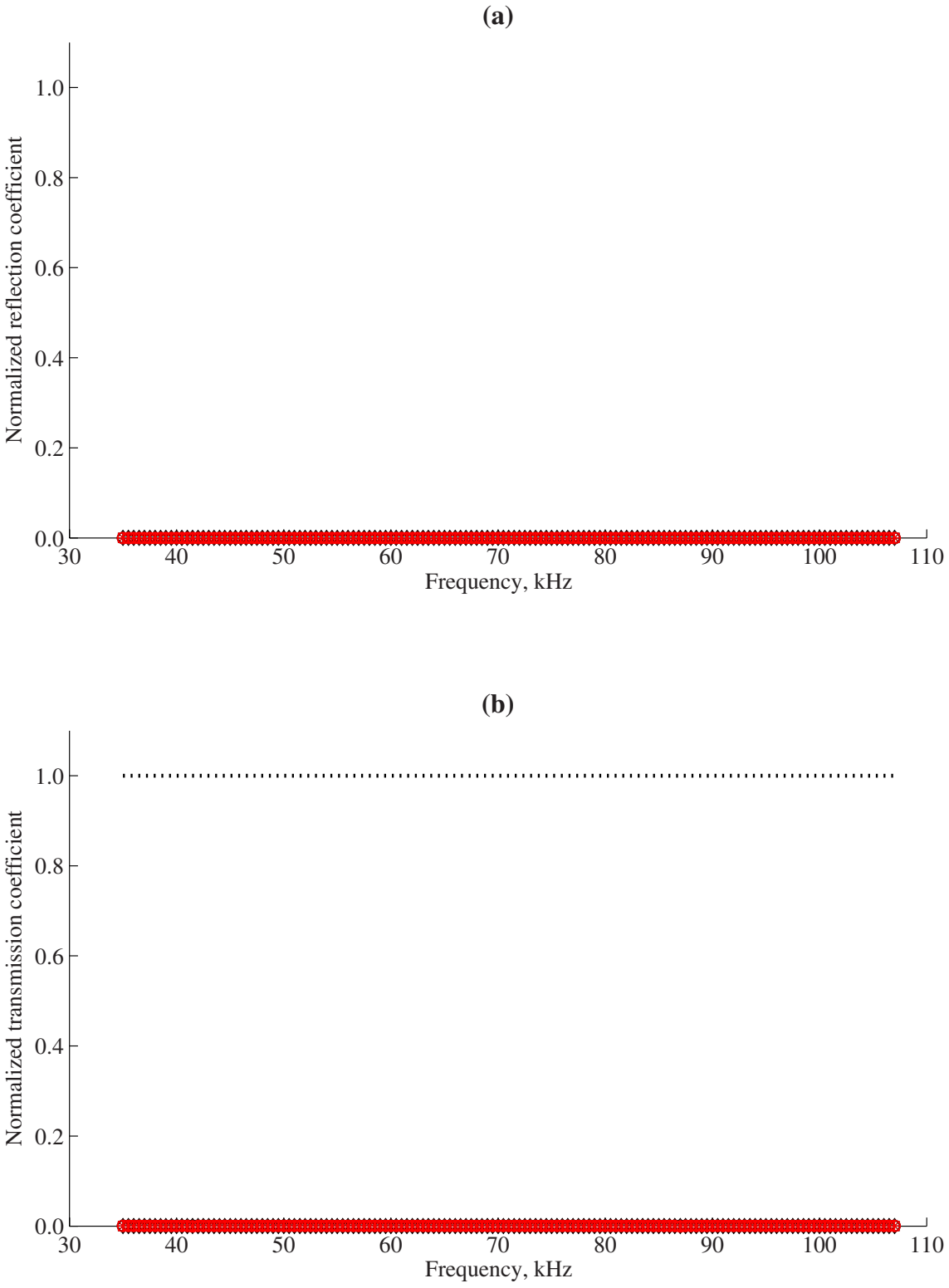

Figure H.32. Normalized reflection and transmission coefficients for the three-dimensional transparency check and the incident L(0,1) mode.

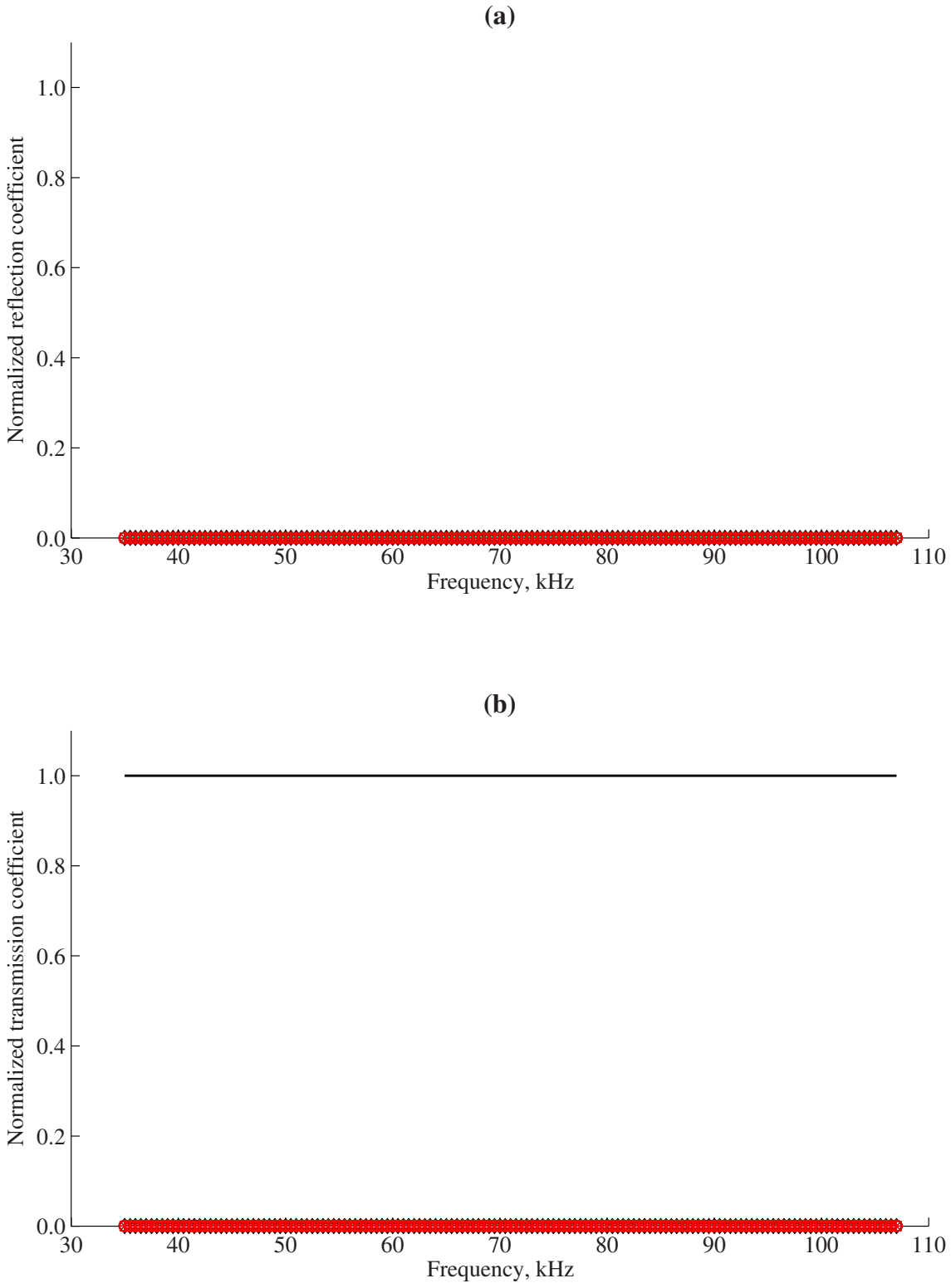

Figure H.33. Normalized reflection and transmission coefficients for the three-dimensional transparency check and the incident L(0,2) mode.

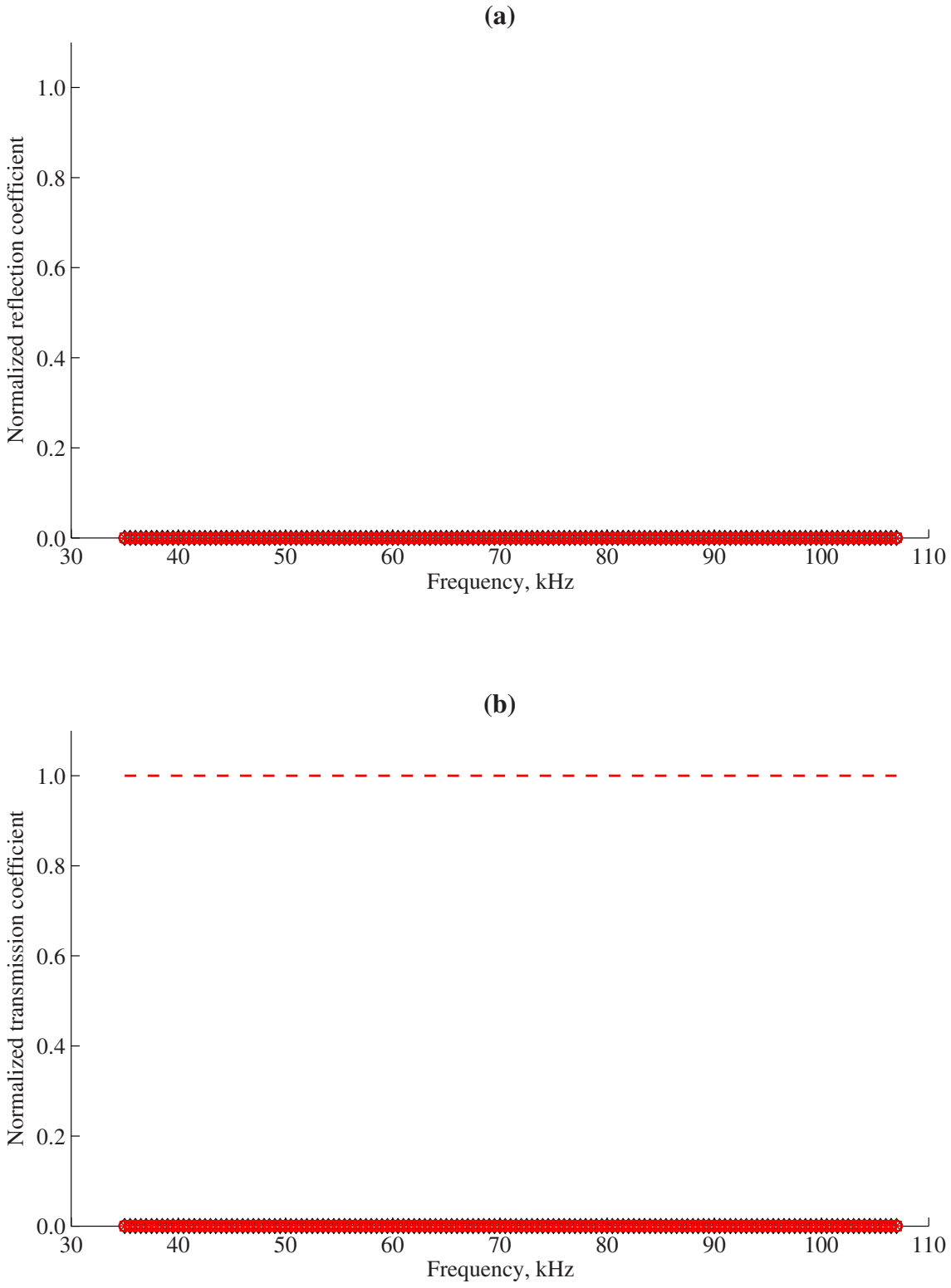

Figure H.34. Normalized reflection and transmission coefficients for the three-dimensional transparency check and the incident F(1,1) mode.

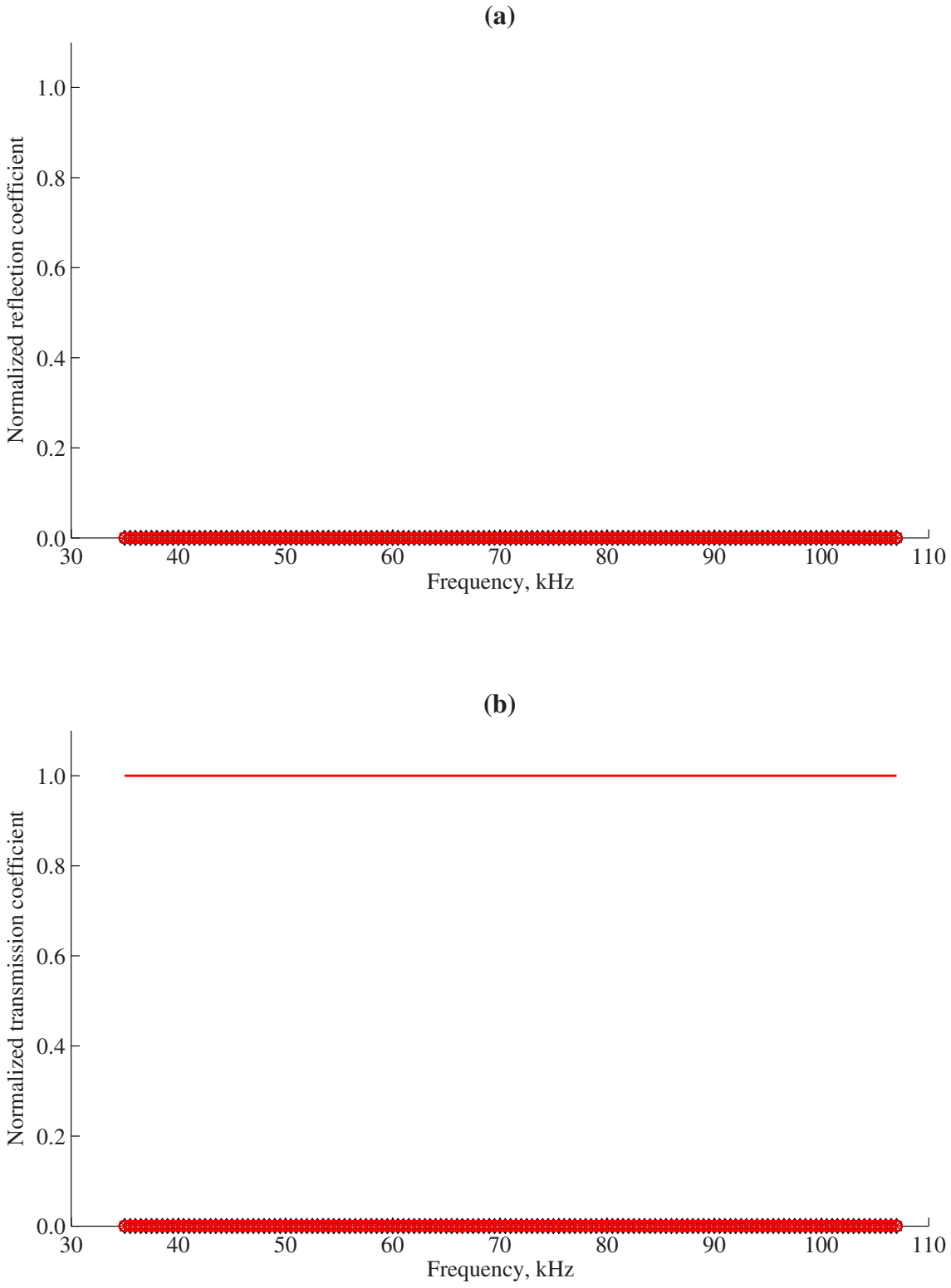

Figure H.35. Normalized reflection and transmission coefficients for the three-dimensional transparency check and the incident F(1,2) mode.

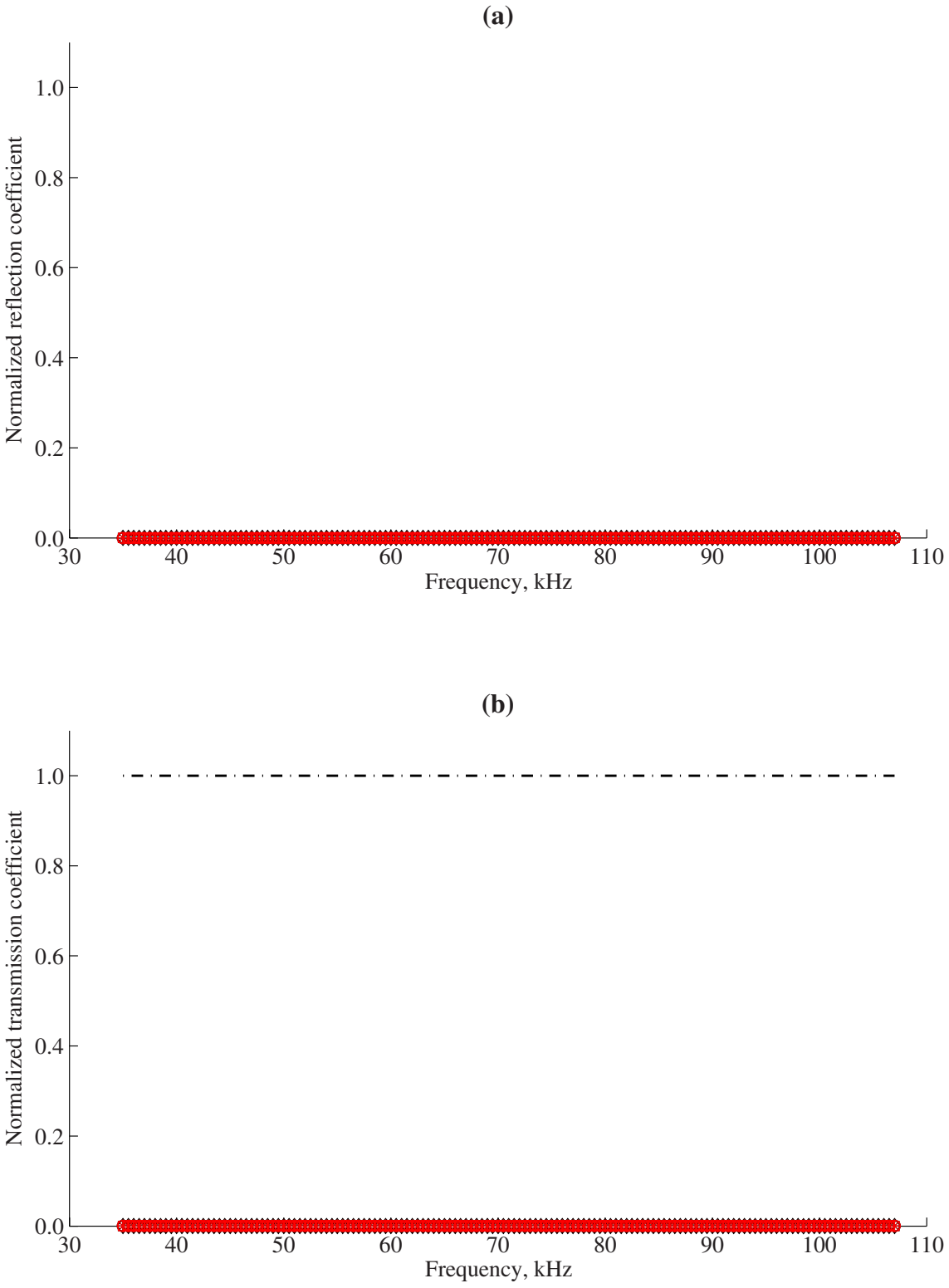

Figure H.36. Normalized reflection and transmission coefficients for the three-dimensional transparency check and the incident F(1,3) mode.

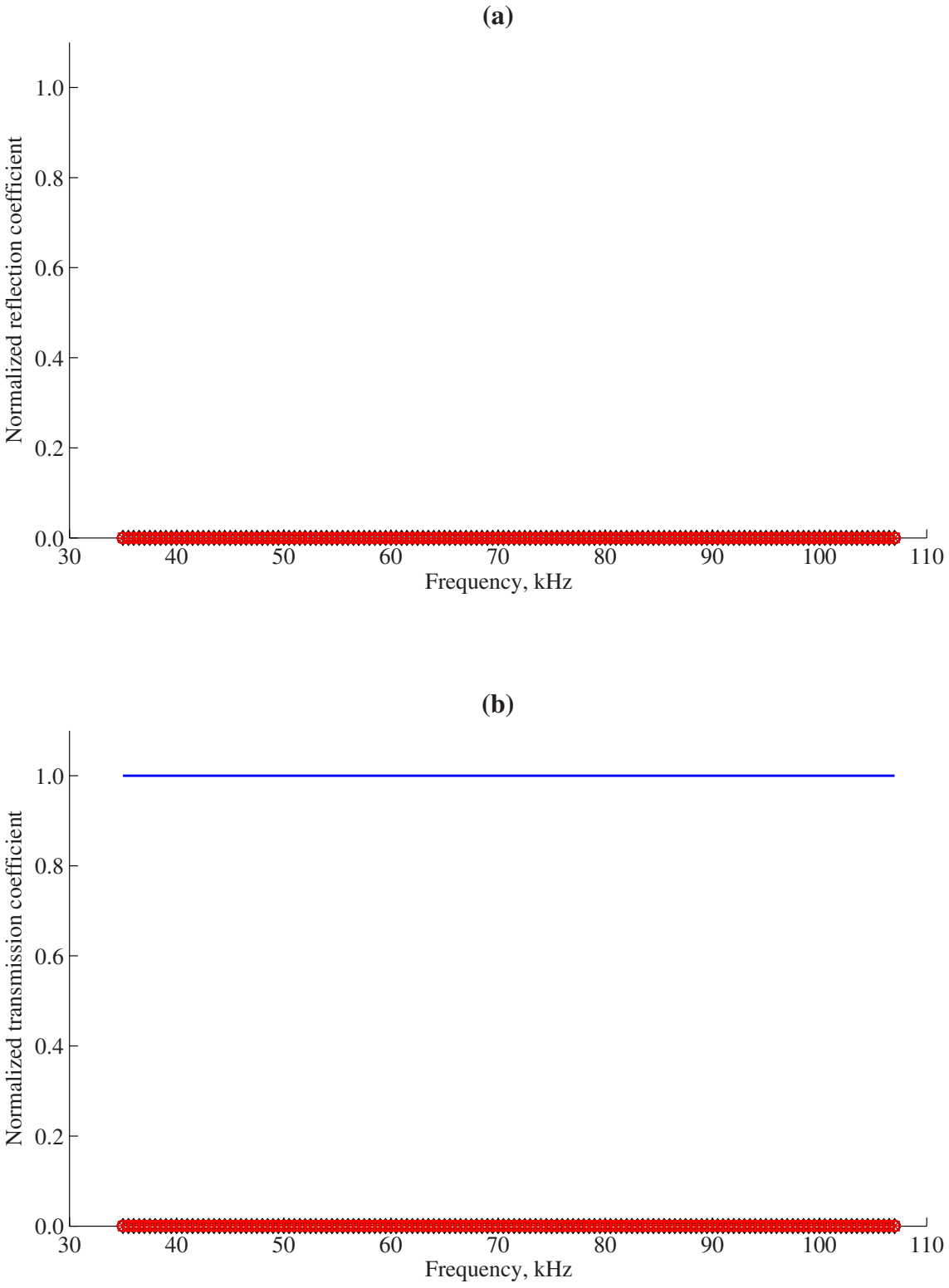

Figure H.37. Normalized reflection and transmission coefficients for the three-dimensional transparency check and the incident F(2,1) mode.

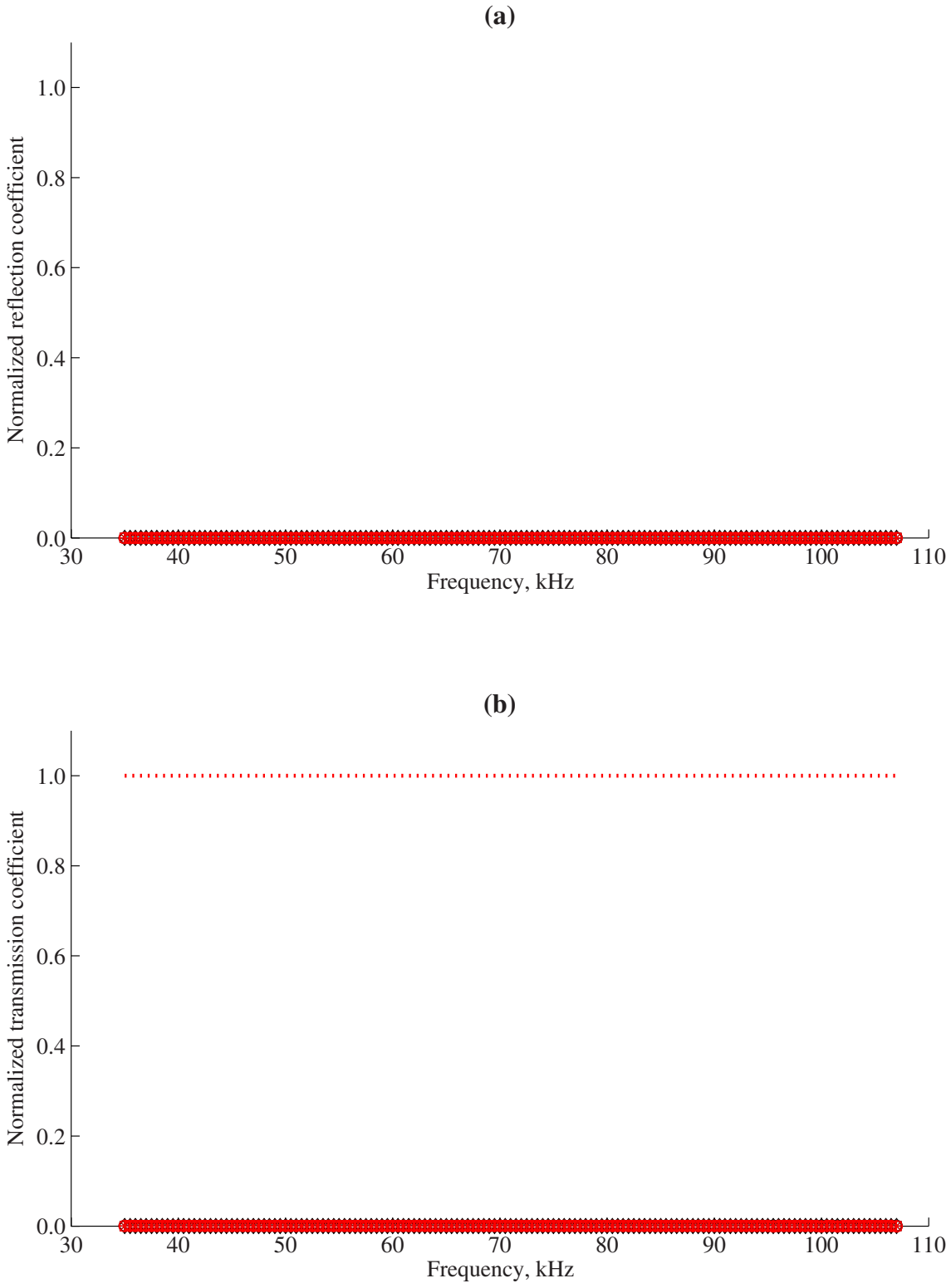

Figure H.38. Normalized reflection and transmission coefficients for the three-dimensional transparency check and the incident F(2,2) mode.

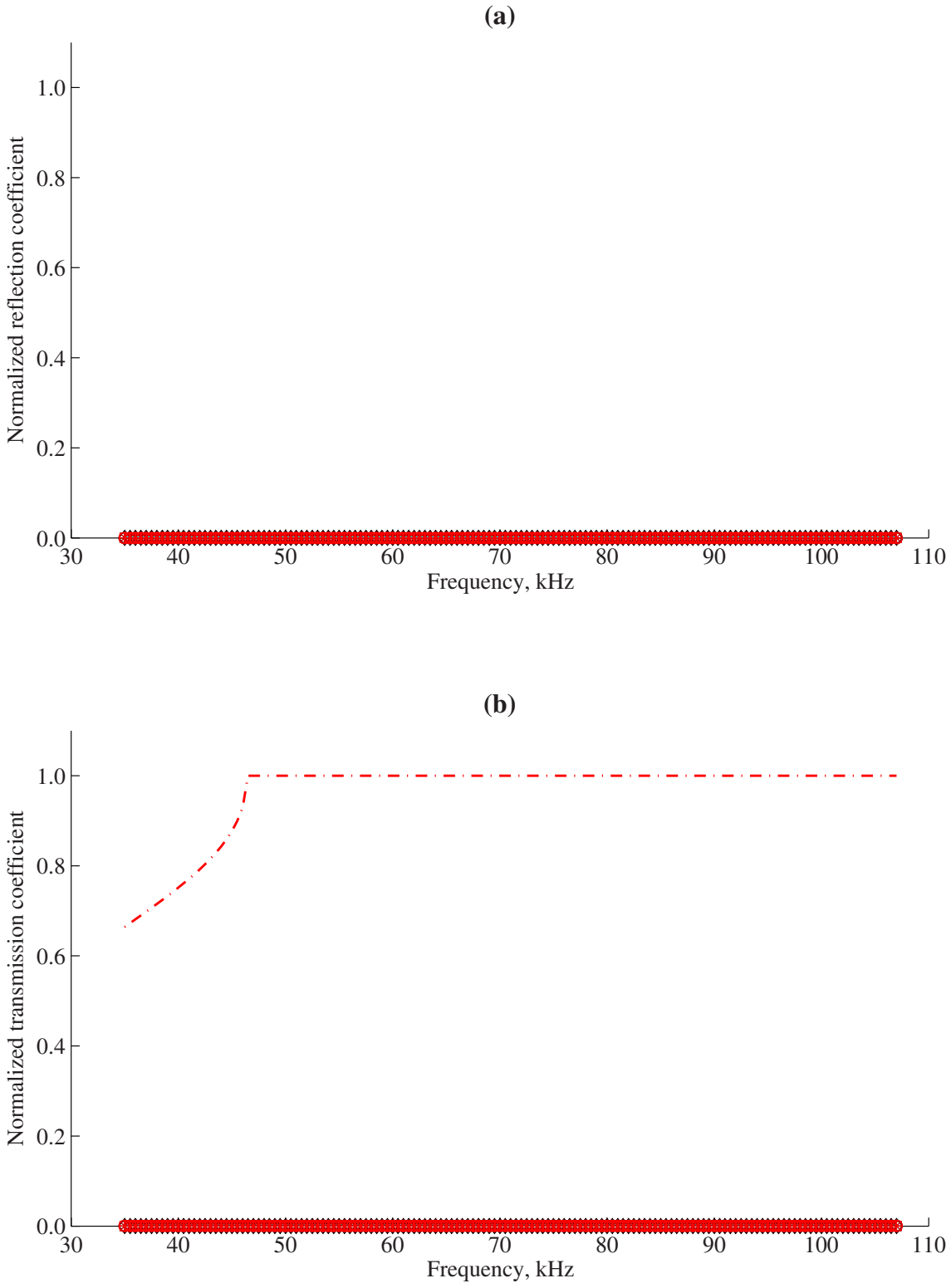

Figure H.39. Normalized reflection and transmission coefficients for the three-dimensional transparency check and the incident F(2,3) mode.

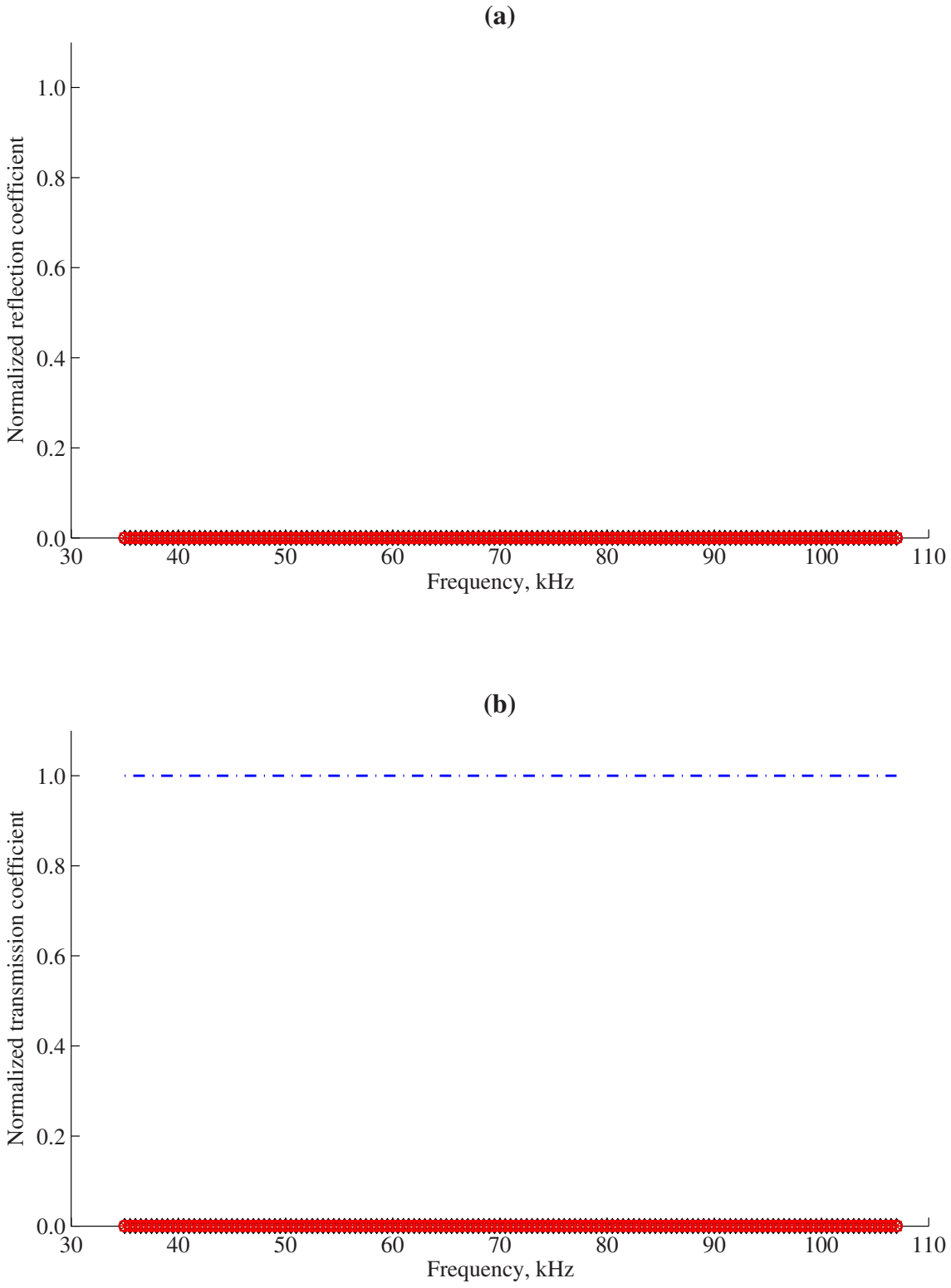

Figure H.40. Normalized reflection and transmission coefficients for the three-dimensional transparency check and the incident F(3,1) mode.

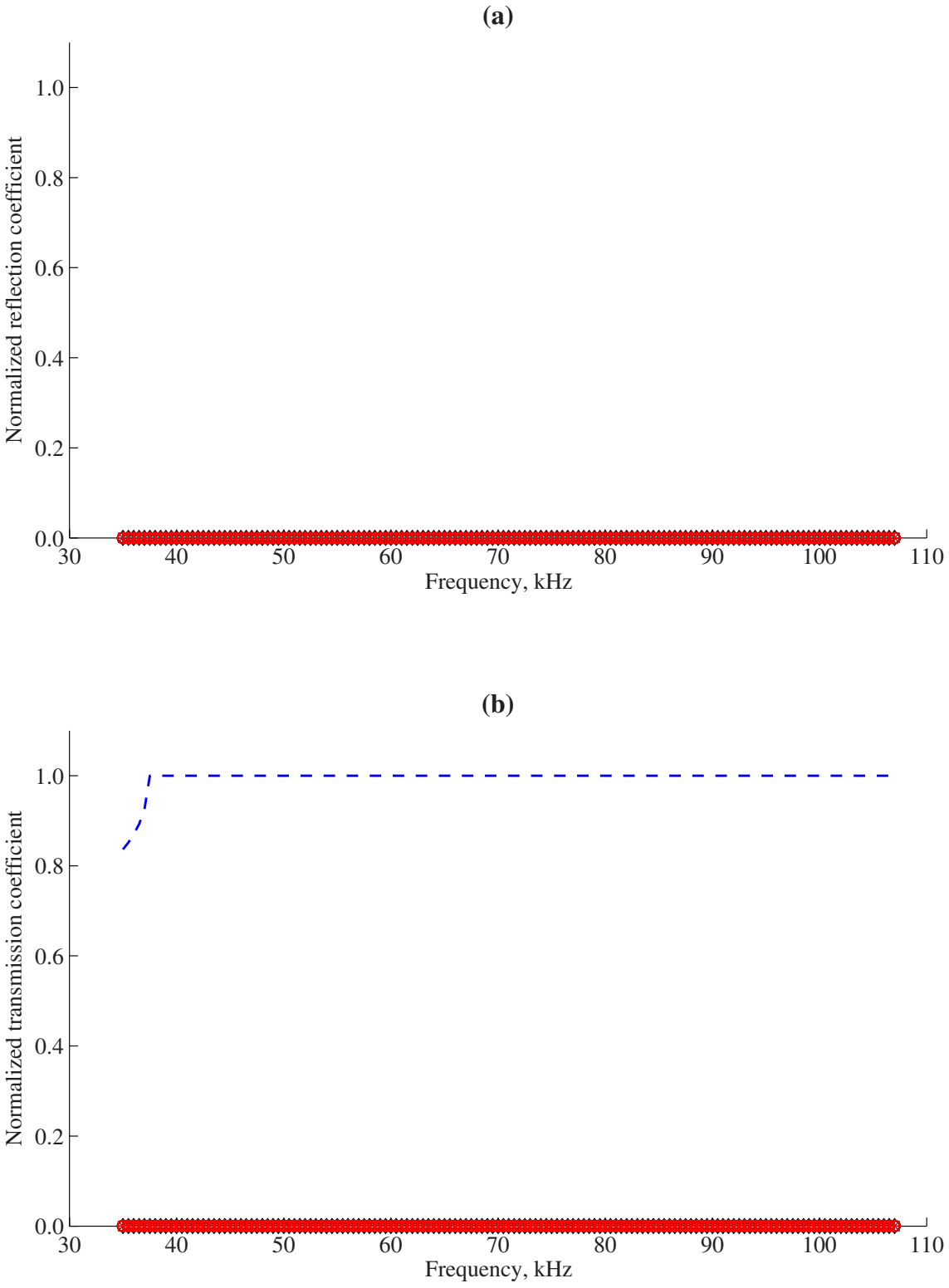

Figure H.41. Normalized reflection and transmission coefficients for the three-dimensional transparency check and the incident F(3,2) mode.

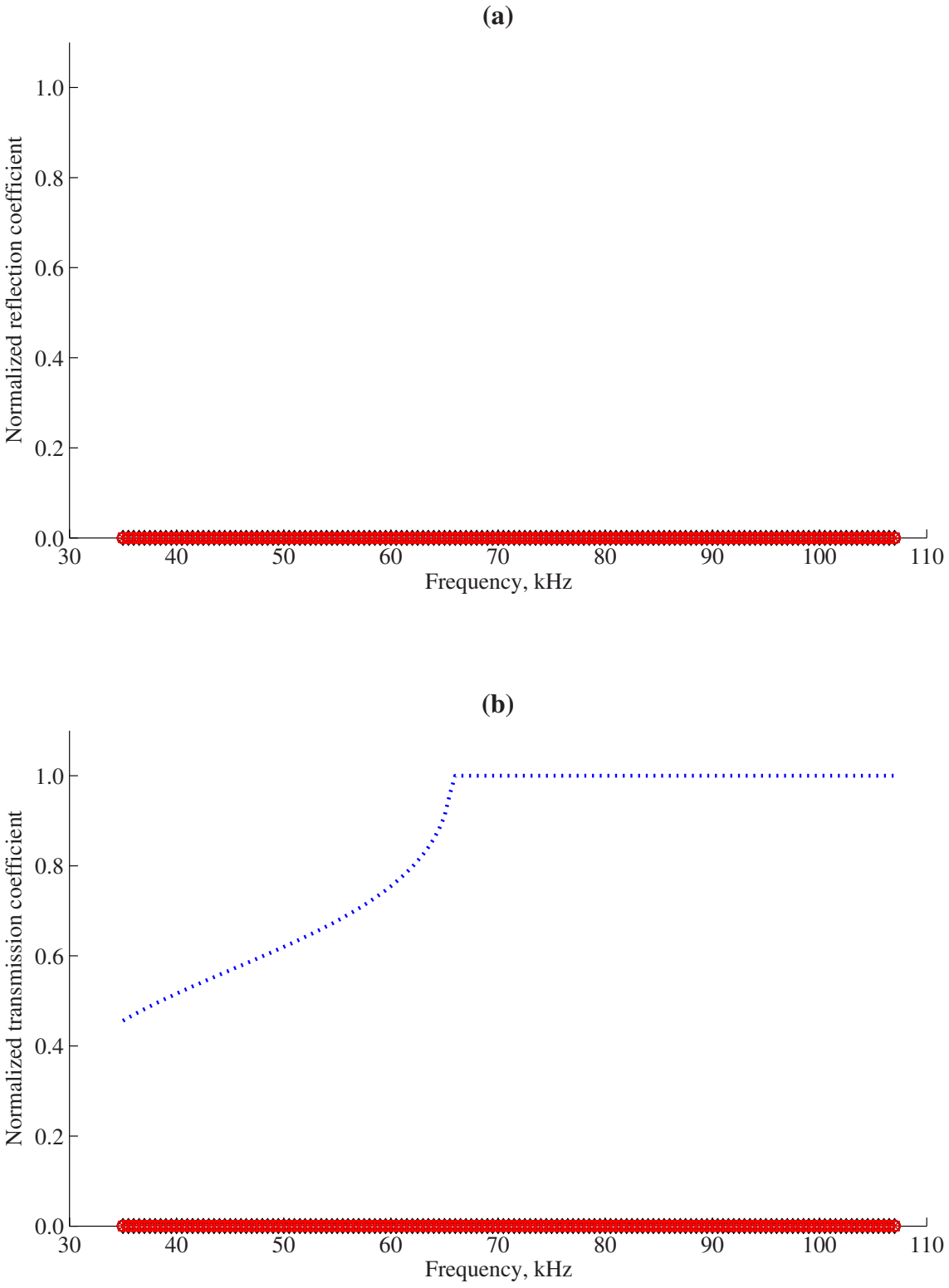

Figure H.42. Normalized reflection and transmission coefficients for the three-dimensional transparency check and the incident F(3,3) mode.

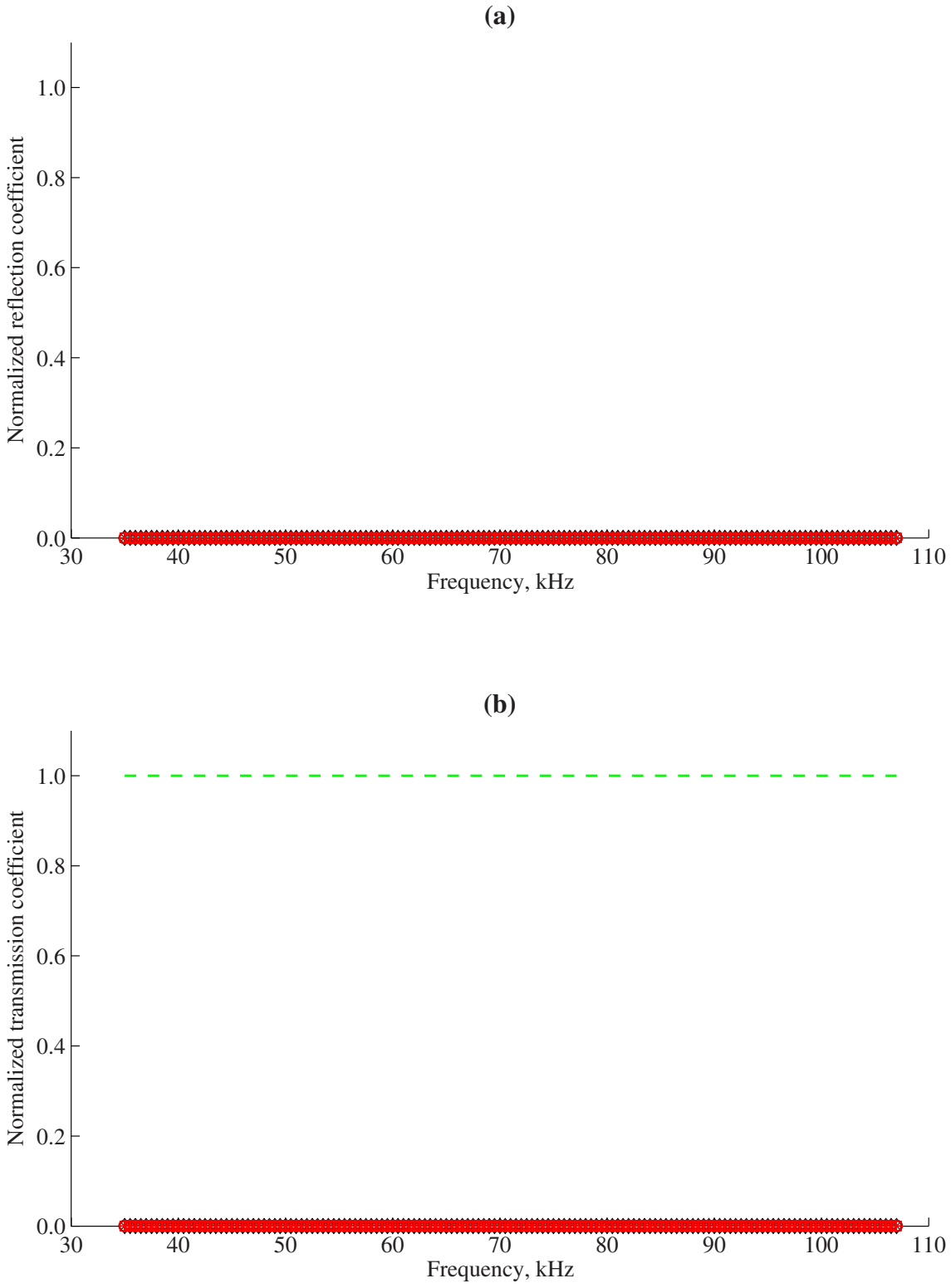

Figure H.43. Normalized reflection and transmission coefficients for the three-dimensional transparency check and the incident F(4,1) mode.

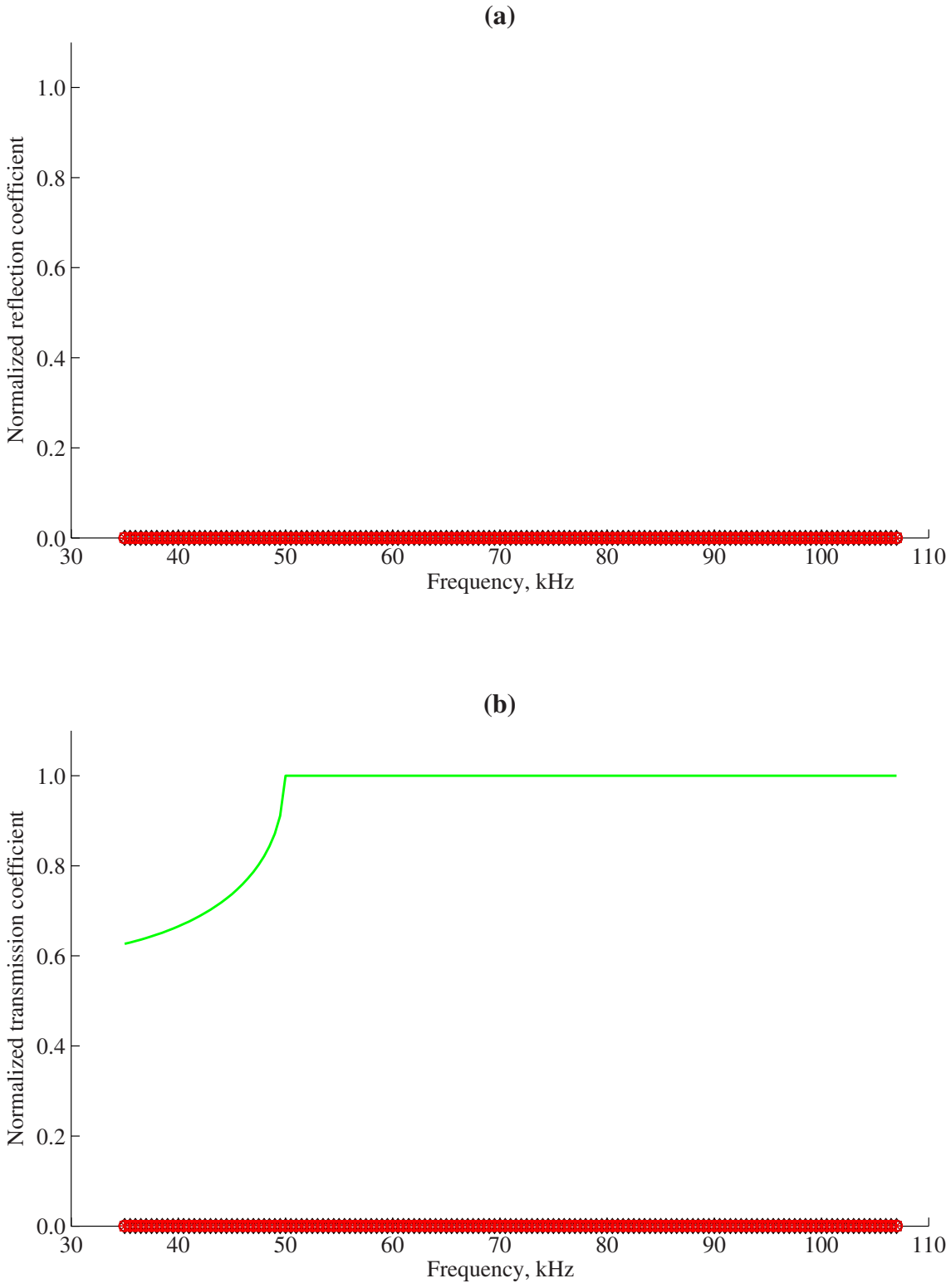

Figure H.44. Normalized reflection and transmission coefficients for the three-dimensional transparency check and the incident F(4,2) mode.

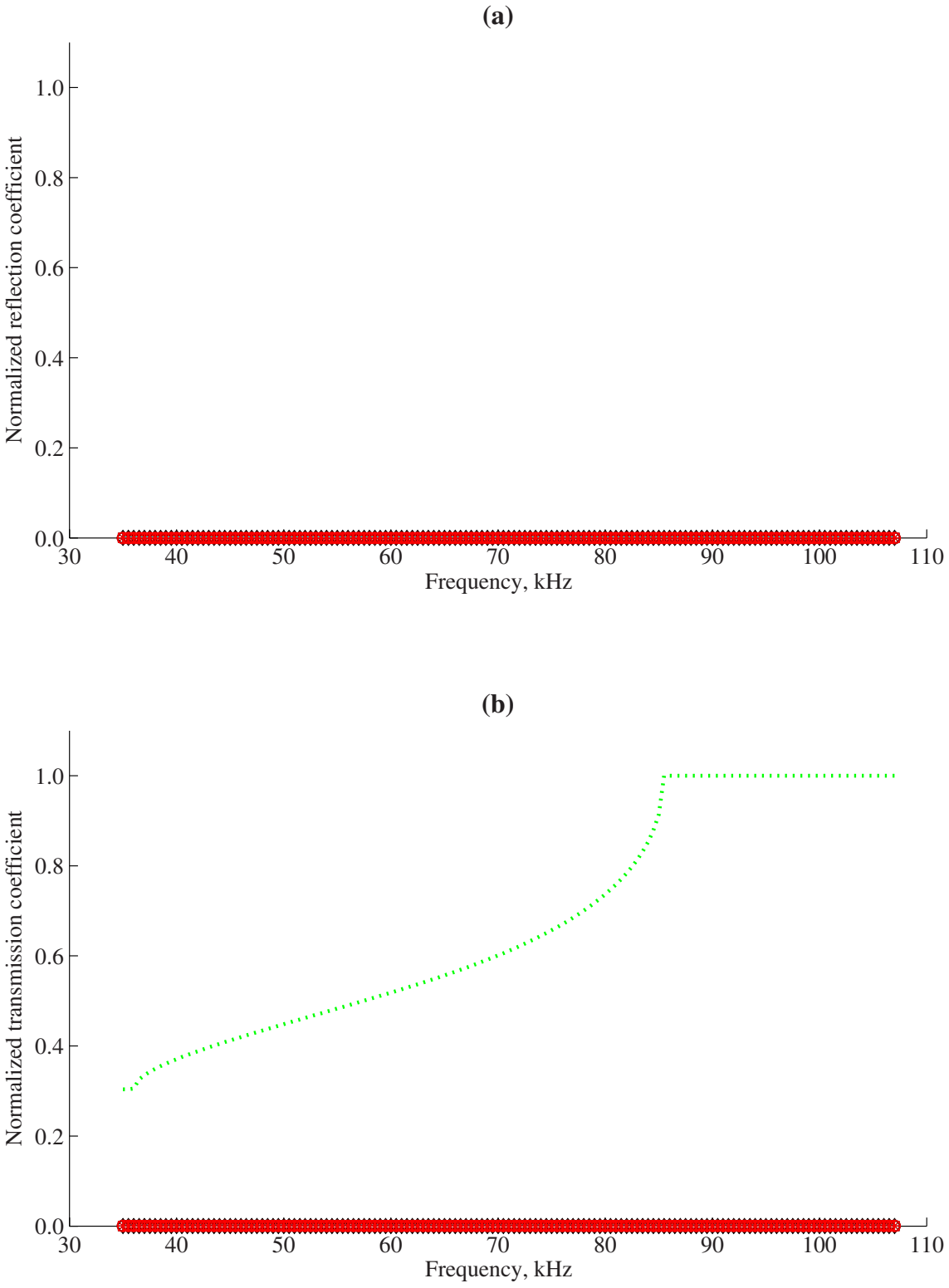

Figure H.45. Normalized reflection and transmission coefficients for the three-dimensional transparency check and the incident F(4,3) mode.

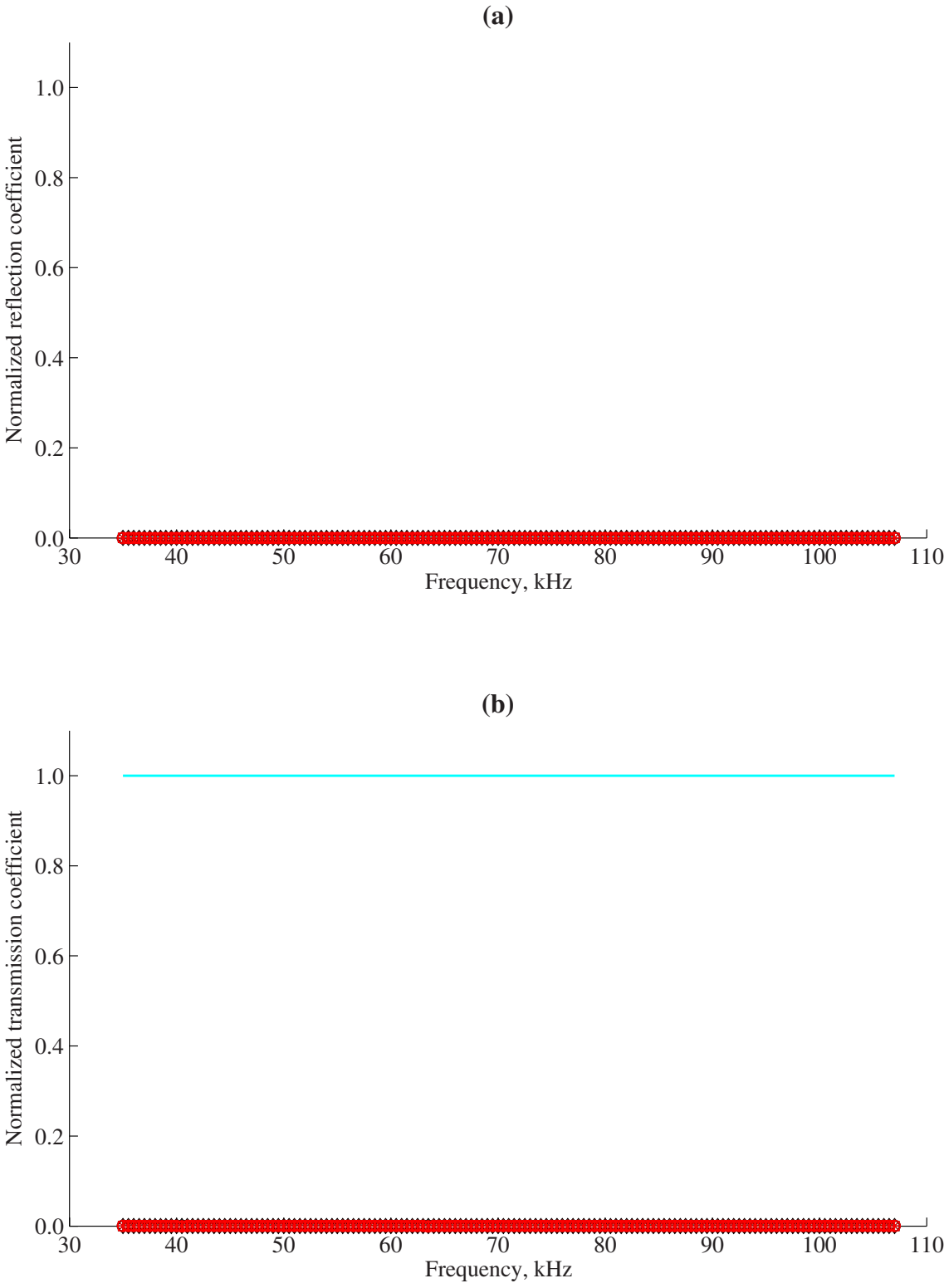

Figure H.46. Normalized reflection and transmission coefficients for the three-dimensional transparency check and the incident F(5,1) mode.

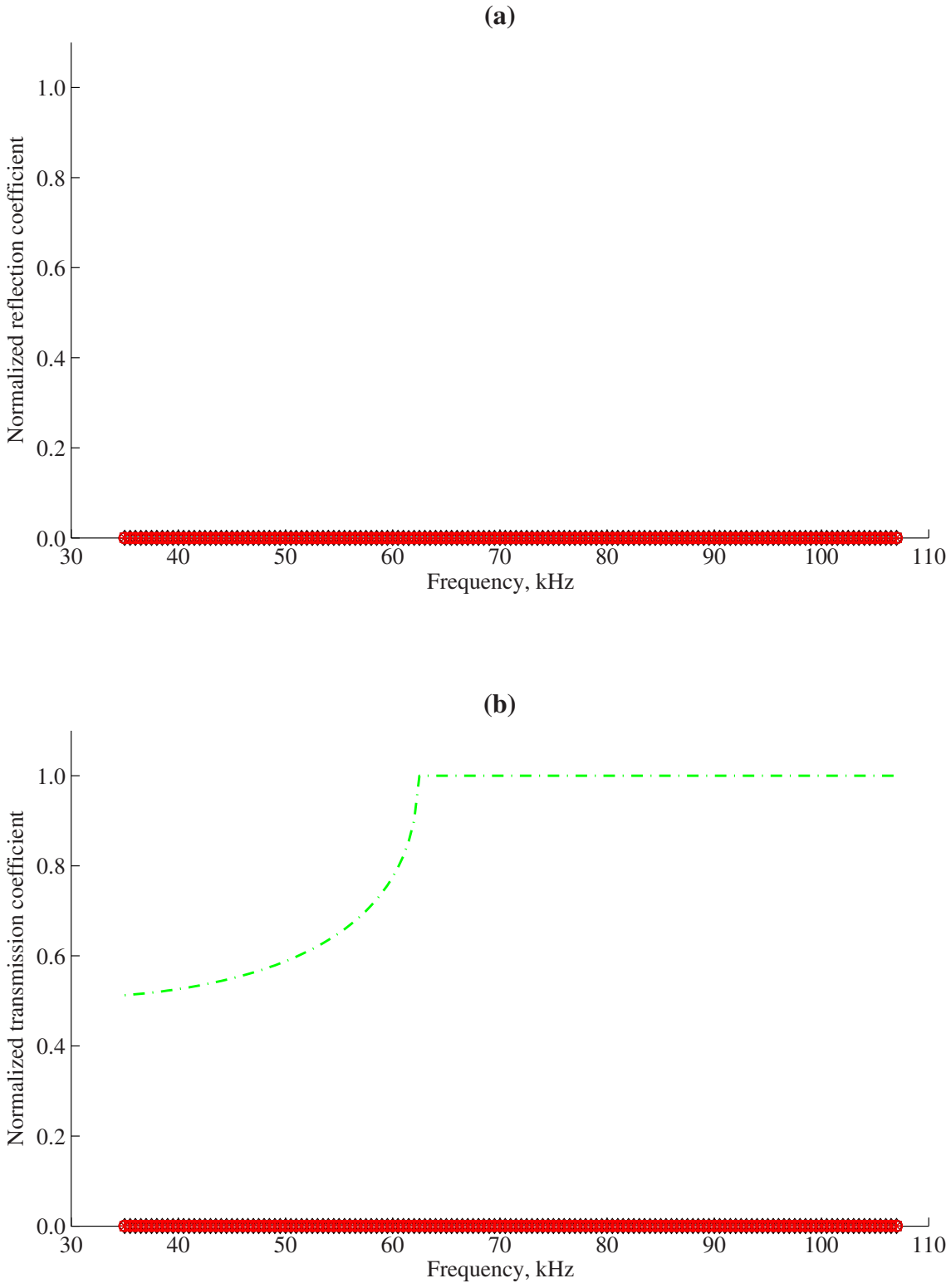

Figure H.47. Normalized reflection and transmission coefficients for the three-dimensional transparency check and the incident F(5,2) mode.

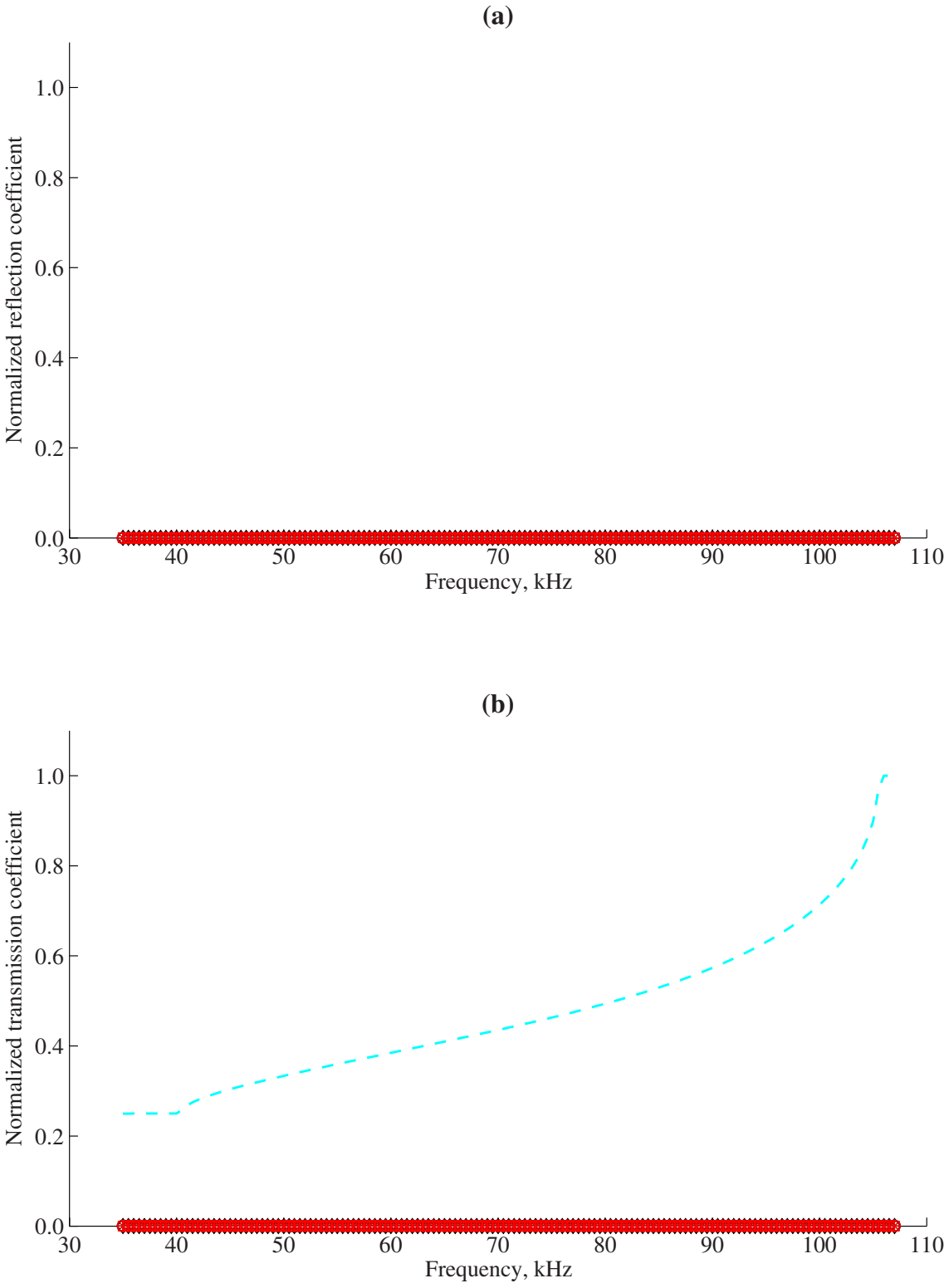

Figure H.48. Normalized reflection and transmission coefficients for the three-dimensional transparency check and the incident F(5,3) mode.

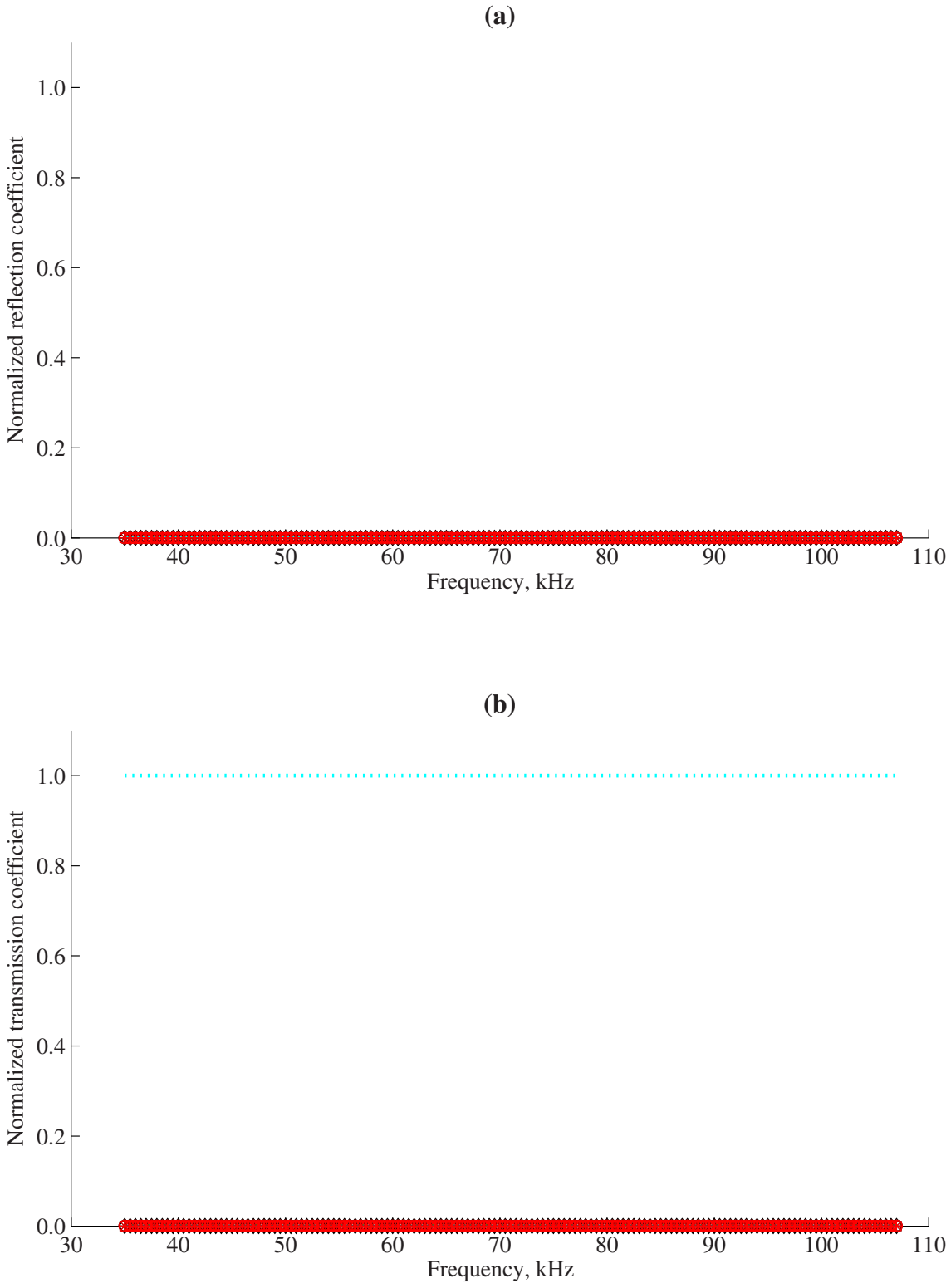

Figure H.49. Normalized reflection and transmission coefficients for the three-dimensional transparency check and the incident F(6,1) mode.

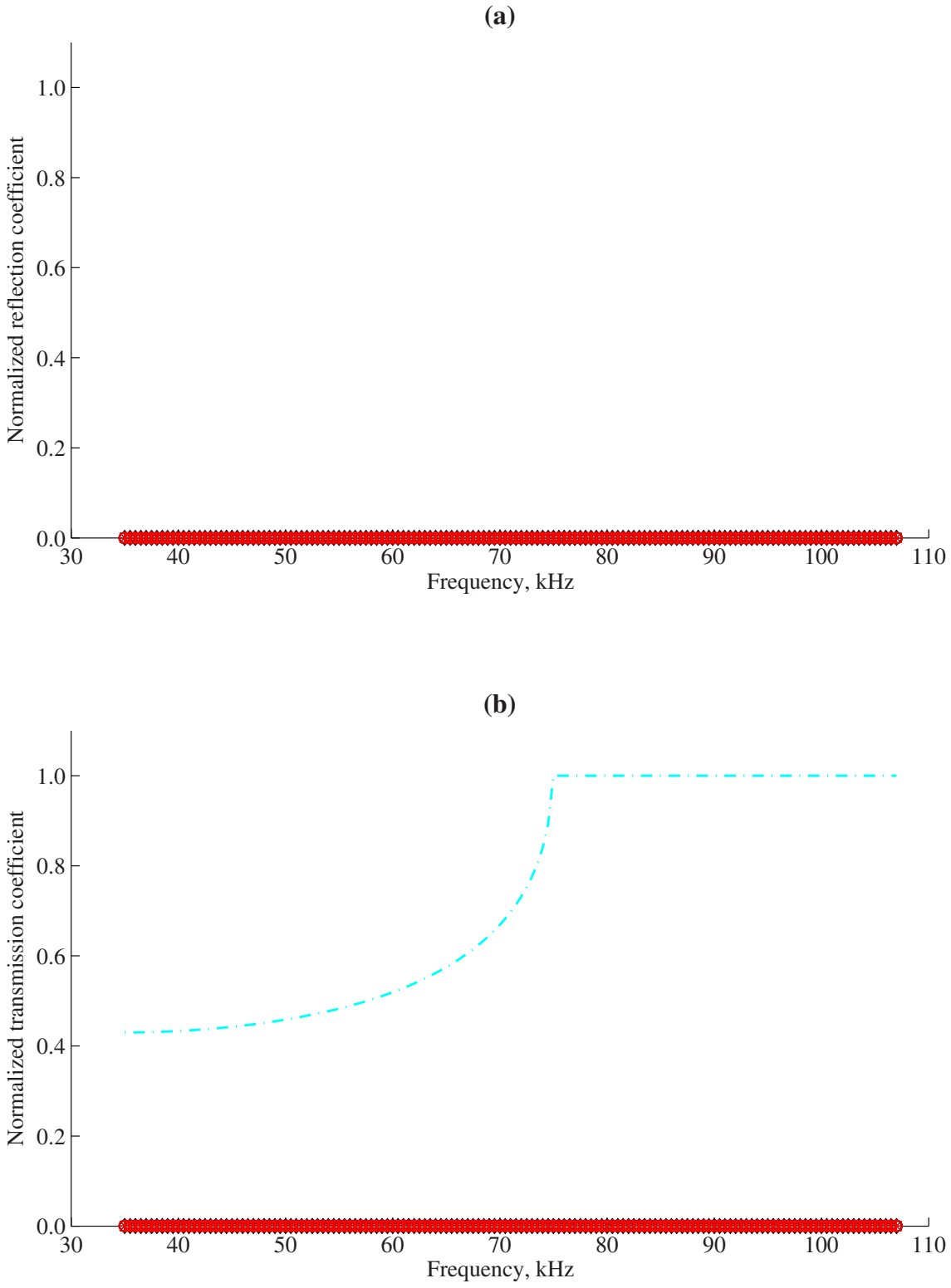

Figure H.50. Normalized reflection and transmission coefficients for the three-dimensional transparency check and the incident F(6,2) mode.

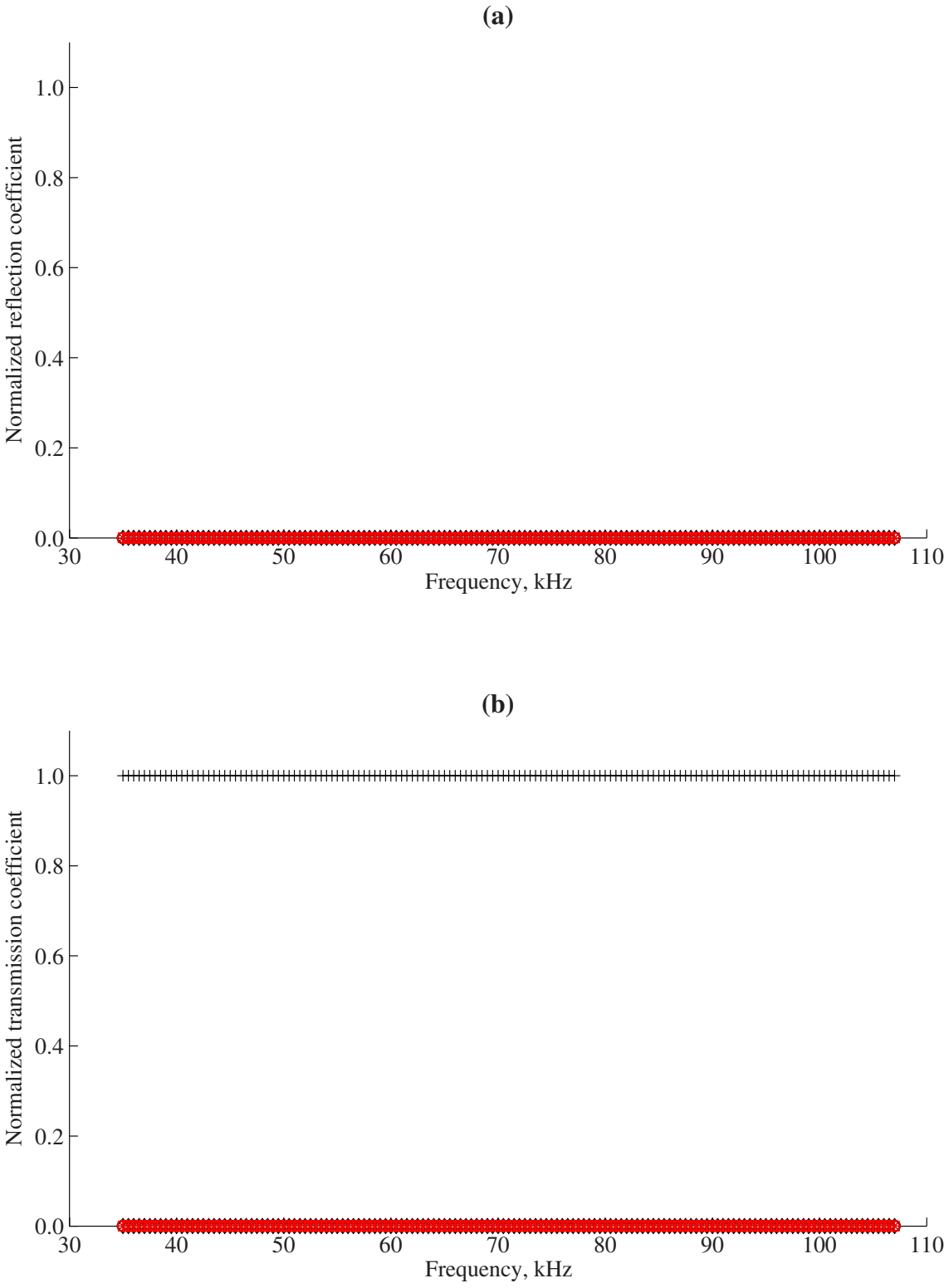

Figure H.51. Normalized reflection and transmission coefficients for the three-dimensional transparency check and the incident F(7,1) mode.

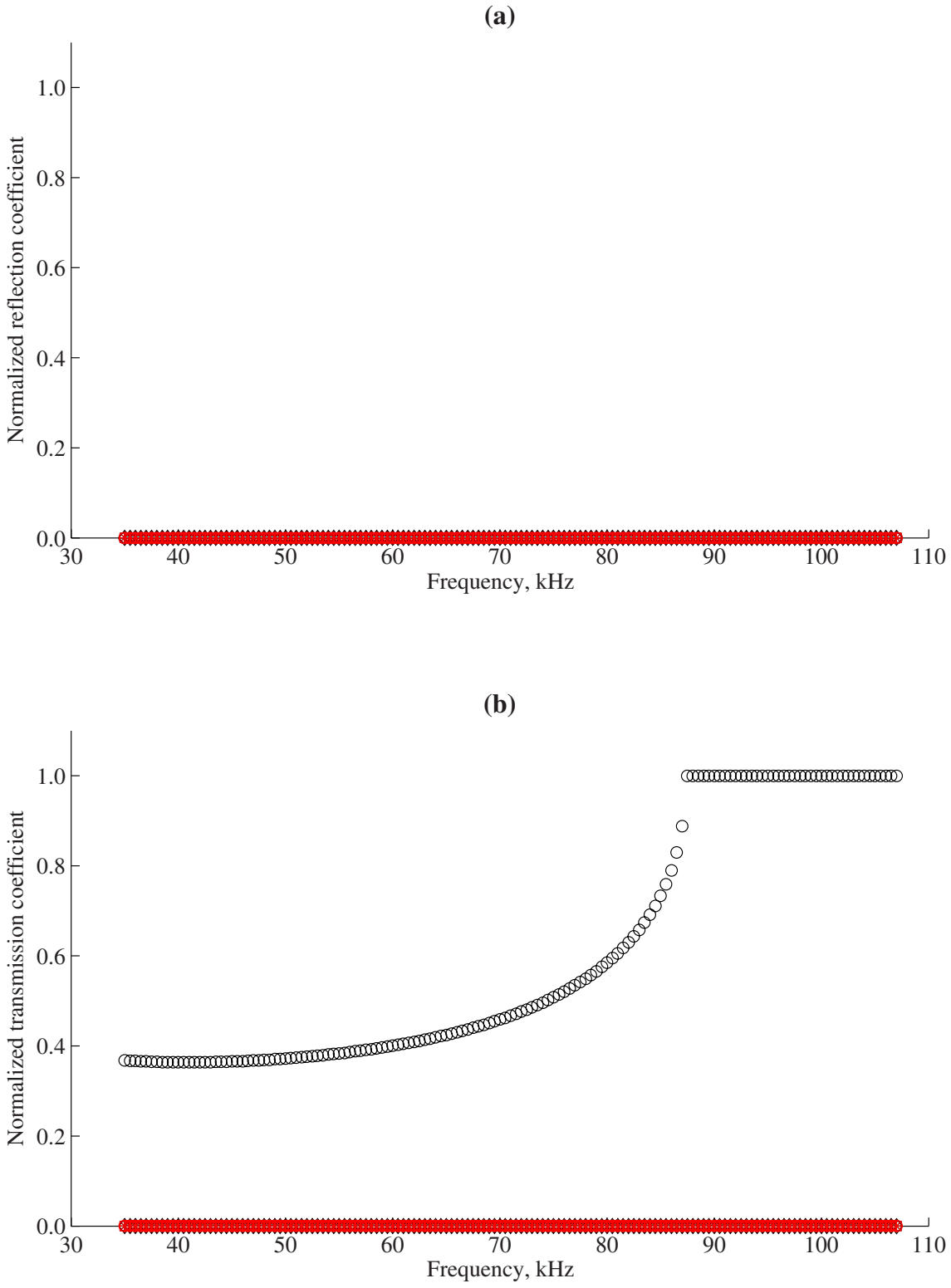

Figure H.52. Normalized reflection and transmission coefficients for the three-dimensional transparency check and the incident F(7,2) mode.

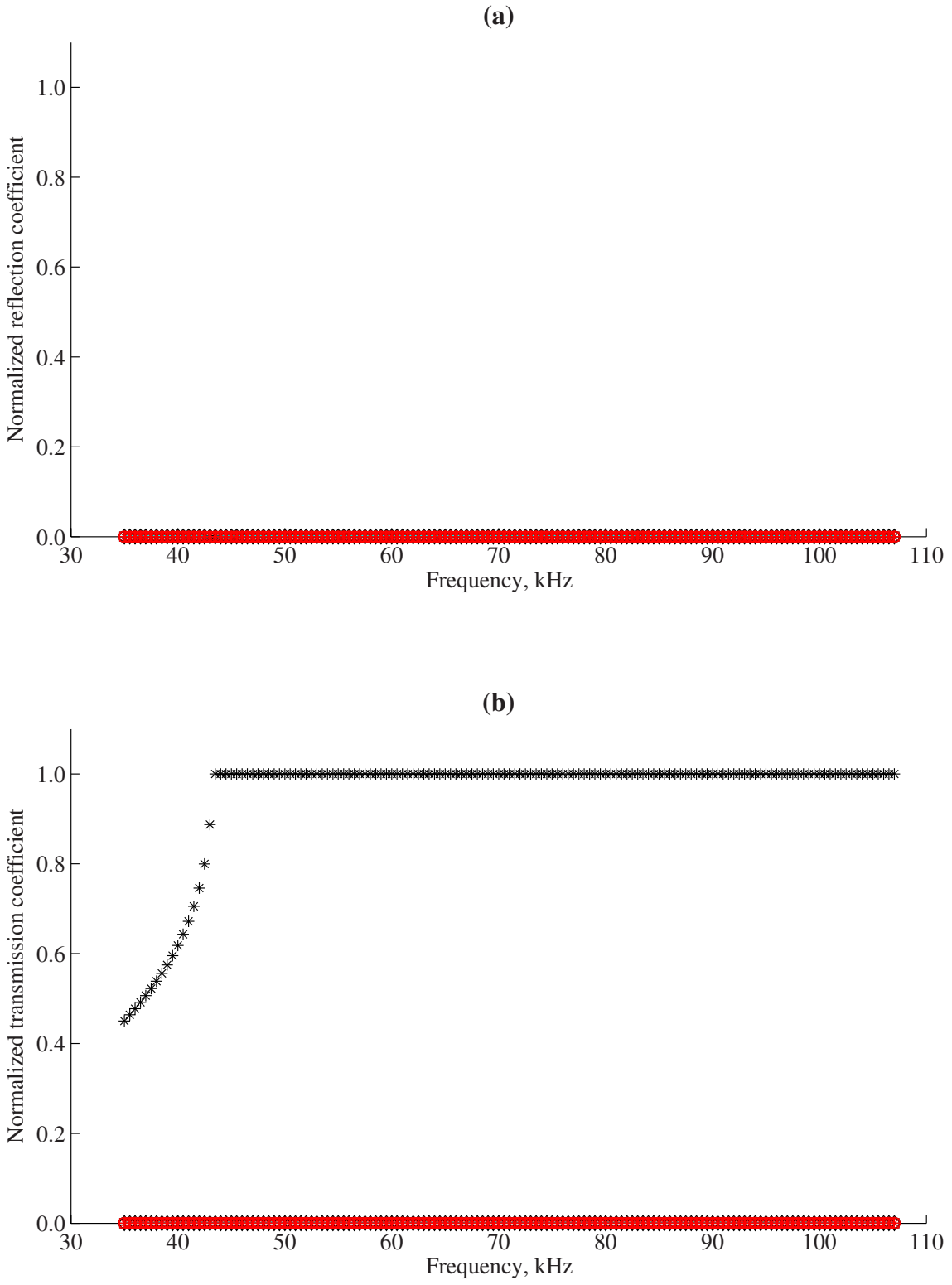

Figure H.53. Normalized reflection and transmission coefficients for the three-dimensional transparency check and the incident F(8,1) mode.

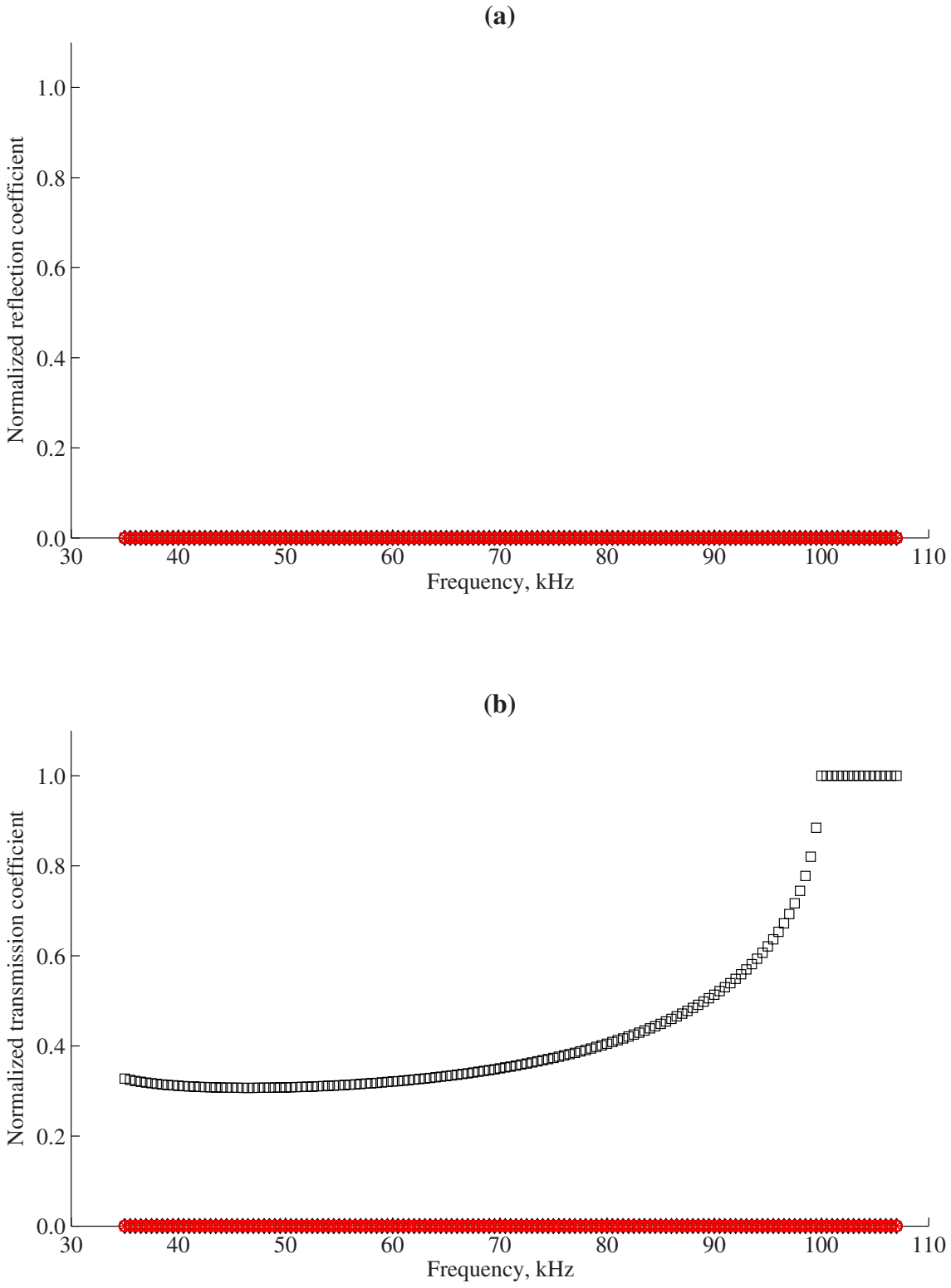

Figure H.54. Normalized reflection and transmission coefficients for the three-dimensional transparency check and the incident F(8,2) mode.

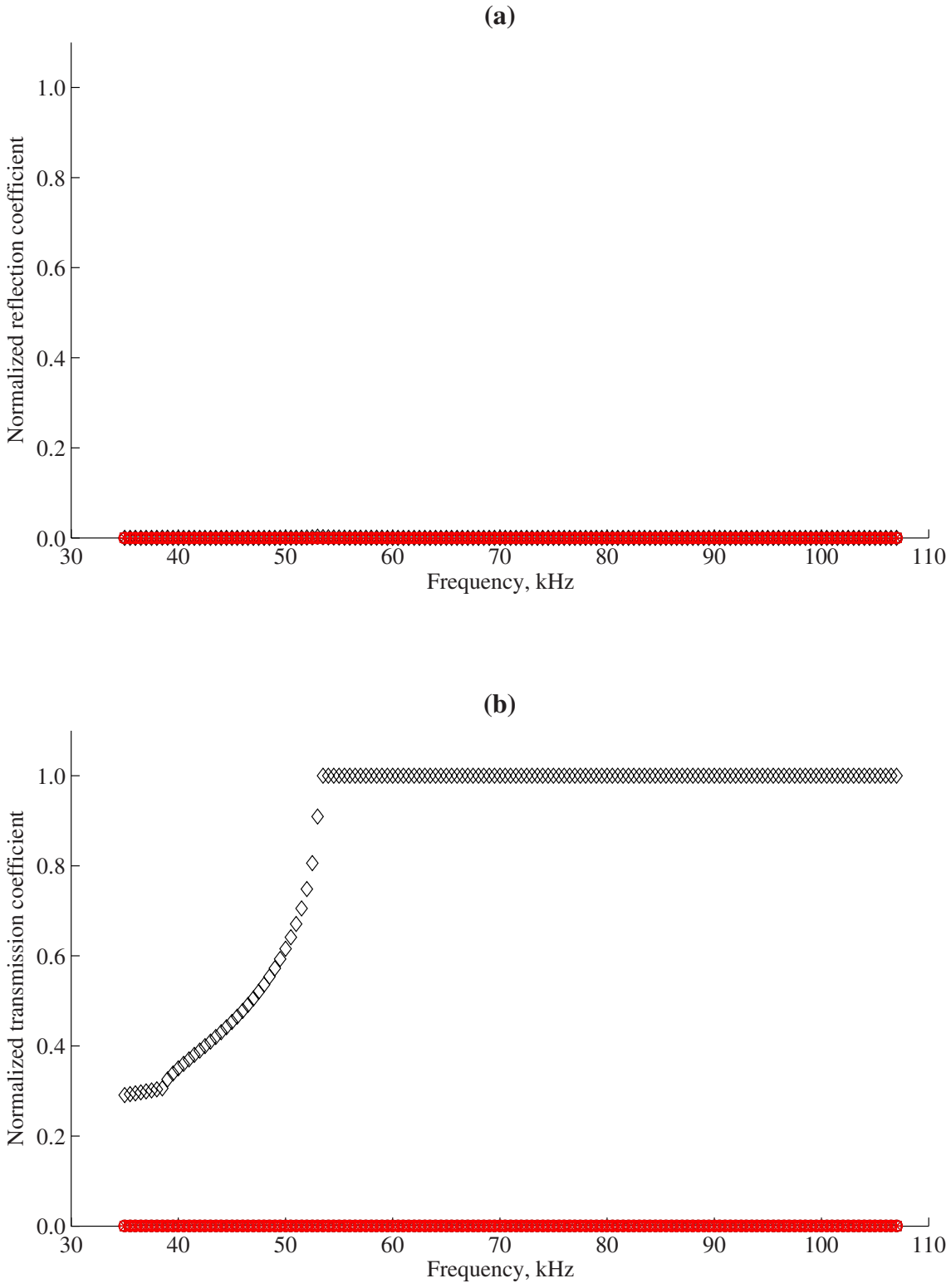

Figure H.55. Normalized reflection and transmission coefficients for the three-dimensional transparency check and the incident F(9,1) mode.

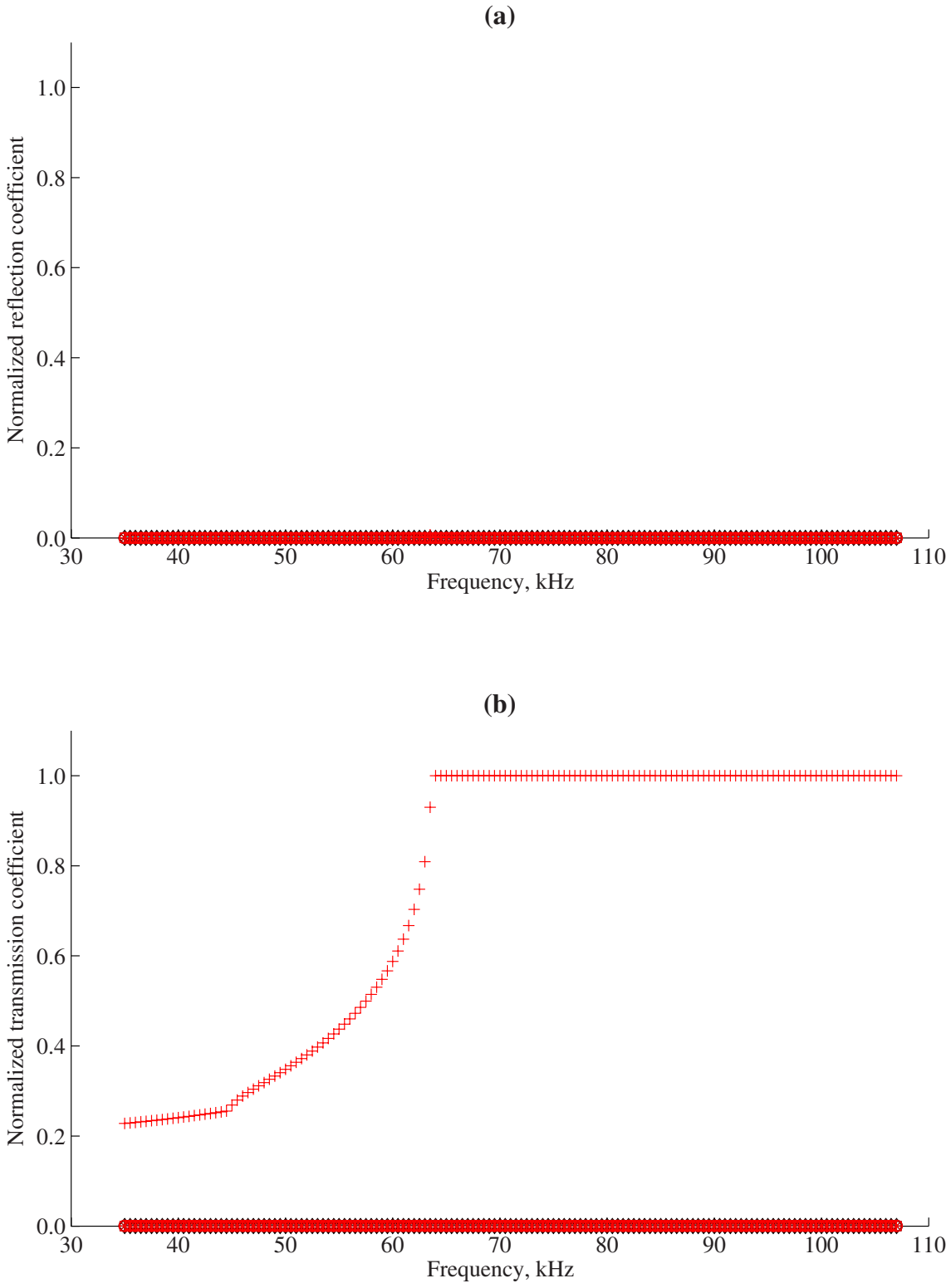

Figure H.56. Normalized reflection and transmission coefficients for the three-dimensional transparency check and the incident F(10,1) mode.

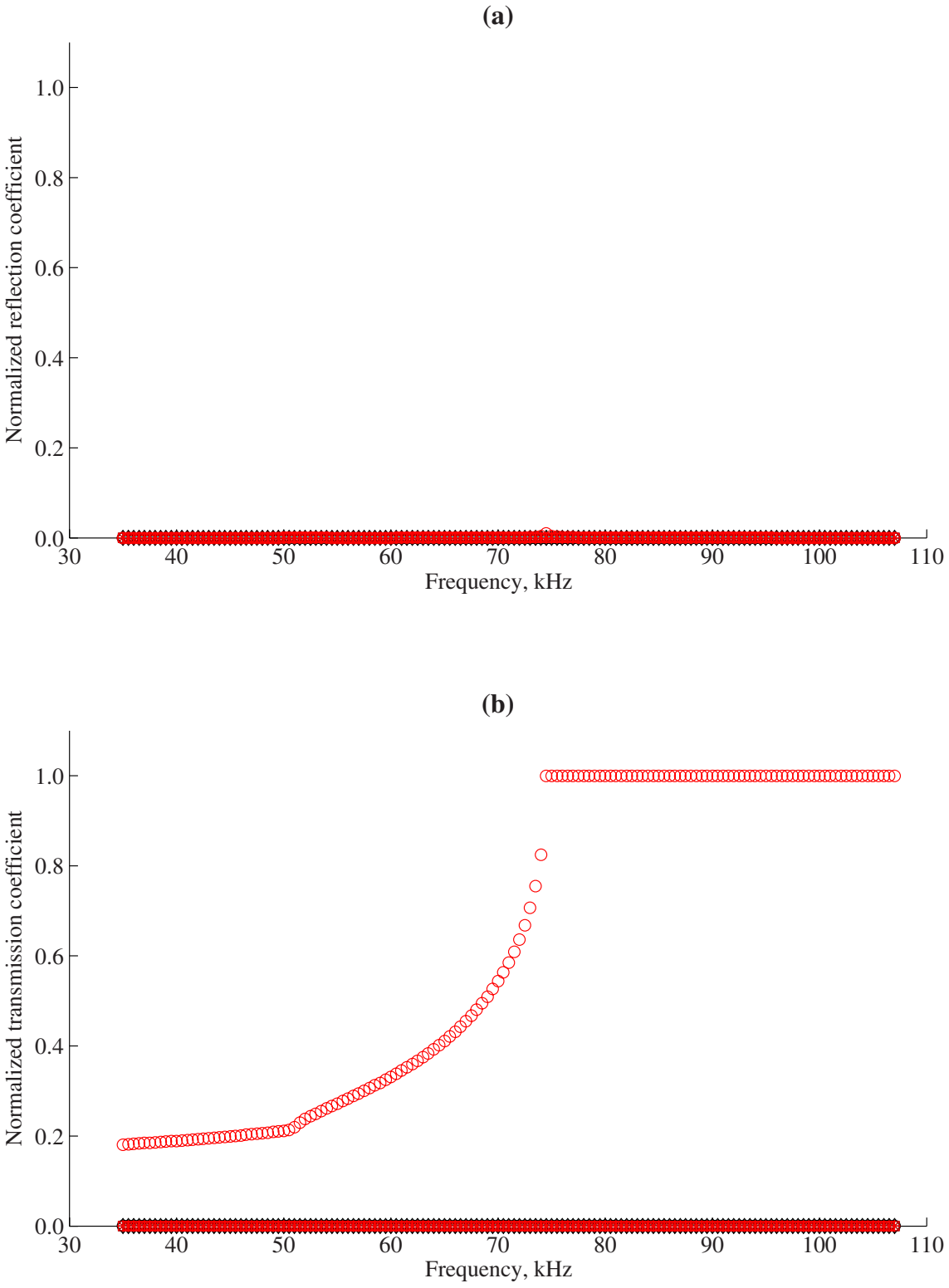

Figure H.57. Normalized reflection and transmission coefficients for the three-dimensional transparency check and the incident F(11,1) mode.

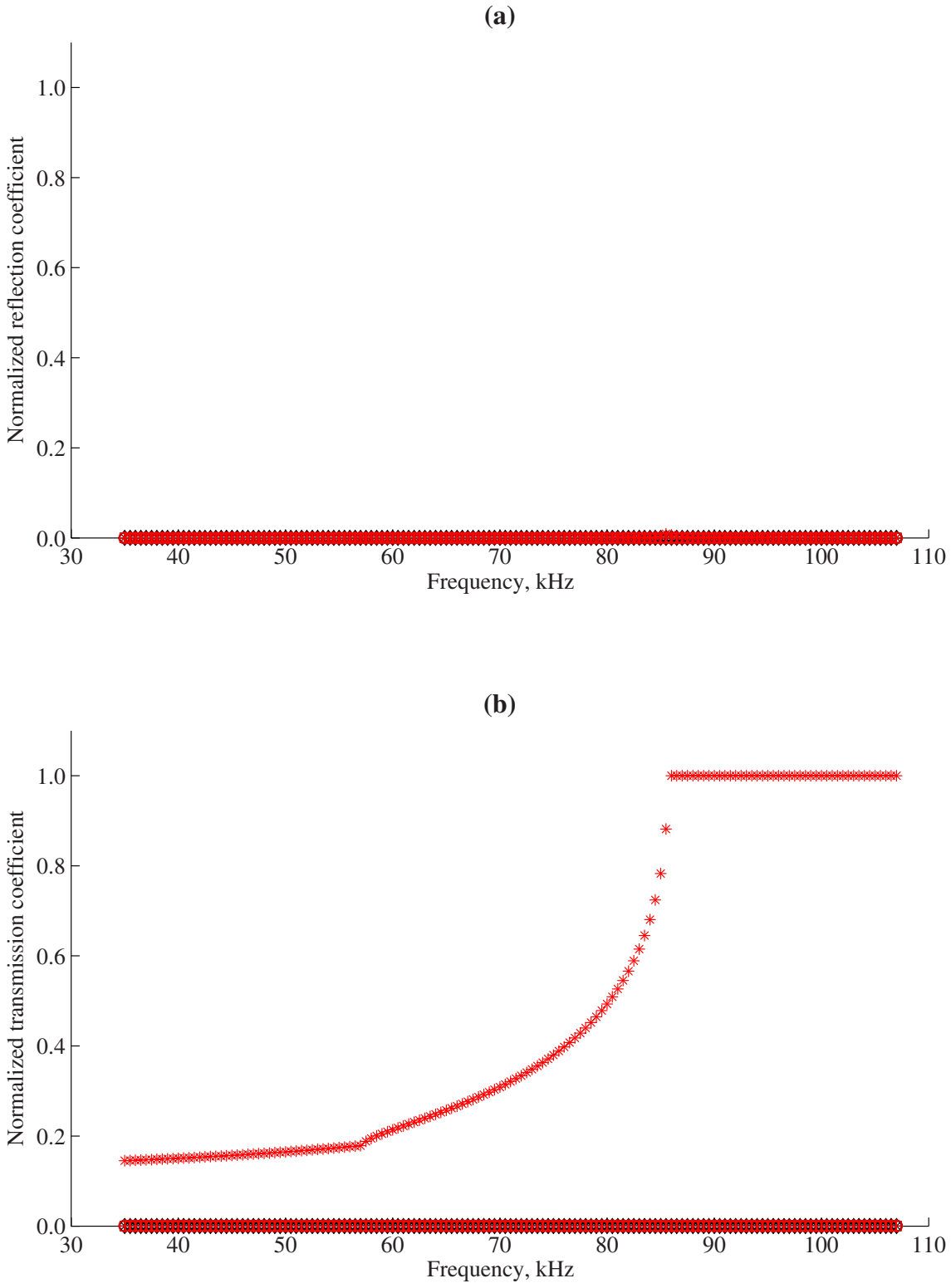

Figure H.58. Normalized reflection and transmission coefficients for the three-dimensional transparency check and the incident F(12,1) mode.

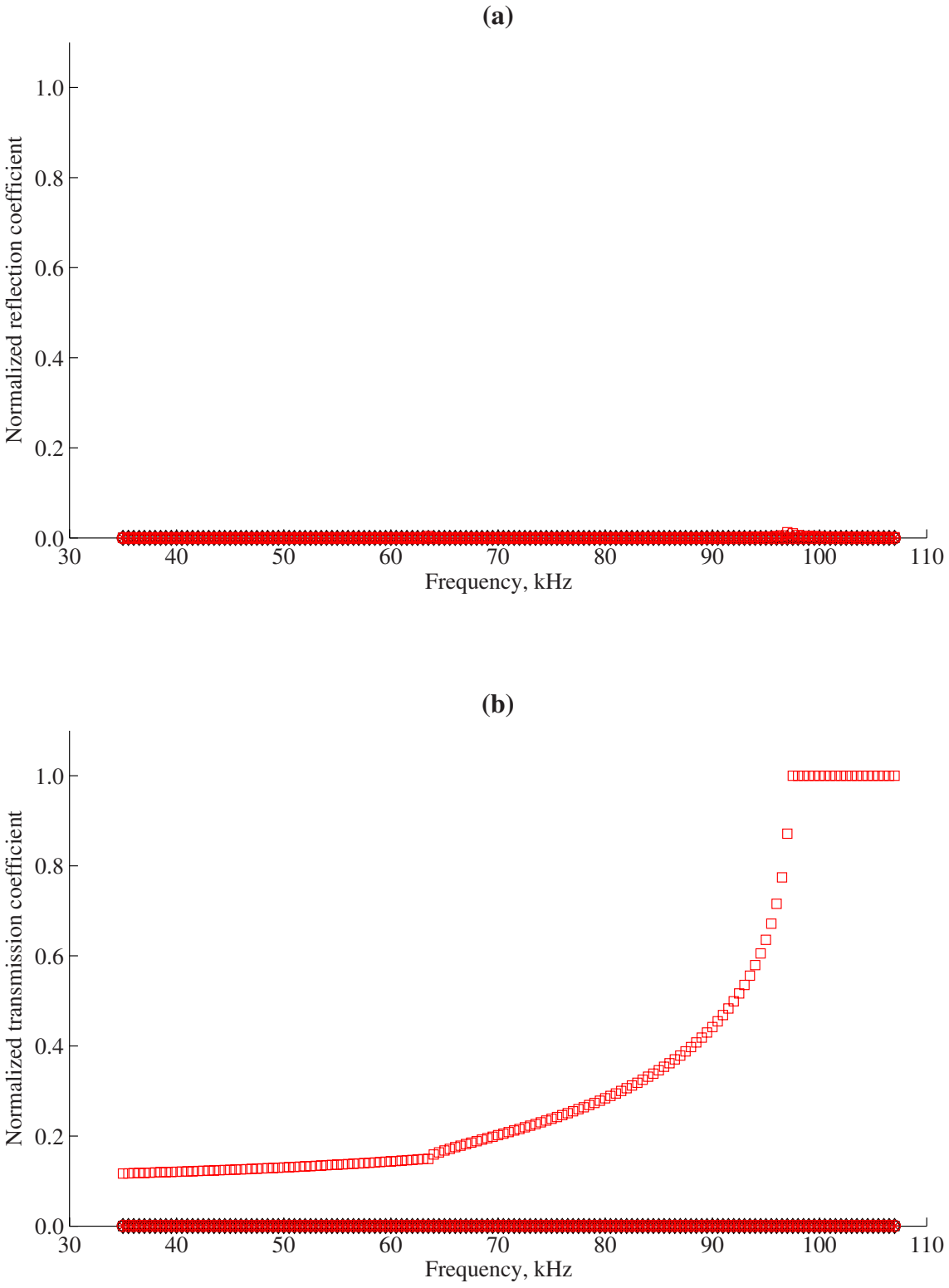

Figure H.59. Normalized reflection and transmission coefficients for the three-dimensional transparency check and the incident F(13,1) mode.

APPENDIX I

REFLECTION AND TRANSMISSION COEFFICIENTS

I.1 Summary

This appendix gives the magnitudes of the normalized reflection and transmission coefficients for selected modes incident on and scattered by the finite element region. The notches are described in Tables 4.1 and 4.5. Modes selected for inclusion have a non-negative circumferential wavenumber and propagate over at least part of the excitation's bandwidth. This selection is compatible with Appendix H. The line and markers used in Figures I.2 through I.59 to denote the various modal reflection and transmission coefficients are indicated in Figure I.1. This last figure duplicates Figure H.1 for convenience. Each incident mode is indicated in a figure's caption.

Figures I.2 through I.4 are interesting in that, as expected, they indicate that no modal conversions between the longitudinal and torsional modes occur for axisymmetric notches. Figures I.4, I.7, I.33, and I.36 show that the F(1,3) mode is reflected less strongly than the L(0,2) mode for each of the two notches considered. This observation supports, in part, the conjecture made in Section 4.3.7.2.

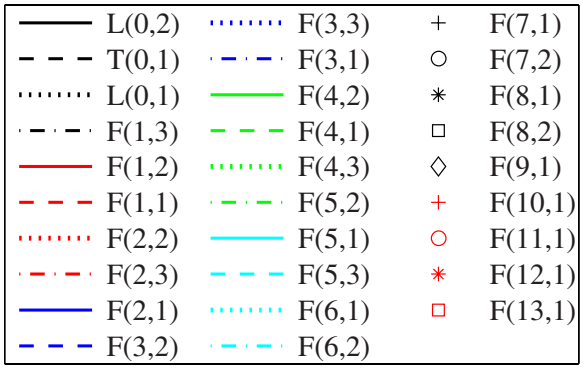

Figure I.1. Legend indicating mode line and marker styles.

I.2 Reflection and Transmission Coefficients for Axisymmetric Notch

Magnitudes of the normalized reflection and transmission coefficients are given in Figures I.2 through I.30 for selected modes incident on and scattered by the axisymmetric notch considered in Section 4.2.8.2. The summary presented in Section I.1 is applicable still.

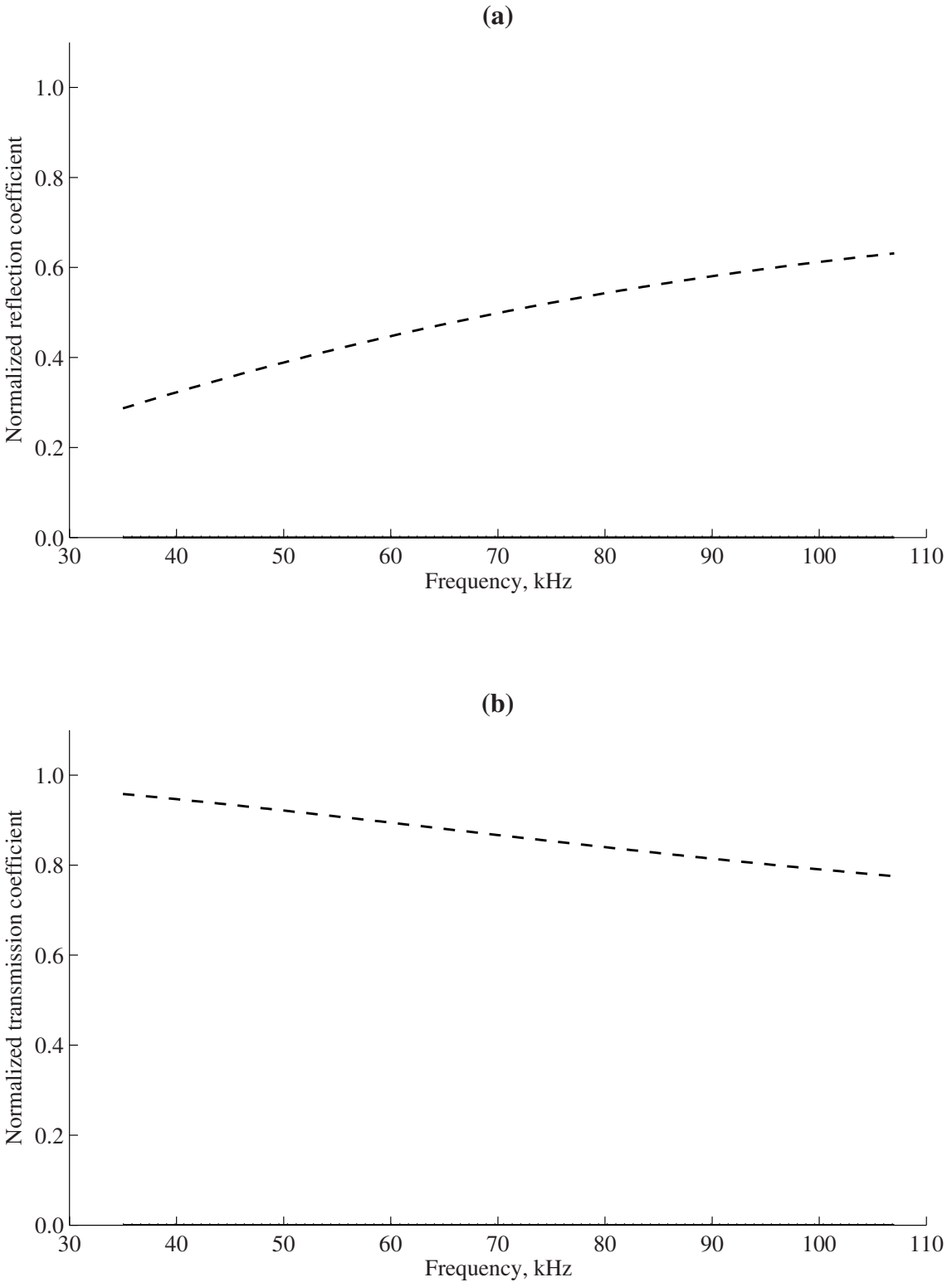

Figure I.2. Normalized reflection and transmission coefficients for the axisymmetric notch and the incident T(0,1) mode.

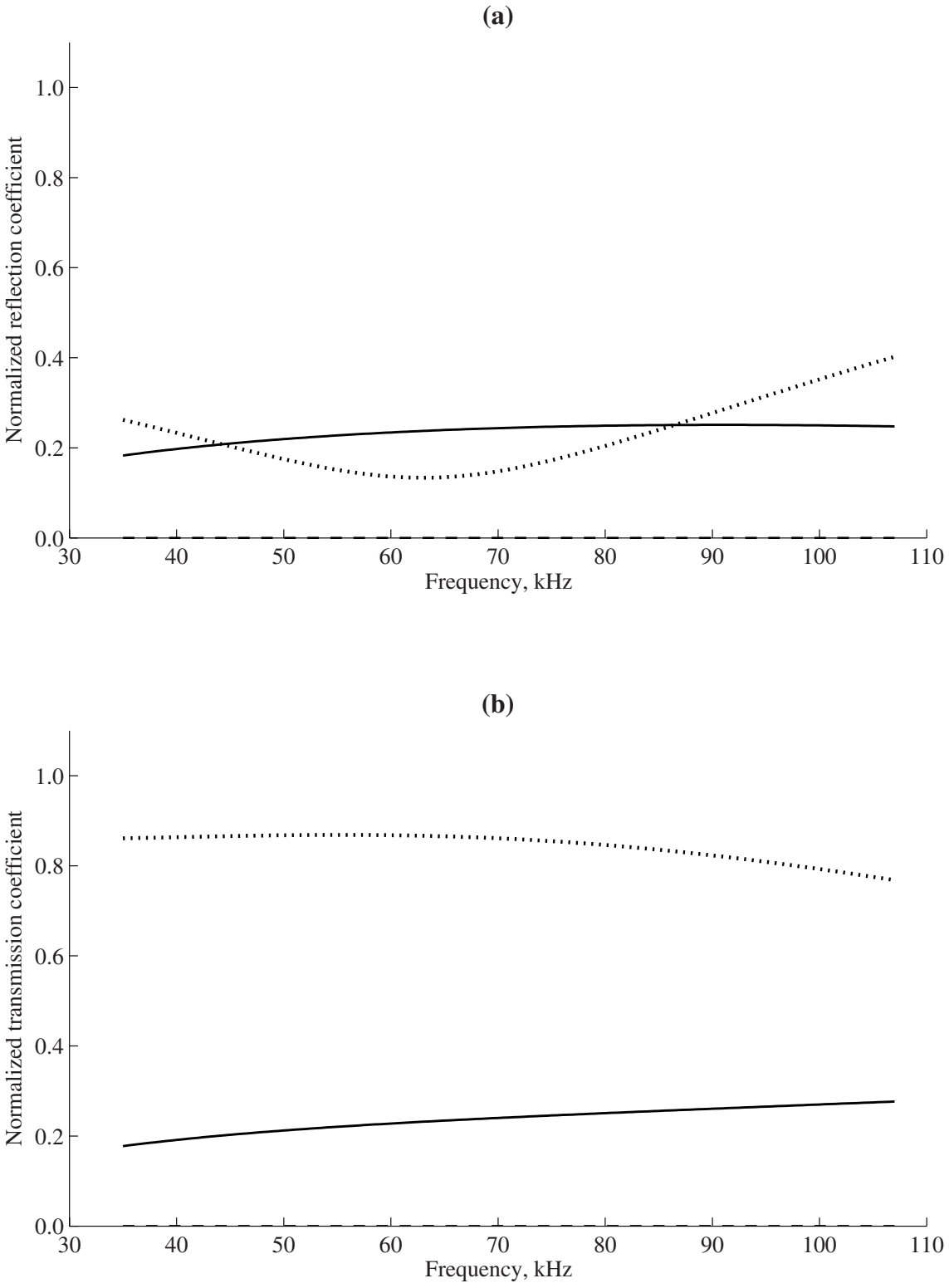

Figure I.3. Normalized reflection and transmission coefficients for the axisymmetric notch and the incident L(0,1) mode.

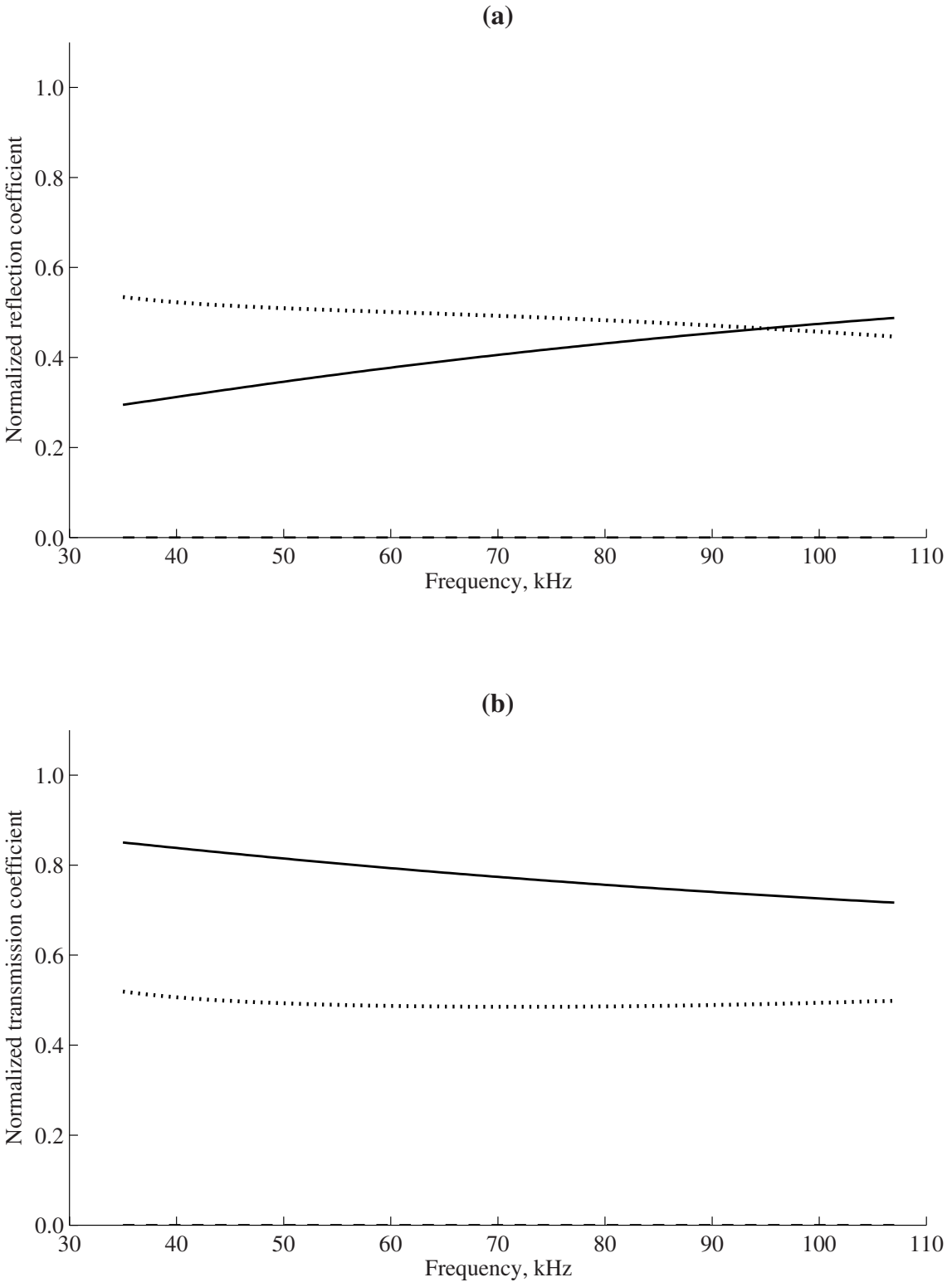

Figure I.4. Normalized reflection and transmission coefficients for the axisymmetric notch and the incident L(0,2) mode.

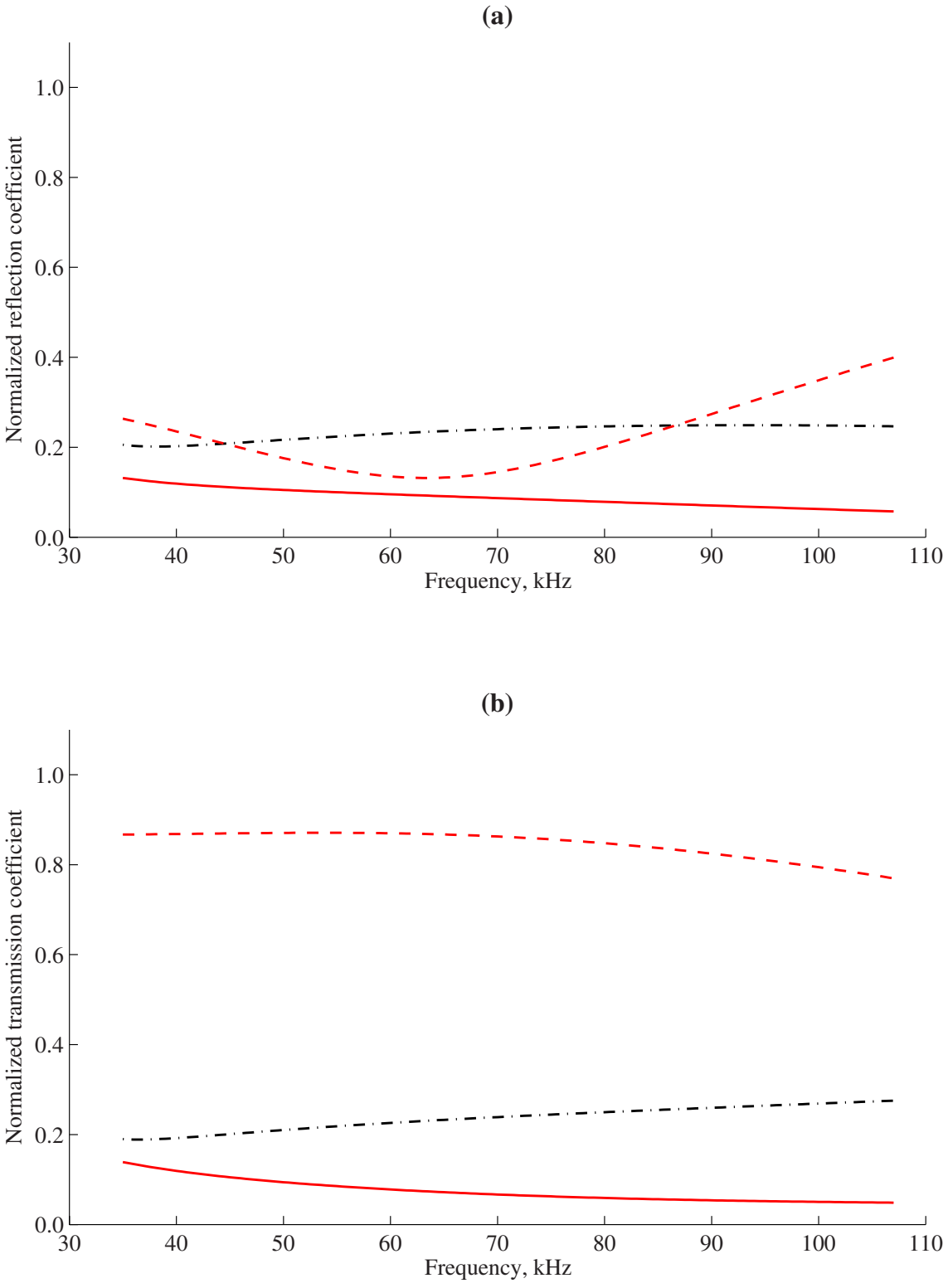

Figure I.5. Normalized reflection and transmission coefficients for the axisymmetric notch and the incident F(1,1) mode.

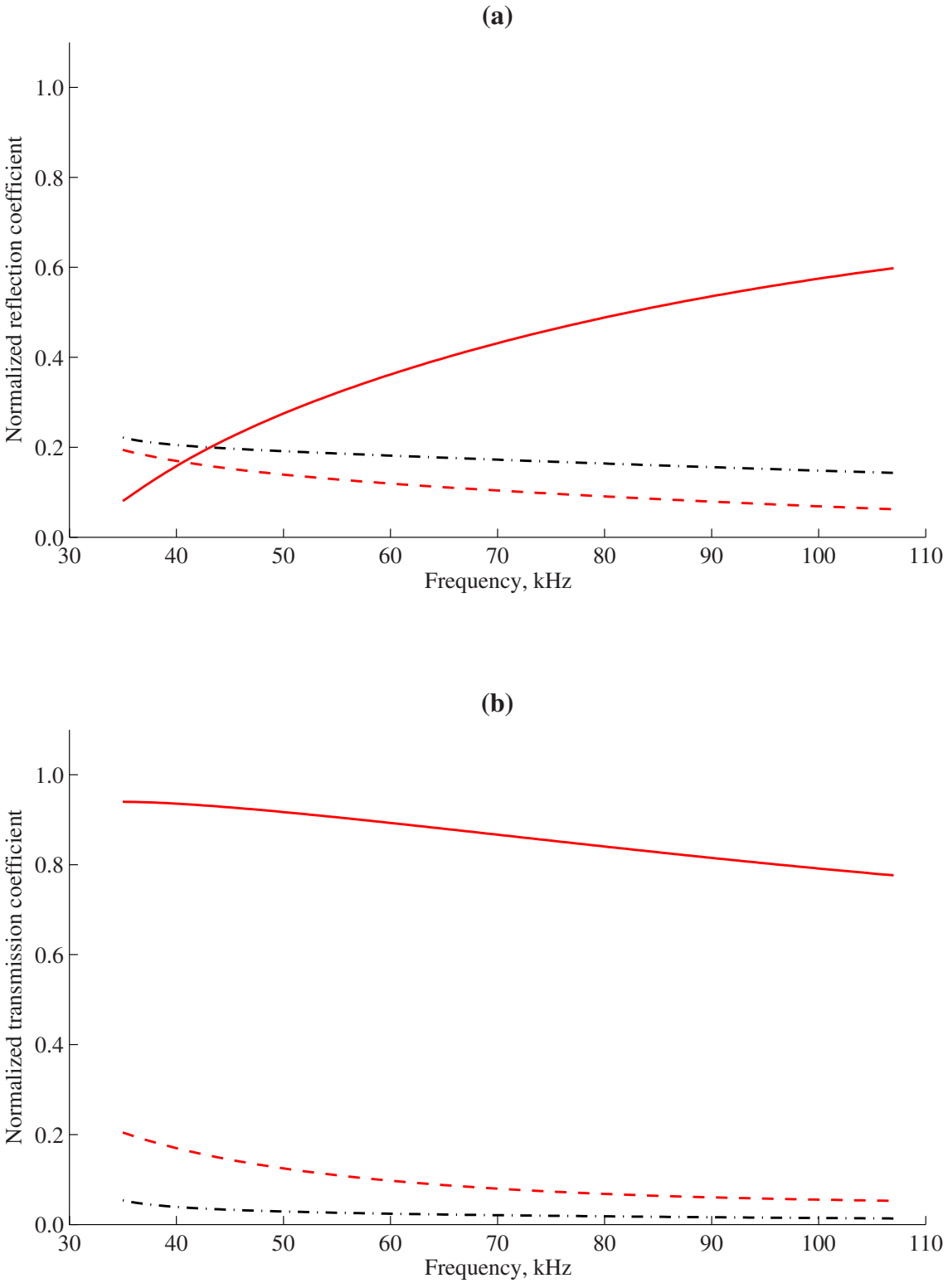

Figure I.6. Normalized reflection and transmission coefficients for the axisymmetric notch and the incident F(1,2) mode.

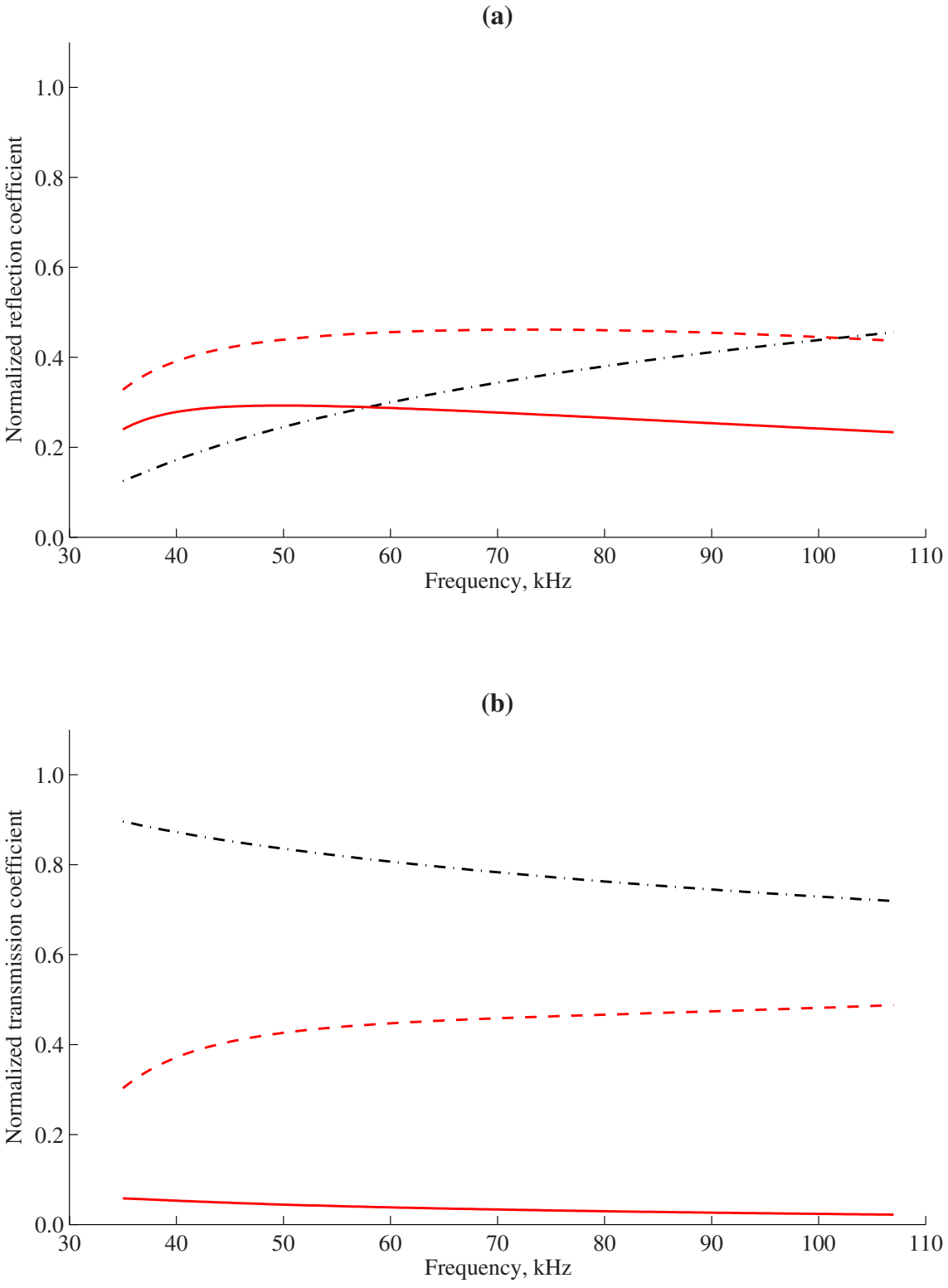

Figure I.7. Normalized reflection and transmission coefficients for the axisymmetric notch and the incident F(1,3) mode.

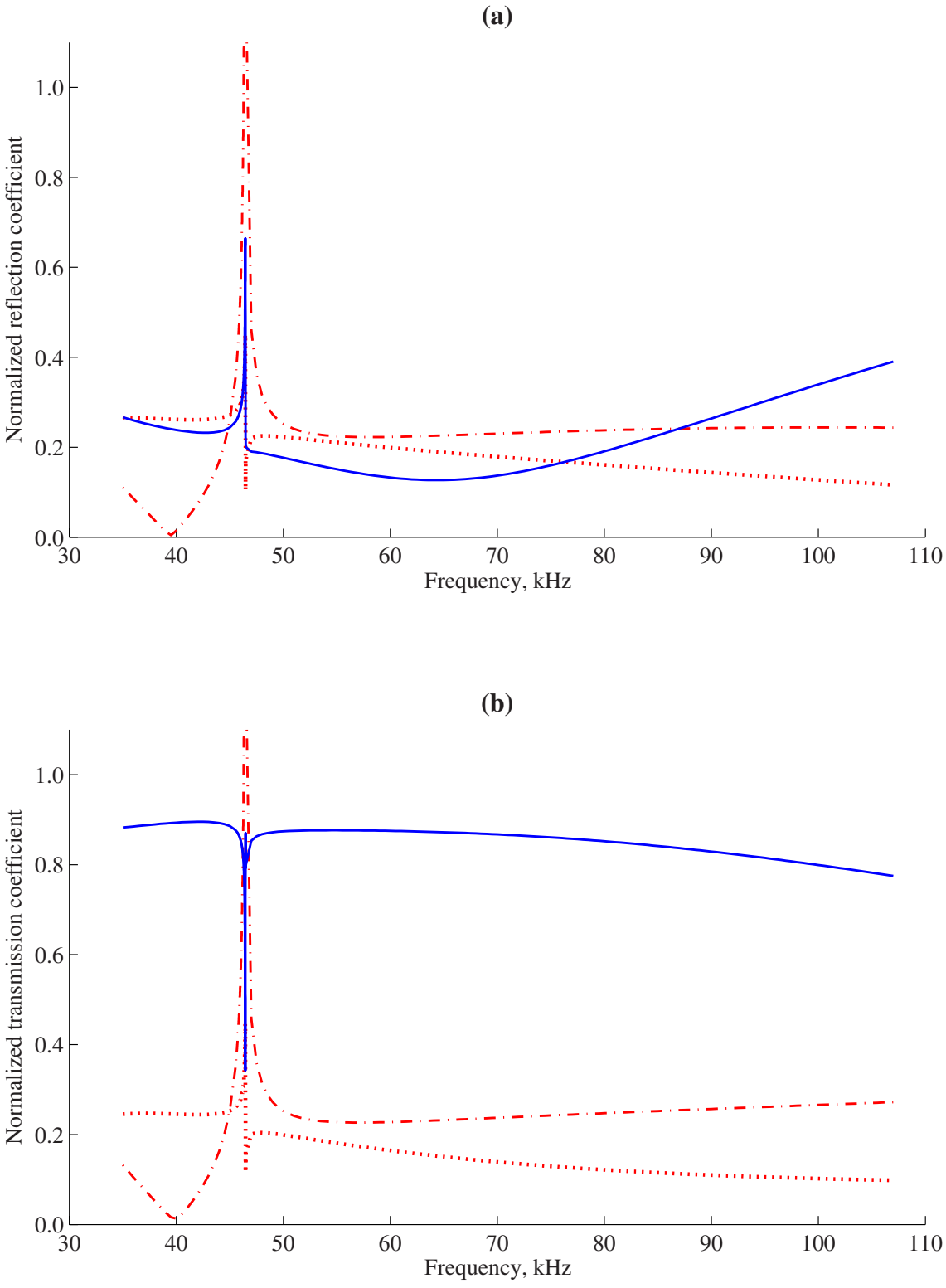

Figure I.8. Normalized reflection and transmission coefficients for the axisymmetric notch and the incident F(2,1) mode.

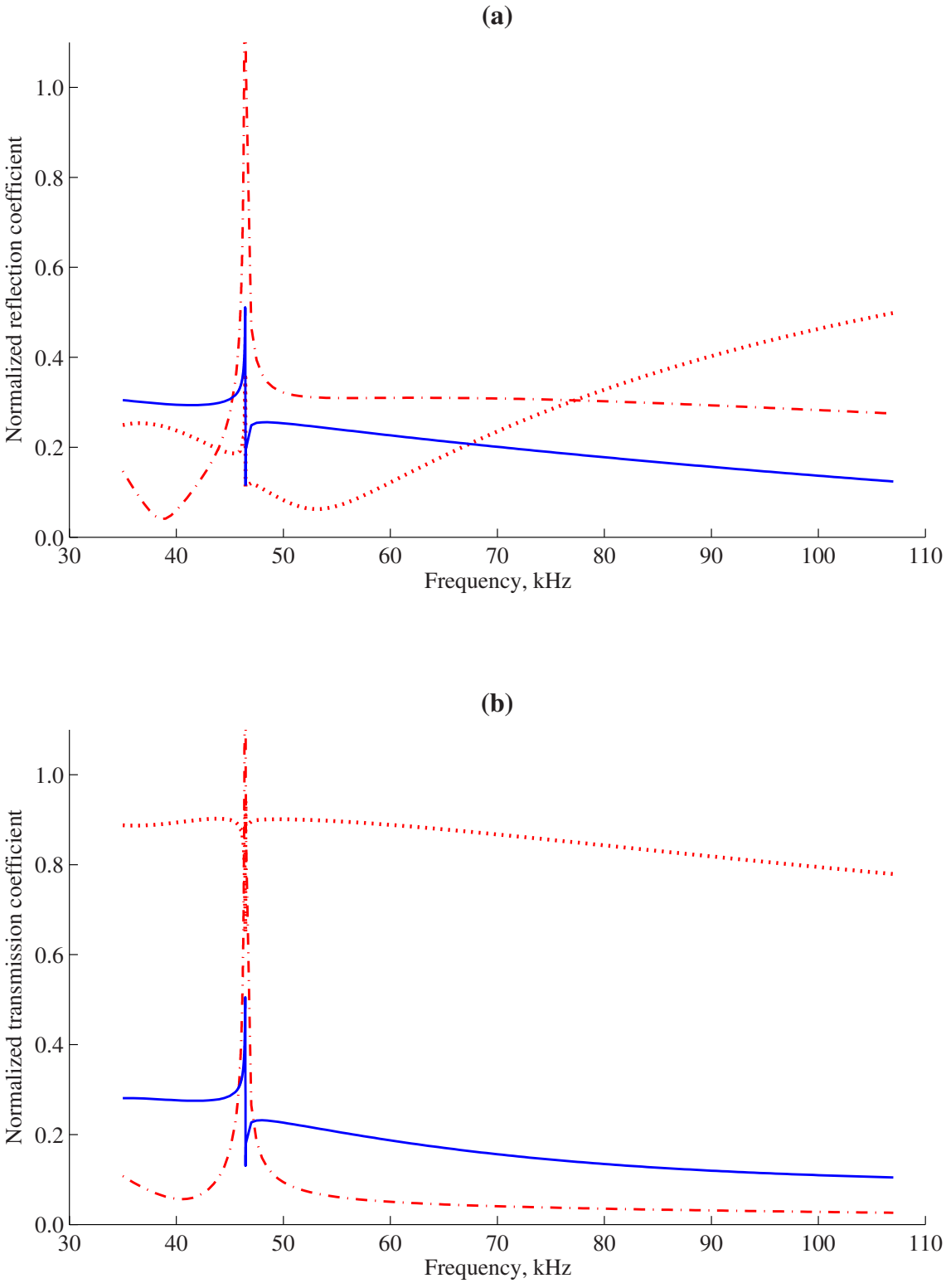

Figure I.9. Normalized reflection and transmission coefficients for the axisymmetric notch and the incident F(2,2) mode.

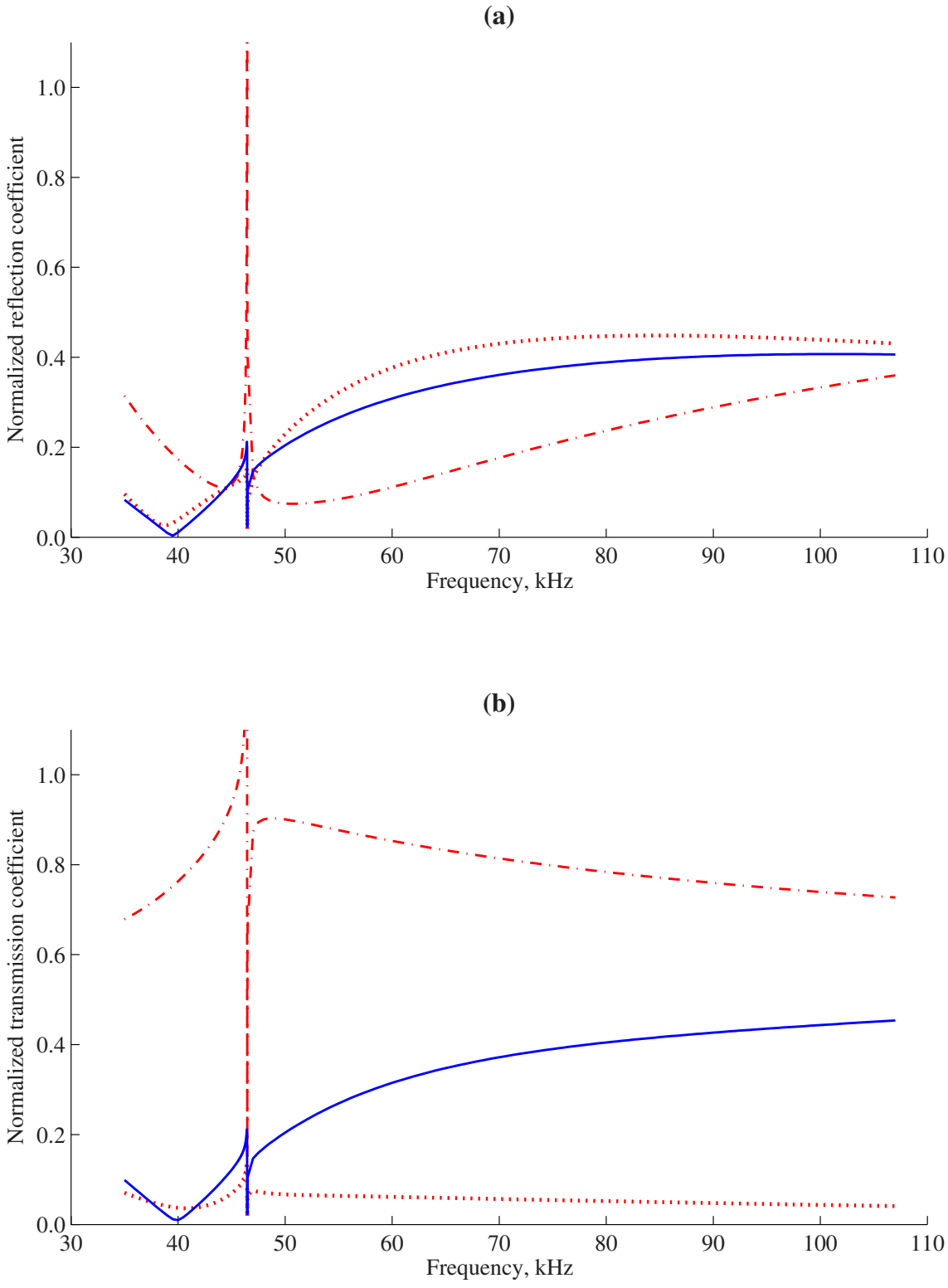

Figure I.10. Normalized reflection and transmission coefficients for the axisymmetric notch and the incident F(2,3) mode.

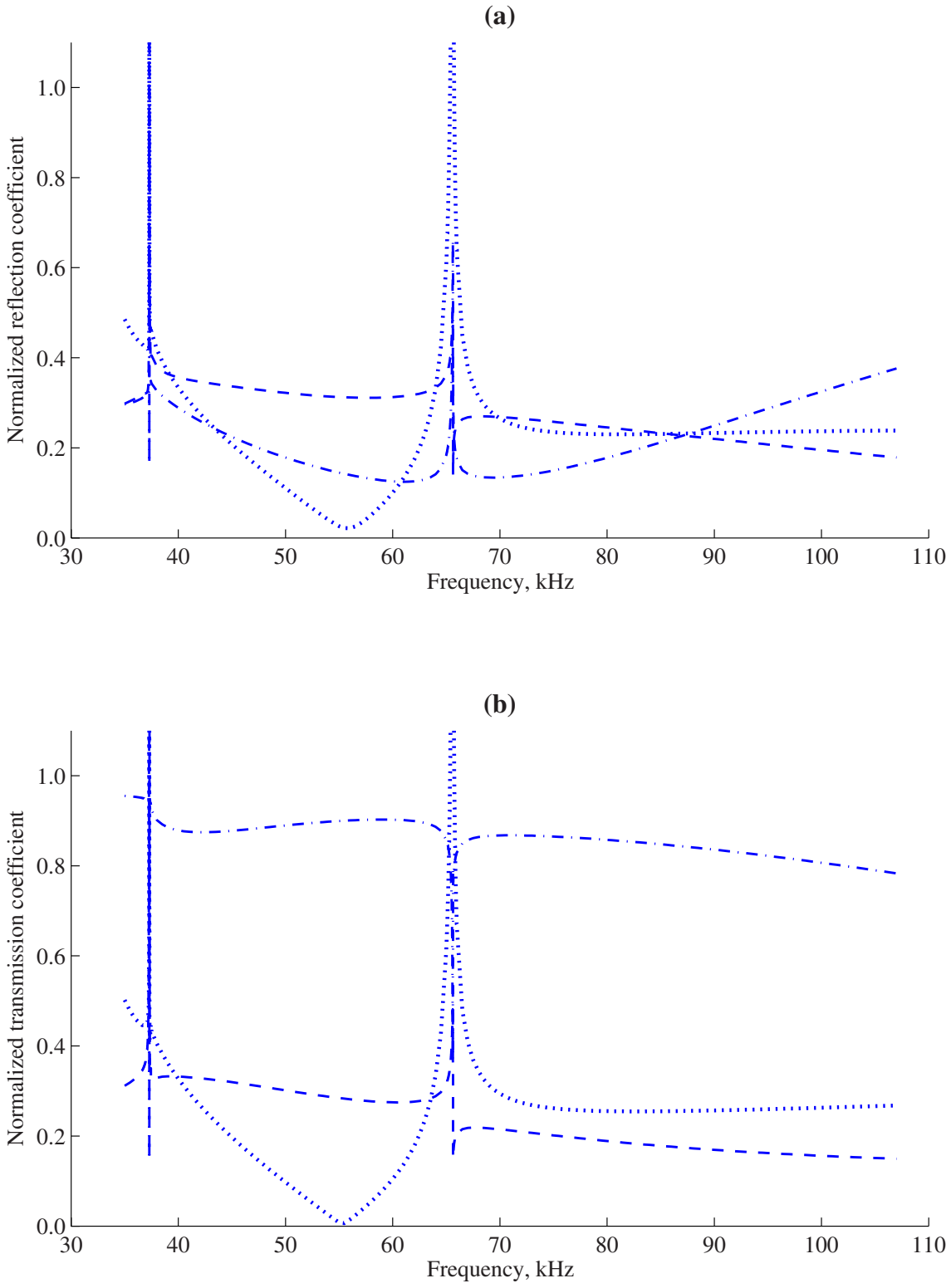

Figure I.11. Normalized reflection and transmission coefficients for the axisymmetric notch and the incident F(3,1) mode.

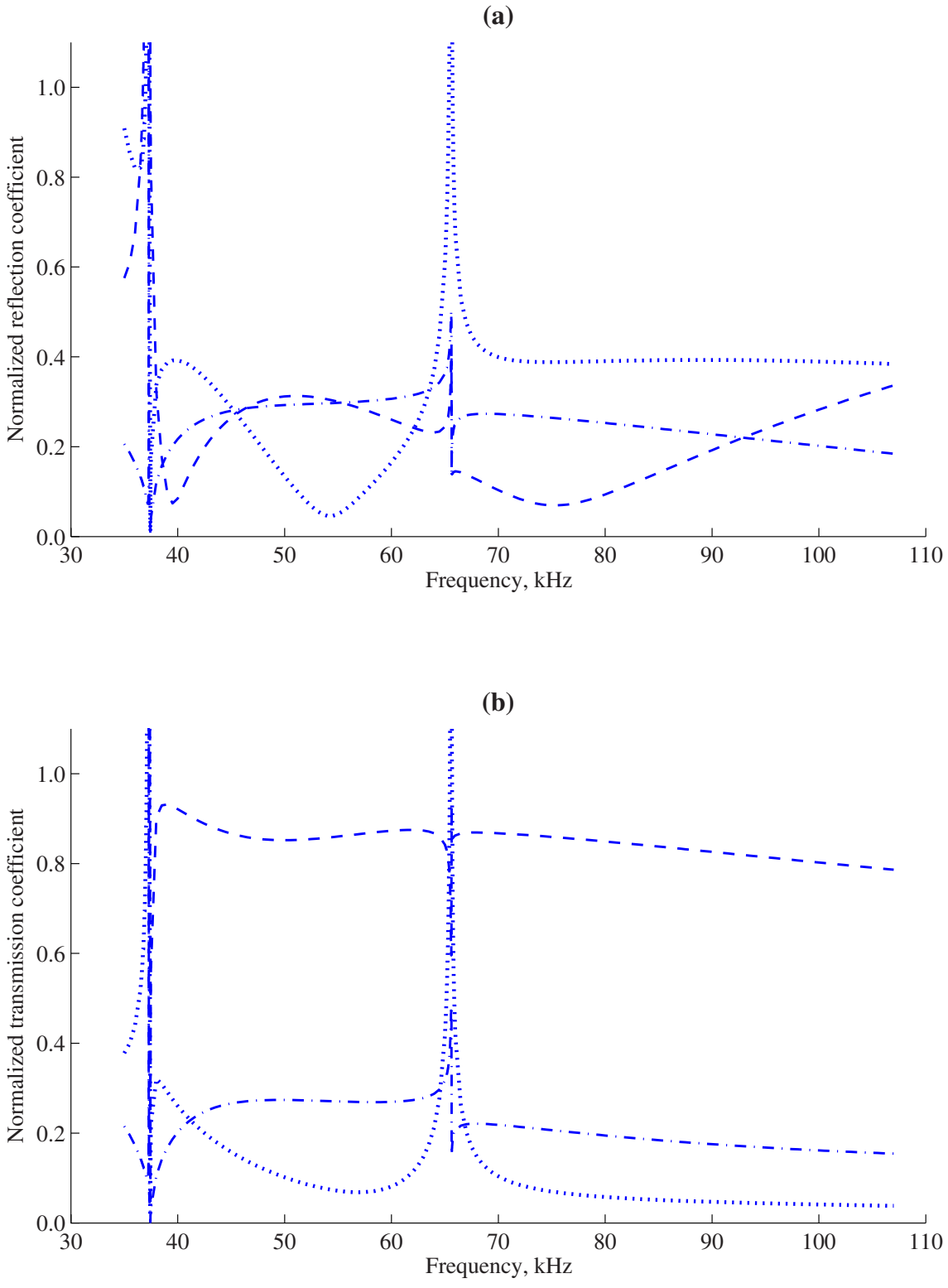

Figure I.12. Normalized reflection and transmission coefficients for the axisymmetric notch and the incident F(3,2) mode.

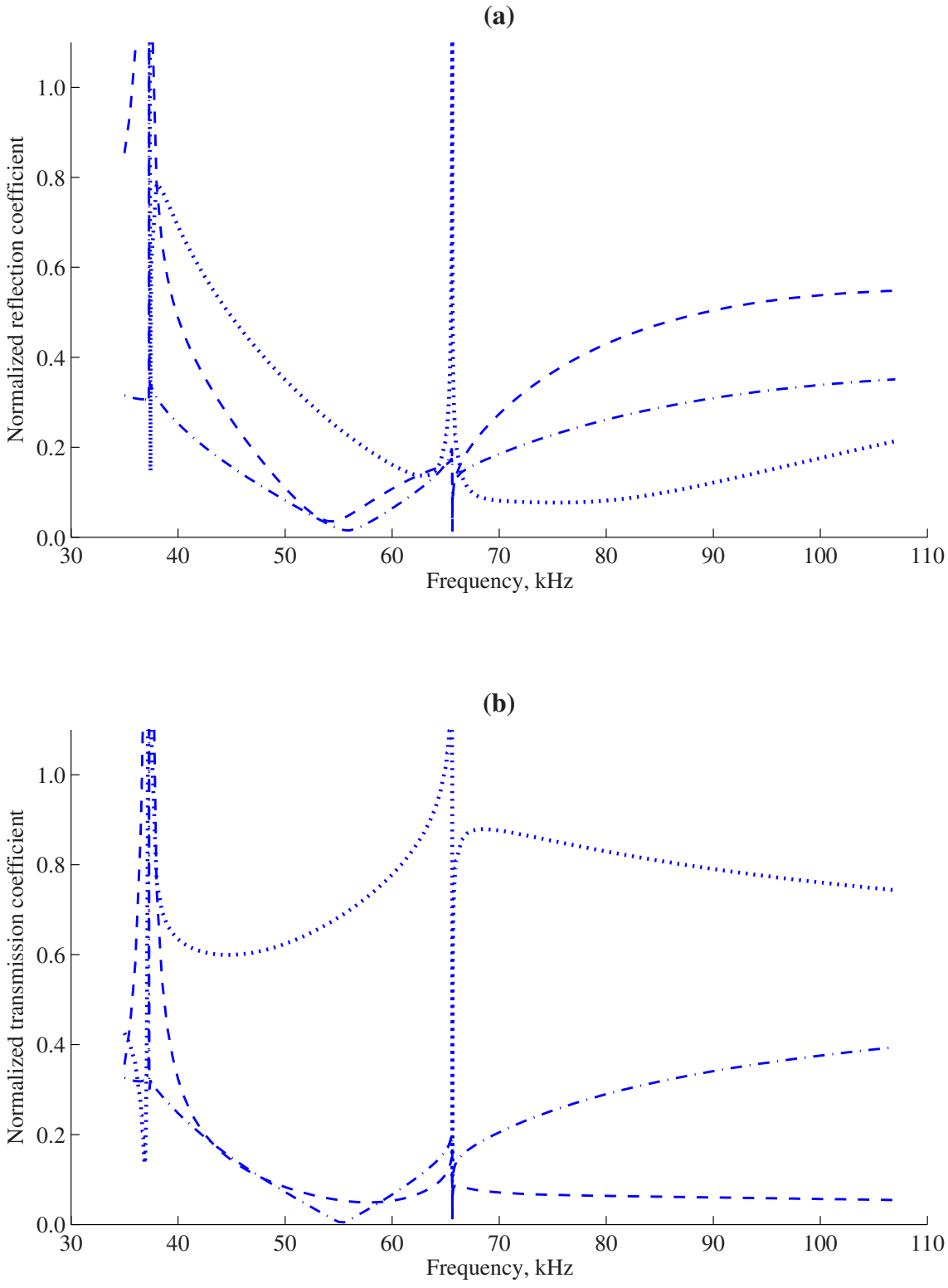

Figure I.13. Normalized reflection and transmission coefficients for the axisymmetric notch and the incident F(3,3) mode.

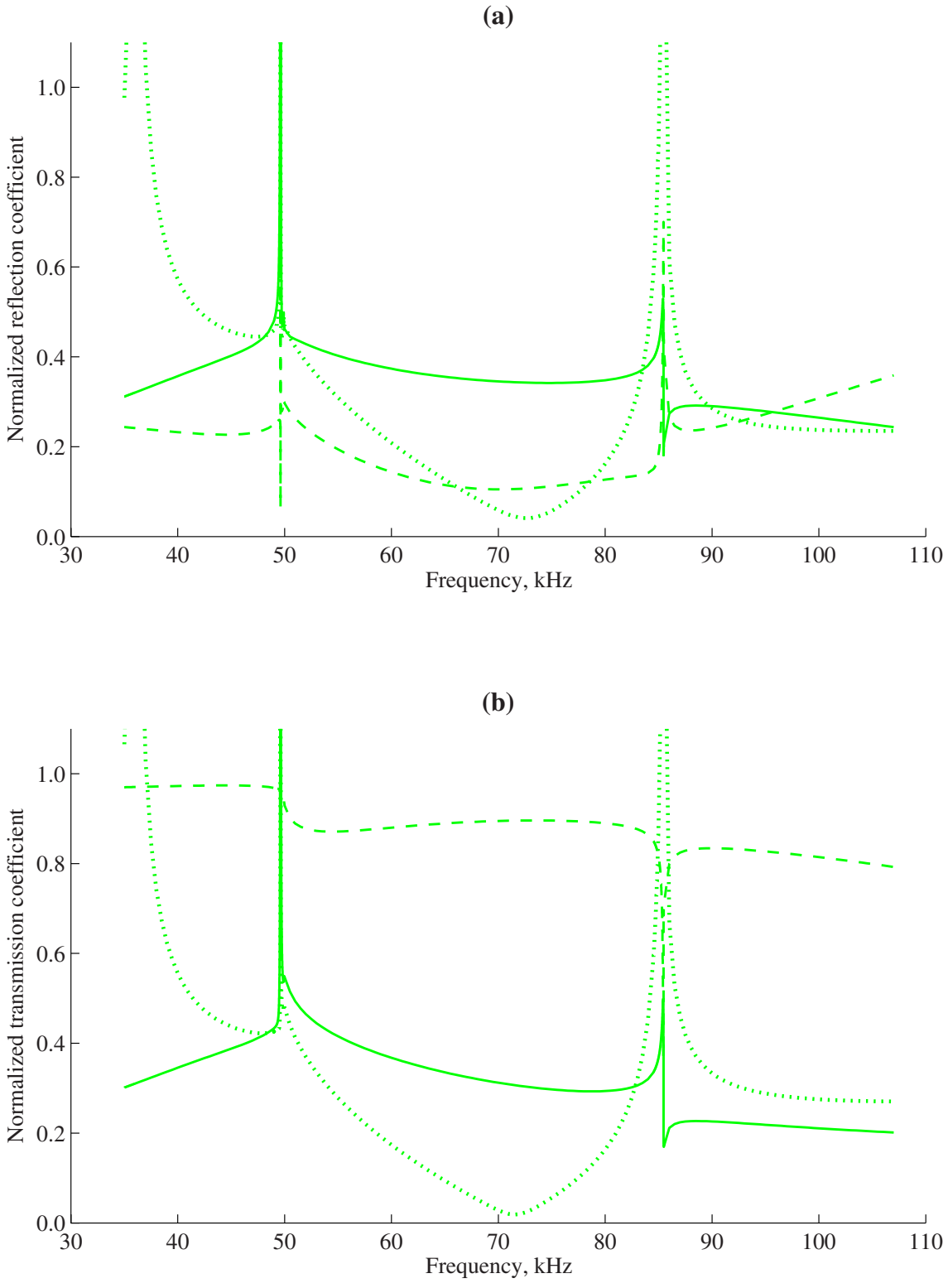

Figure I.14. Normalized reflection and transmission coefficients for the axisymmetric notch and the incident F(4,1) mode.

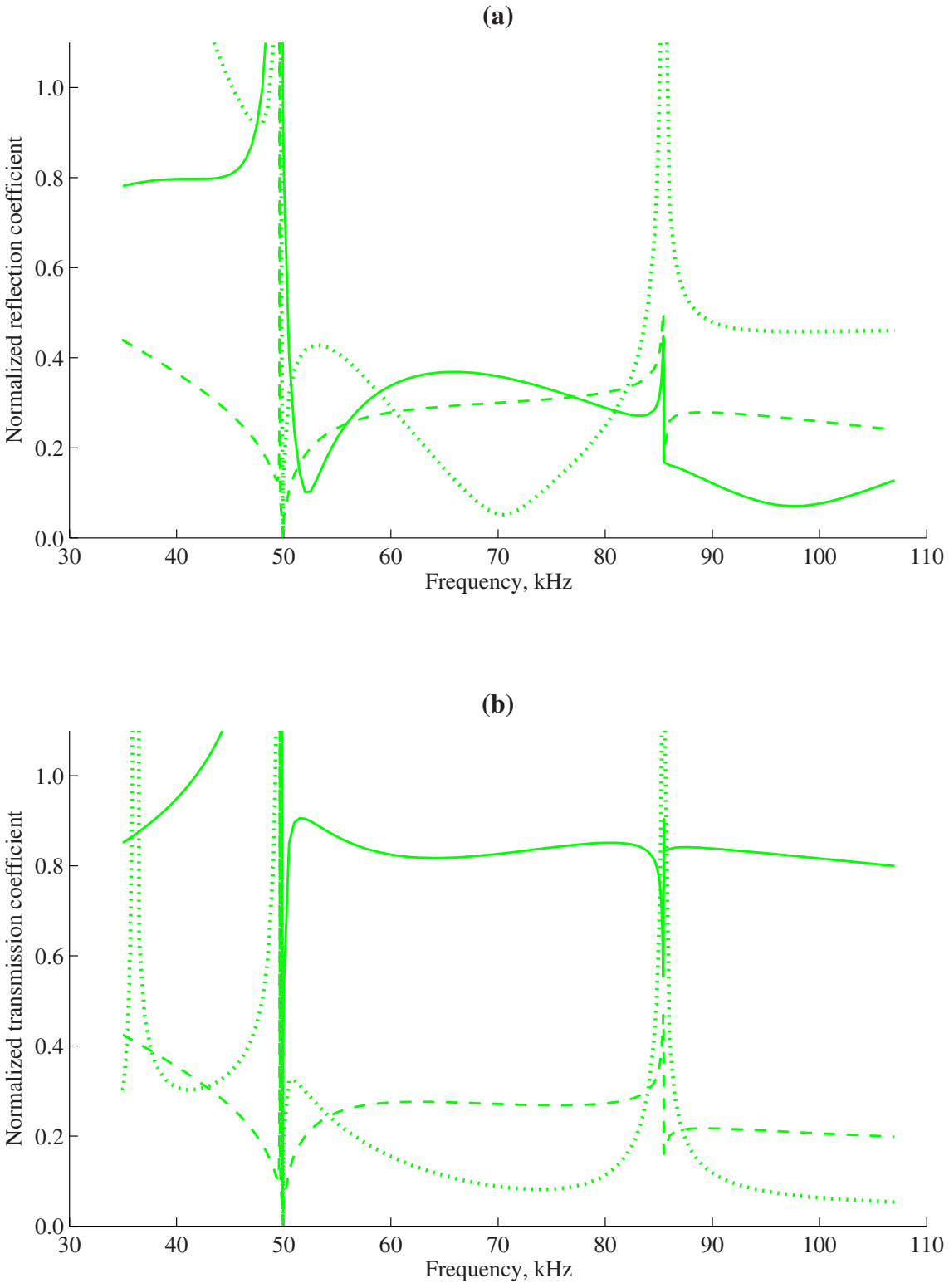

Figure I.15. Normalized reflection and transmission coefficients for the axisymmetric notch and the incident F(4,2) mode.

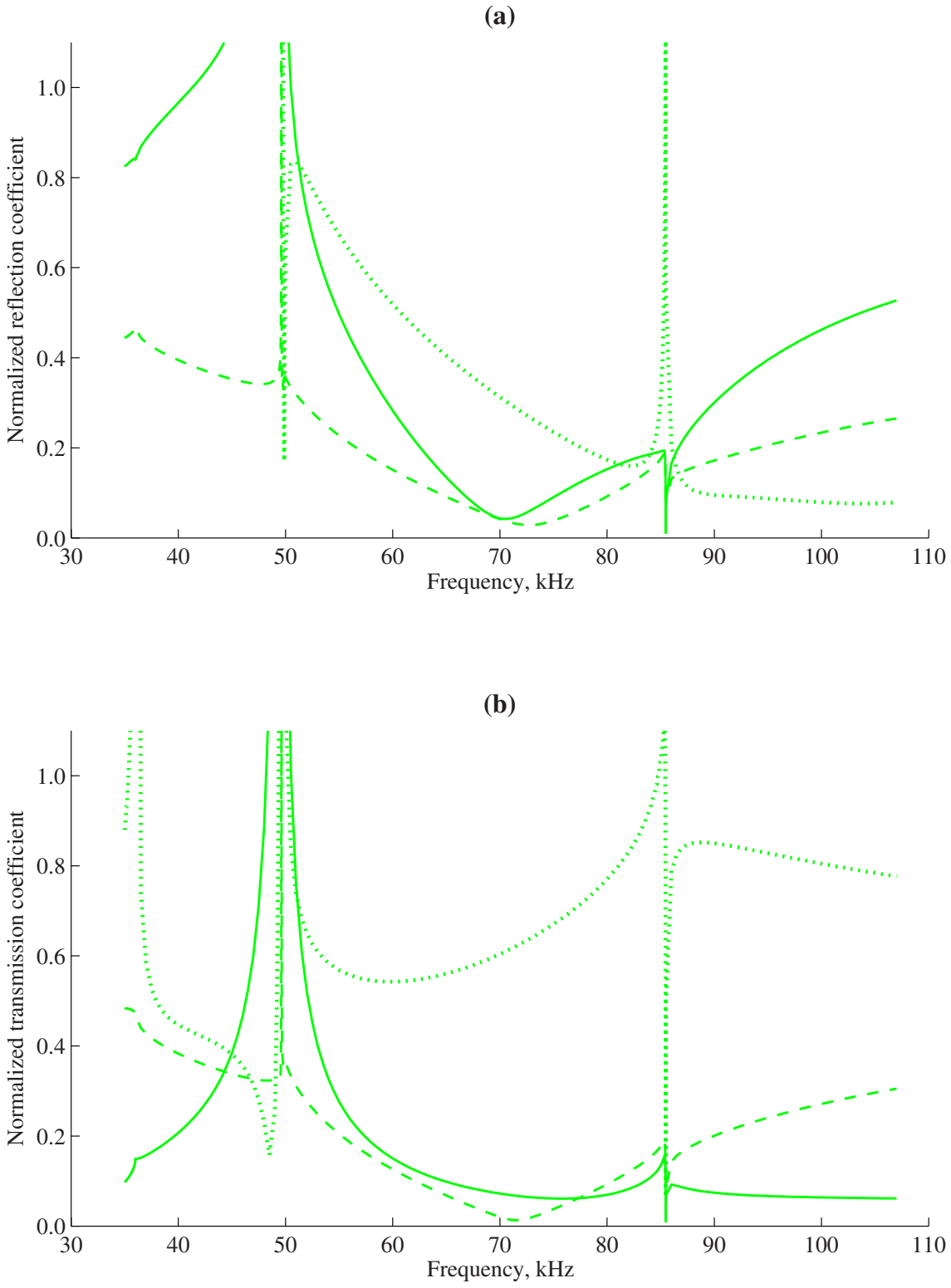

Figure I.16. Normalized reflection and transmission coefficients for the axisymmetric notch and the incident F(4,3) mode.

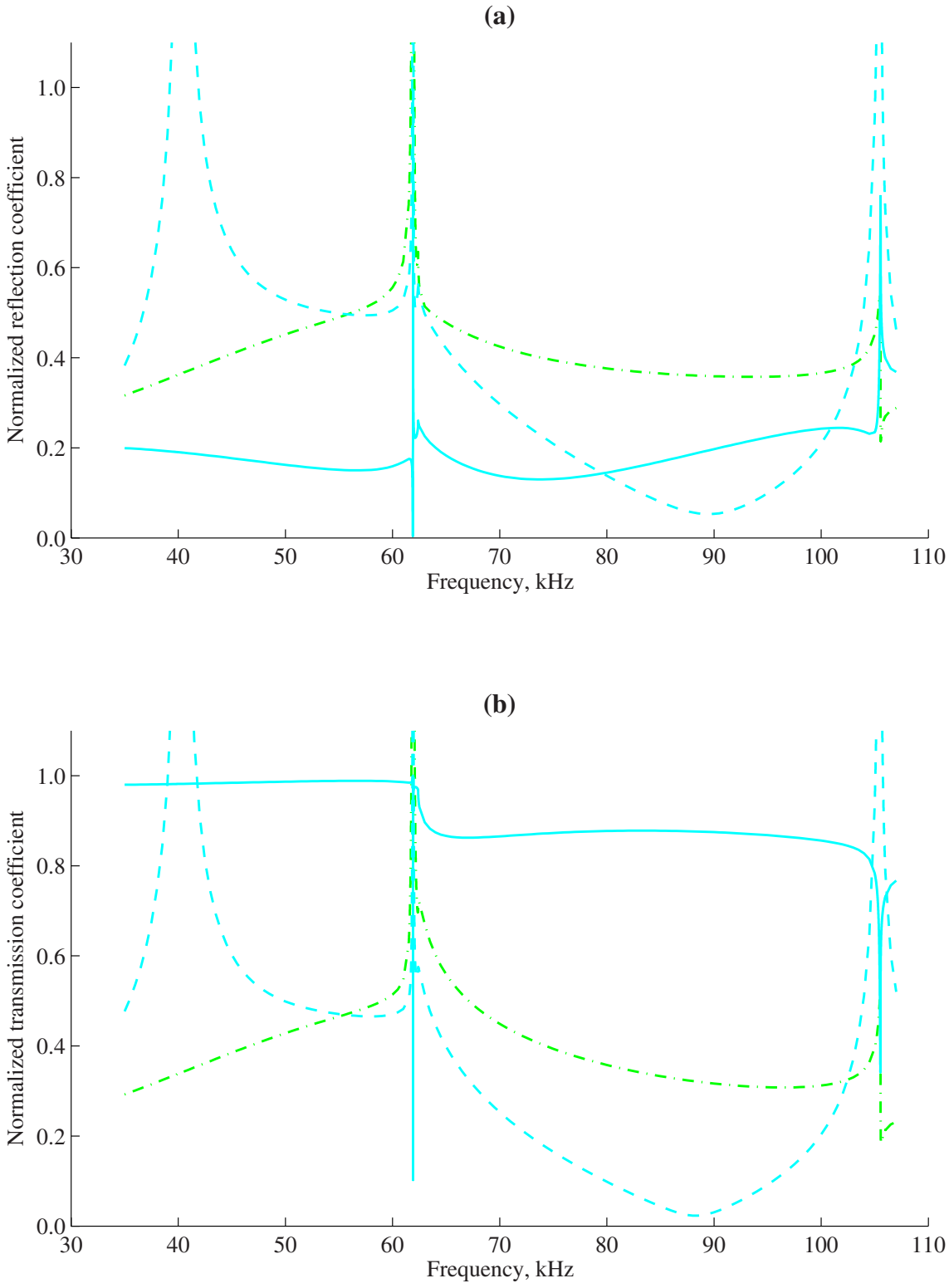

Figure I.17. Normalized reflection and transmission coefficients for the axisymmetric notch and the incident F(5,1) mode.

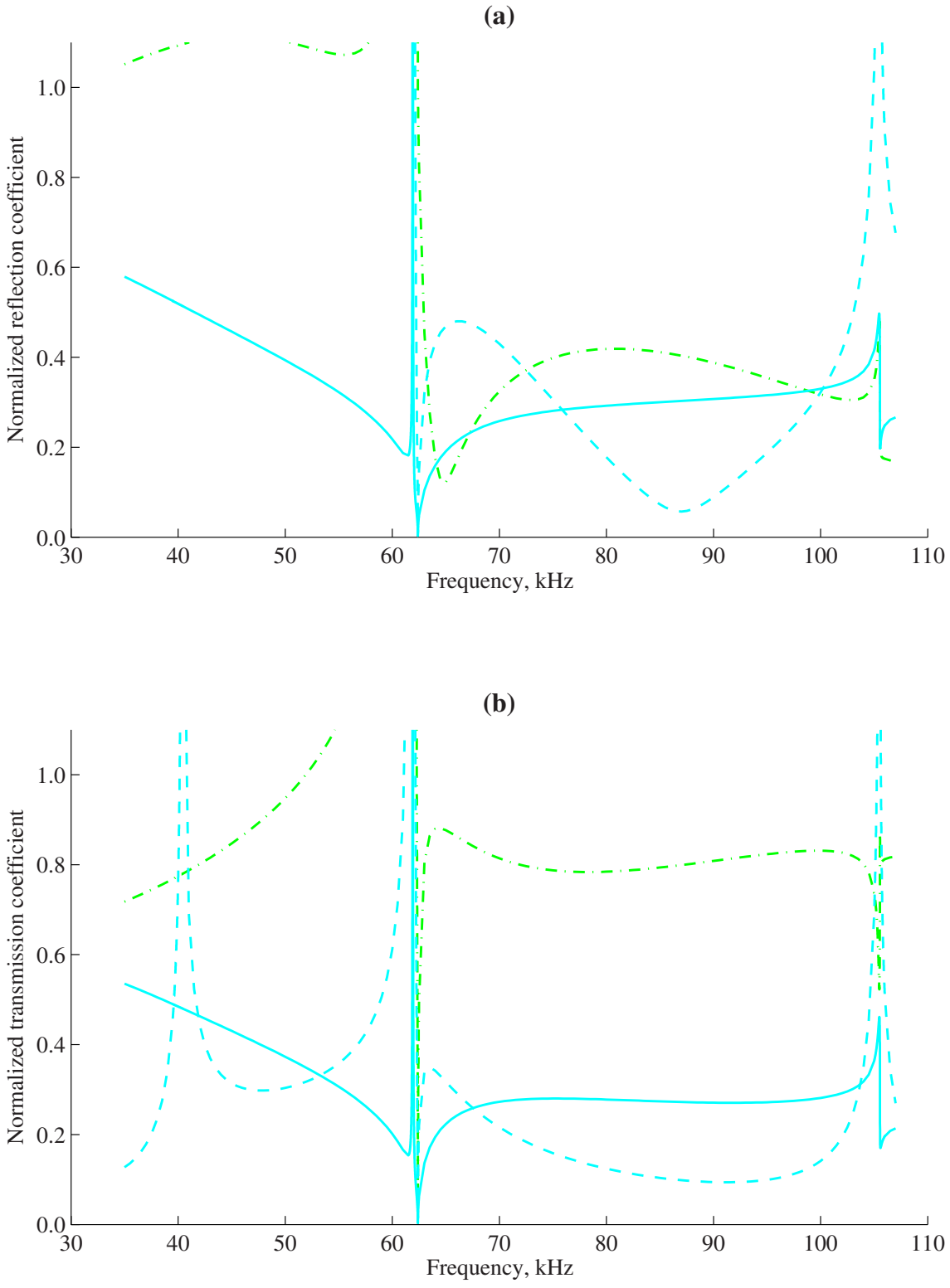

Figure I.18. Normalized reflection and transmission coefficients for the axisymmetric notch and the incident F(5,2) mode.

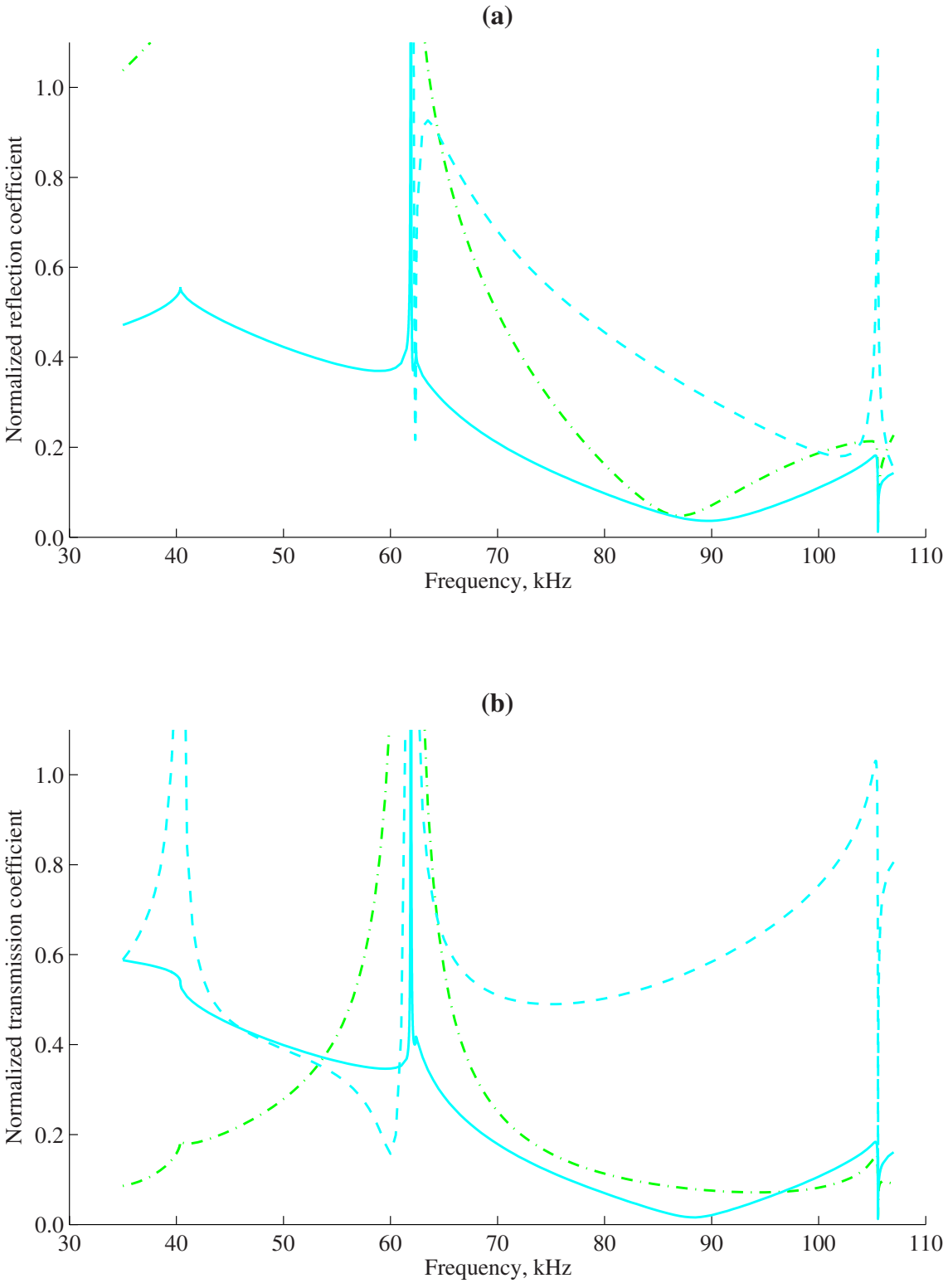

Figure I.19. Normalized reflection and transmission coefficients for the axisymmetric notch and the incident F(5,3) mode.

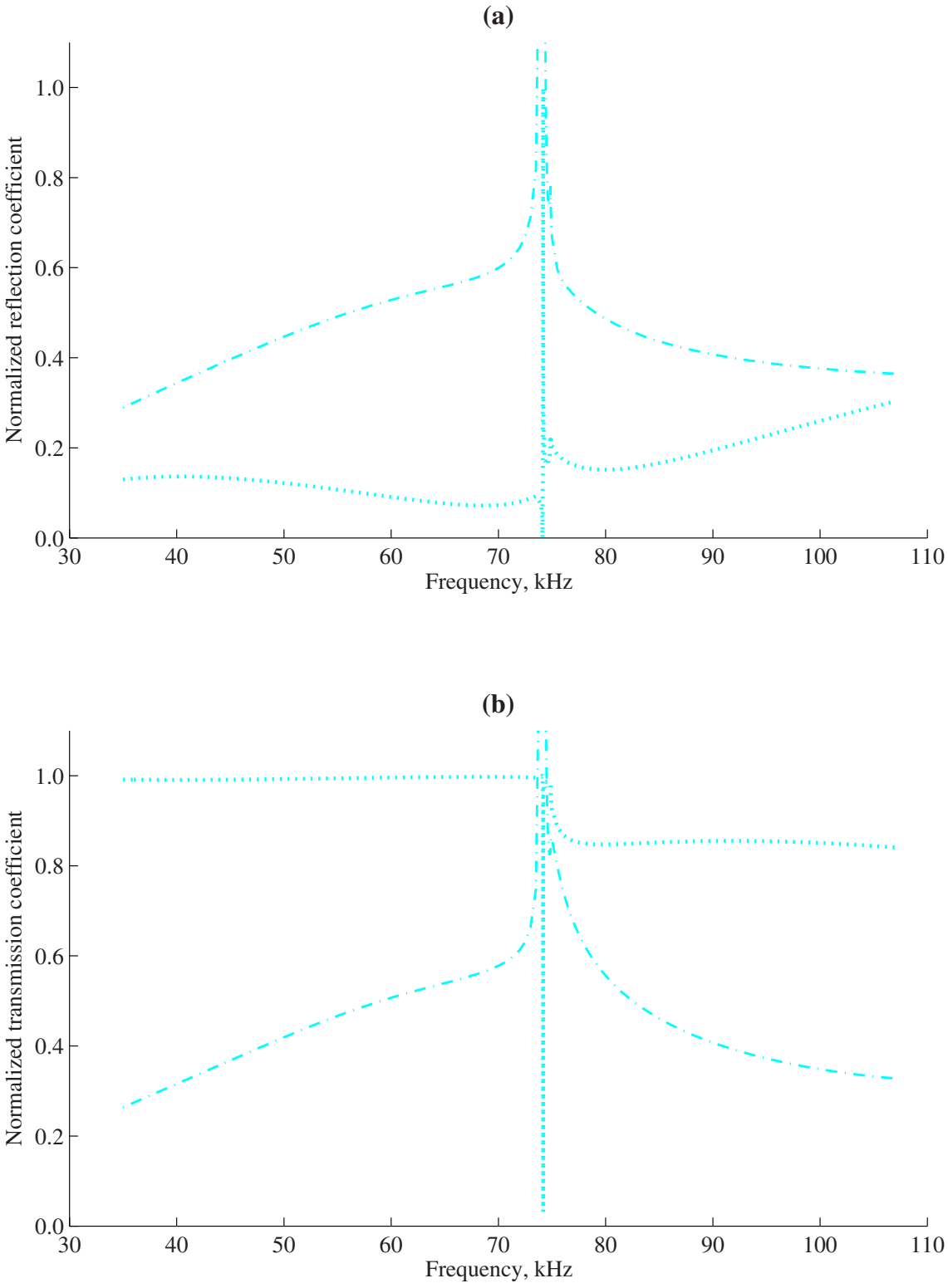

Figure I.20. Normalized reflection and transmission coefficients for the axisymmetric notch and the incident F(6,1) mode.

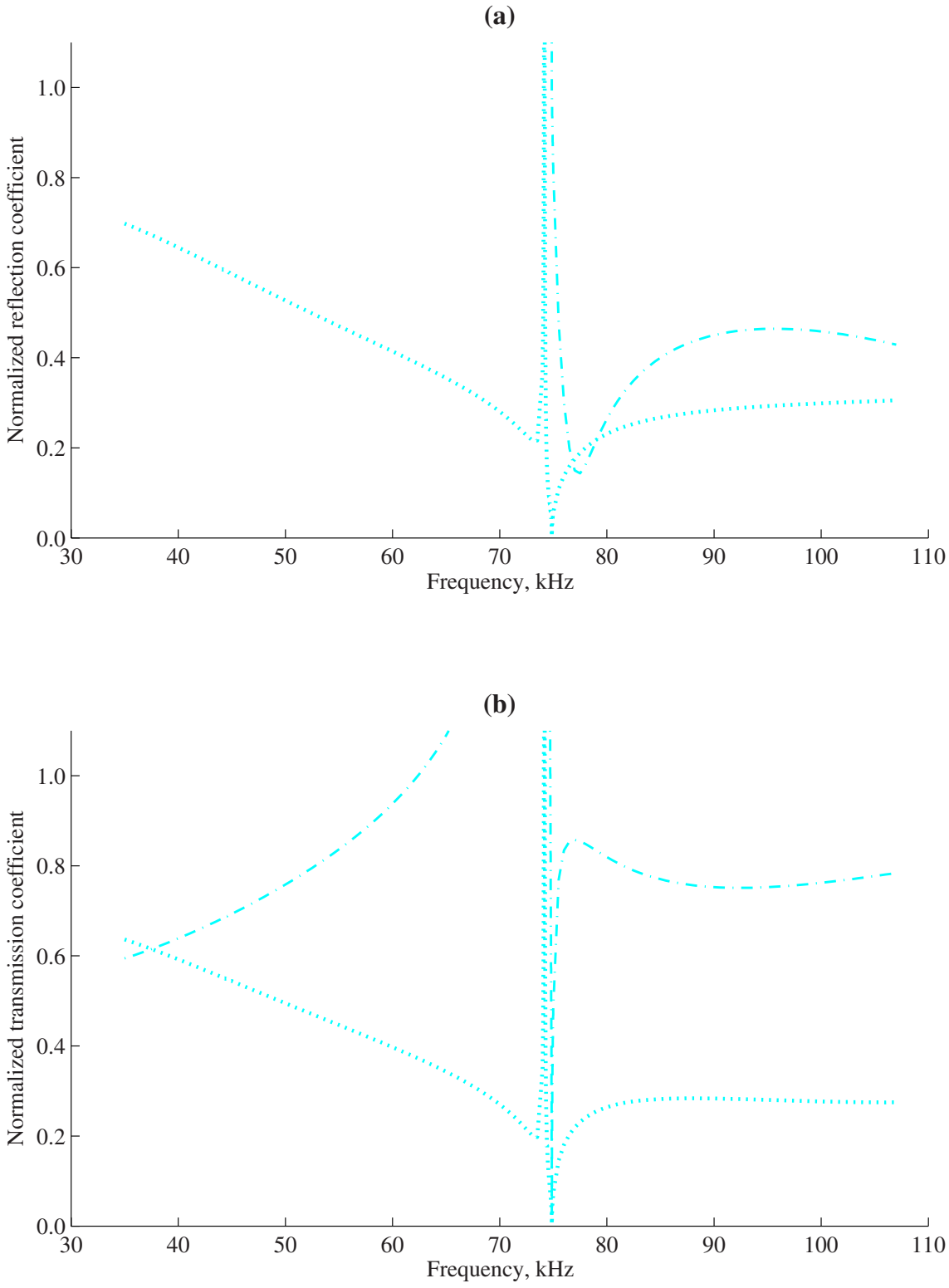

Figure I.21. Normalized reflection and transmission coefficients for the axisymmetric notch and the incident F(6,2) mode.

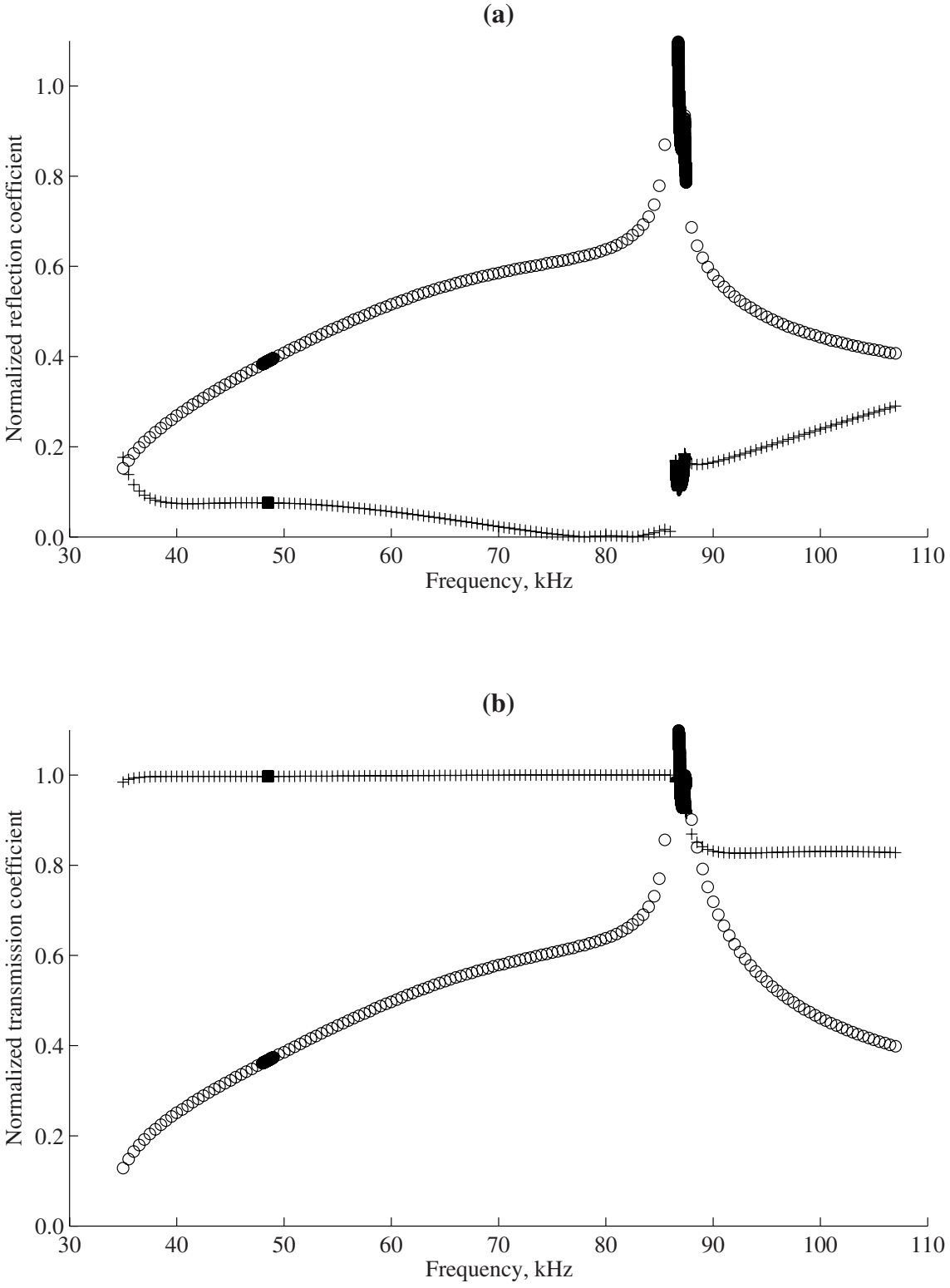

Figure I.22. Normalized reflection and transmission coefficients for the axisymmetric notch and the incident F(7,1) mode.

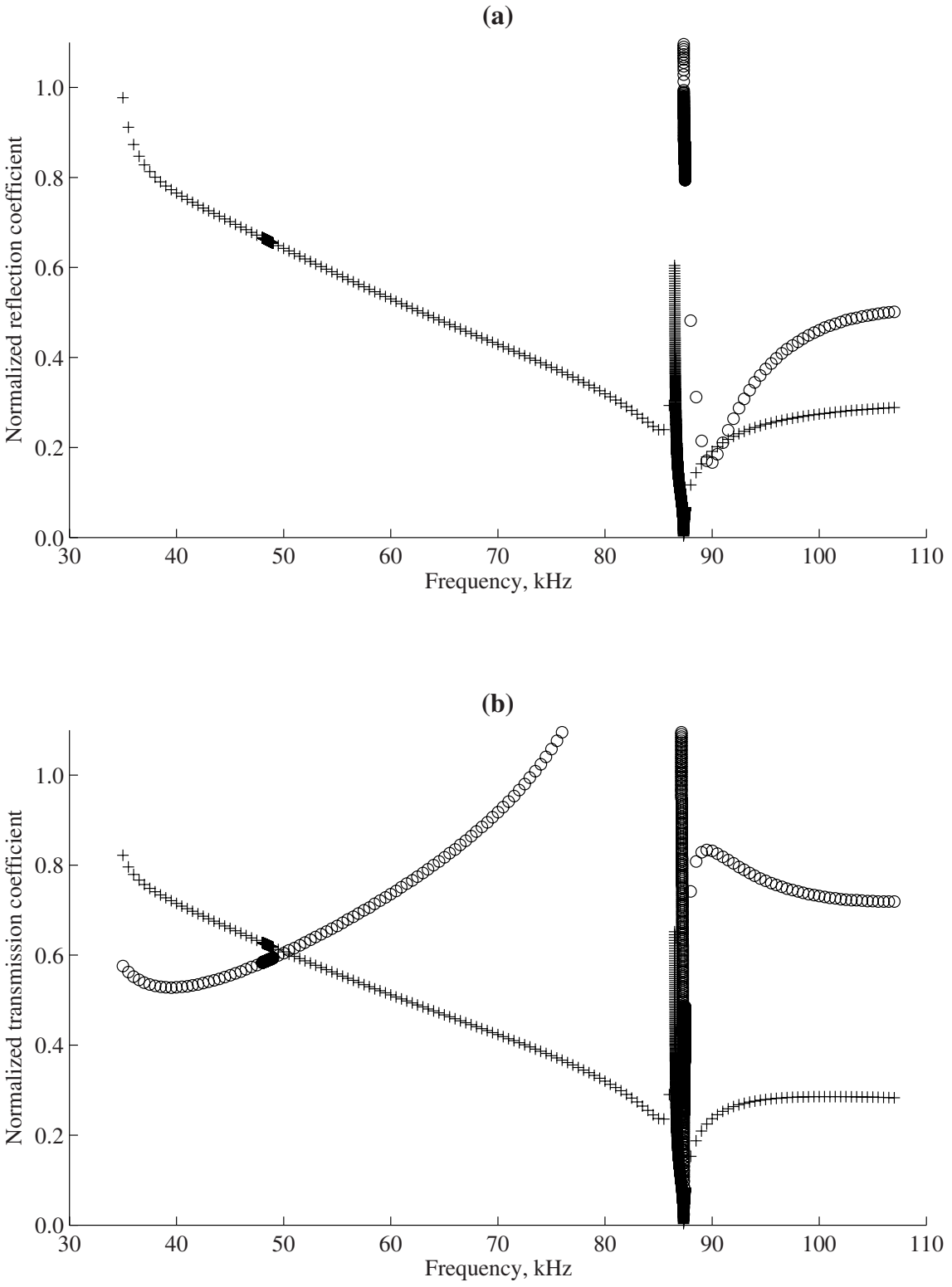

Figure I.23. Normalized reflection and transmission coefficients for the axisymmetric notch and the incident F(7,2) mode.

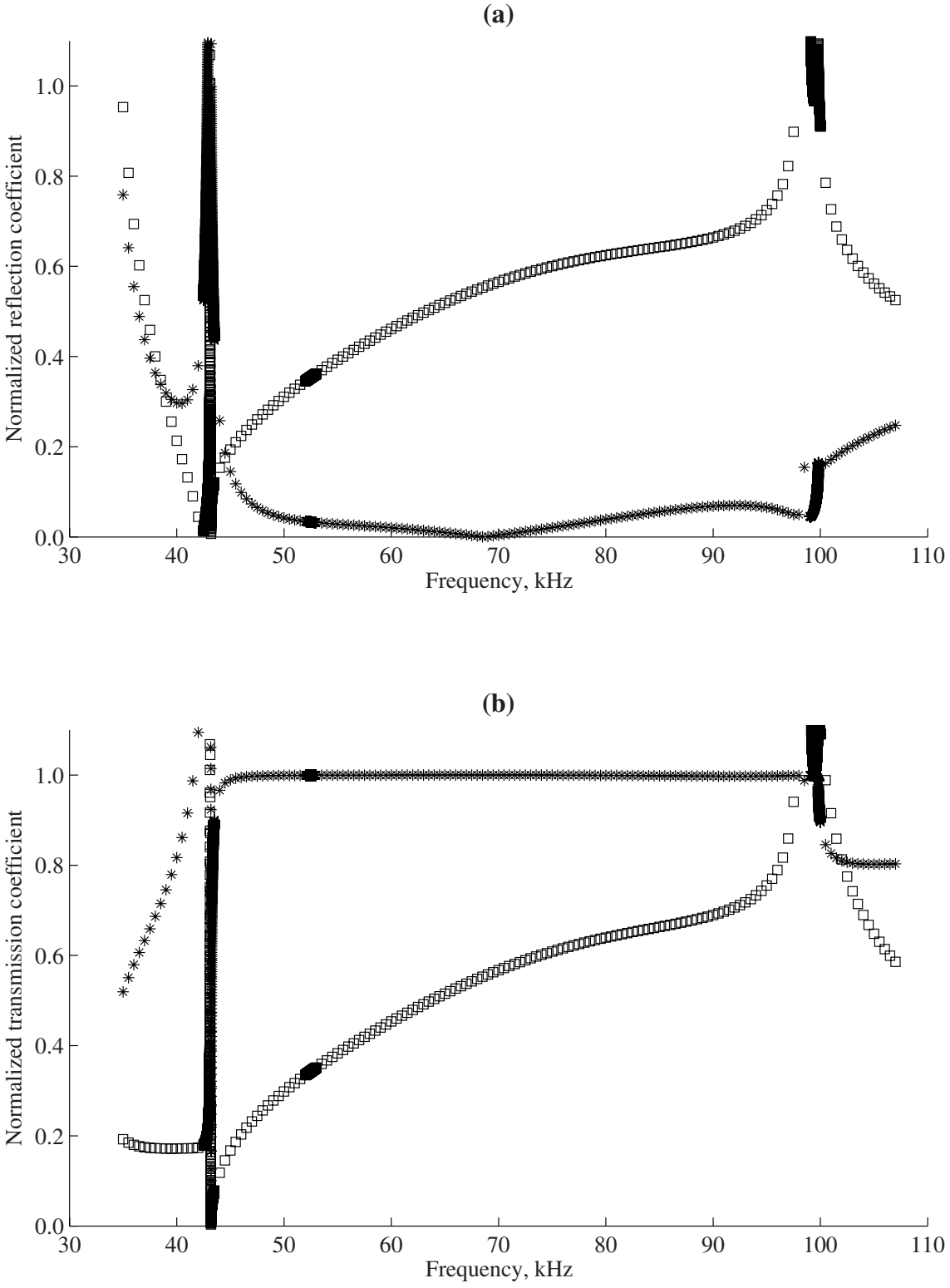

Figure I.24. Normalized reflection and transmission coefficients for the axisymmetric notch and the incident F(8,1) mode.

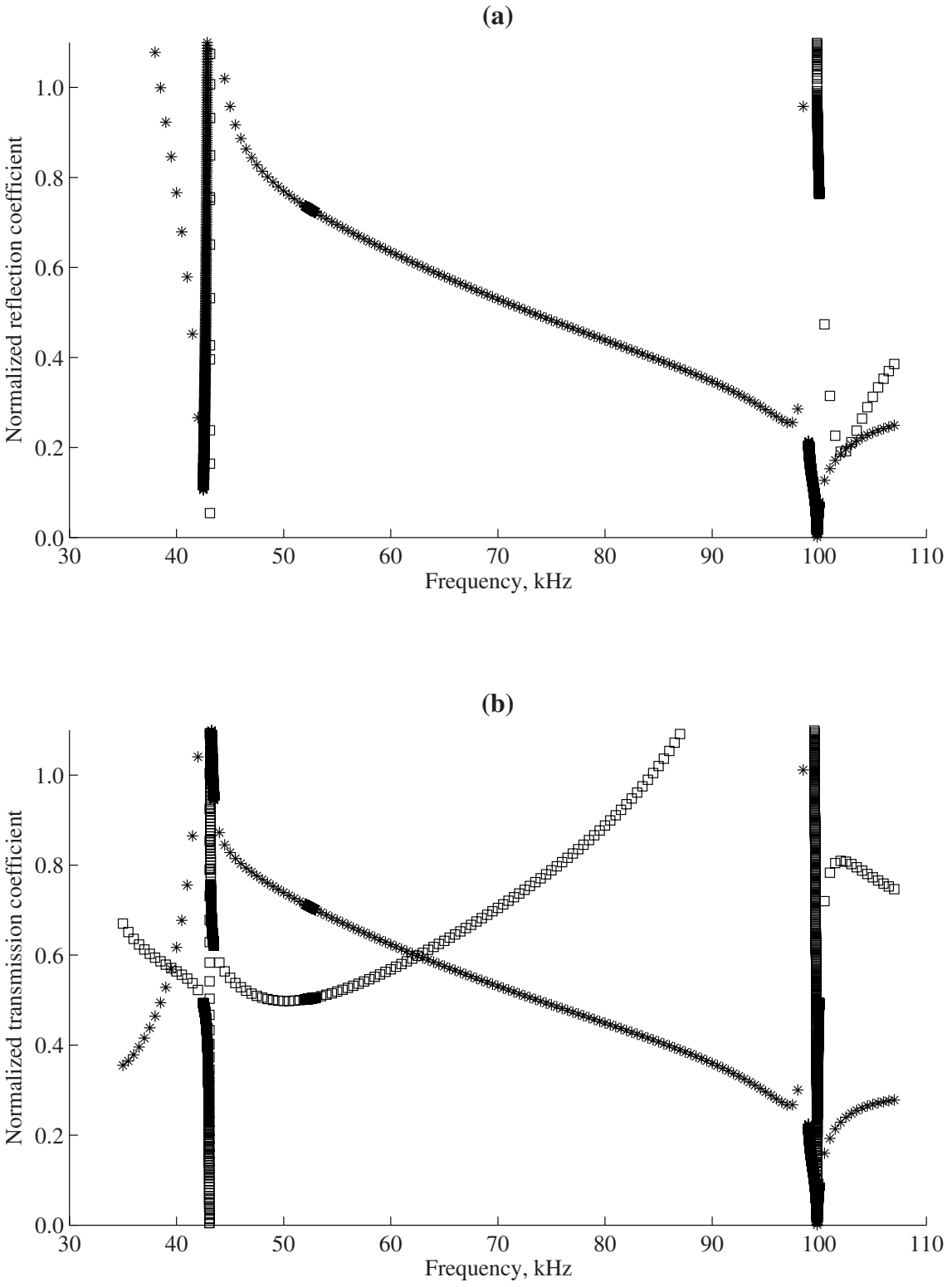

Figure I.25. Normalized reflection and transmission coefficients for the axisymmetric notch and the incident F(8,2) mode.

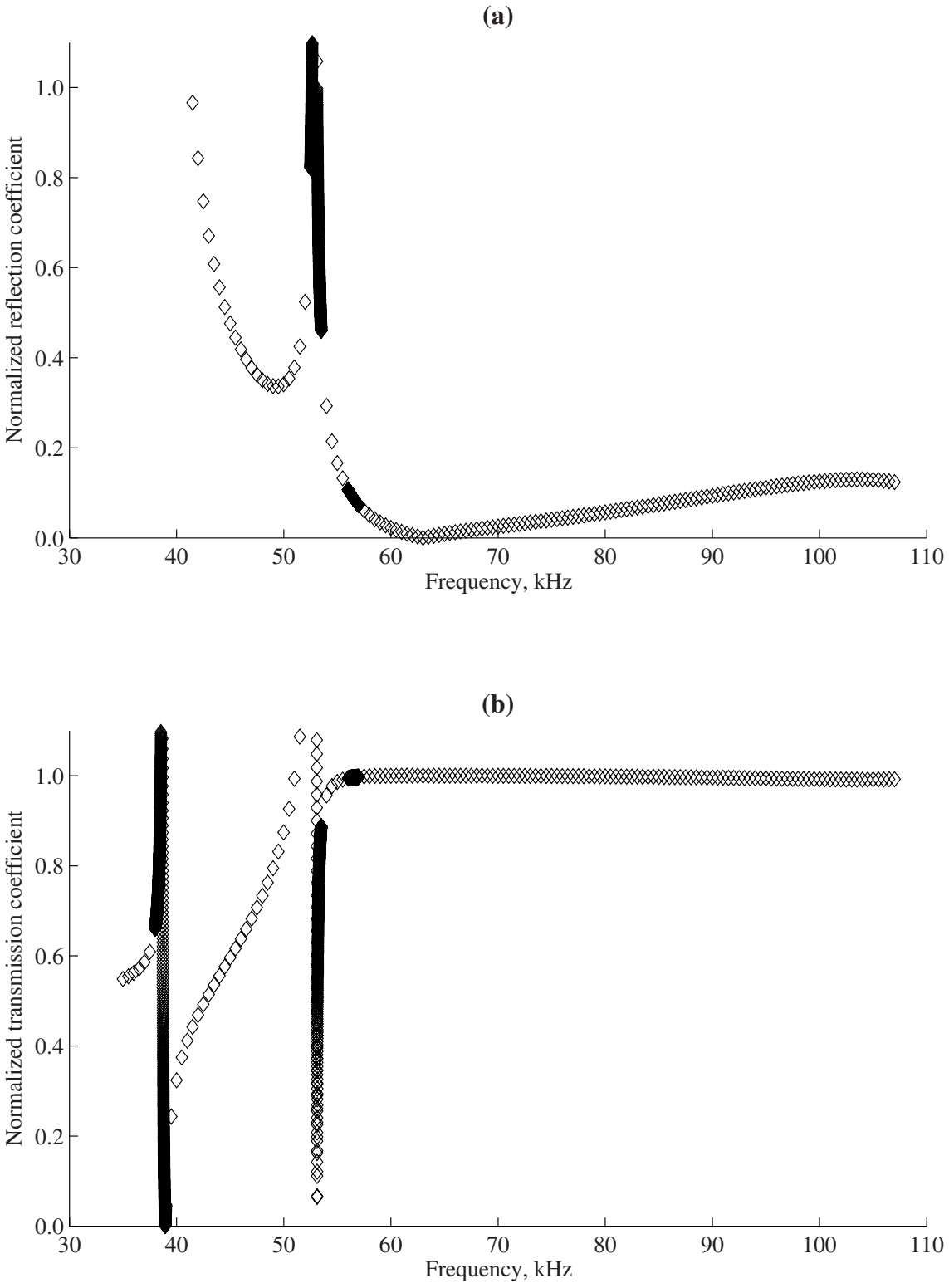

Figure I.26. Normalized reflection and transmission coefficients for the axisymmetric notch and the incident F(9,1) mode.

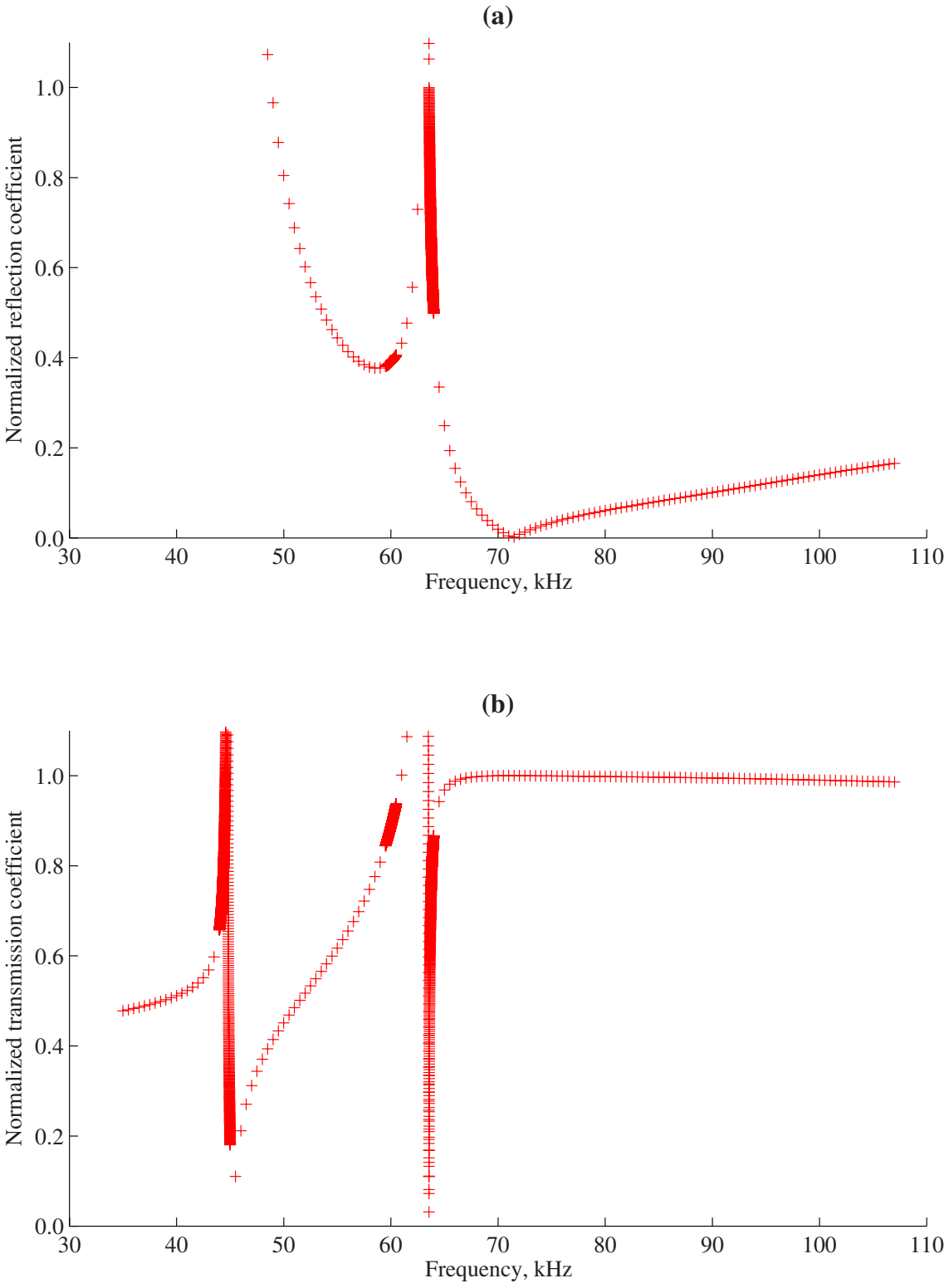

Figure I.27. Normalized reflection and transmission coefficients for the axisymmetric notch and the incident F(10,1) mode.

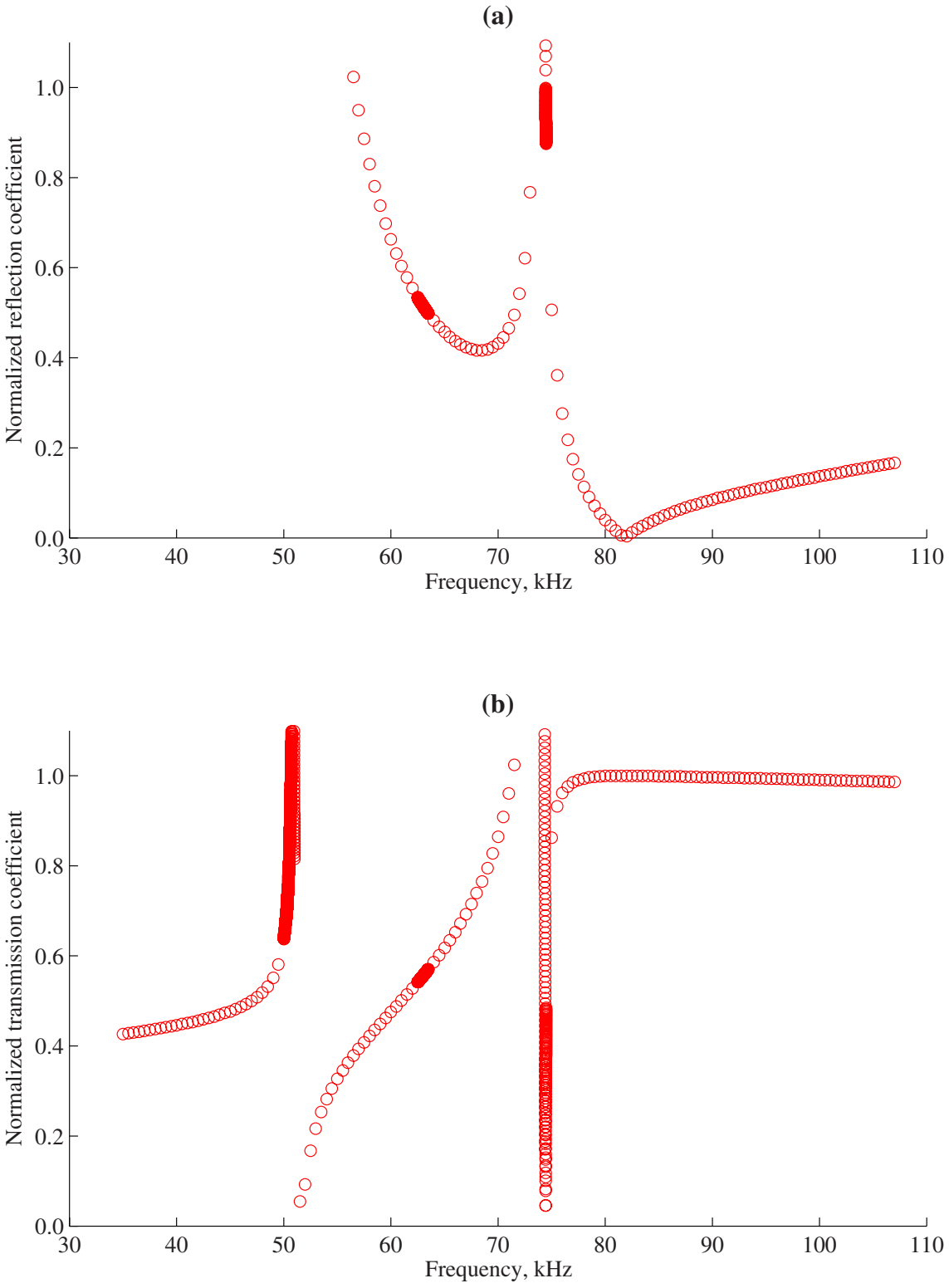

Figure I.28. Normalized reflection and transmission coefficients for the axisymmetric notch and the incident F(11,1) mode.

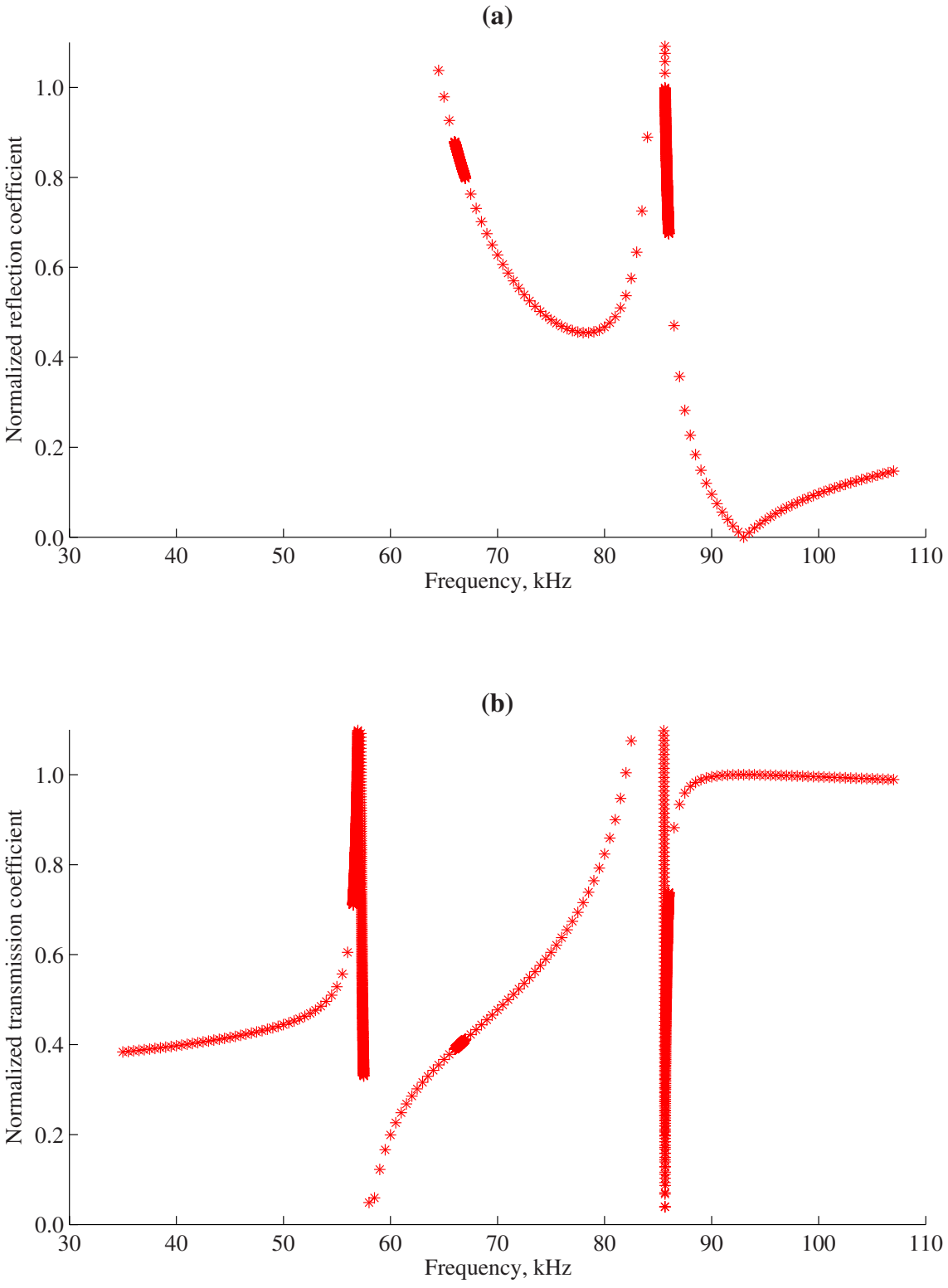

Figure I.29. Normalized reflection and transmission coefficients for the axisymmetric notch and the incident F(12,1) mode.

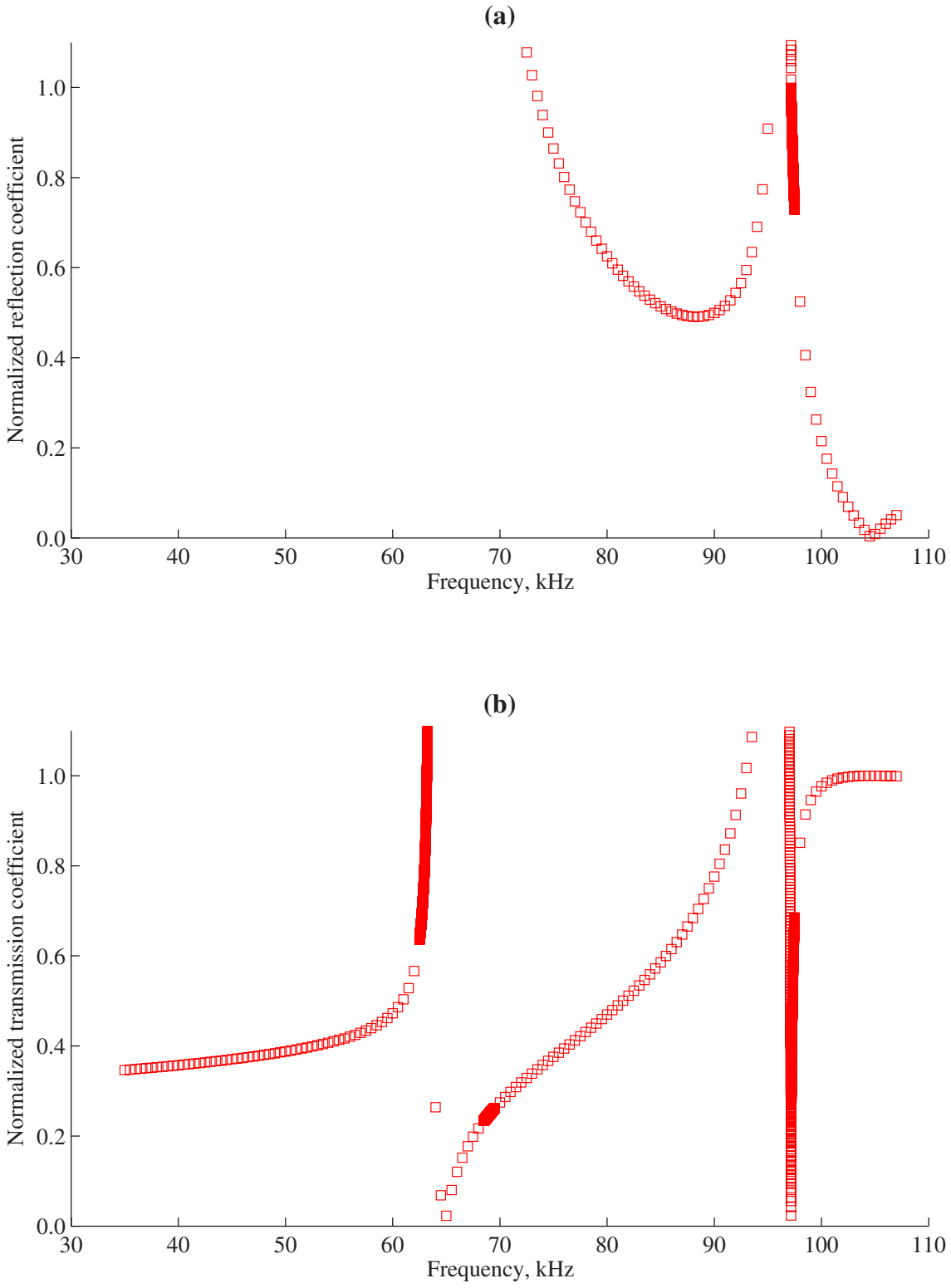

Figure I.30. Normalized reflection and transmission coefficients for the axisymmetric notch and the incident F(13,1) mode.

I.3 Reflection and Transmission Coefficients for Nonaxisymmetric Notch

Magnitudes of the normalized reflection and transmission coefficients are given in Figures I.31 through I.59 for selected modes incident on and scattered by the axisymmetric notch considered in Section 4.3.7.2. The summary presented in Section I.1 is applicable still.

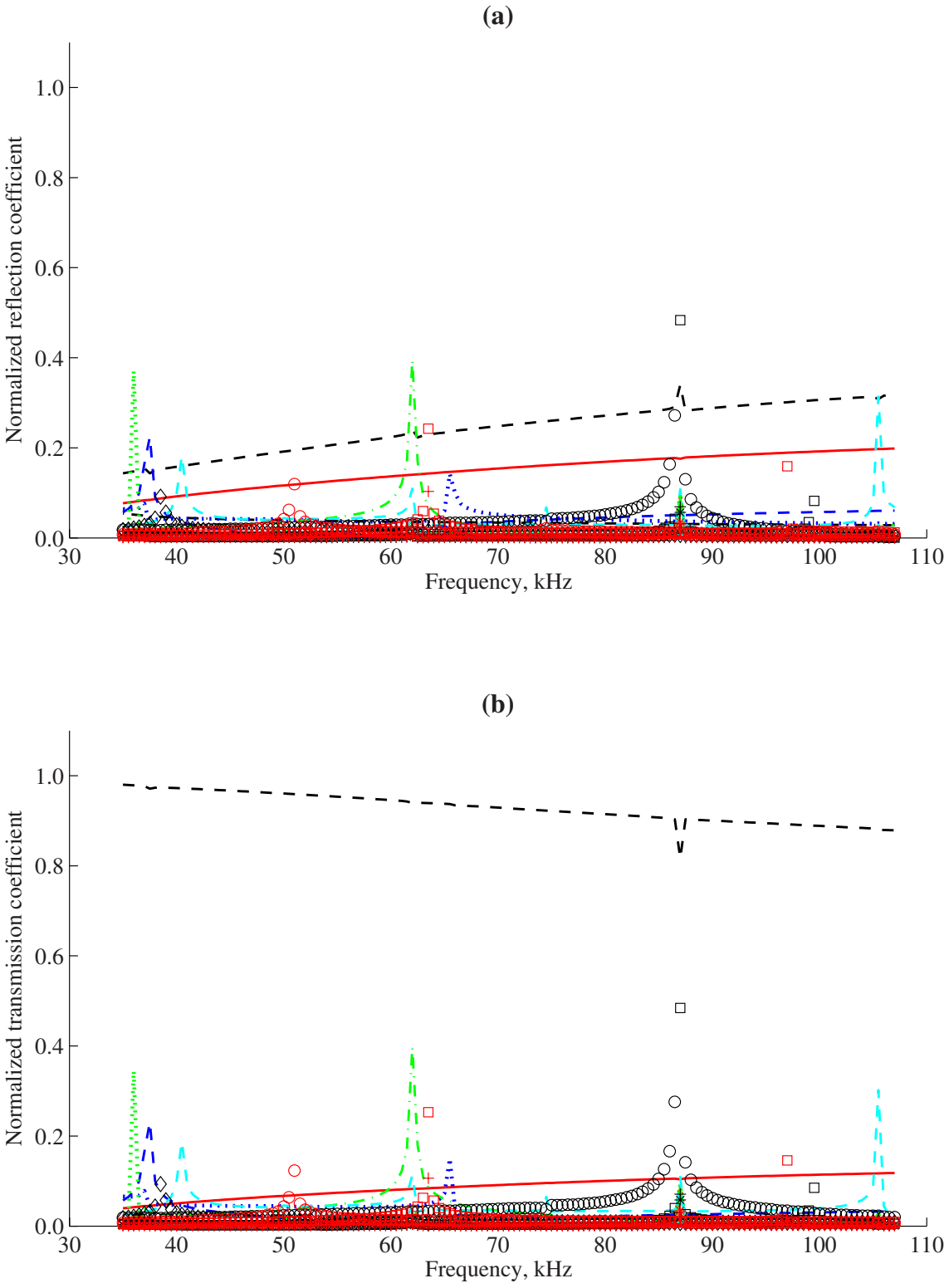

Figure I.31. Normalized reflection and transmission coefficients for the nonaxisymmetric notch and the incident T(0,1) mode.

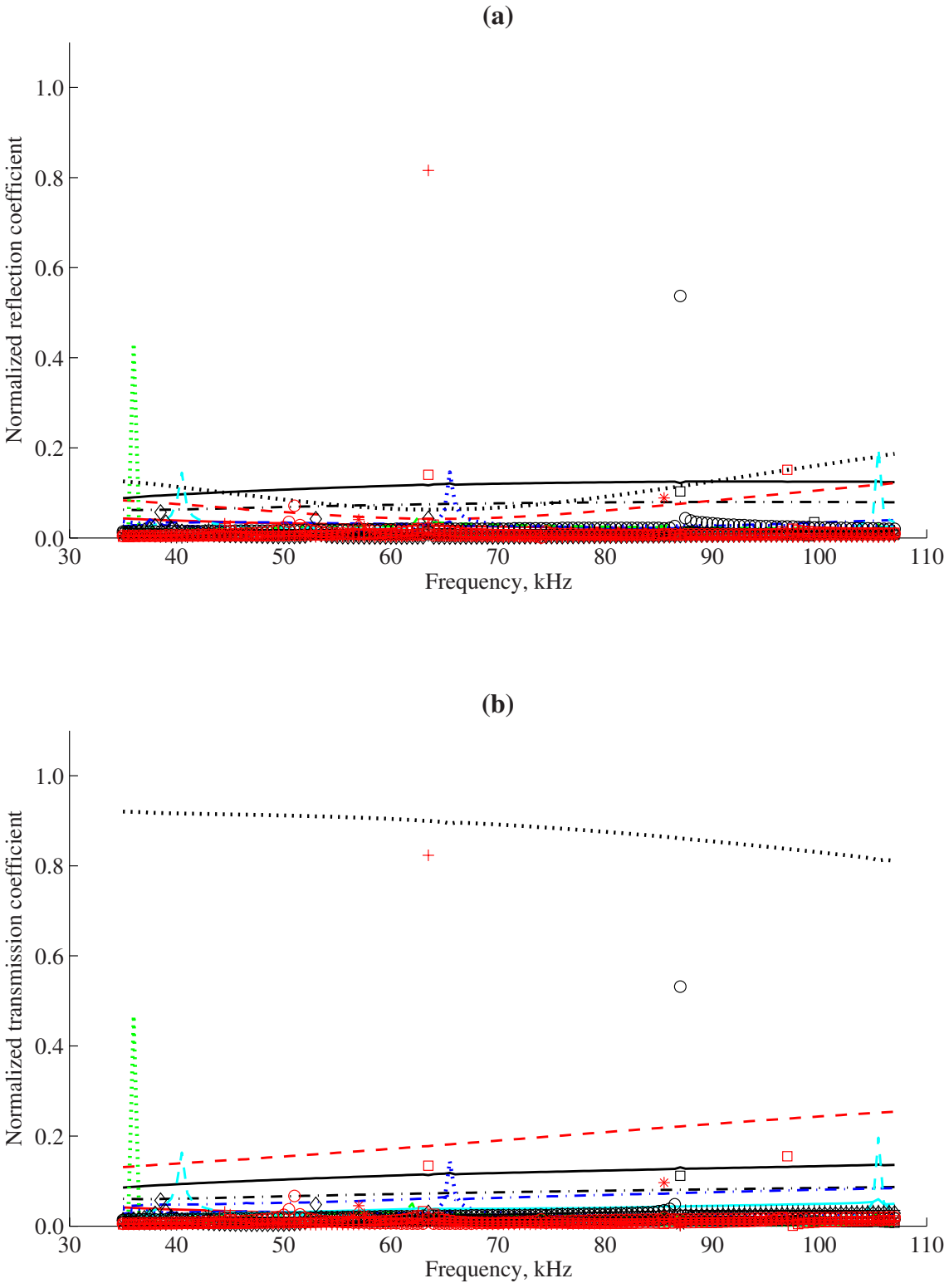

Figure I.32. Normalized reflection and transmission coefficients for the nonaxisymmetric notch and the incident L(0,1) mode.

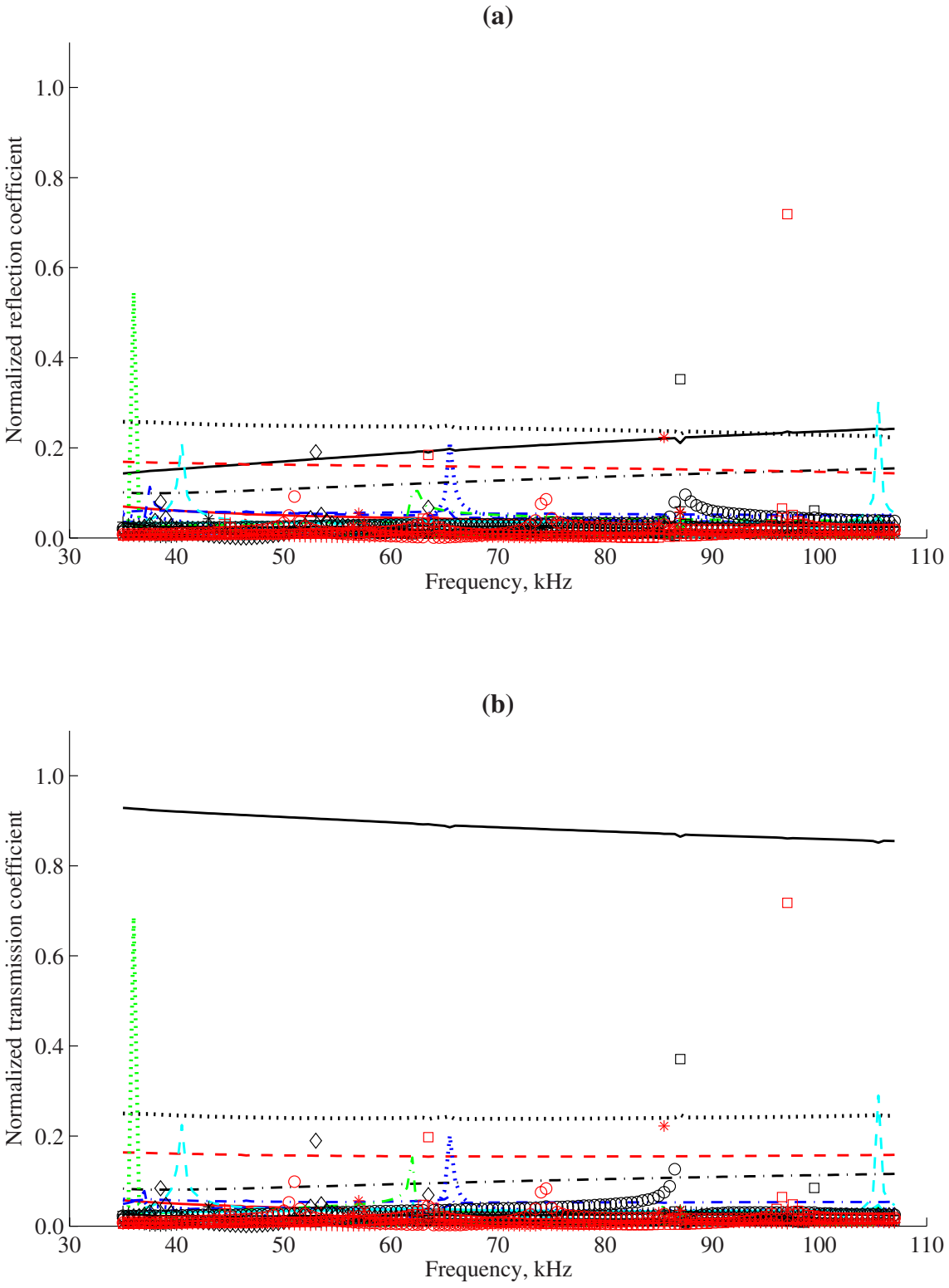

Figure I.33. Normalized reflection and transmission coefficients for the nonaxisymmetric notch and the incident L(0,2) mode.

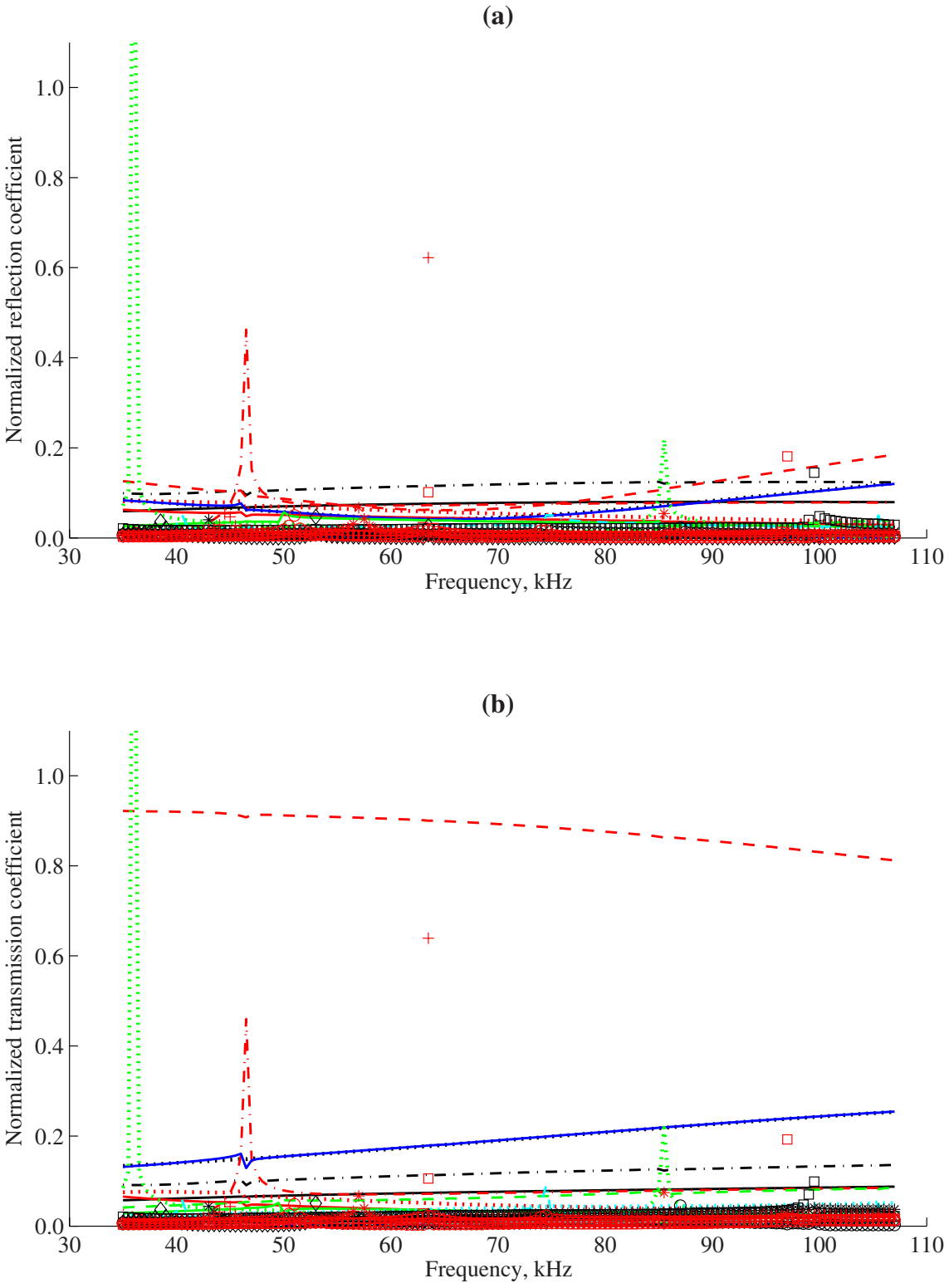

Figure I.34. Normalized reflection and transmission coefficients for the nonaxisymmetric notch and the incident F(1,1) mode.

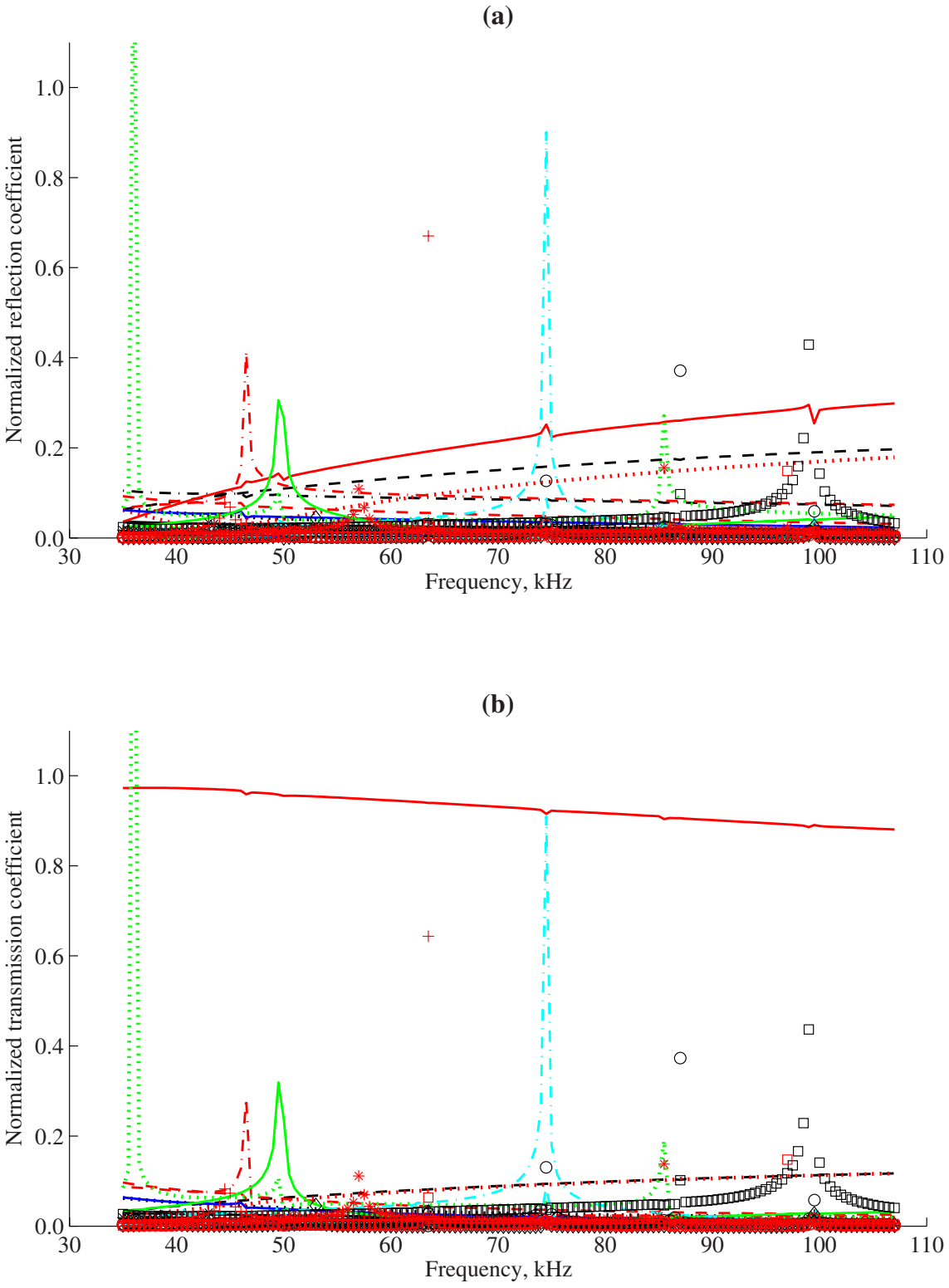

Figure I.35. Normalized reflection and transmission coefficients for the nonaxisymmetric notch and the incident F(1,2) mode.

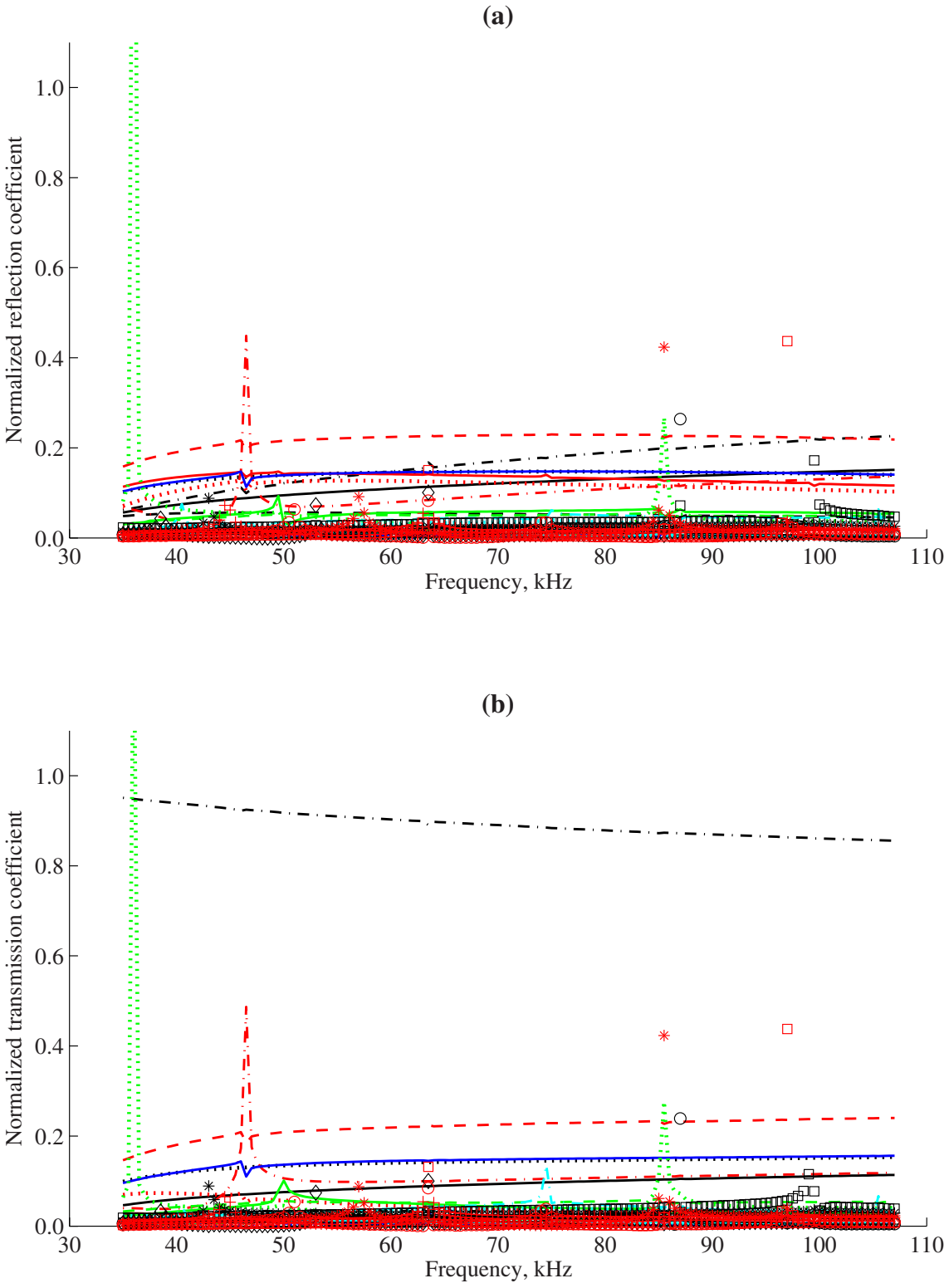

Figure I.36. Normalized reflection and transmission coefficients for the nonaxisymmetric notch and the incident F(1,3) mode.

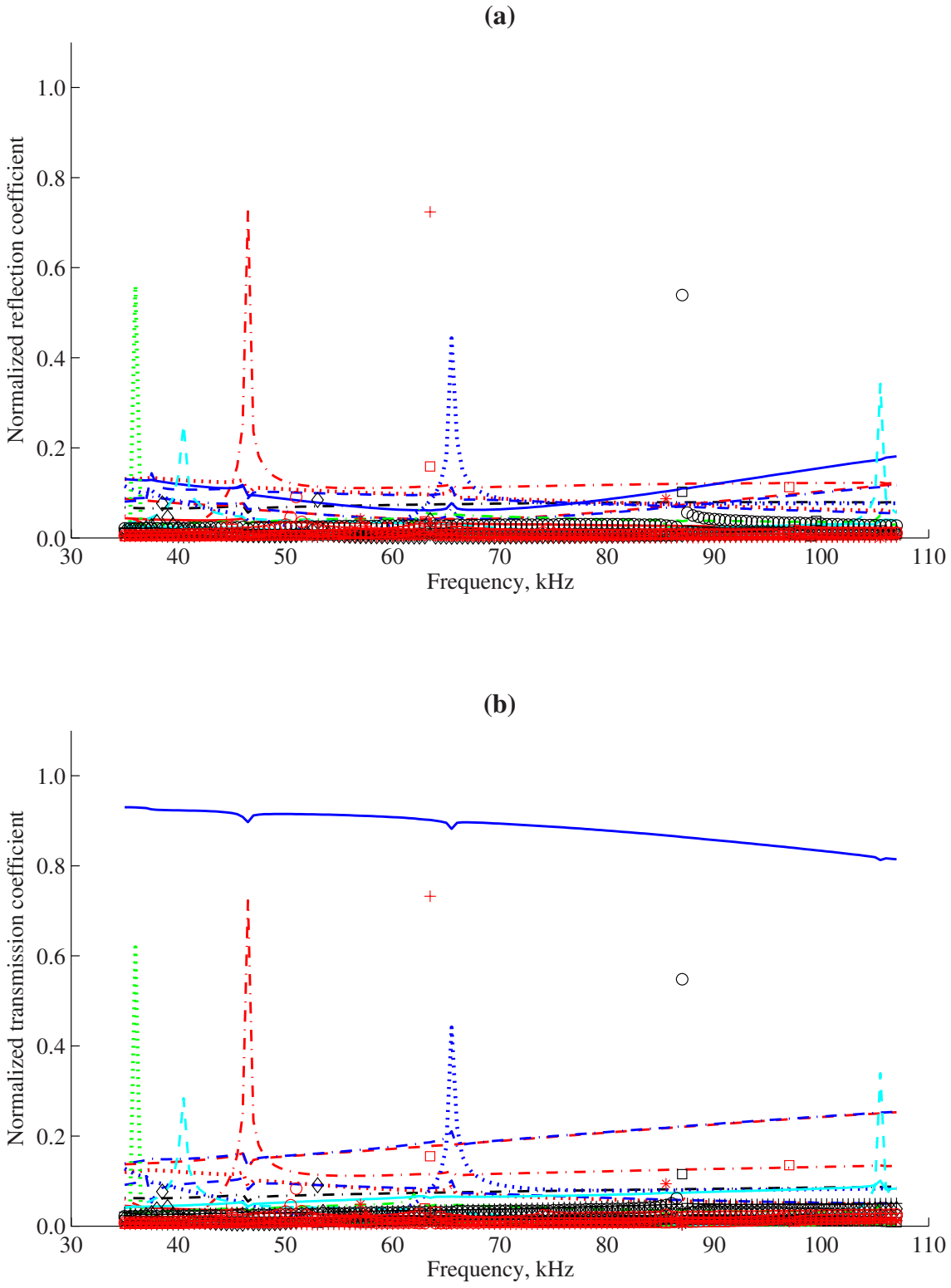

Figure I.37. Normalized reflection and transmission coefficients for the nonaxisymmetric notch and the incident F(2,1) mode.

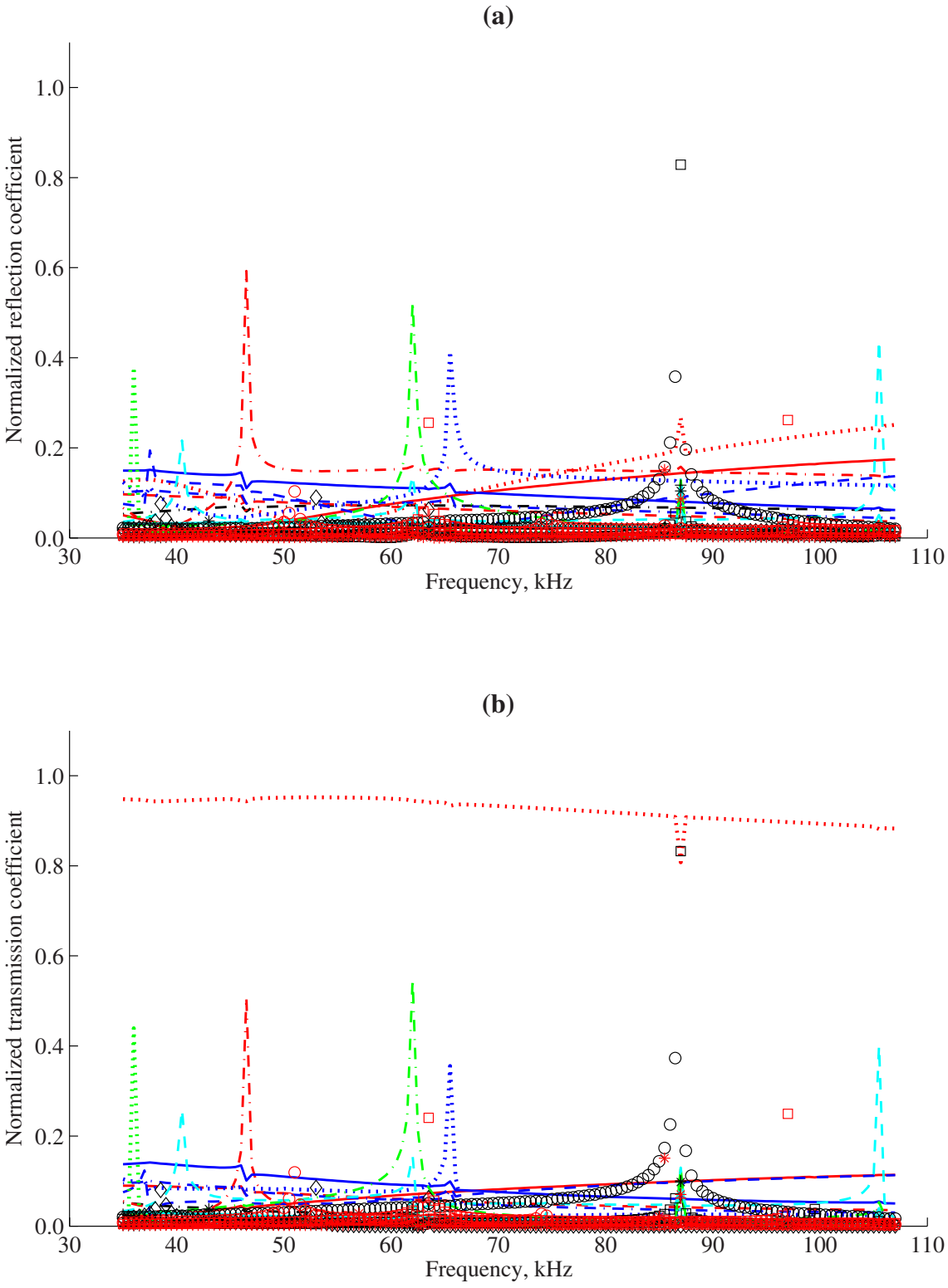

Figure I.38. Normalized reflection and transmission coefficients for the nonaxisymmetric notch and the incident F(2,2) mode.

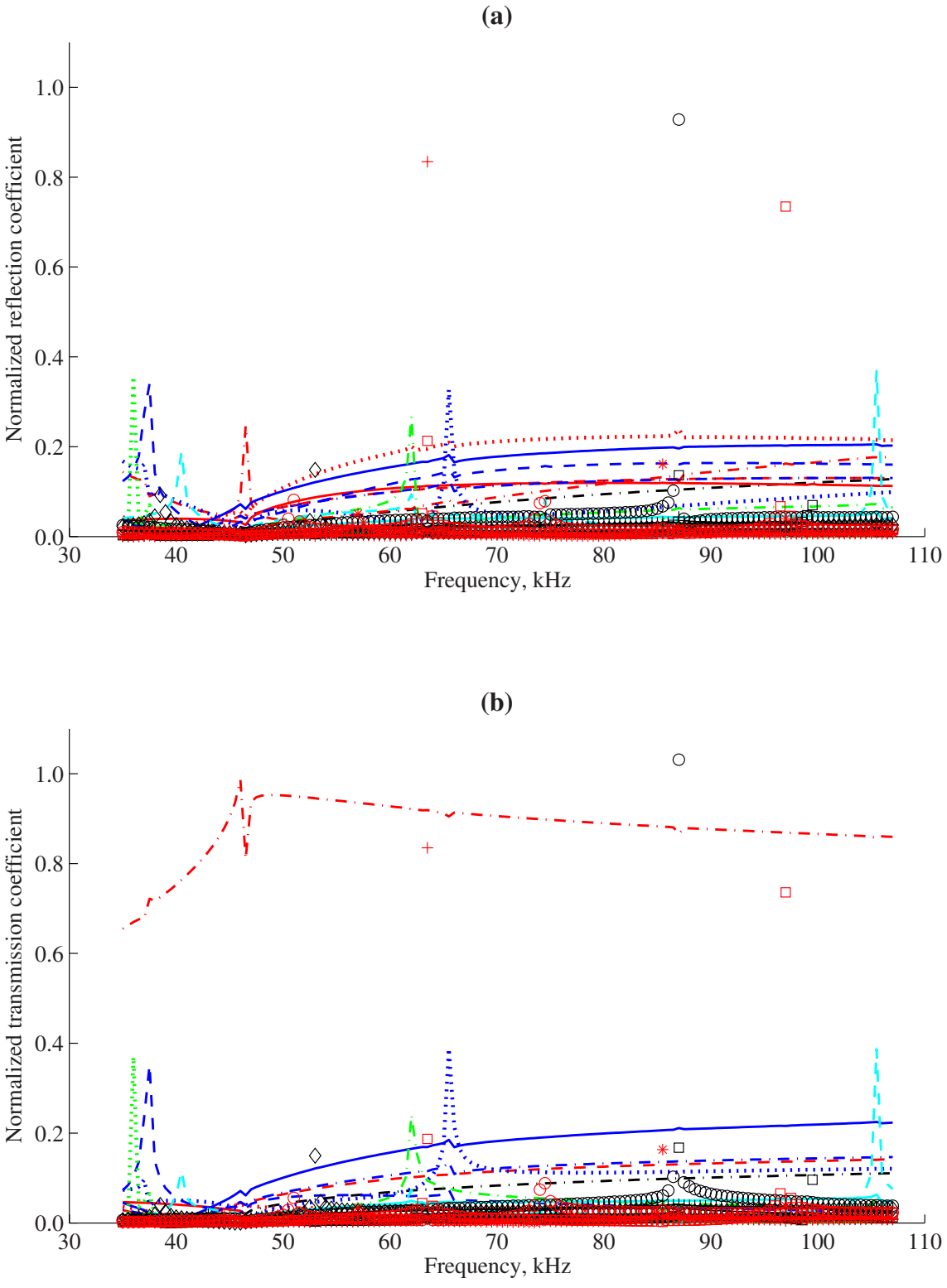

Figure I.39. Normalized reflection and transmission coefficients for the nonaxisymmetric notch and the incident F(2,3) mode.

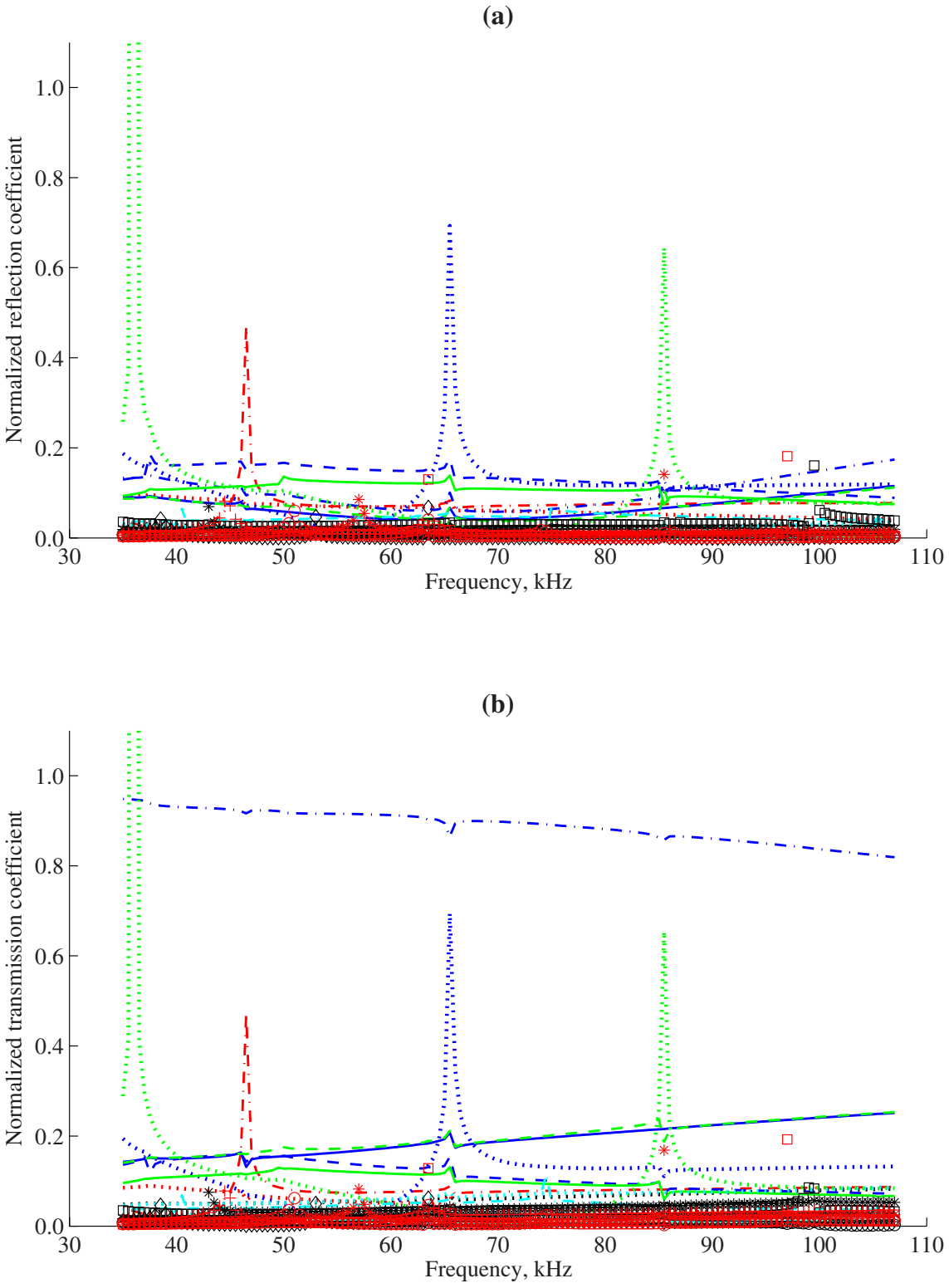

Figure I.40. Normalized reflection and transmission coefficients for the nonaxisymmetric notch and the incident F(3,1) mode.

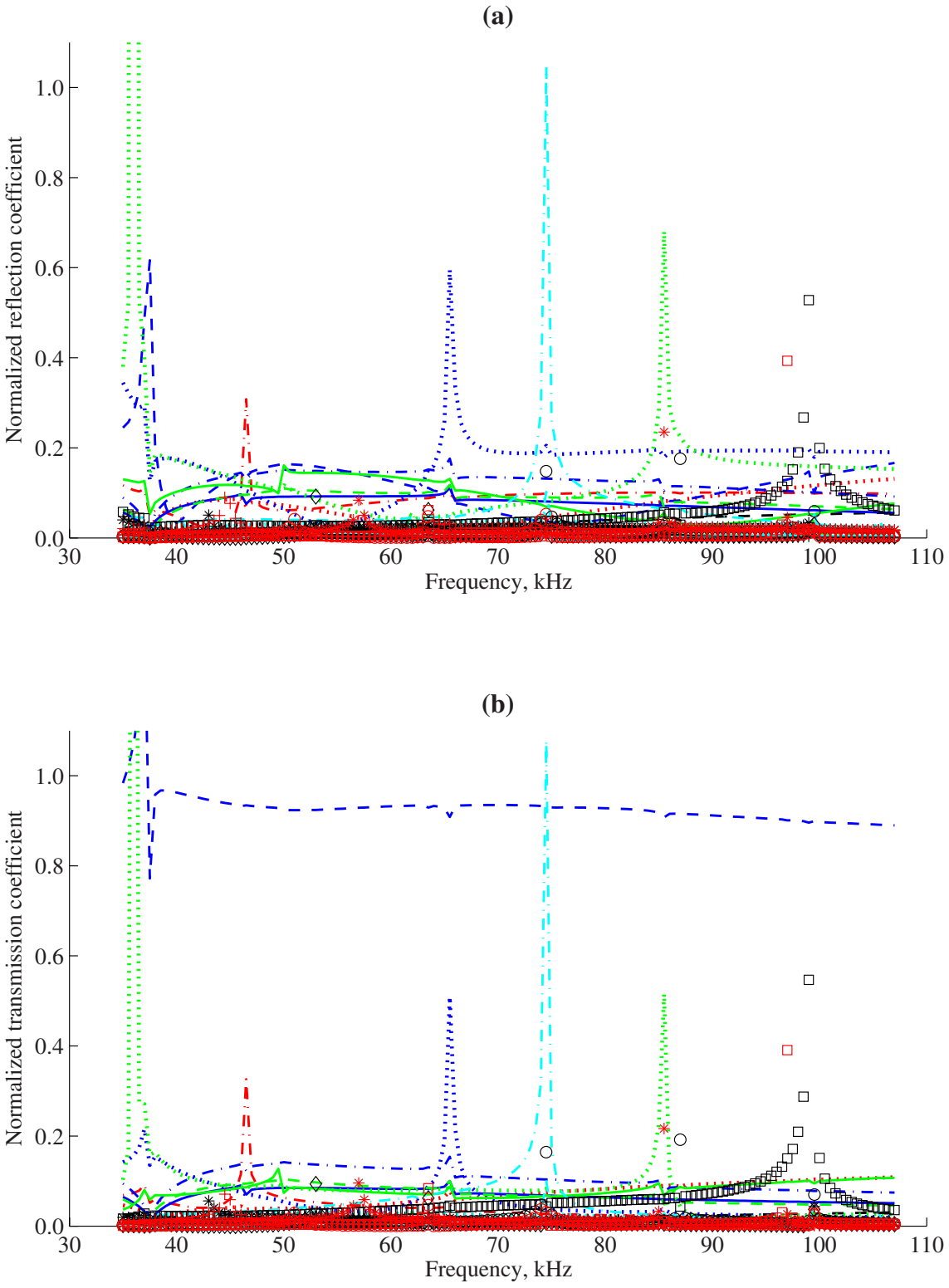

Figure I.41. Normalized reflection and transmission coefficients for the nonaxisymmetric notch and the incident F(3,2) mode.

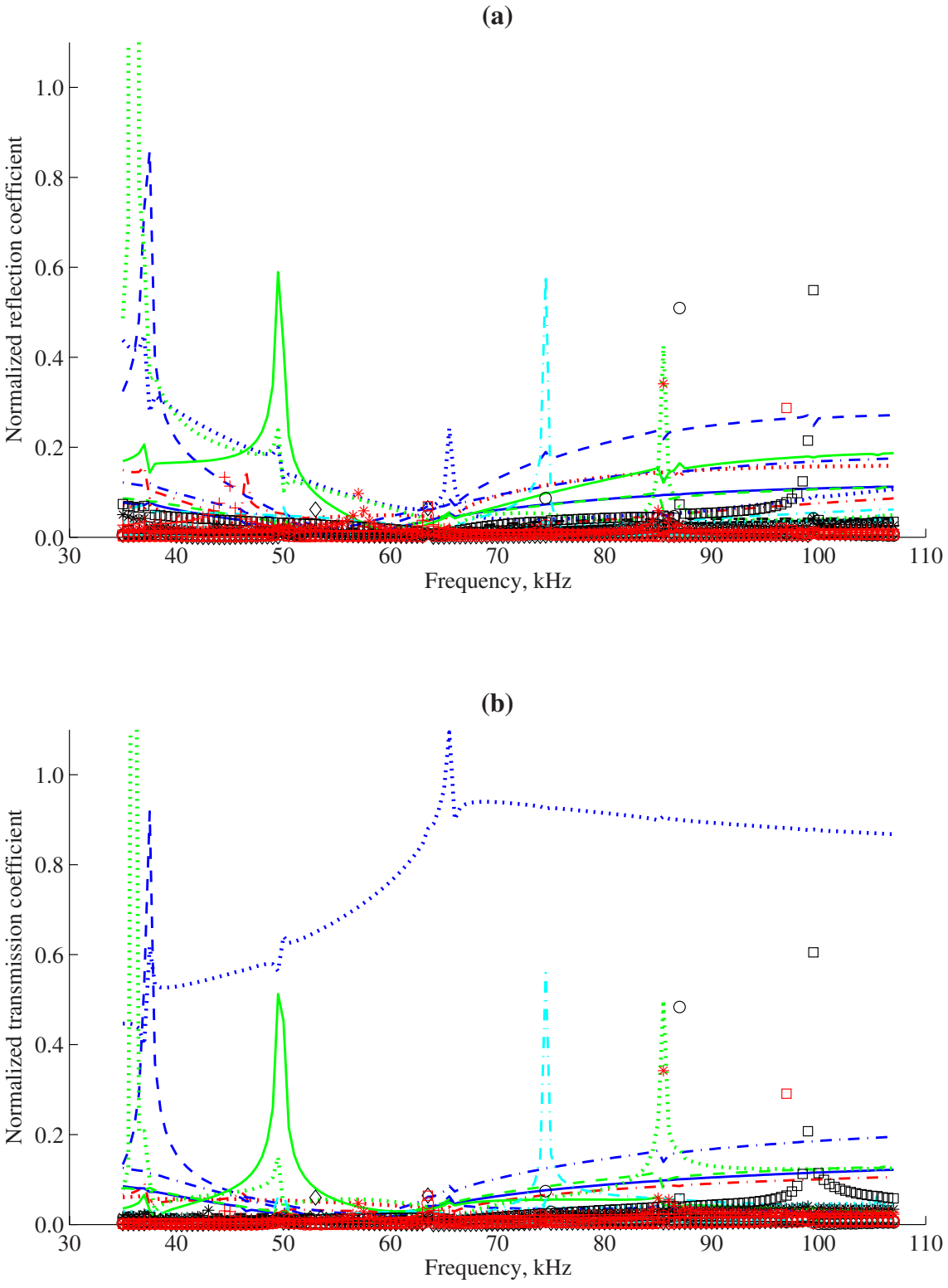

Figure I.42. Normalized reflection and transmission coefficients for the nonaxisymmetric notch and the incident F(3,3) mode.

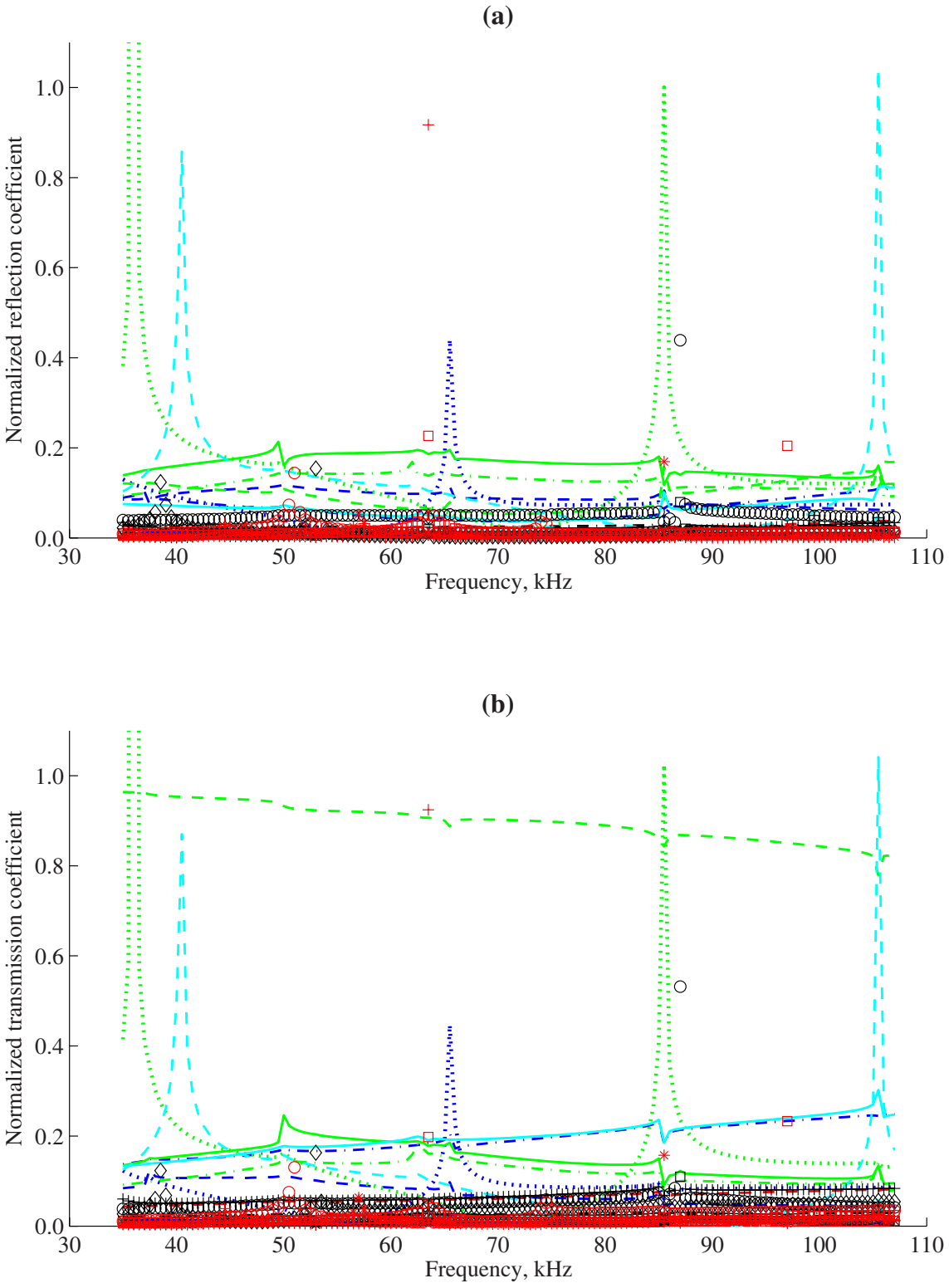

Figure I.43. Normalized reflection and transmission coefficients for the nonaxisymmetric notch and the incident F(4,1) mode.

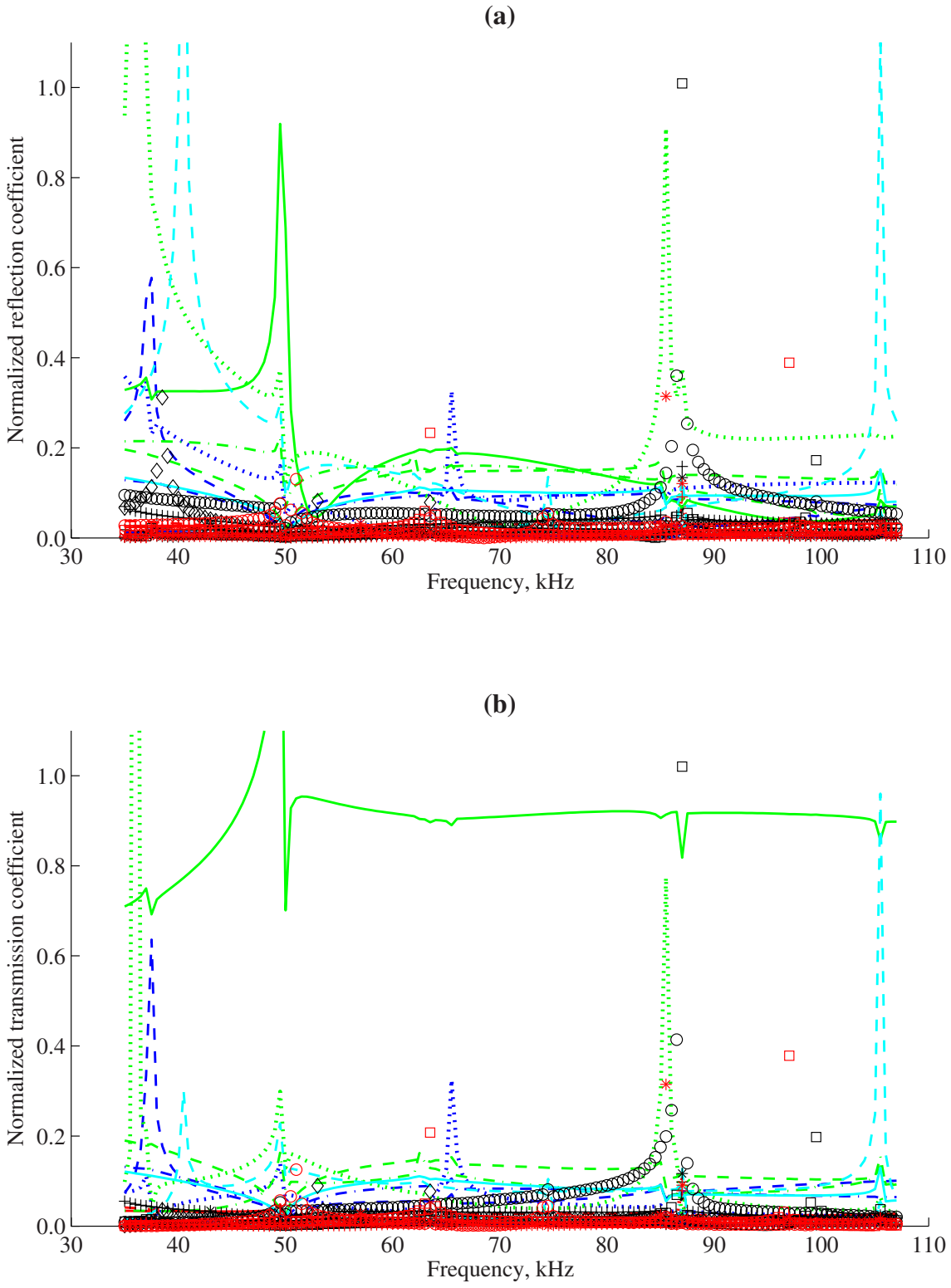

Figure I.44. Normalized reflection and transmission coefficients for the nonaxisymmetric notch and the incident F(4,2) mode.

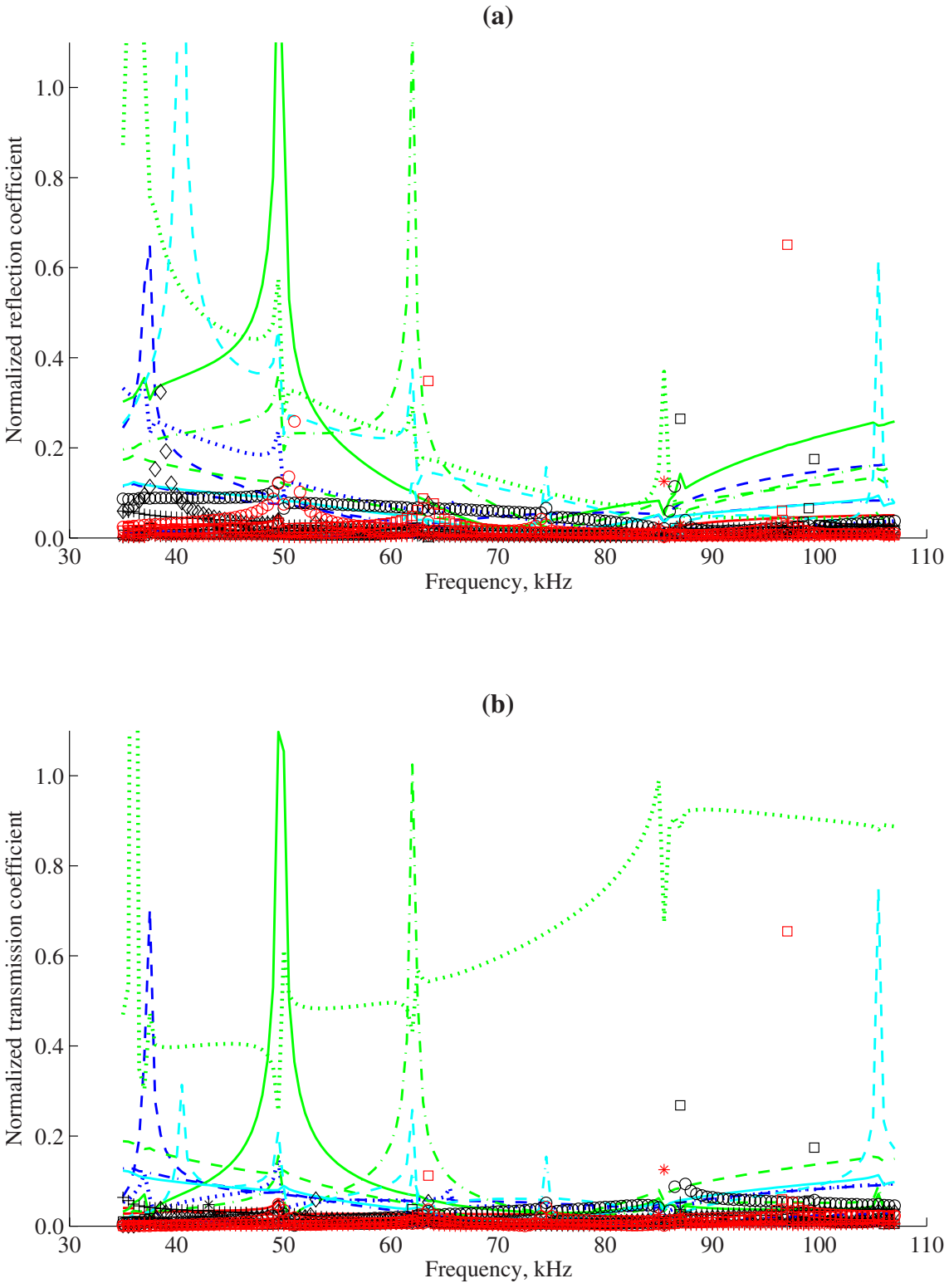

Figure I.45. Normalized reflection and transmission coefficients for the nonaxisymmetric notch and the incident F(4,3) mode.

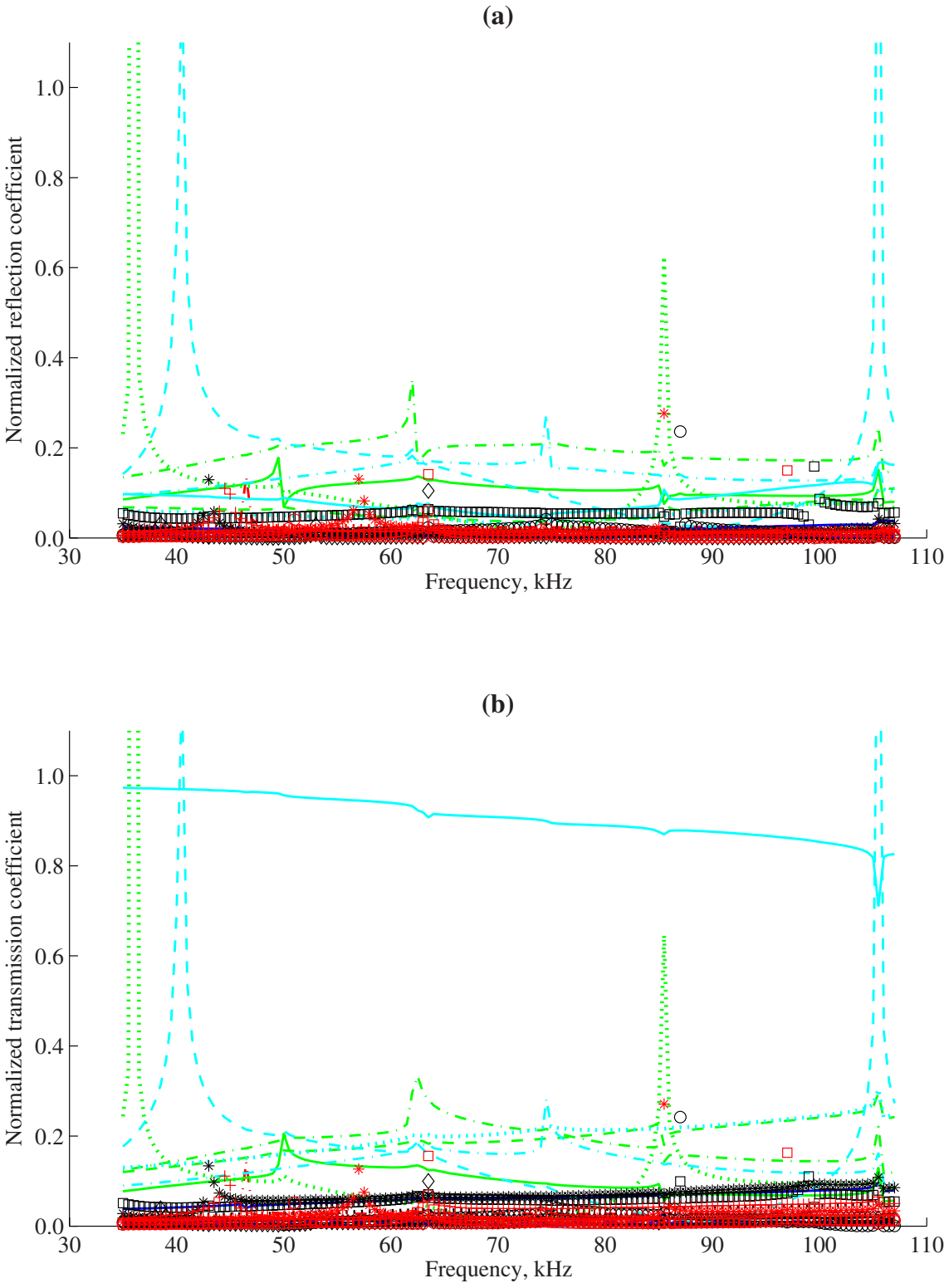

Figure I.46. Normalized reflection and transmission coefficients for the nonaxisymmetric notch and the incident F(5,1) mode.

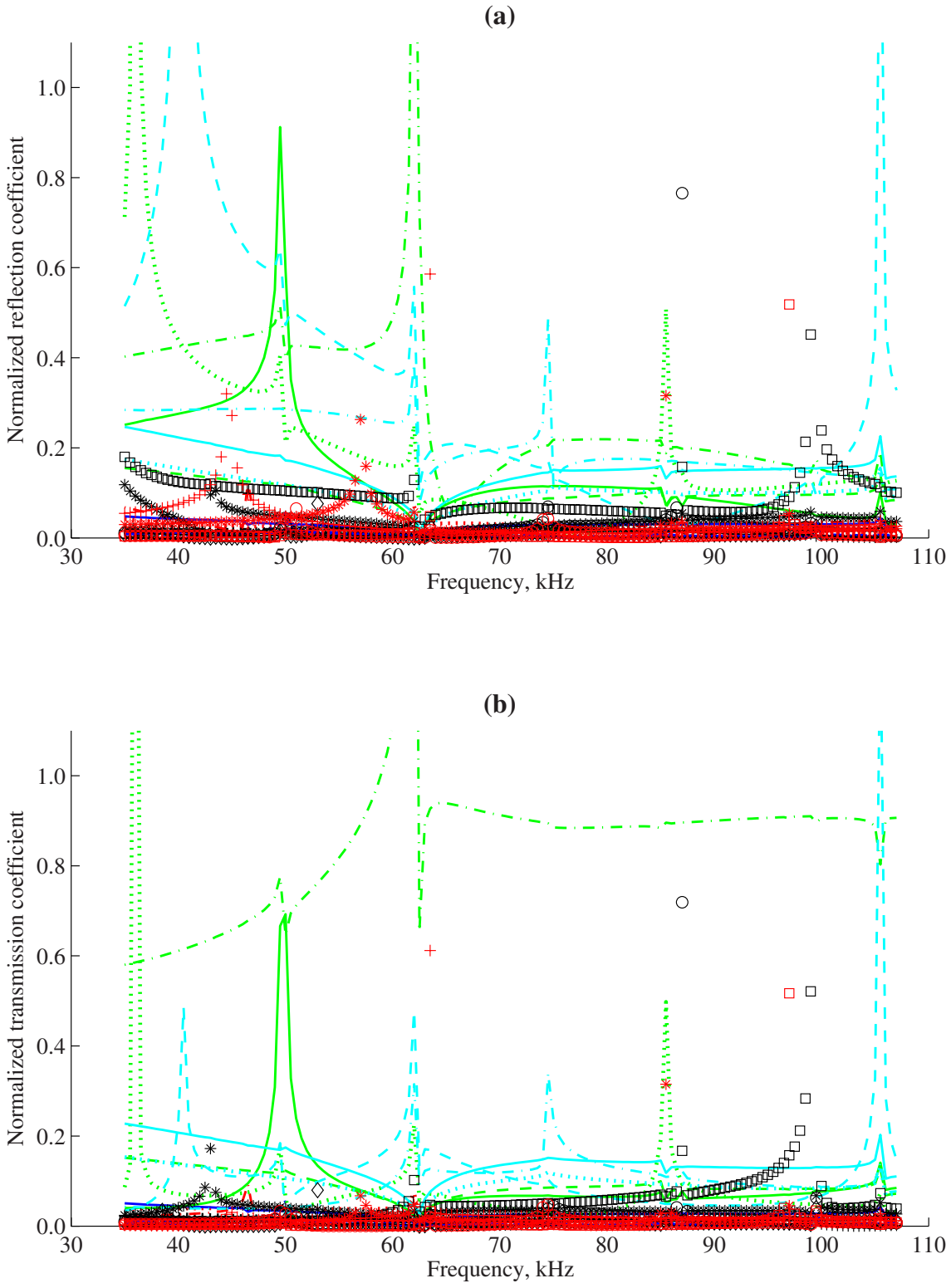

Figure I.47. Normalized reflection and transmission coefficients for the nonaxisymmetric notch and the incident F(5,2) mode.

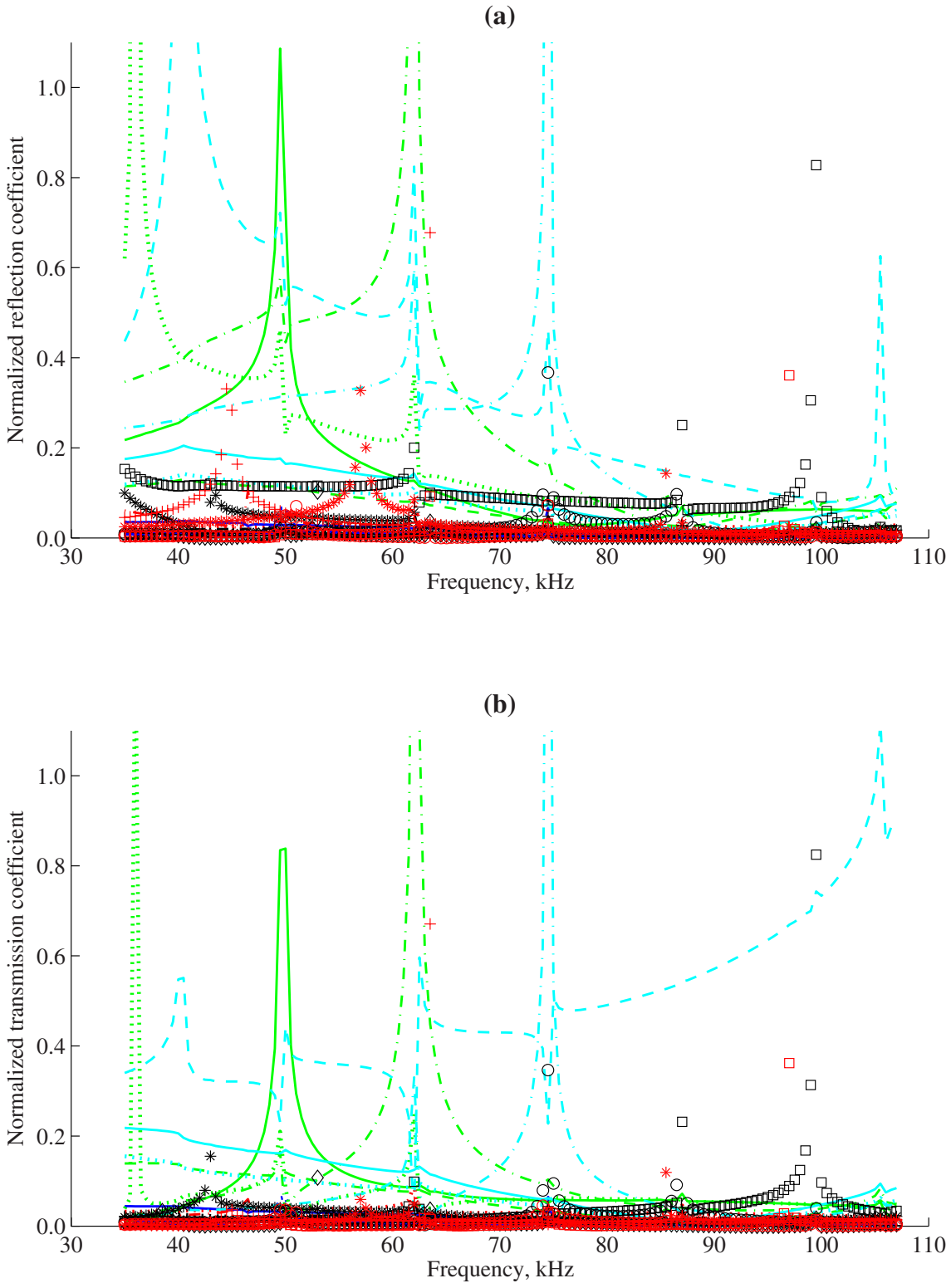

Figure I.48. Normalized reflection and transmission coefficients for the nonaxisymmetric notch and the incident F(5,3) mode.

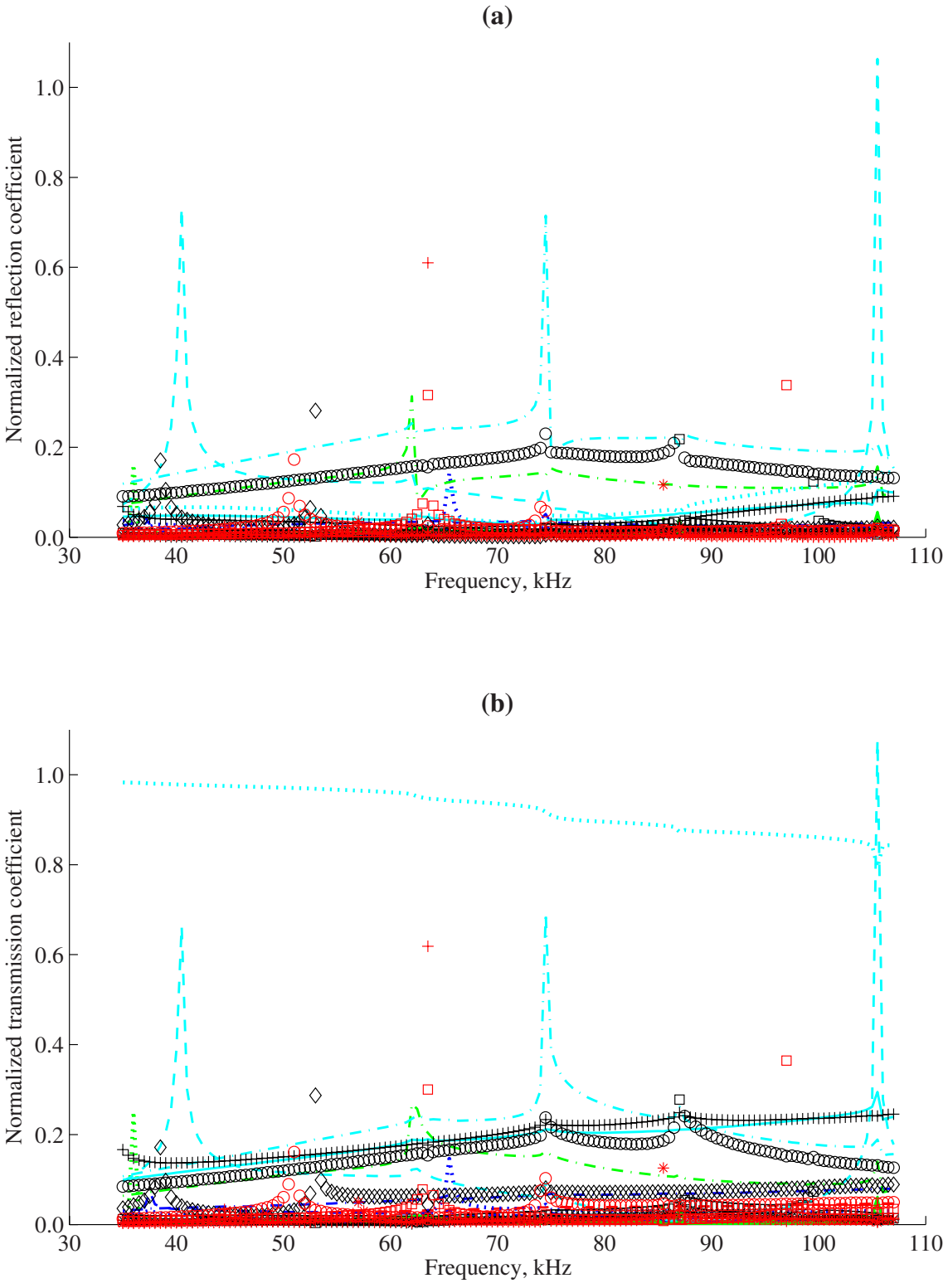

Figure I.49. Normalized reflection and transmission coefficients for the nonaxisymmetric notch and the incident F(6,1) mode.

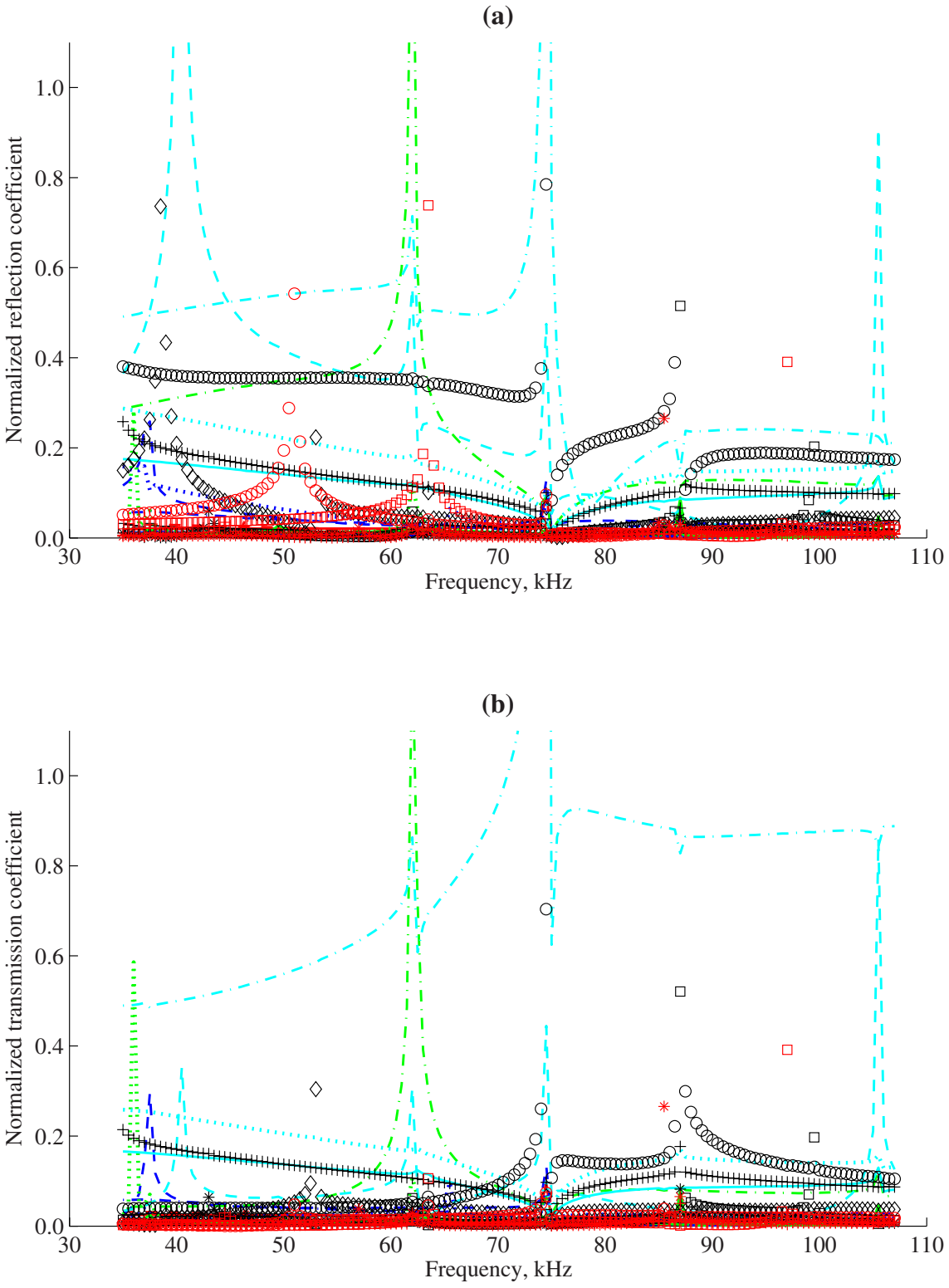

Figure I.50. Normalized reflection and transmission coefficients for the nonaxisymmetric notch and the incident F(6,2) mode.

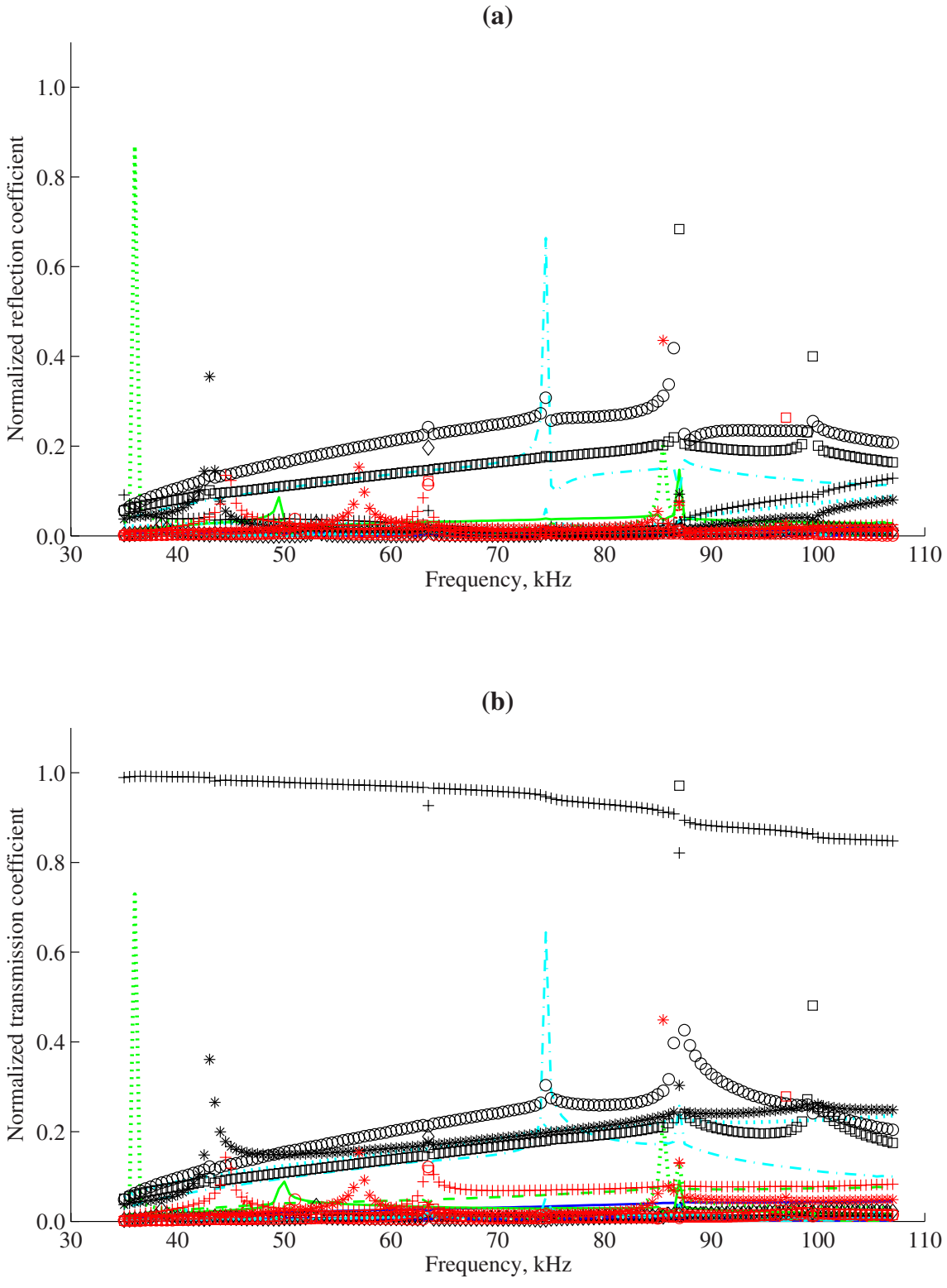

Figure I.51. Normalized reflection and transmission coefficients for the nonaxisymmetric notch and the incident F(7,1) mode.

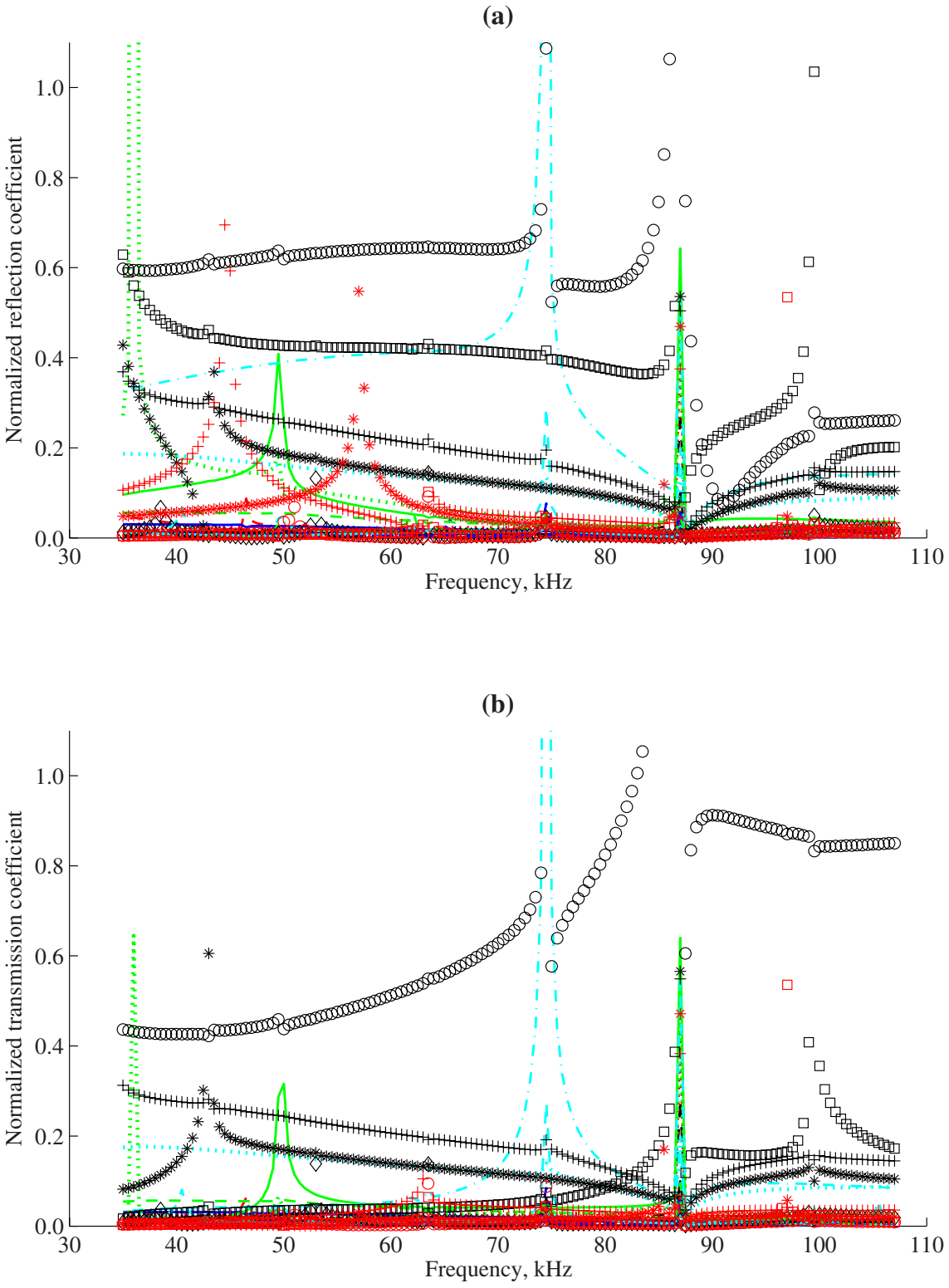

Figure I.52. Normalized reflection and transmission coefficients for the nonaxisymmetric notch and the incident F(7,2) mode.

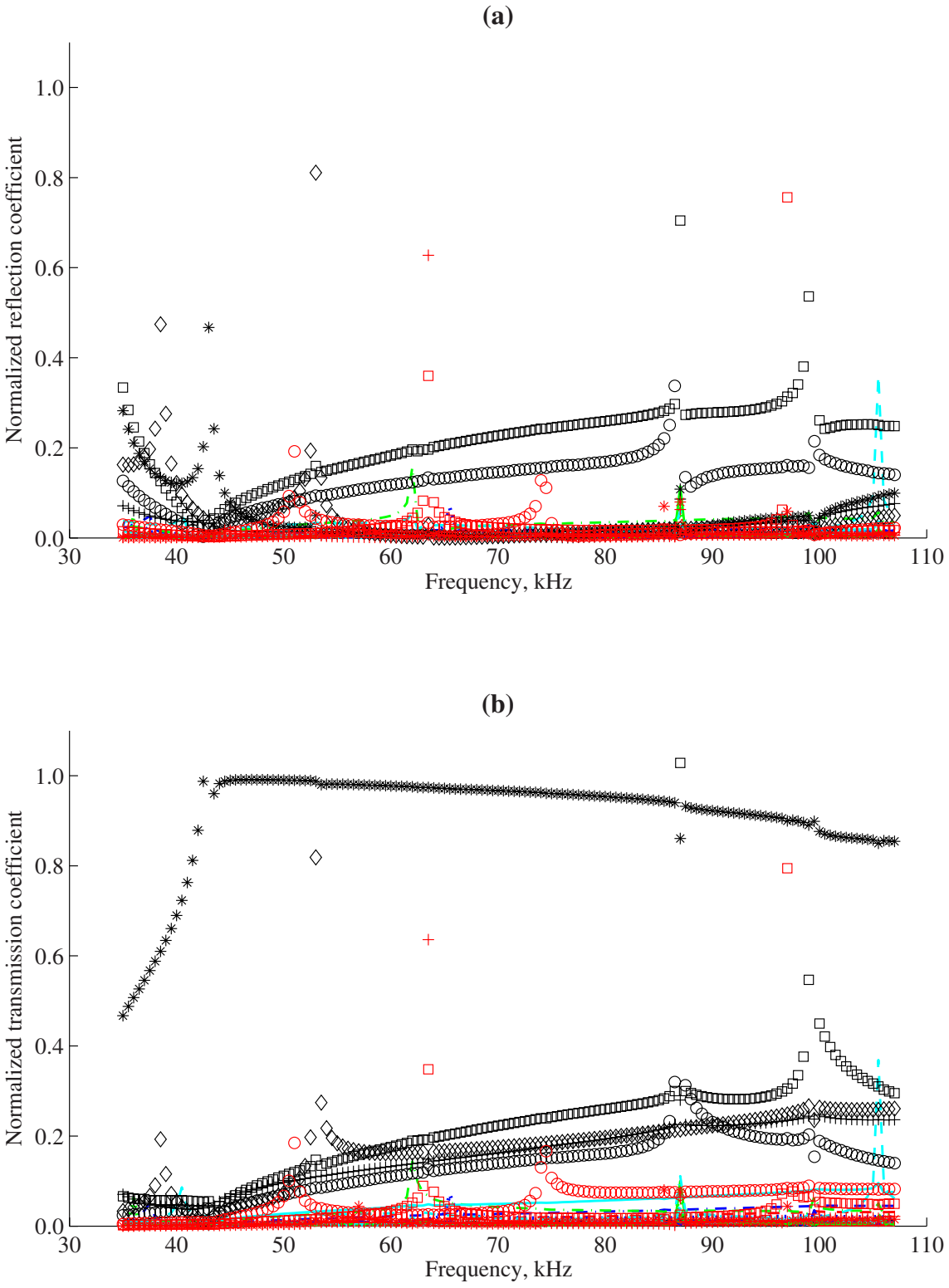

Figure I.53. Normalized reflection and transmission coefficients for the nonaxisymmetric notch and the incident F(8,1) mode.

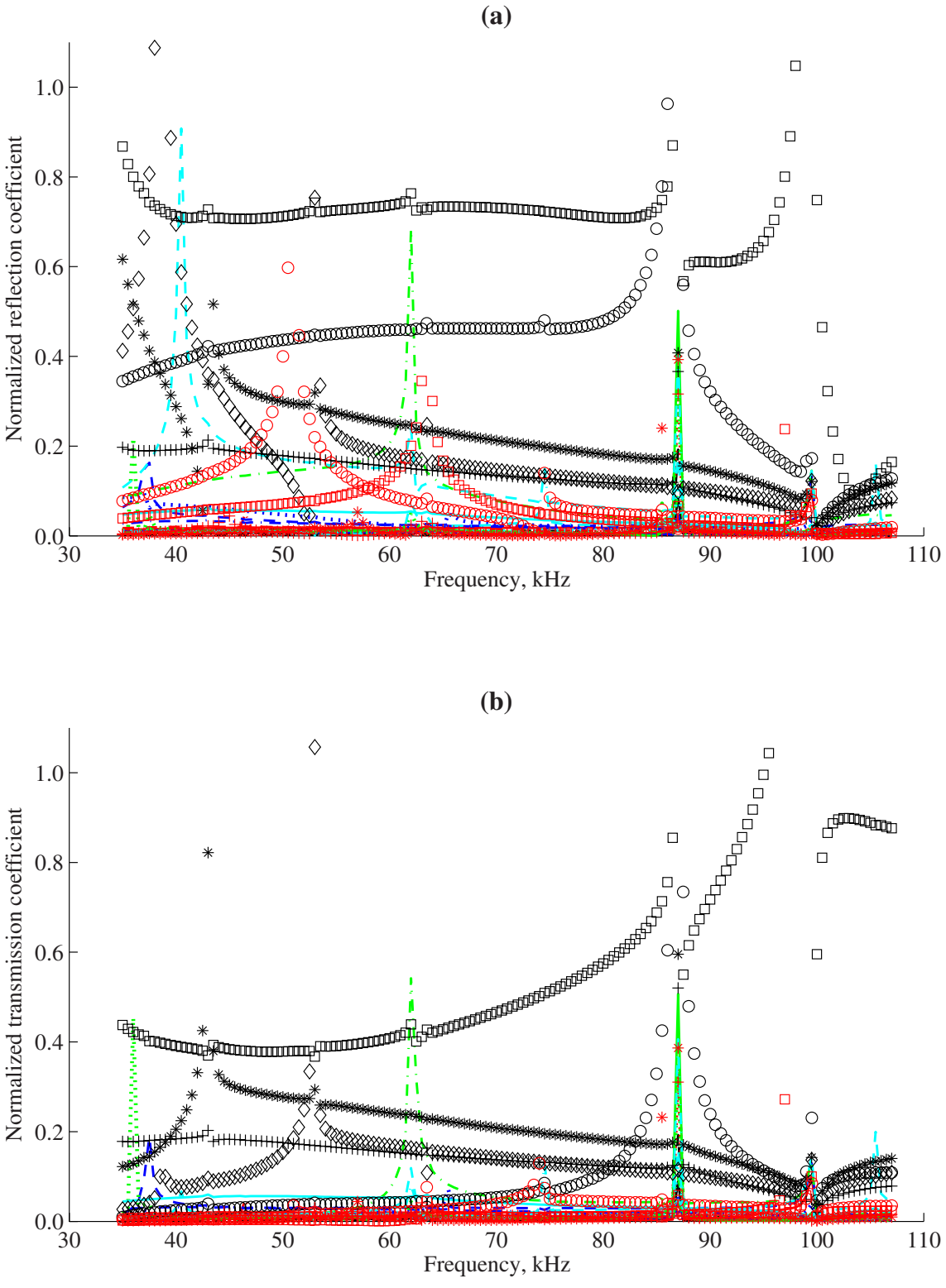

Figure I.54. Normalized reflection and transmission coefficients for the nonaxisymmetric notch and the incident F(8,2) mode.

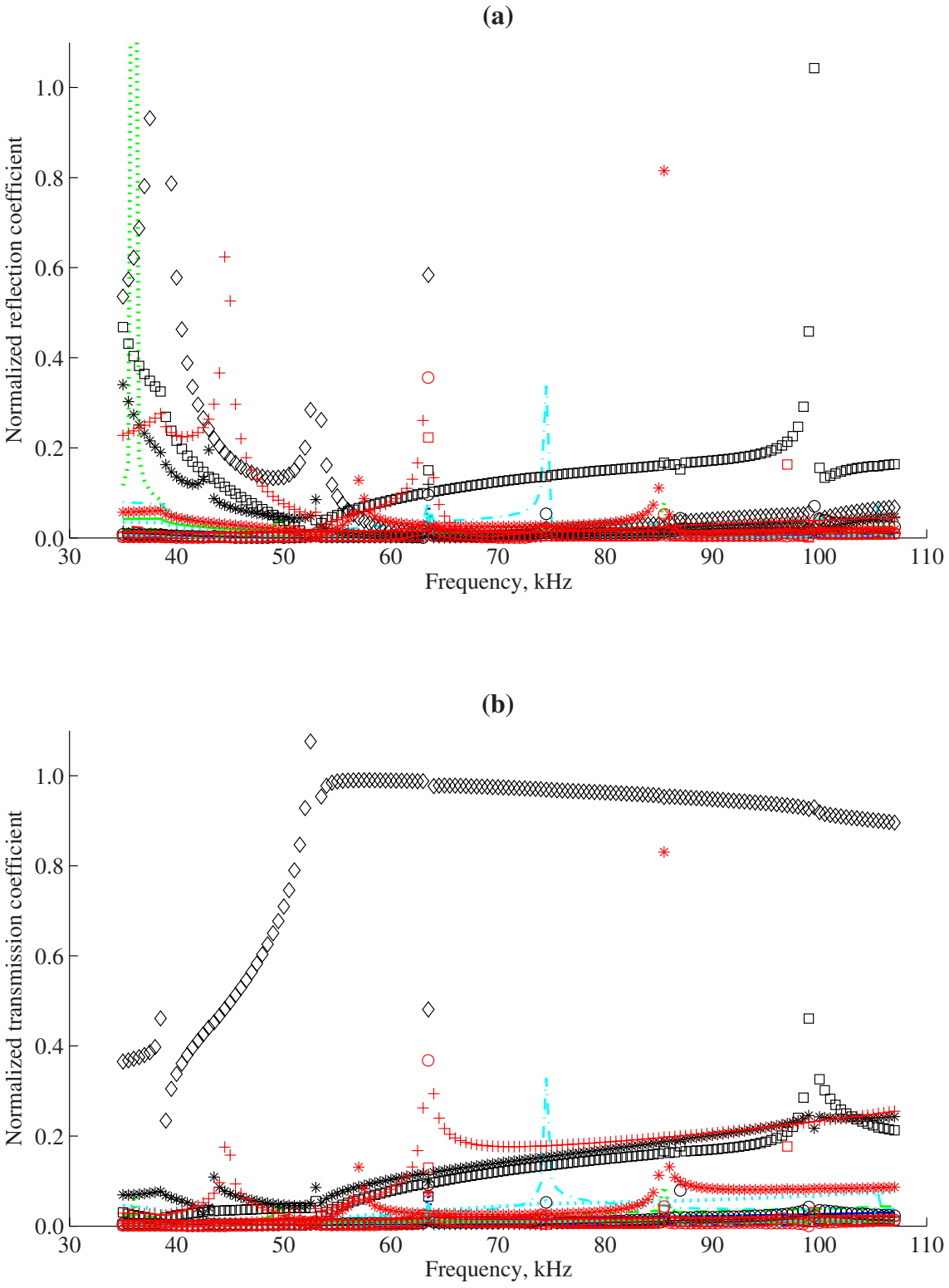

Figure I.55. Normalized reflection and transmission coefficients for the nonaxisymmetric notch and the incident F(9,1) mode.

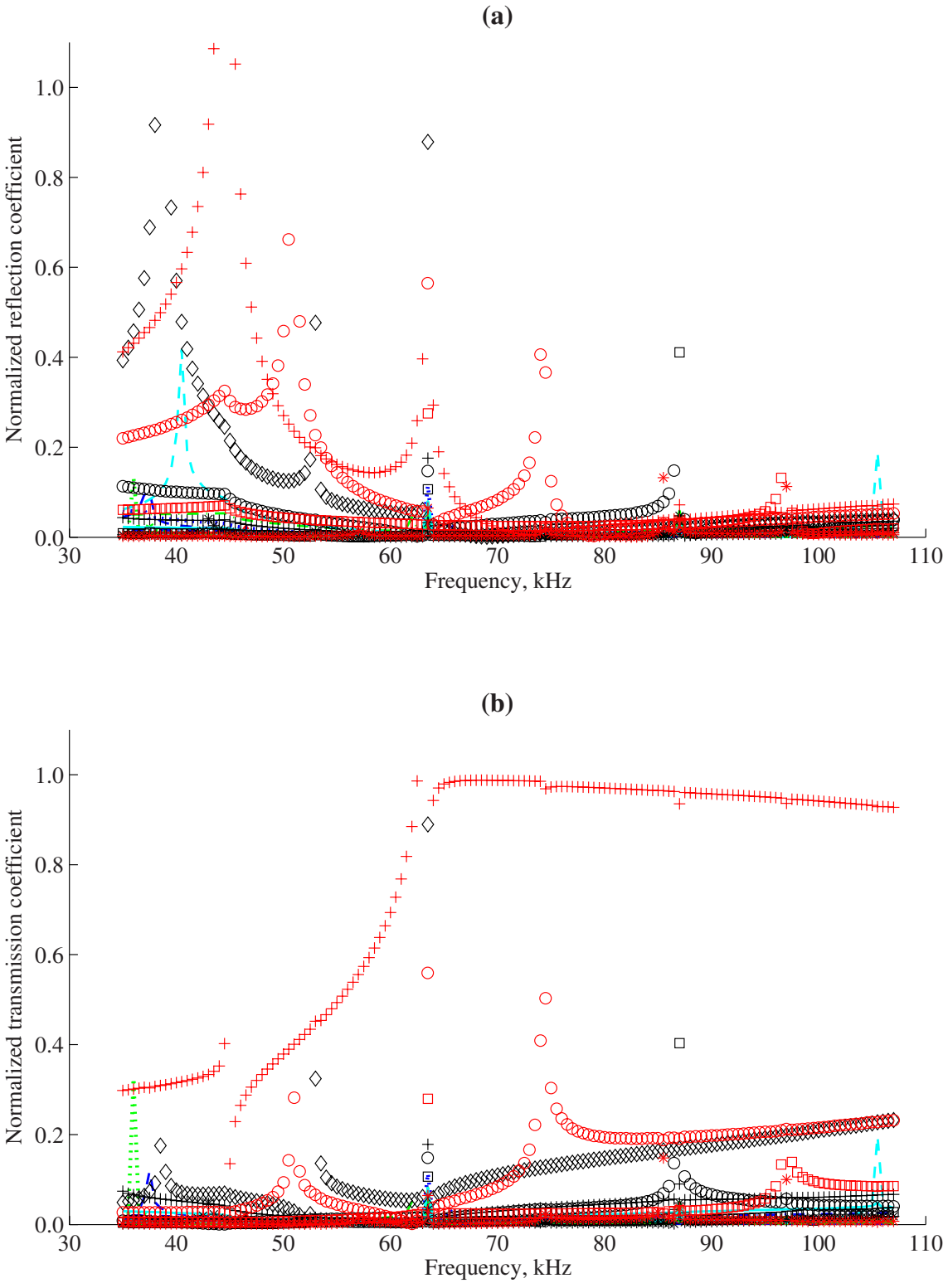

Figure I.56. Normalized reflection and transmission coefficients for the nonaxisymmetric notch and the incident F(10,1) mode.

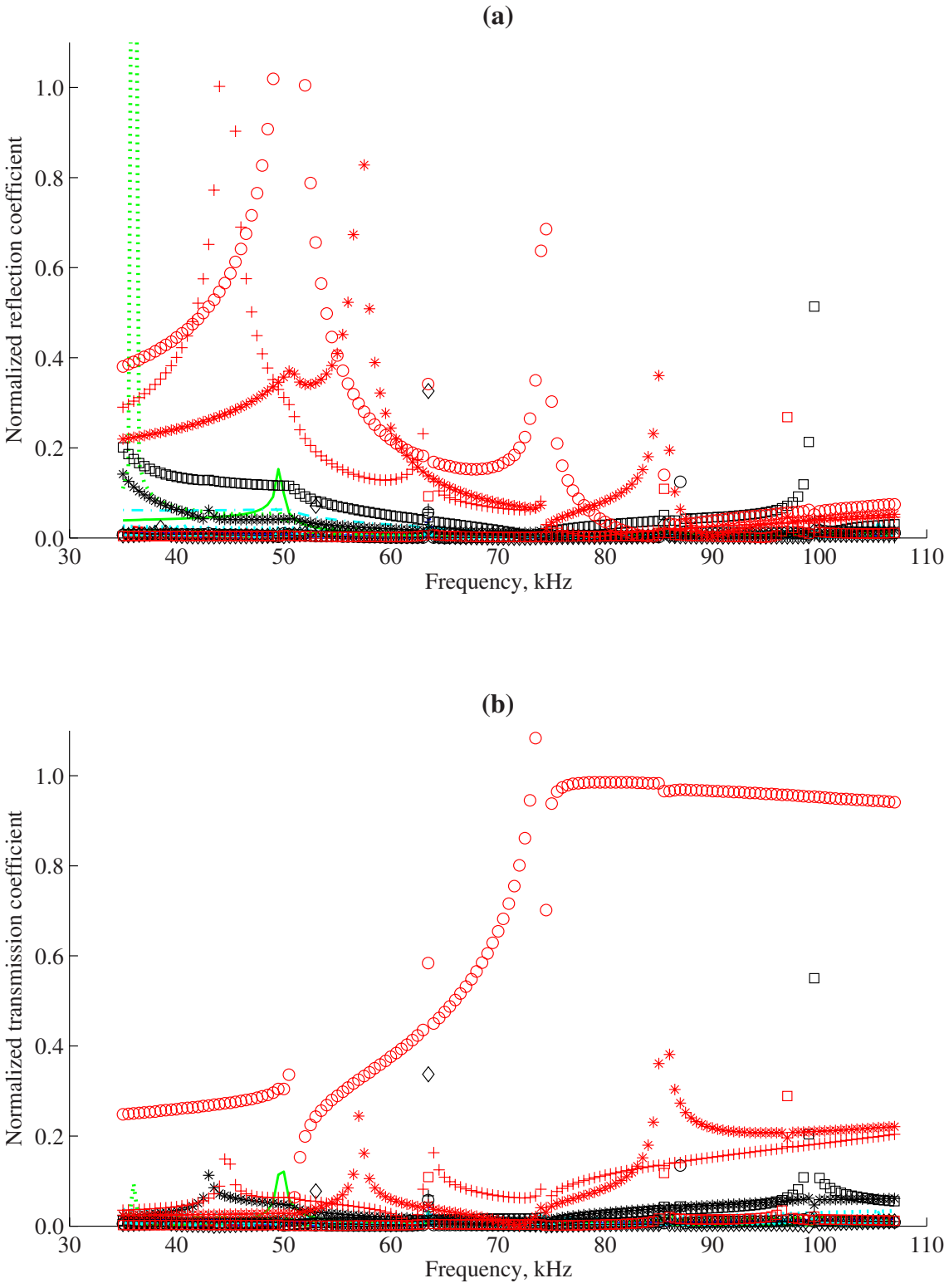

Figure I.57. Normalized reflection and transmission coefficients for the nonaxisymmetric notch and the incident F(11,1) mode.

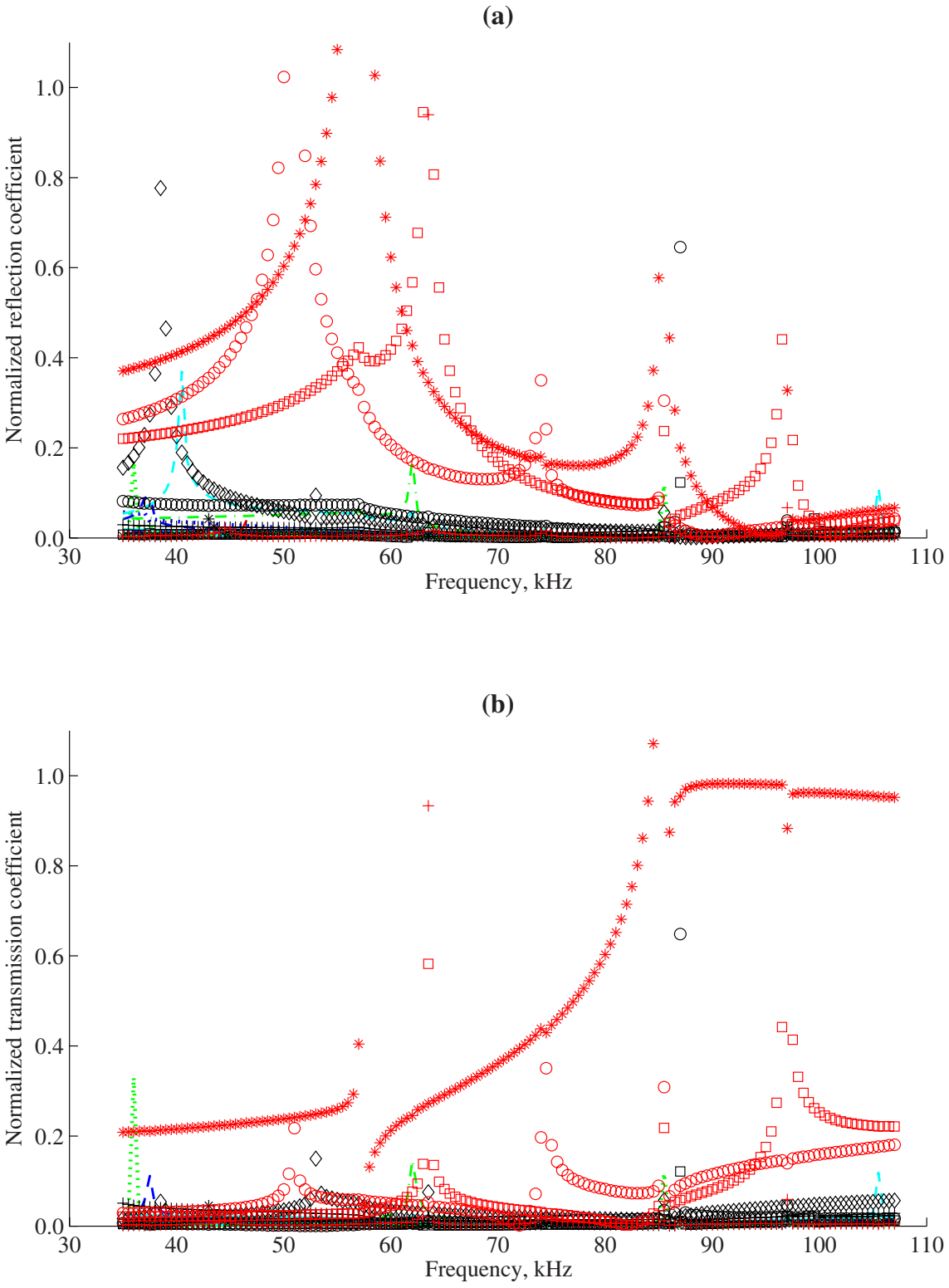

Figure I.58. Normalized reflection and transmission coefficients for the nonaxisymmetric notch and the incident F(12,1) mode.

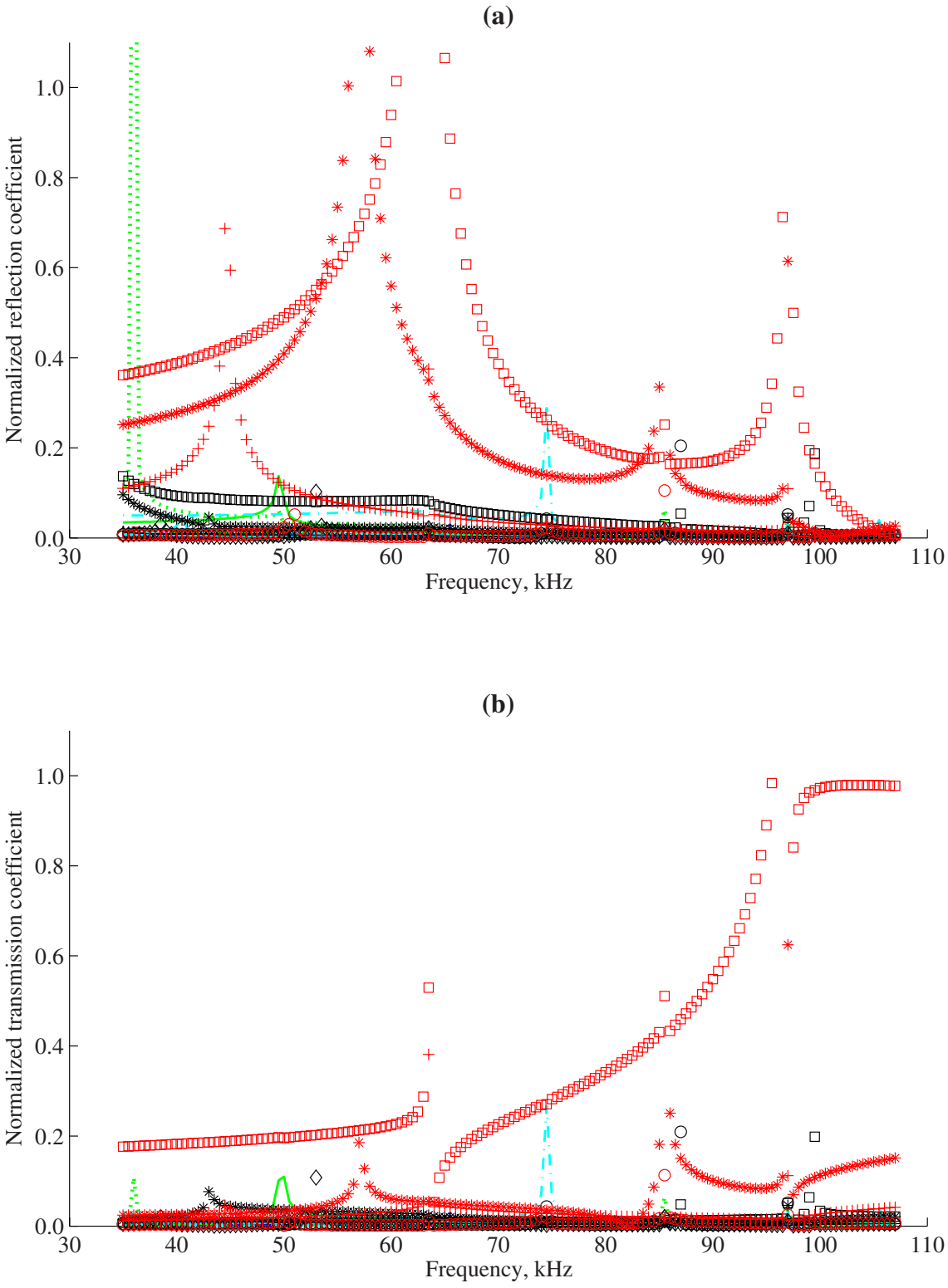

Figure I.59. Normalized reflection and transmission coefficients for the nonaxisymmetric notch and the incident F(13,1) mode.

APPENDIX J

THREE-DIMENSIONAL FINITE ELEMENT MODELLING

J.1 Introduction

The approximate displacement field of a three-dimensional finite element volume is written in this appendix in terms of interpolation functions and a nodal displacement vector. The strain-displacement matrices are introduced to describe the strain and stress fields in terms of the approximate displacement field. Then approximate equations of motion are obtained for no material damping by applying Hamilton's principle to the appropriate functional for complex displacement fields.

J.2 Approximate Displacement Field

The displacement field in the finite element region is approximated first as

$$\mathbf{u}(r,\theta,z,t) = \boldsymbol{\mathcal{N}}(r,\theta,z)\mathrm{e}^{-\mathrm{j}\omega t}\mathbf{U}, \tag{J.2.1}$$

where

$$\boldsymbol{\mathcal{N}}(r,\theta,z) = \begin{bmatrix} \mathbf{N}(r,\theta,z) & \mathbf{0} & \mathbf{0} \\ \mathbf{0} & \mathbf{N}(r,\theta,z) & \mathbf{0} \\ \mathbf{0} & \mathbf{0} & \mathbf{N}(r,\theta,z) \end{bmatrix}. \tag{J.2.2}$$

The $\mathbf{N}$ represent the assembled interpolation functions over the finite element region and $\mathbf{U}$ is the corresponding array of nodal displacements. A time, t, harmonic excitation and displacement response, both having circular frequency ω, have been assumed implicitly in equation (J.2.1). The $\mathbf{N}$ is obtained by a conventional finite assembly process over all

elements. See, for example, [107]. The **U** can be represented, as in Appendix B, by

$$\mathbf{U}_n = \left[\begin{array}{ccc} \mathcal{U} & \mathcal{V} & \mathcal{W} \end{array} \right]^{\mathrm{T}}, \tag{J.2.3}$$

where $\mathcal{U}$, $\mathcal{V}$, and $\mathcal{W}$ are arrays containing the radial, circumferential, and axial nodal displacements, respectively. Isoparametric finite elements are utilized. The interpolation functions, on the other hand, are quadratic Lagrange polynomials. A representative element is shown in Figure J.1 with an illustration of the numbering of the finite element's nodes. Global coordinates, (r, θ, z), are used in Figure J.1 (a), while local coordinates (ζ, η, ξ) are illustrated in Figure J.1 (b).

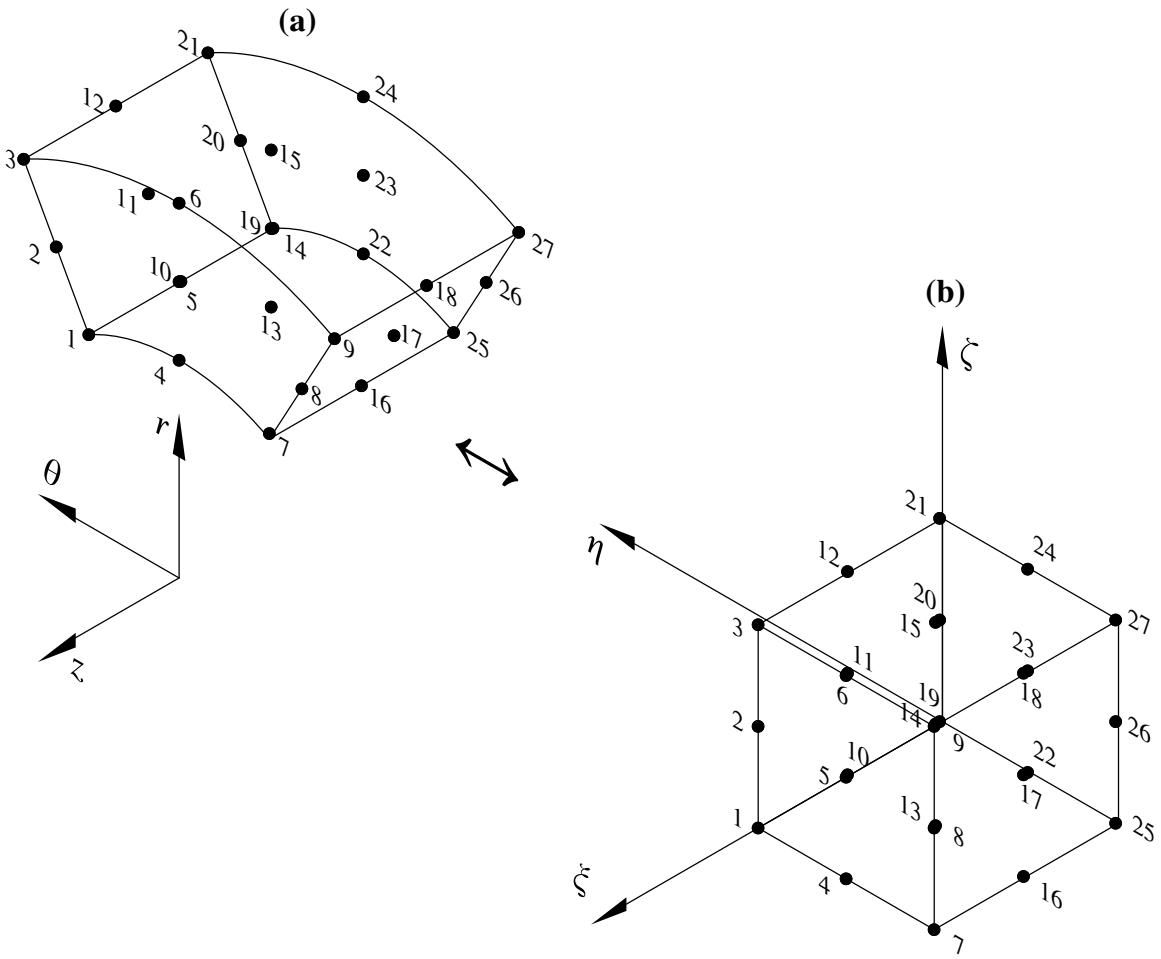

Figure J.1. Showing a representative isoparametric, three-dimensional finite element's nodal numbering in (a) global, and (b) local coordinate frames.

A slightly different approach from the one taken for axisymmetric scatterers is employed. No restrictions[1] are placed on the finite element's nodal coordinates. The shape functions are known immediately from Lagrange's formula [107]. The individual matrix elements of the shape function vector, **n**, used in any finite element can be expressed as

$$n_{1,1} = \frac{1}{8}\xi(\xi+1)\eta(\eta+1)\zeta(\zeta-1), \tag{J.2.4.i}$$

$$n_{1,2} = -\frac{1}{4}\xi(\xi+1)\eta(\eta+1)\left(\zeta^2-1\right), \tag{J.2.4.ii}$$

$$n_{1,3} = \frac{1}{8}\xi(\xi+1)\eta(\eta+1)\zeta(\zeta+1), \tag{J.2.4.iii}$$

$$n_{1,4} = -\frac{1}{4}\xi(\xi+1)\zeta(\zeta-1)\left(\eta^2-1\right), \tag{J.2.4.iv}$$

$$n_{1,5} = \frac{1}{2}\xi(\xi+1)\left(\eta^2-1\right)\left(\zeta^2-1\right), \tag{J.2.4.v}$$

$$n_{1,6} = -\frac{1}{4}\xi(\xi+1)\zeta(\zeta+1)\left(\eta^2-1\right), \tag{J.2.4.vi}$$

$$n_{1,7} = \frac{1}{8}\xi(\xi+1)\eta(\eta-1)\zeta(\zeta-1), \tag{J.2.4.vii}$$

$$n_{1,8} = -\frac{1}{4}\xi(\xi+1)\eta(\eta-1)\left(\zeta^2-1\right), \tag{J.2.4.viii}$$

$$n_{1,9} = \frac{1}{8}\xi(\xi+1)\eta(\eta-1)\zeta(\zeta+1), \tag{J.2.4.ix}$$

$$n_{1,10} = -\frac{1}{4}\eta(\eta+1)\zeta(\zeta-1)\left(\xi^2-1\right), \tag{J.2.4.x}$$

$$n_{1,11} = \frac{1}{2}\eta(\eta+1)\left(\xi^2-1\right)\left(\zeta^2-1\right), \tag{J.2.4.xi}$$

$$n_{1,12} = -\frac{1}{4}\eta(\eta+1)\zeta(\zeta+1)\left(\xi^2-1\right), \tag{J.2.4.xii}$$

$$n_{1,13} = \frac{1}{2}\zeta(\zeta-1)\left(\xi^2-1\right)\left(\eta^2-1\right), \tag{J.2.4.xiii}$$

$$n_{1,14} = -\left(\xi^2-1\right)\left(\eta^2-1\right)\left(\zeta^2-1\right), \tag{J.2.4.xiv}$$

$$n_{1,15} = \frac{1}{2}\zeta(\zeta+1)\left(\xi^2-1\right)\left(\eta^2-1\right), \tag{J.2.4.xv}$$

$$n_{1,16} = -\frac{1}{4}\eta(\eta-1)\zeta(\zeta-1)\left(\xi^2-1\right), \tag{J.2.4.xvi}$$

$$n_{1,17} = \frac{1}{2}\eta(\eta-1)\left(\xi^2-1\right)\left(\zeta^2-1\right), \tag{J.2.4.xvii}$$

[1] It is assumed that the finite elements are not "badly shaped," possess a right handed coordinate system, and have a Jacobian which is defined over the finite element's entire volume and has a positive determinant. See also [107].

$$n_{1,18} = -\frac{1}{4}\eta(\eta-1)\zeta(\zeta+1)\left(\xi^2-1\right), \tag{J.2.4.xviii}$$

$$n_{1,19} = \frac{1}{8}\xi(\xi-1)\eta(\eta+1)\zeta(\zeta-1), \tag{J.2.4.xix}$$

$$n_{1,20} = -\frac{1}{4}\xi(\xi-1)\eta(\eta+1)\left(\zeta^2-1\right), \tag{J.2.4.xx}$$

$$n_{1,21} = \frac{1}{8}\xi(\xi-1)\eta(\eta+1)\zeta(\zeta+1), \tag{J.2.4.xxi}$$

$$n_{1,22} = -\frac{1}{4}\xi(\xi-1)\zeta(\zeta-1)\left(\eta^2-1\right), \tag{J.2.4.xxii}$$

$$n_{1,23} = \frac{1}{2}\xi(\xi-1)\left(\eta^2-1\right)\left(\zeta^2-1\right), \tag{J.2.4.xxiii}$$

$$n_{1,24} = -\frac{1}{4}\xi(\xi-1)\zeta(\zeta+1)\left(\eta^2-1\right), \tag{J.2.4.xxiv}$$

$$n_{1,25} = \frac{1}{8}\xi(\xi-1)\eta(\eta-1)\zeta(\zeta-1), \tag{J.2.4.xxv}$$

$$n_{1,26} = -\frac{1}{4}\xi(\xi-1)\eta(\eta-1)\left(\zeta^2-1\right), \tag{J.2.4.xxvi}$$

and

$$n_{1,27} = \frac{1}{8}\xi(\xi-1)\eta(\eta-1)\zeta(\zeta+1). \tag{J.2.4.xxvii}$$

The radial, r, circumferential, θ, and axial, z, coordinates in a finite element are related to the interpolation functions by

$$r = \mathbf{n}\mathbf{r}_c, \tag{J.2.5a}$$

$$\theta = \mathbf{n}\boldsymbol{\theta}_c, \tag{J.2.5b}$$

and

$$z = \mathbf{n}\mathbf{z}_c, \tag{J.2.5c}$$

where $\mathbf{r}_c$, $\boldsymbol{\theta}_c$, and $\mathbf{z}_c$ are vectors containing the finite element's nodal coordinates.

J.3 Approximate Strain and Stress Fields

The following strain-displacement transformation matrix, **B** is introduced:

$$\mathbf{B} = \begin{bmatrix} 0 & 0 & 0 \\ 1/r & 0 & 0 \\ 0 & 0 & 0 \\ 0 & -1/r & 0 \\ 0 & 0 & 0 \\ 0 & 0 & 0 \end{bmatrix} \boldsymbol{\mathcal{N}} + \begin{bmatrix} 1 & 0 & 0 & 0 & 0 & 0 & 0 & 0 & 0 \\ 0 & 0 & 0 & 0 & 1/r & 0 & 0 & 0 & 0 \\ 0 & 0 & 0 & 0 & 0 & 0 & 0 & 0 & 1 \\ 0 & 1/r & 0 & 1 & 0 & 0 & 0 & 0 & 0 \\ 0 & 0 & 1 & 0 & 0 & 0 & 1 & 0 & 0 \\ 0 & 0 & 0 & 0 & 0 & 1 & 0 & 1/r & 0 \end{bmatrix} \begin{bmatrix} \boldsymbol{\Gamma} & \mathbf{0} & \mathbf{0} \\ \mathbf{0} & \boldsymbol{\Gamma} & \mathbf{0} \\ \mathbf{0} & \mathbf{0} & \boldsymbol{\Gamma} \end{bmatrix} \begin{Bmatrix} \mathbf{N}_{,\zeta} \\ \mathbf{N}_{,\eta} \\ \mathbf{N}_{,\xi} \\ \mathbf{N}_{,\zeta} \\ \mathbf{N}_{,\eta} \\ \mathbf{N}_{,\xi} \\ \mathbf{N}_{,\zeta} \\ \mathbf{N}_{,\eta} \\ \mathbf{N}_{,\xi} \end{Bmatrix} \tag{J.3.1}$$

to simplify the computation of the approximate strain field in the entire three-dimensional finite element volume. The $\boldsymbol{\Gamma}$ in equation (J.3.1) is the matrix inverse of the Jacobian matrix, **J**, which is given by

$$\mathbf{J} = \begin{bmatrix} \frac{\partial r}{\partial \zeta} & \frac{\partial \theta}{\partial \zeta} & \frac{\partial z}{\partial \zeta} \\ \frac{\partial r}{\partial \eta} & \frac{\partial \theta}{\partial \eta} & \frac{\partial z}{\partial \eta} \\ \frac{\partial r}{\partial \xi} & \frac{\partial \theta}{\partial \xi} & \frac{\partial z}{\partial \xi} \end{bmatrix}. \tag{J.3.2}$$

Then the strain and stress tensors in the entire three-dimensional finite element volume can be expressed in vector form as

$$\boldsymbol{\varepsilon} = \mathbf{BU} \tag{J.3.3a}$$

and

$$\boldsymbol{\sigma} = \mathbf{DBU}, \tag{J.3.3b}$$

respectively. The **D** is a symmetric matrix composed of the isotropic, elastic moduli given in equation (B.3.3).

J.4 Application of Hamilton's Principle

Hamilton's principle can be expressed for the entire finite element volume in the form used in equation (B.4.1). Moreover, the kinetic and total potential energies are given still by equation (B.4.2). By following a procedure similar to the one used in Section B.4 to derive equation (B.4.10) from equation (B.4.1), the approximate equations of motions of the complete finite element volume can be shown to be

$$\left(\mathbf{K}_{\mathrm{I}} - \omega^2 \mathbf{M}_{\mathrm{I}}\right)\mathbf{U} = \mathbf{F}. \tag{J.4.1}$$

Equation (J.4.1) is the same as equation (4.2.1) when the $\mathbf{U}$ and $\mathbf{F}$ in the former equation are replaced by $\mathbf{q}$ and $\mathbf{P}$, respectively. The $\mathbf{K}_{\mathrm{I}}$ and $\mathbf{M}_{\mathrm{I}}$ can be computed by evaluating the integrals

$$\mathbf{K}_{\mathrm{I}} = \int_{-z_{\mathrm{FE}/2}}^{0} \int_{-\pi}^{\pi} \int_{r_i}^{r_o} \widetilde{\mathbf{B}}^{\mathrm{T}} \mathbf{D} \mathbf{B} r \mathrm{d}r \mathrm{d}\theta \mathrm{d}z \tag{J.4.2a}$$

and

$$\mathbf{M}_{\mathrm{I}} = \int_{z_{\mathrm{FE}/2}}^{0} \int_{-\pi}^{\pi} \int_{r_i}^{r_o} \rho \widetilde{\boldsymbol{\mathcal{N}}}^{\mathrm{T}} \boldsymbol{\mathcal{N}} r \mathrm{d}r \mathrm{d}\theta \mathrm{d}z. \tag{J.4.2b}$$

The $\mathbf{F}$ in equation (J.4.1) can be found by following the procedure given in [107]. This procedure leads to the integral

$$\mathbf{F} = \int_{-\pi}^{\pi} \int_{r_i}^{r_o} \widetilde{\boldsymbol{\mathcal{N}}}^{\mathrm{T}} \begin{Bmatrix} \tau_{rz} \\ \tau_{\theta z} \\ \sigma_{zz} \end{Bmatrix} r \mathrm{d}r \mathrm{d}\theta \tag{J.4.3}$$

which gives the desired consistent force vector. The $\widetilde{\boldsymbol{\mathcal{N}}}$ in equation (J.4.3) is evaluated on $z = 0$. Moreover, τ_{rz}, $\tau_{\theta z}$, and σ_{zz} are stresses from the wavefunction expansion that act on $z = 0$ because external stresses are applied to the finite element region only on this plane. These stresses may be found for a single mode of the wavefunction expansion region by

applying equations (A.3.2) and (A.4.2) of Appendix A, for that mode, to the displacement field given by equation (B.2.1). The procedure is the same as that described in Section F.4. Collecting the resulting column vectors for all the scattered modes give the matrix $\mathbf{F}_{\text{scat}}$ used in Section 4.3.4. Similarly, $\mathbf{f}^{\text{in}}$ is a single column vector found by applying equation (F.4.4) for a single incident mode.

J.5 Note on Integrating the Finite Element Matrices

The matrices given in equation (J.4.2) are evaluated in practice by "assembling" element matrices. The element matrices take the same form as those used in equation (J.4.2) but have integration limits that span only each finite element's dimensions. As in Section F.5, the integrals of equation (J.4.2) are transformed into functions of only the isoparametric coordinates by using the change of variables theorem from multivariable calculus. The result, for a single element, is

$$\mathbf{K}_{\text{e}} = \int_{-1}^{1}\int_{-1}^{1}\int_{-1}^{-1} \widetilde{\mathbf{B}}^{\text{T}}\mathbf{DBnr}_{\text{c}}\,|\mathbf{J}|\,\text{d}\zeta\text{d}\eta\text{d}\xi \tag{J.5.1a}$$

and

$$\mathbf{M}_{\text{e}} = \int_{-1}^{1}\int_{-1}^{1}\int_{-1}^{-1} \rho \begin{bmatrix} \mathbf{n} & \mathbf{0} & \mathbf{0} \\ \mathbf{0} & \mathbf{n} & \mathbf{0} \\ \mathbf{0} & \mathbf{0} & \mathbf{n} \end{bmatrix}^{\text{T}} \begin{bmatrix} \mathbf{n} & \mathbf{0} & \mathbf{0} \\ \mathbf{0} & \mathbf{n} & \mathbf{0} \\ \mathbf{0} & \mathbf{0} & \mathbf{n} \end{bmatrix} \mathbf{nr}_{\text{c}}\,|\mathbf{J}|\,\text{d}\zeta\text{d}\eta\text{d}\xi, \tag{J.5.1b}$$

where the strain-displacement transformation matrix, $\mathbf{B}$, appearing in equation (J.5.1a) *applies only over a single finite element*. Equation (J.5.1) also makes use of equation (J.2.5a). Evaluating the integrals in equation (J.5.1) in closed form is onerous because the lack of restrictions on the finite element's nodal coordinates greatly complicates the integrands. Numerical, Gaussian integration [107] is used, therefore, to compute approximations for the matrices described in equation (J.5.1). However, the closed form expressions used in Section F.4 for the consistent force matrices are retained. This is because the only modification

required to extend the axisymmetric forces to three-dimensions is that the corresponding integration in the circumferential direction needs to be over solely the three-dimensional finite element's face on the plane $z = 0$ rather than from $-\pi$ to π.

Appendix K

Code Listings and Sketches Implementing hybrid SAFE for Three-dimensional Scatterers

K.1 Overview

This appendix contains annotated code listings and "sketches," in which sections of code are removed for brevity, of illustrative Maple™ and MATLAB® scripts and functions used to implement the hybrid-SAFE method. This method has been described previously in Section 4.3 of Chapter 4 and Appendix J for three-dimensional scatterers. The code listings and sketches demonstrate a work flow that allows a partial automation of writing finite element programs by taking advantage of readily available commercial tools. Moreover, several MATLAB® "best practices," such as preallocating memory for arrays and "vectorizing code" (rather than using a loop) are illustrated as a matter of course in the numerical implementations. Furthermore, the MATLAB® programs in this appendix have been partially "parallelized" (i.e., they run on several computing cores simultaneously). Lines 87, 158, and 109 and 205 of Listings K.2, K.3, and K.4 show the start of the sections of code that run in parallel. A discussion of the effectiveness of these efforts is deferred to Appendix L.

K.2 Annotated Code Listings

An annotated Maple™ code listing to evaluate symbolically the Jacobian, strain-displacement operator, shape function, and radial coordinate matrices for the nonaxisymmetric scattering program is provided in Listing K.1. A high level flowchart for this program is given in Figure K.1. Listing K.2, for which a high level flowchart is shown in Figure K.2, is used to numerically evaluate the (finite) element mass and stiffness matrices and assemble

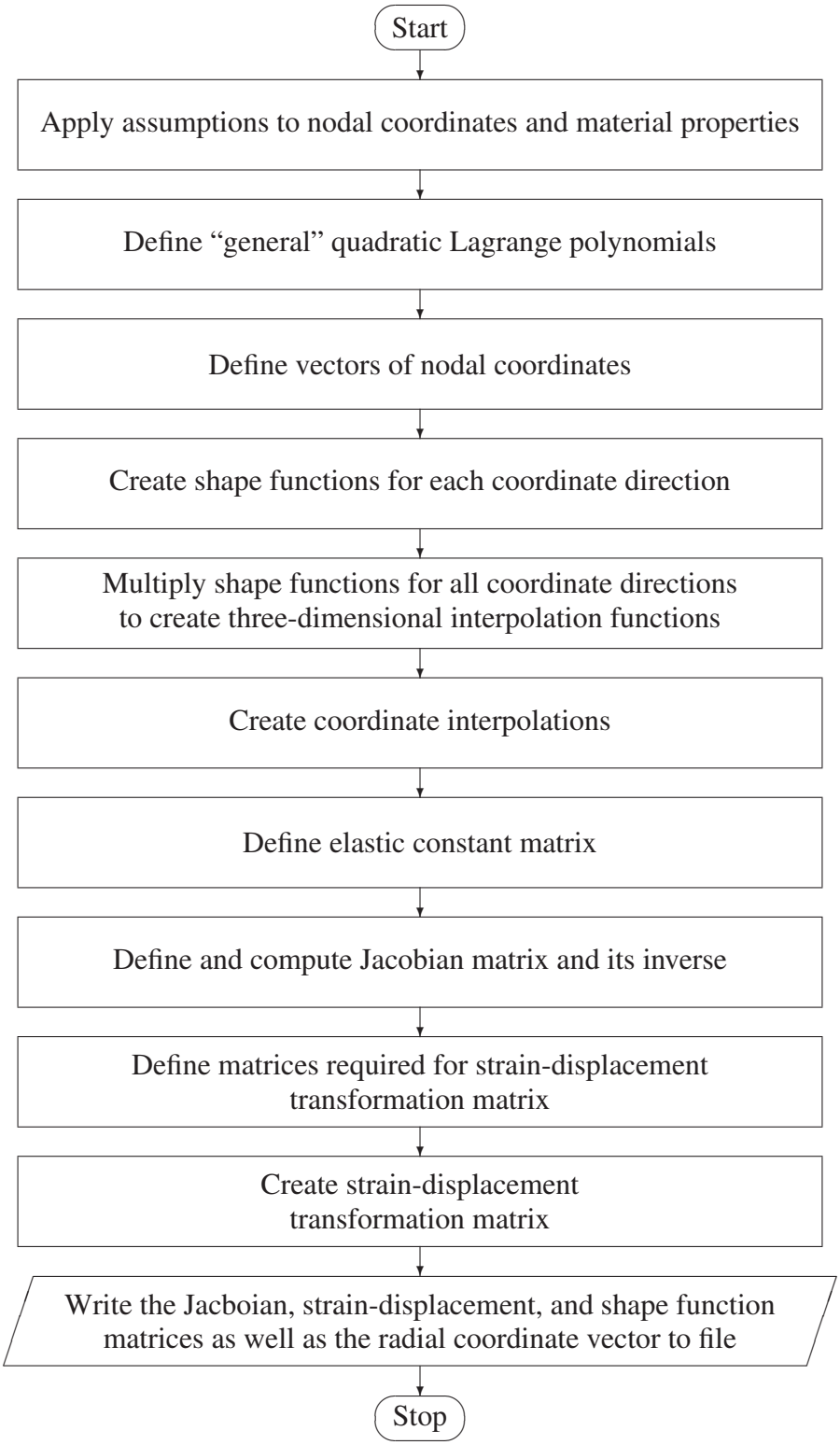

Figure K.1. A high level flowchart for Listing K.1.

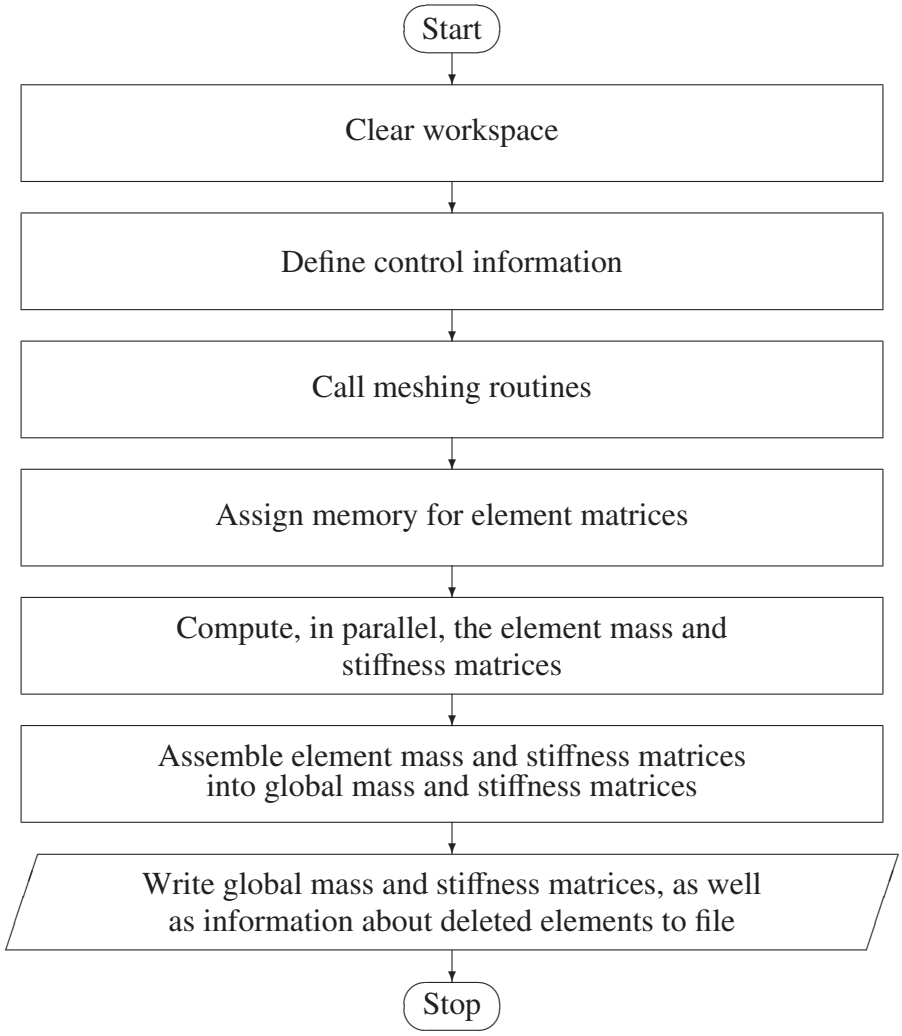

Figure K.2. A high level flowchart for Listing K.2.

them into global mass and stiffness matrices. Listing K.3, on the other hand, is used to condense the internal nodes from the finite element's dynamic stiffness matrix. It is used also to apply the symmetric and antisymmetric boundary conditions on the assumed plane of symmetry. A high level flow chart for this listing appears in Figure K.3. Listing K.4 is the last listing given in this appendix. It is used to interface the finite element volume to the wave function expansion regions by applying continuity conditions on the plane $z = 0$. A flow chart depicting the most important elements of the program appears in Figure K.4.

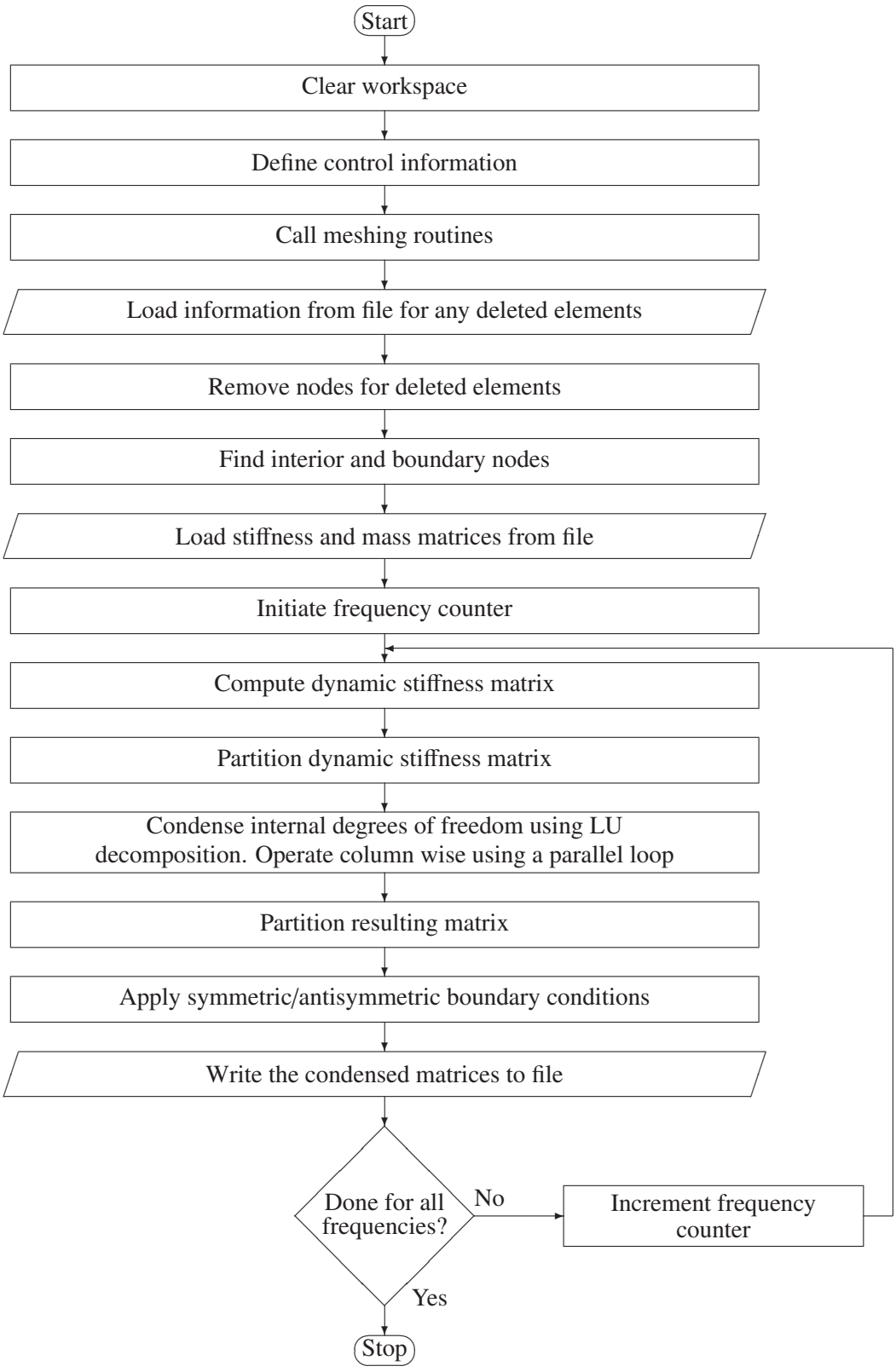

Figure K.3. A high level flowchart for Listing K.3.

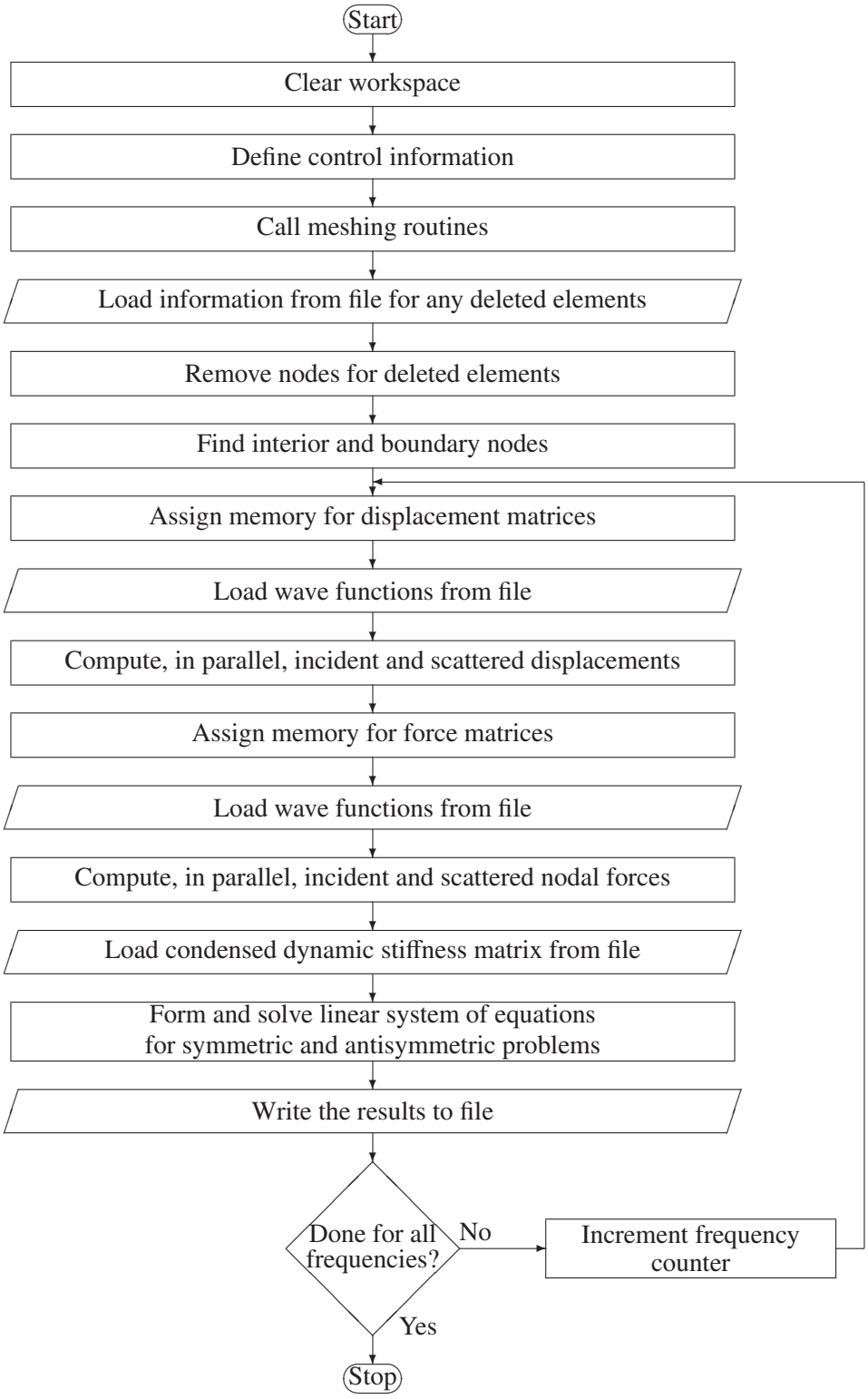

Figure K.4. A high level flowchart for Listing K.4.

Listing K.1. Maple™ code to derive the Jacobian, strain-displacement operator, shape function, and radial coordinate matrices for the nonaxisymmetric scattering program.

```
#Add assumptions to radial coordinates
assume(r1>0);
assume(r2>0);
assume(r3>0);
assume(r4>0);
assume(r5>0);
assume(r6>0);
assume(r7>0);
assume(r8>0);
assume(r9>0);
assume(r10>0);
assume(r11>0);
assume(r12>0);
assume(r13>0);
assume(r14>0);
assume(r15>0);
assume(r16>0);
assume(r17>0);
assume(r18>0);
assume(r19>0);
assume(r20>0);
assume(r21>0);
assume(r22>0);
assume(r23>0);
assume(r24>0);
assume(r25>0);
assume(r26>0);
assume(r27>0);

#Add assumptions to material properties
assume(lambda>=0);
assume(mu>=0);
assume(rho>=0);

#Add assumptions to circumferential coordinates
assume(theta1,real);
assume(theta2,real);
assume(theta3,real);
assume(theta4,real);
assume(theta5,real);
assume(theta6,real);
assume(theta7,real);
assume(theta8,real);
assume(theta9,real);
assume(theta10,real);
assume(theta11,real);
assume(theta12,real);
assume(theta13,real);
assume(theta14,real);
```

(Continued on next page...)

Listing K.1. Maple™ code to derive the Jacobian, strain-displacement operator, shape function, and radial coordinate matrices for the nonaxisymmetric scattering program. (Continued from previous page.)

```
50 assume(theta15,real);
51 assume(theta16,real);
52 assume(theta17,real);
53 assume(theta18,real);
54 assume(theta19,real);
55 assume(theta20,real);
56 assume(theta21,real);
57 assume(theta22,real);
58 assume(theta23,real);
59 assume(theta24,real);
60 assume(theta25,real);
61 assume(theta26,real);
62 assume(theta27,real);
63
64 #Add assumptions to axial coordinates
65 assume(z1,real);
66 assume(z2,real);
67 assume(z3,real);
68 assume(z4,real);
69 assume(z5,real);
70 assume(z6,real);
71 assume(z7,real);
72 assume(z8,real);
73 assume(z9,real);
74 assume(z10,real);
75 assume(z11,real);
76 assume(z12,real);
77 assume(z13,real);
78 assume(z14,real);
79 assume(z15,real);
80 assume(z16,real);
81 assume(z17,real);
82 assume(z18,real);
83 assume(z19,real);
84 assume(z20,real);
85 assume(z21,real);
86 assume(z22,real);
87 assume(z23,real);
88 assume(z24,real);
89 assume(z25,real);
90 assume(z26,real);
91 assume(z27,real);
92
93 #Add assumptions to nondimensional coordinates
94 assume(xi,real);
95 assume(eta,real);
96 assume(phi,real);
```

(Continued on next page...)

Listing K.1. Maple™ code to derive the Jacobian, strain-displacement operator, shape function, and radial coordinate matrices for the nonaxisymmetric scattering program. (Continued from previous page.)

```
#Define general, quadratic Lagrange polynomial
N1:=x*(x-1)/2;
N2:=(x+1)*(x-1)/(-1);
N3:=x*(x+1)/2;

#Define vectors of finite element's nodal coordinates
rc:=Vector[column]([r1,r2,r3,r4,r5,r6,r7,r8,r9,r10,r11,r12,r13,r14,
r15,r16,r17,r18,r19,r20,r21,r22,r23,r24,r25,r26,r27]);

thetac:=Vector[column]([theta1,theta2,theta3,theta4,theta5,theta6,
theta7,theta8,theta9,theta10,theta11,theta12,theta13,theta14,
theta15,theta16,theta17,theta18,theta19,theta20,theta21,theta22,
theta23,theta24,theta25,theta26,theta27]);

zc:=Vector[column]([z1,z2,z3,z4,z5,z6,z7,z8,z9,z10,z11,z12,z13,z14,
z15,z16,z17,z18,z19,z20,z21,z22,z23,z24,z25,z26,z27]);

#Define shape functions in coordinate directions
N1xi:=subs(x=xi,N1);
N2xi:=subs(x=xi,N2);
N3xi:=subs(x=xi,N3);
N1eta:=subs(x=eta,N1);
N2eta:=subs(x=eta,N2);
N3eta:=subs(x=eta,N3);
N1phi:=subs(x=phi,N1);
N2phi:=subs(x=phi,N2);
N3phi:=subs(x=phi,N3);

#Associate shape functions with each nodal coordinate
Nphi:=Vector[row]([N3phi,N3phi,N3phi,N3phi,N3phi,N3phi,N3phi,N3phi,
N3phi,N2phi,N2phi,N2phi,N2phi,N2phi,N2phi,N2phi,N2phi,N2phi,N1phi,
N1phi,N1phi,N1phi,N1phi,N1phi,N1phi,N1phi,N1phi]);

Neta:=Vector[row]([N3eta,N3eta,N3eta,N2eta,N2eta,N2eta,N1eta,N1eta,
N1eta,N3eta,N3eta,N3eta,N2eta,N2eta,N2eta,N1eta,N1eta,N1eta,N3eta,
N3eta,N3eta,N2eta,N2eta,N2eta,N1eta,N1eta,N1eta]);

Nxi:=Vector[row]([N1xi,N2xi,N3xi,N1xi,N2xi,N3xi,N1xi,N2xi,N3xi,
N1xi,N2xi,N3xi,N1xi,N2xi,N3xi,N1xi,N2xi,N3xi,N1xi,N2xi,N3xi,N1xi,
N2xi,N3xi,N1xi,N2xi,N3xi]);

#Combine shape functions
N:=simplify(Nphi*~Neta*~Nxi);

#Define continuous coordinate interpolations
r:=simplify(N.rc);
theta:=simplify(N.thetac);
z:=simplify(N.zc);
```

(Continued on next page...)

Listing K.1. Maple™ code to derive the Jacobian, strain-displacement operator, shape function, and radial coordinate matrices for the nonaxisymmetric scattering program. (Continued from previous page.)

```
#Define matrix of elastic constants
E:=Matrix([[lambda+2*mu,lambda,lambda,0,0,0],
[lambda,lambda+2*mu,lambda,0,0,0],
[lambda,lambda,lambda+2*mu,0,0,0],
[0,0,0,mu,0,0],[0,0,0,0,mu,0],[0,0,0,0,0,mu]]);

#Define Jacobian matrix
J:=Matrix(3);

J[1,1]:=simplify(diff(r,xi));
J[1,2]:=simplify(diff(theta,xi));
J[1,3]:=simplify(diff(z,xi));
J[2,1]:=simplify(diff(r,eta));
J[2,2]:=simplify(diff(theta,eta));
J[2,3]:=simplify(diff(z,eta));
J[3,1]:=simplify(diff(r,phi));
J[3,2]:=simplify(diff(theta,phi));
J[3,3]:=simplify(diff(z,phi));

#Define symbolic inverse of Jacobian matrix
#(numerical values from Jacobian are used
#in the computations)
Gammaa:=Matrix(3,3,symbol=Gamma);

#Get the size of the shape function matrix
tmp:=ArrayTools[Size](N);

#Define shape functions for use in computing strain-displacement
#operators
Nt:=Matrix(3,3*tmp[2]);
Nt[1,1..tmp[2]]:=N;
Nt[2,tmp[2]+1..2*tmp[2]]:=N;
Nt[3,2*tmp[2]+1..3*tmp[2]]:=N;

#Get the size of the inverse of the Jacobian matrix
tmp:=ArrayTools[Size](Gammaa);

#Create a matrix of the inverse of the Jacobian matrix for use
#in computing strain-displacement operators
Gammam:=Matrix(3*tmp[1],3*tmp[2]);

Gammam[1..tmp[1],1..tmp[2]]:=Gammaa;
Gammam[tmp[1]+1..2*tmp[1],tmp[2]+1..2*tmp[2]]:=Gammaa;
Gammam[2*tmp[1]+1..3*tmp[1],2*tmp[2]+1..3*tmp[2]]:=Gammaa;

#Get the size of the shape function matrix
tmp:=ArrayTools[Size](N);
```

(Continued on next page...)

Listing K.1. Maple™ code to derive the Jacobian, strain-displacement operator, shape function, and radial coordinate matrices for the nonaxisymmetric scattering program. (Continued from previous page.)

```
#Compute the operators on the shape function matrix used in
#computing strain-displacement operators
No:=Matrix(9,3*tmp[2]);
No[1,1..tmp[2]]:=simplify(map(diff,N,xi));
No[2,1..tmp[2]]:=simplify(map(diff,N,eta));
No[3,1..tmp[2]]:=simplify(map(diff,N,phi));
No[4,tmp[2]+1..2*tmp[2]]:=simplify(map(diff,N,xi));
No[5,tmp[2]+1..2*tmp[2]]:=simplify(map(diff,N,eta));
No[6,tmp[2]+1..2*tmp[2]]:=simplify(map(diff,N,phi));
No[7,2*tmp[2]+1..3*tmp[2]]:=simplify(map(diff,N,xi));
No[8,2*tmp[2]+1..3*tmp[2]]:=simplify(map(diff,N,eta));
No[9,2*tmp[2]+1..3*tmp[2]]:=simplify(map(diff,N,phi));

#Compute strain-displacement operators
B1:=simplify(Matrix([[0,0,0],[1/r,0,0],[0,0,0],[0,0,0],[0,-1/r,0],
[0,0,0]]).Nt);
B2:=simplify(Matrix([[1,0,0,0,0,0,0,0,0],[0,0,0,0,1/r,0,0,0,0],
[0,0,0,0,0,0,0,0,1],[0,0,1,0,0,0,1,0,0],[0,1/r,0,1,0,0,0,0,0],
[0,0,0,0,0,1,0,1/r,0]]).Gammam.No);
B:=B1+B2;

#Write results to file
save J,"K:\\3Ddevs\\MapleGen\\Jgen.txt";
save B,"K:\\3Ddevs\\MapleGen\\Bgen.txt";
save Nt,"K:\\3Ddevs\\MapleGen\\Ntgen.txt";
save r,"K:\\3Ddevs\\MapleGen\\rgen.txt";
```

Listing K.2. MATLAB® code to compute the finite element stiffness and mass matrices and assemble them into the global matrices for the nonaxisymmetric scattering problem.

```
clear
clc

%Control Information
lambda=113.2E9; %First Lame constant
mu=84.3E9;%Second Lame constant
l_m=lambda/mu; %Ratio of Lame constants
rho=7932;%Mass density
Hp=0.220*25.4E-3;%Wall thickness of pipe
Do=3.4960*25.4E-3;%Outer diameter of pipe
R=(Do-Hp)/2;%Mean radius
H_R=Hp/R;%Wall thickness to mean radius ratio of pipe
wref=1/Hp*sqrt(mu/rho);%Reference frequency

%Common Information
mu=1; %Nondimensional shear modulus
lambda=l_m*mu; %Nondimensional Lame constant
rho=1; %Nondimensional mass density

%Material property matrix
E=[lambda+2*mu,lambda,lambda,0,0,0;
    lambda,lambda+2*mu,lambda,0,0,0;
    lambda,lambda,lambda+2*mu,0,0,0;
    0,0,0,mu,0,0;
    0,0,0,0,mu,0;
    0,0,0,0,0,mu];


%Wave function expansion information
H=1; %Nondimensional wall thickness of pipe
Nr=10; %Number of elements in wave function expansion region

%Finite element region information
Nzfe=2; %Number of elements in the axial direction
Nthetafe=126; %Number of elements in the circumferential direction
Thetafer=pi/180*[0 360]; %Circumferential extent of FE volume
Zfer=[-3.1750E-3/Hp 0];%Axial extent of FE volume
%List of elements to delete to form notch
Edelete=sort([1266:10:1266+10*62 1267:10:1267+10*62 ...
1268:10:1268+10*62 1269:10:1269+10*62 1270:10:1270+10*62]);

%Number of Gauss integration points
Ng=4;

%Define Gauss integration weights as a function of number of Gauss
%points
if Ng==1
    W=[2];
    L=[0];
```

(Continued on next page...)

Listing K.2. MATLAB® code to compute the finite element stiffness and mass matrices and assemble them into the global matrices for the nonaxisymmetric scattering problem. (Continued from previous page.)

```
elseif Ng==2
    W=[1 1];
    L=[-1/sqrt(3) 1/sqrt(3)];
elseif Ng==3
    W=[5/9 8/9 5/9];
    L=[-sqrt(3/5) 0 sqrt(3/5)];
elseif Ng==4
    W=[(18-sqrt(30))/36 (18+sqrt(30))/36 (18+sqrt(30))/36 ...
    (18-sqrt(30))/36];
    L=[-sqrt((3+2*sqrt(6/5))/7) -sqrt((3-2*sqrt(6/5))/7)...
    sqrt((3-2*sqrt(6/5))/7) sqrt((3+2*sqrt(6/5))/7)];
elseif Ng==5
    W=[(322-13*sqrt(70))/900 (322+13*sqrt(70))/900 128/225 ...
    (322+13*sqrt(70))/900 (322-13*sqrt(70))/900];
    L=[-sqrt(5+2*sqrt(10/7))/3 -sqrt(5-2*sqrt(10/7))/3 0 ...
    sqrt(5-2*sqrt(10/7))/3 sqrt(5+2*sqrt(10/7))/3];
else
    error('Unhandled number of Gauss points.');
end

%Call meshing subroutine and return the number of points,
%the number of points on the Finite Element (FE) boundaries,
%the number of interior points, and the radial,
%circumferential, and axial coordinates of the FE nodal points
[Nc,BN,IN,rfe,Thetafe,zfe,Er]=Mesh3D2(Nr,Nthetafe,Nzfe,...
H_R,Thetafer,Zfer);

%Assign memory, for each finite element, to store the global
%stiffness and mass matrices
Ke=zeros(Nr*Nthetafe*Nzfe,81,81);
Me=zeros(Nr*Nthetafe*Nzfe,81,81);

%Open a parallel computing session
matlabpool open

%Loop over (parallized) all finite elements and compute the element
%mass and stiffness matrices
parfor i=1:Nr*Nthetafe*Nzfe
    disp(num2str(i));
    %Convert element number to element position in mesh
    [n,m,o]=ind2sub([Nr Nthetafe Nzfe],i);
    %Get element node numbers
    Nn=Nodes(n,m,o,Nr,Nthetafe);
    %Get node coordinates
    rc=Nc(Nn,1);
    thetac=Nc(Nn,2);
    zc=Nc(Nn,3);
```

(Continued on next page...)

Listing K.2. MATLAB® code to compute the finite element stiffness and mass matrices and assemble them into the global matrices for the nonaxisymmetric scattering problem. (Continued from previous page.)

```
97      %Special case for last circumferential element.  For
98      %convenience, elements run from 2pi to zero.
99      if m==Nthetafe
100         thetac([7 8 9 16 17 18 25 26 27])=0;
101     end
102
103     %Assign memory for the element stiffness and mass matrices
104     Kw=zeros(81,81);
105     Mw=zeros(81,81);
106
107     %Skip any elements that are to be deleted
108     if ~any(i==Edelete)
109
110     %Gauss integration in three dimensions
111     for a=1:1:Ng
112         phi=L(a);
113         Wp=W(a);
114         for b=1:1:Ng
115             eta=L(b);
116             We=W(b);
117             for c=1:1:Ng
118                 xi=L(c);
119                 Wx=W(c);
120                 %Call (numerical) Jacobian subroutine
121                 [J,detJ,Gamma]=Jacobiang(rc,thetac,zc,xi,eta,phi);
122                 %Call (numerical) radial coordinate subroutine
123                 r=rgen(rc,xi,eta,phi);
124                 %Call (numerical) displacement-strain subroutine
125                 B=Bg(rc,xi,eta,phi,Gamma);
126                 %Call (numerical) shape function subroutine
127                 N=Ngen(xi,eta,phi);
128                 %Add increments to element stiffness and mass
129                 %matrices
130                 Mw=Mw+Wp*We*Wx*(N'*N)*rho*r*detJ;
131                 Kw=Kw+Wp*We*Wx*(B'*E*B)*r*detJ;
132             end
133         end
134     end
135
136     end
137
138     %Write element stiffness and mass matrices to global matrices
139     Ke(i,:,:)=Kw;
140     Me(i,:,:)=Mw;
141 end
142
143 %Done with parallel session
144 matlabpool close
```

(Continued on next page...)

Listing K.2. MATLAB® code to compute the finite element stiffness and mass matrices and assemble them into the global matrices for the nonaxisymmetric scattering problem. (Continued from previous page.)

```
%Vectors for each row and column address of each element matrix
RI=zeros(numel(Ke),1);
CI=zeros(numel(Ke),1);
%Assign memory (vectors) for assembly of the global stiffness and
%mass matrices
Ka=zeros(numel(Ke),1);
Ma=zeros(numel(Me),1);


count=1;
%Loop over all finite elements
for i=1:1:Nr*Nthetafe*Nzfe
    disp(num2str(i));
    %Convert element number to element position in mesh
    [n,m,o]=ind2sub([Nr Nthetafe Nzfe],i);
    %Get node numbers for element
    Nn=Nodes(n,m,o,Nr,Nthetafe);
    %Get row and column positions in global matrices for each finite
    %element
    Rows=[Nn;Nn+length(Nc);2*length(Nc)+Nn];
    Cols=Rows;

    %Convert three dimensional array to two dimensional array
    Kw=squeeze(Ke(i,:,:));
    Mw=squeeze(Me(i,:,:));

    %Copy element matrices to global stiffness and mass matrix
    %vectors
    for a=1:1:length(Rows)
        for b=1:1:length(Cols)
            RI(count)=Rows(a);
            CI(count)=Cols(b);
            Ka(count)=Kw(a,b);
            Ma(count)=Mw(a,b);
            count=count+1;
        end
    end
end

%Assemble global stiffness and mass matrices using MATLAB sparse
%command properties
K=sparse(RI,CI,Ka,3*length(Nc),3*length(Nc));
M=sparse(RI,CI,Ma,3*length(Nc),3*length(Nc));

%Remove any fully empty rows and columns of the mass and stiffness
%matrices created by removing finite elements
FNAK=find(full(~any(K)));
FNAM=find(full(~any(M)));
```

(Continued on next page...)

Listing K.2. MATLAB® code to compute the finite element stiffness and mass matrices and assemble them into the global matrices for the nonaxisymmetric scattering problem. (Continued from previous page.)

```
193 K(FNAK,:)=[];
194 K(:,FNAK)=[];
195 M(FNAM,:)=[];
196 M(:,FNAM)=[];
197
198 %Write global stiffness and mass matrices to file
199 save 'KandM.mat' K M
200 %Write deleted element information to file
201 save 'Chole.mat' FNAK FNAM Edelete
```

Listing K.3. MATLAB® code to condense the complete finite element volume's dynamic stiffness matrix for the nonaxisymmetric scattering problem.

```
%Clear workspace
clear
clc

%Control Information
lambda=113.2E9;%First Lame constant
mu=84.3E9;%Second Lame constant
l_m=lambda/mu;%Ratio of Lame constants
rho=7932;%Mass density
Hp=0.220*25.4E-3;%Wall thickness of pipe
Do=3.4960*25.4E-3;%Outer diameter of pipe
R=(Do-Hp)/2;%Mean radius of pipe
H_R=Hp/R;%Wall thickness to mean radius ratio of pipe
wref=1/Hp*sqrt(mu/rho);%Reference frequency

%Common Information
mu=1;%Nondimensional shear modulus
lambda=l_m*mu; %Nondimensional Lame constant
rho=1; %Nondimensional mass density


%Wave function expansion information
H=1; %Nondimensional Wall thickness
Nr=10; %Number of elements in wave function expansion region

%Number of circumferential wavenumbers to use
Mwn=[-15:1:15];

%Finite Element (FE) region information
Nzfe=2; %Number of elements in the axial direction
Nt=126; %Number of elements in the circumferential direction
Thetafer=pi/180*[0 360]; %Circumferential extent of FE volume
Zfer=[-3.1750E-3/Hp 0]; %Axial extent of FE volume

%Call meshing subroutine that returns the number of FE nodal points,
%the number of points on the FE boundaries, the number of FE
%interior points, and the radial, circumferential, and axial
%coordinates of the FE nodal points
[Nc,BN,IN,rfe,Thetafe,zfe,Er]=Mesh3D2(Nr,Nt,Nzfe,H_R,Thetafer,Zfer);

%Load information from file about any deleted elements
load('T:\3D\50H50CA2\Refine\Chole.mat', 'FNAK', 'FNAM', 'Edelete')

%Remove nodal numbers of deleted nodes
Nc(FNAK(1:length(FNAK)/3),:)=[];

%Find nodes that are on boundaries B+ or B-
BN=Nc(:,3)==Zfer(1)|Nc(:,3)==Zfer(2);
%Find interior nodes, i.e., not on boundaries B+ or B-
```

(Continued on next page...)

Listing K.3. MATLAB® code to condense the complete finite element volume's dynamic stiffness matrix for the nonaxisymmetric scattering problem. (Continued from previous page.)

```
IN=~BN;
%Get nodal numbers of nodes on boundaries B+ or B-
BN=(1:1:length(BN)).'.*BN;
BN=nonzeros(BN);
%Get nodal numbers of interior nodes
IN=(1:1:length(IN)).'.*IN;
IN=nonzeros(IN);

%Used to define nodes on mathematical crack face
CN=[];

%Load stiffness and mass matrices from file
load('T:\3D\50H50CA2\Refine\KandM.mat', 'K', 'M')

%Load excitation frequencies to run from file
load('T:\BASEWF\Refine\fHz.mat', 'fall')

freq=2*pi*fall;
clear fall;

%Start routine, noting no excitation frequency point has been run yet
done=false(size(freq));

%Total number of nodes
Nn=length(Nc);
%Number of nodes on the boundaries on boundaries B+ or B-
Rn=length(BN);
%Number of nodes on boundary B+
Pn=sum(Nc(:,3)==Zfer(2));


%Loop until all excitation frequencies are done
while ~all(done)

    %The process can fail, so use try catch block
    try
        %Loop over all excitation frequencies
        for i=1:length(freq)

            %Skip excitation frequencies already done
            if ~done(i)
                disp(['Doing ' num2str(i) '...']);

                %Compute dynamic stiffness matrix
                S=K-(freq(i)/wref)^2*M;

                %Partition S matrix
```

(Continued on next page...)

Listing K.3. MATLAB® code to condense the complete finite element volume's dynamic stiffness matrix for the nonaxisymmetric scattering problem. (Continued from previous page.)

```
99                  SII=[S(IN,IN) S(IN,IN+Nn) S(IN,IN+2*Nn);
100                      S(IN+Nn,IN) S(IN+Nn,IN+Nn) S(IN+Nn,IN+2*Nn);
101                      S(IN+2*Nn,IN) S(IN+2*Nn,IN+Nn)...
102                      S(IN+2*Nn,IN+2*Nn)];
103                 disp('Done SII');
104
105                 SIB=[S(IN,BN) S(IN,BN+Nn) S(IN,BN+2*Nn);
106                      S(IN+Nn,BN) S(IN+Nn,BN+Nn) S(IN+Nn,BN+2*Nn);
107                      S(IN+2*Nn,BN) S(IN+2*Nn,BN+Nn)...
108                      S(IN+2*Nn,BN+2*Nn)];
109                 disp('Done SIB');
110
111                 SBB=[S(BN,BN) S(BN,BN+Nn) S(BN,BN+2*Nn);
112                      S(BN+Nn,BN) S(BN+Nn,BN+Nn) S(BN+Nn,BN+2*Nn);
113                      S(BN+2*Nn,BN) S(BN+2*Nn,BN+Nn)...
114                      S(BN+2*Nn,BN+2*Nn)];
115                 disp('Done SBB');
116
117                 SBI=[S(BN,IN) S(BN,IN+Nn) S(BN,IN+2*Nn);
118                      S(BN+Nn,IN) S(BN+Nn,IN+Nn) S(BN+Nn,IN+2*Nn);
119                      S(BN+2*Nn,IN) S(BN+2*Nn,IN+Nn)...
120                      S(BN+2*Nn,IN+2*Nn)];
121                 disp('Done SBI');
122
123                 %Remove dynamic stiffness matrix from memory
124                 S=[];
125
126                 %Do condensation of internal nodes, using the fastest
127                 %method found to date
128
129                 disp('Starting Sstar');
130
131                 %Assign memory for Sstar
132                 Sstar=zeros(size(SIB));
133
134                 %Do LU decomposition on SII.  See MATLAB
135                 %documentation for descriptions of L, U, p, q, and R
136                 [L,U,p,q,R]=lu(SII,'vector');
137                 %Remove SII from memory
138                 SII=[];
139                 disp('Done LU');
140
141                 %Adjust SIB for scaling from LU decomposition
142                 SIB=(R\SIB);
143
144                 %Remove R from memory
145                 R=[];
146                 disp('Done R\SIB');
```

(Continued on next page...)

Listing K.3. MATLAB® code to condense the complete finite element volume's dynamic stiffness matrix for the nonaxisymmetric scattering problem. (Continued from previous page.)

```
147                     %Reorder SBI to match reordering from LU
148                     %decomposition
149                     SBI=SBI(:,q);
150
151                     %Remove q from memory
152                     q=[];
153
154                     %Open a parallel computing session
155                     matlabpool open 4
156
157                     %Create Sstar by operating on SIB columnwise
158                     parfor n=1:size(SIB,2)
159                         temp=SIB(:,n);
160                         temp=U\(L\temp(p));
161                         Sstar(:,n)=full(temp);
162                     end
163
164                     %Remove SIB from memory
165                     SIB=[];
166
167                     %Next step of finding Sstar
168                     Sstar=-SBI*Sstar;
169
170                     %Remove SBI from memory
171                     SBI=[];
172
173                     %Last step of finding Sstar
174                     Sstar=Sstar+SBB;
175
176                     disp('Done Sstar');
177
178                     %Remove SBB from memory
179                     SBB=[];
180
181                     %Close parallel computing session
182                     matlabpool close
183
184                     %Remove LU decomposition parameters
185                     U=[];
186                     L=[];
187                     p=[];
188
189                     %Partition Sstar matrix
190                     Spp=[Sstar((1:Pn),(1:Pn)) Sstar((1:Pn),(1:Pn)+Rn)...
191                         Sstar((1:Pn),(1:Pn)+2*Rn);
192                         Sstar((1:Pn)+Rn,(1:Pn)) Sstar((1:Pn)+Rn,...
193                         (1:Pn)+Rn)  Sstar((1:Pn)+Rn,(1:Pn)+2*Rn);
194                         Sstar((1:Pn)+2*Rn,(1:Pn)) Sstar((1:Pn)+2*...
```

(Continued on next page...)

Listing K.3. MATLAB® code to condense the complete finite element volume's dynamic stiffness matrix for the nonaxisymmetric scattering problem. (Continued from previous page.)

```
                    Rn,(1:Pn)+Rn)...
                    Sstar((1:Pn)+2*Rn,(1:Pn)+2*Rn)];

                    Spm=[Sstar((1:Pn),(Pn+1:Rn)) Sstar((1:Pn),...
                    (Pn+1:Rn)+Rn) Sstar((1:Pn),(Pn+1:Rn)+2*Rn);
                    Sstar((1:Pn)+Rn,(Pn+1:Rn))...
                    Sstar((1:Pn)+Rn,(Pn+1:Rn)+Rn)...
                    Sstar((1:Pn)+Rn,(Pn+1:Rn)+2*Rn);
                    Sstar((1:Pn)+2*Rn,(Pn+1:Rn))...
                    Sstar((1:Pn)+2*Rn,(Pn+1:Rn)+Rn)...
                    Sstar((1:Pn)+2*Rn,(Pn+1:Rn)+2*Rn)];

                Smp=[Sstar((Pn+1:Rn),(1:Pn)) Sstar((Pn+1:Rn),...
                    (1:Pn)+Rn)  Sstar((Pn+1:Rn),(1:Pn)+2*Rn);
                    Sstar((Pn+1:Rn)+Rn,(1:Pn))...
                    Sstar((Pn+1:Rn)+Rn,(1:Pn)+Rn)...
                    Sstar((Pn+1:Rn)+Rn,(1:Pn)+2*Rn);
                    Sstar((Pn+1:Rn)+2*Rn,(1:Pn))...
                    Sstar((Pn+1:Rn)+2*Rn,(1:Pn)+Rn)...
                    Sstar((Pn+1:Rn)+2*Rn,(1:Pn)+2*Rn)];

                Smm=[Sstar((Pn+1:Rn),(Pn+1:Rn)) ...
                    Sstar((Pn+1:Rn),(Pn+1:Rn)+Rn)...
                    Sstar((Pn+1:Rn),(Pn+1:Rn)+2*Rn);
                    Sstar((Pn+1:Rn)+Rn,(Pn+1:Rn))...
                    Sstar((Pn+1:Rn)+Rn,(Pn+1:Rn)+Rn)...
                    Sstar((Pn+1:Rn)+Rn,(Pn+1:Rn)+2*Rn);
                    Sstar((Pn+1:Rn)+2*Rn,(Pn+1:Rn))...
                    Sstar((Pn+1:Rn)+2*Rn,(Pn+1:Rn)+Rn)...
                    Sstar((Pn+1:Rn)+2*Rn,(Pn+1:Rn)+2*Rn)];

                %Remove Sstar matrix from memory
                Sstar=[];

                %Find Sstar for symmetric and anti-symmetric
                %problems, write matrices to disk
                Sstars=Spp;
                Spp=[];
                Sstara=Sstars;
                Spms=Spm(:,1:(size(Spm,2)*2/3));
                Spma=Spm(:,(size(Spm,2)*2/3+1:size(Spm,2)));
                Spm=[];
                Smms=Smm(1:(size(Smm,1)*2/3),1:(size(Smm,2)*2/3));
                Smma=Smm((size(Smm,1)*2/3+1):size(Smm,1),...
                    (size(Smm,2)*2/3+1):size(Smm,2));
                Smm=[];
                Smps=Smp(1:(size(Smp,1)*2/3),:);
                Smpa=Smp((size(Smp,1)*2/3+1):size(Smp,1),:);
```

(Continued on next page...)

Listing K.3. MATLAB® code to condense the complete finite element volume's dynamic stiffness matrix for the nonaxisymmetric scattering problem. (Continued from previous page.)

```
                    Smp=[];
                    Sstara=Sstara-Spma*(Smma\Smpa);
                    saveSstara(Sstara,i)
                    disp('Done Sstara');
                    Sstara=[];
                    Spma=[];
                    Smma=[];
                    Smpa=[];

                    Sstars=Sstars-Spms*(Smms\Smps);
                    saveSstars(Sstars,i)
                    disp('Done Sstars');
                    Sstars=[];
                    Spms=[];
                    Smms=[];
                    Smps=[];

                    %After successful writes, this excitation frequency
                    %point is done
                    done(i)=true;
                end
            end
        %Handle errors
        catch ME
            disp('Some error detected...');
            ME
            ME.message
            pause(10);
            disp('Trying again...');
            try
                %Try to close matlabpool.  An error is produced if an
                %attempt to start a second instance is made and the
                %matlabpool is already running.
                matlabpool close force
            catch
            end
        end
    end

    %Close parallel computing session
    matlabpool close
```

Listing K.4. MATLAB® code to form and solve the linear system of equations for the nonaxisymmetric scattering problem.

```
%Clear workspace
clear
clc

%Control Information
lambda=113.2E9;%First Lame constant
mu=84.3E9;%Second Lame constant
l_m=lambda/mu;%Ratio of Lame constants
rho=7932;%Mass density
Hp=0.220*25.4E-3;%Wall thickness of pipe
Do=3.4960*25.4E-3;%Outer diameter of pipe
R=(Do-Hp)/2;%Mean radius of pipe
H_R=Hp/R;%Wall thickness to mean radius ratio of pipe
wref=1/Hp*sqrt(mu/rho);%Reference frequency

%Common Information
mu=1;%Nondimensional shear modulus
lambda=l_m*mu;%Nondimensional Lame constant
rho=1;%Nondimensional mass density


%Wave function expansion information
H=1; %Nondimensional wall thickness
Nr=10; %Number of finite elements in wave function expansion region

%Length of eigenvectors, number of axial modes per circumferential
%wavenumber
Na=3*(2*Nr+1);

%Number of circumferential wavenumbers to use
Mwn=[-15:1:15];

%Finite Element (FE) region information
Nzfe=2; %Number of finite elements in the axial direction
Nt=126;%Number of finite elements in the circumferential direction
Thetafer=pi/180*[0 360];%Circumferential extent of FE volume
Zfer=[-3.1750E-3/Hp 0];%Axial extent of FE volume

%Call meshing subroutine that returns the number of FE nodal points,
%the number of points on the boundaries, the number of
%interior points, and the radial, circumferential, and axial
%coordinates of the FE nodal points
[Nc,BN,IN,rfe,Thetafe,zfe,Er]=Mesh3D2(Nr,Nt,Nzfe,H_R,Thetafer,Zfer);

%Load information concerning any deleted elements from file
load('T:\3D\50H50CA2\Refine\Chole.mat', 'FNAK', 'FNAM', 'Edelete')

%Remove nodal numbers of deleted nodes
Nc(FNAK(1:length(FNAK)/3),:)=[];
```

(Continued on next page...)

Listing K.4. MATLAB® code to form and solve the linear system of equations for the nonaxisymmetric scattering problem. (Continued from previous page.)

```
%Find nodes which are on boundaries B+ or B-
BN=Nc(:,3)==Zfer(1)|Nc(:,3)==Zfer(2);
%Find interior nodes, i.e., not on boundaries B+ or B-
IN=~BN;
%Get nodal numbers of nodes on boundaries B+ or B-
BN=(1:1:length(BN)).'.*BN;
BN=nonzeros(BN);
%Get nodal numbers of interior nodes
IN=(1:1:length(IN)).'.*IN;
IN=nonzeros(IN);

%Used to define nodes on mathematical crack face
CN=[];

%Load excitation frequencies to run from file
load('T:\BASEWF\Refine\fHz.mat', 'fall')
freq=2*pi*fall;
clear fall;

%Start routine, noting no excitation frequency point has been run yet
done=false(size(freq));

%Total number of FE nodes
Nn=length(Nc);

%Total number of FE nodes on the boundaries B+ or B-
Rn=length(BN);
%Number of FE nodes on the boundary B+
Pn=sum(Nc(:,3)==Zfer(2));

%Loop until all excitation frequencies are done
while ~all(done)

    %The process can fail, so use try catch block
    try

        %Open a parallel computing session
        matlabpool open

        %Loop over all excitation frequencies
        for i=1:length(freq)

            %Skip excitation frequencies already done
            if ~done(i)
                %Assign arrays for the incident and scattered nodal
                %displacements on B+
                G1pr=complex(zeros(Pn,length(Mwn)*Na));
                G1pt=complex(zeros(Pn,length(Mwn)*Na));
                G1pz=complex(zeros(Pn,length(Mwn)*Na));
```

(Continued on next page...)

Listing K.4. MATLAB® code to form and solve the linear system of equations for the nonaxisymmetric scattering problem. (Continued from previous page.)

```
100
101                     G2r=complex(zeros(Pn,length(Mwn)*Na));
102                     G2t=complex(zeros(Pn,length(Mwn)*Na));
103                     G2z=complex(zeros(Pn,length(Mwn)*Na));
104
105                     %Displacements
106                     disp('Displacements...');
107
108                     %Read wavefunctions from file
109                     parfor p=1:length(Mwn)*Na
110
111                         %Relate circumferential wavenumber to loop
112                         %counter
113                         m=ceil(p/Na);
114
115                         %Relate axial wavenumber counter to loop counter
116                         n=p-(m-1)*Na;
117
118                         %Load wave functions from file into a MATLAB
119                         %structure
120                         LD=load(['T:\BASEWF\Refine\F_' num2str(Mwn(m))...
121                             '_' num2str(i) '.mat'],'phir','phil',...
122                             'kr','kl');
123
124                         %Separate variables from loaded MATLAB structure
125                         phir=LD.phir;
126                         phil=LD.phil;
127                         kr=LD.kr;
128                         kl=LD.kl;
129
130                         %Remove loaded MATLAB structure
131                         LD=[];
132
133                         %Assign memory to operate on columns of
134                         %displacement matrix
135
136                         G1prc=complex(zeros(Pn,1));
137                         G1ptc=complex(zeros(Pn,1));
138                         G1pzc=complex(zeros(Pn,1));
139
140                         G2rc=complex(zeros(Pn,1));
141                         G2tc=complex(zeros(Pn,1));
142                         G2zc=complex(zeros(Pn,1));
143
144                         %Axial coordinate of B+ face
145                         z=zfe(1);
146
147                         %Axial decay terms (always 1 here)
148                         ezr=exp(1i*kr(n)*z);
```

(Continued on next page...)

Listing K.4. MATLAB® code to form and solve the linear system of equations for the nonaxisymmetric scattering problem. (Continued from previous page.)

```
                    ezl=exp(1i*kl(n)*z);
                    %Count row number
                    rstart=1;

                    %Rotate displacements
                    for a=1:1:2*Nt
                        theta=Thetafe(a);
                        et=exp(1i*Mwn(m)*theta);
                        G1prc(rstart:1:rstart+2*Nr)=...
                            phir(1:1:2*Nr+1,n)*et*ezr;
                        G1ptc(rstart:1:rstart+2*Nr)=...
                            phir(2*Nr+2:1:4*Nr+2,n)*et*ezr;
                        G1pzc(rstart:1:rstart+2*Nr)=...
                            phir(4*Nr+3:1:end,n)*et*ezr;

                        G2rc(rstart:1:rstart+2*Nr)=...
                            phil(1:1:2*Nr+1,n)*et*ezl;
                        G2tc(rstart:1:rstart+2*Nr)=...
                            phil(2*Nr+2:1:4*Nr+2,n)*et*ezl;
                        G2zc(rstart:1:rstart+2*Nr)=...
                            phil(4*Nr+3:1:end,n)*et*ezl;

                        %Increment row counter
                        rstart=rstart+2*Nr+1;
                    end

                    %Assign columns to full matrix
                    G1pr(:,p)=G1prc;
                    G1pt(:,p)=G1ptc;
                    G1pz(:,p)=G1pzc;

                    G2r(:,p)=G2rc;
                    G2t(:,p)=G2tc;
                    G2z(:,p)=G2zc;
                end

                %Assemble component matrices into full matrix
                G1=[G1pr;G1pt;G1pz];
                G2=[G2r;G2t;G2z];

                %Assign arrays for the incident and scattered nodal
                %forces on B+

                F1pr=complex(zeros(Pn,length(Mwn)*Na));
                F1pt=complex(zeros(Pn,length(Mwn)*Na));
                F1pz=complex(zeros(Pn,length(Mwn)*Na));

                F2r=complex(zeros(Pn,length(Mwn)*Na));
                F2t=complex(zeros(Pn,length(Mwn)*Na));
```

(Continued on next page...)

Listing K.4. MATLAB® code to form and solve the linear system of equations for the nonaxisymmetric scattering problem. (Continued from previous page.)

```
198                 F2z=complex(zeros(Pn,length(Mwn)*Na));
199
200                 disp('Forces...');
201
202                 %Nodal forces...
203
204                 %Read wavefunctions from file
205                 parfor p=1:length(Mwn)*Na
206
207                     %Relate circumferential wavenumber to loop
208                     %counter
209                     m=ceil(p/Na);
210
211                     %Relate axial wavenumber counter to loop counter
212                     n=p-(m-1)*Na;
213
214                     %Load wave functions from file into a MATLAB
215                     %structure
216                     LD=load(['T:\BASEWF\Refine\F_' num2str(Mwn(m))...
217                         '_' num2str(i) '.mat'],'phir','phil','kr',...
218                         'kl');
219                     %Separate variables from loaded MATLAB
220                     %structure
221                     phir=LD.phir;
222                     phil=LD.phil;
223                     kr=LD.kr;
224                     kl=LD.kl;
225
226                     %Remove loaded structure
227                     LD=[];
228
229                     %Assign memory to operate on columns of
230                     %force matrix
231                     F1prc=complex(zeros(Pn,1));
232                     F1ptc=complex(zeros(Pn,1));
233                     F1pzc=complex(zeros(Pn,1));
234
235                     F2rc=complex(zeros(Pn,1));
236                     F2tc=complex(zeros(Pn,1));
237                     F2zc=complex(zeros(Pn,1));
238
239                     %Axial coordinate of B+ face
240                     z=zfe(1);
241
242                     %Force vectors for one finite element face
243                     Fps=complex(zeros(27,Nr));
244                     Fpi=complex(zeros(27,Nr));
245
246                     %Compute the force vector for the scattered
```

(Continued on next page...)

Listing K.4. MATLAB® code to form and solve the linear system of equations for the nonaxisymmetric scattering problem. (Continued from previous page.)

```
247                         %and incident modes along one radius
248                         for a=1:1:Nr
249                             Ftemp=Forcezp(rfe(2*a+1),rfe(2*a-1),...
250                                 Thetafe(1),Thetafe(3),z,Mwn(m),kr(n),...
251                                 phir([2*a-1:1:2*a+1 2*a-1+2*Nr+1:1:2*...
252                                 a+1+2*Nr+1 2*a-1+4*Nr+2:1:2*a+1+...
253                                 4*Nr+2],n),lambda,mu);
254                             Fps(:,a)=Ftemp;
255                             Ftemp=Forcezp(rfe(2*a+1),rfe(2*a-1),...
256                                 Thetafe(1),Thetafe(3),z,Mwn(m),kl(n),...
257                                 phil([2*a-1:1:2*a+1 2*a-1+2*Nr+1:1:2*...
258                                 a+1+2*Nr+1 2*a-1+4*Nr+2:1:2*a+1+4*...
259                                 Nr+2],n),lambda,mu);
260                             Fpi(:,a)=Ftemp;
261                         end
262
263                         %Rotate forces around all the radii
264                         for a=1:1:Nr
265                             for b=1:1:Nt
266                               et=exp(1i*Mwn(m)*(b-1)*(Thetafe(3)-...
267                                   Thetafe(1)));
268                               Nodes=Nodef(a,b,Nr,Nt);
269                               F1prc(Nodes)=F1prc(Nodes)+Fps(1:9,a)*et;
270                               F1ptc(Nodes)=F1ptc(Nodes)+Fps(10:18,a)*et;
271                               F1pzc(Nodes)=F1pzc(Nodes)+Fps(19:27,a)*et;
272
273                               F2rc(Nodes)=F2rc(Nodes)+Fpi(1:9,a)*et;
274                               F2tc(Nodes)=F2tc(Nodes)+Fpi(10:18,a)*et;
275                               F2zc(Nodes)=F2zc(Nodes)+Fpi(19:27,a)*et;
276                             end
277                         end
278
279                         %Assign columns to full matrix
280                         F1pr(:,p)=F1prc;
281                         F1pt(:,p)=F1ptc;
282                         F1pz(:,p)=F1pzc;
283
284                         F2r(:,p)=F2rc;
285                         F2t(:,p)=F2tc;
286                         F2z(:,p)=F2zc;
287                     end
288
289                     %Assemble component matrices into full matrix
290                     F1=[F1pr;F1pt;F1pz];
291                     F2=[F2r;F2t;F2z];
292
293                     %Solve symmetric and anti-symmetric problems
294
295                     %Load anti-symmetric dynamic stiffness matrix from
```

(Continued on next page...)

Listing K.4. MATLAB® code to form and solve the linear system of equations for the nonaxisymmetric scattering problem. (Continued from previous page.)

```
296                     %file into a MATLAB structure
297                     LD=load(['T:\3D\50H50CA2\Refine\Sstara_'...
298                         num2str(i) '.mat'], 'Sstara');
299
300                     %Form left and right hand sides of linear system of
301                     %equations
302                     LHS=G1'*(LD.Sstara*G1-F1);
303                     RHS=G1'*(F2-LD.Sstara*G2);
304                     %Calculate anti-symmetric solution
305                     Aa=LHS\RHS;
306                     %Remove anti-symmetric dynamic stiffness matrix from
307                     %memory
308                     LD=[];
309
310                     %Load symmetric dynamic stiffness matrix from
311                     %file into a MATLAB structure
312                     LD=load(['T:\3D\50H50CA2\Refine\Sstars_' ...
313                         num2str(i) '.mat'], 'Sstars');
314
315                     %Form left and right hand sides of linear system of
316                     %equations
317                     LHS=G1'*(LD.Sstars*G1-F1);
318                     RHS=G1'*(F2-LD.Sstars*G2);
319                     %Calculate symmetric solution
320                     As=LHS\RHS;
321                     %Remove anti-symmetric dynamic stiffness matrix from
322                     %memory
323                     LD=[];
324
325                     %Compute reflection and transmission coefficients
326                     Rc=(Aa+As)/2;
327                     Tc=(As-Aa)/2;
328
329                     %Save results to file
330                     savescat(As,Aa,Rc,Tc,i);
331
332                     %This excitation frequency completed successfully
333                     done(i)=true;
334                     disp(['Done ' num2str(i)]);
335
336                     %Clean up memory
337                     As=[];
338                     Aa=[];
339                     Rc=[];
340                     Tc=[];
341                     LHS=[];
342                     RHS=[];
343                     G1=[];
344                     G2=[];
```

(Continued on next page...)

Listing K.4. MATLAB® code to form and solve the linear system of equations for the nonaxisymmetric scattering problem. (Continued from previous page.)

```
                F1=[];
                F2=[];
            end
        end
    catch ME %Error handler
        disp('Some error detected...');
        ME
        ME.message
        pause(10);
        disp('Trying again...');
        try
            %Try to close matlabpool.  An error is produced if an
            %attempt to start a second instance is made and the
            %matlabpool is already running.
            matlabpool close
        catch
        end
    end
end

%Close parallel computing session
matlabpool close
```

APPENDIX L

FACILITIES FOR PARALLEL AND DISTRIBUTED COMPUTING

L.1 Overview

As discussed in Chapter 4 and other appendices, the application of the hybrid-SAFE wave function method requires: (i) determining the wave functions (normal modes) of an unblemished waveguide, (ii) developing a conventional finite element model of a volume that (potentially) encloses a flaw, (iii) enforcing displacements and force (stress) continuities between the finite element region and the parent waveguide, where the field equations are written in terms of wave functions, and, finally, (iv) solving the resulting linear equations. This process is implemented computationally here. However, hybrid-SAFE wave function expansion modelling can be expensive in terms of computer wait times. Moreover, depending on the number of finite elements required to model the finite element volume, it can be memory intensive. Indeed, a numerical solution of the final linear equations may require so much memory that they cannot be solved straightforwardly by employing a single computer[1].

Although evolving platforms that invariably involved Personal Computers (PCs) were employed to compute the results given in the main text, a PC equipped with an Intel® Core™ i5 processor, 16 GB of memory, and running 64-bit software was used to generate most of the results. Notwithstanding, techniques are outlined next to ameliorate the previously described difficulties, in a "proof of concept" environment. The "test bed" described in Section L.2 would be suitable for performing all the calculations required to im-

[1]It may be simply impossible to solve the equations by utilizing convenient, conventional linear solvers on a single computer having 32-bit memory addressing. The problem can be alleviated by using 64-bit memory addresses. Note, however, that 64-bit memory addressing does not preclude distribution of memory requirements. It does allow larger problems to be solved before distribution is required providing *sufficient* Random Access Memory (RAM) is available. Parallelization can be beneficial regardless of the memory addressing scheme used.

plement the hybrid-SAFE if the straightforward and relatively inexpensive modifications to the "head" node suggested in Section 5.2 were implemented. Although the methods discussed may seem intuitively obvious, a feasible solution may not be claimed until it is implemented successfully. This appendix documents a "proof of concept" implementation. Further insights are gained by using illustrative examples.

L.2 Description of Computing Cluster

The Wawanesa Mutual Insurance Company generously donated their ageing surplus computers which permitted the assembly of an 18 node computing cluster for a "proof of concept test bed." All nodes use readily available hardware and software—principally MATLAB® and its associated Parallel Computing Toolbox™. The 17 "compute" nodes are nominally International Business Machines (IBM®) Corporation, 8187-WC4 PCs. The total available memory is 16.75 GB, which is distributed between the compute and "head" (controller) nodes. Furthermore 32-bit software is utilized throughout. The computing cluster is shown in Figure L.1. A 100 Mbit Ethernet Transmission Control Protocol/Internet Protocol (TCP/IP) model is used to network the computers.

L.3 Distinction Between CPU and Memory Limited Problems

The hybrid-SAFE scattering technique makes extensive use of spectral decomposition which requires the numerous solution of similar problems (i.e., once for each frequency in the spectral decomposition). Problems which fit into the memory of a single computer are limited by the speed at which computations can be performed and, hence, become Central Processing Unit (CPU) limited. On the other hand, problems not fitting into the memory of a single computer become memory limited. Problems of the first kind can benefit from

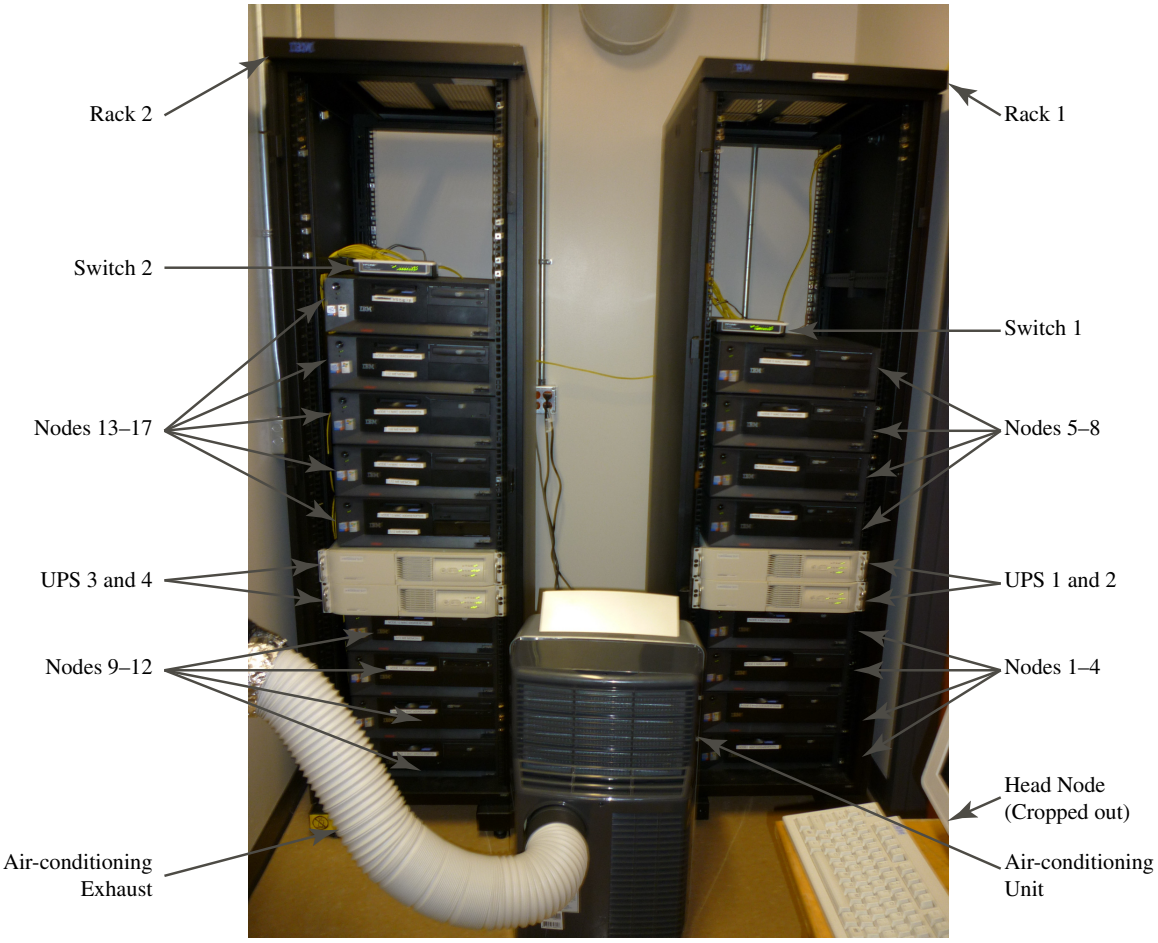

Figure L.1. The assembled computing cluster.

parallelization in which a single occurrence of a problem is run simultaneously on several computers or processing cores. Problems of the second kind are solved more easily if they are distributed so that the memory requirement of a single case is split amongst several computers. The Parallel Computing Toolbox™ of MATLAB® straightforwardly and flexibly implements both types of problems. Its "parfor" structure is useful for the former problems while the "spmd" construct is utilized for the latter problems. The two approaches can be useful at different stages of a given hybrid-SAFE scattering problem, as described next.

L.4 Illustrative Examples

Immediately after assembling the computing cluster described in Section L.2, an early (before optimization) version of the axisymmetric wave scattering program described in Appendix G was modified for parallel execution and run on the cluster. The purpose of this exercise was to assess the potential of using a computing cluster to reduce the wait time. Axisymmetric scattering problems are small enough that they fit into memory and, therefore, are ideal for parallel execution.

Table L.1 gives the "speed up" ratios achieved by using 1, 8, 16, and 17 computing cores in parallel. Figure L.2 shows the same information in graphical form. The speed up ratio, S, is defined as

$$S = \frac{t_{\text{serial}}}{t_{\text{parallel}}}, \tag{L.4.1}$$

where t is the waiting time corresponding to the subscripts "serial" and "parallel" which denote a program run using serial and parallel execution, respectively. Increasing values of S that are larger than unity represent a greater reduction in waiting time with parallelization which, consequently, is increasingly beneficial. However, the overhead associated with starting a distributed computing session and the time taken to distribute data to a remote computer over a network cause the speed up to be less than unity when distributing to merely one core. Notwithstanding, the results shown in Table L.1 and Figure L.2 are generally encouraging as they suggest that distributed computing can be beneficial.

Table L.1. "Speed up" ratios achieved by parallelizing a job that is CPU rather than memory limited.

Computing configuration	Speed up ratio
Serial program	1.0
Distributed to 1 core	0.74[a]
Distributed to 8 cores	5.2
Distributed to 16 cores	8.3
Distributed to 17 cores	9.6

[a] A slow down!

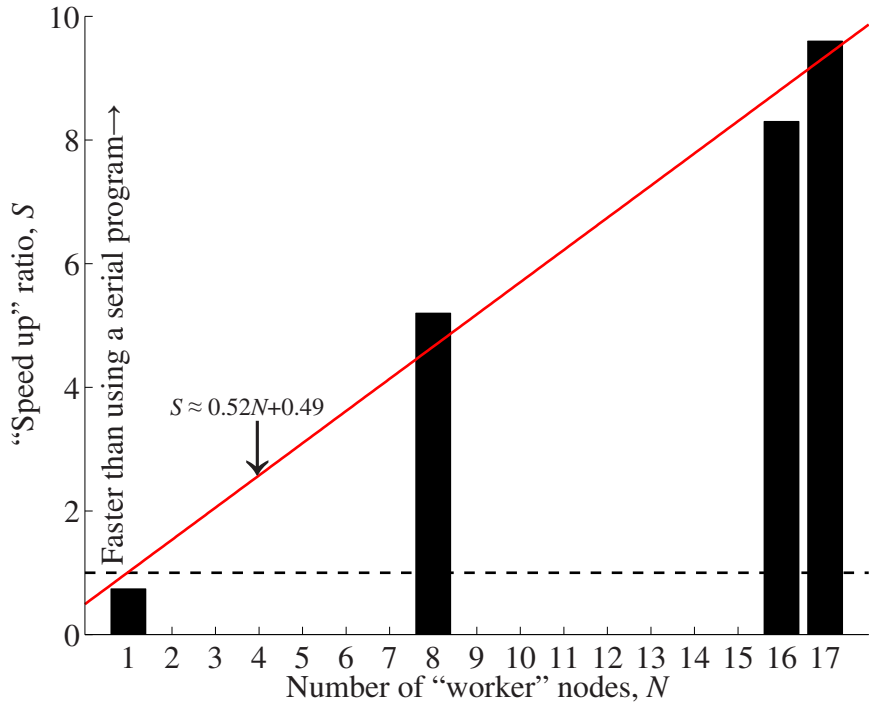

Figure L.2. Graphical illustration of the data presented in Table L.1.

The second step in applying the hybrid-SAFE procedure to wave scattering problems requires a conventional finite element model. The computation of finite element mass and stiffness matrices typically involve modest memory requirements but this process is CPU limited. Consequently parallelization, in a manner similar to the calculation of the wave functions, is beneficial. The computational effort to assemble the global matrices is insignificant compared to the calculation of the element matrices. The assembly results in a large, sparse set of linear equations having the form

$$\begin{bmatrix} \mathbf{S}_{\mathrm{II}} & \mathbf{S}_{\mathrm{IB}} \\ \mathbf{S}_{\mathrm{BI}} & \mathbf{S}_{\mathrm{BB}} \end{bmatrix} \begin{Bmatrix} \mathbf{q}_{\mathrm{I}} \\ \mathbf{q}_{\mathrm{B}} \end{Bmatrix} = \begin{Bmatrix} \mathbf{0} \\ \mathbf{P}_{\mathrm{B}} \end{Bmatrix}. \tag{L.4.2}$$

Here $\mathbf{S}$ is a dynamic stiffness matrix whereas $\mathbf{q}$ and $\mathbf{P}$ are nodal displacement and force vectors, respectively. Furthermore subscripts I and B denote interior and boundary nodes, respectively. A boundary node is one that is common to both the finite element volume and a wave function expansion region. An internal node has no direct connection to either of

the two wave function expansion regions.

Condensation of the internal nodes of the finite element volume presents a formidable challenge. The process can be written mathematically as

$$\left(-\mathbf{S}_{\mathrm{BI}}\mathbf{S}_{\mathrm{II}}^{-1}\mathbf{S}_{\mathrm{IB}} + \mathbf{S}_{\mathrm{BB}}\right)\mathbf{q}_{\mathrm{B}} = \mathbf{P}_{\mathrm{B}}. \tag{L.4.3}$$

The challenge arises in evaluating the matrix product $-\mathbf{S}_{\mathrm{BI}}\mathbf{S}_{\mathrm{II}}^{-1}\mathbf{S}_{\mathrm{IB}}$. Although $\mathbf{S}_{\mathrm{II}}$ is sparse, its inverse is not and, hence, requires significant storage memory. One solution is to distribute the memory requirement among several computers to subsequently perform the required matrix operations. Figure L.3 shows the waiting time required to perform these operations for the computation at a single frequency point with a different number of distributed computer nodes. The illustrative finite element mesh has a total of 790, 27 node quadratic Lagrangian elements. Ten (forty) [two] elements are used in the radial (circumferential) [axial] direction. (Note that this mesh is appropriate only for circumferential wavenumbers

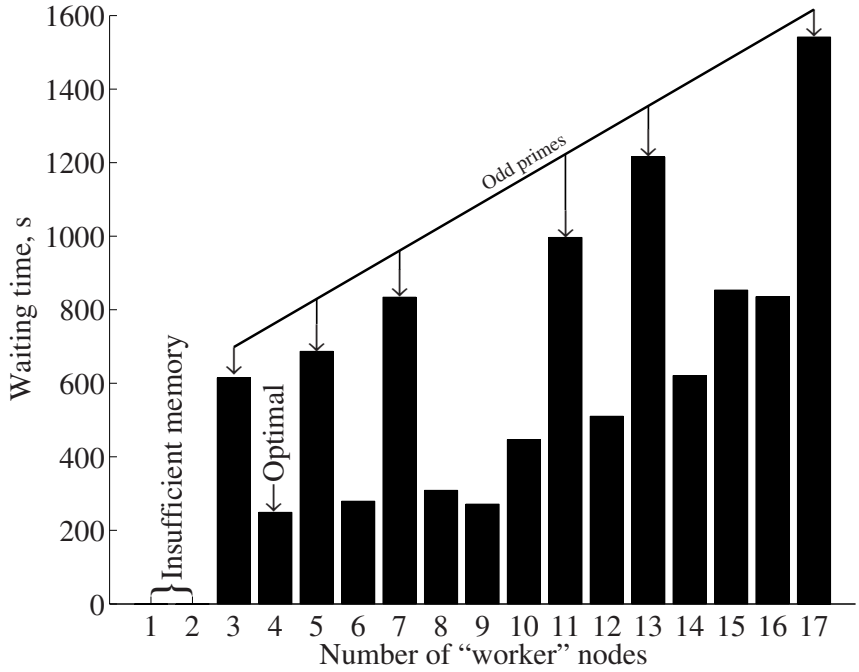

Figure L.3. Time required to invert an illustrative, square dynamic stiffness matrix having order 25,074.

having a magnitude of 4 or less.) Ten elements are removed to idealize a through hole. It is clear from Figure L.3 that the optimal number of distribution nodes *for this particular mesh* is four. To reduce the waiting times further, a combination of distributed and parallelized computing can be performed. A good arrangement for this last approach is to use two "head" nodes, each of which simultaneously controls two jobs distributed to four computer nodes. The configuration is illustrated graphically in Figure L.4, for which four frequency points are evaluated simultaneously.

Two additional examples of the speed up ratios achieved by using parallel computing are shown in Figures L.5 and L.6. The first figure gives the ratios when computing the approximate wavefunctions by using SAFE for a single circumferential harmonic at (a) 145 and (b) 721 frequency points. The mesh for this example is identical to the one used in Chapter 2. The second figure, on the other hand, shows the speed up ratios when solving the axisymmetric scattering problem for a single circumferential harmonic at (a) 145 and (b) 721 frequency points. Then the mesh corresponds to the one employed in Chapter 4. More modest speed up gains are seen in Figure L.6 compared with those given in Figure L.2. In the former case, the program had been improved to be significantly (about a factor of 60

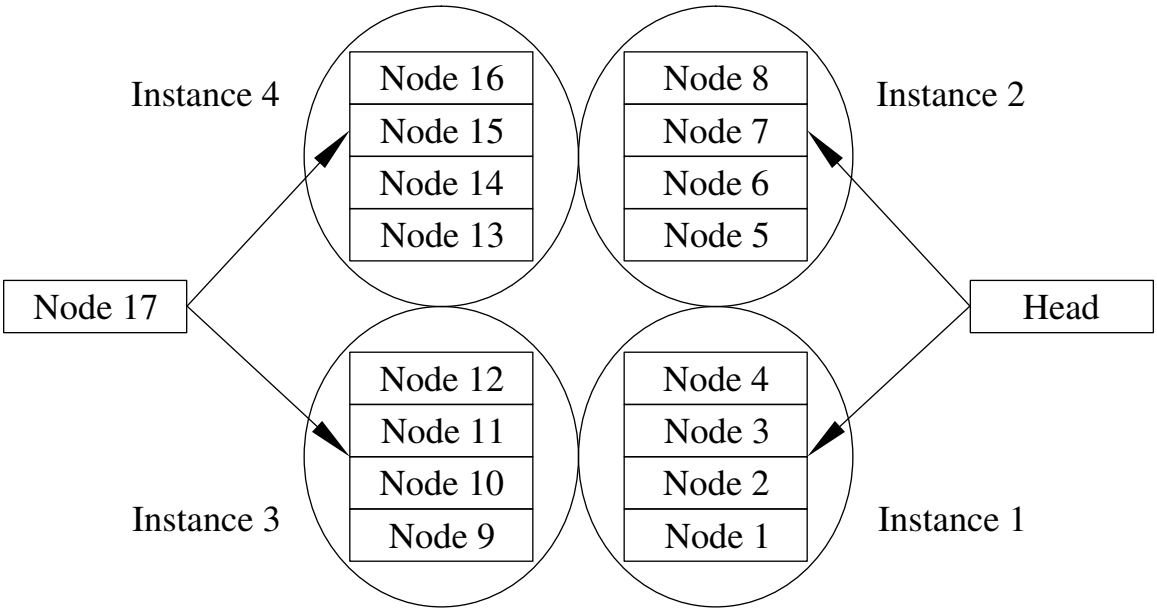

Figure L.4. Optimal computing arrangement for the second illustrative problem.

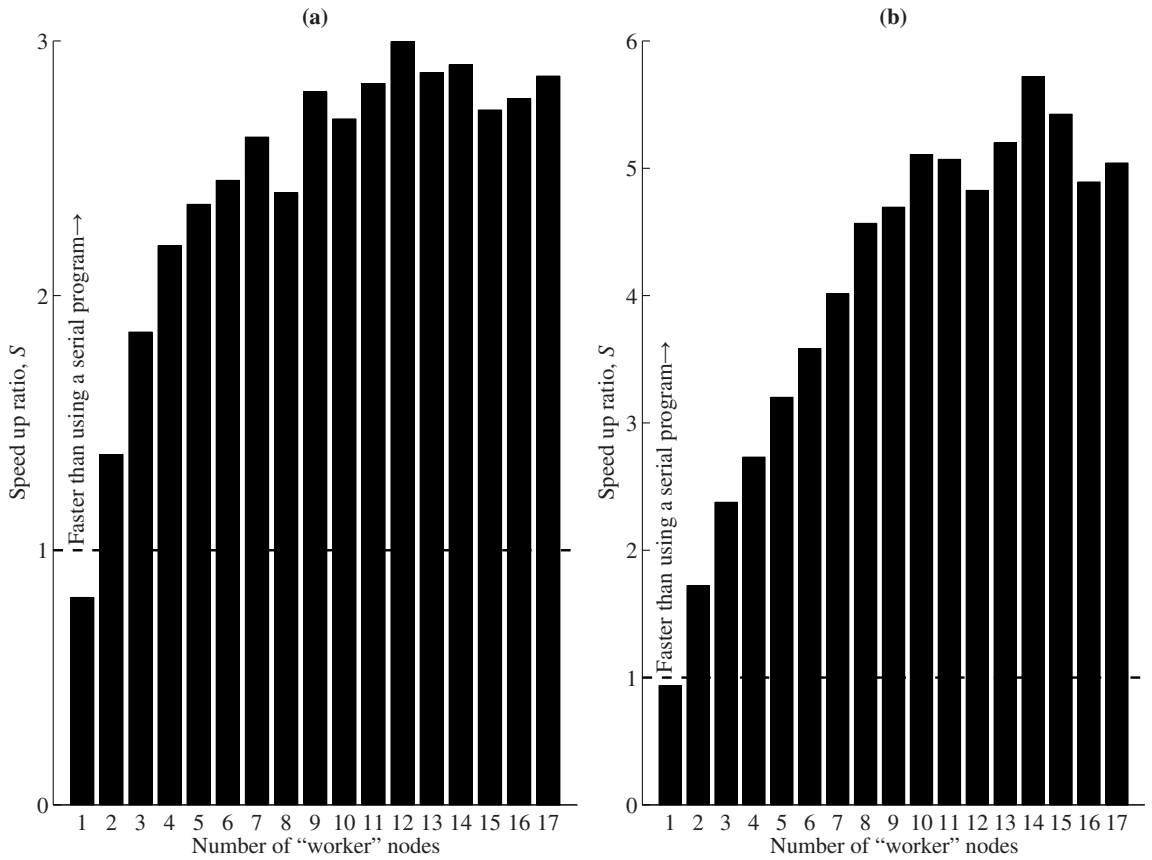

Figure L.5. Speed up ratio, S, achieved when calculating wavefunctions for a single circumferential harmonic at (a) 145 and (b) 721 frequency points.

times fewer floating point operations) more efficient. For this reason, there is significantly more overhead involved in starting and stopping the parallel computations. This overhead is reduced, as a percentage of the total waiting time, with each increase in the time taken for the program to execute a parallel code. This phenomenon explains the larger speed ups seen in Figures L.5 (b) and L.6 (b) relative to those of Figures L.5 (a) and L.6 (a), respectively.

L.5 Conclusions

Illustrative examples have shown that parallel and distributed computing can be applied advantageously to the hybrid-SAFE procedure for wave scattering problems. Two categories of problems were described, CPU and memory limited problems. Parallel computing has

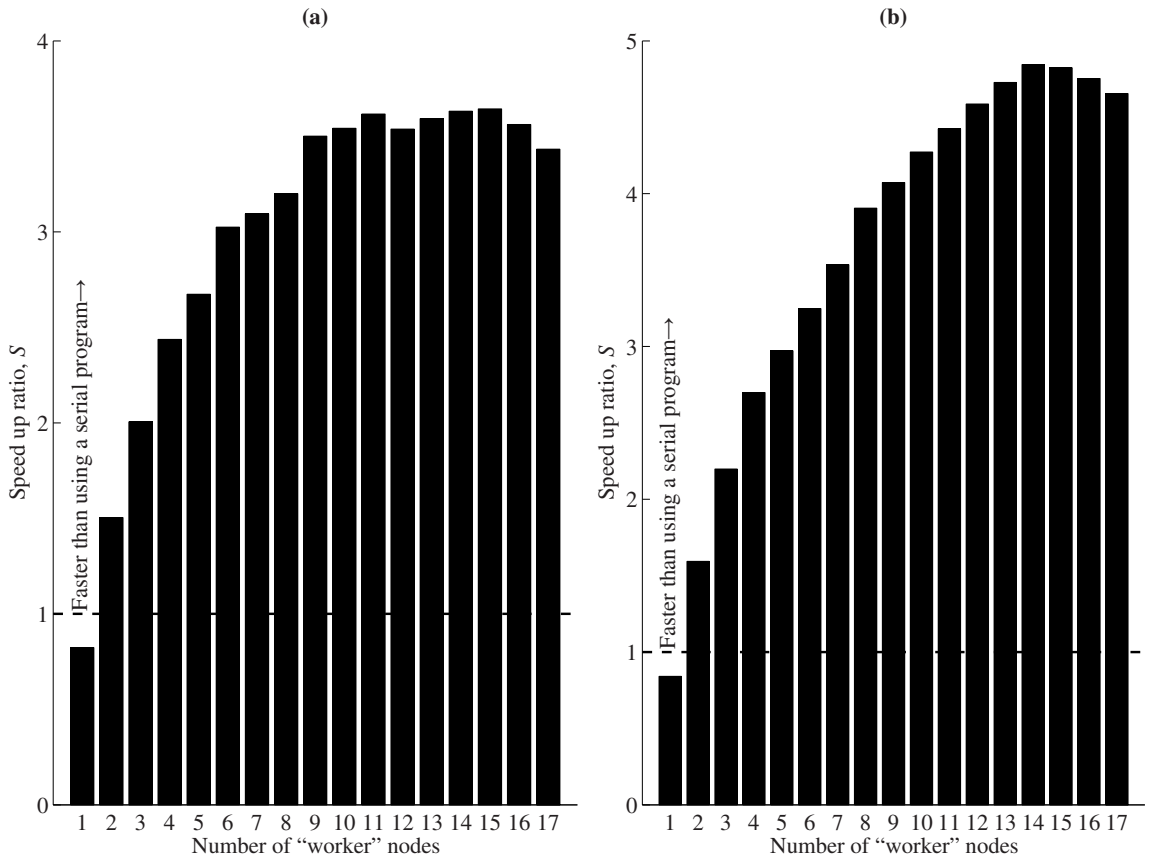

Figure L.6. Speed up ratio, S, achieved when solving the axisymmetric scattering problem for a single circumferential harmonic at (a) 145 and (b) 721 frequency points.

been seen appropriate for the former class but distributed computing was required for the second class. Parallel computing was shown to reduce the waiting time by nearly an order of magnitude when the majority of a program's execution time was spent in parallel executing, i.e., network overhead and serial execution time was negligible. Distributed computing, on the other hand, was demonstrated to be a feasible approach when there was otherwise insufficient RAM to solve a memory demanding problem. However, the optimal allocation of computing resources was not always obvious. Therefore, empirical benchmarking should be used to select an optimal, problem dependent, computing arrangement. The following recommendations are made to further improve the performance of the computing cluster.

1. The "head" node of the present computing cluster should be replaced with a 64-bit Personal Computer (PC) having at least 16 GB of memory,

2. The "compute" nodes of the computing cluster should be upgraded when economically feasible.

3. The cluster's network should be upgraded to "gigabit" speeds when economically feasible.

4. The feasibility of performing hypbrid-SAFE finite element computations by using Graphics Processing Units (GPU) should be explored.